

ANDREAS KÄÄB

Remote Sensing of Mountain Glaciers and Permafrost Creep



Herausgeber:

Prof. Dr. Wilfried Haeberli, Prof. Dr. Max Maisch

Dieser Beitrag basiert auf einer Arbeit, die von der Mathematisch-naturwissenschaftlichen Fakultät der Universität Zürich im Sommersemester 2004 aufgrund der Gutachten von Prof. Dr. W. Haeberli (Universität Zürich), Prof. Dr. M. Bishop (Universität von Nebraska in Omaha), Prof. Dr. R. Dikau (Universität Bonn), und Dr. B. Bindschadler (NASA, Goddard Space Flight Center, Maryland) als Habilitation angenommen wurde.

Für den Inhalt des Textes und der Illustrationen ist der Autor/die Autorin allein verantwortlich.
Die Herausgeber.

ISBN 3 85543 244 9

© Geographisches Institut der Universität Zürich, 2005

Bezugsadresse:

Geographisches Institut der Universität Zürich
Winterthurerstrasse 190
CH-8057 Zürich
Fax: +41 (0)1 635 68 48
E-mail: maisch@geo.unizh.ch

Author contact:

Andreas Kääb
Department of Geosciences
University of Oslo
P.O. Box 1047 Blindern
N-0316 Oslo

kaeaeb@geo.uio.no
<http://folk.uio.no/kaeaeb>

Druck:

Stiftung Zentralstelle der Studentenschaft der Universität Zürich

Titelbild:

Section of the Bhutanese Himalayas taken from the Advanced Thermal Emission and Reflection Radiometer (ASTER) onboard the TERRA satellite. Image courtesy of EROS data center, NASA/GSFC/METI/ERSDAC/JAROS, and the US/Japan ASTER science team.

Summary

At present, monitoring of mountain glaciers and permafrost creep is being confronted with new challenges. High-mountain natural systems that involve surface and sub-surface ice change with rates which are with no historical precedences. Monitoring and decision strategies have to respond to this rapid evolution. New earth observation technologies in combination with geoinformatics have to be adapted or to be developed for glacier and rockglacier monitoring. Permafrost monitoring has to become an integrated part of the global terrestrial observation networks, like glacier monitoring is since many decades.

In this work, an overview is provided of, for the most part, optical air- and spaceborne remote sensing methods, which are suitable for the investigation of mountain glaciers and permafrost creep. The topics covered range from the generation of digital terrain models, to the detection and quantification of terrain changes, to multispectral analyses. It is shown, how geoinformatics and visualization can be used to exploit these data.

In a second main part of this volume, case studies are employed in order to exemplify and discuss the methods presented. On the basis of repeat satellite imagery, the flow of a number of glaciers in the Bhutan Himalaya is examined for the first time. A similar study revealed the surface velocity field of the fast-flowing Kronebreen in Svalbard, and Tasman Glacier, New Zealand. Furthermore, the surge-type movement of Belvedere Glacier, a glacier instability which is exceptional in the European Alps, is analyzed using repeated aerial photography.

A further chapter of case studies discusses and models spatio-temporal high-resolution data on rockglacier deformation in the Swiss Alps. For the first time, rockglacier advance and the evolution of micro-topography on creeping permafrost is investigated in great detail. The sensitivity of rockglacier creep to temperature changes is discussed. Techniques similar to those developed here for rockglaciers are applied to paraglacial rock mass movements also. In this way, it is possible to gain insight into the dynamics and internal structure of such slope instabilities.

Application schemes that combine and exemplify the techniques presented in this volume are compiled for the assessment of glacier- and permafrost-related hazards, and for glacier inventorying based on multispectral imagery.

Research perspectives rising from the methodology shown and from the test studies conducted conclude the individual sections, and the end of this work. Among these perspectives, the global availability of medium- to high-resolution digital terrain models plays a prominent role. The increasing temporal and spatial resolution of earth observation sensors bears a great potential for multidimensional examination and time series analyses of mountain glaciers and rockglaciers.

Acknowledgements

This work would not have been possible without the help of numerous people. I would like to sincerely thank them all.

Wilfried Haeberli enabled this volume with his continuous support and his thoughtful feedback. Frank Paul and Christian Huggel shared fruitful discussions with me and gave mindful comments on the manuscript. Robert Bindschadler, Michael Bishop and Richard Dikau reviewed an earlier version of this work.

My special thanks go to Regula Frauenfelder for her invaluable help during all the years in which the studies of this volume developed.

In addition, I gratefully acknowledge the support that I received in various ways from the following colleagues:

Kurt Brassel
Marta Chiarle
Luke Copland
Trond Eiken
Hans Elsasser
Luzia Fischer
Mirjam Friedli
Thomas Geist
Samuel Guex
Karen Hammes
Klaus Itten
Martin Hoelzle
Jeffrey Kargel
Tobias Kellenberger

Hugh Kieffer
Bernhard Lefauconnier
Kjetil Melvold
Philippe Meuret
Gianni Mortara
Ulrike Müller-Böker
Daniel Nüesch
Bruce Raup
Thekla Reichmuth
Andrés Rivera
Isabelle Roer
Nadine Salzmann
Stefan Schläfli
Kostia Schmutz

Demian Schneider
Oliver Stebler
Tazio Strozzi
Markus Vollmer
Bjørn Wangensteen
Monika Weber
Bruno Weber
Röbi Weibel
Yvo Weidmann
Rick Wessels
Othmar Wigger
Daniel Wirz

Many other colleagues and friends helped me to finish this work, and numerous students assisted with the fieldwork in all types of weather conditions.

Susan Braun-Clarke carefully corrected and improved the language of this volume.

The Swissstopo flight service provided valuable aerial photography, and the NASA/ASTER science team/US Geological Survey likewise provided important satellite data for this work. The studies were supported by the Swiss National Science Foundation under contracts no. 21-54073.98 and no. 21-59045.99 and by the Swiss Federal Office for Education and Science.

The work presented here is based, for the most part, on the author's own research, but also involves students' papers and diploma or doctoral theses under the author's supervision. For this reason, more references to these unpublished works are given as might be common for an international publication. Furthermore, some of the presented case studies were conducted in collaboration with other scientists and institutions. The respective references are given at the beginning of the individual sections in Part III.

Abbreviations

ASL	Above sea level
ASTER	Advanced thermal emission and reflection radiometer
BRDF	Bidirectional reflectance distribution function
BTS	Base (or basal, bottom) temperature of snow
CCD	Charge-coupled device
DEM	Digital elevation model
DHM	Digital height model
DInSAR	Differential interferometric synthetic aperture RADAR
DN	Digital number
DSM	Digital surface model
DTM	Digital terrain model
ETM+	Enhanced Thematic Mapper plus
FCC	False colour composite
GIFOV	Ground-projected instantaneous field of view
GLIMS	Global land ice measurements from space
GNSS	Global navigation satellite system
GPS	Global positioning system
IHS	Intensity-hue-saturation
INS	Inertial navigation system
InSAR	Interferometric synthetic aperture RADAR
IR	Infrared
IRS	Indian remote sensing satellite
LIA	Little ice age
LIDAR	Light detection and ranging
MIR	Middle infrared
MSS	Multi-spectral scanner
RADAR	Radio detection and ranging
RGB	Red-green-blue
RMS	Root mean square error
SAR	Synthetic aperture RADAR
SIRAL	SAR interferometric RADAR altimeter
SPOT	Systeme probatoire pour l'observation de la terre
SRTM	Shuttle RADAR topography mission
SWIR	Short-wave infrared
TIN	Triangular irregular network
TIR	Thermal infrared
TM	Thematic mapper
UTM	Universal transversal Mercator projection
UV	Ultraviolet
VIS	Visible
VNIR	Visible and near infrared
WGMS	World glacier monitoring service

Table of Contents

SUMMARY

ACKNOWLEDGEMENTS

ABBREVIATIONS

TABLE OF CONTENTS

I. INTRODUCTION

1. ABOUT THIS WORK 13

Introduction 13
Structure 14

II. THEORY AND METHODS

2. TERRAIN DIMENSIONS, DATA DOMAINS AND OTHER DEFINITIONS 21

2.1 Geometry, kinetics and dynamics 21
2.2 Kinematic boundary condition at the surface 21
2.3 Data domains, resolution, scale and time 22
 Data domains 22
 Resolution 24
 Time, scale and space-time concepts 24
2.4 Accuracy 25

3. TERRAIN GEOMETRY 27

3.1 Geometry data 27
3.2 Terrestrial methods 27
3.3 Airborne DTM acquisition 28
 3.3.1 Digital photogrammetry of frame imagery 29
 Principle 29
 Application 30
 Accuracy 31
 3.3.2 Digital photogrammetry of airborne pushbroom imagery 35
 Principle 35
 Application and accuracy 35
 3.3.3 Airborne laserscanning (LIDAR) 36
 Principle 36
 Application and accuracy 37
 3.3.4 Airborne interferometric synthetic aperture radar (InSAR) 38
 Principle 38
 Application and accuracy 41
 3.3.5 Analogue and analytical photogrammetry 41
3.4 Spaceborne DTM acquisition 41
 3.4.1 Satellite stereo imagery 42
 Principle 42
 Application 44
 Accuracy 44
 3.4.2 Spaceborne InSAR 48
 Principle 48
 Application and accuracy 50
 Shuttle Radar Topography Mission (SRTM) 50
 3.4.3 Other methods 53
3.5 DTM evaluation and refinement by orthoimage overlay 55
3.6 Digital terrain modelling 55
3.7 Conclusions and perspectives for DTM acquisition 58
 Terrestrial methods 58
 Airborne methods 58
 Spaceborne methods 60
 Sensor-specific problems for high-mountain applications 61
 DTM processing 62

4. CHANGES IN TERRAIN GEOMETRY 63

4.1 Displacements and elevation changes 63
4.2 Vertical DTM differences 63

4.2.1	Filtering 64
4.2.2	DTM matching 65
DTM shift from cross-correlation 65	
DTM shift from statistical adjustment 66	
Numerical correction of DTM differences 69	
4.3	Qualitative analysis of terrain movement 70
4.4	Digital image matching 70
Principles 70	
An alternative approach 72	
Application 73	
Accuracy 75	
4.5	Differential InSAR (DInSAR) 76
Principle 76	
Accuracy and application 79	
4.6	Other methods 79
Terrestrial methods 79	
Analogue and analytical photogrammetry 81	
DTM matching 81	
Others 82	
4.7	Conclusions and perspectives 82
Terrestrial methods 82	
Airborne methods 82	
Spaceborne methods 83	
5.	SPECTRAL CHARACTERISTICS OF TERRAIN 85
5.1	Spectral data 85
5.2	Spectral response 86
Snow 86	
Ice 88	
Rock 88	
Water 88	
Vegetation 88	
Thermal infrared (TIR) 89	
Microwave spectrum 89	
5.3	Classification approaches 91
Hard versus soft classification 91	
Manual, supervised and unsupervised classification 92	
Parametric versus non-parametric classification 92	
Spatial and spectral segmentation 93	
Subpixel classification 93	
Combinations and others 94	
5.4	Image processing for glacial and periglacial surfaces 94
5.4.1	Manual delineation 94
5.4.2	False colour composite (FCC) 94
5.4.3	Calculation of reflectance 94
5.4.4	Spectral transforms 97
Intensity-hue-saturation transformation (IHS) 97	
Principle component transformation (PCT) 97	
Decorrelation stretch 97	
5.4.5	Image algebra and segmentation 99
5.4.6	Unsupervised classification 99
5.4.7	Supervised classification 100
5.4.8	Artificial Neural Networks (ANN) 100
5.4.9	Others and combinations 100
5.5	Conclusions and perspectives 101
6.	MULTIDIMENSIONAL DATA ANALYSIS 103
6.1	Fusion of multiresolution data 103
6.2	Merging spectral and spatial domain data 105
6.3	Merging multitemporal data; change detection 106
Change detection 109	
6.4	Merging spatial, spectral and temporal domain data 111
6.5	GIS integration and numerical modelling 113
6.6	Other methods 114
6.7	Conclusions and perspectives 115

7. VISUALIZATION 117

- 7.1 Visualization domains 117
- 7.2 Cartographic resources 118
- 7.3 Visualization strategies 118
- 7.4 Conclusions and perspectives 120

III. CASE STUDIES AND APPLICATION SCENARIOS

8. GLACIER DYNAMICS 125

- 8.1 Glacier thickness changes from aerial and satellite imagery: Glaciar Chico, Chile, 1975–2001 125
 - Collaboration 125
 - 8.1.1 Introduction 125
 - 8.1.2 Ice thickness changes 126
 - 8.1.3 Conclusions 127
- 8.2 Flow field and speed changes from repeat satellite imagery: Tasman Glacier, New Zealand 130
 - Collaboration 130
 - 8.2.1 Introduction 130
 - 8.2.2 Flow field 130
 - 8.2.3 Variations in speed 132
 - 8.2.4 Conclusions 133
- 8.3 Glacier speed inventorying from repeat satellite imagery: Bhutan Himalaya 134
 - 8.3.1 Introduction 134
 - 8.3.2 Merged DTM from ASTER and SRTM data 134
 - 8.3.3 Flow field of a glacier tongue 135
 - 8.3.4 Glacier speed inventory 136
 - 8.3.5 Conclusions 136
- 8.4 Seasonal velocities on a fast glacier: Kronebreen, Svalbard 137
 - Collaboration 137
 - 8.4.1 Introduction 137
 - 8.4.2 Glacier flow 138
 - 8.4.3 Conclusions 140
- 8.5 Velocity field during the surge-type movement of Ghiacciaio del Belvedere, Italian Alps 141
 - Collaboration 141
 - 8.5.1 Background 141
 - 8.5.2 Elevation changes 142
 - 8.5.3 Ice velocities 144
 - 8.5.4 Conclusions 145

9. ROCKGLACIER DYNAMICS 147

- 9.1 Surface velocity fields of rockglaciers 147
 - 9.1.1 Introduction 147
 - 9.1.2 Gruben rockglacier 147
 - 9.1.3 Suvretta rockglacier 148
 - 9.1.4 Muragl rockglacier 150
 - 9.1.5 Gufer rockglacier 151
 - 9.1.6 Murtèl rockglacier 152
 - 9.1.7 Becs-de-Bosson rockglacier, Val de Réchy 152
 - 9.1.8 Rockglacier speed and slope 153
 - 9.1.9 Discussion and conclusions 158
- 9.2 Rockglacier advance mechanisms: Suvretta and Gruben rockglaciers, Switzerland 159
 - Collaboration 159
 - 9.2.1 Introduction 159
 - 9.2.2 Method 161
 - 9.2.3 Gruben rockglacier front 162
 - 9.2.4 Suvretta rockglacier front 166
 - 9.2.5 Conclusions 168
- 9.3 Observed and modelled seasonal variations of rockglacier speed: Muragl rockglacier, Switzerland 170
 - 9.3.1 Introduction 170
 - 9.3.2 Seasonal velocity variations on Muragl rockglacier 171
 - 9.3.3 Numerical model scheme 172

9.3.4	Temperature variations of one-year cycle	174
9.3.5	Temperature variations of a five-year cycle	175
9.3.6	Conclusions	175
9.4	Deformation of rockglacier surface topography	176
	Collaboration	176
9.4.1	Introduction	176
9.4.2	Transverse ridges on Murtèl rockglacier	177
9.4.3	Transverse ridges on Muragl rockglacier	178
9.4.4	A high-precision profile on Muragl rockglacier	179
9.4.5	A high-precision profile on Suvretta rockglacier	182
9.4.6	Longitudinal ridges on Gruben rockglacier	183
9.4.7	Laboratory experiments	183
9.4.8	Conclusions and perspectives	185
	Rockglacier micro-topography	185
	Perspectives	186
9.5	Permafrost creep within a recently deglaciated glacier forefield: Muragl, Swiss Alps	186
9.5.1	Introduction	186
9.5.2	Study site	187
9.5.3	Surface velocity field	187
9.5.4	Conclusions	187

10. DYNAMICS OF PARAGLACIAL SLOPE DEFORMATION 191

10.1	Kinematics of rock mass creeps at Aletsch and Findelen Glacier, Switzerland	191
	Collaboration	191
10.1.1	Introduction	191
10.1.2	A rock mass creep at Aletsch Glacier	192
10.1.3	A rock mass creep at Findelen glacier	195
10.1.4	Conclusions and perspectives	197

11. SATELLITE-DERIVED GLACIER INVENTORYING 199

	Collaboration	199
11.1	Scheme	199

12. GLACIER- AND PERMAFROST-RELATED HAZARDS 203

	Collaboration	203
12.1	Introduction	203
12.2	Method overview	204
12.2.1	Important factors	204
12.2.2	Airborne remote sensing	205
12.2.3	Spaceborne remote sensing	205
12.2.4	Image classification	206
12.2.5	Digital terrain models	208
	Satellite stereo	208
	Radar interferometry; Shuttle Radar Topography Mission	209
	Aerial photogrammetry	209
	Laserscanning (airborne LIDAR)	209
12.2.6	Terrain elevation changes (DTM differences)	209
12.2.7	Surface displacements	210
12.3	Detection of hazard sources	213
12.4	Modelling of hazard potentials	214
12.5	Disaster management	218
12.6	Conclusions and perspectives	218

IV. CONCLUSIONS

13. GENERAL CONCLUSIONS AND PERSPECTIVES 229

V. REFERENCES

REFERENCES 235

I. INTRODUCTION

Introduction

Surface and subsurface ice occurrences are among the most important features of high-mountain environments:

- Glaciers and permafrost react in a highly sensitive manner to climate changes due to their proximity to melting conditions, and are thus the most important terrestrial indicators of changes in climate conditions (IPCC, 2001a; IPCC, 2001b).
- Glaciers and creeping permafrost are efficient long-term erosion and mass-transport systems which contribute significantly to the evolution of mountain landscapes (Haeberli, 1996; Maisch et al., 1999a; Shroder Jr. and Bishop, 2004; Zemp et al., 2005).
- Land ice influences the water cycle in high mountains and is a crucial factor affecting water supply in some regions. Mountains cover about 25 % of the Earth's continental area but provide roughly 40 % of its fresh water supply (Kaser et al., 2003; UNESCO, 2003; Viviroli and Weingartner, 2003).
- Glacierized mountains attract tourism and can be an important source of income for remote regions.
- Glacier- and permafrost-related hazards endanger human lives, settlements and infrastructures (e.g. Grove, 1987; Haeberli et al., 1997; Richardson and Reynolds, 2000b; Haeberli and Burn, 2003; Huggel, 2004; Kääb et al., 2005c) (see also Chapter 12).

At present, global climate- and hazard-related glacier and permafrost monitoring is being confronted with new challenges (Haeberli, 1998; Haeberli and Beniston, 1998) (cf. Section 12.1):

- Monitoring and decision strategies have to be adapted to rapid environmental changes, which have no historical precedences.
- New earth observation technologies in combination with geoinformatics have to be developed and/or adapted for glacier and permafrost monitoring, and then made operational in order to ensure a sustainable, global long-term monitoring perspective (Williams and Hall, 1998).
- Permafrost monitoring has to become an integrated part of global terrestrial observation networks (GTN-P) (Harris and Haeberli, 2003). Respective methods and strategies must be developed.

Within the framework of the global climate-related observation systems (GTOS/GCOS), a global hierarchical observing strategy of tiers was developed for monitoring terrestrial variables (GHOST, WMO, 1997). According to this system of tiers, the changes in the included variables and their spatio-temporal

representativeness from regional to global scales are meant to be assessed (Haeberli et al., 2002b). The five tiers of GHOST can be viewed as spatio-temporal levels for systematically investigating and monitoring mountain glaciers and permafrost, that is:

- Integrated studies to examine the spatial structure and processes based on large area experiments (tier 1);
- Process understanding and method development; fundamental research at specific sites (tier 2);
- Detecting regional signals through frequent long-term measurements of variables for trend detection; calibration and validation of remotely-sensed variables (tier 3);
- Assessing representativity by infrequent direct measurements of variables; large sample (tier 4);
- Spatial and temporal interpolation, and determination of extent variables by means of remote sensing; frequent, complete (global) coverage (tier 5);

Recent and ongoing developments in earth observation techniques and related geoinformatics constitute significant advances in the investigation of glaciers and permafrost. The present work aims at evaluating the potential of these technologies and at exploring their future perspectives for the understanding and monitoring of glaciers and permafrost creep in high mountains.

For this purpose *high mountains* is defined as the mountain zone above timberline. The main focus, in terms of the observation methods applied, is on panchromatic and multi-spectral optical remote sensing. As *remote sensing* we define all methods for non-contact object measurements and their analysis. In the literature, remote sensing is sometimes more restricted to the measurement and analysis of spectral signals, whereas *photogrammetry* refers then to the (quantitative) spatial or geometric analysis of images. In that sense, the methodological focus of this volume could also be termed *photogrammetry and remote sensing* (cf. definition by the International Society of Photogrammetry and Remote Sensing). Sometimes, remote sensing refers only to the measurement, whilst the data analysis falls then in the disciplines of image processing, computer vision, etc.

The work presented in this volume can be seen under the umbrella of geographic information science (*GIScience*), an interface science between (i) source disciplines such as remote sensing or geodesy, (ii) end-user disciplines from e.g. environmental and earth sciences, and (iii) disciplines with either roles such as cartography or geomorphology (Bishop and Shroder Jr., 2004).

Structure

This work is divided into five parts: (I) this introduction, (II) theory and methods, (III) case studies and application schemes, (IV) conclusions and perspectives, and (V) references. Part II gives an introduction of the terrain and data dimensions, presents methods for measuring terrain geometry and displacement, and provides an overview of the spectral characteristics of typical high-mountain surfaces with the corresponding analyses. Techniques for multidimensional merging of such data are discussed, as are further data analysis and visualization methods. Part II of the work is intended to give a general overview and an application-oriented introduction of Part III. As a first overview Figure 1-1 summarizes a list of remote sensing (and geodesy) methods, which can be applied to high mountains.

Part III of the work evaluates methods outlined in Part II based on case studies and application schemes for:

-
- measuring and analyzing glacier flow fields by means of air- and spaceborne sensors,
 - air- and spaceborne monitoring of ice thickness changes,
 - rockglacier geometry and surface deformation,
 - spatio-temporal variations of deformation, development of micro-topography and advance mechanisms of rockglaciers,
 - dynamics of rock slope deformation caused by glacier retreat,
 - mapping and monitoring of glacier extent from space, and
 - remote assessment of glacier- and permafrost-related hazards.

An important focus of the individual chapters in Parts II, III and IV is the discussion of perspectives for the future use of remote sensing and of geoinformatics in the field of glacier and permafrost creep research.

Figures 1-2 and 1-3 show the locations of study sites referred to in this work.

Platform:	Space			Air			Ground			
	Sensor:	SAR	Altimeter	Optical	SAR	LIDAR	Optical	Laser-scanning	SAR	GNSS; Polar survey
G/FOV:	100-1 m	100-10 m	1000-10 m	1-0.01 m	1-0.1 m	0.1 m	1-0.01 m	0.1-0.01m	1-0.1 m	cm-mm
	Stereo parallaxes, (photoclinometry)	Interferometry	(RADAR, LIDAR, interferometry)	Stereo parallaxes	Interferometry	Laser-scanning, -profiling	Stereo parallaxes	3D point cloud	-	Leveling cm-mm
	Repeat DTM	Repeat DTM	Repeat meas.	Repeat DTM	Repeat DTM	Repeat DTM	Repeat DTM	Repeat DTM	-	Elevation only
	Thickness change	Image matching, (image algebra)	Differential InSAR	-	Image matching, (image algebra, DTM matching)	(Differential InSAR)	DTM matching	Image matching, (image algebra, DTM matching)	Diff. InSAR	Repeat positioning of marked point
	Horizontal surface displacements	Vertical surface displacements	-	Differential InSAR	Image matching in multitemp. stereo models	(Differential InSAR)	(DTM matching)	Image matching in multitemp. stereo models	Diff. InSAR	Repeat positioning of marked point
	Class boundaries	Multispectral segmentation	(Backscatter, polarimetry, multifrequency)	-	(Multi-) spectral segmentation	(Backscatter, polarimetry, multifrequency)	Intensity segmentation	(Multi-) spectral segmentation	-	-
	Surface characteristic	Multi-, hyperspectral analysis, thermal IR	Backscatter, polarimetry, multifrequency	-	Multi-, hyperspectral analysis, thermal IR	(Backscatter, polarimetry, multifrequency)	Intensity (multi-frequency)	Intensity	-	-

Fig. 1-1 Overview of (for the most part) remote sensing methods for obtaining different data types for high-mountain environments, in dependence of the sensor type.

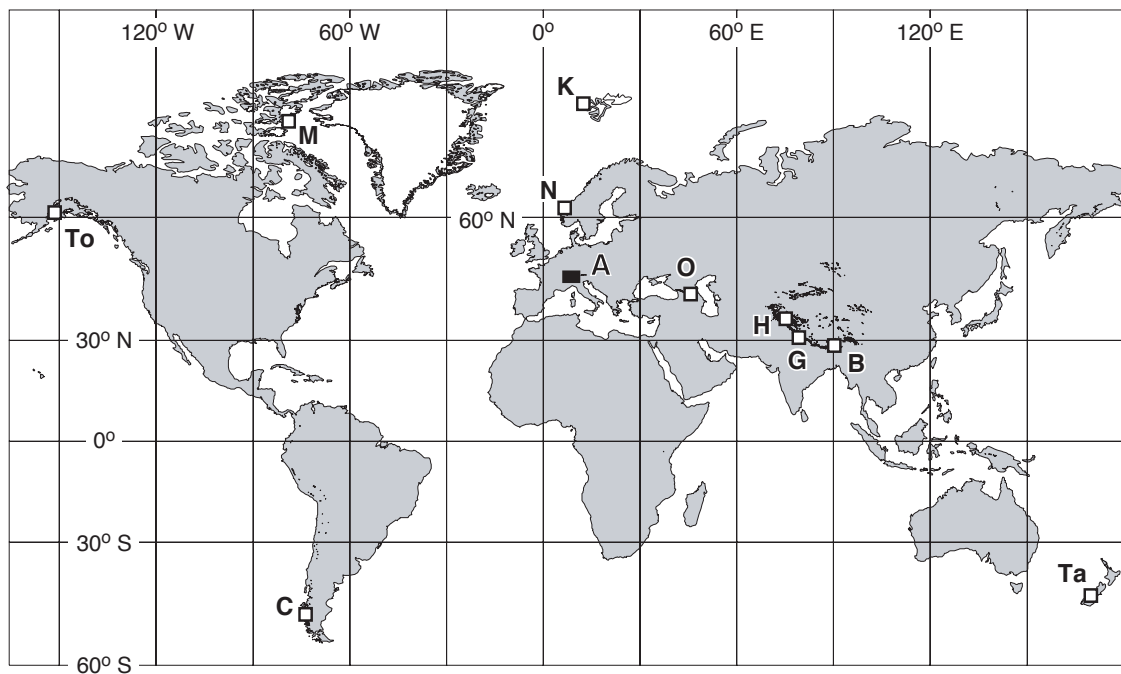


Fig. 1-2 Location of study sites and sample locations in this work:

- A (black inset): Swiss Alps, see Figure 1-3
- B: Bhutan, Himalaya main ridge
- C: Glaciar Chico, Southern Patagonia Icefield
- H: Hispar Glacier, Karakorum, K2 area
- G: Garwhal Himal
- K: Kronebreen, Svalbard
- M: Mittie Glacier, Manson ice cap, Ellesmere Island
- N: Nirgardsbreen, Southern Norway
- O: Karmadon, Caucasus, North Ossetia
- Ta: Tasman Glacier, Mount Cook area
- To: Tordrillo Mountains

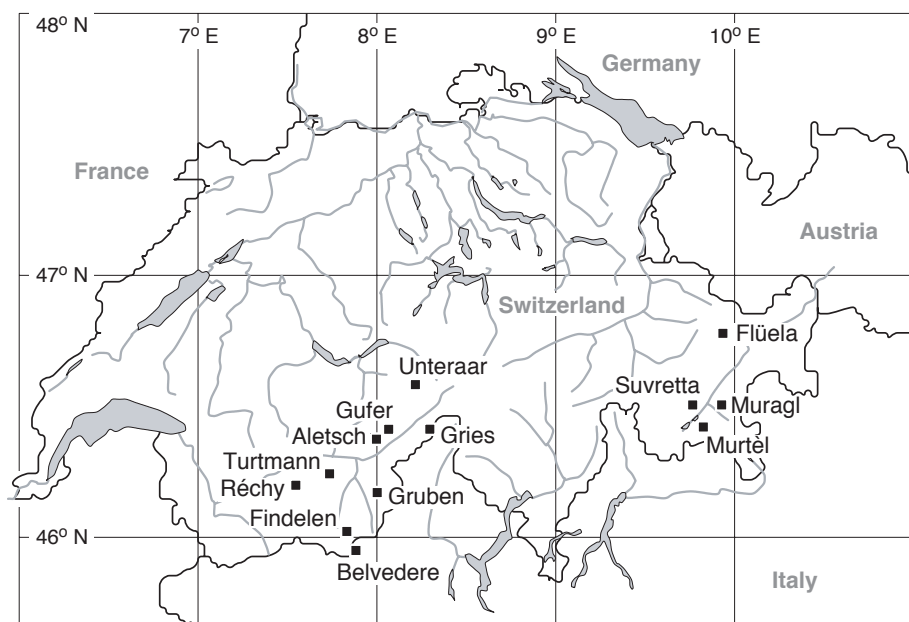


Fig. 1-3 Location of study sites in the Swiss Alps.

II. THEORY AND METHODS

2.1 Geometry, kinetics and dynamics

In this work *geometry* is defined as the spatial extent of an object. Such an object may be a point, a line, a surface or an entire body. *Kinetics* is defined here as the change in geometry with time, e.g. the velocity or velocity field of an object. *Dynamics* involve not only the spatial extent of an object and its changes with time, i.e. kinetics, but also the acting forces. Forces that give rise to, e.g., glacier and permafrost dynamics cannot be directly measured by remote sensing techniques but may be inferred by modelling such data. The measurement or quantitative analysis of kinetics is often called *kinematics*. Kinetics involve both individual velocities and the entire velocity field including gradients of such a field. The first derivative of the velocity field is called *deformation*, described by strain rates.

A different use of the terms 'static' and 'dynamic' was established by visualization science. *Static visualization* is a time-constant representation; *dynamic visualization* is any kind of time-variable representation, also called *animation*.

2.2 Kinematic boundary condition at the surface

Surface kinematics can be understood and analyzed by using the *kinematic boundary condition at the surface*. This relation is especially well suited for analyzing remote sensing data on object geometry and kinetics (Rasmussen, 1988; Kääb, 1996b; Kääb et al., 1998; Gudmundsson and Bauder, 1999; Kääb and Funk, 1999; Reeh et al., 1999; Hubbart et al., 2000; Kääb, 2001). Based on mass continuity, it describes the geometric relation between all components influencing surface kinetics. For the three-dimensional case, the kinematic boundary condition at any surface point is

$$b = \frac{\partial z^s}{\partial t} + v_x^s \frac{\partial z^s}{\partial x} + v_y^s \frac{\partial z^s}{\partial y} - v_z^s \quad (2-1)$$

where b is mass balance at the surface, z^s is surface elevation, $\partial z^s/\partial t$ is change in surface elevation with time, v_x^s and v_y^s are horizontal surface velocity components of a three-dimensional velocity vector $\mathbf{v} = (v_x, v_y, v_z)^T$, $\partial z^s/\partial x$ and $\partial z^s/\partial y$ are surface slope components, and v_z^s denotes vertical velocity at the surface.

The vertical velocity at the surface is

$$v_z^s = \int_{z^b}^{z^s} \frac{\partial v_z}{\partial z} dz + v_z^b, \quad (2-2)$$

where v_z^b denotes vertical velocity at the basal layer with elevation z^b where $|\mathbf{v}|=0$ for $z < z^b$.

With the vertical strain rate $\dot{\varepsilon}_{zz} = \partial v_z / \partial z$, Equation 2-1 can be written as

$$v_z^s = v_x^b \frac{\partial z^b}{\partial x} + v_y^b \frac{\partial z^b}{\partial y} + \int_{z^b}^{z^s} \dot{\varepsilon}_{zz} dz . \quad (2-3)$$

Assuming an incompressible medium, i.e.

$$\dot{\varepsilon}_{xx} + \dot{\varepsilon}_{yy} + \dot{\varepsilon}_{zz} = 0 , \quad (2-4)$$

the vertical velocity at surface v_z^s can, finally, be written as

$$v_z^s = v_x^b \frac{\partial z^b}{\partial x} + v_y^b \frac{\partial z^b}{\partial y} - \int_{z^b}^{z^s} \dot{\varepsilon}_{xx} dz - \int_{z^b}^{z^s} \dot{\varepsilon}_{yy} dz . \quad (2-5)$$

All terms in Equation 2-1 relate to the surface only. Therefore, mass balance b represents the sum of all thawing and freezing processes of ice as well as other mass changes such as erosion or accumulation, as long as they result in a corresponding change in surface elevation. The kinematic boundary condition at the surface does not include internal mass variations that have no influence on surface elevation or flow. Furthermore, media such as structured permafrost or creeping rock masses are – in contrast to massive ice or supersaturated permafrost – not incompressible and, therefore, Equations 2-4 and 2-5 may not be strictly valid. In such cases, the variation of mass density has to be included in Equation 2-1 (see Chapter 10). All terms on the right-hand side of Equation 2-1, except the vertical velocity at surface v_z^s , can be determined by means of surveying, photogrammetry or other remote sensing techniques. Thus, the relation can be used to quantify and understand the potential components of surface kinetics: mass loss or accumulation, mass advection, and three-dimensional straining (Fig. 2-1).

2.3 Data domains, resolution, scale and time

Data domains

In this study, three types of *data domains* are considered (Fig. 2-2):

- the spatial domain,
- the temporal domain, and
- the spectral domain.

The number of *spatial data dimensions* might be 1 (line), 2 (plain), 2.5 (surface) or 3 (i.e. the entire Cartesian space). (The spatial dimension of a surface, 2.5-dimensional, is not strictly a mathematical term). The considered data might cover one, two or multiple points in time (*temporal data dimension*). Representation of an object by remote sensing data might be monospectral (one band, e.g. panchromatic), multispectral (a few broad spectral bands) or hyperspectral (many narrow bands). The number of bands at which a spectral signal is sampled constitute the *spectral data dimension*. The spectral dimension of microwave data is usually one, but may be higher for multifrequency systems or if polarization is considered as well. (Definitions for

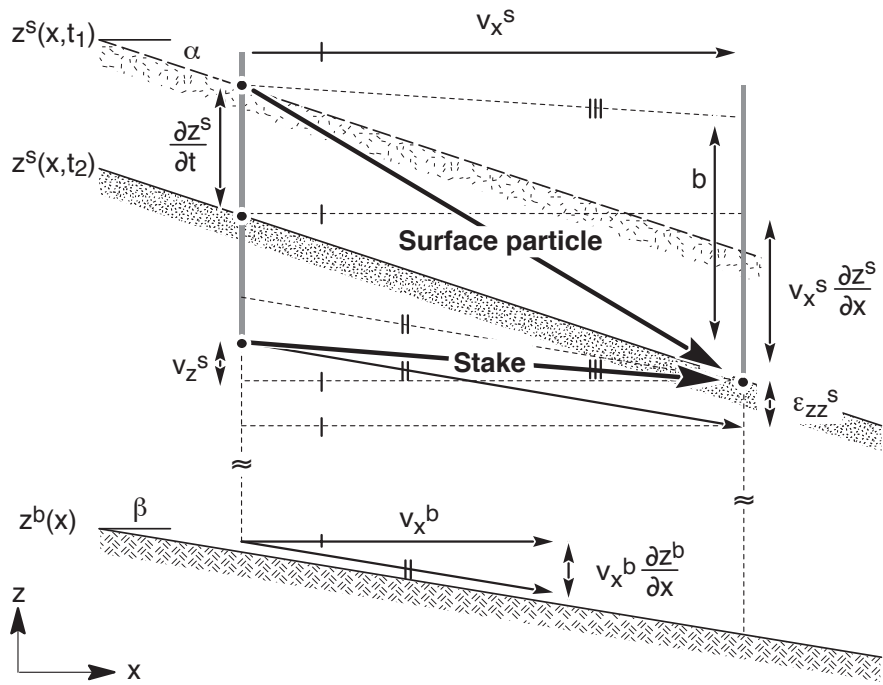


Fig. 2-1 Terms of the kinematic boundary condition at surface, and their relation to terrain changes and their measurement, exemplified for a glacier surface.

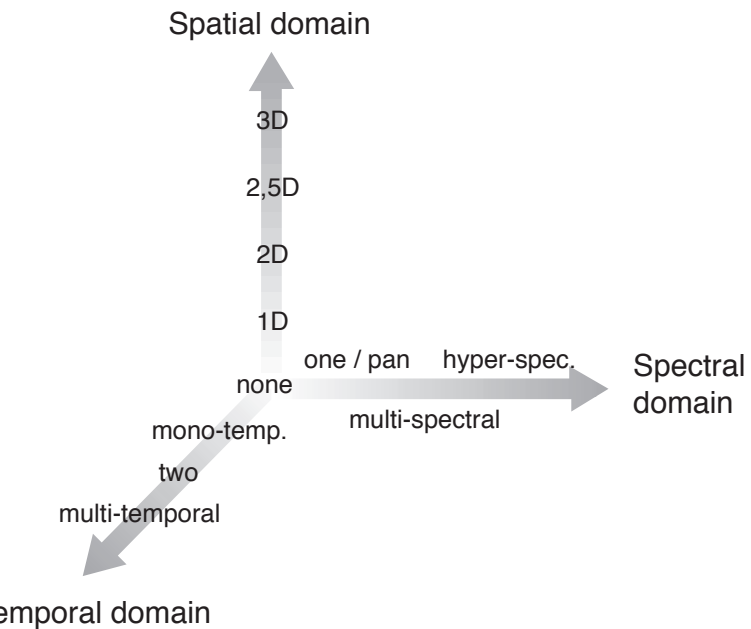


Fig. 2-2 Data domains and their dimensions considered in this work.

spatial, temporal and spectral domains, dimensions and resolution are not unambiguous in the literature, e.g. Schowengerdt, 1997).

Most data sets cover more than one data domain. A multispectral satellite image, for instance, represents the value 'multi' for the number of spectral dimensions, and the value '2' for the spatial dimension. A digital terrain model (DTM; for definition see Section 3.1) may be merged from different multitemporal data sources. The velocity field of a glacier derived from repeat remote sensing data has the temporal dimension

'2' (or more), and the spatial dimension ranges from '1' to '3', depending on the number of velocity components considered.

Since investigating glaciers and creeping permafrost can involve all three data domains, it becomes clear that integrative analysis of a range of data domains and dimensions has a broad potential for defining and clarifying the processes involved (Walsh et al., 1998). This concept, and the corresponding techniques applied, are termed in this volume *multidomain* or *multidimensional data analysis*. In this sense, 'analysis' refers to the widest form of data investigation. *Data fusion* is defined as data combination before further analysis and *data merging* as data combination within the analysis procedure.

Resolution

According to the three data domains above, ground objects are represented with different types of resolutions: the *spatial resolution* is the size of the smallest object, which can be detected from the data set. Depending on the application or data type, the spatial resolution might be somehow approximated as (i.e. it is not equal to) the spatial density of samples, or, for imaging sensors, the ground area covered by one image pixel (ground-projected instantaneous field of view, GIFOV). The *temporal resolution* describes the interval between two consecutive data captures. The *spectral resolution* is the sensor's ability to resolve details in the spectral signal. It depends, among other things, on the location of bands, their spacing interval, and the *bandwidths*. The *radiometric resolution* indicates the number of binary digits at which an original spectral signal is quantized (i.e. bits per pixel). (Entire paragraph: Schowengerdt, 1997; cf. Joseph, 2000).

The minimum pixel size (GIFOV) for the remote sensing data considered here is about 80 m (Landsat MSS: 59 m × 79 m, Landsat TM or ETM+ multispectral bands: 30 m × 30 m). Data sets of coarser resolution are doubtless of great use for a number of regional-scale tasks, but not primarily designed for monitoring the dynamics of mountain glaciers and permafrost creep. In order to characterise spatial resolution, we use here the terms *high resolution* (< 5 m pixel dimension) and *medium resolution* (5–100 m pixel dimension). *Low* (100–1000 m) and *very-low resolution* systems (> 1000 m) are not covered in this contribution.

The temporal resolution of the data treated here ranges from several decades to several weeks or days. The bandwidths, i.e. the width of individual spectral channels applied in this work cover values typical for multispectral sensors (e.g. ASTER visible and short-wave infrared: 40 nm – 100 nm; ASTER thermal infrared: 350 nm – 700 nm; Landsat ETM+ visible and short-wave infrared: 60 nm – 260 nm; Landsat ETM+ thermal infrared: 2100 nm).

See also Section 12.2.1.

Time, scale and space-time concepts

The studies in this work cover different *spatial scales*, ranging from objects of a few metres in size to entire mountain ranges. These scales can be termed *micro-scale* (e.g. individual boulders or rockglacier ridges), *topo-scale* (e.g. a glacier, a rockglacier, or a mountain), and *meso-scale* (e.g. a mountain range) (see Walsh et al., 1998; Wilson and Gallant, 2000; Rasemann et al., 2004). Other scales are the nano-scale and the global-scale. According to the scale considered, the observation techniques and modelling approaches applied extend from detailed high-precision and high-resolution studies to small-scale studies. The terms *small-scale* or *large-scale* are used here in the

mathematical or cartographic sense, i.e. referring to the scale as the ratio between a distance in any representation and its length in an external system (see Equation 3-2).

In a landscape, spatial scale and time are interrelated through the development of landforms over time (*spatio-temporal scale*). Phenomena and processes (not only in high mountains) exist in a dynamic space-time continuum (Bishop and Shroder Jr., 2004). Space, time, spatio-temporal dependencies, and space-time representation in fact underlie all topics of earth and environmental sciences, significantly also cryospheric sciences dealt with in this volume. The concept of *absolute space* views the space as infinite and isotropic. In this concept, time is a static spatial representation at a point in (absolute) time, or a sequence of such representations (*absolute space-time*). However, in a number of earth science disciplines, space-time is – and has to be – treated in relation to events (representing markers) or development stages (*relative space-time*) (Bishop and Shroder Jr., 2004). Through the concept of relative space-time it becomes clear that also scale should be viewed in geosciences as relative and time-dependent, linked to the spatio-temporal development of forms and processes.

2.4 Accuracy

Accuracy is defined as the error for data as related to an external system, e.g. ground coordinates. The internal error of an instrument or algorithm is termed *precision*.

The *standard deviation* s (or mean error of an individual observation) of n members of a Normal population x_1, x_2, \dots, x_n is

$$s = \sqrt{\frac{1}{n-1} \sum_i^n (x_i - \bar{x})^2} . \quad (2-6)$$

The *standard error* $s_{\bar{x}}$ of an unknown population mean is

$$s_{\bar{x}} = \frac{s}{\sqrt{n}} = \sqrt{\frac{1}{n(n-1)} \sum_i^n (x_i - \bar{x})^2} . \quad (2-7)$$

The *root mean square error* (RMS) is

$$RMS = \sqrt{\frac{1}{n} \sum_i^n (x_i - a_i)^2} \quad (2-8)$$

where a is an accepted value. For instance, x_i might be the elevation of a point i of a digital elevation model to be tested, and a_i the corresponding elevation of a reference model. In dependence on the population mean \bar{x} , Equation 2-8 can be written as (Deakin and Kildea, 1999):

$$RMS = \sqrt{\left(\frac{1}{n} \sum_i^n (x_i - \bar{x})^2 \right) + (\bar{x} - a)^2} . \quad (2-9)$$

For a Normal population the probability of an estimate lying within a confidence interval can be computed (e.g. about 68% for $\pm 1 s_{\bar{x}}$, 90% for $\pm 1.64 s_{\bar{x}}$, or 95% for $\pm 1.96 s_{\bar{x}}$). For topographic measurements, the error is sometimes given with respect to such a confidence interval: vertical error is given as linear error (LE), horizontal error as circular error (CE). (E.g. for vertical deviations: linear error at 90% confidence level, LE90, which is equal to $\pm 1.64 s_{\bar{x}}$ for a Normal distribution).

3.1

Geometry data

This chapter focuses on the acquisition of elevation information as the basic parameter of 'terrain'. Automatic methods for delineation of planimetric data are treated in Chapter 5. *Digital height models* (DHM) or *digital elevation models* (DEM) describe the three-dimensional position of surface points, but also sub-surface objects. Most air- and spaceborne remote sensing sensors receive radiation reflected or emitted from the boundary between earth surface and atmosphere, i.e. including, for instance, buildings and vegetation. Related elevation values refer, thus, to a *digital surface model* (DSM). The reduction of such model to the terrain surface is called *digital terrain model* (DTM). Since glacial and periglacial terrain is in general not covered by, for instance, buildings or high vegetation, remote sensing techniques often produce DTMs directly. Whether the term 'terrain' should refer to the glacier surface or the glacier bed depends on the application. A DTM contains both the original data points and rules for the surface geometry between them, leading to a continuous description of the surface geometry. There exists no uniform nomenclature for the terms DEM, DHM, DTM, etc., across the various disciplines. The here-used definitions follow for the most part the accepted usage in photogrammetry.

Information on the terrain geometry is available in the form of points, lines or continuous surfaces. These data structures relate to – and may vary with – the *sensor characteristics*, the *data model*, and the *data representation*. The sensor might record a continuous surface geometry down to the sensor's spatial resolution. Further analysis steps might then reduce the surface description to selected surface points or lines (e.g. raster, triangular irregular network (TIN), or breaklines). A later representation might, then, once again interpolate a continuous surface from the latter discrete points and lines (e.g. contour lines or hillshades). DEMs are usually characterized by their spatial resolution (point density), point distribution e.g. in relation to the topographic forms (e.g. raster, TIN, breaklines), and horizontal and vertical accuracy.

3.2

Terrestrial methods

Modern ground-based methods for measuring terrain geometry include:

- combined distance and angle measurements (polar survey, triangulation),
- terrestrial laserscanning,
- satellite-based surveying (global navigation satellite system, GNSS, e.g. global positioning system, GPS),
- terrestrial photogrammetry, and
- optical levelling.

Terrestrial surveying with theodolites and laser rangers (polar survey based on totalstations) provides the geometry of selected points with an accuracy of a few centimetres or better for close range applications and net settings with redundancy (e.g. Zick, 1996; Koning and Smith, 1999; Konrad et al., 1999; Gudmundsson et al., 2000; Krainer and Mostler, 2000) (see also Sections 9.2, 9.3 and 9.4). This method requires direct access to the measuring points with a reflector, except for forward intersection or application of reflector-less laser rangers.

For close-range applications, *terrestrial laserscanning* is able to provide DSMs with a spatial resolution of some millimetres to centimetres without requiring direct access to the object under investigation (Paar et al., 2001; Bauer et al., 2003; Janeras et al., 2004).

Differential satellite-based surveying (GNSS; e.g. GPS, GLONASS, and the planned GALILEO) is suitable for point-by-point measurements similar to polar survey, reaching an accuracy of several millimetres to a few centimetres even over longer distances (e.g. Eiken et al., 1997; Berthling et al., 1998; Frezzotti et al., 1998; Hagen et al., 1999; Gao and Liu, 2001; Lambiel and Delaloye, 2004).

Terrestrial photogrammetry, in principle working similar to airborne photogrammetry (Sections 3.3.1 and 3.3.2), is a very flexible quantitative remote sensing technique and offers a number of potential applications to high mountains, in particular where the terrain is not accessible to aircrafts or their employment is too expensive (Fig. 6-7; Section 4.6) (e.g. Rentsch et al., 1990; Brecher and Thompson, 1993; Kaufmann and Ladstädtter, 2004; Pitkänen and Kajutti, 2004). Direct visibility and access, topographic situation, and weather conditions are important factors determining the applicability of either method.

Optical levelling can be used for high-precision DEMs where millimetre-accuracy is required (Kääb and Weber, 2004) (see Section 9.4).

3.3 Airborne DTM acquisition

Methods for airborne DTM acquisition include:

- analogue and analytical photogrammetry based on hardcopy photography (Section 3.3.5),
- digital photogrammetry based on digital cameras or digitized photography (frame imagery) (Section 3.3.1),
- digital photogrammetry based on other digital sensors (e.g. linear arrays) (Section 3.3.2),
- laser profiling and scanning (Section 3.3.3), and
- interferometric synthetic aperture radar (Section 3.3.4).

In principle, the airborne methods discussed in this chapter work in most cases for different platform types such as surveying aeroplanes, small amateur aeroplanes, helicopters, or model aeroplanes and helicopters. For very mobile and unstable platforms special acquisition and processing techniques might be required, which are not discussed in this volume. In particular in terms of cost efficiency, for objects with difficult access by larger aeroplanes, and/or where airborne close-range techniques are required, such methods might, however, be suitable for high mountain applications.

In the case studies of Part III, digital photogrammetric methods based on digitized aerial frame photography and digital satellite imagery are applied in most cases.

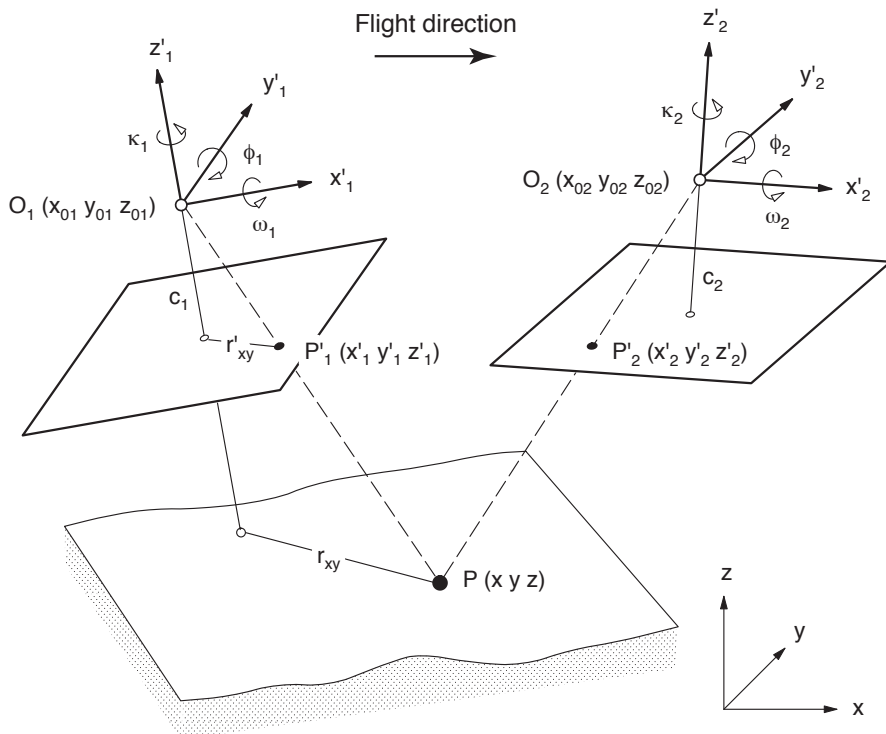


Fig. 3-1 Principle of photogrammetric DTM generation: points in space are determined by the intersection of oriented rays from overlapping photography.

3.3.1 Digital photogrammetry of frame imagery

Principle

DTMs can be automatically derived from overlapping digital images. Frame images represent central projections of the terrain (Fig. 3-1):

$$\mathbf{x} - \mathbf{x}_o = \lambda \mathbf{R} (\mathbf{x}' - \mathbf{x}'_o) \quad (3-1)$$

where

$\mathbf{x} = (x, y, z)^T$ are coordinates of a terrain point in ground coordinates,

$\mathbf{x}_o = (x_o, y_o, z_o)^T$ are the ground coordinates of the projection centre,

$\lambda = \frac{(z - z_o)}{(-z'_o)}$ is the image-to-ground scale,

$\mathbf{R} = f(\omega, \phi, \kappa)$ is a 3×3 rotation matrix depending of the orientation angles ω, ϕ and κ ,

$\mathbf{x}' = (x', y', z')^T$ are image coordinates of an image point,

$\mathbf{x}'_o = (x'_o, y'_o, z'_o)^T$ are the image coordinates of the projection centre, and

$-z'_o = c$ is the calibrated focal length of the camera.

Equation 3-1 represents a three-dimensional vector through the projection centre, the direction of which is given by three orientation angles. A terrain point is determined by the *intersection in space* of two or more vectors originating from different images (Fig. 3-1).

The orientation parameters can be computed from a set of ground control points (GCP) by solving Equation 3-1 or are directly inferred from on-board differential satellite navigation (usually GPS) and inertial navigation systems (INS).

Image scale M is defined as

$$M = \frac{1}{\lambda} = \frac{c}{(z_0 - z)} = \frac{r'_{xy}}{r_{xy}}, \quad (3-2)$$

where

- r_{xy} is the horizontal (radial) distance of a terrain point from the sensor nadir,
- λ is the scale number,
- r'_{xy} is the radial distance between the image centre and the projection of a terrain point into the image,
- $(z_0 - z)$ is sensor height above ground, and
- c is the sensor focal length.

Equation 3-1 is often applied to orthoprojection by solving for x and y of individual image points. This approach requires a DTM for introducing z into the otherwise under-determined equation system. As a basic feature of orthoimage generation, vertical errors in terrain elevation are transformed into horizontal deviations in pixel location:

$$\frac{\partial r_{xy}}{\partial z} = \frac{r_{xy}}{(z_0 - z)} = \frac{r'_{xy}}{c}. \quad (3-3)$$

Equation 3-3 represents a simplification assuming exact nadir imagery (cf. Fig. 3-28). The effect of Equation 3-3 implies that errors increase towards the image margins. For photogrammetric wide-angle cameras (focal length 0.15 m) with 23 × 23 cm image size, for instance, the ratio between a vertical DTM error ∂z and the corresponding horizontal deviation ∂r_{xy} in the orthoimage amounts nearly 1:1 for the outermost image corners.

Application

Automatic DTMs from frame imagery can be computed from digitized analogue photographs or directly from digital imagery. Digital photogrammetric cameras can consist of one charge-coupled device (CCD) array combined with one lens system (e.g. the Emerge/Applanix Digital Sensor System) or can be composed of several CCD array cameras (e.g. the ZI Imaging Digital Mapping Camera System). Respective image resolutions range currently from about 4,000 × 4,000 to 14,000 × 8,000 pixels. For the latter ZI Imaging Digital Mapping Camera, for example, this resolution corresponds to about 0.1 m GIFOV per 1,000 m above ground. (For comparison: digitizing an 23 × 23 cm analogue aerial photo at 30 µm corresponds to an image dimension of approximately 8,000 × 8,000 pixels).

For the studies in this work digitized airphotos and the Socet Set commercial photogrammetric software is used (formerly Leica-Helava Systems, San Diego, California, USA, currently BAE Systems, UK). Multiple image sets were oriented and adjusted as one image segment as a special measure to improve the relative accuracy between multitemporal imagery and the corresponding products (in general cf. Toutin, 1995a; Aniello, 2003). For this purpose, only stable terrain points, i.e. not on glaciers, rockglaciers or other slope movements, were used for ground control points and multitemporal image tie-points (Kääb and Vollmer, 2000; Kääb, 2002). The methodology of subsequent automatic DTM extraction and orthophoto generation from digital stereo imagery is well established and described (e.g. Grün and Baltsavias, 1987; Grün and Baltsavias, 1988; Baltsavias, 1996; Chandler, 1999). The measurement of individual terrain heights is based on the automatic assignment of corresponding terrain features in two (or more) overlapping images. For the final

measurement, the related correlation procedures focuses on the comparison of image sections of only a few pixels in size (in this study usually 15 pixels). Hence, heights can best be derived where the optical contrast on the digital images is sufficient, e.g. not diminished due to fresh snow, and, secondly, where terrain sections look similar on the different photographs and are not strongly distorted. Height computation fails where terrain parts are occluded on one or more photographs so that they are only visible in only one image. In summary, the accuracy of the resulting DTM is generally low on steep slopes or in shadow zones.

Automatic aerophotogrammetric DTMs have been derived and investigated for Arctic glaciers and ice caps (e.g. Etzelmüller et al., 1993; Bacher et al., 1999), ice sheets (e.g. Wrobel and Schlüter, 1997; Fox and Gooch, 2001), and for glaciers, rockglaciers and slope instabilities in high mountains (e.g. Baltsavias et al., 1996a; Kääb, 2000; Kääb and Vollmer, 2000; Weber and Herrmann, 2000; Baltsavias et al., 2001; Kaufmann and Ladstädter, 2002; Ødegård et al., 2004).

Accuracy

Figures 3-2 and 3-3 show the comparison between DTMs computed using digital photogrammetry and DTMs from traditional, analytical photogrammetry where terrain heights are measured by a human operator. Operator-measured DTMs are characterized by high accuracy and reliability of individual elevation values. In Figure 3-2 the vertical differences between an automatic DTM and an analytical one are given for Muragl rockglacier, Swiss Alps (Kääb and Vollmer, 2000). 1:6,000-scale aerial photography was applied for the test, and scanned at 30 μm for the automatic DTM (i.e. approximately 0.2 m ground resolution). Average block size on the rockglacier is in the order of few decimetres. While the reference data were measured from one stereo-pair of photographs (60% overlap), the digital DTM generation was performed using three overlapping images (80% overlap each). The RMS of the vertical differences is ± 1.4 m, maximum errors range from -16 m to +9 m. Large differences are mainly found in areas with less favourable terrain conditions, i.e. steep slopes, rough topography or low optical contrast, e.g. due to snow cover. Under favourable terrain conditions, for instance on rock-glacier lobes, the RMS amounts to approximately ± 0.6 m and maximum vertical DTM differences are in the range of approximately ± 1.5 m. The inferred average error of the reference DTM is estimated to be ± 0.2 m (Kääb, 1996b). Thus, a majority of the vertical differences between the automatic DTM and the reference elevation data is not significant.

A further test is presented for a typical glacier surface. Figure 3-4 shows the comparison between a DTM that was manually measured using analytical photogrammetry, and an automatic DTM using Socet Set. Both 25 m gridded DTMs were derived from 1:18'000-scale black-and-white imagery of 1975. The vertical accuracy of the manual DTM is estimated to approximately ± 0.5 m RMS (Kääb, 1996b). For the entire study site (approximately 1,000 points), an RMS of ± 2.4 m and an error range between -20 m and +34 m was found (manual DTM minus automatic DTM). For the glacier itself an RMS of ± 1.2 m and an error range between -7.5 m and +4.5 m is obtained. Thereby, errors are significantly larger for debris zones where blocks of up to several metres in diameter cover the ice compared to the block size of a few decimetres for the Muragl rockglacier discussed above. The vertical deviations amount to ± 0.7 m RMS ranging from -2.2 to +3.6 m for the clean-ice zones.

Figure 3-5 shows the vertical differences between a DTM from analytical photogrammetry and a DTM from digital photogrammetry for a region of typical high-mountain terrain. The two DTMs have been acquired using different imagery.

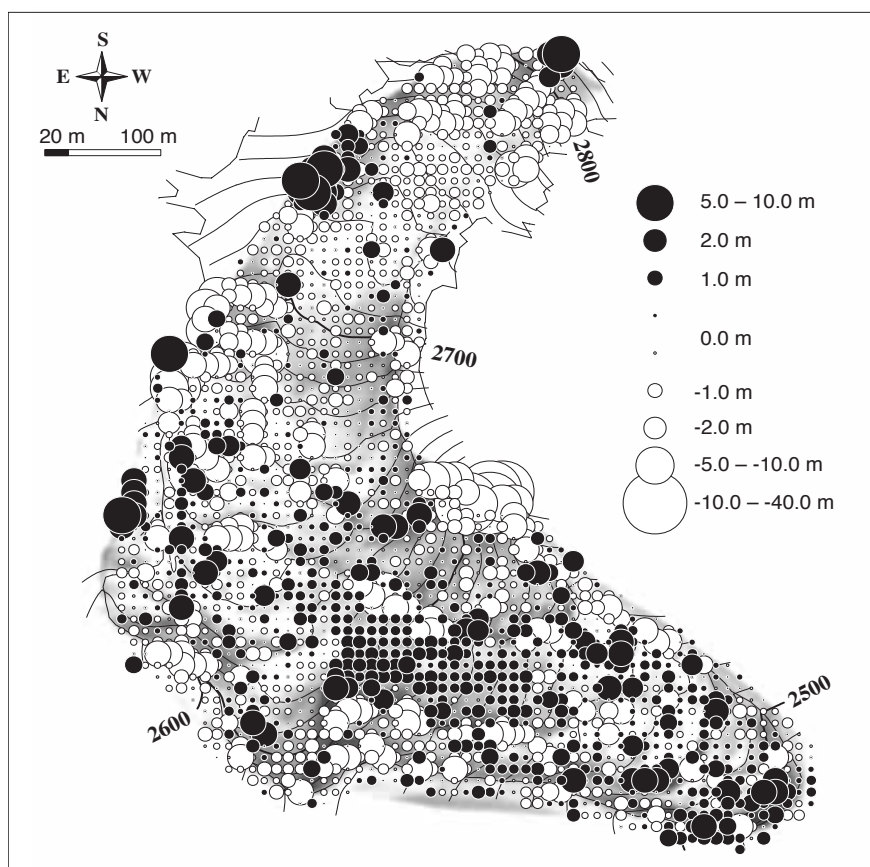


Fig. 3-2 Muragl rockglacier, Swiss Alps: raw differences between a reference DTM (operator-measured using analytical stereo-photogrammetry) and a DTM automatically derived from digitized imagery (digital photogrammetry). Note that maximum differences are not depicted in a linear scale.

The manually-measured DTM is based on approximately 1:30,000-scale infrared aerial photography from 1991. DTM accuracy is estimated at $\pm 1\text{--}2$ m (Kääb, 1996b). The automatic DTM was derived using Socet Set from approximately 1:18,000-scale colour imagery from 1999 scanned at $30\text{ }\mu\text{m}$ (i.e. approximately 0.5 m pixel size). For glacierized terrain, the vertical DTM differences 1991–1999 reflect changes in ice thickness rather than DTM deviations. Except for the glaciers, however, the terrain can be considered stable to a large extent. For the entire region of Figure 3-5 the vertical differences between the two 25 m gridded DTMs (22,000 points) range between -95 m and +105 m with ± 8 m RMS. For the large inset in Figure 3-5 (c. 8,000 grid points) where the terrain is not affected by glacier fluctuations between the image acquisitions, the DTM differences range between -58 m and +88 m (± 7.5 m RMS). The small inset (c. 2,000 points) consists of more moderate high-mountain topography with no steep flanks. Corresponding vertical DTM differences range between -25 m and +22 m (± 3.5 m RMS).

Considering all three test studies, a vertical RMS for automatic aerophotogrammetric DTMs corresponding to 1–3 times the image pixel size can be achieved for moderate high-mountain topography, and an RMS corresponding to 5–7 times the image pixel size for rough topography. For steep flanks with cast shadow or snow cover, maximum vertical errors in the order of 60–100 times the image pixel size may be encountered.

3.3 Airborne DTM acquisition

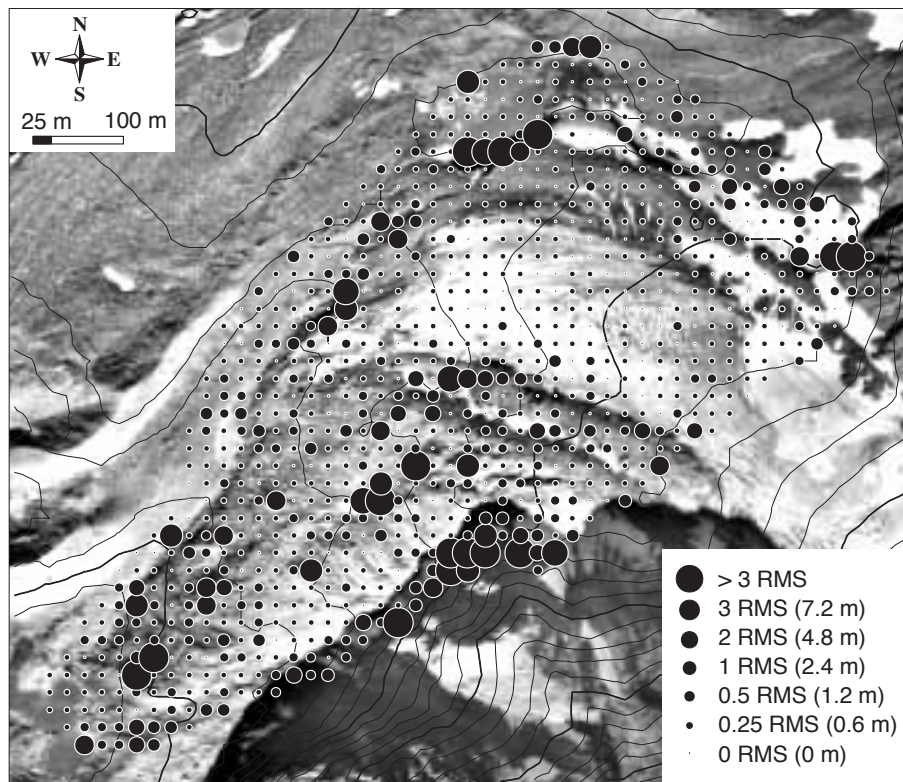


Fig. 3-4 Comparison between an operator-measured analytic DTM and an automatic one for the Gruben glacier tongue, Swiss Alps. Deviations are depicted in relation to their overall average (RMS).

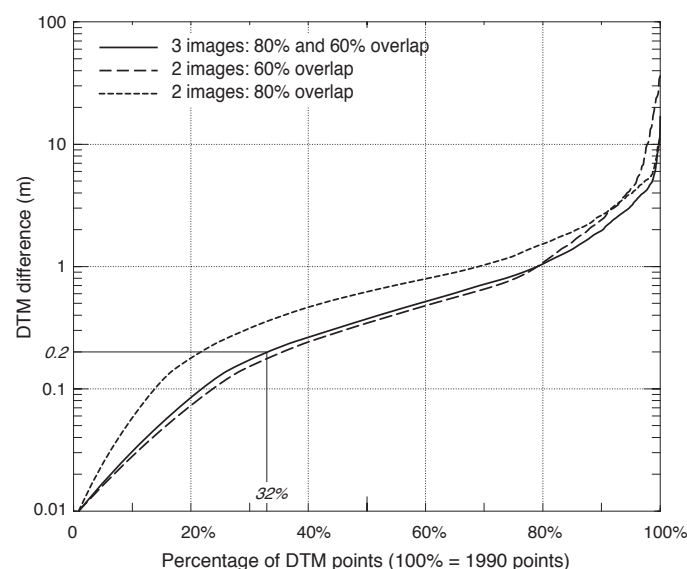


Fig. 3-3 Cumulative histogram of differences ($|\partial z^S|$) between an analytically- and an automatically-measured DTM for Muragl rockglacier (see Fig. 3-2). The automatic DTM was compiled in three versions: from two images with 60% overlap, from two images with 80% overlap, and from all three images. The 80%-overlap DTM shows larger deviations from the manually-measured DTM, presumably due to its less favourable geometric constellation (smaller intersection angle of the projection vectors). For the three-image DTM, 32% of the compared points show vertical deviations smaller than the (horizontal) pixel size of 0.2 m of the applied imagery.

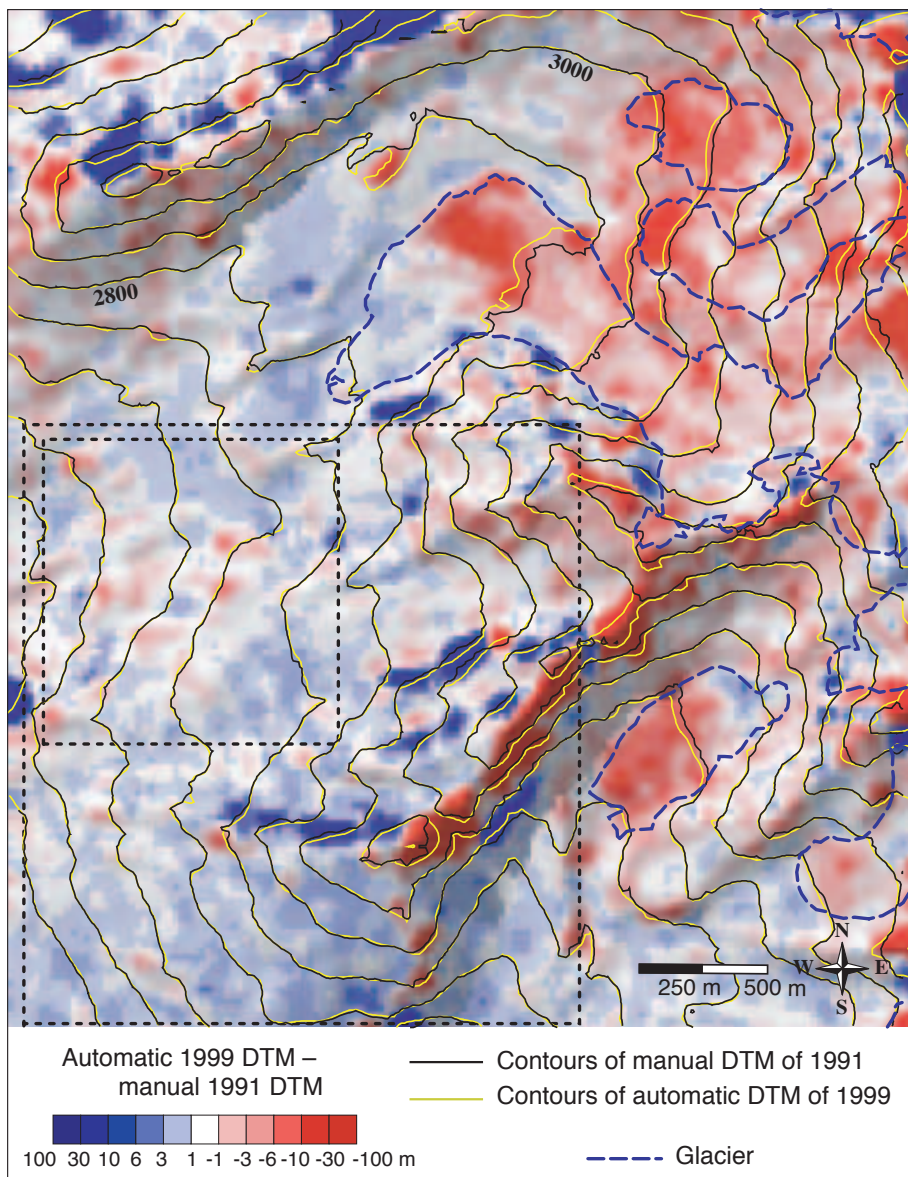


Fig. 3-5 Comparison between an operator-measured analytic DTM and an automatic one for the Gruben region, Swiss Alps. The brightness of the colour-coded vertical deviations between the two DTMs is modulated with a hillshade from the operator-measured DTM. Note that the analytic DTM is from imagery from 1991, while the automatic one is from 1999 imagery. Deviations on glacierized terrain, therefore, are influenced by changes in ice thickness. DTM differences have been analyzed for the entire extent, and for two subsets (dashed rectangles).

There is usually no reference DTM available for assessing the accuracy of an obtained DTM. For optical stereo methods, DTM errors can be estimated by comparing orthoimagery computed from the identical DTM but applying different stereo images (Baltsavias, 1996; Kaufmann, 1998b; Ladstädter, 2001; Kaufmann and Ladstädter, 2002). The procedure is explained in more detail in Section 3.5.

See Baltsavias et al. (1996a; 1996b; 2001) for further tests on automatic aerophotogrammetric DTMs of high-mountain terrain.

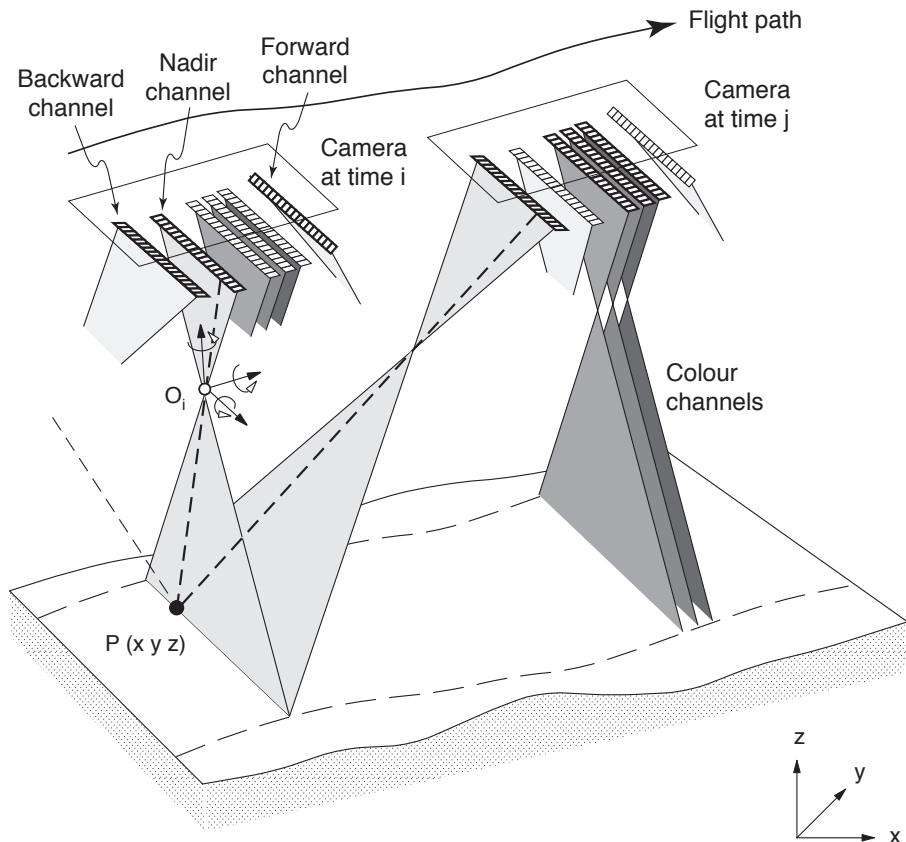


Fig. 3-6 Principle of a pushbroom sensor with three multispectral nadir lines and panchromatic backward, nadir and forward stereo lines.

3.3.2 Digital photogrammetry of airborne pushbroom imagery

Principle

In addition to photogrammetry of digital or digitized frame imagery, the author considers photogrammetry of digital *pushbroom sensors* (also called *linear array CCD sensors*) to play an increasingly important role in the air- and spaceborne determination of DTMs. Other non-frame techniques are not discussed here.

A pushbroom array (i.e. a cross-track line of detectors) can be viewed as a two-dimensional central projection (see Equation 3-1). In contrast to frame imagery, however, the orientation parameters \mathbf{x}_o , \mathbf{R} and λ change for every line. These effects are usually corrected by determining $\mathbf{x}_o(t)$, $\mathbf{R}(t)$ and $\lambda(t)$ from on-board differential satellite navigation and inertial navigation systems (INS). Similar to photogrammetry of frame imagery, terrain points can be computed from along-track pushbroom arrays with different view angles (two-, three-, or multiple-line cameras) providing ray intersections at individual terrain points (Fig. 3-6). Pushbroom cameras may also record multispectral information. (Entire paragraph: Cosandier, 1999; Hauber et al., 2000; Grün and Zhang, 2002; Poli, 2002).

Application and accuracy

Airborne, multiple-line cameras (nadir, back-looking, and/or forward-looking pushbroom lines) such as the HRSC-A (by DLR) or ADS40 (by Leica Geosystems) currently reach spatial ground resolutions in the order of one decimetre GIFOV per 1,000 m above ground. Corresponding DTMs have a spatial resolution between one

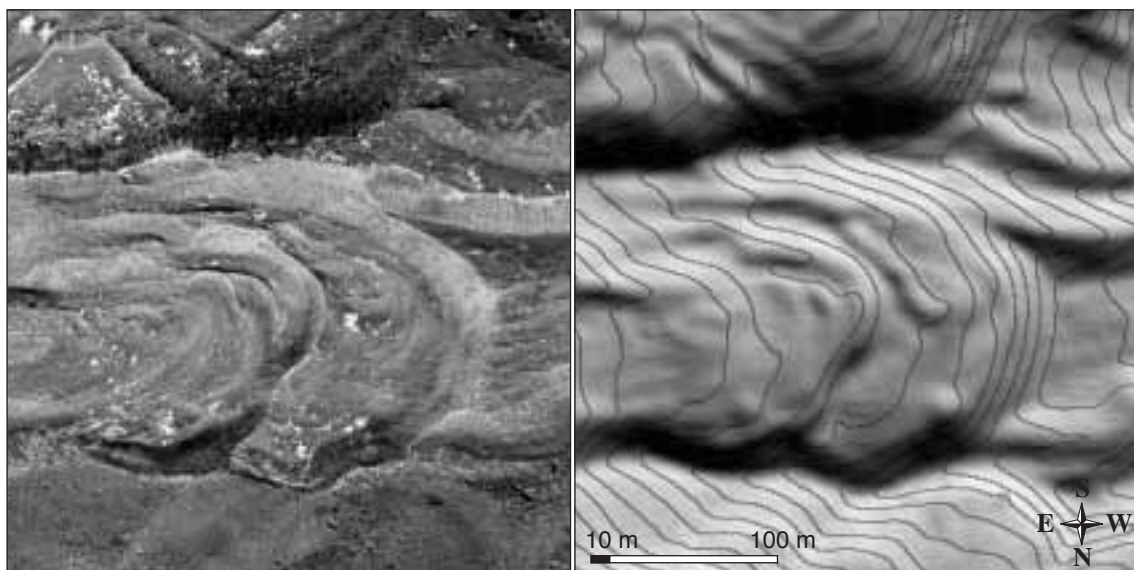


Fig. 3-7 Section of a orthophoto (left) and DTM hillshade (right) derived from the HRSC-A pushbroom camera. Rockglacier front, Turtmann valley, Swiss Alps. Contour line interval is 5 m. Data courtesy of Department of Geography, University of Bonn. (See Roer et al., 2005b).

and a few metres with a vertical accuracy of approximately one decimetre per 1,000 m above ground (e.g. Hauber et al., 2000; Grün and Zhang, 2002; Zhang and Grün, 2004). The general characteristics of DTMs from two- or three-line cameras are similar to those from frame imagery, where low-contrast areas or steep slopes often cause DTM errors. First tests for high-mountain terrain gave very promising results (Hauber et al., 2000; Roer et al., 2005b) (Fig. 3-7).

3.3.3 Airborne laserscanning (LIDAR)

Principle

The distance between sensor and terrain surface can be estimated from the travel time of a laser impulse sent from an aircraft sensor, reflected at the terrain surface, and received again at the aircraft sensor (light detection and ranging, LIDAR) (Fig. 3-8):

$$\mathbf{x} - \mathbf{x}_o = \mathbf{r}_u c_l \Delta t / 2 \quad (3-4)$$

where

- $\mathbf{x} = (x, y, z)^T$ are coordinates of a terrain point in ground coordinates,
- $\mathbf{x}_o = (x_o, y_o, z_o)^T$ are the ground coordinates of the LIDAR sensor centre,
- $\mathbf{r}_u = f(\omega, \phi, \kappa)$ is a unit vector depending of the orientation angles ω , ϕ and κ ,
- c_l is the travel speed of the laser impulse, and Δt is the measured travel time.

At present, air- and spaceborne LIDAR systems apply impulse run-times and phase measurements for ranging. In contrast to analogue and digital imagery, LIDAR uses active sensors. Thus one measurement alone is able to determine a terrain point. From a larger sample of measured points the terrain surface can be reconstructed. The orientation parameters are obtained from on-board differential satellite navigation and INS. For a general introduction to laserscanning, see Baltsavias (1999) and Wehr and Lohr (1999).

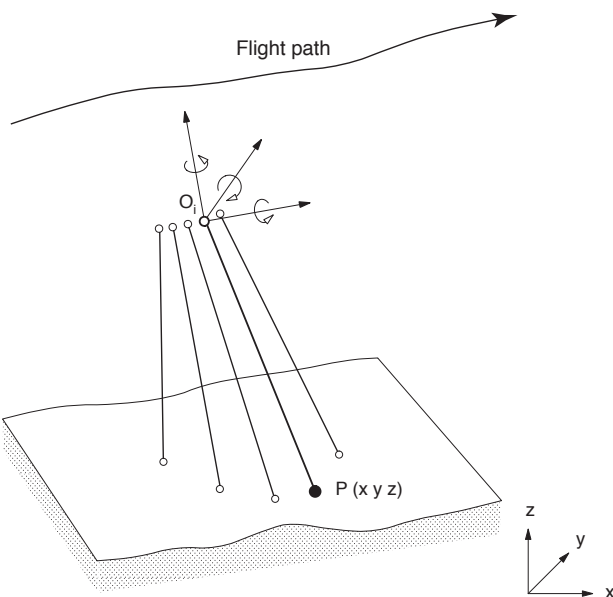


Fig. 3-8 Principle of laserscanning: the three-dimensional position of individual terrain points is determined by their range and direction relative to the sensor.

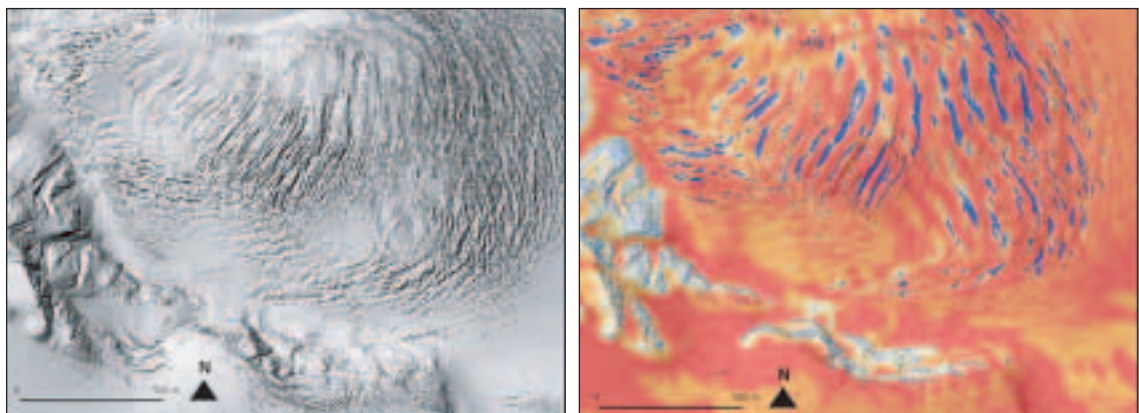


Fig. 3-9 Left: Shaded DTM of a section of Engabreen, Norway, from laserscanning (September 2001). Right: Vertical DTM differences from laserscanning of September 2001 and May 2002 for the same terrain section as left panel. Red colours indicate thickening, blue colours thinning between the data acquisitions. Thickening is mainly due to snow accumulation between autumn and spring, thinning due to the advection of crevasses leading to a pattern of elevation increases and corresponding decreases at crevasses (see Section 4.3). (With kind permission from Geist et al., 2003).

Application and accuracy

The terrain surface can be measured with one laser ray fixed with respect to the sensor, which results in a terrain profile (*laser profiler*), or with a scanning, rotating or optical fibre-bundle laser resulting in stripe-wise terrain coverage (*laser scanner*). Laserscanning provides a DSM with a spatial resolution of one to a few metres (Fig. 3-9), and a typical vertical and horizontal accuracy (RMS) ranging from several centimetres to decimetres, depending on the flying height above ground. Footprint size of the laser beam is in the order of some decimetres per 1000 m flying height above ground. Some LIDAR sensors are able to record multiple returns of the same laser pulse (e.g. first/last pulse). These data are e.g. useful for vegetation tomography (Lefsky et al., 1999).

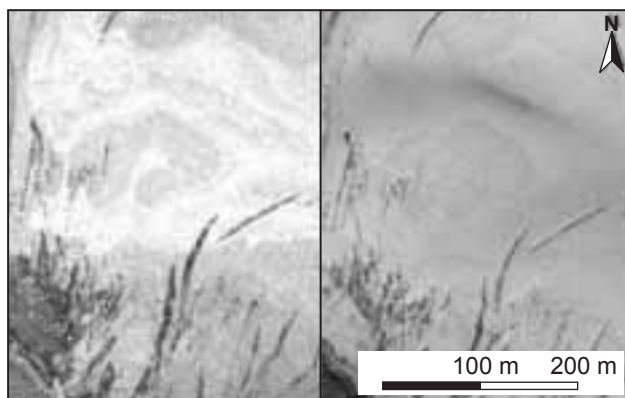


Fig. 3-10 Section of Svartisheibreen, Norway. Left: measured laser intensity distribution; right orthoimage of the same glacier section. (From Lutz et al., 2003).

By recording of the signal intensity it is possible to gather further information about the scanned terrain (Fig. 3-10) (Lutz et al., 2003). The signal intensity at sensor is among others a function of surface characteristics such as reflectivity, incidence angle (angle between surface normal and laser vector), footprint size and range between sensor and footprint (Lutz et al., 2003). The flying height above ground is limited by the laser power. However, advanced signal processing and additional hardware enable flying to be conducted currently at heights of up to some km above ground. It is sometimes still difficult to obtain complete coverage by laser scans over terrain with large elevation differences.

Airborne LIDAR was extensively tested and used for deriving glacier topography and glacier thickness changes in arctic environments (e.g. Garvin and Williams, 1993; Krabill et al., 1995; Echelmeyer et al., 1996; Adalgeirsdotir et al., 1998; Van der Veen et al., 1998; Bindschadler et al., 1999; Conway et al., 1999; Arendt et al., 2002). Recent experiments with laserscanning for deriving glacier and high-mountain DTMs produced very promising results (Kennett and Eiken, 1997; Favey et al., 1999; Baltsavias et al., 2001; Geist et al., 2003; Geist and Stötter, 2003; Janeraas et al., 2004).

3.3.4 Airborne interferometric synthetic aperture radar (InSAR)

Principle

Active radar sensors determine the *distance (range) from the sensor to the terrain surface* by run-time measurements of microwave signals. Combination of the radar backscatter in range direction (i.e. cross track, slant range direction) along the flight track of the sensor (i.e. azimuth direction) results in a radar image. The antenna aperture (electromagnetically receiving area) can be extended synthetically by continuously combining the antenna positions in flight direction (*synthetic aperture radar, SAR*) (Curlander and McDonough, 1991).

More details on the characteristics and applications of microwave remote sensing for exploring glaciers and permafrost are given in Sections 3.4.2, 4.5 and 5.2. Here, the focus is on DTM generation from SAR interferometry (*InSAR*). In contrast to amplitude-based DTM derivation from (passive) optical imagery, InSAR relies on the signal's phase. The InSAR technique is based on the fact that for a given terrain point the backscatter phase depends on the distance of this point to the sensor. Thus, if the terrain point is measured from two different antenna positions (separated by a spatial baseline \mathbf{B}) the interferometric phase difference depends on the respective slant range difference (Bamler and Hartl, 1998) (Fig. 3-11):

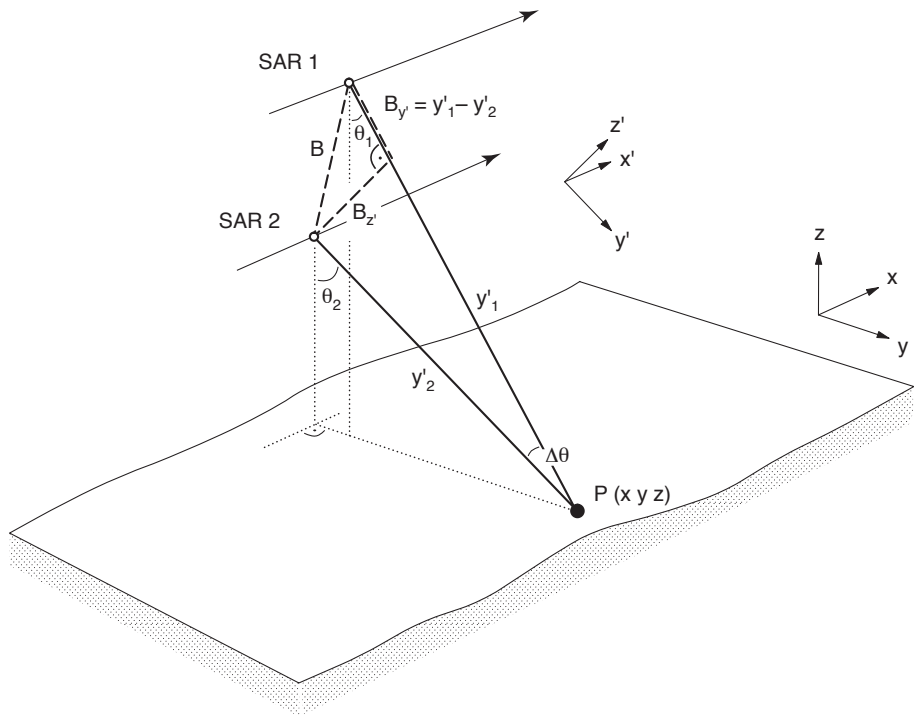


Fig. 3-11 Geometric principle of interferometric SAR using two antennas, SAR1 and SAR2, simultaneously (single pass) or in repeat passes (repeat-pass InSAR).

$$\phi = \varphi_1 - \varphi_2 = \frac{4\pi}{\lambda}(y'_1 - y'_2) \quad (3-5)$$

where

ϕ is the interferometric phase for a given point P ,
 φ_1 and φ_2 are the phases of the two SAR images for the given point P ,
 λ is the radar wavelength, and
 y'_1 and y'_2 are the slant range distances from the scatterer to the two antennas.

For a stable terrain section, the interferometric phase can be linearized to

$$\phi = \frac{4\pi}{\lambda} B_{y'} + \frac{4\pi}{\lambda} \Delta y'_{atmosphere} + \phi_{noise} \quad (3-6)$$

where

$B_{y'}$ is the baseline parallel component with the line-of-sight between sensor and scatterer P , i.e. the slant range (y') component of \mathbf{B} ,
 $\Delta y'_{atmosphere}$ is the apparent range difference due to different atmospheric conditions between sensor 1 and scatterer, and sensor 2 and scatterer, and
 ϕ_{noise} is a noise term which becomes zero for single-pass InSAR (i.e. most airborne SAR campaigns).

On airborne platforms, the two SAR sensors can be mounted together, so that the interferometric phase is usually determined during one overflight (*single-pass interferometry*), and the atmospheric effect $\Delta y'_{atmosphere}$ can be neglected. For terrain points with different azimuth coordinates x' and slant range coordinates y' located in one SAR interferogram $\phi(x', y')$, the baseline parallel component $B_{y'}$ changes, and thus ϕ changes. The change in $B_{y'}$ is a function of slant range and incidence angle. When the influence of interferometric phase change with range change is subtracted using a DTM approximation (usually a reference ellipsoid; ‘flat earth’), the remaining phase

is a function of terrain elevation. For a spatially continuous sequence of phase cycles (fringes), these can be inverted to elevation differences when wavelength, slant range and baseline are known (*phase unwrapping*) (Gens and van Genderen, 1996) (Fig. 3-12). Differentiation of the first term of Equation 3-6 for terrain height z gives

$$\frac{\partial \phi}{\partial z} = \frac{4\pi}{\lambda} \frac{B_{z'}}{y' \sin \theta} \quad (3-7)$$

where

$B_{z'}$ is the baseline normal component to the line-of-sight, and
 θ is the incidence angle from nadir.

Differentiation of Equation 3-6 for slant range distance gives

$$\frac{\partial \phi}{\partial y'} = \frac{4\pi}{\lambda} \frac{B_{z'}}{y' \tan \theta}, \quad (3-8)$$

that is the fringe frequency in slant-range direction for a flat surface. The height difference corresponding to a phase change of 2π (i.e. one fringe) is, as can be derived from Equation 3-7:

$$\Delta z_{2\pi} = \frac{\lambda y' \sin \theta}{2B_{z'}}. \quad (3-9)$$

Similarly, the following relations can be obtained from Equation 3-8 for one fringe:

$$\Delta y'_{2\pi} = \frac{\lambda y' \tan \theta}{2B_{z'}}, \text{ or } \Delta y_{2\pi} = \frac{\lambda y' \tan(\theta - \alpha)}{2B_{z'}}, \text{ respectively,} \quad (3-10)$$

where

α is the terrain slope, and
 y is the horizontal ground projection of y' .

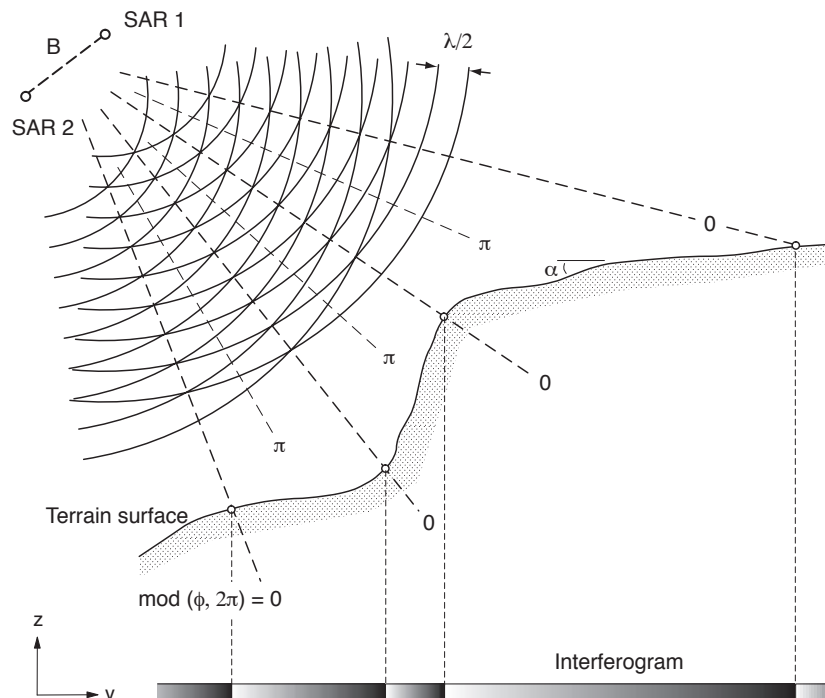


Fig. 3-12 Principle of a SAR interferogram as caused by terrain relief.

The absolute elevation shift z_0 is deduced, for instance, from ground information. The DTM is then derived from the integration of Equation 3-7 (Fig. 3-12).

SAR sensors are side-looking sensors used to resolve terrain points by range measurements. This side-looking principle causes some geometric restrictions such as foreshortening, shadow and layover, which are especially effective for mountainous terrain (see Section 3.7). On the other hand, airborne single-pass SAR systems offer the opportunity for free choice of flight track. To overcome the above geometric restrictions, airborne SAR DTMs are usually derived from multiple overflights with different flight directions. (For a more thorough introduction to InSAR see Gens and van Genderen, 1996; Bamler and Hartl, 1998).

Application and accuracy

The resolution of airborne SAR DTMs is in the order of metres or even less, and their vertical accuracy for mountainous terrain in the order of decimetres to metres, both depending on the wavelength applied (Faller and Meier, 1995; Madson et al., 1995; Hofmann et al., 1999; Schwäbisch and Moreira, 1999; Sties et al., 2000; Wimmer et al., 2000). Current systems (e.g. AeS-1, GeoSAR) use X- to P-band SAR (i.e. around 3 to 80 cm wavelength). A major advantage of SAR as microwave technique lies in its all-weather capability.

Radar penetration into the ground is a function of the ground properties, and the applied wavelength and polarization (see Section 5.2). The penetration might vary significantly, especially for vegetation and snow cover. Although this might not be the desired effect, it can be exploited for deriving surface characteristics (e.g. SAR tomography) (König et al., 2001). Only a few airborne SAR campaigns focusing on ice and snow, or mountain terrain have been performed so far (Vachon et al., 1996; Bindschadler et al., 1999; Eckert and Kellenberger, 2002; Stevens et al., 2003; Barmettler et al., 2004; Stebler et al., 2004).

3.3.5 Analogue and analytical photogrammetry

Analogue and analytical photogrammetry are well-established tools for measuring DTMs of glaciers and permafrost, and have been applied for decades (e.g. Finsterwalder, 1931; Hofmann, 1958; Finsterwalder and Rentsch, 1980; Ebner, 1987; Rentsch et al., 1990; Kersten and Meister, 1993; Kääb, 1996b; Fox and Nuttall, 1997; Kääb et al., 1997; Kääb and Funk, 1999; Kääb, 2001). Although digital techniques may sooner or later fully replace photogrammetry that is based on analogue photography, it should be mentioned that analytical photogrammetry still is very useful or even superior for applications where human interpretation is necessary to back up image measurements. This situation arises because of the lower resolution of digital imagery compared to photographic films, and the lower resolution and display quality of computer displays compared to optical display systems.

3.4 Spaceborne DTM acquisition

DTMs can be derived from space by

- satellite stereo imagery (Section 3.4.1),
- interferometric SAR (Section 3.4.2),
- LIDAR altimetry (Section 3.4.3),
- RADAR altimetry (Section 3.4.3), and
- other methods (Section 3.4.3).

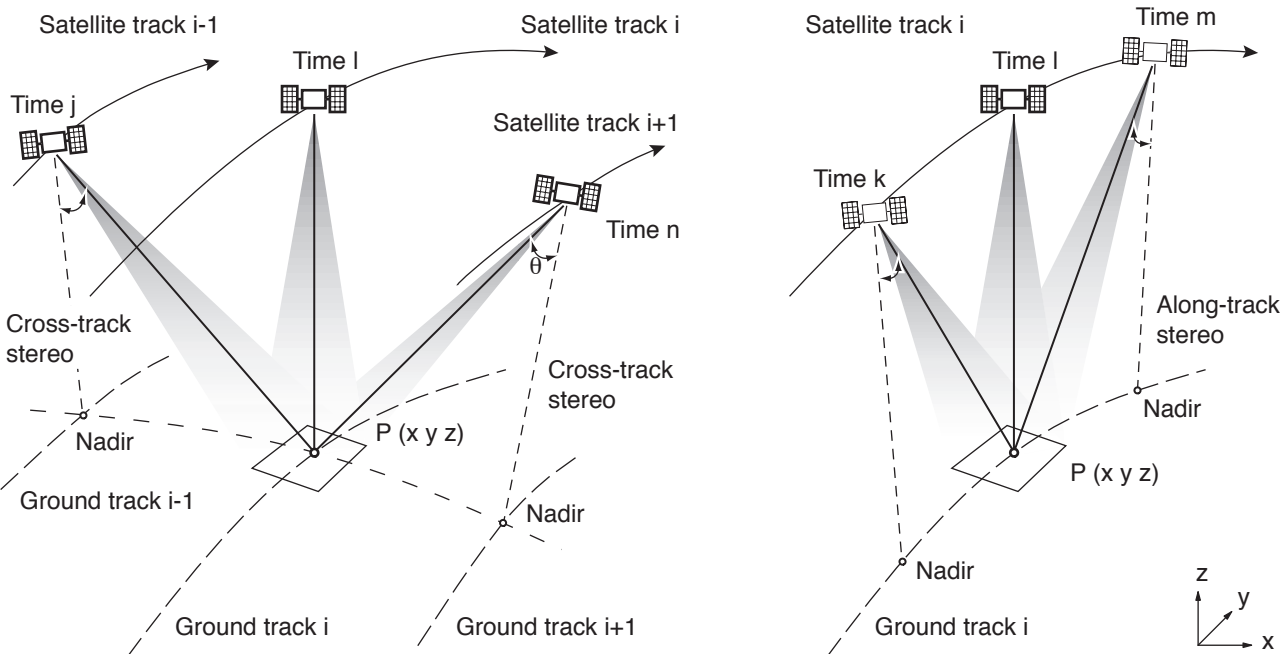


Fig. 3-13 Principles of optical satellite stereo: cross-track stereo, left or right, from different satellite tracks with time differences ranging from days to months (left panel), and along-track stereo, forward or backward, taken during one overflight, i.e. with acquisition time differences in the order of seconds to minutes (right panel).

3.4.1 Satellite stereo imagery

Principle

Optical satellite stereo imagery is usually obtained from scanning or pushbroom sensors. A stereo image is either recorded from repeat imaging of the terrain with different viewing angles, i.e. from different satellite tracks (*cross-track stereo*), or during one overflight by nadir-, forward- and/or backward-looking *along-track stereo* (Fig. 3-13). In particular, multitemporal SPOT data from different pointing-angles have been widely employed for DTM generation over mountainous terrain, but data from other sensors have also been used (e.g. Simard, 1987; Al-Rousan and Petrie, 1998; Bishop et al., 2000; Toutin, 2001; Toutin, 2002a; Toutin and Cheng, 2002; Zomer et al., 2002). The techniques applied for extracting DTMs from satellite stereo are comparable to those from aerial imagery (Sections 3.3.1 and 3.3.2). In contrast to airborne methods earth rotation, earth curvature, etc. have considerable effects (Fig. 3-14) (Toutin, 1995a; Toutin, 2004). However, the flight track of a satellite is disturbed much less by high-frequency variations than are airborne platforms.

If available, along-track stereo is preferable for most applications in glaciology, since the data can be obtained during one overflight without marked terrain changes. During the much longer time spans between the stereo partners of cross-track stereo imagery (up to months), the terrain conditions could change significantly and complicate image correlation, for instance, due to snowfall or snowmelt.

SPOT5 (10 m resolution) or ASTER (15 m resolution), which is used in this study, carry along-track stereo sensors (Fig. 3-15).

In order to compute 2- or 3-dimensional ground point positions from 2-dimensional images, two principle classes of mathematical models are applied (Toutin, 2004).

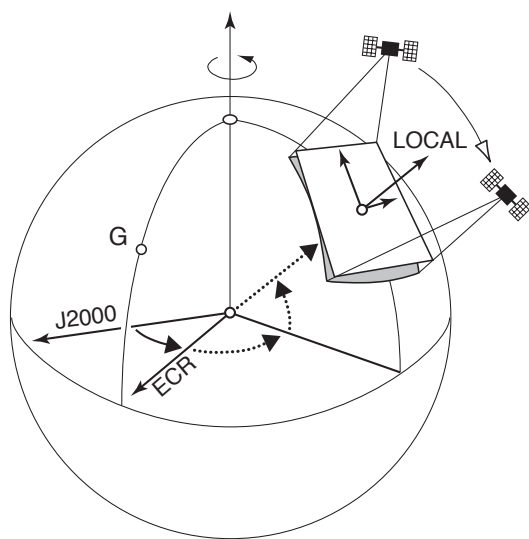


Fig. 3-14 Transformation of satellite imagery onto global or local terrestrial coordinate systems involves (1) transformation from an inertial space system (e.g. J2000) in which the satellite is manoeuvred into an earth-centred rotating system (ECR), and (2) further rotation and shift onto a locally centred system.

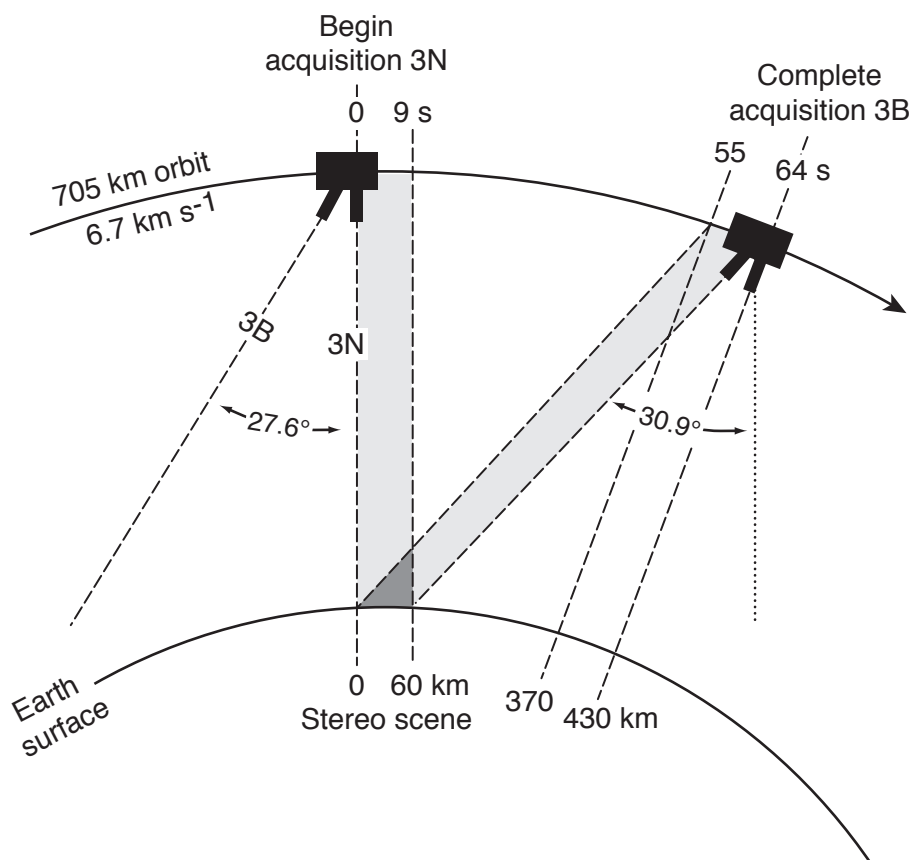


Fig. 3-15 ASTER stereo geometry and timing of the nadir-band 3N and the back-looking sensor 3B. An ASTER nadir scene of approximately 60 km length, and a corresponding scene looking back at a 27.6° off-nadir angle and acquired about 60 seconds later together form a stereo scene. Figure not drawn to scale. (After ERSDAC, 1999a; ERSDAC, 1999b; Hirano et al., 2003).

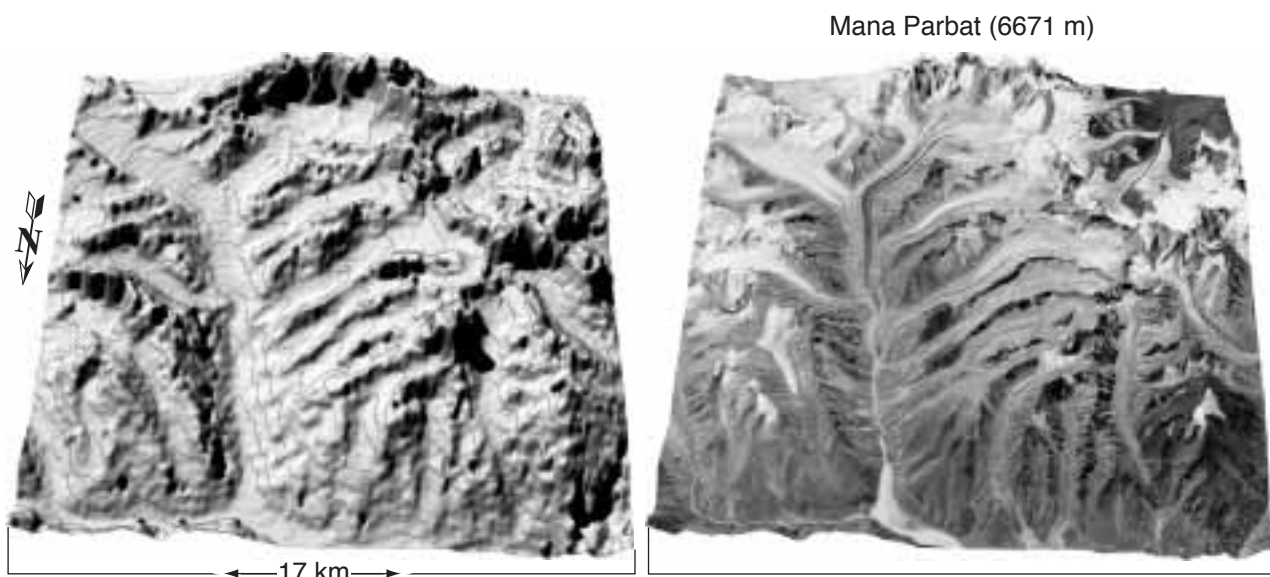


Fig. 3-16 Example of a DTM from ASTER along-track stereo data. Left: oblique hillshade of the DTM with superimposed 200 m contours. Right: oblique view of an ASTER RGB false colour composite (FCC) of bands 321, converted to grayscale, and draped over the DTM. Mana Bamak glacier in the Garhwal Himal, India, is located in the upper left. Most depicted glaciers (right panel) exhibit very small accumulation areas at the acquisition date of 9 September 2001.

These models can be used for any kind of image (optical, SAR, etc.), and are not only valid for optical satellite imagery (Toutin and Gray, 2000).

- Empirical models, such as 2D and 3D polynomial or rational functions. These models do not reflect the actual acquisition geometry but directly transform image coordinates without any a priori information.
- Physical (or rigorous) models, which try to fully reflect the imaging geometry, for instance Equations 3-1 and 3-4. Sensor position and rotation might be modelled from GCPs, given ephemeris, or on board GNSS/INS, e.g. in the form of piecewise polynomials.

Application

For generating DTMs from ASTER data, either corrected level 1B data or level 1A data were used in this study. Level 1A data are destriped using the respective parameters provided by the image header. Orientation of the 3N and corresponding 3B band (Fig. 3-15) from GCPs, transformation to epipolar geometry, parallax-matching, and parallax-to-DTM conversion is done using the PCI Geomatica 8.0 Orthoengine software (see Toutin and Cheng, 2001). In areas with no sufficient ground control available such information is computed directly from the given satellite position and rotation angles. In such cases, the line-of-sight for an individual image point is intersected with the earth ellipsoid. The resulting position on the ellipsoid is corrected for the actual point elevation, which, in turn, is estimated from the 3N-3B parallax of the selected GCP. Such GCPs are, then, imported into PCI Geomatica for bundle adjustment. An example of an ASTER-derived DTM is given in Figure 3-16. (Entire paragraph: Kääb, 2002; Kääb et al., 2003a; Kääb, 2005).

Accuracy

Figure 3-17 shows the comparison of an ASTER DTM with a reference DTM which was derived with 25 m grid-spacing from 1:30,000-scale aerial photography by

analytical photogrammetry (Section 3.3.1) (Kääb, 2001). The ASTER DTM was generated from data of 24 August 2001. The depicted test area around Gruben Glacier in the Swiss Alps represents rugged high-mountain conditions with elevations of 1,500 to 4,000 m ASL, steep rock walls, deep shadows and snow fields without contrast. Therefore, the test area is considered to represent a worst case for DTM generation from ASTER data.

Visual inspection and quantitative analysis show that severe vertical errors of the ASTER DTM of up to 500 m occur for sharp peaks having steep northern slopes. These errors are not surprising, considering that northern slopes are heavily distorted (or even totally hidden) in the 27.6° back-looking band 3B, and lie in shadow at the same time. The two ASTER DTMs were generated from level 1A (L1A, raw image data) and level 1B (L1B, destriped and projected to UTM, ERSDAC, 1999a; ERSDAC, 1999b). The accuracy obtained for the ASTER DTMs compared to the aerophotogrammetric reference DTM amounts to ± 78 m RMS (for the L1A DTM; for the L1B DTM: ± 68 m RMS) (Fig. 3-19). Maximum errors range between -220 m and +630 m (for the L1B DTM between -230 m and +510 m). The vertical differences between the L1A and L1B-derived DTMs amount to ± 33 m RMS (range: -380 m to +180 m). For a subsection with moderate high-mountain topography (rectangle in Fig. 3-17), an accuracy of ± 15 m RMS (for the L1B DTM: ± 19 m) and maximum errors of 100 m were found (for the L1B DTM: 105 m). For the subset, the vertical differences between the L1A- and L1B-derived DTMs lie in the range of ± 11 m RMS, with maximum errors between -30 m and +50 m. These maximum errors occur at sharp moraine ridges or deep stream channels. Exact numbers for these comparisons vary slightly with parameter variation for the DTM generation.

The tests presented above are based on ASTER DTMs derived using a grid spacing of 2 pixels (i.e. 30 m). While such resolution was found to improve the accuracy and representation of terrain details, coarser DTMs showed reduced gross errors. For vertical deviations smaller than about 100 m from the reference DTM (about 90% of the total point number) an ASTER DTM of the Gruben area derived with 60 m resolution gave larger deviations compared to the corresponding 30 m DTM (Fig. 3-19). However, for the remaining 10% of DTM points with vertical deviations larger than 100 m the 60 m DTM shows better vertical accuracy compared to the 30 m DTM (maximum error of 60 m DTM: 430 m; Fig. 3-20).

A second test study was conducted for the Gries Glacier area in the Swiss Alps (Fig. 3-19 and 3-18). This region represents less rugged high-mountain topography compared to the Gruben area. Nevertheless, the image section used contains a greater number of low-contrast snow and ice areas. By comparing an ASTER DTM from 24 August 2001 data with the 'DHM25 level 1' by Swisstopo, maximum errors of up to 500 m were found in two small areas. Elsewhere, the errors were significantly lower, and an RMS of ± 35 m was achieved. Compared to the Gruben ASTER DTM, the Gries ASTER-DTM reveals significantly fewer gross errors, but a lower accuracy for large terrain sections (Fig. 3-19). This might be due to the lower optical contrast in the Gries area compared to the Gruben area at image acquisition time (clean glaciers, snow coverage, etc.). Furthermore, the reference DTM DHM25 level1 applied is less accurate than a photogrammetrically operator-measured one (Paul, 2004) and thus also infers errors into the comparison.

As shown in Figure 3-31, northern slopes appear strongly shortened or even hidden in the back-looking stereo channel of the ASTER satellite sensor during its descending orbit. Such systematic distortion suggests a dependency of DTM errors

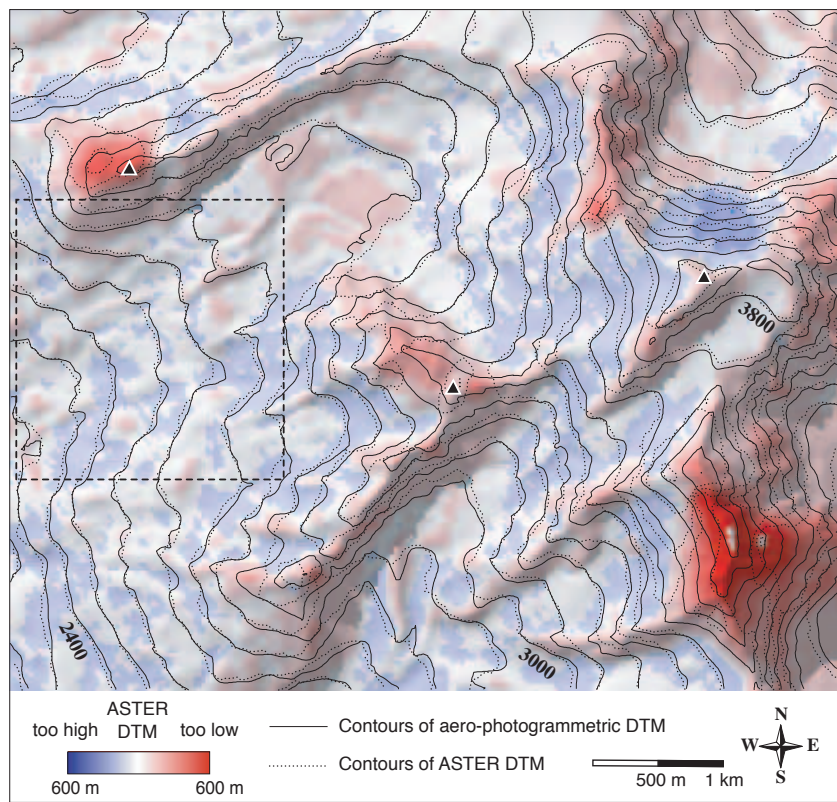


Fig. 3-17 Colour-coded elevation differences between an aerophotogrammetric reference DTM and an ASTER L1B-derived DTM of Gruben area (Swiss Alps), superimposed on a hillshade of the reference DTM. Continuous lines: 200 m contours of the photogrammetric DTM; dotted lines: 200 m contours of the ASTER DTM. Largest errors (dark red and dark blue) of up to 500 m occur at sharp peaks. For a subset (dashed rectangle) maximum errors of about 100 m and an RMS of ± 15 m were found. The general trend of a too-high (= blue colours) ASTER DTM towards the higher terrain parts (left part of figure) points to some model distortion, which was absent if ASTER L1A data were used. For the triangles see Fig. 3-31.

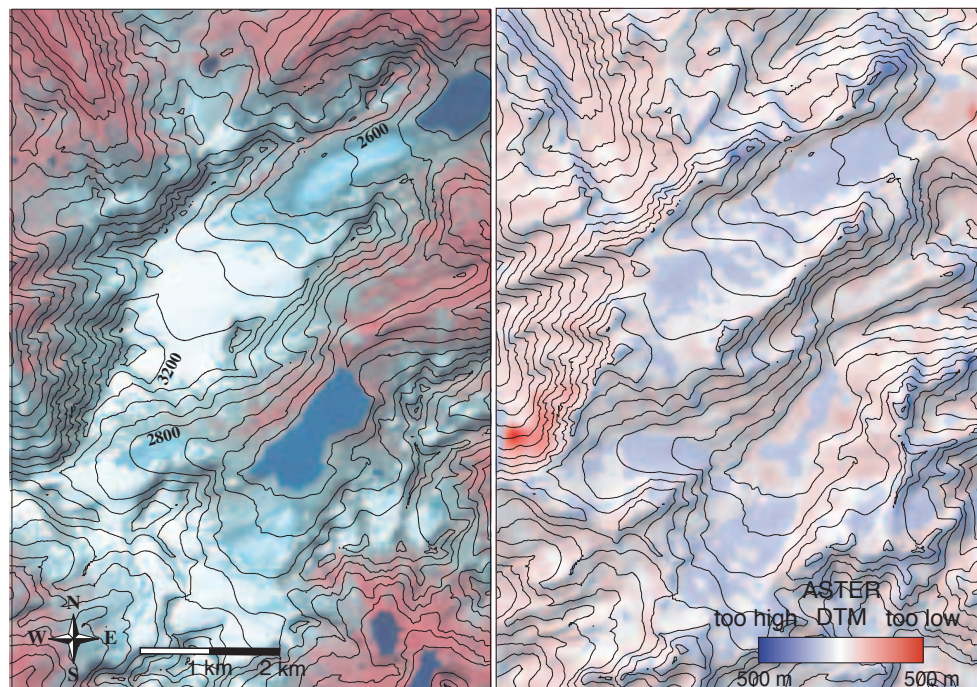


Fig. 3-18 RGB-composite of ASTER bands 321 (left) showing the Gries glacier area, Swiss Alps. Right: colour-coded vertical deviations of an ASTER L1B-derived DTM from the DHM25 of swisstopo (permission BA057212). ASTER data of 24 August 2001.

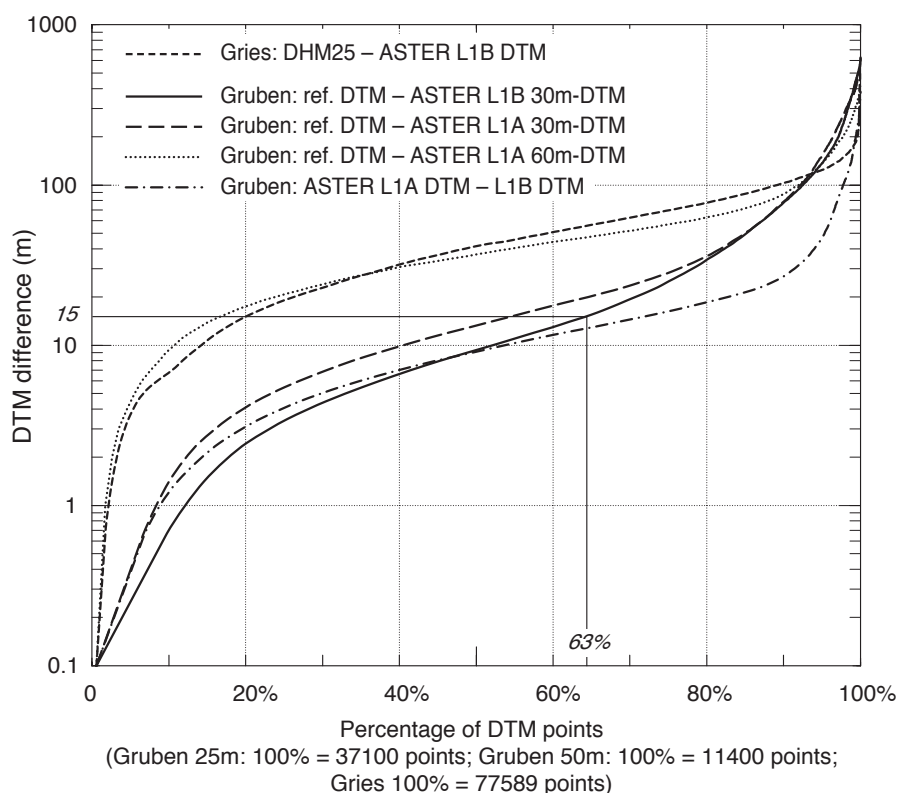


Fig. 3-19 Cumulative histogram of vertical deviations between reference DTMs and ASTER L1A- or L1B-derived DTMs. For the ASTER L1B-derived DTM of the Gruben area, for instance, 63% of the points show a vertical deviation of ± 15 m RMS or smaller, i.e. the ASTER pixel size in the visible and near-infrared spectrum (VNIR).

on aspect and slope. Indeed, Rivera et al. (2005) found a sinusoidal variation of DTM errors with aspect, which they also applied for correction of the respective ASTER DTMs (see also Section 4.2.2). Furthermore, severe DTM errors are also expected for sharp peaks. These are represented by too few pixels in the comparably coarse satellite imagery to allow reliable DTM matching.

It should be noted that the above accuracy assessments of ASTER DTMs are valid only for the applied PCI Orthoengine software. In particular, the obtained gross errors in the order of hundreds of metres, which are partially absent in coarser DTM levels, point to deficiencies in the blunder detection algorithm within the module. (For further evaluations of DTMs from ASTER and other satellite stereo optical sensors see: Toutin, 2001; Eckert and Kellenberger, 2002; Toutin, 2002b; Aniello, 2003; Bolch and Kamp, 2003; Hirano et al., 2003; Zollinger, 2003; Berthier et al., 2004; Eisenbeiss et al., 2004; Gamache, 2004; Stevens et al., 2004; Weidmann, 2004; Cuartero et al., 2005; Eckert et al., 2005).

For optimal DTM generation from satellite stereo multiple DTMs should be computed from one stereo data set with different resolutions (e.g. 30 m, 60 m and 120 m) and different sizes for the image block used for DTM matching (chip size; level of DTM detail) (Figs. 3-20 and 3-21). These DTM levels and the score channels containing the matching correlation coefficients for individual DTM points are then compared to each other and statistically analysed in order to detect gross errors (e.g. Cuartero et al., 2005). Finding such DTM errors can be supported by overlay of orthoimages computed from the DTMs and multi-incidence-angle data. Within such orthoimages DTM errors become visible as horizontal distortions, which among

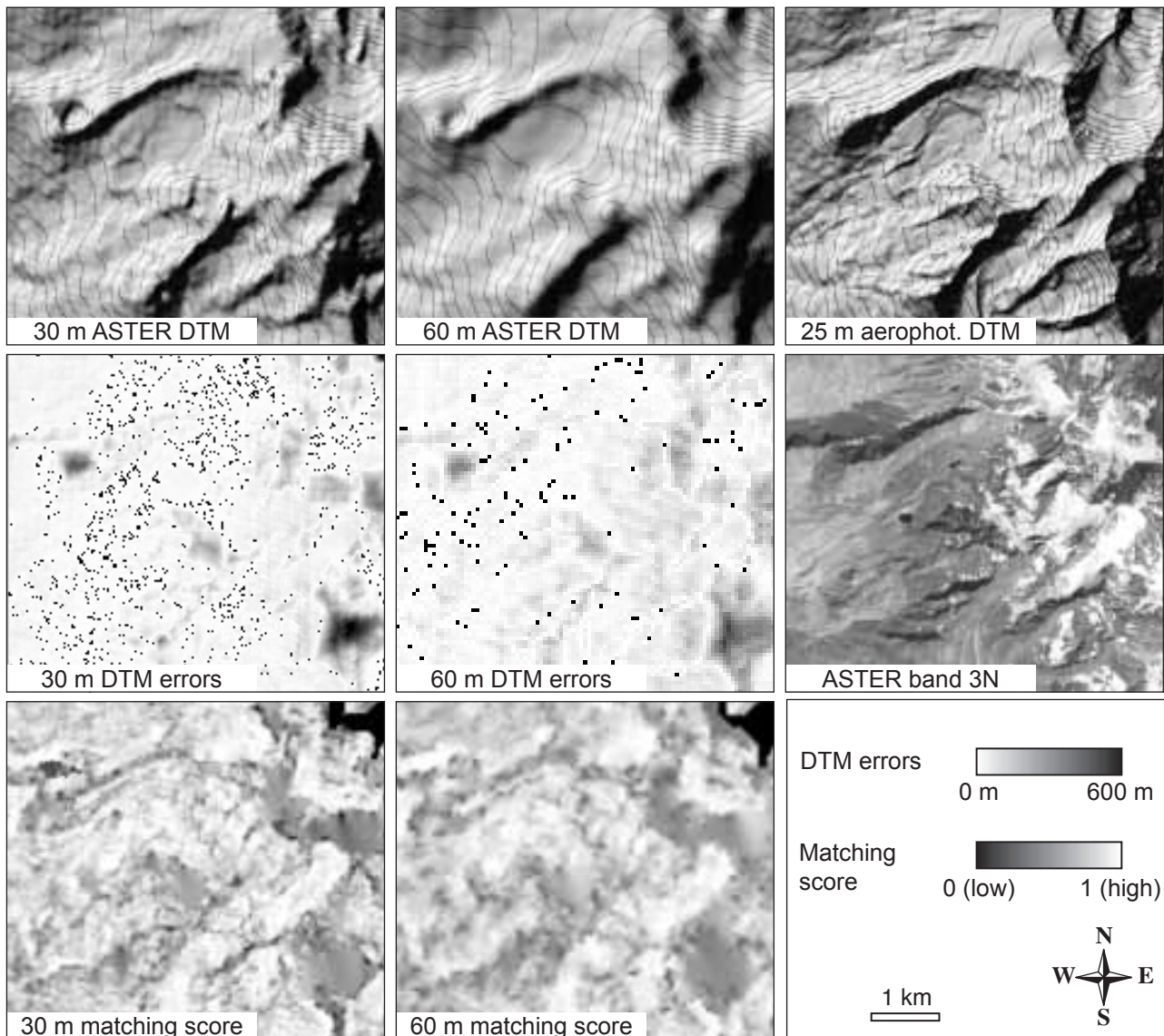


Fig. 3-20 First row: 30 m ASTER DTM (left), 60 m ASTER DTM (middle), aerophotogrammetric DTM (right; see text for description). Contour interval is 100 m. Second row: Grayscale-coded vertical DTM differences between the aerophotogrammetric DTM and the ASTER DTMs of first row (left and middle). Right: ASTER band 3N orthoimage. Third row: Score channels of DTM matching correlation. The darker the pixel the worse the correlation. Severe vertical DTM errors and matching problems are more pronounced for the 30 m ASTER DTM, which on the other hand shows more terrain details (see also Fig. 3-19).

others are proportional to the DTM errors and the incidence angle (see Sections 3.5 and 8.3). Further geomorphometric analyses can be applied to detect and fill unnatural spikes, sinks, etc. in the DTMs (Zollinger, 2003). Finally, the different DTMs and additional ones (e.g. the SRTM DTM; see Sections 3.4.2 and 8.3) (Weidmann, 2004) can be combined (Fig. 3-22) or gross errors masked out.

3.4.2 Spaceborne InSAR

Principle

The principle of spaceborne InSAR for DTM acquisition is similar to the one explained before for airborne InSAR (see Section 3.3.4). In contrast to airborne SAR sensors, the two antennas required can usually not be mounted on one platform due

3.4 Spaceborne DTM acquisition

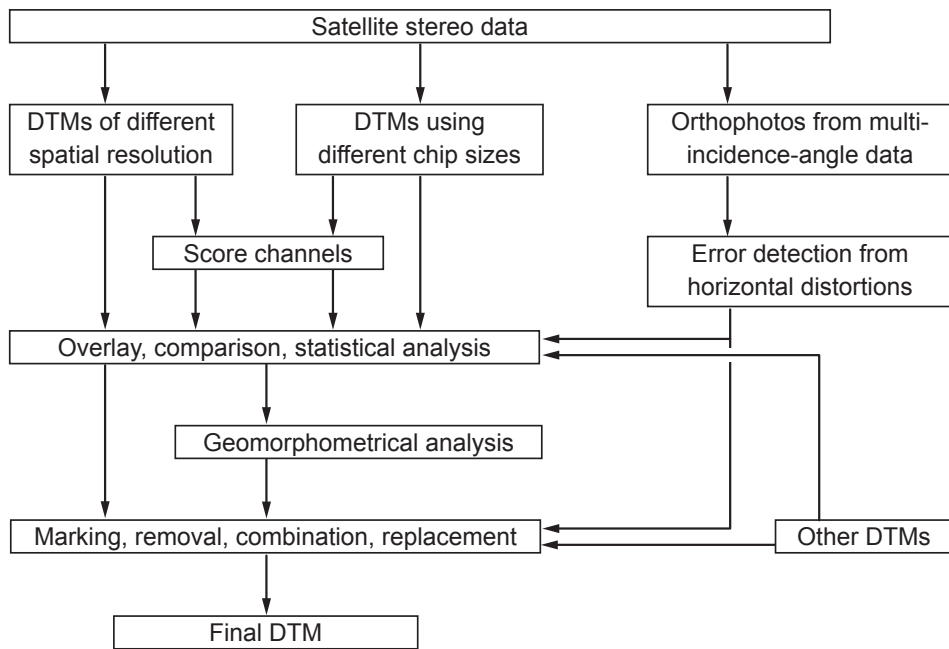


Fig. 3-21 Scheme of possible processing steps in order to detect severe errors and improve DTMs derived from satellite stereo.

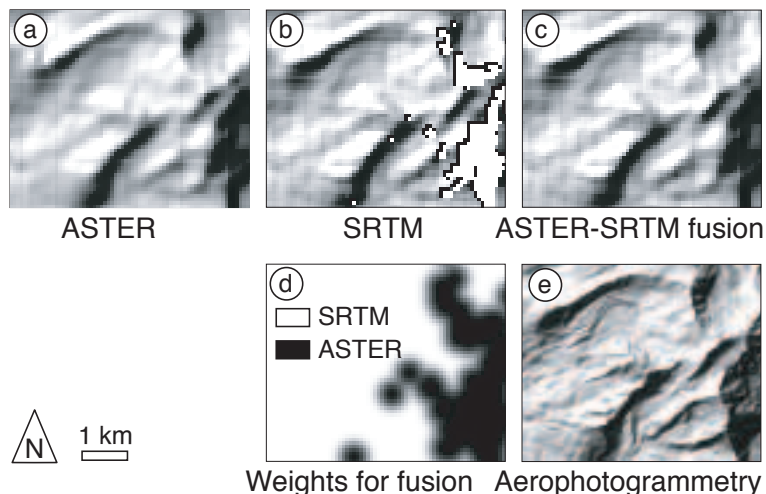


Fig. 3-22 Fusion between a DTM from ASTER stereo and SRTM. (a) hillshade of an ASTER DTM of the Gruben area, Swiss Alps, derived at 60 m resolution; (b) SRTM DTM with data gaps in white; (c) fusion between both DTMs; (d) fusion weights for filling the SRTM gaps with ASTER DTM data (white: SRTM is used, black: ASTER is used; grey: weight of SRTM elevation values with respect to ASTER DTM); (e) aerophotogrammetric DTM for comparison.

to technical restrictions relating to baseline length. Spaceborne InSAR has, therefore, to apply repeat-pass SAR imagery. In such cases, the interferometric phase is potentially affected by changes in terrain geometry and atmospheric conditions:

$$\phi = \frac{4\pi}{\lambda} B_{y'} + \frac{4\pi}{\lambda} \Delta y'_{displace} + \frac{4\pi}{\lambda} \Delta y'_{atmosphere} + \phi_{noise} \quad (3-11)$$

where

$\Delta y'_{displace}$ is the displacement of the scatterer in the line-of-sight direction.

An exception of such spaceborne repeat-pass InSAR is the Shuttle Radar Topographic Mission (SRTM, see below for details), and to some extent tandem missions with SAR sensors following each other within a short time interval and on similar tracks.

Application and accuracy

For DTM generation, terrain displacement disturbs the interferometric phase and thus the derived terrain elevation. The most crucial condition for applying repeat-pass InSAR is the phase preservation between the SAR images of an interferometric pair. This coherence is connected to changes in surface properties. It might be lost after seconds to minutes for dense vegetation under windy conditions, or after hours for melting snow (e.g. Pulliainen et al., 2003). For dry debris or rock that is not, or is only sparsely, vegetated – conditions frequently found in high mountains – coherence might be preserved or recovered over a period of months to years (e.g. Rott and Siegel, 1999; Kenyi and Kaufmann, 2001; Rignot et al., 2002; Strozzi et al., 2004). For cold snow, firn and ice, maximum coherence times lie in the range of weeks (e.g. Joughin et al., 1996; Engeset, 1999), for temperate ice and snow in the range of days (Rignot et al., 1996; Kelley et al., 1997; Joughin et al., 1999a; Strozzi et al., 2003a). Phase coherence is sensitive to changes in the dielectric surface and volume properties (Gens and van Genderen, 1996). Under glacial and periglacial conditions such variations are among other things due to high-frequency terrain destruction (e.g. local sliding and settlement) and changes in surface humidity from rainfall, snowfall, snow and ice-melt, or dew and hoarfrost (e.g. Moorman and Vachon, 1998). Interferometric coherence is also dependent on the signal polarisation (Stebler et al., 2002). Best results for DTM generation from spaceborne repeat-pass InSAR were usually achieved from the ERS 1/2 tandem mission with a minimal temporal baseline of 24 hours. The coherence sensitivity is also dependent on the wavelength used. The larger the wavelength, the more robust the coherence tends to be (e.g. Coltelli et al., 1996; Strozzi et al., 2004).

The spatial resolution and accuracy of DTMs from spaceborne InSAR lies in the order of metres to tens of metres (Renouard et al., 1995; Gens and van Genderen, 1996; Bindschadler, 1998; Sties et al., 2000; König et al., 2001; Crosetto, 2002; Stevens et al., 2003; Strozzi et al., 2003d). In contrast to airborne SAR, spaceborne SAR azimuth is restricted to the satellite track. Geometric influences such as shadow or layover that complicate DTM derivation can, therefore, be reduced only partially from combining ascending and descending orbits (e.g. Renouard et al., 1995; Toutin and Gray, 2000; Crosetto, 2002).

Shuttle Radar Topography Mission (SRTM)

The single-pass InSAR campaign SRTM of February 2000 provides a unique DTM for large sectors of the continents (60° N - 54° S, e.g. Van Zyl, 2001). The mission specifications lead one to expect a DTM resolution of several tens of metres with an absolute vertical accuracy of ± 16 m (LE90), a relative vertical accuracy of ± 6 m (LE90), and a horizontal positional accuracy of about ± 20 m (circular error, LE90) (Rabus et al., 2003). The SRTM included two SAR systems, one employing C-band SAR (5.6 cm wavelength, 225 km ground path width), the other X-band SAR (3.1 cm wavelength, 50 km ground path width). The C-band derived SRTM DTM is available in two spatial resolutions: the SRTM1 with 1 arcsecond (approximately 30 m) and the SRTM3 with 3 arcseconds (approximately 90 m). Vertical reference of these SRTM DTMs is the WGS84 EGM96 geoid.

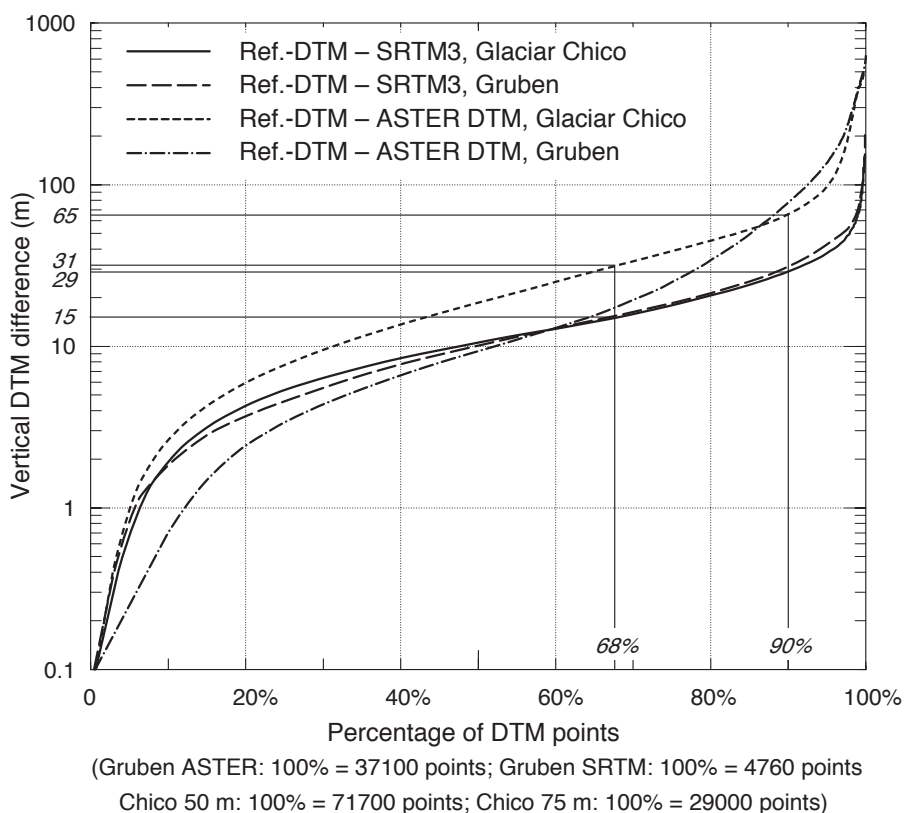


Fig. 3-23 Cumulative histograms of vertical deviations between aerophotogrammetric reference DTMs and ASTER or SRTM3 DTMs, respectively, for Glaciar Chico and Gruben. For Glaciar Chico, 68 % of the points have vertical deviations smaller than ± 15 m for the SRTM3 DTM, or smaller than ± 31 m for the ASTER DTM. For the 90 % level (LE90), the corresponding numbers are ± 29 m for SRTM3, and ± 65 m for ASTER.

Initial assessment of SRTM DTMs shows that the mission specifications were well fulfilled (Rignot et al., 2003; Sun et al., 2003). For the Gruben test site (see Sections 3.3.1 and 3.4.1), Strozzi et al. (2003d) compared the X-band derived SRTM DTM and the automatic aerophotogrammetric DTM that is also evaluated in Section 3.3.1. They obtained an average height difference of 7.2 m, a standard deviation of height difference of 36.2 m, and maximum errors of up to 285 m.

Here, the C-band SRTM3 DTM is evaluated for the Gruben and Glaciar Chico test sites (Fig. 1-2). For Gruben, vertical differences between the SRTM3 for February 2000 and an operator-measured aerophotogrammetric reference DTM for 1991 (see Sections 3.3.1 and 3.4.1) were calculated. Both DTMs were resampled to 75 m grid spacing beforehand. The average elevation difference obtained is -2.3 m, the standard deviation of the vertical differences is ± 20 m (RMS), and the minimum or maximum values are -193 m or +143 m, respectively (Figs. 3-23 and 3-24). The greatest errors or data gaps are found in the slopes facing east, which correspond to the back slopes of SAR illumination (see Strozzi et al., 2003d). In addition, an alternating pattern of too-high elevation values for the northern or north-western slopes and too-low values for the southern or south-eastern slopes suggests some error in horizontal position (see Strozzi et al., 2003d; Weidmann, 2004). For a subsection of the test area (Fig. 3-24) with moderate high-mountain topography (see also Fig. 3-17), the standard deviation of elevation differences is ± 12 m with minimum and maximum vertical deviations of -54 m and +41 m, respectively. The cumulative histogram in Figure 3-23 suggests that a DTM derived from ASTER L1B satellite stereo imagery (Section 3.4.1) is competitive with the SRTM3 DTM for

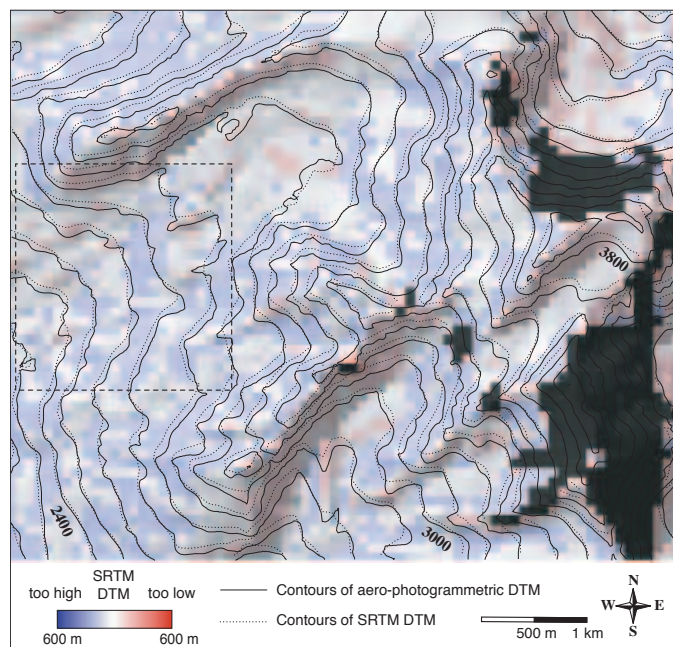


Fig. 3-24 Colour-coded elevation differences between an aerophotogrammetric reference DTM and the SRTM3 DTM, superimposed on a hillshade of the reference DTM for the Gruben area. Black areas indicate missing data in the SRTM3 DTM. The dashed rectangle marks a subset with more moderate topography (see text). The colour-coded elevation differences are displayed with a linear scale (100 m steps), but colours are also modulated from fusion with the hillshade (see Fig. 3-17).

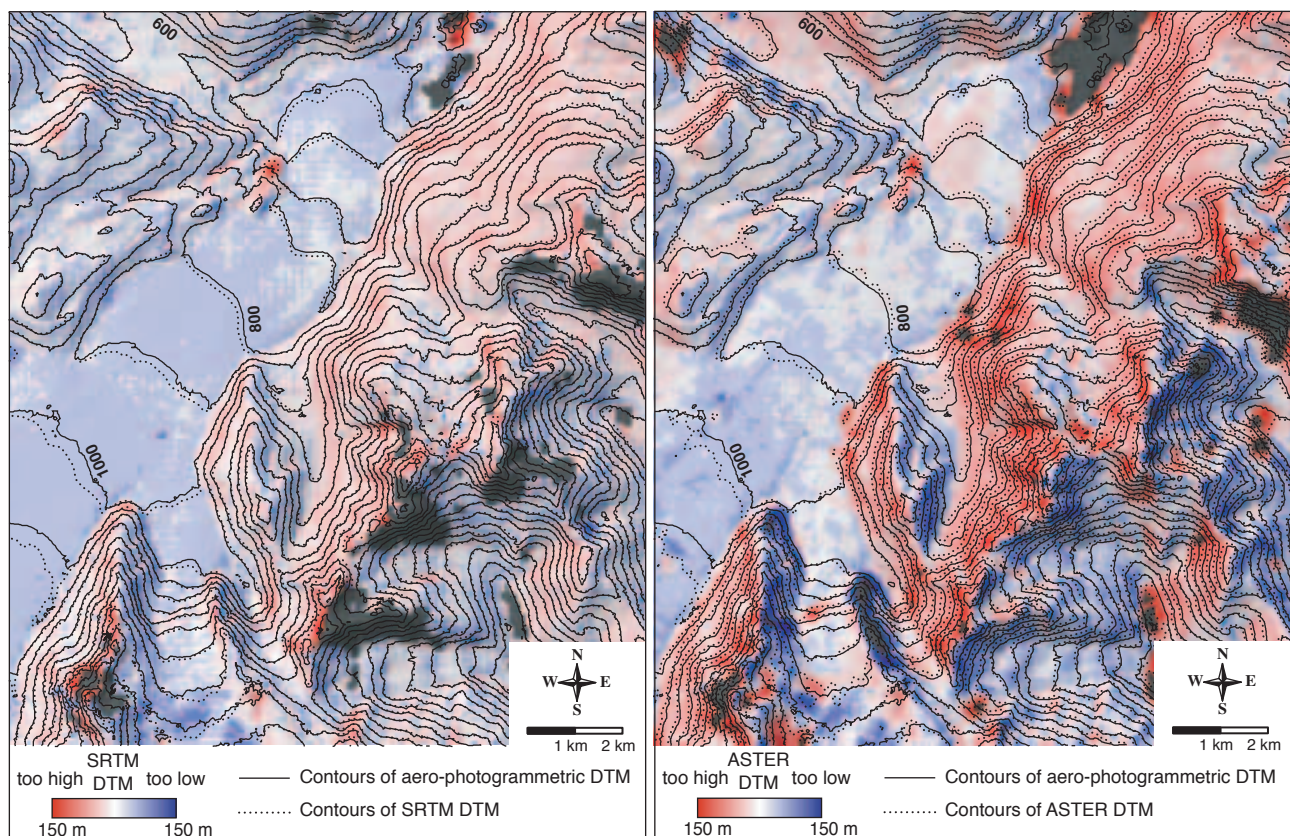


Fig. 3-25 Colour-coded elevation differences between an aerophotogrammetric reference DTM and the SRTM3 DTM (left) and an ASTER DTM (right). Colour brightness is modulated from a shaded relief of the reference DTM for Glaciar Chico. Black areas indicate missing data in the SRTM3 DTM (left), or deviations greater than ± 150 m for the ASTER DTM (right). The colour-coded elevation differences are displayed on a linear scale (20 m steps), but colours are also altered by hillshading. (See also Figs. 8.4 and 8.5).

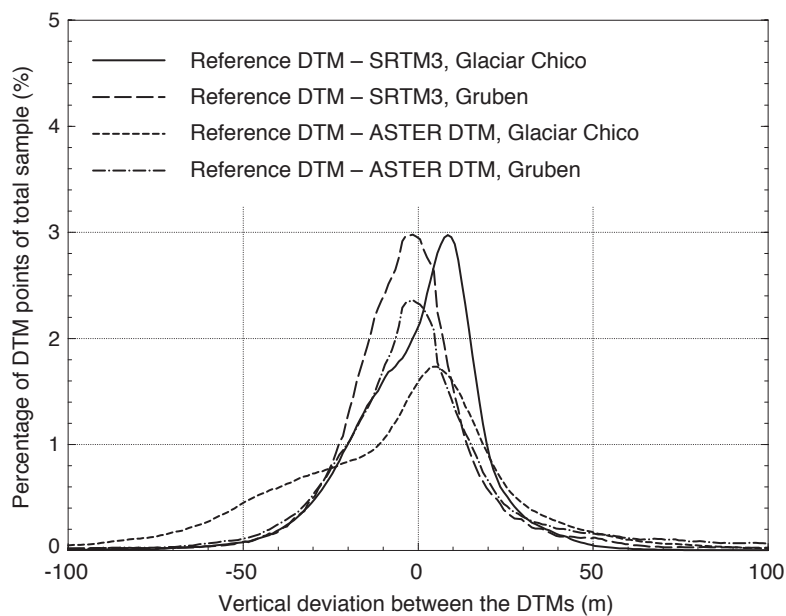


Fig. 3-26 Histograms of vertical deviations between aerophotogrammetric reference DTMs and ASTER or SRTM3 DTMs. Point density is given in percent of each individual DTM.

about 60–70 % of the points. The SRTM3 DTM, however, includes significantly fewer large errors.

For the terminus area of Glaciar Chico, Southern Patagonia Icefield (see Section 8.1), an automatically-derived photogrammetric DTM from airphotos of 1997 was compared to the SRTM3 DTM (Fig. 3-25 left) and an ASTER-derived DTM of 2001 (Fig. 3-25 right) (see also Kääb, 2005). The standard deviation for vertical differences between the aerophotogrammetric DTM and the ASTER DTM is ± 31 m (see Section 4.2.2), and the corresponding value for the SRTM3 DTM is ± 15 m with maximum deviations of up to 150 m. The cumulative histogram of vertical deviations Figure 3-23 reveals a better SRTM3 DTM compared to the ASTER DTM. At the acquisition time of the ASTER scene large sections of the terrain were snow-covered, which complicated the corresponding DTM generation (Fig. 8-3). The regular pattern of vertical deviations both for the SRTM and the ASTER DTM suggest horizontal offsets compared to the reference DTM (see Section 4.2).

Histograms of the vertical deviations between the aerophotogrammetric DTMs and the SRTM3 or ASTER DTMs studied in this section are given in Figure 3-26.

3.4.3 Other methods

Photoclinometry (also called 'shade-to-shape') can be used to convert image brightness values to surface slopes. Selected surface elevations have to be known in order to enable the surface slopes to be integrated along the illumination direction. This technique works best for small slopes, low Sun elevations and homogeneous surface cover (e.g. snow), conditions which are frequently found on ice sheets (Bindschadler, 1998). In this case, the method can be used to interpolate DTMs from single spot heights or elevation profiles, e.g. from satellite altimetry. The method works, in principle, for optical and SAR images (Toutin and Gray, 2000). The azimuthal terrain slope can be estimated also from the co-polarimetric signature recorded at a fully polarimetric SAR system (*polarimetry*), and the terrain surface then integrated similar to photoclinometry (Schuler et al., 1998; Toutin and Gray, 2000).

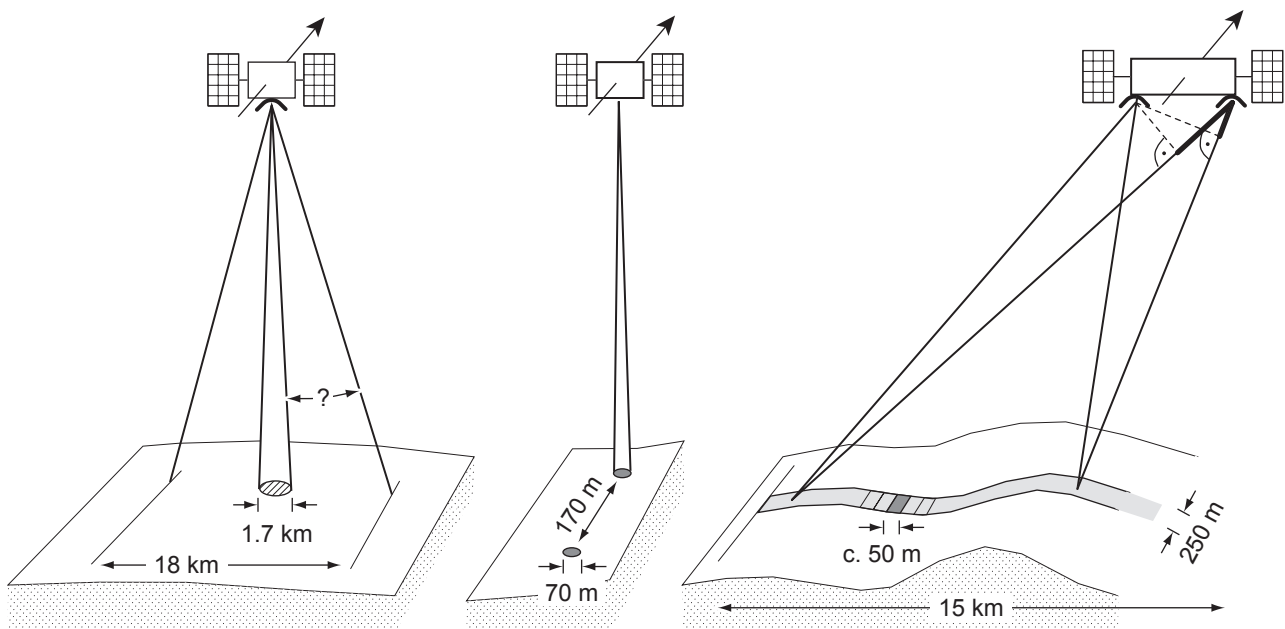


Fig. 3-27 Schemes of a spaceborne RADAR altimeter (left), LIDAR altimeter (middle), and interferometric RADAR altimeter (right). Numbers for footprint size and cross-track window approximately refer to the RA-2 onboard ENVISAT, the LIDAR altimeter onboard ICESAT, and the SIRAL instrument onboard CRYOSAT (meanwhile failed).

Satellite LIDAR and RADAR altimetry are not dealt with in detail in this work as they are not suitable (at the present time) for monitoring complex high-mountain terrain with sufficient resolution and accuracy (cf. Bindschadler, 1998; König et al., 2001). Both LIDAR and RADAR altimetry determine the terrain height from the travel time of a nadir-looking laser or microwave beam, respectively. The footprint of the RADAR altimeter is approximately 2 km in width (e.g. RA-2 aboard ENVISAT, Benveniste et al., 2001). The footprint ground location within the radar beam ground track of about 20 km cannot be measured. Such RADAR altimeters are thus not suitable for resolving rough terrain. Ground elevation accuracy is in the order of a decimetre for flat terrain and in the order of several metres for more complex terrain.

The LIDAR footprint is several tens of metres in size (e.g. 70 m for GLAS aboard ICESAT, Zwally and others, 2002). The along-track horizontal distance between footprints is about 170 m. Altimeter sensors cover for the most part only the nadir of their track, so that overlapping measurements or a spatial coverage are difficult to obtain, especially for lower latitudes. The satellite altimeter missions are designed for, among other things, the monitoring of ice sheets and sea ice, rather than for high-mountain terrain (e.g. Bamber et al., 1998; Davis et al., 2000; Stenøien and Bently, 2000).

The first RADAR altimeter which potentially is able to resolve also more undulated topography is of the type of the SAR Interferometric RADAR Altimeter (SIRAL) on board of the failed CRYOSAT. In its InSAR mode it uses two antennas to measure simultaneously the distance to ground and the incidence angle of the return signals (Fig. 3-27; cf. Fig. 3-11).

3.5 DTM evaluation and refinement by orthoimage overlay

For many applications, generated DTMs cannot be tested against existing reference DTMs. If, in such cases, imagery from different sensor positions is available (multi-incidence angle images), DTMs may be tested through the overlay of orthoimages generated from that image data. Such orthoimagery has to be computed from the DTM to be tested and from two (or more) source images taken from different sensor positions (e.g. Baltsavias, 1996; Aniello, 2003; Kääb, 2005). For a correct DTM, the two (or more) orthoprojections of corresponding image pixels perfectly overlap (Fig. 3-28). Vertical DTM errors, on the other hand, translate into horizontal shifts between the orthoprojected pixels of the source images (Fig. 3-28, Eq. 3-2). A DTM error is without effect in the case of nadir projection vectors. The horizontal projection shifts between the orthoimages from different source imagery can be visualized by change detection techniques (e.g. ratio images, Fig. 3-29; see also Section 6.3), or animation techniques (e.g. image flickering, Section 7.3; see also Section 8.3)(Kääb, 2005). For areas showing significant differences between the orthoimages, the underlying DTM may be flagged, masked out or improved.

For known projection geometry, the resulting planimetric differences may also be measured and re-projected in order to refine the underlying DTM (Norville, 1996; Kaufmann and Ladstädter, 2002; Georgopoulos and Skarlatos, 2003).

3.6 Digital terrain modelling

DTMs are necessary for a large number of tasks in remote sensing and geoinformatics, e.g. radiometric and geometric corrections (Sections 5.1 and 5.4.3), models (this section, and Section 12.4), multidimensional classification (Sections 6.2 and 6.4), visualization (Chapter 7), but also for understanding the terrain itself.

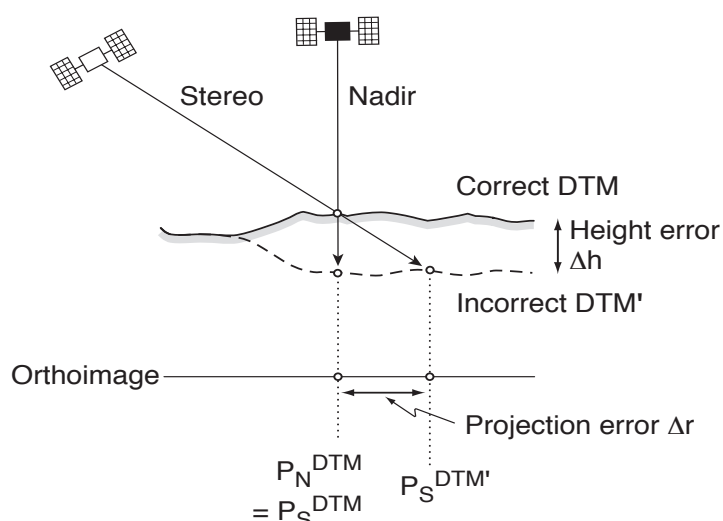


Fig. 3-28 Errors of the underlying DTM lead to horizontal distortions in orthoimages that are computed using this DTM. Such a distortion in the orthoprojection linearly depends on the vertical DTM error and on the look-angle of the original image. Thus, an identical DTM error causes different distortions in different orthoprojections.

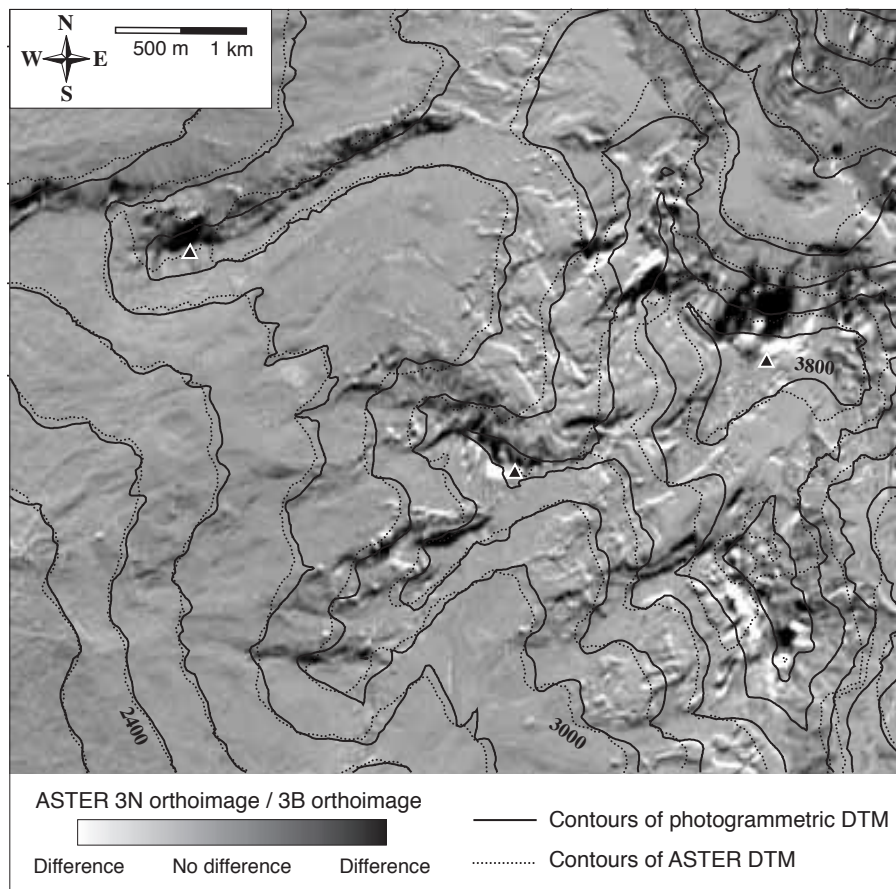


Fig. 3-29 Ratio image between two orthoimages of the Gruben area, computed from ASTER imagery. A DTM derived from ASTER L1B was used as the height source for both orthoprojections. One orthoimage was computed from the ASTER 3N nadir band, the other from the corresponding ASTER 3B back-looking band. The ratio-image reflects similar DTM errors compared to the ones found using a reference DTM (Figure 2.14). The multiangle orthoimage approach is an efficient method for qualitatively assessing DTMs where no reference data are available.

Quantitative terrain analysis based on DTMs (termed *geomorphometry*, *quantitative geomorphology*, or *digital terrain modelling*) involves

- local DTM derivatives,
- DTM residuals,
- hydro-geomorphological parameters,
- spatio-temporal dependencies,
- terrain classification, and
- complex process models or statistical models.

In addition to the elevation itself, the topographic parameters most often used for analyzing high-mountain terrain are *local DTM derivatives*: slope, aspect, flow direction, curvature, convexity and concavity (e.g. Guth, 1995; Wilson and Gallant, 2000). Such terrain attributes are already of great importance for many mountain applications (e.g. Etzelmüller, 2000; Bishop et al., 2001; Etzelmüller et al., 2001b; Mulders, 2001; Ødegård et al., 2004). Terrain slope and aspect, for instance, influence the incoming potential short-wave radiation (e.g. Hoelzle, 1992). Slope is a crucial parameter for assessing and modelling terrain instabilities (e.g. Van Westen, 1994; Mantovani et al., 1996; Duan and Grant, 2000). In principle, flow direction can be applied to many mass transport processes. In addition to the direct use of local DTM derivatives, such

derivatives are also inferred in DTM classification (see below), or integrated in multidimensional data merging (Chapter 6).

Analysis of *DTM residuals* includes elevation means and ranges, difference and deviation from mean elevation, standard deviation, percentile, or others (Wilson and Gallant, 2000). These attributes are usually computed within rectangular or circular windows. The resulting values directly represent glaciological parameters (e.g. Bishop et al., 2001; Kääb et al., 2002b), or are applied to characterizing terrain roughness (e.g. Van der Veen et al., 1998; Etzelmüller, 2000; Bishop et al., 2001).

For large relief, water flow and other flow-type processes such as debris flows or avalanches are fundamental processes. Thus, *hydro-geomorphological DTM analyses* are of special importance in mountain research. Corresponding computations involve drainage analyses such as flow accumulation, catchment area, drainage basin delineation, flow width and flow path length (e.g. Nogami, 1995; Pike, 2000; Wilson and Gallant, 2000). Both *upslope* (contributing area) and *downslope* (affected area) algorithms are applied. Flow modelling is of major importance, in particular for hazard assessment. Lake outburst floods and related debris flows can be modelled (Huggel et al., 2002; Huggel et al., 2003c). Flow accumulation and catchment area analyses aid in the detection of potential starting zones and in the modelling of periglacial debris flows (Dikau et al., 1996b; Zimmermann et al., 1997; Gamma, 2000; Oswald, 2001). Hydrological flow models can be modified to simulate, for instance, ice avalanches or rockfall (e.g. Krummenacher and Keusen, 1997; Meissl, 1998; Salzmann et al., 2004).

The investigation of *spatio-temporal dependencies* in DTMs is gaining importance as a means of improving the understanding of landscape. Related analyses include, in particular, the questions of topographic scaling. Terrain self-similarity may be described by semi-variograms, fractal dimensions or wavelets applied to DTMs or DTM derivatives (e.g. Evans and McClean, 1995; Bishop et al., 1998). The fractal structure that is often observed in the context of water runoff networks and related landscape forms may be attributed to self-organization processes. The according concept of self-organized criticality relates spatio-temporal chaos and process periodicity to fractal scaling in space and time (Phillips, 1995; Pike, 2000) (cf. Section 2.3).

Classification techniques similar to those applied to spectral data from remote sensing (Section 5.3) are also applied to DTMs in order to delineate and characterize terrain units. In this process, the included data sets may be the terrain elevation itself, or the local DTM derivatives, DTM residuals, or hydro-geomorphological attributes (e.g. Dikau et al., 1995; Brändli, 1996; Walsh et al., 1998; Schmidt and Dikau, 1999; Bishop et al., 2001; Etzelmüller et al., 2001b). Furthermore, scale parameters play an important role in terrain classification. Similar to spectral classification, the applied techniques range from algebraic expressions, to likelihood classification, to artificial neural networks (see Section 5.4 for more details). Provided that suitable DTMs are available, such terrain classification solely based on height information is already of great value for different tasks in mountain research, for instance, for landslide detection or geomorphological mapping. However, DTMs acquire even more importance when they are merged with other geometric, spectral and temporal domain data (e.g. Chorowicz et al., 1995; Dikau et al., 1996a) (Chapter 5).

Process-based or *statistical models* significantly extend the applicability of DTMs. In contrast to the primary DTM derivatives and classifications mentioned above, such second-order DTM products may include spatio-temporal natural processes (e.g. Richards et al., 1995) and, to some extent, physical laws. Examples of such models

which are important for mountain research include wetness indices, stream-power indices, radiation models (Funk and Hoelzle, 1992; Moore, 1992), ice-flow models (Etzelmüller and Björnsson, 2000), flood and debris-flow models (Gamma, 2000; Huggel et al., 2002; Huggel et al., 2003c), avalanche models (Gruber, 2001; Salzmann, 2002; Salzmann et al., 2004), and permafrost models (Hoelzle, 1992; Gruber, 2000; Etzelmüller et al., 2001a). Respective results may also be inferred into a DTM classification (see above paragraph) or combined within a multidimensional merger (see Chapter 5).

For further model examples see Section 12.4.

3.7 Conclusions and perspectives for DTM acquisition

Terrestrial methods

Ground-based methods have to be applied for measuring DTMs with a millimetre-to-centimetre degree of accuracy. This usually refers to differential satellite-based surveying, polar surveying, or – increasingly – terrestrial laserscanning. The latter is especially promising for monitoring changes in the geometry of small terrain sections (e.g. erosion, debris accumulation, rockfall, creep, etc.). Since the method is not restricted to a small sample of measuring points, changes can be detected virtually area-wide (Paar et al., 2001; Bauer et al., 2003). In particular, terrestrial laserscanning is able to provide new insights in the geometry and related changes of steep ice/rock walls where the application of vertical air- and spaceborne techniques is often limited.

Airborne methods

Airborne methods provide DTMs with spatial resolutions of up to several metres, and with a vertical accuracy in the order of several centimetres to decimetres (Table 3-1). If the DTMs are derived from image data (i.e. through photogrammetric methods in their widest definition) the applied imagery can also be used for further analyses and products such as interpretation, classification, orthoproduction, or terrain displacement measurements.

Photogrammetry. Photogrammetric methods based on optical imagery are well established and robust. However, they break down when there is no optical contrast, for instance, on fresh snow. Direct digital data acquisition, e.g. by CCD array cameras or airborne pushbroom sensors, will gain in importance. The fully digital data flow allows for DTM (and orthoimage) delivery in a short time. If such a sensor also provides multispectral data, automatic image-analysis techniques become even more valuable.

Laserscanning. If there is a low optical terrain contrast (e.g. snow or firn cover) and if only a DTM is needed, laserprofiling or -scanning is preferable to passive optical methods. In contrast to photogrammetric DTM generation, laserscanning or -profiling works especially well on snow and firn due to their high reflectivity. It is, among other things, depending on the flying height above ground and the applied laser power if the laser reflection is strong enough to allow for DTM measurement. Most airborne LIDAR sensors have to be flown relatively low to the ground because laser power is limited due to a number of reasons. Thus, terrain with significant elevation differences is not yet accessible for area-wide airborne LIDAR. However, this problem is currently being resolved as advances are being made in optoelectronics and signal-processing, so that flying heights above ground of up to

several kilometres appear feasible. Furthermore, recording and analyzing the amplitude and phase of the laser signal support terrain characterization (Lutz et al., 2003), or improve the accuracy of the laser distance measurement. Multispectral laser systems employing two or more light frequencies could help to improve the range measurement accuracy and the interpretation of the ground characteristics (Zwally and others, 2002).

Synthetic aperture radar. To date, only scant experience has been made with airborne interferometric SAR applications for DTM generation in high mountains. The problems posed by foreshortening, layover and radar shadow require overlapping overflights with different look-directions. Narrow valleys cannot be covered due to the side-looking character of InSAR sensors. The all-weather capability of SAR sensors may be of minor advantage in rough high mountains when visual flight conditions are required anyway for the aeroplane the sensor is mounted on. However, from a technical point of view airborne InSAR might well play an increasing role in high mountain research. Beside DTM generation, the ground characterization from multifrequency and multipolarization SAR systems might in particular gain importance (Barmettler et al., 2004; Stebler et al., 2004).

Combination of aerial photography and laserscanning. For future glaciological monitoring tasks in high mountains the author favours a combination or even integration of digital photogrammetry and laserscanning, possibly acquired during the same overflight. Optical imagery is required for interpretation and visualization, as well as for products such as orthoimages and terrain displacements. Nevertheless,

Table 3-1 Summary of DTM accuracy assessments in this volume. All numbers are given in meters and are approximately. Exact values vary with DTM generation parameters.

Method	Site (Section)	Min. elev.	Max. elev.	Std. dev.	Max. neg. DTM err.	Max. pos. DTM err.	RMS DTM err.	Image pixel
Digit. aero- photogr.	Muragl	2480	2840	±75	-16	9	±1.4	0.2
Digit. aero- photogr.	Gruben	1990	4000	±400	-95	105	±8	0.5
ASTER stereo	Gruben	1990	4000	±400	-230	510	±68	15
ASTER stereo	Gruben	2270	3000	±165	c. -100	c. 100	±19	15
ASTER stereo	Gries	1850	3370	±265	c. -500	c. 500	±35	15
ASTER stereo	Chico	70	2400	±435	c. -300	c. 300	±31	15
SRTM	Gruben	1990	4000	±400	-193	143	±20	
SRTM	Gruben	2270	3000	±165	-54	41	±12	
SRTM	Chico	70	2400	±435	c. -150	c. 150	±15	

laserscanning is able to provide DTMs with higher resolution and accuracy (Baltsavias, 1999). Technically, the two systems, and thus their advantages, can be combined (Kraus, 2002).

Spaceborne methods

Satellite optical stereo. In principle, along-track satellite stereo is preferable to cross-track stereo due to its simultaneous stereo channel acquisition. However, a combination of both methods would reduce the effects of perspective distortion or hidden terrain sectors. For along-track stereo in middle and low latitudes, mainly northern or southern slopes are affected from perspective distortion; for cross-track stereo eastern or western slopes are affected. A combination of both methods could be achieved for selected terrain sectors by pointable along-track stereo-sensors, thus also allowing for combined along- and cross-track stereo. Such a procedure is, for instance, possible for ASTER equipped with a back-looking along-track stereo which can be pointed cross-track by 24°. An alternative is given by the combination of overlapping imagery from different optical sensors with comparable spatial resolution (e.g. SPOT, Landsat ETM+ pan, ASTER, IRS) and application of general photogrammetric multi-image techniques (Maas, 1997; Grün and Zhang, 2002; Zhang and Grün, 2004).

The problem of distorted or even hidden terrain parts in along-track stereo channels can be partially overcome by introducing two stereo channels, i.e. a forward- and a backward-looking one. At present, such a procedure can be simulated from ASTER data taken during (local) summer in high latitudes where both the ascending and descending orbit cover the same target during daylight. One nadir, one or two along-track (back- and/or forward), and one or two cross-track sensors (left and/or right) can be run simultaneously on one platform (cf. multiangle imaging spectroradiometer, MISR, Zong et al., 2002). A combination of two back- (or forward-) looking stereo-sensors with different off-nadir angles could optimize the merits of good stereo-ratio (i.e. large off-nadir angle) and small distortions (i.e. small off-nadir angle).

Synthetic aperture radar: The major disadvantage of VNIR and SWIR satellite data that they rely on cloud-free daytime conditions is overcome by the all-weather capabilities of active microwave sensors. In that respect, satellite InSAR has clear advantages for DTM generation where no further optical information is needed. In addition, SAR as an active sensor does not depend on optical ground contrast. A combination of SAR data from ascending and descending orbits enables the effects from layover or shadow to be minimized. In the future, combined strategies for DTM generation from satellite optical stereo and InSAR might gain importance in glaciology (see Section 8.3). Due to the small coherence times for temperate snow and ice, repeat-pass InSAR usually requires tandem missions.

Shuttle Radar Topography Mission: Both satellite stereo and InSAR provide DTMs with a comparable spatial resolution of several 10 m, and a similar order for accuracy. The SRTM, and cross-track stereo from 1m-resolution-class optical sensors such as Ikonos or QuickBird (e.g. Toutin, 2001; Fraser et al., 2002; Eisenbeiss et al., 2004) are currently among the most accurate civil systems for spaceborne DTM generation. The SRTM DTM, indeed, represents a “breakthrough” (Van Zyl, 2001) or “new class of digital elevation models” (Rabus et al., 2003) where it is available. SRTM DTMs also have specific problems for high-mountain topography, but show considerably smaller gross errors compared to, for instance, ASTER-derived DTMs. Since ASTER DTMs seem competitive to SRTM3 DTMs (approximately 90 m spatial resolution) for moderate high-mountain topography, fusion or merging of both data

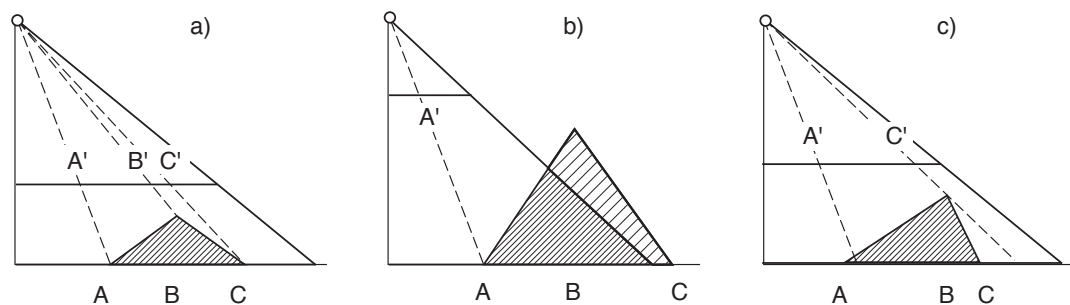


Fig. 3-30 Typical problems relating to optical sensors in high-mountain relief. Left: perspective distortion as depending on terrain slope relative to the sensor. Middle: cut-off of terrain parts due to low flying height, and/or small focal length, respectively. Right: Optical shadow for steep terrain directed away from the sensor.

sets might gain importance (see Section 8.3). Even if a SRTM DTM is not sufficient for a specific application, it is still an invaluable source of first-order DTMs to be refined by other methods (e.g. Section 3.5).

Satellite altimetry. Satellite LIDAR or RADAR altimetry is not likely to become a feasible tool for high-mountain relief in the near future due to their large footprints and/or large distances between individual tracks and the subsequent small profile density. It might, however, turn out that new LIDAR altimeters such as GLASS aboard ICESAT or SIRAL (first planned for the failed CRYOSAT) provide some useful additional information on thickness changes for large glaciers, ice caps and ice fields, although they are mainly designed for ice sheets.

Sensor-specific problems for high-mountain applications

Figures 3-30, 3-31 and 3-32 summarize typical problems relating to high-mountain applications for optical and SAR sensor types.

DTM processing

DTM uncertainty and errors. Digital terrain modelling will increasingly have to consider DTM uncertainty and errors, and their propagation into further DTM products. The increasing number of available DTMs with different characteristics, and the increasing number of applications utilizing DTMs, makes further efforts necessary for characterizing and modelling DTM uncertainty. The applied DTM analysis tools, on the other hand, will have to be able to cope with uncertainty and error propagation, and reflect these in their output (Gyasi-Agyei et al., 1995; Etzelmüller, 2000; Wechsler, 2000).

DTM compression and representation. New airborne sensors, in particular laserscanning or digital cameras, are able to provide DTMs with a resolution and speed which exceeds the currently available storage and processing capabilities. Advanced methods for DTM compression and DTM representation have, therefore, to be further developed (e.g. Briese and Kraus, 2003; Lenk, 2003). Accordingly, DTM analysis algorithms, which for the most part are based on raster and contour data at present, have to be adapted (e.g. Weibel and Brändli, 1995; Tucker et al., 2001).

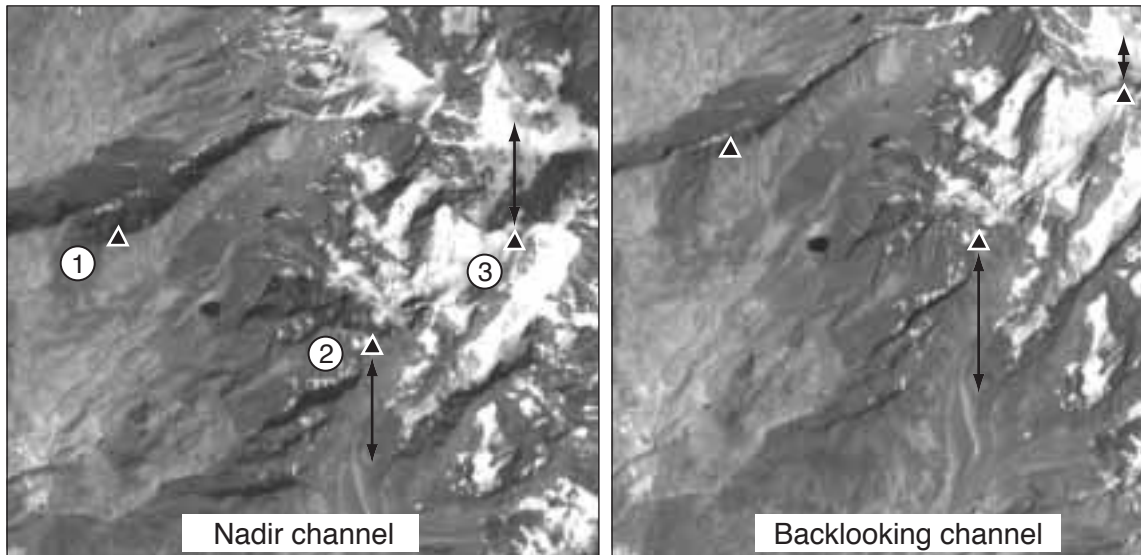


Fig. 3-31 ASTER 3N nadir band (left) and 3B back-looking band (right) of the Gruben area, Swiss Alps. ASTER daytime data are taken during the descending orbit, i.e. the 3B band is north-directed. The slope north of point 1 is totally hidden in the 3B image. On the southern slope at point 2, the distance to a glacier tongue (arrow) is strongly extended in the 3B image, and viceversa for the northern slope at point 3.

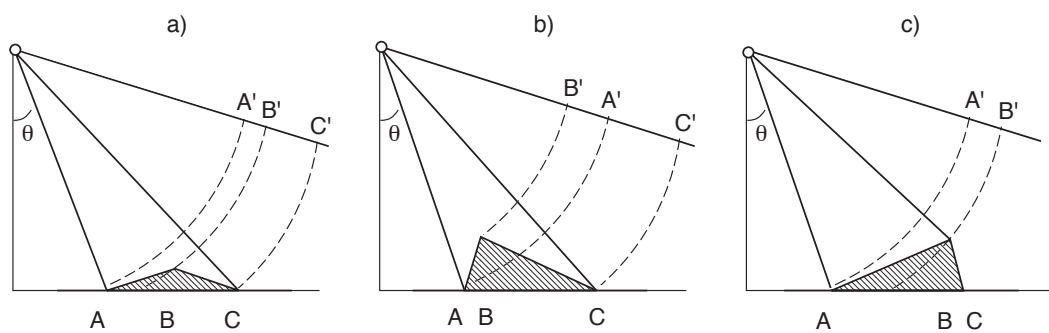


Fig. 3-32 Typical problems relating to SAR sensors in high mountains. Left: foreshortening from perspective distortion. Middle: layover due to first radar-signal return from elevated terrain parts. Right: radar shadow for steep terrain directed away from the sensor.

4.1 Displacements and elevation changes

As can be seen from the kinematic boundary condition at the surface (Eq. 2-1 and Fig. 2-1), the *change in terrain elevation* $\partial z^s / \partial t$ and the vertical component v_z^s of the *three-dimensional displacement* $\mathbf{v}^s = (v_x^s, v_y^s, v_z^s)^T$ of an individual particle on the surface describe different kinematic quantities. A change in elevation at a defined terrain position may originate from mass balance, three-dimensional straining and/or mass advection. The latter is a function of terrain displacement and geometry. From Equations 2-1 to 2-5 it becomes clear that a full examination of the kinetics of terrain requires information on both the elevation changes and the horizontal displacements. Changes in elevation are usually detected as differences between DTMs.

Terrain displacements can be determined by different methods. These provide one or more components of the three-dimensional velocity vector:

- vertical differences between multitemporal DTMs (Section 4.2),
- qualitative analysis of movements (Section 4.3),
- digital matching of repeat optical imagery (Section 4.4),
- differential SAR interferometry (DInSAR) (Section 4.5),
- repeat terrestrial and satellite geodesy (Section 4.6),
- analogue and analytical photogrammetric methods (Section 4.6),
- DTM matching (Section 4.6),
- terrestrial SAR (Section 4.6), and
- mechanical methods (Section 4.6).

The first four methods are described in more detail in the ensuing sections.

4.2 Vertical DTM differences

The differences between repeat (multitemporal) DTMs reveal the change in elevation between the corresponding times of data acquisition. To minimize vertical shifts between the multitemporal datasets that are not related to actual terrain changes, these may be corrected using stable terrain sectors. In the case where photogrammetric techniques are applied even better results are achieved when all imagery used is included in one multitemporal bundle adjustment before deriving the DTMs (Section 3.3.1) (Kääb and Vollmer, 2000).

Examples of elevation changes for glacial, peri- and paraglacial phenomena are given in Sections 8.1, 8.5, 9.4, Chapter 10, and Fig 12-4. See also Section 12.2.6. Elevation changes can also be directly measured by differential InSAR (Section 4.5).

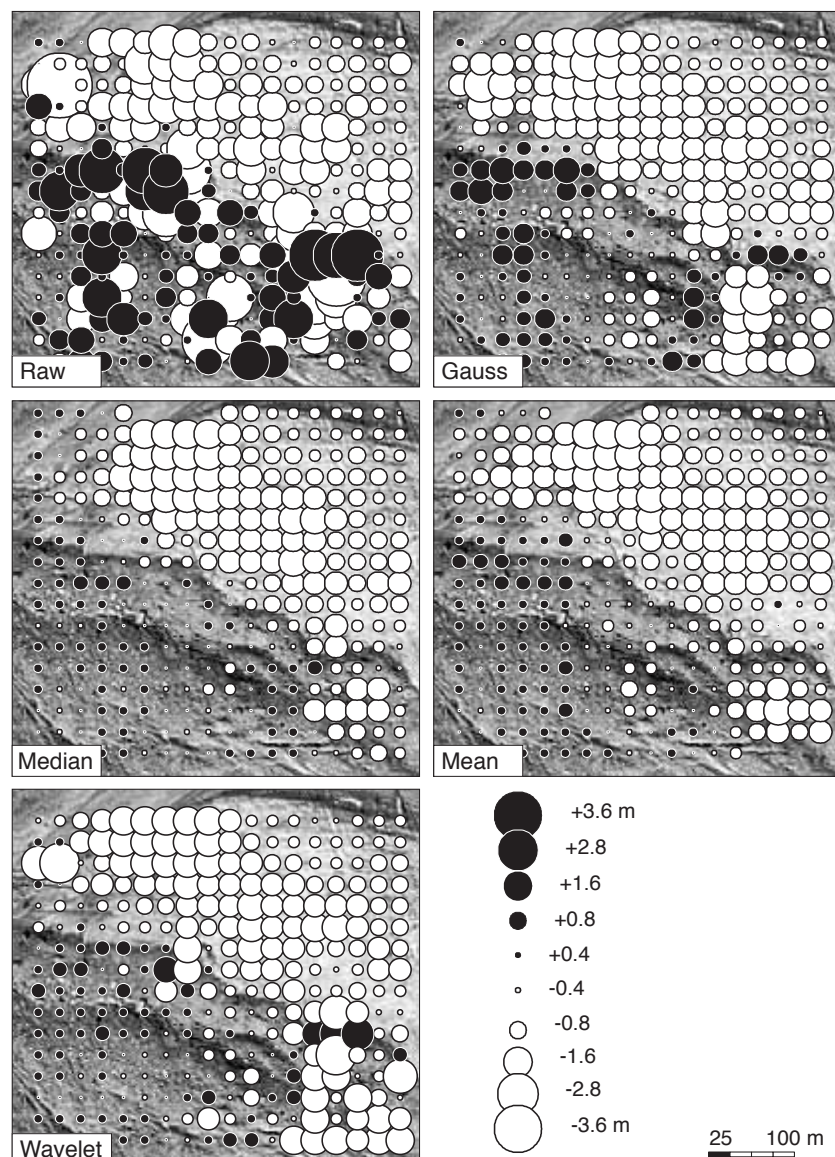


Fig. 4-1 Elevation differences 1991–1992 on a section of Gruben glacier, Swiss Alps. Upper left: raw elevation differences from two raster DTMs; upper right: filtered by a 3×3 Gaussian filter; middle left: filtered by a 3×3 median filter; middle right: filtered by a 3×3 mean filter; lower left: de-noised after decomposition by a Meyer wavelet. The choice of the filter applied strongly depends on the intended further data application. The raw data, for instance, might be too noisy in order to allow identification of overall trends. A median filter, on the other hand, might remove important high-frequency signals. The noise from elevation differences is significantly slighter on the smooth debris-free glacier surface to the upper right compared to the debris-covered ice with rough micro-topography.

4.2.1 Filtering

When two multitemporal DTMs represent independent measurements, the RMS of an individual elevation difference Δh is $RMS_{\Delta h}^2 = RMS_{h1}^2 + RMS_{h2}^2$, i.e. the resulting field of elevation differences is more strongly affected by noise than the individual DTMs (Etzelmüller, 2000). For glaciers or ice-rich permafrost, a smooth field of elevation differences can often be expected due to dynamic coherence and thermal inertia. It might, therefore, be useful to apply a low-pass filter to the resulting differences. A median filter, for instance, is able to eliminate single outliers. A Gaussian filter smooths the obtained result field without disregarding individual values (Fig. 4-1) (Kääb, 1996b).

A group of other methods filters the data in the frequency space after applying Fourier or Wavelet transformations to it (Fig. 4-1). The Wiener filter, for instance, results in the cutoff of wavelengths above a certain threshold in the Fourier space. The threshold is estimated from the power spectrum (e.g. Vaseghi, 1996; Kääb et al., 1997; Gudmundsson and Bauder, 1999). The filters may also be applied to data other than DTM differences such as velocity fields. De-noising or other filtering in the frequency space offers various possibilities to adjust the filter to the data characteristics and analysis purpose. The lower left panel in Figure 4-1 shows the results of only one possible parameter set for one possible Wavelet.

4.2.2 DTM matching

If the signal-to-noise ratio is insufficient in order to determine the spatial variation of DTM differences at a reliable level, it might still be possible to estimate the mean elevation difference for a larger terrain section. For that purpose it has to be assumed or to be assured by adjustment measures that the error term in the individual DTM differences contains only a random component. Repeat DTMs might have systematic differences, in particular if they originate from different sensors or different orientation procedures. Systematic error terms such as vertical and horizontal shifts between the DTMs have to be subtracted, or terms of higher order such as vertical and horizontal scales or rotations, can be estimated from comparing the elevation of stable terrain through matching techniques (see below). The DTM(s) can then be corrected by, for instance, simple shifts or a vertical 1D and a horizontal 2D Helmert transformation, both constructed from the DTM residuals (cf. Pilgrim, 1996a; Pilgrim, 1996b; Li et al., 2001; Mitchell et al., 2002; Schenk et al., 2002; Berthier et al., 2004; Weidmann, 2004). After Fourier or Wavelet transformations of the DTM differences, the wavelength cutoff-threshold can be chosen large enough that only signals concerning, for instance, the entire glacier width remain in the filtered data set.

Below, three possibilities for correcting/shifting DTMs to be compared are discussed in more detail:

- DTM shift from cross-correlation
- DTM shift from statistical adjustment
- numerical correction of DTM differences

The first two approaches are applied beforehand DTM subtraction, the third is applied to the DTM differences after subtraction.

DTM shift from cross-correlation

Figure 4-2 shows the residual vectors from matching the SRTM3 DTM and an ASTER DTM onto an aerophotogrammetric reference DTM from 1997. For DTM and site description see Sections 3.4.2 and 8.1, and Figures 3-25, 8-2 and 8-3. For the results depicted in Figure 4-2 quadratic DTM sections of 750 m size were matched on the reference DTM using a procedure similar to Equation 4-2 (Weidmann, 2004). Subpixel accuracy was obtained by constructing a polynomial surface for each grid point through the individual correlation coefficients and interpolating the position of the maximum correlation (see also Sections 4.4 and 4.6). When matching the entire SRTM3 or ASTER DTM for the Glaciar Chico tongue as one block (10×12 km) on the reference DTM average offsets of $dx = -13$ m and $dy = -29$ m result for the SRTM DTM, and $dx = +85$ m and $dy = +30$ m for the ASTER DTM. After correcting the DTMs by these shifts the RMS of the DTM deviations compared to the reference DTM become about 10% smaller for both the SRTM and the ASTER

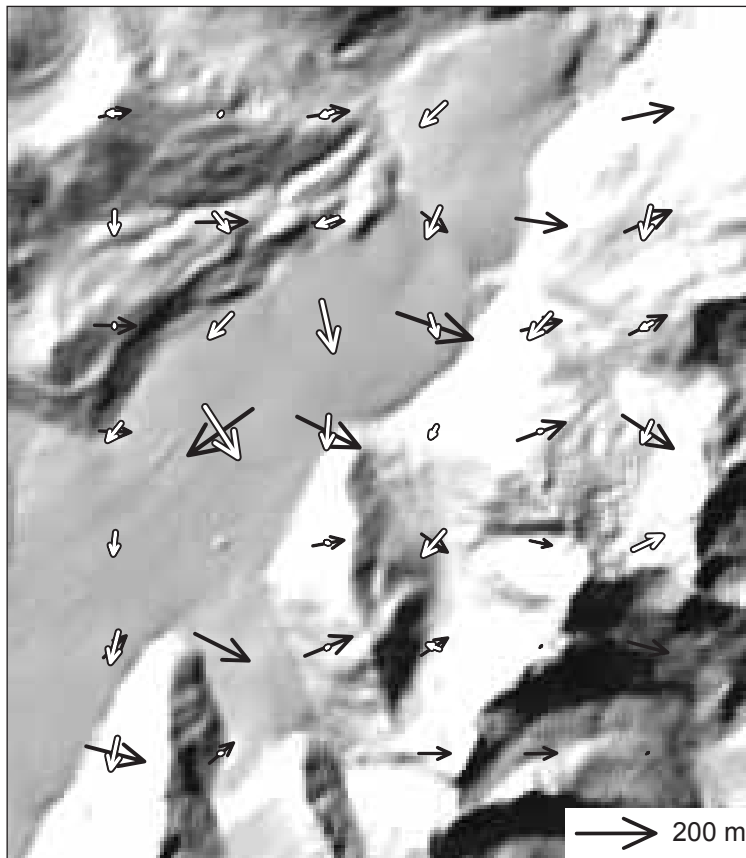


Fig. 4-2 Horizontal residuals from matching the SRTM3 DTM (white arrows) and an ASTER DTM (black arrows) onto an aerophotogrammetric reference DTM. Glaciar Chico. Matching grid width used was 1500 m, matching chip size was 750 m. For the flat glacier obvious mismatches occur due to missing relief contrast. No residual vectors are available for the SRTM DTM in the lower right section due to data gaps.

DTM. Figure 3-25 (right) shows the vertical DTM differences without the above shift applied. Figure 8-3 shows ice thickness changes derived from aerophotogrammetry and ASTER data, both using the original and the shifted ASTER DEM according to the cross-correlation.

Alternatively to cross-correlation, least-squares matching can be applied.

DTM shift from statistical adjustment

Figure 4-3 shows for the same DTMs as in the above paragraph, that the vertical deviations between the aero-photogrammetric DTM from 1997 and the ASTER DTM from 2001 are to a significant extent dependent from the terrain aspect with largest vertical deviations to the East and West (upper left panel). At the same time the vertical deviations show a clear positive dependency from slope α (upper right panel). A linear regression gives $|\Delta h| = 9.2 + 64 \sin \alpha$, or $|\Delta h| = 10.0 + 1.03 \alpha^\circ$. Both, the sinusoidal dependency of height differences from terrain aspect and the dependency from slope suggest a shift between both DTMs. The dependency between a height error ∂h , on the one hand, and an uniform vertical shift ∂s_z and horizontal shift ∂s_{xy} , on the other hand, is (Fig. 4-4):

$$\partial h = (\partial |\mathbf{s}| \cdot \cos(Az_s - \beta)) \cdot \tan \alpha + \partial s_z \quad (4-1)$$

with $\mathbf{s} = (s_x, s_y, s_z)$: shift vector, Az_s : Azimuth of shift vector, α : terrain slope, and β : terrain aspect.

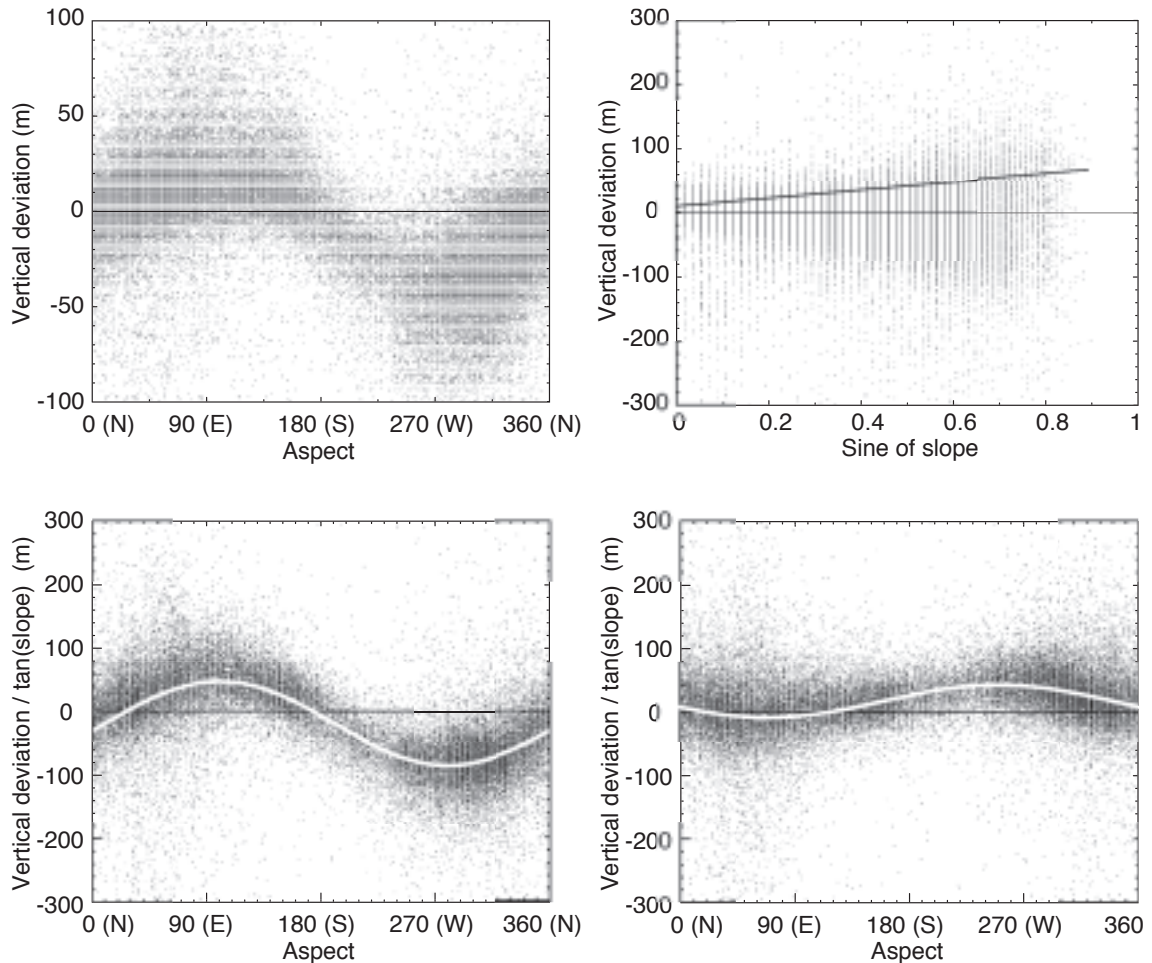


Fig. 4-3 Scatter plots of vertical deviations between an aero-photogrammetric DTM from 1997 and an ASTER DTM from 2001, tongue of Glaciar Chico (cf. Fig. 3-25, Section 3.4.1, Fig. 4-2, Section 8.1). Upper left: Vertical deviations between the two DTMs as a function of terrain aspect. Upper right: Vertical deviations between the two DTMs as a function of the sine of terrain slope. The regression line is computed for the absolute values of the vertical differences $|\Delta h|$. Lower panels: Values of $\Delta h/\tan(\alpha)$ as a function of terrain aspect; left: uncorrected DTMs, right: ASTER DTM shifted. The white lines are fits of the form $y=a+b\cdot\cos(\alpha+c)$. (Cf. Equation 4-1).

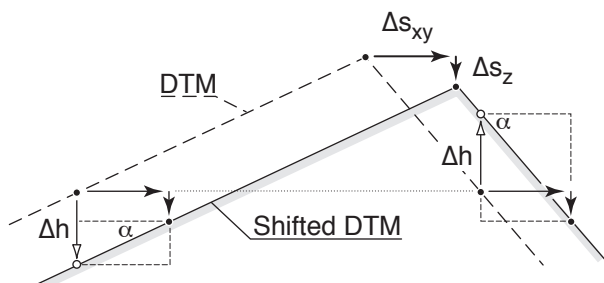


Fig. 4-4 Height errors between two DTMs due to horizontal and vertical shifts.

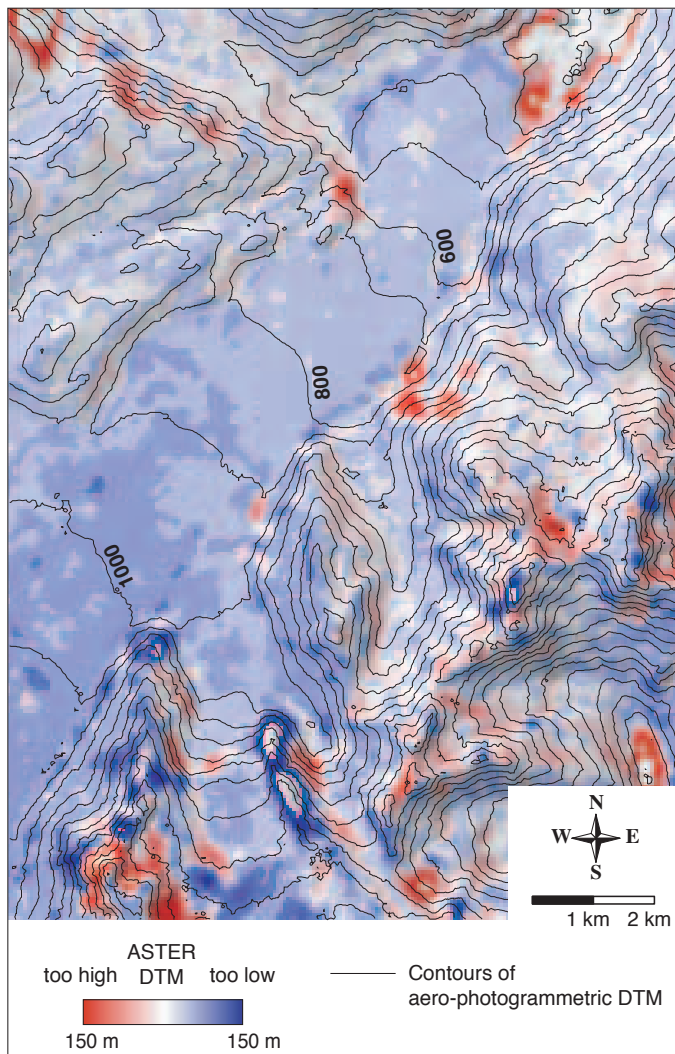


Fig. 4-5 Vertical deviations between an aerophotogrammetric DTM from 1997 and an ASTER DTM from 2001 after initial correction of the ASTER DTM for a horizontal and vertical shift. Glaciar Chico. The figure depicts a slightly smaller terrain section than Figure 3-25 (right), which shows the raw, un-shifted DTM differences. In addition, the vertical differences were smoothed by an 3×3 average filter. (Cf. Figs 3-25 and 4-3).

The length of the shift vector $|\mathbf{s}|$ and its azimuth $A_{\mathbf{z}_s}$ can, hence, be estimated from a cosine fit through the values $\Delta h / \tan(\alpha)$ plotted against terrain aspect (Fig. 4-3, lower left panel). Alternatively, a least-square adjustment can be performed for estimating the unknowns $|\mathbf{s}|$, $A_{\mathbf{z}_s}$ and ∂s_z from the vertical deviations Δh between two DTMs using Equation (4-1). In contrast to the above cross-correlation approach, the approach of statistical adjustment does not directly provide the final shift values between the DTMs. Rather, it has to be applied iteratively, because the vertical deviations have to be computed newly after each DTM-shift and the adjustment has to be repeated using the new values for Δh .

Figure 4-3, lower right panel, shows the residuals of the DTM differences after a first iteration step of estimating the shift and applying it to the ASTER DTM ($|\mathbf{s}| = 66$ m; $A_{\mathbf{z}_s} = 100^\circ$). Obviously, some aspect-dependency of the vertical deviations is still present. Figure 4-5 shows the DTM differences of a similar terrain section as in Figure 3-25 (right) but with the above initial shift applied to the ASTER DTM (see also Section 8.1). Before the DTM shift, the vertical RMS between the aerophotogrammetric and the ASTER DTM is ± 41 m, after the shift it becomes ± 31 m.

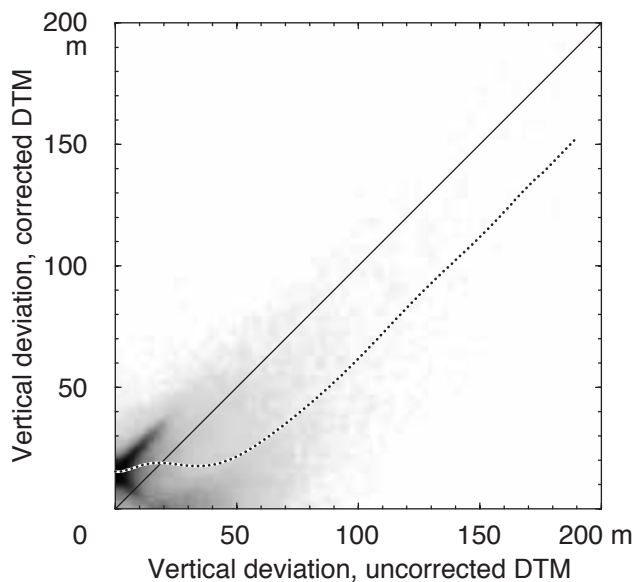


Fig. 4-6 2D-histogram of vertical deviations $|\Delta h|$ between a 1997 aero-photogrammetric DTM and a 2001 ASTER DTM, Glaciar Chico. X-axis: uncorrected elevation differences (see Fig. 3-25); y-axis: elevation differences after correcting the offset of the ASTER DTM (see Fig. 4-5). Dotted line: running average of $|\Delta h|$.

(i.e. improvement by about 22 %). Severe errors of $\Delta h > 300$ m are excluded in this estimation because they represent for the most part errors introduced at the data set margins due to the shift. The two-dimensional histogram of uncorrected versus corrected DTM differences shows, that the initial offset correction for the ASTER DTM significantly improves all $|\Delta h| > 20$ m (Fig. 4-6).

Because the relation $\Delta h / \tan(\alpha)$ becomes infinite for $\alpha=0$ and noise in Δh is too much exaggerated for small slopes α , Equation 4-1 cannot not be used to estimate a DTM shift for terrain sections with low slope angle. Therefore, terrain with $\alpha < 10^\circ$ was excluded from the above calculations. In addition, through that procedure most glacier parts in the study area, which could have experienced natural (and thus correct) elevation changes between 1997 and 2001, were excluded. Indeed, the glaciated areas become well visible in the corrected DTM differences (Fig. 4-5) suggesting some ice thickness loss (see also Section 8.1).

Numerical correction of DTM differences

Instead of actually shifting one DTM beforehand DTM subtraction to best fit the other DTM to which it should be compared, vertical corrections can be computed from the estimated offset vector \mathbf{s} , and be applied to each elevation value or elevation difference as a function of aspect, or aspect and slope (Rivera et al., 2005). Such procedure might be particularly comfortable if not a map of elevation differences is desired but rather some statistical analysis of elevation differences (e.g. distribution with height, etc.) (e.g. Rivera et al., 2005).

4.3 Qualitative analysis of terrain movement

Qualitative and semi-quantitative detection of terrain movement may be both a valuable tool for process understanding, and a first step for preparing the application of quantitative techniques. Available methods include:

- detection and interpretation of terrestrial indicators,
- automatic change detection techniques, and
- image overlay.

Geomorphodynamic indicators for terrain movement in high mountains are manifold and range from complete geomorphological forms such as, for example, rockglaciers, glaciers or landslides to individual expressions within these forms such as folding, cracks, crevasses, fresh fine material, etc. (e.g. Bindschadler, 1998; Frauenfelder et al., 1998; Strozzi et al., 2004). *Absolute and relative dating methods* applied to surface or subsurface material provide indirect qualitative or semi-quantitative indications about terrain movement (Haeberli et al., 2003): for instance, C^{14} radio-carbon dating (e.g. Haeberli et al., 1999b), measurement of Schmid-hammer rebound values (Frauenfelder et al., 2003b; Laustella et al., 2003), measurement of weathering-crust thickness (Brazier et al., 1998; Frauenfelder et al., 2003b; Laustella et al., 2003), lichenometry (Haeberli et al., 1979; Bull et al., 1994; Martin et al., 1994; Sloan and Dyke, 1998; Laustella et al., 2003), and vegetation mapping (Guglielmin et al., 2001; Burga et al., 2004).

Automatic *change detection techniques* based on repeat datasets are able to indicate terrain movement (Section 6.3). For horizontal displacements, the change pattern detected shows some typical characteristics such as features repeating themselves as negative and positive anomalies (Fig. 4-7). The *animated overlay of repeat orthoimages* or imagery taken from similar positions, also called flickering, is considered by the author to be one of the most efficient and instructive methods for detecting and exploring horizontal terrain displacements (Kääb et al., 2003b). Two or more orthoimages, possibly radiometrically adjusted, are overlain sequentially in short time intervals. Such a procedure can be controlled manually using any image display software allowing for multiple layers, or can be automated with various tools for image flickering or animation.

4.4 Digital image matching

Principles

An efficient method for measuring terrain displacements is the comparison of repeat optical imagery. If original imagery is used, the displacements obtained have then to be rectified using the corresponding sensor model and orientation parameters (Kääb, 1996b; Kääb et al., 1997; Kääb and Funk, 1999; Kaufmann and Ladstädter, 2002). If orthoimages are used, the image comparison directly provides the horizontal components of the displacement vector, v_x^s and v_y^s . The approach is, in principle, applicable to terrestrial, air-, and spaceborne imagery.

Basically, two techniques are used for digital comparison between multitemporal (ortho-) images:

- block (or area-based) matching techniques, or
- feature matching techniques.

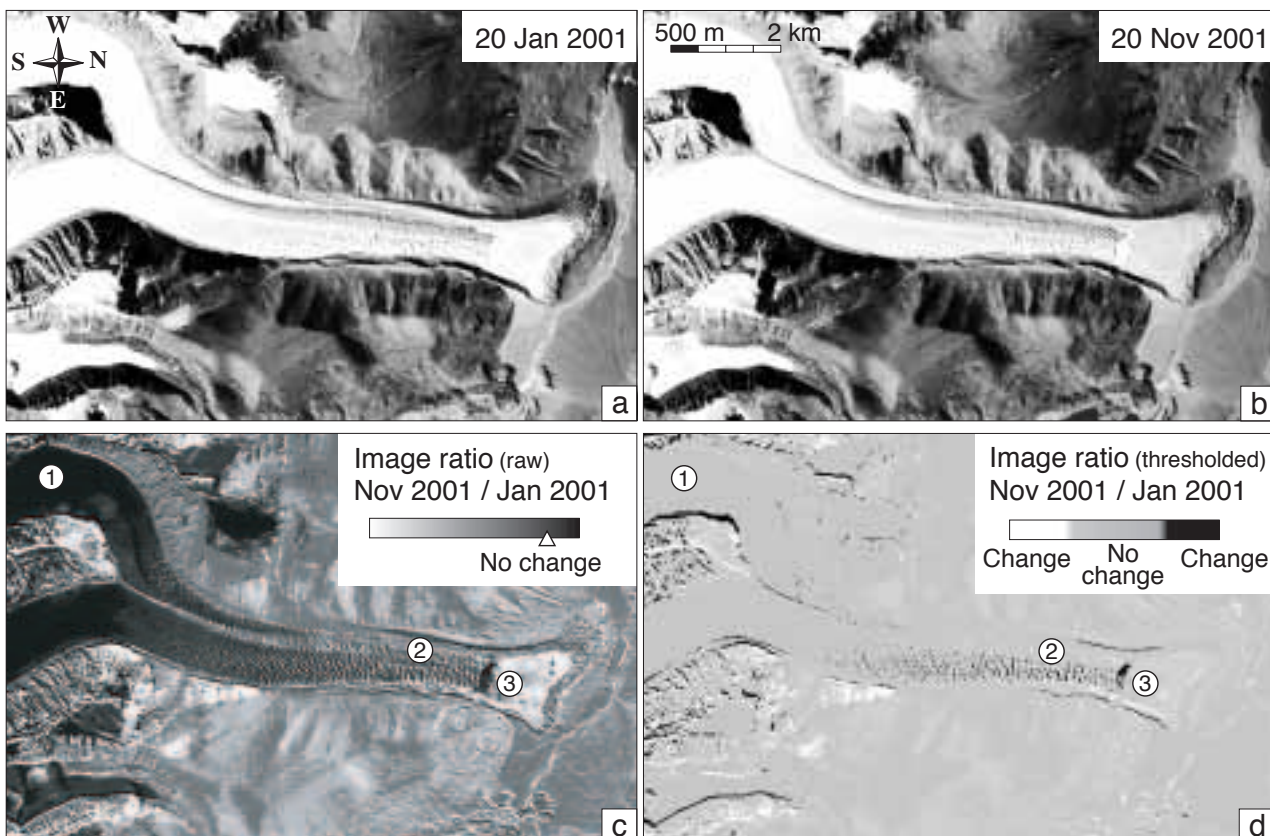


Fig. 4-7 Raw (panel c, lower left) and thresholded (panel d) ratio images between repeat ASTER imagery (panels a and b) of an unnamed glacier in Bhutan, northern basin. The image ratios reveal virtually no change for snow-covered terrain (1). On the glacier (2) a typical transverse black-and-white pattern of positive and negative changes indicates the movement of crevasses. In this way, the displacement can be detected (change detection) and also be measured from individual change features (see Fig. 8-7). At point (3), glacier retreat can be detected clearly as change.

Block matching compares complete grey-value arrays, i.e. image sections, to each other. *Feature matching* compares geometric forms such as edges or polygons extracted beforehand from the imagery in a pre-processing step. Block matching techniques include two-dimensional cross-correlation, least-squares matching or matching of Fourier or wavelet functions decomposed from the original image (e.g. Grün and Baltsavias, 1987; Crippen, 1992; Scambos et al., 1992; Frezzotti et al., 1998; Evans, 2000; Kääb and Vollmer, 2000; Van Puymbroeck et al., 2000; Kaufmann and Ladstädter, 2002; Netanyahu et al., 2004; Stevens et al., 2004). Before performing the block matching, it might be useful to apply filters to the raw imagery such as contrast and edge enhancements, interest operators, or other global, regional and adaptive radiometric adjustments (e.g. Förstner, 2000).

Here, the horizontal displacements of individual terrain features are derived from multitemporal digital orthoimages using the Correlation Image Analysis (CIAS) software (Vollmer, 1999; Kääb and Vollmer, 2000). The measurement of an individual horizontal displacement vector basically follows two steps (Fig. 4-8): (1) an image section (so-called *reference block*) with sufficient optical contrast is chosen in the orthophoto of time 1. The ground coordinates of the central pixel are known from the orthophoto georeference. (2) The corresponding image section (so-called *test block*) is searched for in a sub-area (so-called *test area*) of the orthophoto of time 2. If successfully detected, the differences in central pixel coordinates directly give the horizontal displacement vector between time 1 and 2 (Fig. 4-8).

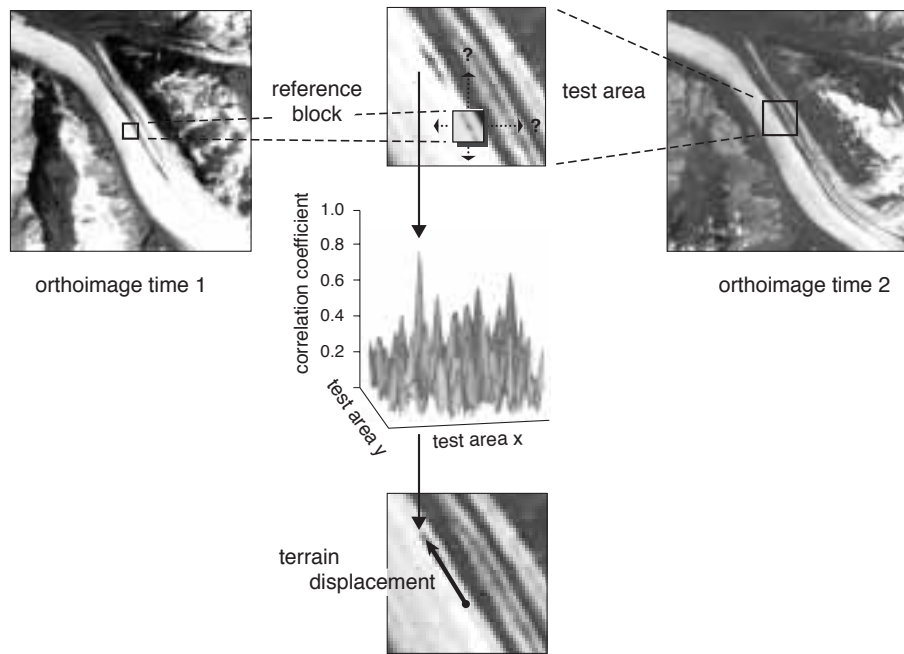


Fig. 4-8 Principle of measuring horizontal terrain displacements from grey-scale matching between repeat orthoimagery.

For identifying corresponding image blocks in both (or more) images, a double cross-correlation function based on grey values of the images is used:

$$\Phi(i,k) = \frac{\sum_j \sum_l s\left((i+j, k+l) - \left(\frac{T_{test}}{N_{test}}\right)\right) \cdot m\left((j,l) - \left(\frac{T_{ref}}{N_{ref}}\right)\right)}{\sqrt{\sum_j \sum_l s^2\left((i+j, k+l) - \left(\frac{T_{test}}{N_{test}}\right)\right) \cdot \sum_j \sum_l m^2\left((j,l) - \left(\frac{T_{ref}}{N_{ref}}\right)\right)}} \quad (4-2)$$

where

- Φ is the double cross-correlation function,
- (i,k) and (j,l) are the coordinates inside the test and reference block,
- s is the spatial grey-value function of the test block,
- $s(i,k)$ is the corresponding grey value at location (i,k) ,
- m is the spatial gray-value function of the reference block,
- $m(j,l)$ is the corresponding grey value at location (j,l) ,
- T is the sum of grey values of the test or reference block, and
- N is the number of pixels of the test or reference block ($N_{ref} = N_{test}$).

The global maximum of Φ is supposed to indicate the displaced terrain block of time 1. The T -over- N terms in Equation 4-2 normalize the grey values of test and reference blocks and ensure that overall differences in grey-value do not affect the correlation result.

An alternative approach

Combining matching techniques that are applied to orthoimages with repeat DTMs provides both the horizontal displacements and the surface elevation changes (see Eq. 2-1 and Fig. 4-9). A combination of simultaneous multitemporal and multiangle image matching where a surface particle is measured in all overlapping images of all image acquisition dates is, in fact, able to deliver the three-dimensional surface

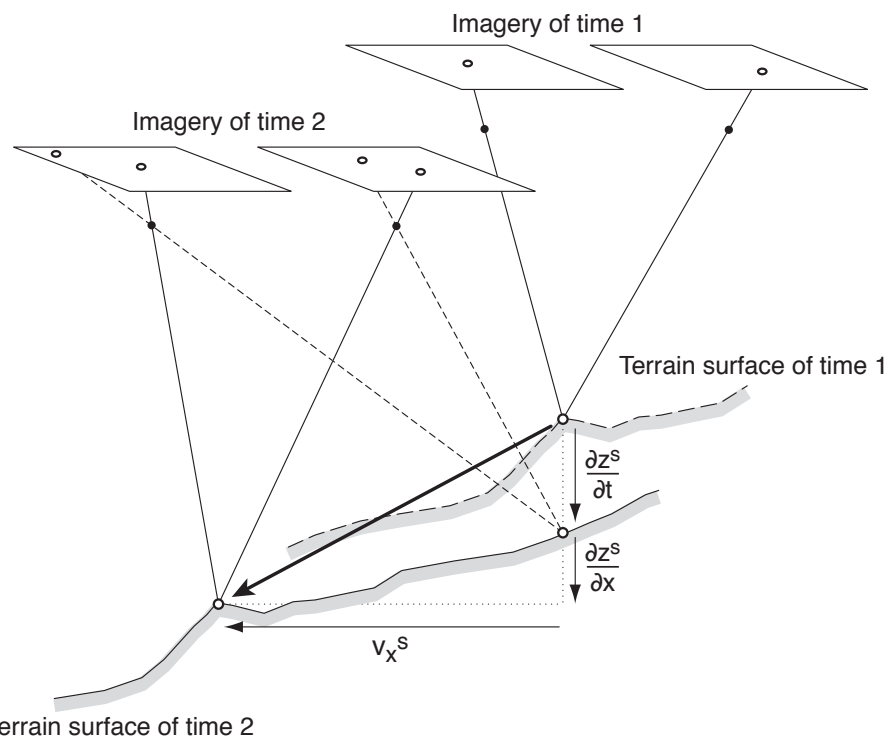


Fig. 4-9

Two basic principles for the digital measurement of three-dimensional surface displacements from repeat optical stereo-imagery. (1) Computation of multitemporal DTMs and orthoimages: vertical DTM differences provide elevation changes $\partial z^s / \partial t$. Orthoimage matching contributes the horizontal displacement component v_x^s . The terrain slope component of the particle movement $\partial z^s / \partial x$ has to be interpolated from the resulting DTMs. (2) Simultaneous matching of a surface particle both in multitemporal and multiangle imagery provides the exact three-dimensional vector of the particle movement. The change in terrain elevation has to be interpolated from DTMs.

particle displacements. Such a procedure can be simplified substantially by introducing approximated orthoimages (i.e. orthoimages computed from coarse DTMs; also called "pseudo-orthoimages") instead of the original imagery (Kaufmann, 1998a; Ladstädter, 1999; Kaufmann and Ladstädter, 2002). This procedure and the approach presented above converge if DTMs with a spatial resolution of a few image pixels are used for the methods. (1) Horizontal surface displacements and (2) surface elevations at the start and end points of the velocity vectors obtained can also be measured and improved iteratively. The accuracy of this approximation is determined by the ratio of surface roughness to image pixel size, or, in other words, the representativeness of the DTM used as compared to the actual terrain geometry.

Application

The size of the test area has to be chosen according to the expected maximum displacement to ensure that the test block, which corresponds with the reference block, can be found in the test area. The size of the reference and test block has to be chosen according to the textural characteristics of the ground surface depiction. If the reference-block size is too small, Φ has no clear maximum (Fig. 4-10); if the reference block size is too large, computing time soars drastically. Typical reference block sizes in this study range from 7×7 pixels to 30×30 pixels. As a consequence of the ratio between typical sizes of terrain features, such as rocks and crevasses, and the spatial image resolution, smaller block sizes should be used for satellite imagery (spatial resolution in the order of metres to tens of metres) and larger ones for aerial

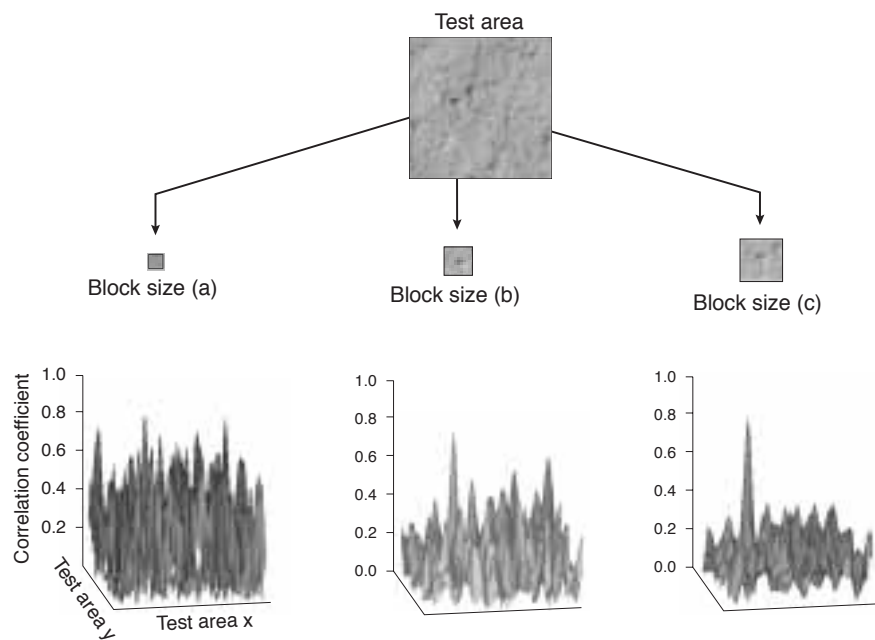


Fig. 4-10 An optimal block size has to be found for matching terrain displacements. Large image blocks lead to more distinct correlation peaks, but increase computing time drastically. The displacements determined by larger image blocks represent the movement of a larger area and thus smear fine details of the displacement field.

imagery (spatial resolution in the order of decimetres to centimetres). The example in Figure 4-10 points out the influence of block size on the Φ -surface and the corresponding characteristics of global and regional maxima of Φ . In order to obtain some sub-pixel accuracy for the matching, the final level of the image pyramid used is computed here from cubic interpolation of the original image.

Matching blunders are detected and eliminated from analysis of the correlation coefficients and from application of constraints, such as expected range for flow speed and direction. In the case of coherent displacement fields, additional spatial filters may be applied such as median or RMS thresholds (see Section 4.2). Glaciers and creeping permafrost usually show such coherent velocity fields due to the stress-transferring properties of ice.

Digital motion measurements from repeat optical imagery have been applied

- for ice sheets using satellite imagery (e.g. Lucchitta and Ferguson, 1986; Scambos et al., 1992; Bindschadler et al., 1994; Whillans and Tseng, 1995; Bindschadler et al., 1996; Frezzotti et al., 1998) (see Bindschadler, 1998; König et al., 2001),
- for Arctic glaciers using satellite imagery (e.g. Lefauconnier et al., 1994; Rolstad et al., 1997; Dowdeswell and Benham, 2003; Kääb et al., 2005b) (see König et al., 2001) (Fig. 4-11, Section 8.4),
- for mountain glaciers using satellite, aerial or terrestrial imagery (e.g. Seko et al., 1998; Nakawo et al., 1999; Evans, 2000; Kääb and Vollmer, 2001; Kääb, 2002; Kääb et al., 2003a; Skvarca et al., 2003; Vadon and Berthier, 2004; Berthier et al., 2005; Kääb, 2005) (Fig. 4-12, Sections 8.2, 8.3, and 8.5),
- for rockglaciers using aerial imagery (Kääb, 2000; Kääb and Vollmer, 2000; Ladstädter, 2001; Kääb, 2002; Kääb et al., 2002a; Kaufmann and Ladstädter, 2002; Kääb et al., 2003c; Kaufmann and Ladstädter, 2003; Kääb and Weber, 2004; Roer et al., 2005a; Roer et al., 2005b) (Chapter 9, Fig. 12-6), or

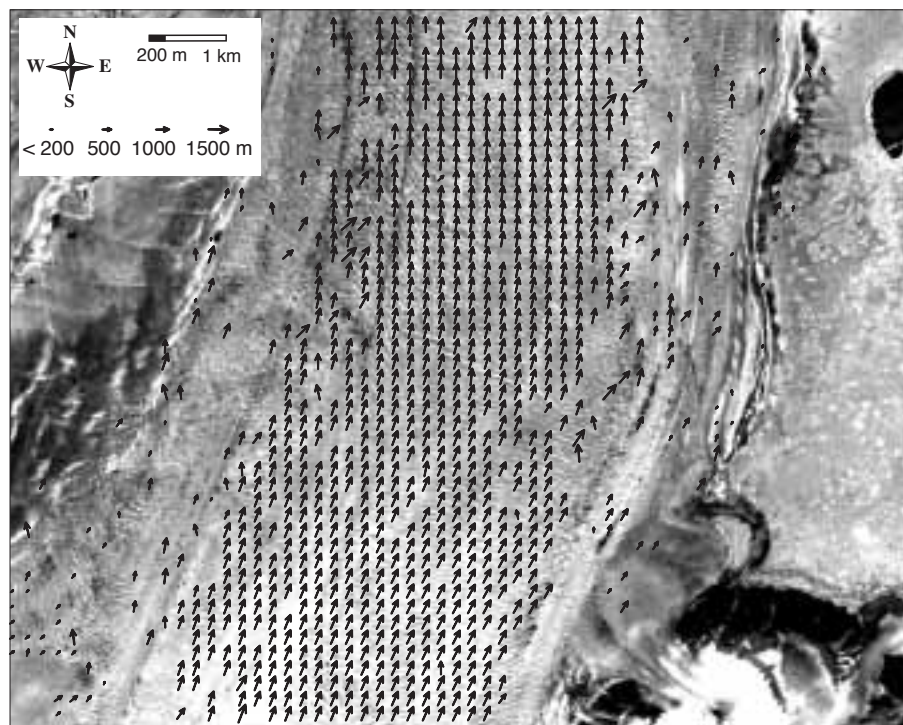


Fig. 4-11 Velocity field for a section of Mittie glacier, Manson ice cap, Ellesmere Island, Canadian High Arctic, computed from Landsat ETM+ pan orthoimagery of 13 July 1999 and 27 June 2000 (15 m resolution). Displacements amount to 1500 m. Original measurements were performed with 100 m spacing, but are depicted with 200 m spacing for better readability. Mittie glacier was surging during the observation period (Copland et al., 2003). The Landsat imagery was processed and provided by Luke Copland, Department of Earth and Atmospheric Sciences, University of Alberta, Edmonton. For location see Figure 1-2.

- for other mass movements and slope deformation using satellite or aerial imagery (e.g. Crippen, 1992; Mantovani et al., 1996; Powers et al., 1996; Baum et al., 1998; Vadon and Massonnet, 2000; Van Puymbroeck et al., 2000; Kääb, 2002; Casson et al., 2003; Delacourt et al., 2004) (Chapter 10).

For matching of repeat SAR imagery see Section 4.5.

Accuracy

In order to avoid distortions between the multitemporal products, all imagery is best adjusted as one image block connected by multitemporal tie-points (see Section 3.3.1). For the multitemporal model connection, these tie-points are placed on stable terrain. For details see also Kääb and Vollmer (2000). From comparison with ground measurements and analytical photogrammetry (e.g. Fig. 4-13), and from the noise within coherent flow fields (e.g. Fig. 4-14) an RMS of 0.5 to 1 times the image pixel size was found for the horizontal displacement measurements. Figure 4-14 gives the standard deviation of the displacement magnitude within a 3×3 mask for the Mittie glacier flow field (Fig. 4-11). Identical analysis of the Nigardsbreen flow field (Fig. 4-12) reveals standard deviations of less than 0.2 m for the central parts. It is important to note that the accuracy of such image matching is often restricted by terrain properties and related changes with time, and not only by the precision of the algorithms applied.

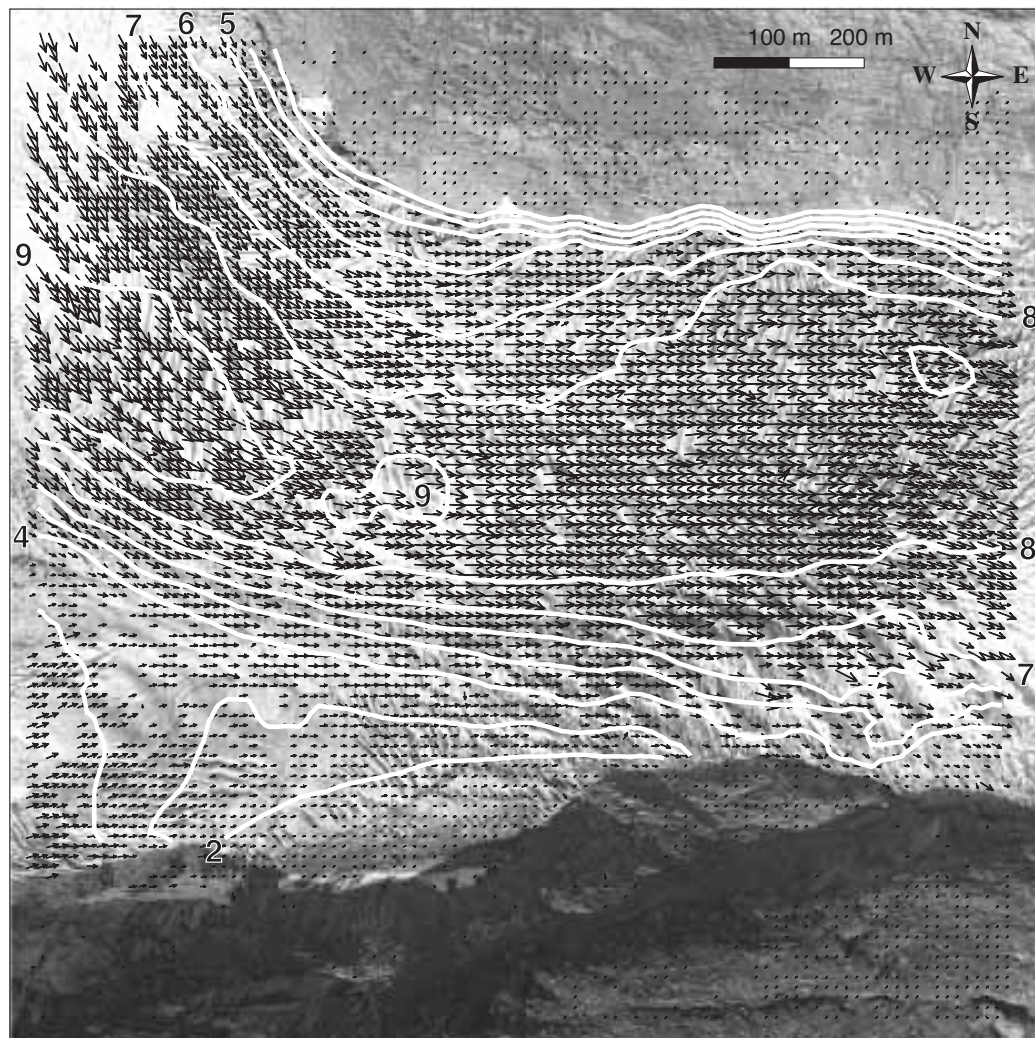


Fig. 4-12 Velocity field for a section of Nigardsbreen, Southern Norway, computed from matching between repeat airborne orthoimagery of 19 and 29 August 2001. The numbered contours give the absolute displacement in metre units. Spacing between the vectors is 12 m. The applied orthoimages have 0.3 m ground resolution. The orthoimagery was provided by Bjørn Wangensteen and Trond Eiken, Department of Physical Geography, University of Oslo, and was acquired within the GLACIORISK-project. Aerial imagery © Department of Physical Geography, University of Oslo, Norway. For location see Figure 1-2.

4.5 Differential InSAR (DInSAR)

Principle

If the antenna positions of two (or more) repeat-pass SAR images are identical, a possibly remaining interferometric phase can only be explained by coherent surface displacements and/or atmospheric influences (Eq. 3-11). For baselines $|B| > 0$, the baseline component B_y can be computed from known sensor positions and a DTM. The synthetic interferogram calculated from an existing DTM is compared to the real one from two repeat-pass SAR images (two-pass DInSAR). Alternatively, the terrain elevation information is inferred from additional interferograms. In this process, one of the two interferograms to be compared forms the reference, for example, a reference or master interferogram with a short temporal baseline and assumed minimal displacement influence (three- and four-pass DInSAR) (Wegmüller

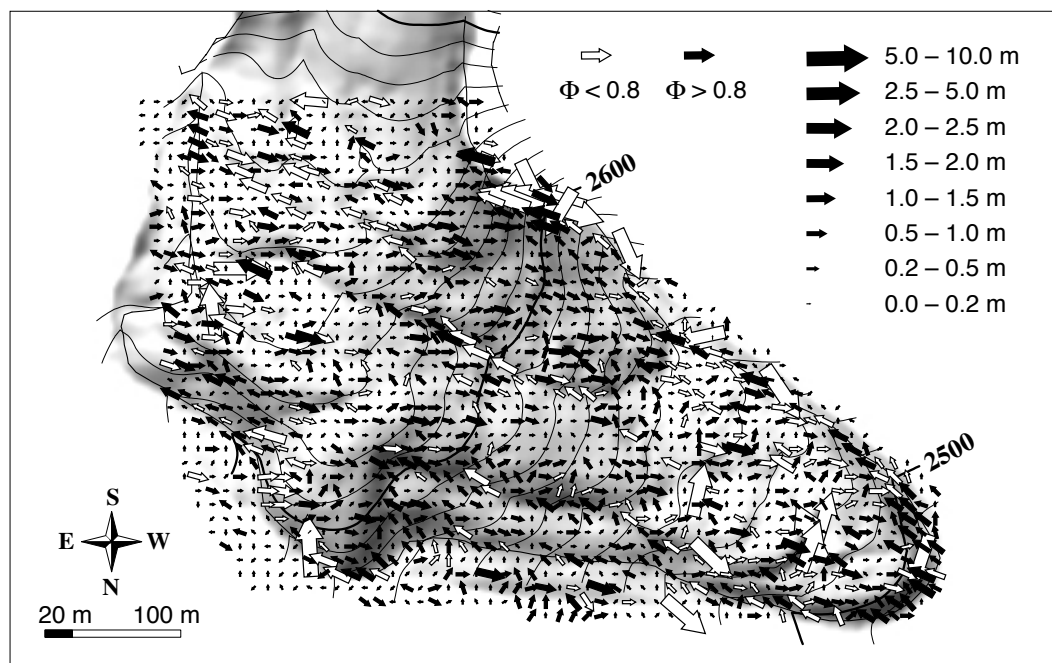


Fig. 4-13 Two-dimensional deviations between surface displacements that were (1) operator-measured from analytical photogrammetry (Kääb et al., 1997) and (2) automatically matched from repeat orthoimagery (see Fig. 9-3). The same original imagery was applied for both procedures. The white arrows indicate automatic measurements that have a correlation coefficient below 0.8. Muragl rockglacier, Swiss Alps.

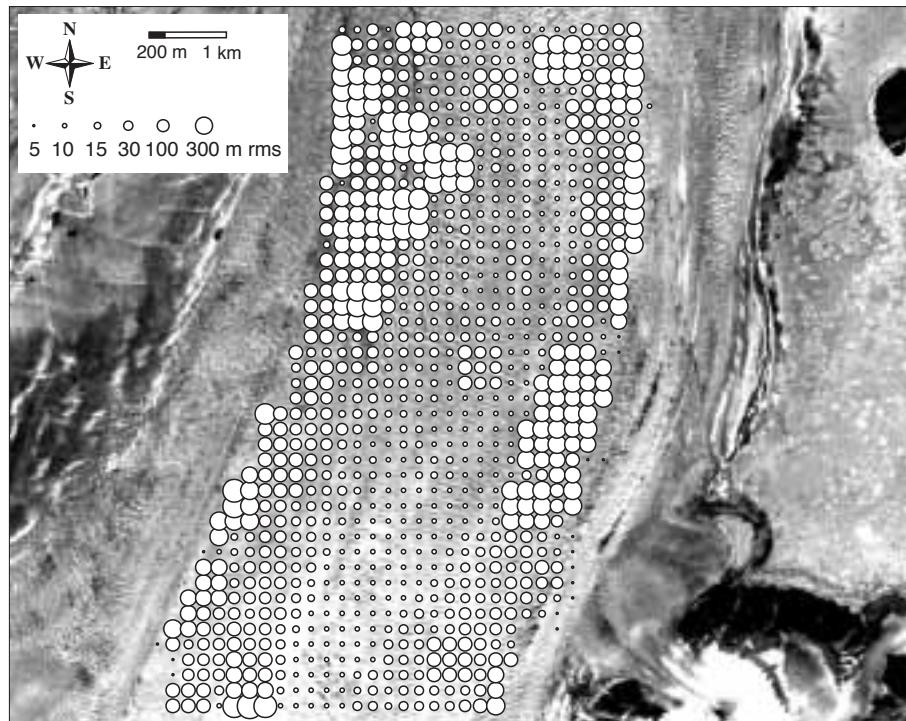


Fig. 4-14 Standard deviation of vector magnitude within a quadratic filter of 3 by 3 pixels over the Mittie glacier velocity field shown in Figure 4-11. In the centre, the measurement noise estimated thus is clearly below the image pixel size of 15 m. Strong transverse ice straining leads to increasing deviations towards the margins.

et al., 1998)). Suitable SAR data have to fulfill spatial and temporal requirements. For terrain displacement detection using DInSAR, (a) a small baseline is advantageous. On the other hand, for InSAR DTM generation the choice of baseline length has to consider (b), the geometric setting that changes with length and (c), the probability of volume decorrelation effects that increase with baseline length. The period between SAR acquisitions has to be long enough to (d), allow for the detection of displacements that exceed the significance level. On the other hand, (e) long temporal baselines often lead to the coherence degradation (Section 3.4.2). To meet these InSAR and DInSAR requirements, either repeat passes of the same sensor or tandem missions (e.g. ERS 1 and 2) are usually chosen. (For an overview of DInSAR applied to glaciers see König et al., 2001).

As can be seen from Equation 4-3, the terrain displacement component in the line-of-sight direction can be *unwrapped* from the differential interferogram, similar to the InSAR DTM generation (Fig. 4-15). For sufficiently different azimuths of ascending and descending orbits (i.e. for high latitudes), two components of the displacement vector can be derived and thus the horizontal displacement direction can be computed (Joughin et al., 1999a). The vertical component of the terrain displacement can be estimated by assuming, for instance, that surface-parallel movement or vertical thickness changes only will take place (e.g. Strozzi et al., 2001; 2003a; 2004).

$$\Delta y = \frac{\Delta y'_{\text{displace}}}{\sin \theta}, \text{ or } \Delta z = -\frac{\Delta y'_{\text{displace}}}{\cos \theta}, \text{ or } \Delta y_\alpha = \frac{\Delta y'_{\text{displace}}}{\sin(\theta + \alpha)} \quad (4-3)$$

where

- Δy is the horizontal displacement component,
- Δz is the vertical displacement component,
- α is the (negative) surface slope, and
- Δy_α is the surface-parallel displacement component (Fig 4-15).

In addition to the *phase unwrapping* applied above on differential SAR interferograms, techniques such as *phase correlation*, *speckle tracking* or *permanent scatter* based on repeat

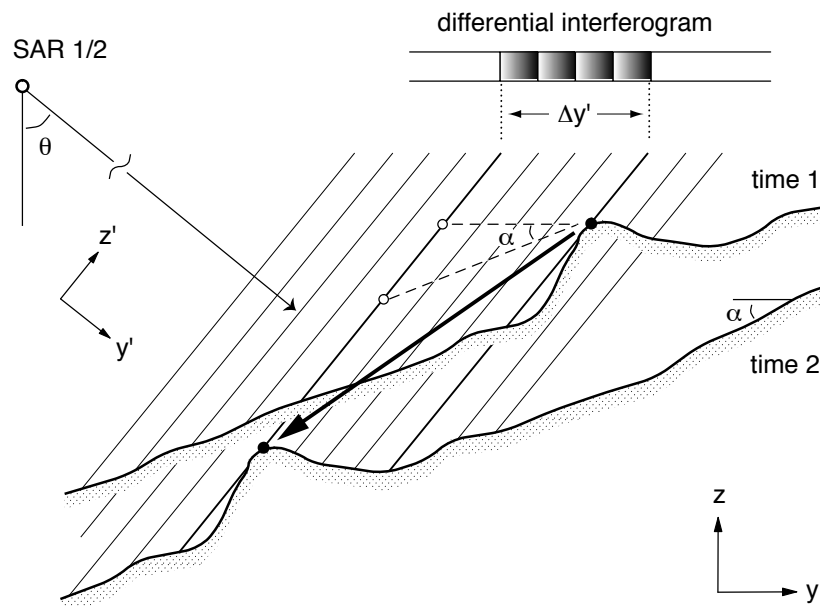


Fig. 4-15 Principle of measuring terrain surface displacement from differential SAR interferograms derived from repeat SAR acquisitions. An assumption has to be made about the three-dimensional direction of the displacement if no data from orbits with sufficiently different azimuth exist.

SAR imagery can be used to measure surface displacements (Michel and Rignot, 1999; Ferretti et al., 2001; Luckman et al., 2002; Murray et al., 2002; Strozzi et al., 2002; Colesanti et al., 2003; Luckman et al., 2003). Speckle tracking exploits SAR amplitude images in a way that is similar to the image matching method described in Section 4.4 (see Tab. 4-1). It can serve to complement DInSAR for terrain sections where phase decorrelation between the repeat SAR data prevents DInSAR application. The permanent scatterer approach intends to minimize the phase decorrelation effects due to acquisition geometry (geometric decorrelation) and due to time between the data captures (temporal decorrelation), and atmospheric artefacts by isolating phase-stable point-wise radar targets from long time-series of SAR interferograms.

Accuracy and application

For a coherent DInSAR phase, the line-of-sight displacements can be determined to some fraction of the applied wavelength, i.e. with an accuracy of some millimetres to centimetres. For the permanent scatterer technique accuracy is in the sub-millimetre order because tens of interferograms are used within one deformation analysis (Colesanti et al., 2003). However, the required density of potential permanent radar scatterers (5–10 per km²) might not be given on a regular basis for high-mountain environments.

Because of good coherence preservation and minimal topographic effects, spaceborne DInSAR is frequently applied for measuring ice speed for ice sheets, ice caps, ice fields, and large glaciers in high latitudes (e.g. Goldstein et al., 1993; Rignot et al., 1996; Rott and Siegel, 1997; Bindschadler, 1998; Mohr et al., 1998; Dowdeswell et al., 1999; Forster et al., 1999; Joughin et al., 1999b; König et al., 2001; Luckman et al., 2002; Murray et al., 2002; Eldhuset et al., 2003; Forster et al., 2003). Vertical permafrost heave and subsidence is also measured from DInSAR (Moorman and Vachon, 1998; Wang and Li, 1998; Wang and Li, 1999). Under mid-latitude alpine conditions, loss of coherence due to ice- and snowmelt, topographic effects from high relief, and smaller glacier size with respect to the SAR spatial resolution complicate spaceborne DInSAR application for glacier monitoring (Fig. 4-16) (Mattar et al., 1998; Strozzi et al., 2003a; Strozzi et al., 2004).

Similar factors complicate the application of spaceborne DInSAR to rockglacier creep and paraglacial slope instabilities (Figs. 4-16 and 12-5) (Fruneau et al., 1996; Rott and Siegel, 1999; Kenyi and Kaufmann, 2000; Kenyi and Kaufmann, 2001; Nagler et al., 2002; Rignot et al., 2002; Colesanti et al., 2003; Squarzoni et al., 2003; Strozzi et al., 2004).

Overall advantages and problems of DInSAR compared to optical image matching are summarized in Table 4-1.

4.6

Other methods

Terrestrial methods

Terrestrial or satellite-aided geodesy are traditional techniques for determining terrain displacements. The methods deliver fully three-dimensional surface displacement vectors for selected points with an accuracy in the order of millimetres to centimetres. To ensure this accuracy, measuring points have to be marked, for instance, by rock bolts or ablation stakes. For the latter signalling work and for the measurements themselves (except for the forward intersection method and touchless

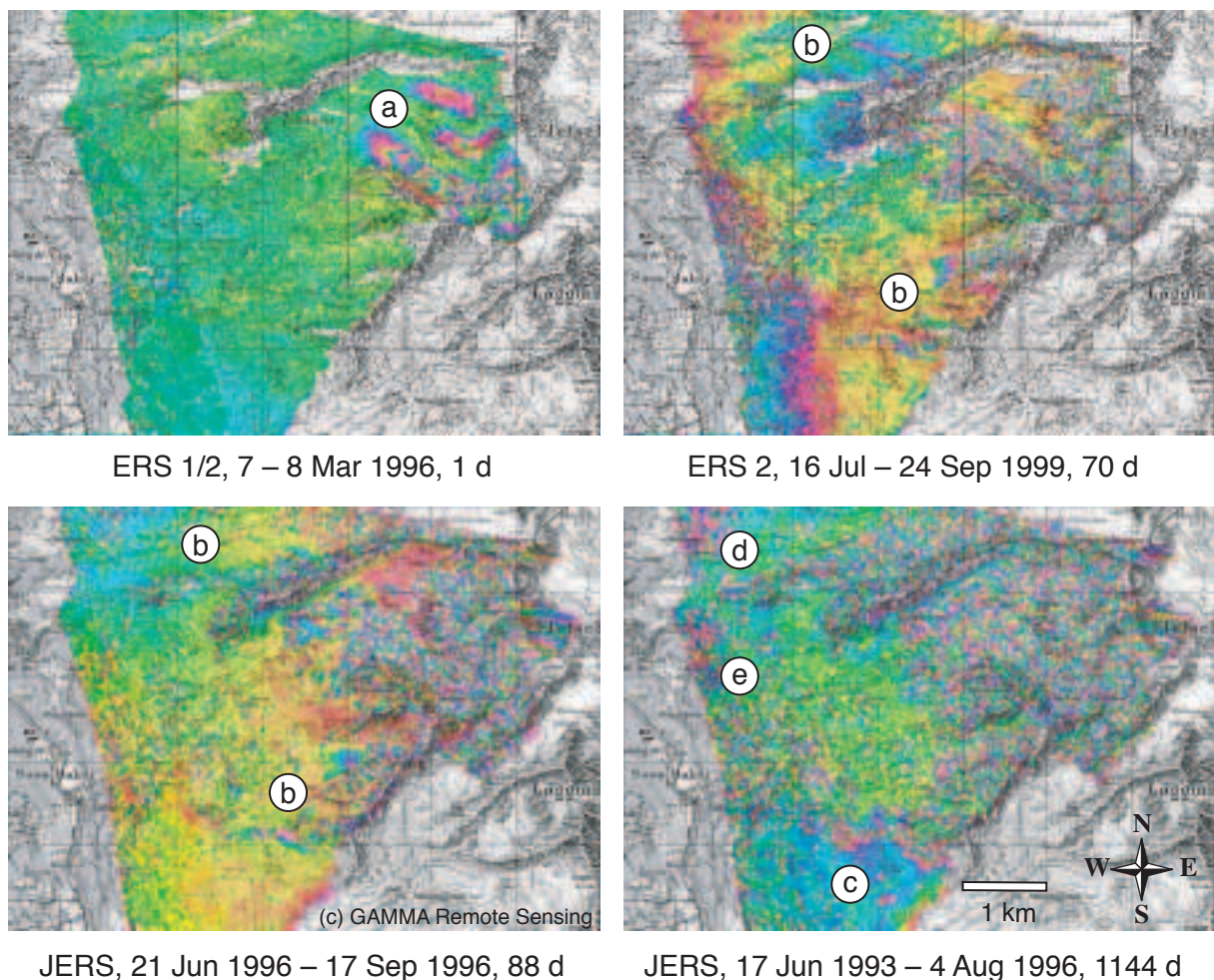


Fig. 4-16 Differential interferograms from different SAR sensors and time bases applied to Gruben area, Swiss Alps. For a 1-day repeat time (upper left panel) the movement of glaciers can be detected (a). The same glaciers show decorrelation for all other interferograms. Longer time bases reveal the movement of rockglaciers (b). Using JERS DInSAR with about 3 years time base, the movement of rockglaciers, which have been classified as “inactive” from in-situ and photogrammetric surveys (c and d), and a rock mass movement (e) become detectable (Strozzi et al., 2003a; 2003b; 2003c; 2004). ERS SAR data courtesy A03-178, © ESA, processing GAMMA, JERS SAR data courtesy J-2RI-001, © NASDA, processing GAMMA. Background map by swisstopo (permission BA057212).

laser rangers), direct access to the object under study is usually required. Polar survey and GNSS are common tools applied for glacier flow measurements (e.g. Frezzotti et al., 1998; Gudmundsson et al., 2000; Gao and Liu, 2001), for deriving rockglacier movement (e.g. Zick, 1996; Berthling et al., 1998; Sloan and Dyke, 1998; Koning and Smith, 1999; Konrad et al., 1999; Krainer and Mostler, 2000; Kääb et al., 2003c; Kääb and Weber, 2004), and other periglacial slope instabilities (e.g. Mora et al., 2003). Terrestrial laserscanning is discussed in Sections 3.2 and 3.7, and in the section below on DTM matching. For close-range applications simplified but very cost-efficient displacement measurements are possible by using hand-held laser rangers. They provide one displacement component if single distances are measured repeatedly, or two or three displacement components if multiple distances are measured and combined (arc intersection method).

Image matching techniques (Section 4.4) are applicable also to all kinds of terrestrial imagery, such as terrestrial frame imagery, digital and analogue amateur images, or

video stills. Particularly interesting for glacier and permafrost research might be the employment of automatic cameras (Fig. 6-7). (See also following paragraph).

Analogue and analytical photogrammetry

Before digital photogrammetry was available, a number of analogue or analytical methods were developed for displacement measurements:

- displacement parallax measurements from analogue terrestrial photos (e.g. Finsterwalder, 1931; Melvold, 1992) or airphotos (e.g. Hofmann, 1958),
- manual or analogue photogrammetric point-by-point measurements (aerotriangulation, e.g. Messerli and Zurbuchen, 1968; Barsch and Hell, 1975; Brecher, 1986; Rentsch et al., 1990; Gorbunov and Titkov, 1992; Whillans et al., 1993),
- direct analogue comparison of repeat images (Flotron, 1979),
- computer-based, point-by-point measurements (e.g. Grün and Sauermann, 1977; Kaufmann, 1998a; Krummenacher et al., 1998),
- computer-based simultaneous comparison (Armenakis, 1984; Haeberli and Schmid, 1988; Kääb et al., 1997; Knizhnikov et al., 1998; Kääb and Funk, 1999).

DTM matching

With upcoming metre to sub-metre spatial resolutions for DTMs from airborne digital photogrammetry, laserscanning or InSAR, it becomes increasingly possible to detect terrain displacements from the matching between repeat DTMs. The DTMs can be coded as grey-value images and image-matching techniques can be applied (see Section 4.4; Fig. 4-2). DTM matching does, in principle, provide only an approximation of the terrain displacement, since change in elevation, which such procedure tracks, is not equivalent to terrain displacement (see kinematic boundary condition, Eq. 2-1). Terrain displacements can only be detected if the respective multitemporal DTMs include individual and corresponding terrain features such as rocks or crevasses (Abdalati and Krabill, 1999; Bauer et al., 2003; Geist et al., 2003) (Figs. 3-9 and 4-17).

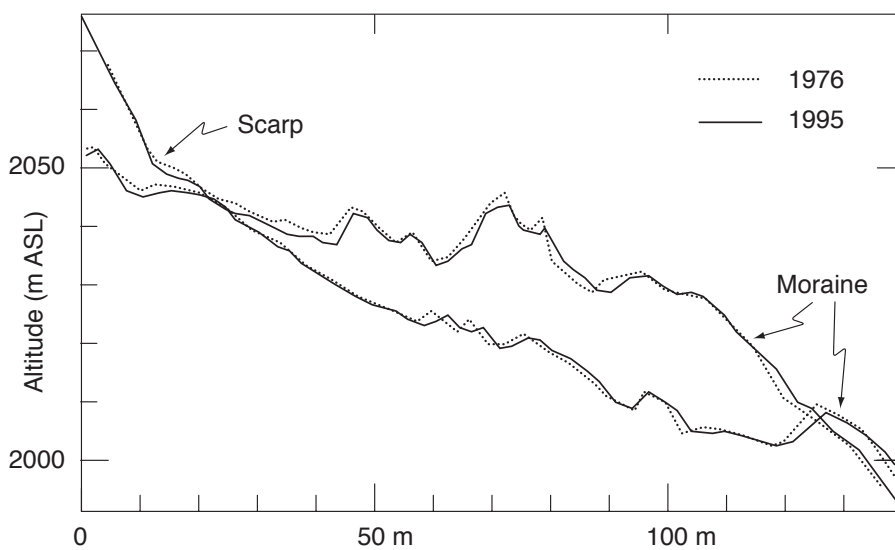


Fig. 4-17 Sections of two longitudinal elevation profiles over a rock mass creep near Aletsch Glacier, Swiss Alps, as derived from analytical photogrammetry of 1976 and 1995 imagery (see Chapter 10). The repeat high-resolution profiles with 1 m horizontal spacing reveal not only the vertical changes but also the three-dimensional displacements of distinct topographic features.

Others

Initial attempts have been made with terrestrial DInSAR. This technique involves the installation of a SAR instrument on a fixed sled and will, therefore, to be used mainly for monitoring slow landslides. For suitable terrain, the technique has the potential to provide area-wide terrain displacement with an accuracy yet unknown (Tarchi et al., 2003).

Mechanical close-range techniques such as steel tapes or strain wires have also been used for deformation or displacement measurements on rockglaciers (e.g. Haeberli, 1985; White, 1987) or glaciers (Röthlisberger and Aellen, 1970).

4.7 Conclusions and perspectives

Terrestrial methods

Differential satellite-aided surveying, e.g. differential GNSS, and motorized total stations can be used for automated displacement measurements with high temporal resolution (e.g. Gudmundsson et al., 2000). Such applications open new perspectives for investigating short-term velocity variations of flow, creep or other slope-movement processes. For special applications in glaciology, continuous elevation monitoring by digital levels might become of interest, for instance, for monitoring terrain heaving and settlement due to frost action or water pressure, for detecting the onset of glacier surges or other instabilities, or for monitoring water levels.

Terrestrial laserscanning is especially promising for monitoring changes in geometry for small terrain sectors such as rockglacier fronts (Bauer et al., 2003). Since the method is not restricted to a small sample of measuring points, changes can be detected quasi area-wide with high resolution and accuracy, both in the order of centimetres. Because of the high spatial resolution of terrestrial laser scans, which also depict small terrain features, both elevation changes and three-dimensional displacements can be detected (see above DTM-matching, Bauer et al., 2003). In particular, terrestrial laserscanning is able to provide new insights in the geometric changes of steep ice/rock walls (erosion, frost weathering, rock fall, ice break-offs, etc.) where the application of vertical air- and spaceborne techniques is often hampered.

Airborne methods

Deriving elevation changes using repeat DTMs from aerial optical imaging is a well-established method. Repeat airborne laserscanning will become a method of choice for the operational monitoring of volume changes of glaciers and frozen ground. For such tasks, even one or a few repeat scan tracks along a central flow line are sufficient. The combination of repeat laserscanning and optical imagery provides a promising tool for monitoring elevation changes and displacements simultaneously with high resolution and accuracy (Section 3.7) (see also Kraus, 2002). Since repeat laser profiles hardly ever overlap perfectly, laser profiling is difficult to apply for measuring elevation changes when the topography variations exceed the elevation differences to be measured between the acquisition dates. However, for topography with few low-frequency components the method is very successful (e.g. Arendt et al., 2002).

The author is not aware of any airborne DInSAR applications for monitoring high-mountain surface displacements, but consider the approach to be suitable and promising.

Spaceborne methods

Satellite LIDAR and RADAR altimetry, designed besides sea surface applications for arctic and antarctic applications, presumably will not become operational in the near future for detecting elevation changes of small glaciers and frozen ground in steep terrain. Related problems mainly originate from the large footprints, the profiling characteristics, and/or the long repetition cycles. A first step toward applicability of satellite altimetry for detecting elevation changes in more undulated topography is SAR interferometric radar altimetry.

The most crucial parameter for applying image-matching techniques using satellite optical imagery is the spatial image resolution, or the discernibility of individual corresponding features (see Bindschadler et al., 2001). There it becomes clear that sensors such as IRS pan (7 m), SPOT 5 pan (2.5 m), Ikonos (1 m) or QuickBird (0.6 m) bear a high potential for detecting terrain displacements from space by optical means (see Fig. 5-5) (Delacourt et al., 2004).

The substantial capability of spaceborne DInSAR to detect terrain displacements on glaciers, rockglaciers or slow mass movements is well proven. Due to their different characteristics, DInSAR and satellite image matching show little overlap in terms of applicability. Moreover, they turn out to be highly complementary tools for terrain displacement measurements, as Table 4-1 demonstrates (cf. Vadon and Massonnet, 2000). The detection and investigation of small and very small surface movements in the glacial, peri- and paraglacial environment by DInSAR is able to provide new insights in glacier, rockglacier and landslide dynamics. DInSAR might, for instance, support the spaceborne discrimination of debris-covered ice from paraglacial debris by displacement detection. For such purpose, the coherence degeneration of the RADAR phase is already a valuable signal (see Gruben Glacier in Fig. 4-16, upper right panel), and unwrapping of the differential phase and, thus, quantification of the terrain movement is not necessarily required.

Table 4-1 Repeat satellite image matching and spaceborne DInSAR: Inter-comparison of their capability for terrain displacement measurements.

High-resolution satellite image matching	Spaceborne DInSAR
– accuracy: in the order of 1 m – 10 m	+ accuracy: in the order of mm – cm (for speckle tracking: in the order of 10 m) (for permanent scatterer techn.: 0.1–1 mm)
+ 2-dimensional horizontal displacements	– 1-dimensional displacements (2-dimensional using ascending and descending orbits in high latitudes)
+ nadir view	– side-looking (overlay, shadow, etc.)
– only for clear sky and daytime	+ all-weather and night-time
– optical contrast required	+ works also on snow etc.
+ coherence robust against melt, little snow, etc.	– sensitive coherence (fast coherence loss due to vegetation, humidity, melt, etc.)
o large displacements only (> image pixel size)	o small displacements only (otherwise coherence loss)
+ large, increasing number of suitable imagery available	– special acquisition characteristics required for many applications (e.g. tandem missions, or short baseline and time lag)
+ easy processing	– complex processing at present

5.1 Spectral data

In this work, the section of the electromagnetic spectrum from visible light to microwaves is considered, i.e. from approximately $0.3\text{ }\mu\text{m}$ to 1 m wavelengths.

The radiation recorded at a sensor depends on:

- the radiation source,
- the signal transmission through the atmosphere,
- the signal interaction with the terrain surface, which among other things is a function of the reflecting or emitting objects and their neighbours, and
- the sensor characteristics.

The primary *radiation sources* used in remote sensing are the sun, the earth's surface and the sensor itself. While *active sensors* (e.g. SAR or LIDAR) emit their own signals, *passive sensors* register the radiation reflected from the ground (e.g. visible and near infrared, VNIR, or short-wave infrared, SWIR, sensors) or the radiation emitted from the ground (e.g. thermal infrared, TIR, or passive microwave sensors).

The total spectral irradiance at the Earth surface E_λ is a composite of three components (Bishop et al., 2004):

$$E_\lambda = E_\lambda^b + E_\lambda^d + E_\lambda^t \quad (5-1)$$

During the atmospheric passage, the radiation is modified by *atmospheric scattering* and *absorption* by gases and particles (direct solar irradiance E_λ^b). Both effects decrease the signal intensity, among other things as a function of the wavelength. The atmospheric transmittance depends on the passing wavelength and the atmospheric conditions. In mountains, the direct solar irradiance is influenced by (i) the incidence angle of illumination and (ii) the vector normal to the surface. The *atmospheric windows* for the optical part of the spectrum are shown in Figure 5-1. Visible (VIS), infrared (IR) and thermal infrared radiation (TIR) are not or only partially able to penetrate clouds, whereas microwaves are. (Entire paragraph: Schowengerdt, 1997; Lillesand and Kieffer, 2000; Bishop et al., 2004).

Due to scattering processes the atmosphere produces hemispherical irradiance (diffuse skylight irradiance E_λ^d), depending on the relative geometry between illumination source and atmosphere, and atmosphere composition. Both components E_λ^b and E_λ^d interact with the terrain leading to a third irradiance source (adjacent terrain irradiance E_λ').

At the terrain surface, the incoming radiation is partly reflected (direct, or diffuse = scattered), and partly absorbed, depending on the ground emissivity. The ground reflectance varies, among other things, with the incidence angle of the radiation

source and the terrain geometry with respect to the sensor position (bidirectional reflectance distribution function, BRDF), and depends on the wavelength and the physical properties of the ground surface material (e.g. for glacier ice: Greuell and de Ruyter de Wildt, 1999). The variation of reflection with wavelength determines the spectral signature of the surface material. Figures 5-2 and 5-3 show some selected spectral signatures useful for optical remote sensing of high mountains. For microwaves, the backscatter is among others a function of the complex dielectric properties of the ground, which are influenced, *inter alia*, by the water content and surface roughness. Compared to visible and infrared light, microwaves can penetrate into the ground depending on the wavelength and the physical ground properties. The degree of absorbed energy or backscatter influenced in this way provides information about the ground. (Entire paragraph: Lillesand and Kieffer, 2000).

Here, a signal is considered to be characterized in the spectral domain by its wavelength (or wavelength segment), its intensity (amplitude), its phase and its polarization, where the latter two apply primarily to active microwave sensors. Accordingly, a sensor can also be characterized by the part of the spectral domain it records.

5.2 Spectral response

The spectral response of the ground cover determines the possibility for its spectral discernibility. Schematic reflection curves in dependence on the wavelength are given in Figures 5-2 and 5-3.

Snow

Fresh snow reflects up to 95% of the incoming VIS and about 50–80% of the near infrared (NIR) radiation with nearly a Lambertian reflectance (isotropic reflection, i.e. 100% diffuse reflection). In the VIS spectrum, snow reflectance decreases with dust contamination, and less with increasing grain size (Warren, 1982; Hall et al., 1989). In the NIR, the corresponding influence of dust contamination decreases, and the influence of grain size increases. In the short-wave infrared, the reflectance of snow is very low with a marked dependency on grain size, but a low one on snow

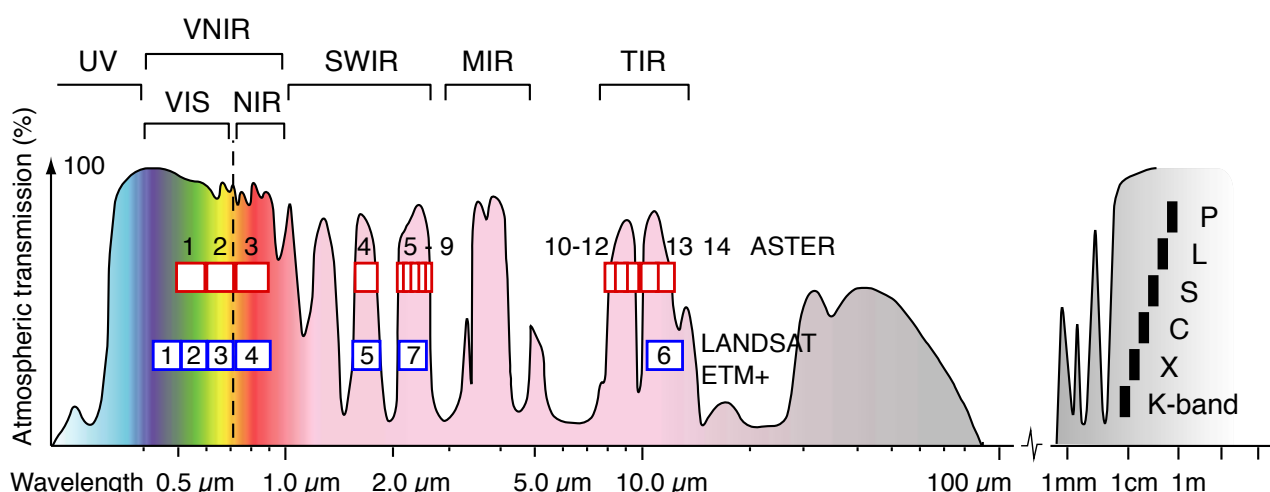


Fig. 5-1 Atmospheric transmission, sections of the optical and microwave spectrum, and spectral range of Landsat ETM+ and ASTER bands. UV: ultraviolet; VIS: visible; NIR: near infrared; SWIR: short-wave infrared; MIR: middle infrared; TIR: thermal infrared.

5.2 Spectral response

contamination (Dozier, 1989; Bourdelles and Fily, 1993; Salisbury et al., 1994). This large contrast between the VIS and SWIR spectral signature is exploited for snow classification (e.g. Rott, 1976; Dozier, 1989; König et al., 2001). The TIR and passive microwave emission of snow and ice is governed by the fact that the surface temperature is at or below 0° C. (See also Bindschadler, 1998; König et al., 2001).

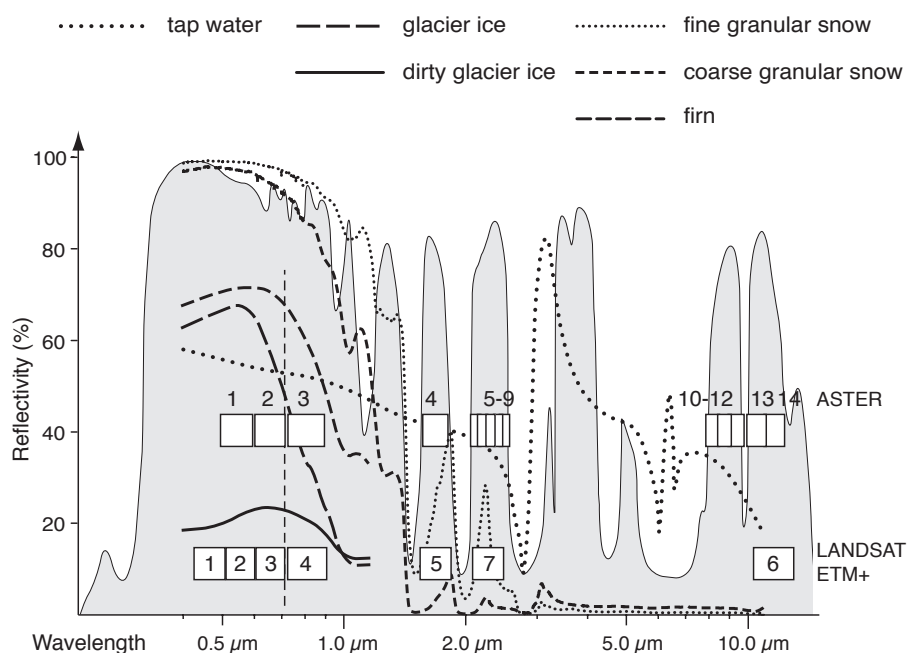


Fig. 5-2 Simplified spectral signatures of water and different types of snow and ice for passive optical sensors. Atmospheric transmission and Landsat ETM+ and ASTER bands are also shown. Spectral data are taken from the ASTER spectral library, Zeng et al. (1983), and Hall et al. (1988).

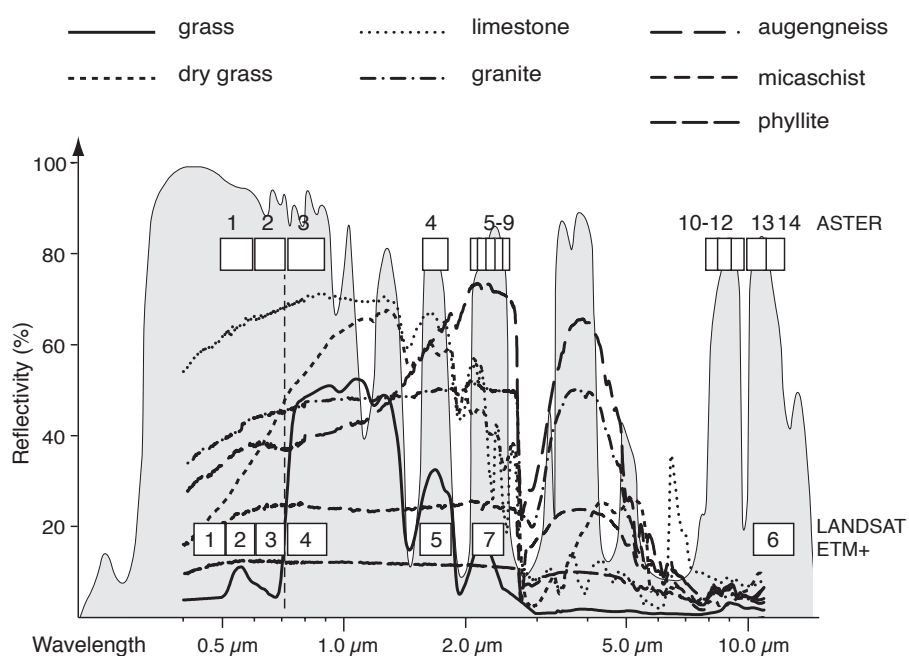


Fig. 5-3 Simplified spectral signatures of different types of grass and rock for passive sensors. Atmospheric transmission and Landsat ETM+ and ASTER bands are also shown. Spectral data are taken from the ASTER spectral library.

Ice

As a consequence of the reflectance properties of snow, bare glacier ice has a lower reflectance than snow in the VIS spectrum because of the accumulation of optically active contaminants. This effect increases towards dirty glacier ice (Zeng et al., 1983; Koelemeijer et al., 1993). In the NIR and SWIR, the dependency of reflectance on increasing grain sizes from snow to ice is effective. In addition, the presence of liquid water on the ice surface might lead to reduced reflectivity in the NIR (Rott, 1976; Winther et al., 1999; König et al., 2001). For debris-covered ice, the spectral signature of debris may prevail over the ice signature depending on the percentage of the debris-covered surface area. If the ice surface within a pixel is covered with debris by more than several ten percents of surface area it can hardly be separated from pixels of periglacial debris or bedrock using multispectral data.

Rock

Compared to snow and ice, rock or debris-covered surfaces show a significantly different reflectance in the VNIR and SWIR. This fact usually allows for good spectral discernibility of such surfaces against clean snow and ice. The highly variable reflectance, or emissivity, respectively, of different mineral and rock types in the VNIR, SWIR and TIR forms the base for geology mapping from multi- and especially hyperspectral imagery (e.g. Clark, 1999; Sabins, 1999; Rencz et al., 2003; Rowan and Mars, 2003; Volesky et al., 2003). Knowledge of the geology of a high-mountain area supports geomorphological and geomorphodynamical analyses in various ways (e.g. detection of erosion processes). There are also direct applications for glaciological investigations. Detection of the spatial distribution and the type of surface debris on glaciers or rockglaciers, for instance, enables material origin and transport paths to be discovered provided that the size of the spectral features examined sufficiently exceeds the sensor resolution (e.g. Bishop et al., 1995). Conclusions can be drawn concerning present dynamics and past dynamics (e.g. Fig. 5-7, right, and Fig. 5-8).

Water

Reflection of open water in the VIS is highly variable depending among other things on its turbidity. In the NIR and SWIR, water strongly absorbs radiation, nearly independent of its turbidity. The ratio of NIR to SWIR reflection of water is similar to that of snow and ice, which involves the risk of misclassification. Inclusion of the VIS thus facilitates separation into two categories (Huggel et al., 2002; Paul, 2004). Turbidity and temperature of glacial lakes, an important element in their characterization, can be derived from VIS and thermal infrared (TIR) data (Wessels et al., 2002). (For other applications see also Keller et al., 1998; Pietroniro and Leconte, 2000; Frohn et al., 2005).

Vegetation

Much research on multi- and hyperspectral remote sensing of vegetation in mountainous environments is available (e.g. Frank, 1988; Kurnatowska, 1998; Ustin et al., 1999). Related vegetation mapping usually takes advantage of a strong increase in reflectivity in the NIR. In glaciological research, the existence of vegetation itself might be the most interesting result since it potentially indicates, for instance, comparably stable surfaces, plant succession or lack of surface abrasion. First-order vegetation mapping may be applied for excluding distinct areas from further analyses or removing misclassifications (e.g. Figures 5-6, 5-7, 6-4, and 6-5).

Thermal infrared (TIR)

Until present, the thermal infrared spectrum has been barely exploited for investigating mountain glaciers and permafrost (Lipton and Ward, 1997; Bishop et al., 2004). Compared to ice, the strong thermal emission of debris under incoming direct short-wave radiation has a strong effect on the TIR signal of debris-covered ice. The extent to which TIR data can be used to distinguish glacier ice under loose or thin debris-cover from respective cooling of the superimposed debris is presently under investigation (Taschner and Ranzi, 2002; Ranzi et al., 2004) (cf. Lougeay, 1974; Lougeay, 1982). Figures 5-7 (right) and 5-8 show examples of how the inclusion of TIR in image interpretation and classification supports mapping of the lithological composition of the surface (cf. Hook et al., 1992; Schmugge et al., 1998; Hook et al., 1999).

During daytime, the long-wave radiation emitted from the terrain surface depends mainly on the short-wave incoming radiation (e.g. Mittaz et al., 2000; Hoelzle et al., 2001). Therefore, nocturnal or early morning TIR imagery might represent the emissivity differences of the ground material in a better way. In Figure 5-4 ASTER night-time TIR data are compared to daytime data from Landsat ETM and a DTM hillshade. Indeed, in the nocturnal TIR data some glacier tongues that are debris-covered in parts (e.g. glacier tongue to the south-east, Capps Glacier) show less long-wave emission than the surrounding paraglacial debris. In contrast, in the daytime TIR data the supraglacial debris shows similar emission and reflectivity compared to the terrain surrounding the glacier. Comparing the satellite optical data with the DTM hillshade (sun azimuth and elevation as during the ETM data acquisition) confirms the significant influence of incoming short-wave on emitted long-wave radiation.

Because objects differ with respect to emissivity (effectiveness in translation of absorbed radiation into temperature, and temperature into emitted radiation), observed radiation does not translate directly in temperature differences (Wan and Dozier, 1989; Campbell, 2002; Bishop et al., 2004). Through multitemporal TIR studies (e.g. the above comparison between day- and night-time data) the thermal inertia of objects can be analysed.

Microwave spectrum

In the microwave spectrum, the ground response is a function of the applied wavelength, polarization, incidence angle in relation to the topography orientation, and the complex dielectric constant of the surface material (Lillesand and Kieffer, 2000). The latter describes the reflectivity and conductivity of the material. The reflectivity depends, among other influences, on the surface roughness in relation to the wavelength applied. While roughness in the cm-order appears rough for the K-band (i.e. large fraction of diffuse reflection), it appears smooth in the L-band (i.e. large fraction of specular reflection). Platforms with multifrequency SAR sensors, which simultaneously cover different bands, thus, allow for deriving surface characteristics from backscatter differences (e.g. SIR/X-SAR C, L, X-band: Coltell et al., 1996; Floricioiu and Rott, 2001)

The material conductivity in the microwave spectrum is mainly dependent on the liquid water content. A cold and dry snow pack may be invisible for microwaves so that the main reflection happens at the underlying material, whereas the penetration into wet firn or ice is very small and surface reflectivity is high (Mätzler, 1987; Marshall et al., 1995; Kelley et al., 1997; Engeset, 1999; Friedman et al., 1999; König et al., 2001; Piesbergen, 2002; Zahnen et al., 2003; König et al., 2004). Mountain lakes

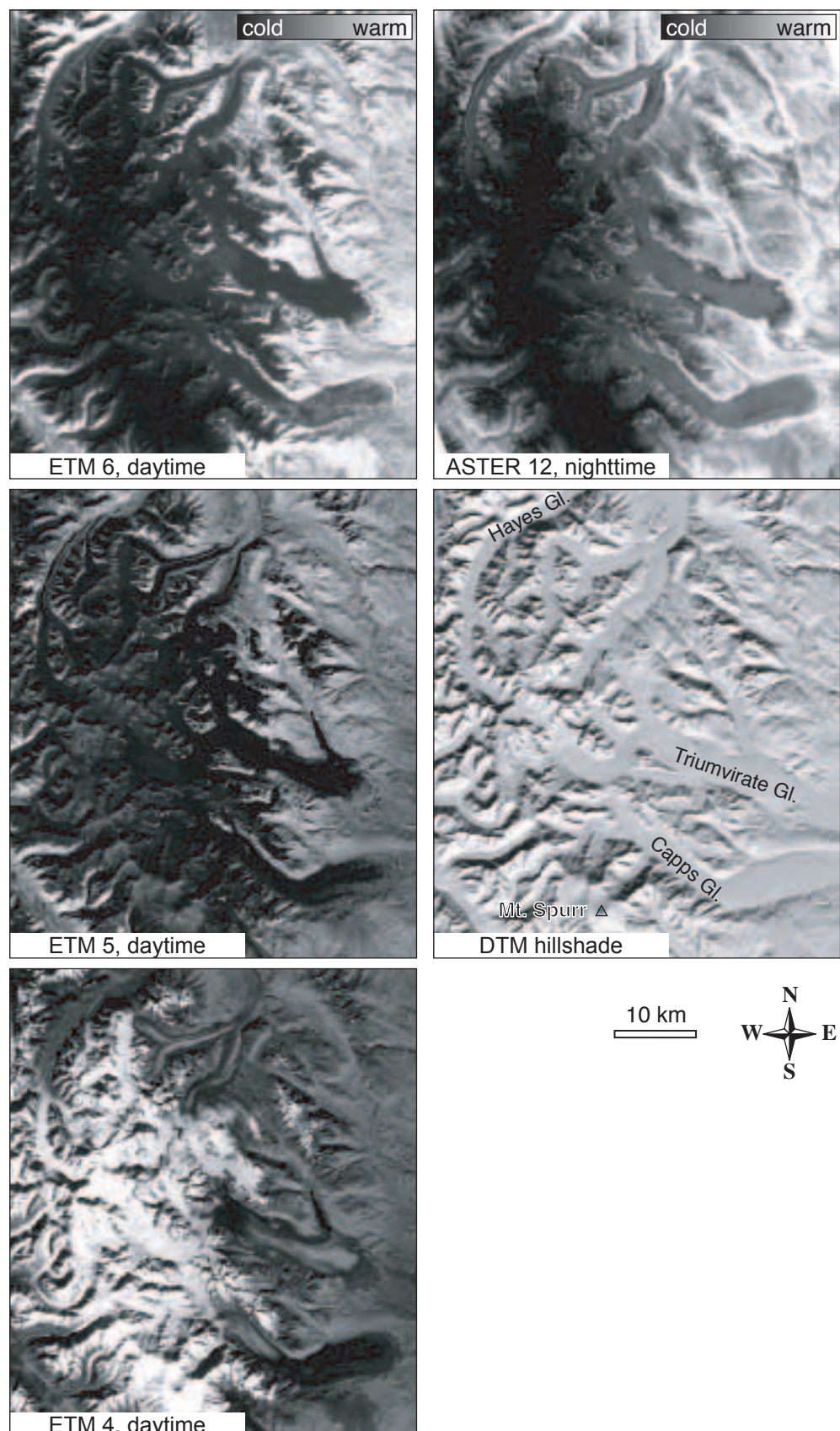


Fig. 5-4 Tordrillo Mountains, Alaska (61.5°N , 152°W). Left column: Landsat ETM+ channels 6 (TIR), 5 (SWIR), and 4 (NIR) of 06 September 2001, 12:19 local time. Right column: ASTER band 12 (TIR) of 28 August 2002, 22:35 local time, and hillshade of a DTM by the US Geological Survey. Dark colours in the TIR data indicate low long-wave emission. DTM illumination angles as for the time of the ETM+ acquisition (sun elevation 34.2° , azimuth 164.3°).

often represent a relatively smooth surface with respect to the microwave wavelength thus leading to specular reflection and a dark signature in the SAR image (Pietroniro and Leconte, 2000).

Polarization of the emitted and received radar signal (typically measured in an orthogonal reference system; H: horizontal, V: vertical) is also able to decompose the measured signal in different scattering mechanisms (Rott, 1994; Floricioiu and Rott, 2001; König et al., 2001; Stebler et al., 2002). If a clear polarisation or depolarisation in the backscatter signal from a polarimetric SAR system can be observed for a terrain section, certain surface characteristics can be inferred (e.g. a blocky surface acting as corner reflectors). Depolarisation can be among others due to a rough terrain surface with respect to wavelength, or volume scattering from a inhomogenous ground medium. Decomposition of terrain characteristics can be supported by polarimetric SAR in an interferometric mode (Pol-INSAR: Cloude and Papathanassiou, 1998; Stebler et al., 2002).

See also Section 12.2.

5.3 Classification approaches

The surface signature in the spectral domain is used to (i) describe and (ii) distinguish surface types and conditions. Such classifications may be characterized (Schowengerdt, 1997; Campbell, 2002) by terms such as:

- hard / soft classification,
- manual / supervised / unsupervised classification,
- parametric / non-parametric classification,
- spatial / spectral segmentation,
- pixel / subpixel classification, and
- multispectral / hyperspectral classification.

Hard versus soft classification

Hard classification means that a terrain point is assigned to only one category, producing sharp boundaries between classes. In *soft classification*, likelihood values alone are given for a pixel to belong to certain classes. In alpine environments, both discrete (hard) and fuzzy (soft) transitions exist, thus suggesting application of both classification types. In nature, the boundaries between, for instance, glacier and rock, or snow and bare soil are in general very distinct (see Fig. 5-5). The classification goal is then to determine the boundary location as accurate as possible. On the other hand, the transitions are smooth, for example, from dead ice to moraine or from sparse to dense vegetation cover, with the result that making a change in the class probability might serve to reflect the conditions in nature in a much better way (e.g. Fig. 5-5)

The choice of hard versus soft classification strategies depends not only on the natural characteristics of the boundary between two surface categories, but also on the spectral properties and spatial resolution of the sensor applied, and the scale considered. A category transition in nature might be discrete in one part of the spectrum, but fuzzy in another part (see Section 5.2). If the spatial resolution of a sensor (i.e. GIFOV) is significantly larger than the spatial variations of a category, an image pixel contains a mixed signal of more than one ground category (mixed pixel), regardless of whether the category transitions are discrete or fuzzy. Such mixed pixels

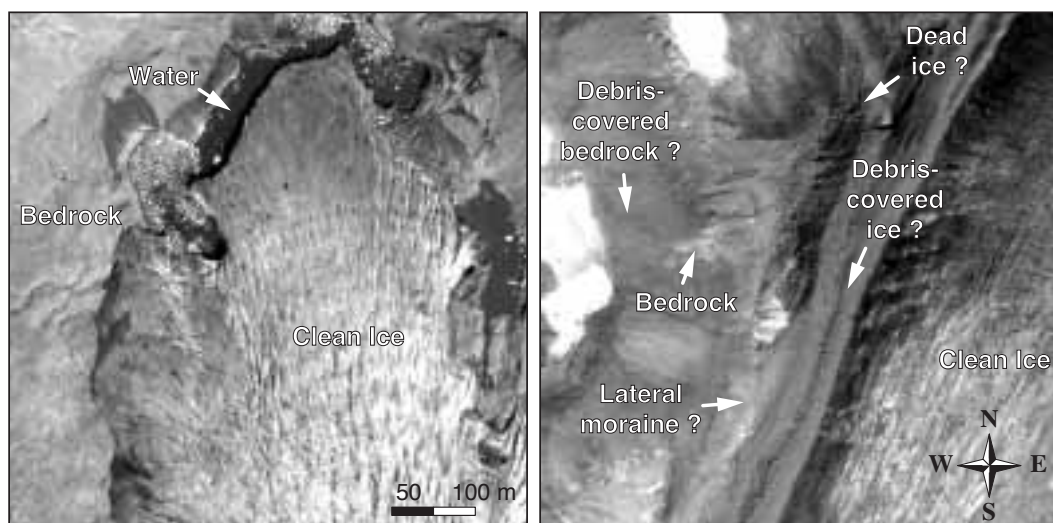


Fig. 5-5

Two sections of an Ikonos image of 17 September 2000 (© Space Imaging Europe, Swiss National Point of Contact) in the Susten region, Swiss Alps. Classification of distinct (hard) boundaries (e.g. between clean ice and bedrock; left panel) requires different approaches than classification of uncertain (soft) transitions between two major ground types (e.g. clean ice vs. debris-covered ice vs. debris-covered dead ice vs. debris-covered bedrock vs. bedrock; right panel).

can be classified as hard (e.g. by a threshold) or soft (e.g. by giving category percentages).

Manual, supervised and unsupervised classification

Manual delineation of categories is done by combining human interpretation and digitizing. Manual delineation is used for simple classifications, but also for accuracy assessments, ground truth acquisition, or completion or correction of other classifications. *Supervised classification* is an application-driven method. Training areas of the categories to be mapped are operator-selected in order to develop the spectral signatures of these classes. Discernibility analysis is applied to test if the selected categories can be distinguished significantly from one another. Overlapping signatures have to be separated artificially. The spectral signatures are then used to automatically segment the entire imagery. During *unsupervised classification* the image is automatically segmented in concentrations of spectral vectors. These so-called clusters represent artificial categories. Unsupervised classification is, therefore, a data-driven method. The automatic clusters have then to be assigned to classes of user interest. All three classification strategies may also be combined.

Parametric versus non-parametric classification

Parametric classification assumes a certain statistical distribution of a particular class (e.g. mean spectral vector and covariance). The statistical class parameters are estimated from training areas within the image under analysis or are inferred. An individual pixel is assigned to a certain class according to its statistical proximity with respect to the class parameters (e.g. nearest mean, or maximum likelihood). In the case of *non-parametric classification*, the membership in a class is decided not on the basis of statistical parameters, but on the basis of simple boundaries, e.g. boxes, in the spectral space as defined around training data, or on the basis of Euclidean distance to training pixels. Artificial neural networks (ANN) are non-parametric classifications where the decision boundaries between the classes are determined iteratively by minimizing an error criterion on the given training data (see Section 5.4.8).

Spatial and spectral segmentation

Supervised and unsupervised, parametric and non-parametric classifications primarily rely on the spectral characteristics of individual pixels. Image segmentation can also be done using neighbourhood relations of pixels (*spatial segmentation*). Edge detection or feature extraction algorithms are able to detect class boundaries (pattern recognition). Areas of the same class membership may be aggregated by region growing algorithms where individual pixels are joint according to algebraic rules (e.g. based on spectral characteristics). Some spatial algorithms work also for panchromatic imagery. The spectral and spatial approaches can be combined to *spatial-spectral segmentation*, for instance, by applying spectral classification to pixel areas aggregated beforehand, by spatially filtering the classification results, or – more advanced – by applying *integrated object-oriented image classifications* (e.g. eCognition, Frohn et al., 2005).

Subpixel classification

Hard classification methods assign each pixel to exactly one category. Quantifying the categories contributing to the spectral signature of a mixed pixel leads to *subpixel classification*. In terms of subpixel accuracy, a distinction must be made between spectral subpixel resolution ('which categories contribute, and how much?') and geometric subpixel resolution ('where are the categories?'). In principle, the location of the contributing categories within a pixel cannot be resolved from a mixed pixel. However, corresponding assumptions might be drawn, including the spatial context of a pixel, or expert knowledge about the typical characteristics of a boundary. Some kind of such geometric subpixel accuracy may be achieved by *post-classification editing* of class boundaries that were originally determined with pixel-accuracy. Simple approaches of that type consist in interpolation or smoothing of classification results. For instance, the pixel-wise (i.e. planimetrically stepped) classification between glacier ice and adjacent bedrock might be represented by interpolating a smooth horizontal curve separating both classes. In practice such procedure is often complicated by a number of classification problems, and might require knowledge-based interpolation algorithms. The success of the approach depends, among other things, on the ratio between GIFOV and the spatial resolution at which the category boundaries should be mapped.

Linear unmixing strives to determine for individual pixels the fraction f_{ij} of idealized pure signatures (endmembers) contributing to its actual spectral composition. After Schowengerdt (1997) the mixed signature of a pixel in a linear mixing model is:

$$DN_{ij} = E f_{ij} + \varepsilon_{ij} \quad (5-2)$$

where

DN_{ij} is the digital number of a pixel at ij ,

E is the $k \times l$ matrix of the k -dimensional spectral signatures for l endmembers,

f_{ij} is the l -dimensional vector of endmember fractions within a pixel ij , and

ε_{ij} is a residual error.

The endmember signatures can be derived from extreme pixels assumed to consist of only one endmember class (i.e. pure unmixed), or inferred from laboratory data or spectral libraries (e.g. Painter et al., 2003). *Fuzzy set classification* follows the opposite approach to the linear mixing concept by allowing one pixel to be member of multiple categories with a certain probability connected to each membership.

Combinations and others

The classification approaches listed here can be applied on *multippectral* data with a small number of comparably broad bands as well as on *hyperspectral* data with a large number of narrow bands. However, some of the classification methods are especially suited for hyperspectral data (e.g. linear unmixing), and a number of additional algorithms exist for hyperspectral data (Schowengerdt, 1997; Lillesand and Kieffer, 2000).

Classification approaches can be combined or applied sequentially. Instead of using only spectral data, some classification algorithms also permit the inclusion of spectral derivatives (e.g. band ratios instead of the bands themselves, or multitemporal data) or non-spectral data (e.g. DTMs (Brown et al., 1998); see multidimensional merging, Chapter 6).

5.4 Image processing for glacial and periglacial surfaces

In this section, selected classification approaches based on optical data are summarized that have already been tested for glaciological applications in high mountains (see Paul, 2001; Albert, 2002; Paul et al., 2002):

5.4.1 Manual delineation

Manual delineation of panchromatic or multispectral image features might be useful for highly complex classifications where expert knowledge is needed, for instance, for distinguishing rockglaciers, dead ice, debris-covered ice and periglacial debris from one another (e.g. Fig. 12-1). An analyst is able to include experience, knowledge and complex logical rules in the decision process, also relying on non-spectral, i.e. multidimensional data or knowledge. Manual delineation is often needed to complement and correct automatic classifications, and has been applied to glacier delineation in numerous studies (e.g. Rott and Markl, 1989; Hall et al., 1992; Williams et al., 1997; Paul, 2002a).

5.4.2 False colour composite (FCC)

False colour composites may take advantage of differences between the spectral signatures of the categories prevailing in the multispectral image (Pohl and Van Genderen, 1998). For instance, in an ETM 543 RGB-composite (red: channel 5, green: channel 4, blue: channel 3) snow and ice are clearly separated from debris, rock or vegetation because ice and snow show a significant step in reflectance between VNIR and SWIR as compared to the other materials (e.g. Figs. 5-6, 5-7 and 5-9). FCCs can be used for facilitating manual delineation. They work well for clean ice and snow (e.g. Della Ventura et al., 1983; Williams et al., 1991). Instead of FCCs, IHS-transforms or decorrelation stretches might be helpful (see Section 5.4.4).

5.4.3 Calculation of reflectance

Derivation of the ground reflectance at each pixel requires the following steps (cf. Section 5.1):

(1) Calculation of the effective planetary reflectance at the sensor from the raw DNs of the image. Beforehand, the DNs have to be transformed into radiance at the sensor using the calibration coefficients 'gain' and 'offset' (Markham and Barker, 1985).



Fig. 5-6 FCCs of ASTER bands 321 (left) and 432 (right) as RGB. Unteraar Glacier, Grimsel region, Swiss Alps. In the 321-FCC, vegetation (red) can be more easily identified. In the 432-FCC, ice and snow (blue) are more easily distinguishable from debris (light pink).

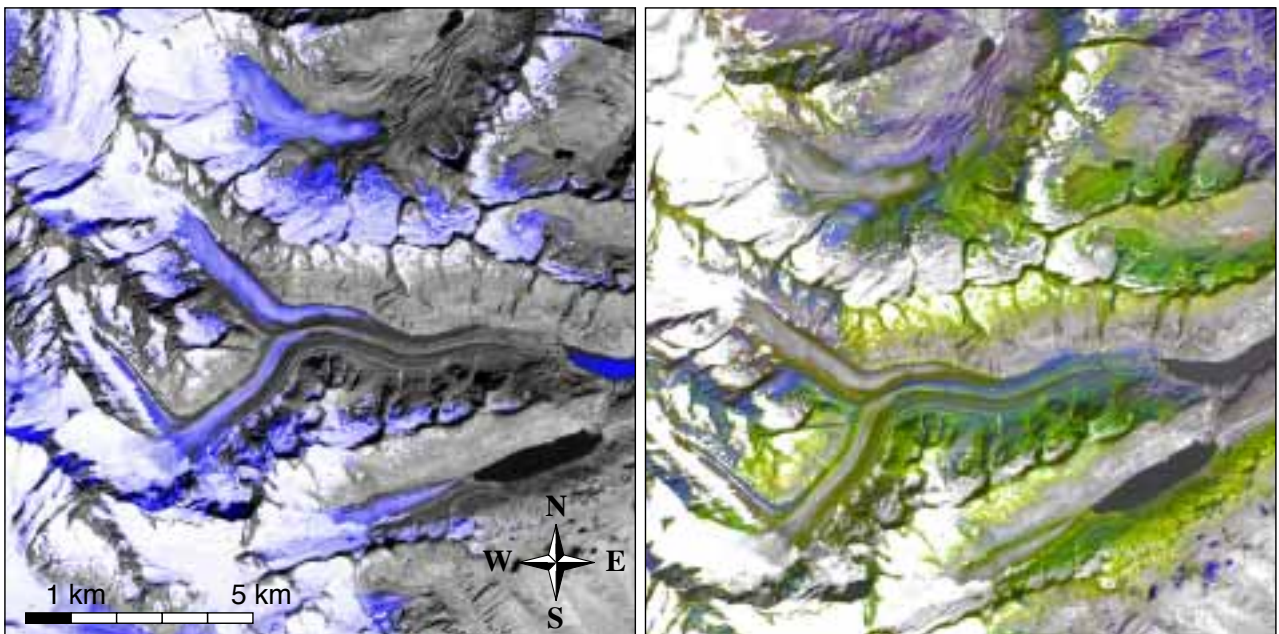


Fig. 5-7 Left: composite of a thresholded ratio-image ASTER 3 / ASTER 4 (blue colour) with the intensity taken from ASTER band 3. The procedure is used to highlight debris-free glacier ice. The reservoir in front of Unteraar glacier is misclassified by the band ratio. Right: RGB-FCC of ASTER bands 4 (SWIR), 9 (SWIR) and 10 (TIR), IHS-fused with the ASTER band 3 (intensity). Vegetated areas as identified by the NDVI, and ice- and snow-covered areas as identified by a thresholded ASTER 3 / ASTER 4 ratio-image have been de-saturated. Thus, only rock and debris surfaces are depicted in colour. The resulting image corresponds well with the main geologic units in the region: granite surfaces rather appear in yellow (image centre and right) and gneiss surfaces rather in blue (left part of the image section). As seen from the bluish colours on the debris-covered tongue of Unteraar glacier, the supraglacial debris originates from the upper glacier parts that are surrounded by gneiss.

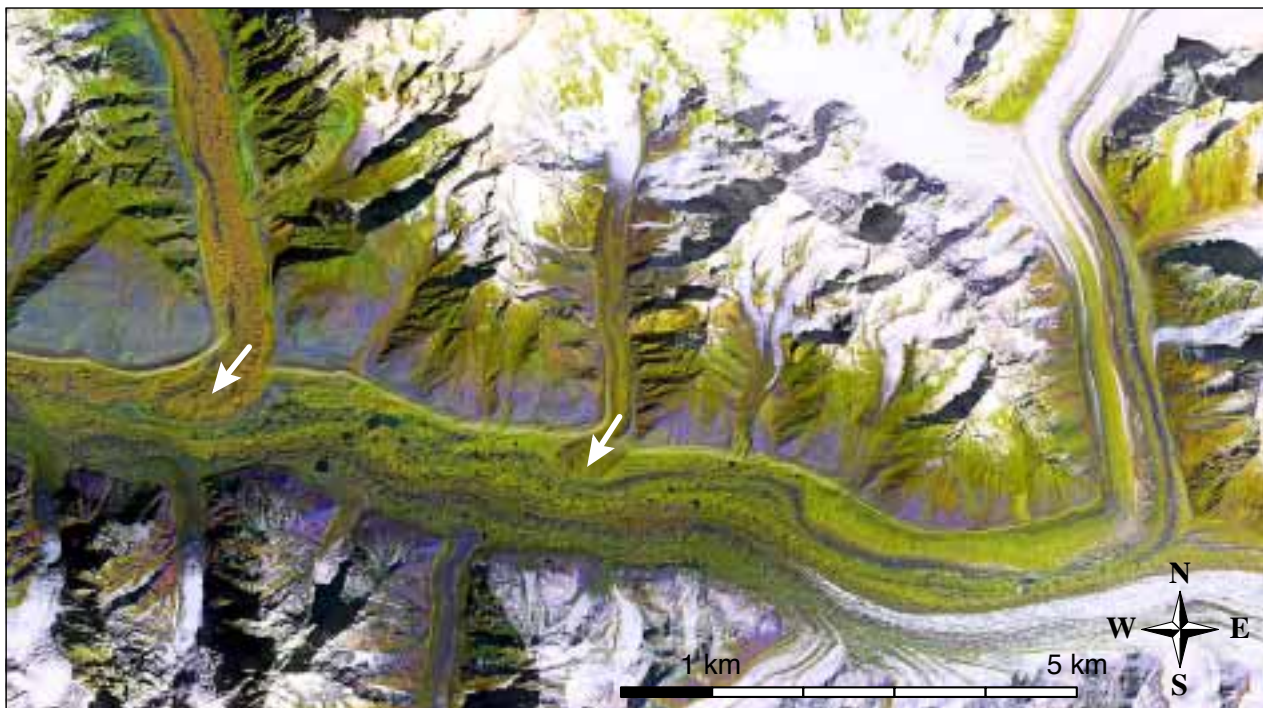


Fig. 5-8 Hispar glacier, Karakorum, Pakistan. Surface lithology shows especially good discernibility in the SWIR and TIR (see Fig. 5-3). That characteristic can be used to identify differences in surface rock and debris type, and thus to map geologic properties (see Fig. 5-7, right). Such an approach may also be used to detect differences in debris-cover type on glaciers. Corresponding results are able to provide insight into past and present glacier dynamics by reflecting the source areas and travel path of the material. The figure shows a RGB-FCC of ASTER bands 4 9 10, with the intensity taken from ASTER band 3. The two northern tributary glaciers in the middle and to the left have recently advanced (in surge-type mode?) as can be seen from the moraine deformation on the main east-west directed glacier stream (arrows, see Wake and Searle, 1993).

(2) Atmospheric correction of the reflectance due to content of aerosols, water vapour and others (e.g. Hall et al., 1989; Hall et al., 1990; Vermote et al., 1997; Bishop et al., 2004). This step improves the correspondence of satellite with in-situ measurements.

(3) Topographic correction to account for bias in illumination due to slope and aspect effects (anisotropic reflectance correction) (Sandmeier and Itten, 1997; Bishop et al., 2004).

Steps (1)-(3) can be summarized as *radiometric corrections*.

(4) Image co-registration to other data sets, georeferencing and/or orthoprojection (also termed (ortho-)rectification) represent *geometric corrections* of spatial distortions, which are however not related to the calculation of reflectances.

Comparing the remote sensing derived reflectance to that obtained from in situ measurements, or to theoretical predictions from spectral signatures (see Section 5.2), allows to some extent for surface interpretation from the corrected image. This approach has been used mostly to characterize snow and ice facies, or their albedo, respectively (Hall et al., 1988; Gratton et al., 1990; Hall et al., 1990; Gratton et al., 1993; Koelemeijer et al., 1993; Winther, 1993; Knap et al., 1999; König et al., 2001; Paul, 2001; Paul, 2004; Paul et al., 2005).

5.4.4 Spectral transforms

Intensity-hue-saturation transformation (IHS)

For better visual interpretation, image manipulation or subsequent classification, it can be useful to enhance RGB images by transforming them into another three-axes colour space. The colour space most often applied in that context is the intensity (image brightness), hue (colour), saturation (colour purity) colour space (IHS). The IHS components of an RGB image pixel can be computed from geometric projections of an RGB colour vector into the IHS colour space (Schowengerdt, 1997; Pohl and Van Genderen, 1998). The IHS image layers can be manipulated and then inversely transformed back into the RGB space. This technique is, for example, used for image fusion where the intensity layer of the original image is replaced by the intensity layer of an image with higher resolution (Section 6.1). In addition, the components I, H or S of an image might be individually inferred into a classification (e.g. Paul, 2004; Salzmann et al., 2004).

Principle component transformation (PCT)

Multispectral image bands are often highly correlated due to the spectral similarity of the ground material within an entire wavelength range, due to topographic effects (e.g. shading) and due to the spectral resolution of the sensor applied. Principle component (PC) transformation aims at transforming the original image linearly to minimize the inter-band correlation (Richards, 1993; Schowengerdt, 1997):

$$DN_{PC} = W_{PC} DN \quad (5-3)$$

where

DN is the k -dimensional vector of digital numbers of an image pixel in k different bands,

DN_{PC} is the vector of this pixel in the PC-transformed system,

W_{PC} is an image-specific $k \times k$ -matrix of PC-coefficients that minimize the inter-band correlation, and

k is the number of image bands.

PCT can be applied to reduce the size of a multi- or hyperdimensional data set by sorting the data into layers ranging from high spatial variance to layers with little spatial variance. In this way, redundant information can be excluded from the original data set. By reducing the spectral image redundancy, PCs are able to facilitate visual interpretation or automatic classification approaches (Fig. 5-10) (Sidjak and Wheate, 1999). Direct assignment of PCT-results to classes of glaciological interest is, however, difficult because the principal components depend on the individual image and the image section chosen for analysis (Paul, 2004). Like the IHS transform, PCT is thus an image enhancement or preprocessing method rather than a classification tool by itself.

Decorrelation stretch

Decorrelation stretch is an application of the PC or IHS transformation to reduce correlated and thus redundant information of multispectral imagery (Gillespie et al., 1986; Schowengerdt, 1997). It allows for better visual exploitation of multispectral imagery and supports the manual delineation as well as preparation and selection of further classification methods (Figs. 5-9 and 5-10). The multispectral bands are PC transformed at first for decorrelation stretching. The respective PCs are then stretched to fill the colour-space in an optimal way, and inversely transformed by

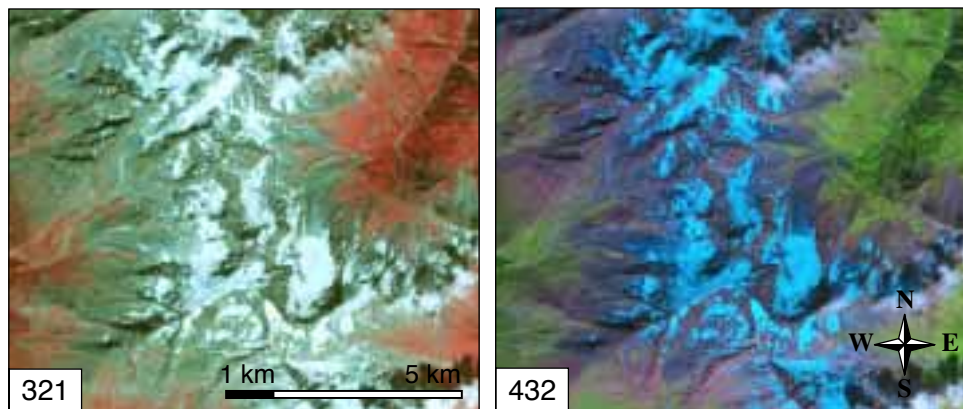


Fig. 5-9 RGB-FCCs of ASTER bands 321 (left) and 432 (right) of the Gruben area, Swiss Alps. The FCCs are given for comparison of the visual information content with the principle components and decorrelation stretch in Figure 5-10.

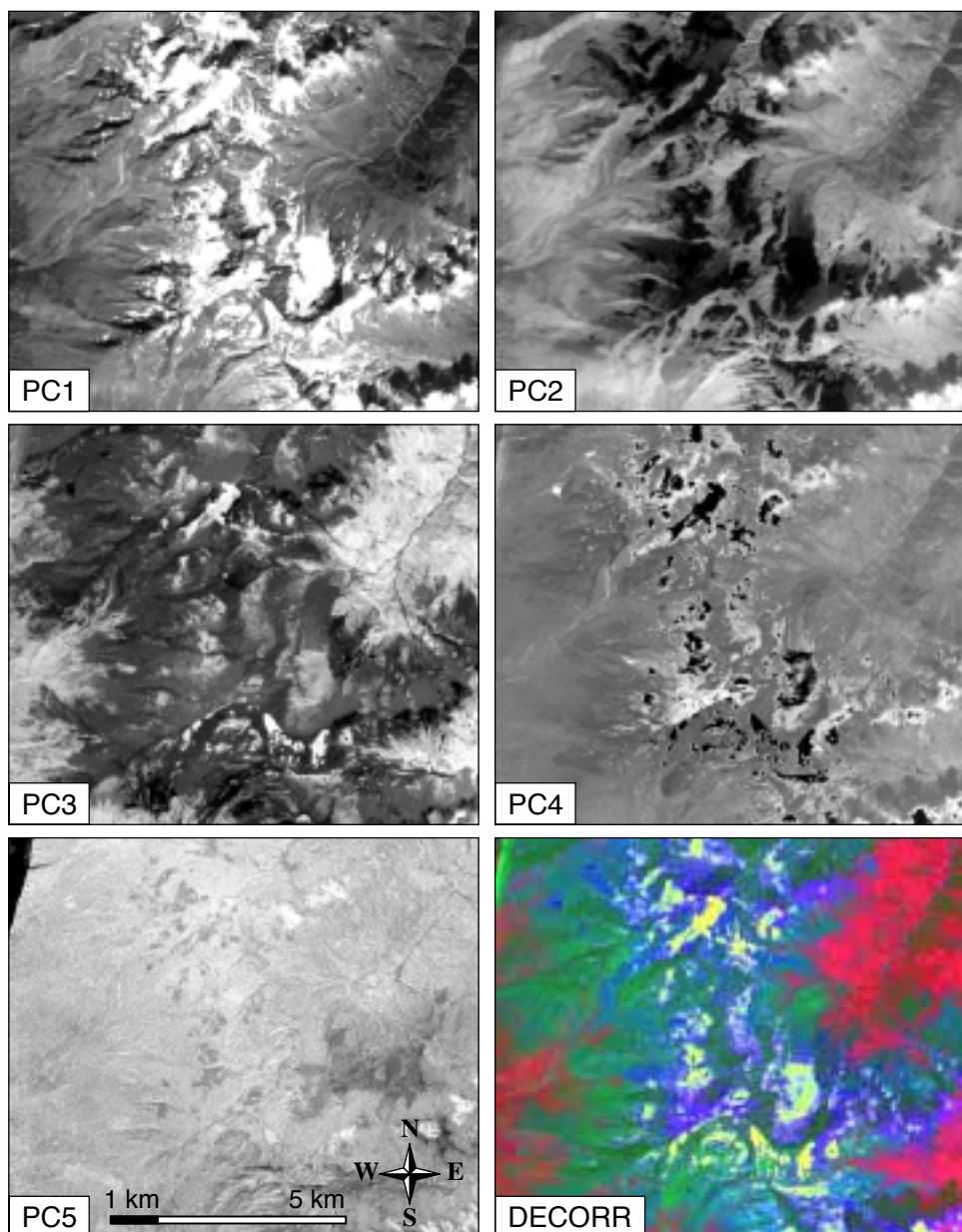


Fig. 5-10 Principle components 1-5 of ASTER bands 1-9 of the Gruben area, and decorrelation stretch (R: PC1, G: PC2, B: PC3). PC1 and PC2 reflect approximately the VNIR, or SWIR variability, respectively. PC3 shows some correlation with vegetation cover, PC4 mainly with different snow and ice facies. PC5 contains high-frequency variation such as fine objects or sensor noise.

W_{PC}^{-1} (see Eq. 5-3) into the RGB colour space. Decorrelation stretches are, for instance, available as ASTER Level 2 products.

5.4.5 Image algebra and segmentation

Spectral bands may be inferred in different algebraic algorithms, among which band ratios R

$$R_{ij} = \frac{DN_i}{DN_j}, \text{ or} \quad (5-4)$$

$$R_{ij} = \frac{(DN_i - DN_{\min(i)})}{(DN_j - DN_{\min(j)})}, \quad (5-5)$$

and normalized differences indices (NDI , or modulation ratios) are the most widespread (Schowengerdt, 1997)

$$NDI_{ij} = \frac{R_{ij} - 1}{R_{ij} + 1} = \frac{(DN_i - DN_j)}{(DN_i + DN_j)}, \quad (5-6)$$

where

DN_i and DN_j are digital numbers of two bands i and j that show high discernibility for the category to be classified with respect to other categories in the image, and

DN_{\min} are the minimum (i.e. darkest) DNs of an individual band.

For band ratios, subtraction of the minimum DN for each band applied reduces the illumination differences from atmospheric scattering (Crippen, 1988). Similarly, the results of normalized differences might be improved by subtraction of the band-specific minimum DNs. For ice and snow, usually bands in the VNIR versus bands in the SWIR are applied (e.g. TM 2, 3 or 4 versus TM 5: Della Ventura et al., 1987; Bayr et al., 1994; Rott, 1994; Jacobs et al., 1997; Paul, 2001; Albert, 2002; Paul, 2002a; Paul et al., 2002; or ASTER 3 versus ASTER 4: Kääb et al., 2003a; Paul, 2004; Paul and Kääb, 2005).

The normalized difference snow index (NDSI) for TM is defined as $(TM2 - TM5)/(TM2 + TM5)$ (Dozier, 1989; Hall et al., 1995a; Sidjak and Wheate, 1999). Water can be detected by means of the normalized difference water index (NDWI: $(TM4 - TM1)/(TM4 + TM1)$, Huggel, 1998; Kääb et al., 2000a; Kääb et al., 2000b; Huggel et al., 2002), which is similar to the well-established NDVI for vegetation (e.g. $(TM4 - TM3)/(TM4 + TM3)$, Hardy and Burgan, 1999). Classification of water or vegetation might be useful for eliminating misclassifications from the above band ratios for ice and snow (e.g. Figs. 5-7, 6-4 and 6-5) (Paul et al., 2002). Band ratios and NDIs partly eliminate atmospheric and topographic influences when these affect the used bands in a similar way (e.g. Holben and Justice, 1981). Thresholds have to be chosen for final segmentation of the ratio or normalized difference image. Image algebra and segmentation algorithms are especially robust (Paul, 2001; Albert, 2002). To gain better control on the results further terms might be added to Equations 5-4, 5-5, or 5-6, possibly including further bands. (Examples in Figs. 3-29 and 4-7)

Other image algebra methods, which are for instance used for image fusion (Section 6.1), include adding and multiplication (Pohl and Van Genderen, 1998).

5.4.6 Unsupervised classification

Unsupervised classification methods tend to be successful for relatively homogeneous terrain with few categories only (e.g. clean-ice glaciers), whereas problems often occur for variable terrain with many classes (e.g. clean ice, dirty ice, debris-covered ice, or clean ice in cast shadow: Paul, 2001; Paul, 2004). The unsupervised categories have to be assigned to classes of user-interest, which leaves the major classification problems for terrain with low discernibility still to the analyst. Unsupervised ISODATA classification was applied by Aniya (1996) for glacier inventorying of the Southern Patagonia Icefield using Landsat TM bands 1, 4 and 5. Albert (2002) applied the same technique on an ice cap in Peru. In general, unsupervised classifications for glaciological purposes seem suited for initial data exploration rather than for final classifications.

5.4.7 Supervised classification

Supervised classification often works accurately for high-mountain terrain with reasonable spectral discernibility. Yet, as for all spectral classifications, it cannot solve problems such as debris-covered ice. Good results with supervised classification may be achieved by including not only spectral bands but also derivatives such as band ratios, principle components or normalized differences (e.g. Bronge and Bronge, 1999; Sidjak and Wheate, 1999). The choice of training areas is especially crucial for inhomogeneous terrain, as it is often found in alpine environments. In general, the spectral class signatures trained from one scene cannot be applied for other scenes, which reduces the automation capability or requires radiometric adjustments. A number of studies on supervised classification of mountain glaciers have been performed so far (Gratton et al., 1990; Binaghi et al., 1993; Paul, 2001; Albert, 2002; Paul, 2004).

5.4.8 Artificial Neural Networks (ANN)

In ANN classification the decision boundaries are not fixed in a deterministic way from training signatures, but obtained in an iterative fashion by minimizing an error criterion on the labelling of the training data (Schowengerdt, 1997). ANN classification is not restricted to spectral data. Other input data, such as spatial relations of pixels, multitemporal data, DTMs or DTM derivatives can be used. For glacial and paraglacial terrain, ANN classifications from data of a single domain (spectral or DTM) have been tested (Bishop et al., 1995; Brown et al., 1998; Bishop et al., 1999; Paul et al., 2004). However, the main potential of ANN application in glaciology might lie in the integration of multidimensional data (see Paul et al., 2004).

5.4.9 Others and combinations

Klein and Isacks (1999) used spectral unmixing for classification of snow and ice, Binaghi et al. (1997) fuzzy set theory. Brown et al. (1998) applied maximum-likelihood and ANN classification using a DTM of a glaciated landscape. Among other techniques, Albert (2002) tested linear spectral unmixing for mapping an ice cap area.

Often, classification procedures can (or have to) be combined either by fusing different approaches or by performing them sequentially. As mentioned for the supervised classification, spectral derivatives or results from other pre-processing classifications may be combined as input layers. Sidjak and Wheate (1999), for instance, achieved good results for glacier mapping from a supervised maximum-

likelihood classification using the PCs 2–4 of TM bands 1–7, a TM4/TM5 band ratio, and the NDSI. An often used chain of sequential classification approaches is to complete and correct automatic classifications manually. Such a procedure is, for instance, unavoidable for the mapping of debris-covered ice. Band ratios for glacier mapping, for instance, may result in misclassifications for vegetation in shadow and turbid water, which in turn can be eliminated by applying NDVI and NDWI (Paul, 2004). Postprocessing of the results using, for instance, spatial-domain filters may follow automatic classifications (e.g. Section 5.3, subpixel classification) (Paul et al., 2002).

5.5 Conclusions and perspectives

Classification approaches based on multispectral imagery are well developed and strongly established. Further significant progress can be expected from newly developed combinations of input layers and combinations of classification algorithms. For ice and snow applications, inclusion of thermal bands has rarely been tested and should be investigated further.

Paul (2002a; 2002b) and Albert (2002) found band ratios to be an especially simple, robust and fast method for glacier mapping over large areas. Manual adjustment of the necessary threshold seems to be preferable to thresholds automatically optimized from training areas (Rott and Markl, 1989). For complicated situations adaptive threshold variations over one scene depending on variations of the ground or illumination properties might be investigated.

There is still a large potential from spectral data and its derivatives alone, but multidimensional classification including DTMs may be most promising since they best reflect the nature of high-mountain phenomena and processes. The increasing availability of suitable DTMs supports this trend. The manual application of expert knowledge for delineation will decline gradually but never become redundant (Rott and Markl, 1989).

There is no doubt that hyperspectral analysis of the glacial, peri- and paraglacial environment will provide major impulses for classification, but also for understanding numerous phenomena and processes. While promising results are already available for geological applications, only little is known about the hyperspectral response of alpine environments with rugged topography (Keller et al., 1998; Schläpfer et al., 2000). In contrast to multispectral applications, hyperspectral ones may lead much further beyond the human ability for visual interpretation. Due to the complex topographic conditions, advances in multi- and hyperspectral remote sensing of high mountains will in particular be accompanied by or be due to the combined modelling of the spectral BRDF and the terrain (Bishop et al., 2004).

Microwave sensors respond in a particularly sensitive way to the liquid water content of snow and ice. Thus, microwave remote sensing has a high potential for characterizing snow and ice. Spectral fusion of optical and SAR data might be especially promising for that task (Rott and Strobl, 1992; Rott, 1994; Hall et al., 1995b; König et al., 2001). However, much research is still needed on the complex dielectric properties of snow and ice under various conditions to allow for linking the recorded microwave response to ground characteristics.

As defined in Section 2.3, any combined data analysis including more than one spatial data set and covering the same terrain section is considered as multidimensional data *merging*, or, more generally, as *multidimensional data analysis*. Such data can originate from different domains (spatial, temporal, spectral), have different dimensions within one domain ('1', '2', '3', 'mono', 'multi', etc.), or have differing dimension values only (point in time, wavelength, frequency, resolution, etc.). If the data merging is performed ahead of any further analysis step it is referred to as *fusion*. The term *multisensor* – often used in the context of fusion and merger (Pohl and Van Genderen, 1998; Hellwich, 1999) – denotes the combination of data from different sensors and often implies, for instance, different spatial resolutions and/or wavelengths covered.

Data merging can be characterized by two pairs of contrasting approaches:

- On the one hand, the *original data* of different domains and dimensions are merged (for images: pixel level, cf. Pohl and Van Genderen, 1998), or its *derivative products* (for images: feature level, decision level, cf. Pohl and Van Genderen, 1998).
- On the other hand, *pixel-wise information* alone or *spatial relations* may be utilized for merging.

6.1 Fusion of multiresolution data

Data fusion within one domain may consider different spectral, spatial or temporal dimensions or resolutions. Multispectral data fusion and merging (i.e. combination of different wavelengths) is discussed in Chapter 5. Multitemporal data merging is dealt with in Section 6.3. In this section, the focus is on the *fusing of spectral data with different spatial resolution*. This type of data fusion is usually applied to combine remote sensing data of higher spectral but of lower spatial resolution with data of higher spatial but lower spectral resolution. The procedures aim to combine the advantages of systems with competing constraints in one resulting data set. Principally (Toutin, 1995b; Schowengerdt, 1997; Pohl and Van Genderen, 1998; Simone et al., 2002), the applied methods can be divided into

- spatial domain fusion, and
- spectral domain fusion.

Spatial domain fusion transfers the high-frequency content as extracted by spatial filters from a high resolution image to a lower resolution image (Figs. 6-1 and 6-2). Schowengerdt (1997) gives a general approach for spatial domain fusion as

$$R_{ijk} = M_{ijk} + K_{ijk} \cdot HPH_{ij} \quad (6-1)$$

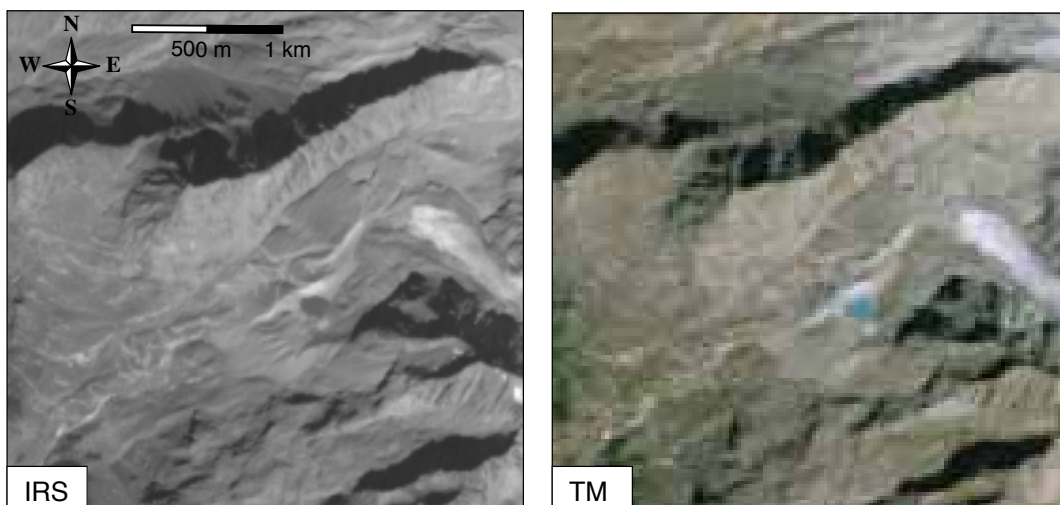


Fig. 6-1 Panchromatic IRS satellite image with 5 m resolution (left) and RGB-composite of Landsat TM bands 3 2 1 with 30 m resolution (right). Gruben area, Swiss Alps.

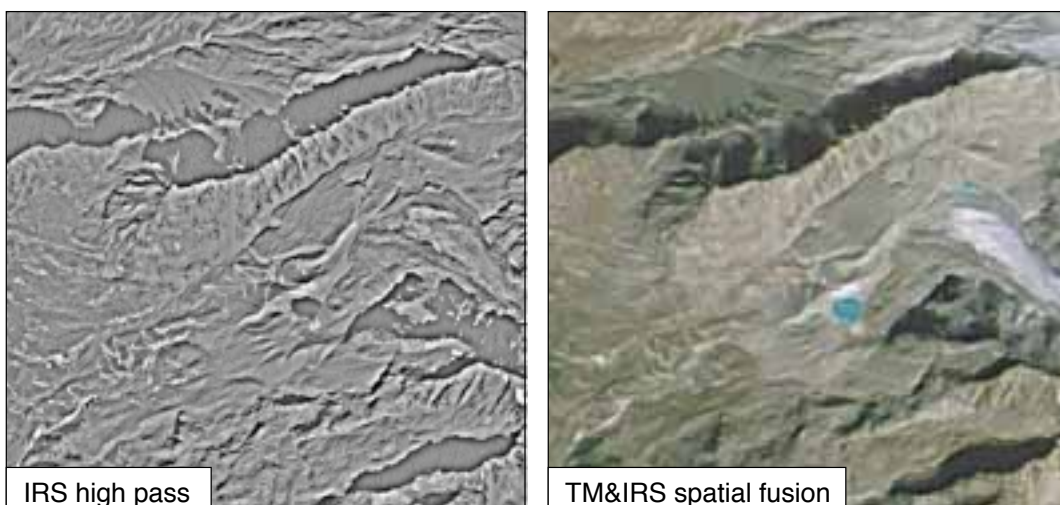


Fig. 6-2 Spatial domain fusion of a high-pass filtered IRS pan image (left; see Fig. 6-1 left) and a Landsat TM RGB composite of bands 3 2 1 (see Fig. 6-1 right). The fusion result is displayed in the right panel.

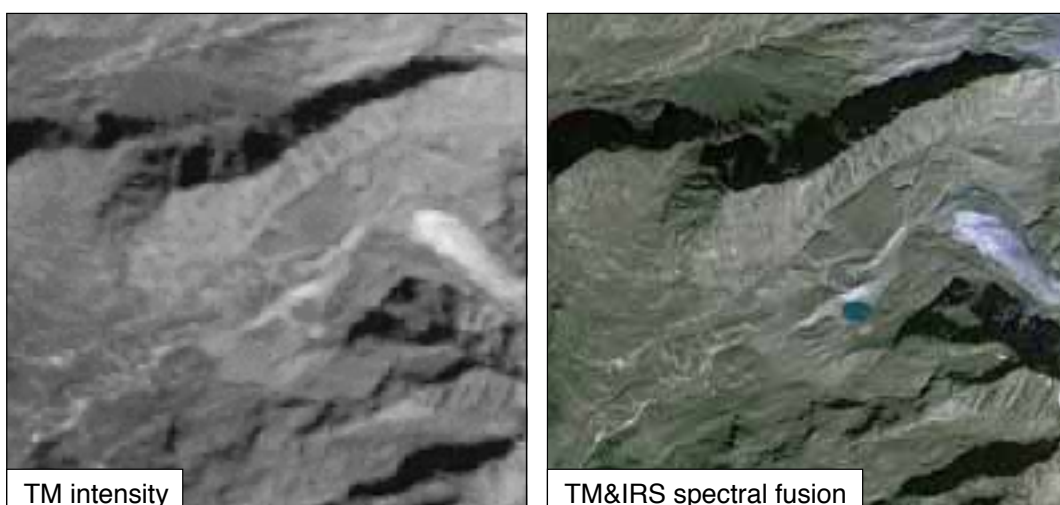


Fig. 6-3 IHS fusion of an IRS image (see Fig. 6-1 left) and a Landsat TM image (see Fig. 6-1 right). The intensity component of the Landsat 3 2 1 composite (left) is replaced by the IRS pan image (see Fig. 6-1 left). The fusion result is displayed in the right panel.

where

- R_{ijk} is the fused image matrix ij of band k ,
- M_{ijk} is the lower resolution image,
- HPH_{ij} is a high-pass version of the high resolution image H_{ij} , and
- K_{ijk} is a spatially variable weight function, for instance, normalising M_{ijk} and H_{ij} .

Similarly, wavelet or Fourier transformation of the two images with different resolutions may be combined and re-transformed, so that the high-frequency content is inferred into the lower resolution image in the frequency domain instead of the pixel domain (Pohl and Van Genderen, 1998; Ranchin and Wald, 1998; Zavorin and Le Moigne, 2005). A Fourier transform expands an image (or other data set) into a sum of cosine and sine functions, which cover the entire data set (i.e. global functions). A wavelet transform expands an image (or other data set) into a sum of functions with variable length (i.e. local filter windows) (see Section 4.2).

Spectral domain fusion transforms the lower resolution image into a new spectral space – for instance principle components (PC fusion) or IHS colour space (IHS fusion; cf. Section 5.4.4) – in which one dimension is best correlated with the high resolution image to be merged. This respective spectral dimension of the lower resolution image (e.g. PC1 or I-component) is then replaced by the high resolution image, and, if needed, transformed back into the original spectral space (Fig. 6-3) (e.g. Pellemans et al., 1993; Toutin, 1995b; Yocky, 1996; Gross and Schott, 1998; Pohl and Van Genderen, 1998; Zhou et al., 1998; Nunez et al., 1999).

Other fusion techniques apply image algebra based on different images or image bands, e.g. adding, multiplication, differences or ratios (Section 5.4.5), or various combinations (Munehika et al., 1993; Pohl and Van Genderen, 1998). Also, classification techniques might be used for image fusion (feature level fusion), e.g. spectral unmixing (Zhukov et al., 1999) (cf. Section 5.3).

Multiresolution fusion might also be applied for DTMs of different resolutions, when, for instance, the coarser DTM is of higher absolute accuracy, but the finer DTM of higher relative accuracy (e.g. Honikel, 1999; Honikel, 2002; Mitchell et al., 2002; Buckley et al., 2004).

6.2 Merging spectral and spatial domain data

The merging techniques between spectral and geometric data are various, ranging from algebraic expressions, to combined classifications (e.g. McDermid and Franklin, 1994; McDermid and Franklin, 1995; Wheatley et al., 2000), to artificial neural networks (e.g. Bishop et al., 1999) (see also Section 5.4). As numerous as the merging techniques are, so great is also the variety of data combinations and applications. Therefore, only some examples are given in the following section.

Steep glaciers – a potential source of ice avalanches – can be detected by combining an ice classification result (i.e. a point derivative of spectral data; see Section 5.4) with the local slope (i.e. the derivative of a DTM) (Fig. 6-4, right). In this way, empirical slope thresholds are applied to characterize the potential stability of a glacier (Salzmann, 2002; Salzmann et al., 2004). Similarly, steep debris reservoirs, a potential source of debris flows, can be detected by combining spectral debris classification with slope data (Gruber, 2000; Huggel et al., 2004c). Misclassifications from multispectral glacier detection might be eliminated partly by application of an altitude threshold for areas below the minimum elevation of glaciers in the region (i.e. the original DTM values) (e.g. Binaghi et al., 1997). Rock walls and active flood planes

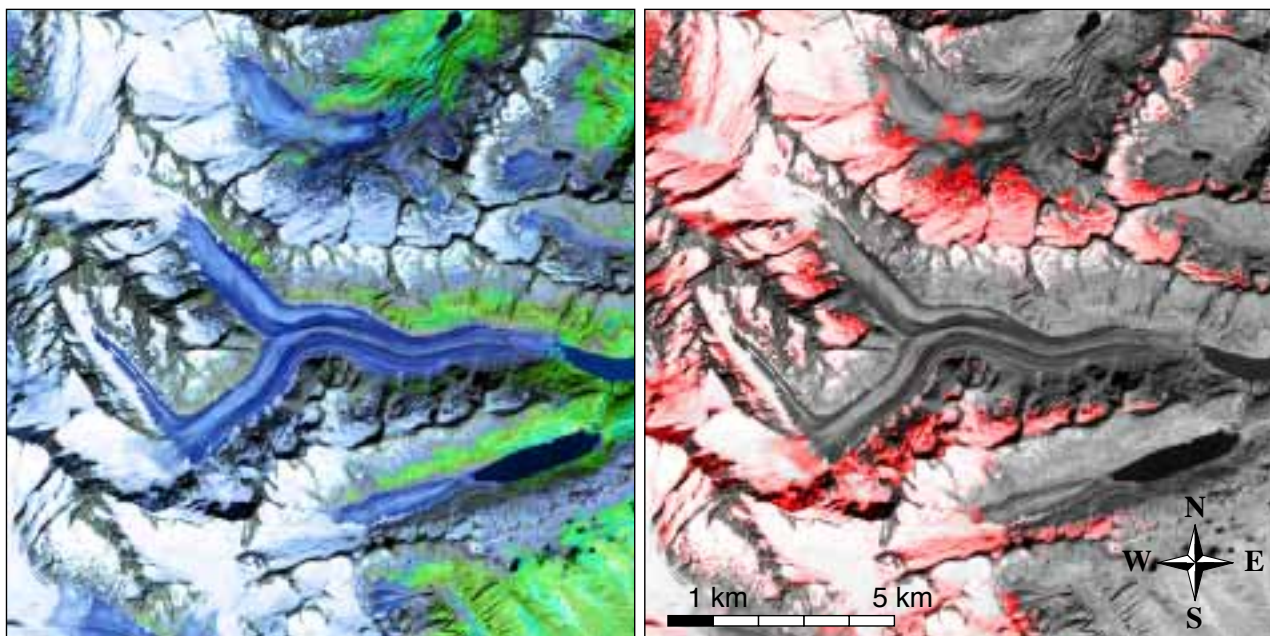


Fig. 6-4 Left: IHS-fusion of spectral and DTM data for Unteraar glacier, Grimsel area, Swiss Alps. Blue: sum of a thresholded ratio-image ASTER 3 / ASTER 4 (marking clean ice and snow; see Fig. 5-7) and a thresholded slope image marking areas with less than 20° slope. Green: NDVI. Intensity component from ASTER band 3. The result shows the potential of the integration of DTM and spectral data for classifying debris-free and -covered glacier parts in one.
Right: Steep glaciers as determined by a combination of a thresholded ASTER 3 / ASTER 4 ratio-image and a thresholded slope map with slope greater than 30° . The resulting image was coloured red and the intensity component taken from ASTER band 3. Detection of steep glaciers is e.g. a prerequisite for the modelling of ice-avalanche hazard potentials.

can be detected as non-vegetated areas with slope above and below a certain threshold (Stumm, 2001; Zemp et al., 2002). Combination of geomorphometric parameters with multispectral information from remote sensing can support analysis and simulation of mountain permafrost distribution and periglacial processes (Etzelmüller et al., 2001b; Gruber and Hoelzle, 2001).

Debris-covered ice may be classified as ‘non-clean ice’ and ‘non-vegetated terrain’ (i.e. spectral data products) below a certain threshold for slope (i.e. a DTM derivative), and in direct contact with clean ice (i.e. a spatial relation; Fig. 6-4, left; Figs. 6-5 and 6-6) (Paul, 2004; Paul et al., 2004). Analogously, promising results for combined detection of clean ice and debris-covered ice may be obtained from supervised classification using spectral bands, band ratios, PCs and a DTM, or DTM derivatives (Rick Wessels, personal communication 2002, cf. Sidjak and Wheate, 1999). Fusing spectral products with DTMs has a special importance for parameterizing classification results, for instance, for attributing elevation, slope or aspect information to multispectrally detected glaciers (e.g. Mennis and Fountain, 2001; Kääb et al., 2002b; Paul et al., 2002; Paul, 2004). Spectral-geometric merging may also consider more complex derivatives such as results from GIS models, for instance, for permafrost distribution or flow accumulation (see Section 3.6).

See also Section 12.3.

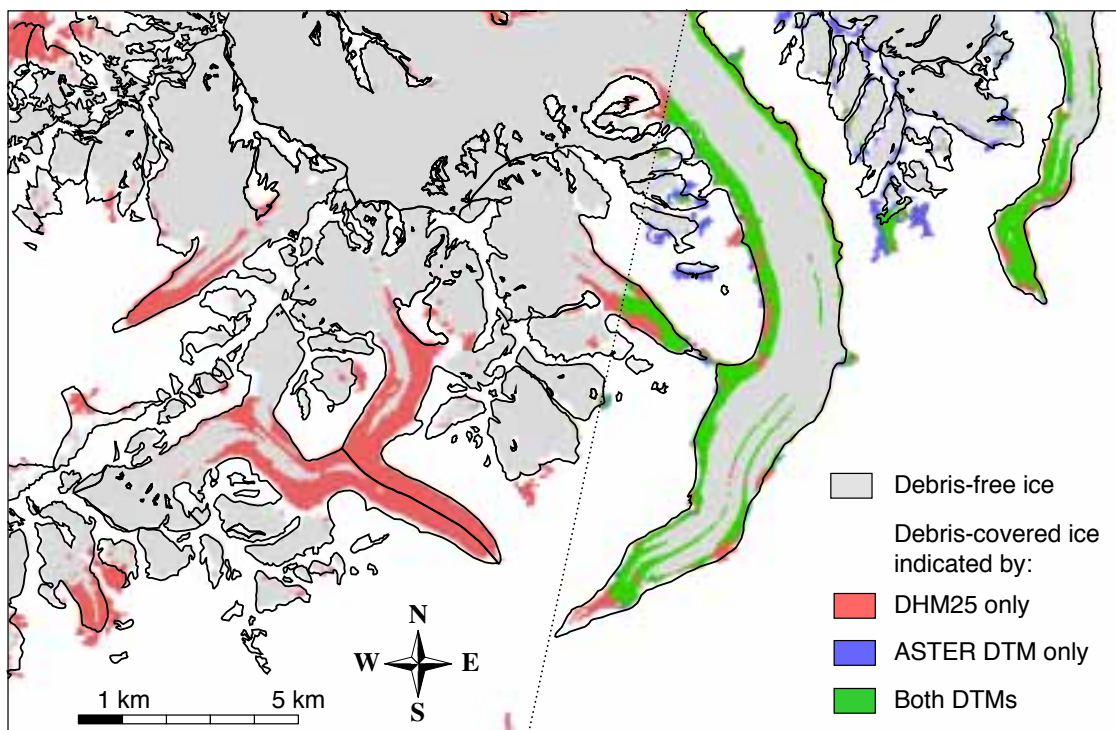


Fig. 6-5 Automatic mapping of debris-covered ice from merging spectral data and DTM-slope. Areas that (1) have a slope $< 23^\circ$, (2) are not vegetated according to the NDVI, and (3) are in direct contact with debris-free ice as mapped from a thresholded TM 4 / TM 5 ratio-image are classified as debris-covered ice (Paul et al., 2004). The procedure was performed using the DHM25 of Swisstopo (permission BA057212) for the entire section, and also using a DTM from ASTER satellite stereo data, which was available only for the right part. The black outlines are taken from the 1973 Swiss glacier inventory (Maisch et al., 1999b). Classification provided by Frank Paul, Department of Geography, University of Zurich. (See Fig. 6-6).

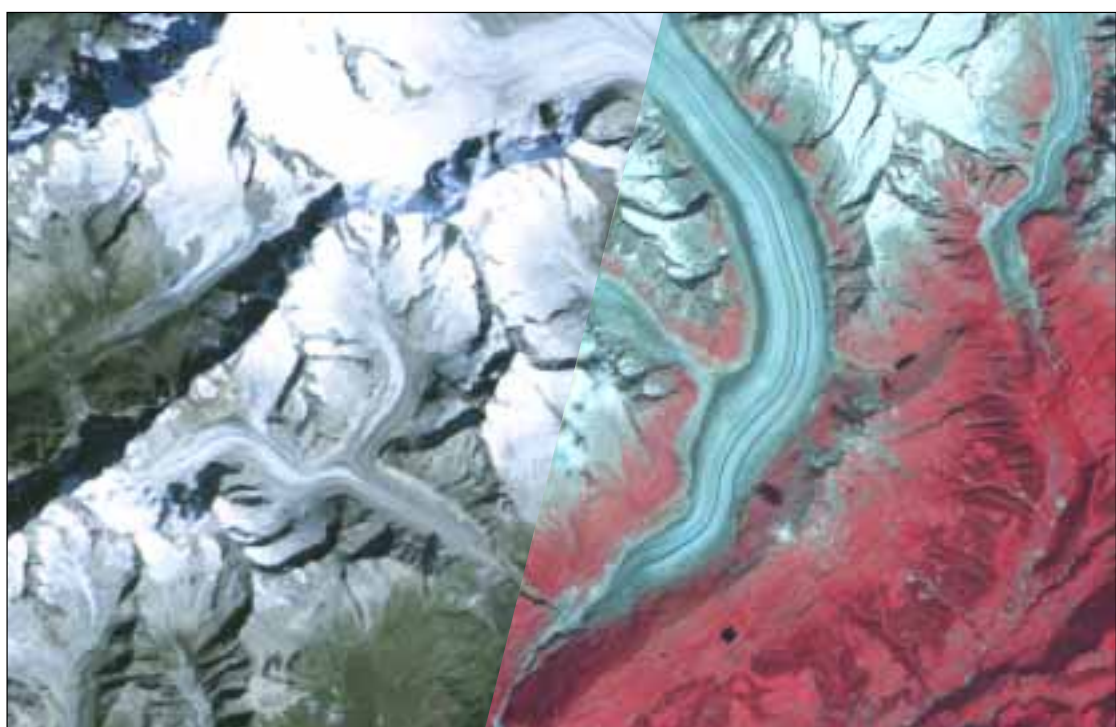


Fig. 6-6 Landsat TM (left) and ASTER scene (right) of the study area of Figure 6-5.

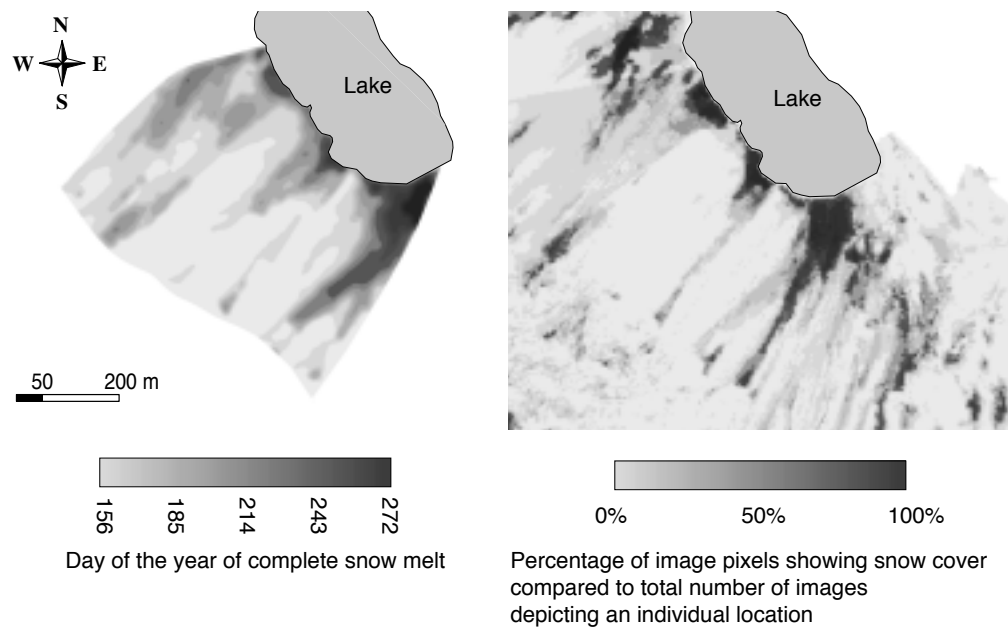


Fig. 6-7 Debris slope at Flüela pass, Swiss Alps. Left: A multitemporal merger of daily repeat imagery from an automatic terrestrial camera is used to document the snowmelt progress. Right: Overlay and normalization of various orthoimages in order to compare the snow-cover pattern of different years. The image sources are aerial photography of various scales and terrestrial non-frame amateur photography. For both maps, the orthoimagery constructed has been segmented in the two classes "snow" and "no snow" (Lerjen et al., 2003).

6.3 Merging multitemporal data; change detection

The merging of either spectral or spatial domain data of different acquisition times is termed as *multitemporal data merging*. A basic multitemporal merger in the spectral domain consists in the overlay of repeat imagery. Figure 6-7, left, shows the overlay of repeat imagery from an automatic terrestrial camera in order to monitor the snowmelt progress on a scree slope. For assessing the representativity of this data observed for only one season, various images of different sensors and different spatial coverage, over a time range of several decades, were combined (Fig. 6-7, right). To allow multitemporal overlay, the imagery was orthorectified and classified for both studies. (See also Figs. 12-1, 12-2 and 12-3).

Two other important multitemporal merging methods have already been discussed in Chapter 4: measurement of *elevation changes* and *terrain displacements*. Further merging of such multitemporal geometry data facilitates the understanding and modelling of terrain dynamics. For instance, the combining of elevation changes and displacements for a glacier-affected rockglacier reveals the different material properties and terrain behaviour (Fig. 6-8) (Kääb et al., 1997; Kääb and Haeberli, 2001). This data can be quantitatively combined with the kinematic boundary condition at the surface (e.g. Kääb et al., 1998; Gudmundsson and Bauder, 1999; Kääb and Funk, 1999; Kääb, 2001) (see Sections 9.4 and 10.1).

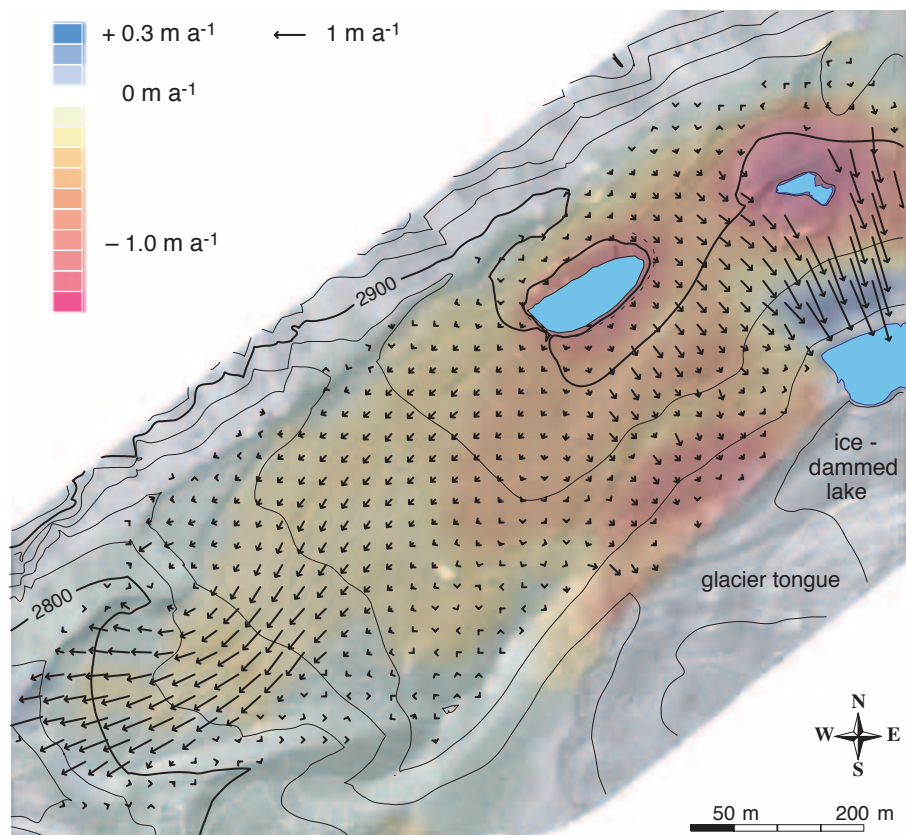


Fig. 6-8 Gruben rockglacier, Swiss Alps. Overlay of the horizontal surface velocities (vectors) and the colour-coded changes in elevation, both for 1970 to 1995. The multitemporal three-dimensional data merging clearly reveals differences within the rockglacier in terms of dynamics and thermal equilibrium. To the north-east, a patchy distribution of horizontal velocities and high rates of thaw settlement indicate dead ice occurrences that are not in thermal equilibrium. To the south-west, a coherent flow field and almost constant thickness point to creeping permafrost in thermal equilibrium (Kääb et al., 1997).

Change detection

Another group of multitemporal data fusion and merging techniques consists in *change detection* (Singh, 1989; Mouat et al., 1993; Pohl and Van Genderen, 1998; Lillesand and Kieffer, 2000):

- postclassification comparison,
- multitemporal classification,
- multitemporal principle component analysis,
- multitemporal false colour composites,
- algebraic expressions,
- change vector analysis, and
- change axis analysis.

Although mainly designed for application in the spectral domain, some of the above strategies can also be applied to other data types.

Common spectral and non-spectral classification procedures (see Sections 5.3 and 5.4) may be applied separately on data sets of different times, and the classification results compared thereafter (*postclassification comparison*). For instance, glacier-covered areas can be detected by multispectral classification from a satellite image of time 1, and again from a satellite image of time 2. The areas of glacier change can be

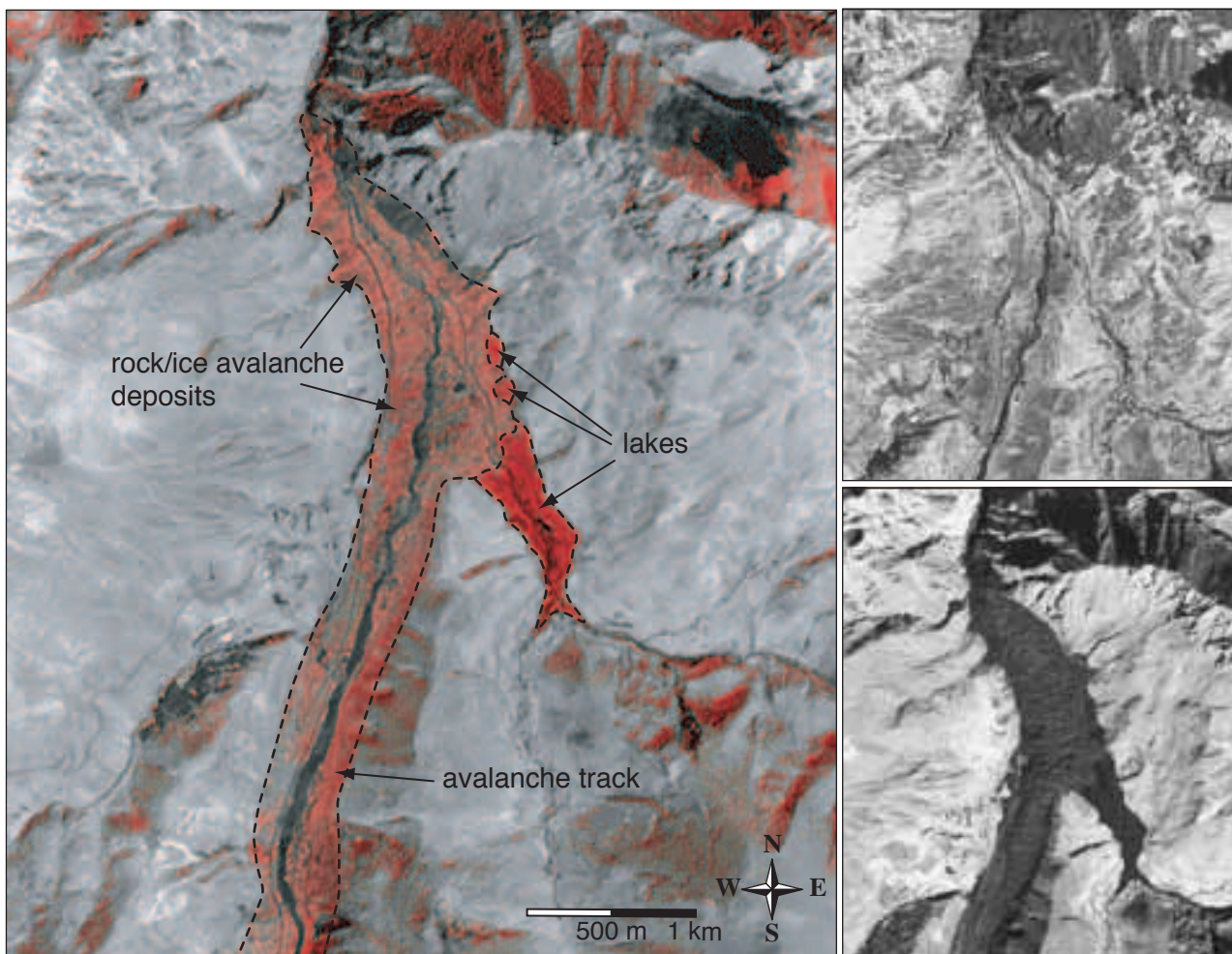


Fig. 6-9 Deposits of the 20 September 2002 rock/ice-avalanche at Karmadon, North Ossetian Caucasus. Change detection is done by a multitemporal RGB-composite. R: ASTER band 3 of 22 July 2001 (upper right image); G and B: ASTER band 3 of 13 October 2002 (lower right image). Avalanche track and deposits, as well as lakes dammed by these deposits become visible in the FCC. The dashed outline marks the avalanche path running from south to north, the deposits in front of a gorge at the upper edge of the image, and the lakes, which were dammed by the avalanche deposits (Kääb et al., 2003d). Red-coloured changes in northern slopes are due to different shadow/illumination conditions between the acquisition dates.

extracted and quantified by simple algebraic expressions (Kääb et al., 2002b; Paul, 2002b; Paul, 2002a).

Instead of comparing results after the classification, terrain change can also be detected by merging the multitemporal data within one classification procedure and by defining *change classes* and *non-change classes* (*multitemporal classification*).

The individual bands (or layers) of multitemporal data can be combined into one new multilayer data set (Fujimura and Kiyasu, 1999). *Principle component analysis* of this new data set may then enable the changed terrain sectors to be detected as minimally correlated components of the multilayer data set. Such an approach is of particular use when change has to be extracted from a large number of data (Marshall et al., 1995) (cf. Sections 5.4.4 and 6.1).

Multitemporal false colour composites represent a powerful tool for visualizing change between two or three images (Fig. 6-9) (Section 5.4.2). Such FCCs might directly form the basis for mapping, or serve as preparation and evaluation of other change detection algorithms. The number of data acquisition dates included in a

multitemporal FCC is restricted to three. Multitemporal FCCs may also be used to visualize and investigate results of other change detection techniques. Multitemporal FCCs are, for instance, constructed from repeat optical or SAR imagery. The latter is in particular useful for snow classification (e.g. König et al., 2001) or flood mapping.

Algebraic expressions such as subtraction and ratios between two or more multitemporal data sets are often used for change detection (cf. Sections 5.4.5 and 6.1). Detecting elevation differences from repeat DTMs is a simple example of temporal data subtraction (Section 4.2). Spectral differences between repeat imagery indicate terrain changes, but are also affected by different illumination and atmospheric conditions. Under some circumstances, ratios of multitemporal imagery tend to normalize for some effects such as cast shadow (cf. Crippen, 1988). Figure 4-7 shows an example of detecting glacier movement from repeat ASTER imagery from a multitemporal band ratio. Thereby, change is detected from the displacement of individual terrain features such as crevasses (*spatial change*). Change may also be detected from the general change in spectral signature, for instance when an area becomes ice-free due to glacier retreat (*spectral change*).

The change detection approaches mentioned above are applied to the raw image data, but also to corrected imagery (e.g. for illumination and atmosphere), or further transformed or processed products (e.g. orthoimagery, see Fig. 3-29, filter products, PCs). Application of change detection algorithms can also be restricted to certain areas masked by some previous classification (Lillesand and Kieffer, 2000).

For a given pixel of a multispectral image or multilayer data set, two or more spectral variables can be plotted against each other for individual acquisition dates. A *change vector* connects the resulting points in the chosen variable space. The magnitude and direction of this vector (or vector cluster for a group of pixels) may be characteristic for a certain type of change, for instance, plant succession in glacier forefields, development of the snow pack, or glacier retreat (Fig. 6-10). (Entire paragraph: Lillesand and Kieffer, 2000).

A two- (or multi-) dimensional scatter plot of a spectral band at time 1 versus the same band at time 2 approximates the plot diagonal in case of no changes between the two acquisition dates (Fig. 6-11, left). For significantly changed pixels, the respective plot points lie apart from this diagonal, forming clusters typical for individual change types (Fig. 6-11, right). *Change axis analysis* defines a *non-change axis* (the above diagonal, or a parallel or slightly rotated axis) and perpendicular *change axes*. Threshold coordinates in the change-axes space are then used to classify individual changed, or non-changed pixels (Lillesand and Kieffer, 2000). The method is also sensitive to changes not aimed at by detection, e.g. changes in illumination conditions.

For all change detection approaches, accurate uniform geometry for the repeat data sets is crucial. Such techniques are thus usually applied using imagery of the same sensor and same sensor position (e.g. repeat tracks) or orthoimages. Location differences between the compared data sets substantially influence the change detection results.

6.4 Merging spatial, spectral and temporal domain data

The merging of spatial and spectral domain data discussed above might be the most common multidomain merging (e.g. Mulders, 2001). However, inclusion of the temporal domain is able to provide additional information about continuously

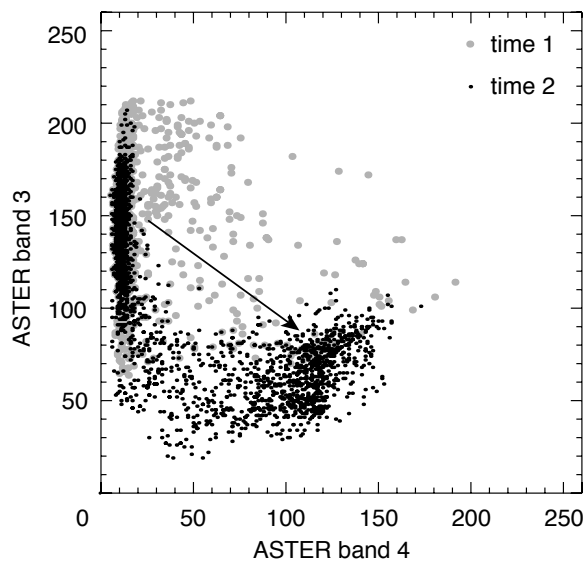


Fig. 6-10 Change vector analysis for the retreating tongue of Damma Glacier, Swiss Alps, from repeat ASTER scenes. The figure depicts the dependency between ASTER bands 3 and 4 for individual pixels. The glacier pixels show low to medium digital numbers (DN) in band 4 and medium to high DNs in band 3. For pixels with ice disappearance between times 1 and 2, or emergence of rock or debris, the position in the scatter plot has changed to medium DNs for both ASTER 3 and 4. The resulting change vector for one individual pixel is given as an example.

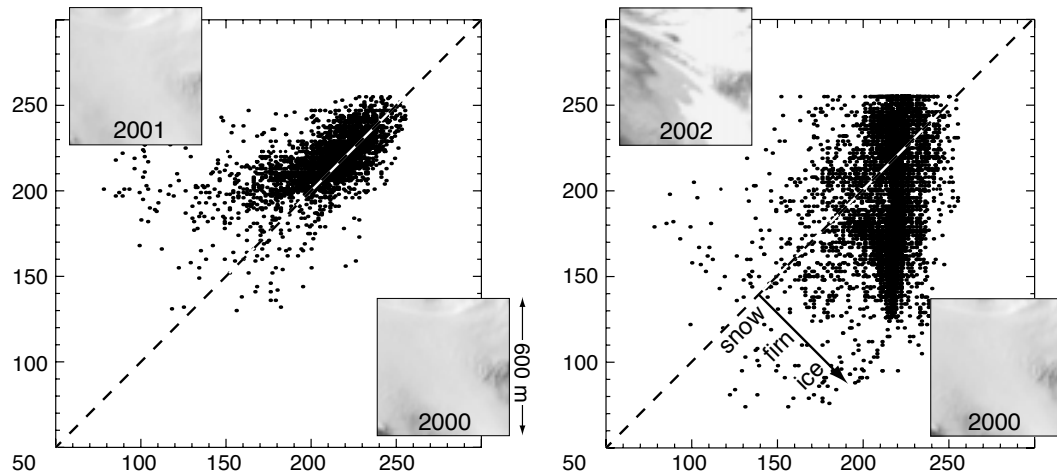


Fig. 6-11 Change axis analysis from three repeat ASTER bands 3 for a glacier section.
Left: in 2000 and 2001 the area was equally snow-covered resulting in a scatter of the individual pixels around the diagonal (i.e. $DN\ 2000 \approx DN\ 2001$).
Right: in 2002 the bare ice has become partly exposed, leading to spectral deviations of the pixel positions from the diagonal (i.e. $DN\ 2000 \neq DN\ 2002$). The degree of deviation can be used to characterize the change occurred.

changing environments such as cold mountains. Again, the number of possible strategies and applications is too large to give more than a few examples.

The spectral signature of rockglaciers (non-vegetated, scarcely weathered rock) and their geometric signature (typical elevation and slope range, size), for instance, characterizes these features. The decision as to whether a rockglacier or a part of it is active or inactive might then be supported by data on elevation changes and

displacements, i.e. temporal domain data (e.g. Figs. 4-16 and 6-8) (Kääb and Vollmer, 2000; Strozzi et al., 2004).

Similarly, the distinction between (a) debris-covered glacier ice, (b) debris-covered dead ice, and (c) adjacent periglacial debris can be supported by multitemporal data: the sum of all three surface types can be detected by spectral and geometric analysis. In the temporal domain, however, they differ: (a) glacier ice shows horizontal movement, and possibly elevation changes; (b) elevation loss prevails for dead ice; and (c) ice-free debris is comparably stable (e.g. Kääb et al., 1997; Kääb, 2001; Kääb and Vollmer, 2001).

The results of merging spectral data and a DTM for detecting debris-covered ice (see Section 6.2) can be improved by introducing change detection from repeat imagery. Retreat or advance of glaciers affects also debris-covered parts that cannot be detected from spectral data alone. Mapping of glacier retreat or advance from change detection techniques helps to refine the classification results from spectral-spatial data merging. By using such procedure, it is possible, at least in part, to distinguish active glacier parts and dead ice occurrences from one another, and exclude glacier parts that were misclassified by a slope criterion (Paul, 2004; Paul et al., 2004). Furthermore, matching of repeat optical imagery or DInSAR analysis may be introduced into such classification in order to distinguish glacier parts that are debris-covered and other debris surfaces from the movement of debris covered ice.

6.5

GIS integration and numerical modelling

The fusion and merger methods discussed above consider only discrete points in time (i.e. the acquisition dates) and only simple spatial relations. Enhanced detection and classification of terrain and related processes is possible by integrating numerical process models that cover the space and/or time domain. When image data or other spatial data sets are involved, such analyses are most efficiently performed within a GIS-type software, which is able to deal with raster and vector data, as well as with two- or three-dimensional spatial algorithms.

The models applied differ from one another by the domain of processes they simulate:

- mass relocation (e.g. rockfall; rock, ice or snow avalanches; debris flows; water; erosion),
- energy transport and exchange (e.g. radiation; energy balance; thermal conditions; permafrost),
- transport and reaction of chemical substances, and
- forces and stresses,

to list only some abiotic types. These models may be applied

- as part of the classification procedure (*intra-classification process modelling*), or
- using previously classified data (*post-classification process modelling*).

In view of the numerous possibilities and applications, some examples are given here only.

The geomorphological details of terrain are a result of mass relocation by removal, transport and deposition. Thus, the applied algorithms often model such mass relocation processes. Detection of a debris cone by its spectral (i.e. fresh debris) and geometric signature (i.e. typical slope and curvature) may not be clear. *Rockfall* modelling based on a DTM is, then, able to support in distinguishing debris cones

from similar features such as moraines, alluvial fans or rockglaciers (intra-classification mode; e.g. Stumm, 2001; Zemp et al., 2002).

On the other hand, rockfall modelling might already be the desired final product within, for instance, a hazard assessment study (e.g. Meissl, 1998; Bottino et al., 2002; Dorren and Seijmonsbergen, 2003). Prior to the rockfall model the potential starting zones (i.e. rock walls) may be detected as steep terrain (i.e. using a slope threshold) without vegetation cover (i.e. using multispectral classification, post-classification mode; e.g. Zemp et al., 2002; Frauenfelder, 2004).

Similar analysis strategies can be applied for *ice avalanches* (e.g. originating from steep glaciers, as detected using geometric and spectral data) (Salzmann et al., 2004), *periglacial debris flows* (originating from steep debris reservoirs; Gamma, 2000; Gruber, 2000; Oswald, 2001; Huggel et al., 2004c), *glacier lake outburst floods* (originating from lakes; Huggel et al., 2002; Huggel et al., 2003b; Huggel et al., 2003c), or *rockglacier evolution* (originating from debris fans, Frauenfelder, 2004). This group of kinematic or dynamic process models is based on DTMs. Mass relocation is modelled to follow strictly or with a certain probability the steepest slope, and is affected by certain parameters for energy gain and loss (Quinn et al., 1991; Quinn et al., 1997; Iverson et al., 1998; Huggel et al., 2003c).

Other process models range from parameterization schemes (e.g. Haeberli and Hoelzle, 1995; Hoelzle and Haeberli, 1995), to numerical integration and finite differences (e.g. Olyphant, 1983; Oerlemans et al., 1998), to two- and three-dimensional finite element models (e.g. Blatter, 1995; Gudmundsson, 1997).

Another group of spatial models simulates non-kinematic processes, for instance, involving energy balance or thermal conditions. Illumination models are applied for respective correction of satellite imagery (Sandmeier and Itten, 1997; Bishop et al., 2004). The results of statistical or empirical permafrost modelling (e.g. Etzelmüller et al., 2001a) combined with the classification of steep debris assists in the assessment potential starting zones of debris flows, which in turn may then be simulated by mass transport models (Zimmermann et al., 1997; Oswald, 2001).

6.6

Other methods

In this work, the focus is on data concerning the terrain surface. It is clear, however, that a full understanding of terrain dynamics requires subsurface information also, as obtained, for instance, from geophysical investigations. Such data usually range in the spectral domain (electrical current, wave propagation, temperatures etc.). Spatial data such as internal layers and boundaries are then modelled from such spectral data (e.g. Hauck, 2001). More seldom, spatial subsurface data can be accessed directly from boreholes or trenches (e.g. Arenson et al., 2002). In addition, multitemporal acquisition of such data is applied (e.g. Hauck, 2001). Merging such subsurface data with surface data in the spectral, spatial and temporal domain clearly has the greatest potential as a means of monitoring and understanding glacier- and permafrost-related processes (e.g. Section 9.4) (Kääb and Funk, 1999; Kääb, 2001; Kääb and Kneisel, 2005). In contrast to surface data, availability of subsurface data is presently restricted to small terrain sections.

6.7 Conclusions and perspectives

On the one hand, an increasing amount of high-mountain terrain data with increasingly different characteristics will be available in the future. On the other hand, continuously improved analysis methods and tools facilitate the respective data exploitation. In view of these two developments, multidimensional data fusion and merging is clearly a research field of special need and, at the same time, of great potential.

Future data sets available for high-mountain research are characterized by

- an increasing number of ground-, air- and spaceborne sensors,
- an increasing number of spectral bands, increasing radiometric resolution, and smaller bandwidths (for optical sensors),
- an increasing number of available microwave bands and polarizations (for microwave sensors),
- an improving spatial resolution, data precision and geolocation accuracy, and
- an improving temporal resolution from coverage by different or pointable sensors.

Fusion and merging techniques adapted for use in high-mountain environments are needed in order to profit from this rapidly growing database for monitoring purposes and research. Considering high mountains to be an especially dynamic environment, enhanced inclusion of multitemporal data in the mergers seems to have special potential. Because microwave and optical data characterize ice and snow in very different ways, efforts to implement the merger between these two spectral data types should be made (Rott, 1994; Renouard et al., 1995; Honikell, 2002; Ostir et al., 2003). Without any doubt, the merging of DTMs within or after the classification process will gain further importance due to the increasing availability of high-resolution and high-precision DTMs (see SRTM, Section 3.4.2). Finally, the convergent characteristics of air- and spaceborne sensors in terms of digital data acquisition, multispectral imaging, or spatial resolution, for example, will draw more attention to the fusion between air- and spaceborne sensors for down-scaling approaches or for closing spatial and temporal gaps, for instance.

For the analysis methods and tools, the author expects a further integration of typical GIS and typical remote sensing tool capabilities, either by the software producers or by the users. GIS should increasingly be able for analyzing multispectral data, or viceversa for remote sensing software. In view of the large data volumes involved in such multidimensional analyses, efforts are needed towards more efficient data models (e.g. compression) and algorithms (e.g. matrix operations).

Advances in multidimensional data analysis approaches, including the merging of spatial, spectral and temporal data at various spatio-temporal resolutions will confront the user increasingly with questions of spatial scale, spatio-temporal scale and space-time dependencies (cf. Section 2.3) (Bishop et al., 2004).

7.1 Visualization domains

Similar to the data domains introduced in Section 2.3, visualization may be characterized by different domains as well (Fig. 7-1)(Käab, 1998b):

- the structure or process to be presented (cartographic variable),
- the object on/in which this information is placed, and
- the visualization approach.

A monotemporal *information* to be displayed may be one-dimensional (point information), two-dimensional, or three- (and more-) dimensional (information vector). Similarly, a *process* to be depicted may be one-dimensional (e.g. vertical elevation changes), two-dimensional (e.g. horizontal displacements), or three-dimensional (e.g. flow of particles). Both monotemporal information and time-dependent processes can be visualized in combination, for instance, by overlay.

The *object* (i.e. terrain or terrain sector) where the information is placed or where the process takes places may be one-dimensional (point), two-dimensional (e.g. a lake

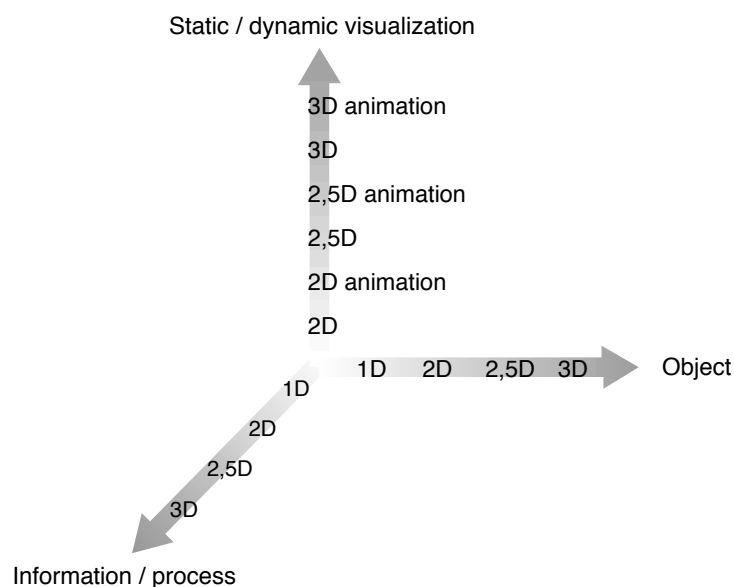


Fig. 7-1 Visualization domains: object, information/process and visualization technique. For instance, elevation changes (i.e. a one-dimensional vertical process) is overlain on a contour plot and/or orthoimage (i.e. a two-dimensional static visualization) of the corresponding glacier surface (i.e. a 2.5-dimensional object).

surface or terrain profile), 2.5-dimensional (a surface; see Section 2.3), or three-dimensional (an entire body).

The *visualization approach* to depicting information and objects can be characterized by its spatial and temporal dimension: two-dimensional static (e.g. planimetric map), two-dimensional dynamic (e.g. planimetric animation), 2.5-dimensional static or dynamic (e.g. oblique view or animation), or three-dimensional (e.g. physical laboratory model or virtual reality).

For example, changes in elevation (1D information) of a glacier surface (2.5D object) might be represented in planimetric projection (2D visualization). Or, a field of horizontal displacements (2D information) can be draped over a DTM (2.5D object) in oblique perspective (2.5D visualization).

7.2 Cartographic resources

The cartographic resources for visualizing high-mountain phenomena and processes include colour, annotations, point symbols, outlines, iso-lines, iso-areas, vectors and streamlines, polygons, raster filling and images, hillshading, or continuous (or quasi-continuous) transitions.

When dealing with temperatures and ice, the colour red is often used for high temperatures or ice melt, and the colour blue for cold temperatures or ice gain. Since the overlay of cartographic elements is usually limited to a small number for reasons of readability, the combined visualization of different or complex information is restricted (Häberling, 1999; Hurni et al., 2000; Huber and Sieber, 2001; Häberling and Hurni, 2002; Buckley et al., 2004).

Stereo viewing techniques applied to original or computed stereo imagery such as anaglyph images (red-green glasses), image polarization, image flickering, shutter glasses, active matrix glasses, autostereoscopic liquid crystal display, or holography can also be considered as a cartographic resources (Falk et al., 1986; Buchroithner and Kirschenbauer, 1998).

7.3 Visualization strategies

Static visualization uses time-constant representation. It is clear that a visualization approach requires special abstraction techniques for displaying time-dependent processes. These difficulties grow with increasing information/process dimension and with increasing object dimensions. *Dynamic visualization*, also called (*cartographic*) *animation* uses a sequence of static visualizations. It is able to depict time-dependent processes with less abstraction than necessary for static visualization, and permits the transmission of more or more complex information (e.g. Dransch, 1997; Buziek et al., 2000; Kaufmann and Plösch, 2000; Winter, 2001; Isakowski, 2003; Kääb et al., 2003b; Buckley et al., 2004). In cartographic animations, time, variables, and/or the object space might be dynamic or static, i.e. animated or not (Lobben, 2003).

Planimetric changes (e.g. in glacier or lake area) can be presented by the overlay of repeat outlines or polygons with colour or pattern filling (e.g. Fig. 7-2, right, Figs. 12-1 and 12-3). Such repeat information can be draped over a shaded DTM in oblique perspective (e.g. Kääb, 1998b; Huber et al., 2003; Kääb et al., 2003b; Paul et al., 2003). Various possibilities exist for visualization of 1D information (see Tab. 7-1), for example, iso-lines or iso-areas, profiles, colour coding or colour transitions. In many cases, natural information or processes might be represented best by means of

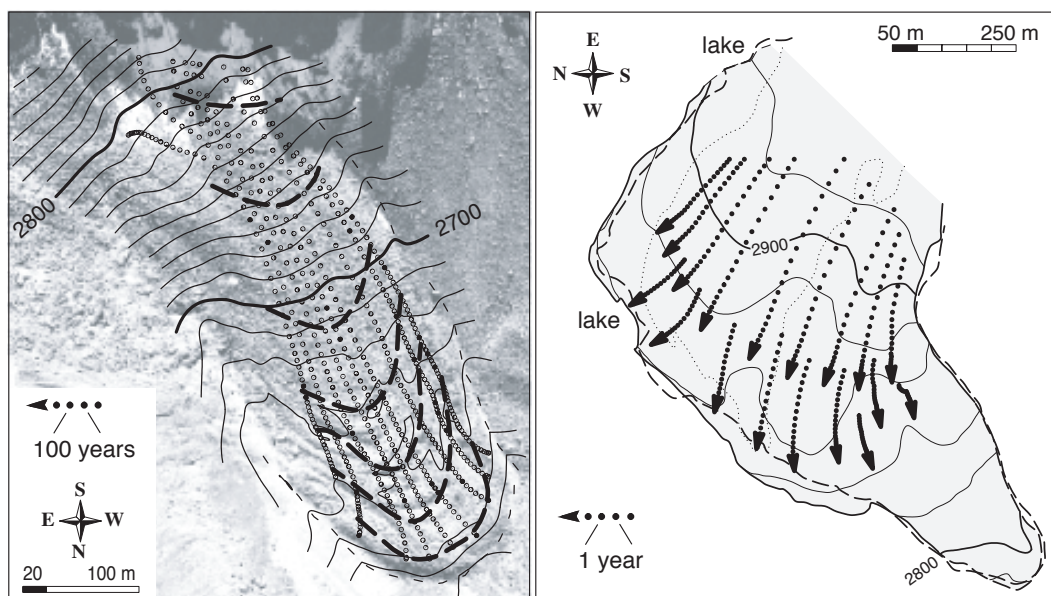


Fig. 7-2 Streamlines and trajectories can be used to visualize displacement fields. They allow for different analyses as compared to vector plots. Left: streamlines interpolated from the horizontal velocity field 1987–1996 on Murtel rockglacier (Fig. 9-5). Streamlines reflect the hypothetical journey of individual surface particles in a monotemporal velocity field. The velocity field is, in this case, assumed to remain constant with time. Right: trajectories depict the actual particle path. The trajectories on the Gruben glacier tongue for 1973 to 1992 have been interpolated from repeat velocity fields that showed a significant change with time (Käab, 2001). The dashed glacier outline is of 1973, the solid one of 1992. Both streamlines and trajectories include the travel path as well as the travel time. For Murtel rockglacier (left) hypothetical isochrones of 1 ka interval (dashed line) have been interpolated from the streamlines (Käab et al., 1998).

continuous transitions instead of the artificial sharp boundaries (e.g. Fig. 6-8). However, such techniques usually require the interpolation of the original discrete information and may thus lead to interpolation artefacts. Therefore, point-wise visualization may be closer to the original data and in some cases facilitate initial data exploration by experts. Changes in terrain surface elevation, for instance, can be displayed as scaled circles (e.g. Fig. 4-1). In this case, the radius r of an individual circle symbol is calculated from a variable value x as

$$r = m \cdot x^n \quad (7-1)$$

where m is the general symbol scale and n is chosen to suit the visualization purpose. The larger n , the more distinct spatial variations in the data become visible (Käab, 1998b; Isakowski, 2003; Käab et al., 2003b).

In contrast to 1D information, the possibilities for visualizing 2D information are more limited. In many cases, the 2D information can be transformed and separated into two 1D components (e.g. magnitude and direction of a displacement). Arrows are most often used for indicating velocities, possibly colour-coded or overlain by isolines or colour transitions for their magnitude (e.g. Fig. 4-12). Such vectors may also be combined for a time-dependent velocity field (Käab, 1998b; Käab, 2001). In addition, velocity fields can be represented by streamlines, showing the hypothetical path of selected particles as interpolated from the displacement field (Fig. 7-2, left) (Käab, 1996b; Käab, 1998b; Käab et al., 1998; Käab and Vollmer, 2001; Käab et al., 2003c). If the path of individual particles is in fact tracked over a certain period of time such path lines are called trajectories (Fig. 7-2, right) (Käab, 1998b). For streamlines or trajectories, the particle speed, or respective time intervals, can be indicated by single symbols for each time step (Fig. 7-2), or by the thickness or colour

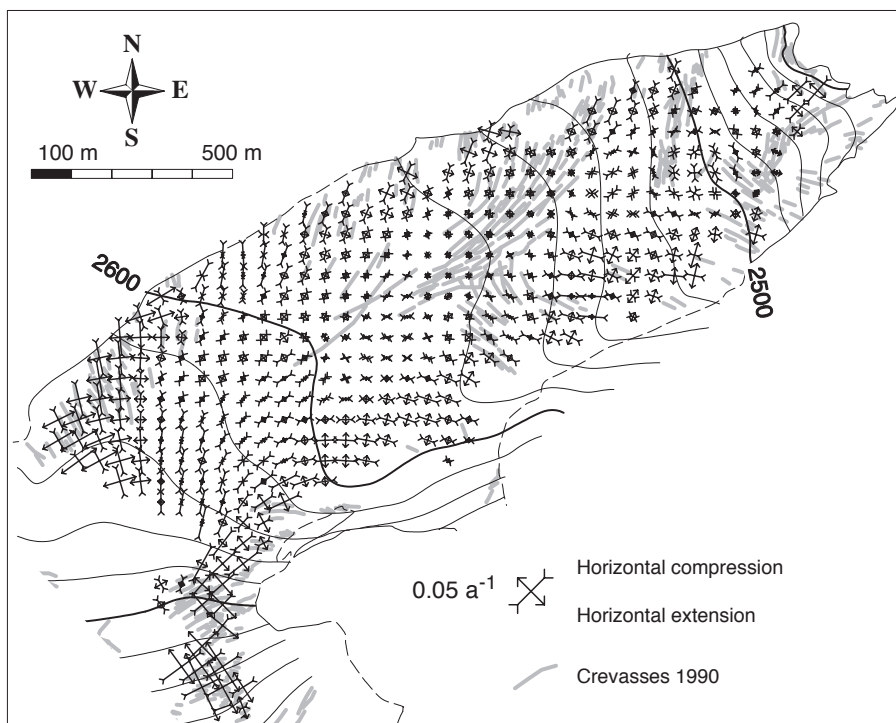


Fig. 7-3 Strain-rate rosettes can be used to visualize two-dimensional strains and stresses. Strain-rate magnitude and direction correspond with the development of glacier crevasses (Käab, 1996b). The strain rates on the Gries Glacier tongue, Swiss Alps, are calculated from the photogrammetrically-determined surface velocity field of 1990 to 1991 (Käab and Funk, 1999).

of the line (“stregenels”, Knizhnikov and Nikitin, 1997). Two-dimensional strain rates, i.e. the derivatives of the velocity field, are often shown as rosettes, representing the principle axis of the strain rates (Fig. 7-3).

To a limited extent, different visualizations may be superimposed. Furthermore, the current information is often combined with terrain information such as shading, contour lines or orthoimages for the sake of better orientation (Hurni et al., 2000; Buchroithner, 2002a; Häberling and Hurni, 2002; Huber et al., 2003; Paul et al., 2003; Buckley et al., 2004). Similarly, a point or vector information might be combined with a vector or spatial information, respectively. Such an approach represents one of the few possibilities for visualising 3D information by splitting it into 1D and 2D information (e.g. Käab, 2000).

Another class of visualization approaches, which is particularly suited for analysing remote sensing data and DTMs, are statistical plots such as scatter plots (e.g. Figs 6-10 and 6-11) and 1D and 2D histograms (e.g. Figs 3-3, 3-19, 3-23, and 3-26).

Table 7-1 gives a selection of possibilities for visualizing glacier- and permafrost related information and processes. The different presentation methods are not exclusive but may be combined.

7.4 Conclusions and perspectives

The possibilities for *static visualization* of high-mountain phenomena and processes are well established and highly developed (Hurni et al., 2000; Häberling and Hurni, 2002; Buckley et al., 2004), but, for principal reasons, are of limited use for reflecting the usually complex three-dimensional nature of such information. In this sense, the author considers the further development and application of *dynamic visualization* to

be both a special requirement and a promising perspective for the improved exploration and better understanding of multidimensional data (Kääb et al., 2003b; Buckley et al., 2004). Enhanced *stereo-viewing techniques* are also able to significantly upgrade visualization by inferring an additional dimension. Animated stereo viewing, a virtual reality technique, combines both perspectives described above. The main task of high-mountain research consists in adapting the tools already available in computer vision and animation (e.g. computer games), rather than developing new techniques.

Table 7-1 High-mountain phenomena and processes, and selected approaches for their visualization.

Information/process dimension	Examples	Static visualization	Dynamic visualization
1D	ablation / accumulation, terrain height, elevation change, glacier speed, vertical strain rate, panchromatic image	point symbols annotation isolines, iso-areas profiles raster image (continuous) colour coding (hill-) shading planimetric projection oblique perspective stereo viewing	symbol animation (scale-variation) colour transitions (variation of hue, saturation or intensity) sequential image animation (e.g. flickering) morphing (interpolation) rotation of oblique perspectives fly through stereo viewing
2 D	horizontal displacements, horizontal strain rates, change in area outline	splitting in two 1D-components line overlay draping on 2.5D surfaces vectors or rosettes streamlines “stregenels”	sequential image animation particle path animation symbol animation (deformation) splitting in two 1D-animations stereo viewing
3 D, and more	flow, creep, sliding, falling, multi- or hyperspectral data	splitting in 1D and 2D information colour composites	particle path animation splitting in 1D and 2D animation

III. CASE STUDIES AND APPLICATION SCENARIOS

8.1 Glacier thickness changes from aerial and satellite imagery: Glaciar Chico, Chile, 1975–2001

Collaboration

This study was conducted in collaboration with Andrés Rivera (Glaciology Centre; University of Bristol; Departamento de Geografía, Universidad de Chile, Santiago; Centro de Estudios Científicos, Valdivia, Chile). He provided the aerial photography and ground control information used in this section. (See also Rivera et al., 2005).

8.1.1 Introduction

For many decades, repeat aerial stereo photography has been the best established method for monitoring changes in glacier thickness over time (see Section 4.2). However, this approach has serious disadvantages in terms of costs and technical feasibility when monitoring large glaciers, many glaciers at once and glaciers in remote or large areas. Spaceborne techniques, on the other hand, have the potential to overcome these problems, at least in parts. Vertical DTM differences for Glaciar Chico, Chile, derived from digital aerial photography are compared here with vertical DTM differences from ASTER along-track stereo in order to assess the suitability of satellite stereo imaging for monitoring glacier thickness changes.

Glaciar Chico is a north-eastern outlet glacier of the Southern Patagonia Icefield (Aniya et al., 1996), partially calving into a branch of the Lago O’ Higgins. In the past 50 years significant retreat and thinning of the icefield glaciers has been observed (Aniya, 1999). This deglaciation trend has been associated (Aniya et al., 1997) with atmospheric warming observed during the last century in Patagonia (Rosenblüth et al., 1997). Until recently (Rignot et al., 2003), quantitative studies on ice thickness changes have been available only for a few glaciers of the Southern Patagonia Icefield, all of them conducted for the ablation areas. Most measurements indicated high thinning rates of the glaciers (Casassa et al., 2002). Casassa et al. (1997) compiled a glacier change record for Glaciar O’ Higgins, the northern neighbour of Glaciar Chico. Rignot et al. (2003) derived thickness changes for both Patagonian Icefields from photogrammetric contour-line maps and SRTM data. Rivera et al. (2005) derived ice elevation changes for Glaciar Chico from ASTER satellite data, digital aerial imagery and ground-based GPS data. The following evaluation forms an integral part of the latter study.

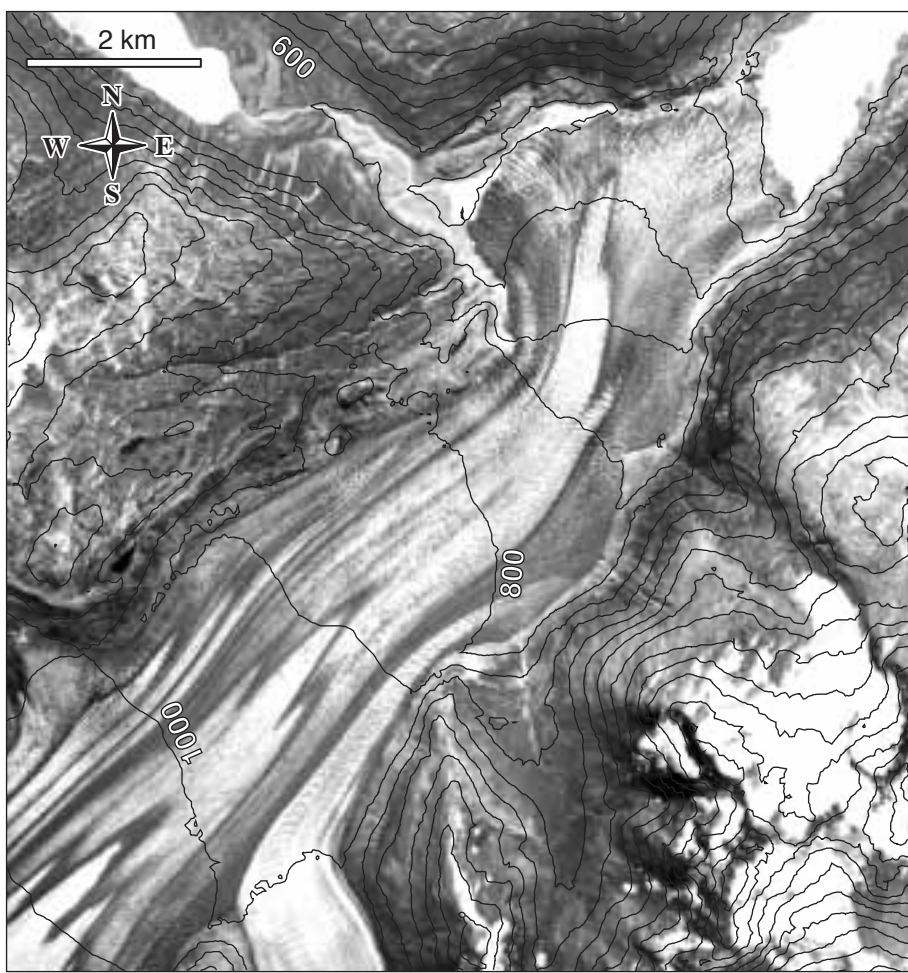


Fig. 8-1 Orthoimage of the tongue of Glaciar Chico, Southern Patagonia Icefield, with 100 m contours superimposed. The orthoimage and the DTM have been computed from aerial photography of 15 March 1975. Imagery provided by Andrés Rivera.

8.1.2 Ice thickness changes

Using digital photogrammetry (Section 3.3.1), 50 m DTMs were generated based on aerial photography from 15 March 1975 (scale 1:75,000; Fig. 8-1) and 15 March 1997 (scale 1:70,000; Fig. 8-2). Noise from the vertical DTM differences of 1975–1997 on the tongue of Glaciar Chico was suppressed by installing a Gaussian filter (Fig. 4-1). From empirical values (Section 3.3.1) and the remaining deviations from zero for stable terrain outside the glacier, the RMS of the photogrammetry-derived ice thickness changes was estimated to be about ± 3.5 m (0.16 m a^{-1}). At the very end of the glacier terminus towards the lake, thickness loss of -3 m a^{-1} and more was observed for 1975–1997 (Fig. 8-2). As a comparison with the underlying orthoimages shows, this ice loss is associated with a horizontal glacier retreat of up to 500 m (approximately 20 m a^{-1} annual average) at calving sections. Other parts of the front are grounded on a small island, which first became visible in 1975. The calving activity of Glaciar Chico is much slighter than for other calving glaciers of the Southern Patagonia Icefield (Rivera et al., 2002).

Above the very terminus, the ice thickness loss decreases smoothly from -3 m a^{-1} to between -2 and -1 m a^{-1} at 12 km upstream.

As a comparison, a DTM was also constructed based on ASTER imagery from 14 October 2001. Ice thickness changes were calculated between this satellite-derived



Fig. 8-2 Contours of annual ice-elevation changes in 1975–1997 for Glaciar Chico. The 1975 and the 1997 DTMs have both been digitally derived from aerial photography. The underlying orthoimage and the 100 m contours are based on the 15 March 1997 imagery. Aerial photography provided by Andrés Rivera.

DTM and the 1975 aerophotogrammetric DTM (Fig. 8-3). Before subtracting both DTMs the ASTER DTM was shifted to optimal match the aerophotogrammetric DTM (see Section 4.2, and Figs. 4-2 and 8-3).

Based on empirical values (Section 3.4.1) and the deviations from zero for stable terrain outside the glacier, the accuracy for the ice thickness changes from 1975 to 2001 is estimated to about ± 15 m (0.6 m a^{-1}). The resulting pattern of ice loss is, in general, very similar to the one obtained for 1975 to 1997. The ASTER DTM is associated with considerable noise, which makes the interpretation of details difficult. Due to the low slope of the glacier tongue, even small vertical DTM errors translate into large horizontal position errors for the isolines of elevation change. The significance level for the ice elevation changes derived between the 1997 aerophotogrammetric DTM and the 2001 ASTER DTM is estimated to be about ± 15 m RMS. Thus, a potential thickness loss in the order of 5–12 m as expected for 1997–2001 cannot be detected reliably on a pixel-by-pixel base. However, after advanced postprocessing of the DTMs and the vertical differences 1997–2001, zones of ice thickness changes become detectable (cf. Section 4.2, Fig. 4-5).

8.1.3 Conclusions

Figure 8-4 shows the histogram of deviations between the ice elevation changes obtained for 1975–1997 and 1975–2001. Non-glacierized areas have been masked out

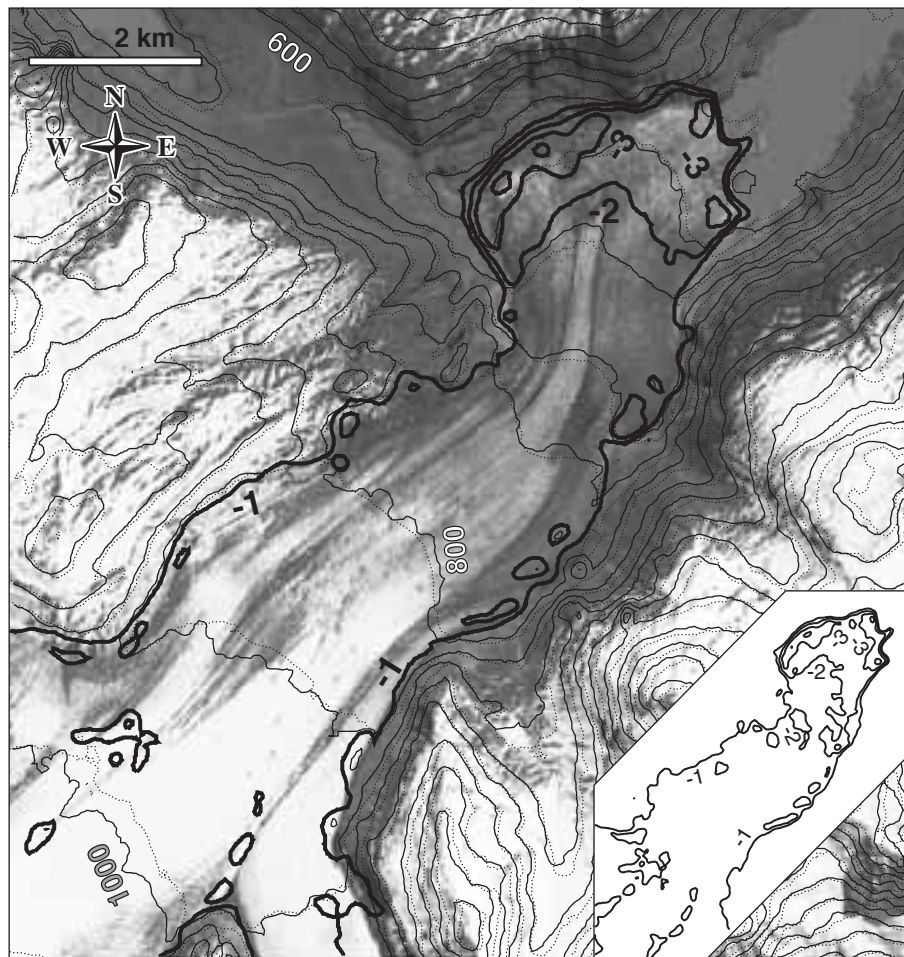


Fig. 8-3 Contours of annual ice-elevation changes of 1975 to 2001 for Glaciar Chico. The 1975 DTM has been derived digitally from aerial photography. The 2001 DTM is computed from ASTER satellite stereo data and was horizontally shifted to better match the aerophotogrammetric DTM (see Section 4.2). The underlying ASTER orthoimage is based on imagery of 14 October 2001. The solid elevation contours are derived from the 2001 ASTER DTM, the dotted contours are from the 1997 aerophotogrammetric DTM (see Fig. 8-2). The inset to the lower right shows the ice thickness changes obtained without shift of the ASTER DTM.

for this comparison. For 68% of all points (i.e. the one-sigma level) the deviations are less than $\pm 0.45 \text{ m a}^{-1}$. This result is better than the above a-priori accuracy estimate of $\pm 0.6 \text{ m a}^{-1}$. For 78% of all glacier points the deviations are less than $\pm 0.6 \text{ m a}^{-1}$. As it is less accurate, the ASTER DTM contributes most of the deviations between the two elevation-change measurements. The comparison between the a-priori accuracy estimate deduced from the studies in Section 3.4.1 and the actual deviations obtained here suggests that the ASTER DTM for the tongue of Glaciar Chico is better than other ASTER DTMs of mountainous terrain. Furthermore, the ASTER DTM is more accurate for the glacier tongue itself as compared to the terrain surrounding it. For flat glaciers with sufficient optical contrast (e.g. from ash layers in the case of Glaciar Chico, or debris cover), the RMS of ASTER DTMs may be in the order of $\pm 8\text{--}10 \text{ m}$.

The ice elevation change of -30 m to over -80 m since 1975 as observed for the glacier tongue coincides well with other intermediate aerophotogrammetric DTMs and GPS measurements obtained for the glacier (Rivera et al., 2005). The results for Glaciar Chico are in the same order of magnitude as the thickness loss of other glaciers of the Southern Patagonia Icefield. Rignot et al. (2003) measured average

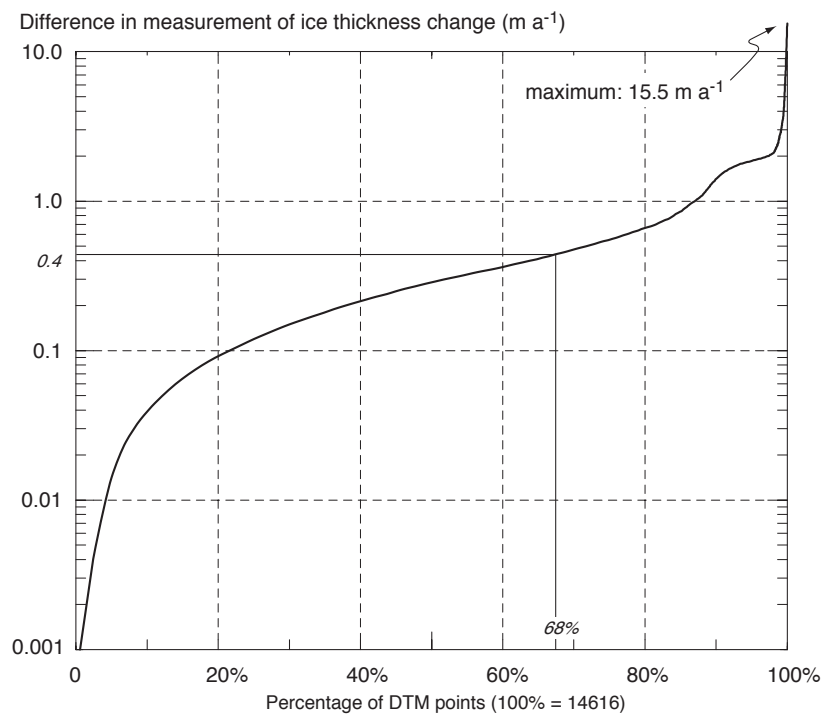


Fig. 8-4 Glaciar Chico: histogram of deviations between ice elevation changes as derived from aerial photography of 1975 and 1997, and ice elevation changes as derived from 1975 aerial photography and 2001 ASTER satellite stereo data. 68% of all points on the glacier (i.e. the one sigma range) show deviations smaller than $\pm 0.45 \text{ m a}^{-1}$.

rates of changes in ice thickness for the entire Southern Patagonia Icefield using the SRTM DTM and aerophotogrammetric DTMs. For the elevation zone 600–1000 m ASL considered here, their study revealed average thinning of about -2 m a^{-1} during the 1975–2000 period (-5 m a^{-1} for 1995–2000). The number for the 1975–2000 period coincides well with the measurements of ice thickness change presented here for Glaciar Chico. However, exact comparisons between different glaciers are difficult due to the large influence of calving on the behaviour of individual glaciers of the Southern Patagonia Icefield.

Inclusion of more base data, other aspects of DTM evaluation and a thorough glaciological interpretation of the results are given in (Rivera et al., 2005).

At present, optical satellite stereo from medium-resolution instruments such as ASTER can rarely be used alone to monitor glacier thickness changes. To be detectable at a significant level, elevation changes between image acquisition dates have to clearly exceed the pixel size of the applied imagery, which – if at all – is expected for decadal scales rather than for annual or pluriannual scales. Nevertheless, our study shows that a comparison of modern satellite imagery to pre-existing aerial photography, some decades old, does indeed reveal massive glacier thickness changes at a reliable level – at least for ablation areas (cf. Fig. 12-4). Advanced postprocessing might allow to detect different zones of ice thickness changes even after a few years (cf. Section 4.2, Fig. 4-5). This procedure opens new perspectives for glacier monitoring in remote areas where old photographs (or maps) are available but no such data exist for the present time. Where available, SRTM or SPOT 5 DTMs might be preferable to ASTER data for studies of this sort (see Section 3.4.2)(Berthier et al., 2004). For selected areas, application of high-resolution satellite stereo (e.g. Ikonos, Quickbird) makes it possible to greatly reduce the significance level of elevation changes in the order of one metre.

8.2 Flow field and speed changes from repeat satellite imagery: Tasman Glacier, New Zealand

Collaboration

Martin Kirkbride, Department of Geography, University of Dundee, supported the glaciological interpretation of the measurements from this study.

8.2.1 Introduction

As shown in Section 4.4, flow fields of medium- to large-sized glaciers can be measured from repeat optical satellite imagery. If the repeat imagery is not taken from identical camera positions, another identical projection – usually orthorectification – is required for such procedure. Therefore, a DTM of the study area has to be available in most cases. Such requirement makes instruments with stereo capability especially suitable for deriving glacier movement since they simultaneously deliver the images and DTMs needed. Where available, the SRTM DTM is a valuable alternative to the DTM from satellite stereo. This section presents a discussion of the flow field of Tasman Glacier, New Zealand, as derived from repeat ASTER imagery and of speed variations between two adjacent years.

Tasman Glacier, the largest glacier in New Zealand, is situated in the central Southern Alps near Mount Cook (3754 m ASL). It has the longest and most detailed historical record of any New Zealand glacier starting from 1862 (see Kirkbride and Warren, 1999). Similar to most large valley glaciers in the Southern Alps, it is covered with an extensive supraglacial debris mantle and following the 20th-century retreat now terminates in an ice-contact lake (Kirkbride and Warren, 1999). In the mid-1980s, the terminus lake (now called Lake Tasman) started to develop from supraglacial ponds, which first occurred in the late 1950s (Kirkbride, 1993), and is now over 5 km long (ASTER imagery of 2001). The only substantial bare ice zone in approximately the lower 10 km of the glacier, just below the inflow of Hochstetter Glacier, seems to have diminished since the 1890s. It was completely covered by the deposits of a large rock avalanche from the east flank of Mount Cook in December 1991 (McSaveney et al., 1992; Kirkbride and Warren, 1999).

8.2.2 Flow field

Figure 8-5 depicts the surface displacements between April 2000 and April 2001 for Tasman Glacier. The displacement vectors were measured automatically from orthorectified ASTER data from 29 April 2000 and 7 April 2001 using image correlation techniques (Section 4.4). The fact that one of the ASTER images was acquired in nadir mode but the other with 8.5° cross-track pointing led to some low-frequency distortions between the orthoimages, presumably from errors in exterior orientation. In order to avoid these distortions, the displacements were derived section-wise. For the individual sections, planimetric orthoimage-to-orthoimage transformations were determined from apparently stable terrain points. The parameters of the section-wise transformations were then applied to correct the raw displacement vectors. A threshold for individual correlation coefficients to be accepted was applied, and the few obvious mis-matches were deleted manually. Figure 8-5 depicts the measurements resulting from these procedures without further filters applied. The automatic cross-correlation was not particularly

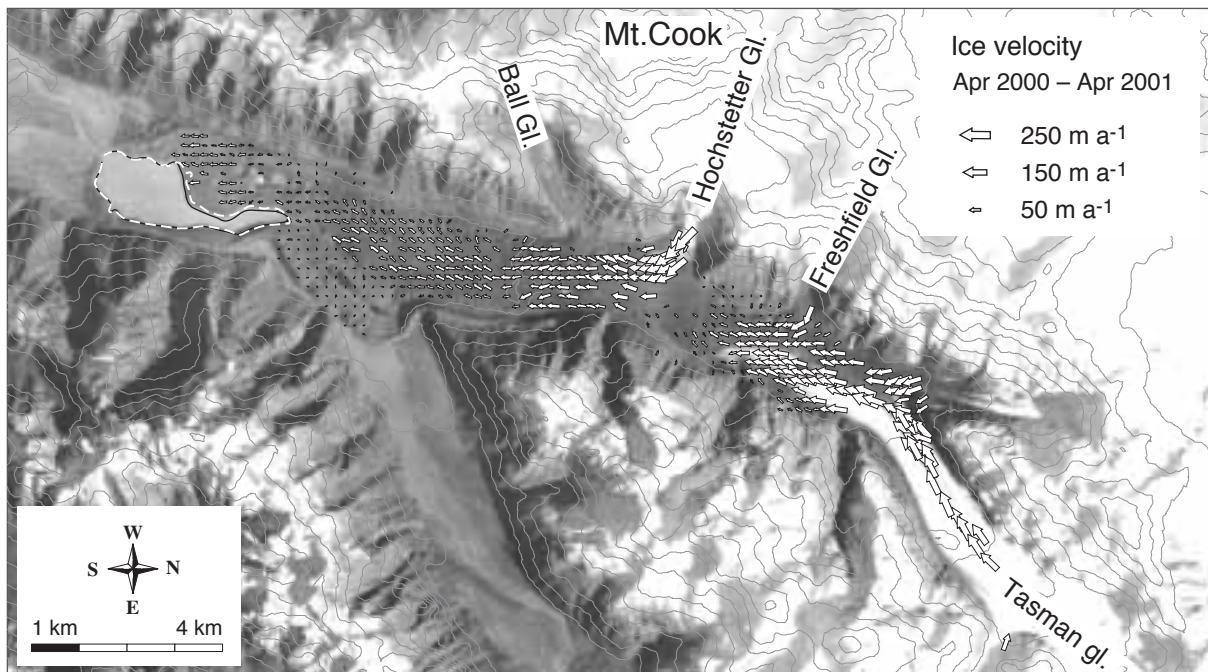


Fig. 8-5 Ice flow vectors for Tasman and Hochstetter Glacier, New Zealand, derived from ASTER images of 29 April 2000 and 7 April 2001. The original 100 m spacing of the raw measurements is resampled to 200 m spacing. Ice speeds amount to 250 m a^{-1} . At the glacier terminus lake, a dashed line marks the lake extent of 7 April 2001 superimposed on the 29 April 2000 orthoimage. The observed lake growth towards the ice front amounts to 130 m.

successful for clean ice because the images showed no corresponding features between the two acquisition times. The upper glacier parts were snow-covered in April 2000 especially.

In the upper part of the glacier, ice speeds of up to 230 m a^{-1} were observed (Fig. 8-6), continuously decreasing towards the central part of the depicted image section, where velocities are below the significance level of approximately one image pixel size ($\pm 15 \text{ m}$). The distinctive ice inflow of 250 m a^{-1} (or even more) from the western tributary, Hochstetter Glacier, might play an important role in this process. Velocities decrease again towards the lake at the glacier front below the glacier confluence. An area with very low or even zero velocities can be recognized, presumably consisting of ice-free moraine or stable dead ice to the north-east of the lake.

A striking feature of the Tasman Glacier flow field is the decrease in ice speed just above the confluence with Hochstetter Glacier. It is possible that (1) the ice supply from Tasman Glacier stops, for the most part, at the confluence area, or that (2) the ice transport from Tasman Glacier is pressed partially under, or incorporated into the Hochstetter Glacier. Scenario (1) can be assessed in more detail on the basis of mass conservation considerations by comparing estimated mass flux to estimated mass loss from ablation. The assumption of a semi-circular cross-section of Tasman Glacier at the inflow of Freshfield Glacier and a speed distribution with depth symmetrical to the one at surface yields a total ice flux of roughly $15 \text{ million m}^3 \text{ a}^{-1}$. A vertical ice loss of roughly -4 m a^{-1} would be necessary, in order to totally remove this mass from a glacier area of approximately $3\text{--}4 \text{ million m}^2$ between the Freshfield and Hochstetter Glacier inflows. For the lower 10 km (approx.) of Tasman Glacier, Kirkbride and Warren (1999) found annual ablation rates between -2 and -17 m a^{-1} , strongly depending on the thickness of the debris cover. It seems thus well possible that the ice flux from Tasman Glacier is consumed by ablation before it reaches

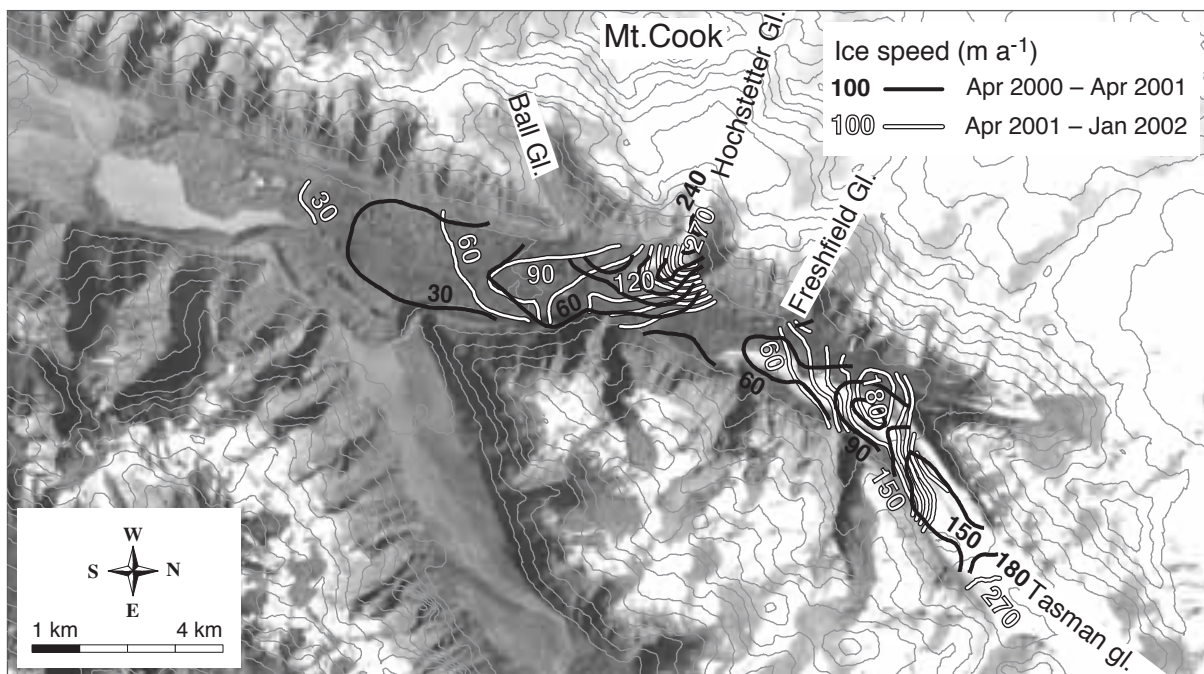


Fig. 8-6 Isolines of glacier surface speed on Tasman Glacier, New Zealand, derived from repeat ASTER imagery. Black lines indicate the average speed between 29 April 2000 and 7 April 2001, white lines the average speeds between 7 April 2001 and 29 January 2002. A significant increase in speed could be observed in the interval between the two periods.

Hochstetter Glacier (i.e. suggesting hypotheses 1). The thickness of the debris mantle on Tasman Glacier between Freshfield and Hochstetter Glaciers, which is unknown to us, is presumably strongly influenced in some parts by the 14 December 1991 rock avalanche deposits (McSaveney et al., 1992).

A glaciological interpretation of the confluence discussed here has also to consider the general mass balance gradient in the area. New Zealand has a humid maritime climate, with the Southern Alps lying across the path of the prevailing westerly winds. This situation creates steep, eastward precipitation gradients and a strong föhn effect. Mean annual precipitation reaches its maximum of 15,000 mm or more in the western part of the Southern Alps, a few kilometres west of the main divide. From this maximum, precipitation diminishes approximately exponentially to, for instance, about 4,000 mm at Mount Cook Village, south of Lake Tasman (Griffiths and McSaveney, 1983). Tasman Glacier is thus less well nourished than Hochstetter Glacier. From that point of view, dynamical separation of the two glacier tongues in an east-west direction, i.e. across the main valley and in direction of the tributary valley, can be expected rather than a flow-parallel separation, i.e. along the main valley. The latter represents the common situation for many other glaciers which incorporate confluences. Thus the so-called Tasman Glacier terminus at Lake Tasman is, in fact, the Hochstetter Glacier terminus, whereas the Tasman Glacier terminus is most likely to be situated somehow above the confluence area with Hochstetter Glacier (cf. Kirkbride and Warren, 1999).

8.2.3 Variations in speed

The above velocity field obtained for April 2000 to April 2001 was also compared to a velocity field derived from ASTER data of 7 April 2001 and 29 January 2002 using the same techniques (Fig. 8-6). It should, however, be stated clearly that due to

radiometric differences from different illumination conditions, the 2001–2002 measurements have a smaller signal-to-noise ratio than the 2000–2001 measurements. Therefore, at individual points variations in speed can seldom be derived to a reliable degree. Thus, the speed contour lines of 2001–2002 depicted in Figure 8-6 have to be interpreted with caution. However, the spatial distribution of speed differences reveals a consistent overall increase in flow speed from 2000–2001 to 2001–2002 in the order of up to 50% with respect to the first period – both for Tasman and Hochstetter Glacier.

The ice velocities measured from the ASTER data can be compared to a selection of terrestrial and photogrammetric velocity measurements available for Tasman Glacier (Kirkbride, 1995; Kirkbride and Warren, 1999). For the lowermost 2–3 km of the glacier tongue the velocities observed from ASTER data seem to be similar within the measurement accuracy to those observed for 1971 to 1986 and 1957 to 1971. Terrestrial velocity measurements for May to December 1986 at a region c. 10 km upvalley of the front gave $90\text{--}100 \text{ m a}^{-1}$. Velocities at the same place derived from ASTER data approximate 50 m a^{-1} for April 2000 to April 2001, and 60 m a^{-1} for April 2001 to January 2002. Earlier measurements in the same zone by T.N. Brodrick in 1890 and P.W. Anderton during 1971–73 gave ice speeds of about 170 m a^{-1} , or $60\text{--}90 \text{ m a}^{-1}$ respectively. The variations at the 10 km section indicate a marked difference in ice speed. It is not clear if this is, in fact, due to a general change in ice flow regime or just due to seasonal velocity variations. Note that the terrestrial surveying of 1986 and the ASTER measurements cover different segments of a year. Similarly, at this point it is not possible to attribute the change in speed observed in the ASTER data of 2000, 2001 and 2002 to either a general increase in ice flow or to seasonal effects.

During April 2000 to April 2001, and again during April 2001 to January 2002, the glacier front retreated by up to 130 m at the ice-contact lake (Fig. 8-5). The measured flow field and retreat rates of Tasman Glacier provide a possibility to forecast the evolution of the pro-glacial lake (Kirkbride and Warren, 1999; Purdie and Fitzharris, 1999). This kind of lake evolution mainly consists of a balance between ice melt and break-off (calving), on the one hand, and ice supply from glacier flow, on the other.

Near the inflow of Ball Glacier a conspicuous transverse ridge can be recognized on the applied ASTER imagery. That ridge might have been part of the outline of the deposits of the December 1991 Mount Cook rock avalanche and been deformed over time by glacier movement. Comparison of the 2001 ridge position to the position of the rock avalanche deposits in 1991 (McSaveney et al., 1992; Kirkbride and Warren, 1999) gives a potential downstream advection of roughly 1 km. The order of magnitude for the resulting average surface speed of 100 m a^{-1} fits well to the speed observed in the ASTER imagery of 2000–2002 (Fig. 8-6).

8.2.4

Conclusions

The Tasman Glacier study revealed an as yet little known characteristic of its flow field, thereby adding to the improved understanding of its dynamics, structure and potential future behaviour under conditions of climate change. The identification of seasonal versus long-term variability is necessary for the interpretation of observed changes in glacier speed. To this end, further image data will be included in the study.

Medium-resolution satellite imagery such as ASTER data still has a coarse resolution compared to the size of typical glacier surface features such as crevasses or rocks, or compared to the resolution of aerial imagery. The present work shows that corresponding velocity measurements are, nevertheless, able to provide novel

glaciological findings about glacier dynamics. The potential of such space imagery to cover almost any glaciated area of the world opens new perspectives for investigating glacier dynamics in regions rarely studied to date. Further, it is shown that striking variations in ice speed can be monitored on the basis of repeat space imagery, even on an annual basis. Such perspectives are greatly improved when high-resolution is included (e.g. Ikonos, Quickbird, SPOT 5).

8.3 Glacier speed inventorying from repeat satellite imagery: Bhutan Himalaya

See also Kääb (2005).

8.3.1 Introduction

Investigations about the Tasman Glacier flow field (Section 8.2) pointed out the broad potential of spaceborne optical imagery for observing glacier flow for a large number of glaciers. The Tasman Glacier study worked well because features of the debris cover on the glacier were preserved over time. In the following study focusing on parts of the Bhutan Himalaya it was of particular interest to test whether such flow fields may also be derived for clean glacier ice and simultaneously for entire mountain ranges.

Glaciers in the Bhutan Himalaya have only rarely been investigated due to naturally and politically complicated access; in particular, very little is known about their dynamics. The northernmost section of the Himalayan main ridge (called "Lunana"; roughly 28° N, 90–91° E)(Gansser, 1970), marks the center of the study area, separating the Tibet plateau to the north from the central Bhutan Himalayas to the south (Fig. 8-8). The lowest terrain parts studied of about 3,700 m ASL lie in the valleys south of the main ridge. The northern sections towards the Tibet plateau show minimum elevations of around 5,000 m. Highest peaks are around 7,300 m. Thus, the study area represents one of the highest mountain relieves found on Earth.

Most northern glaciers are directed to the north, most southern glaciers to the south. The glacier tongues investigated are found at minimum elevations of 5,000 m to the north, and 4,000 m to the south of the main Bhutan watershed. 80 to 90 % of the total annual precipitation in the southern valleys (Lunana; 500–700 mm a⁻¹) falls during March to October (Mool et al., 2001b; Karma et al., 2003; Meyer et al., 2003). Floods from glacier lake outburst are one of the severest natural hazards in Lunana and among the most important processes of sediment redistribution and evacuation in the area (Gansser, 1970; Watanabe and Rothacher, 1996; Ageta et al., 2000; Mool et al., 2001b).

8.3.2 Merged DTM from ASTER and SRTM data

For orthorectification of the used repeat ASTER data a combined DTM was merged from an ASTER-stereo derived DTM and the SRTM3 DTM. The ASTER DTM of the study region was computed using ASTER imagery from 20 November 2001. Comparison between the SRTM3 DEM, and ASTER 30 m and 120 m DTMs for the site show that the ASTER 120 m DTM includes significantly less gross errors than the ASTER 30 m DTM (see Section 3.4.1). As a result data gaps in the SRTM3 DTM were filled with the ASTER 120 m DTM. DTM merging was done by replacement of SRTM3 no-data cells with the corresponding ASTER DTM cells. The resulting master-DTM was evaluated by comparing multi-incidence angle orthophotos derived

from ASTER 3N and 3B data (Section 3.5). Details on the methodology applied can be found in Kääb (2005).

8.3.3 Flow field of a glacier tongue

Figure 8-7 shows the surface displacements on a glacier tongue on the northern slope of the main ridge of the Bhutan Himalayas (the glacier is labelled Teri Kang no. 15 in the World Glacier Inventory and out-gr-42 in Mool et al. (2001b)). The glacier has only sparse debris coverage. In this study, the applied image matching technique (Section 4.4) mainly relies on crevasses which are well preserved over the observational period. The glacier surface velocities have been measured on the basis of ASTER imagery from 20 January 2001 and 20 November 2001. Velocities obtained for the period between 20 November 2001 and 22 October 2002 yielded no significant differences, and are thus not presented.

The observed velocity magnitude amounts to 70 m a^{-1} and decreases to 40 m a^{-1} at the calving glacier front. Speeds on the eastern tributary are higher than on the western one. They show sharp transverse gradients towards the glacier boundary but are otherwise largely uniform on the glacier. This characteristic clearly indicates a high basal component of the observed ice speed. Such velocity distribution with depth is also confirmed by the good preservation of crevasses over time, which in turn facilitates the measurements (see Fig. 4-7).

Between January 2001 and November 2001 the calving front retreated in places by up to 150 m, between November 2001 and October 2002 by up to 110 m. Maximum total retreat for January 2001 to October 2002 was up to 220 m.

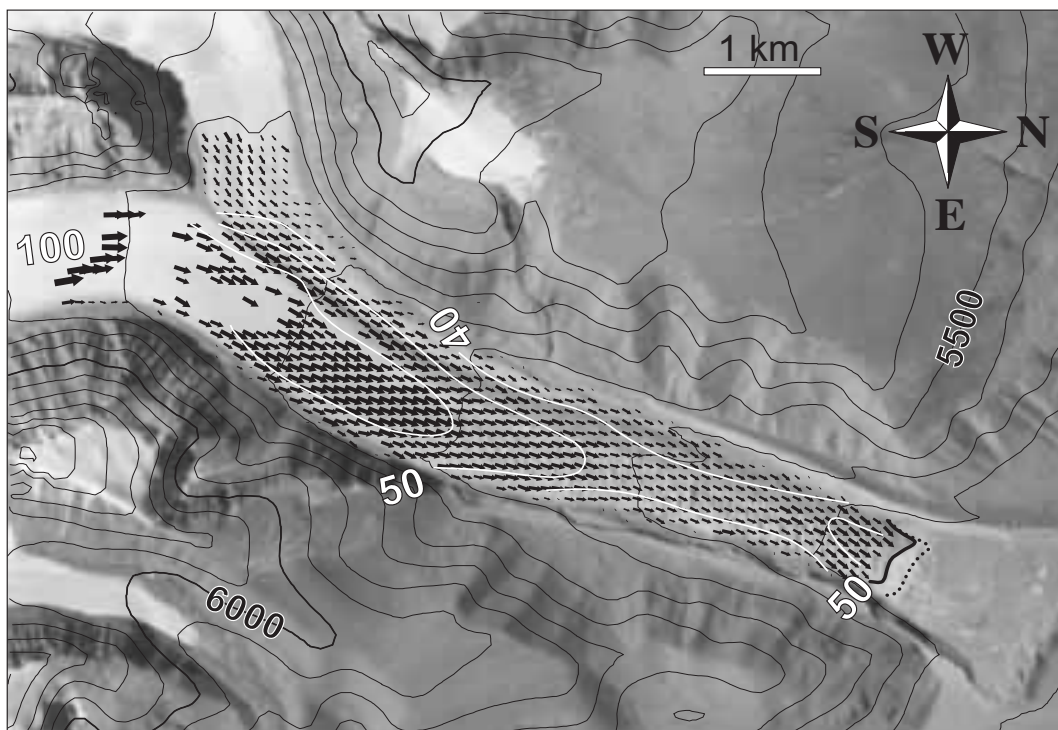


Fig. 8-7 Horizontal surface velocities on a glacier with unpublished name on the northern slope of the Bhutan Himalaya, derived from ASTER data of 20 January 2001 and 20 November 2001. Both the high ice speeds of over 40 m a^{-1} at the terminus and over 60 m a^{-1} 6 km above the terminus, and the sharp transverse speed gradients towards the glacier margins, indicate high basal glacier speeds. The dotted line at the calving front marks its position in January 2001; the bold line is the November 2001 position. For image location see Figure 8-8.

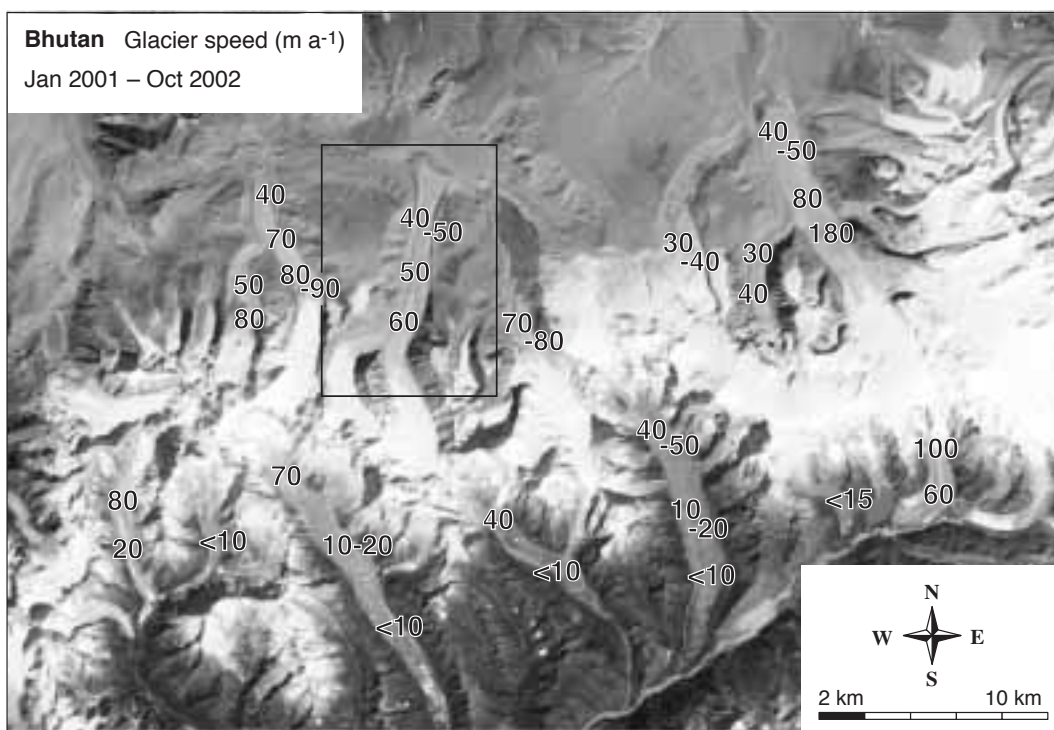


Fig. 8-8 Inventory of average glacier speeds for the main ridge of the Bhutanese Himalaya derived from ASTER data of 20 January 2001, 20 November 2001 and 22 October 2002. Northbound glacier tongues flow significantly faster than the debris-covered southbound ones. The inset marks the section shown in Figure 8-7.

8.3.4 Glacier speed inventory

Measurements similar to those for the glacier tongue shown above were performed for all large glaciers on the main ridge of the Bhutan Himalaya (Fig. 8-8)(Kääb, 2005), and the measurements on the northern slope turned out to be equally successful. On the southern slope, where glacier tongues are mostly heavily covered by debris and thermokarst features, significantly larger surface changes over time reduced the number of corresponding surface features in the repeat imagery. For better visibility, Figure 8-8 depicts only the average velocity magnitude for selected glacier zones over the period January 2001 to November 2001 to October 2002. No significant speed changes were observed during this period but inclusion of three image dates improved the measurement accuracy, or the number of corresponding features.

Clearly, the investigated glacier tongues on the northern slope show speeds of higher magnitude than the debris-covered glacier tongues on the southern slope (Kääb, 2005). Speeds of 40 m a^{-1} and more on the southbound glaciers are found for ice falls and other steep glacier parts. However, speeds on the debris-covered tongues rarely exceed the significance level of the measurement which is approximately 10 m a^{-1} .

8.3.5 Conclusions

For the Bhutanese Himalaya, it was found that glacier tongues on the northern and southern slope differed significantly, both in surface characteristics and in dynamics. Southbound glacier tongues are mostly heavily debris-mantled and covered by thermokarst features such as rapidly changing depressions and supraglacial ponds (cf. Chikita et al., 1999; Benn et al., 2000; Reynolds, 2000). In their terminus zones, glacier speed is near the significance level of the applied method, i.e. in the range of

10–20 m a⁻¹. Higher speeds are only reached in steep glacier parts above the tongues. Northbound glacier tongues show higher speeds of several tens to over 100 m a⁻¹. Velocity magnitude and surface velocity fields hint at a large percentage of basal velocity for the northern glaciers. These glaciers have almost no debris-coverage. Their light-blue ice colour – similar to that of arctic glaciers – indicates a comparably high content of air bubbles reflecting the sunlight, and thus cold glacier ice. The dry-cold continental climate in the northern basin and its elevation of over 5,000 m ASL suggests the existence of discontinuous permafrost (Xin et al., 1999; Brown et al., 2001). In contrast to the southern glaciers, the margins of the northern ones might be frozen to the ground – a fact that is known to favour high subglacial water pressure and thus basal sliding (e.g. Haeberli and Fisch, 1984). Surface slopes of the southern and northern glacier tongues are likewise in the order of a few degrees. Thus, different surface slopes can largely be excluded as the reason for the large speed differences observed. The speed differences might, on the contrary, point to different basal processes. For the calving glacier tongues, the uniform and comparably high speed might also be linked to a far-reaching influence of lake water pressure reducing the basal drag. For a thorough glaciological interpretation see also Kääb (2005).

The presented study shows that velocities of mountain glaciers can be measured from repeat satellite imagery also on clean glacier ice, at least under cold and dry conditions and for high sliding ratios, both of which support the preservation of surficial ice features such as crevasses (see Fig. 4-7). Applied to a large number of glaciers, this possibility opens new perspectives for observing and understanding spatio-temporal variability of glacier speed within different glaciers. Fresh insight into the topographic, climatic or geologic control of glacier dynamics can be gained from such regional-scale inter-comparisons (Kääb, 2005). It now seems feasible indeed to include glacier speed as a parameter into satellite-derived glacier inventories as is foreseen e.g. for the GLIMS project (“glacier speed inventorying”) (Raup et al., 2001). Such data could, for instance, help to assess the potential reaction of individual glaciers on climate impact. However, thorough goals and strategies for glacier speed inventorying have yet to be developed.

8.4 Seasonal velocities on a fast glacier: Kronebreen, Svalbard

Collaboration

Bernard Lefauconnier, Le Sappey en Chartreuse, France (formerly with the Norsk Polar Institute), and Kjetil Melvold, Department of Geography, University of Oslo, supported the glaciological interpretation of the results obtained in this study and provided comparative data. See also Kääb et al. (2005b).

8.4.1 Introduction

On fast glaciers, flow velocity exceeds the noise level obtained for displacement measurements from repeat satellite imagery in a way that makes observation of seasonal velocities feasible (see Section 4.4). On the other hand, measurement of displacements over longer time intervals is complicated or even made impossible by the destruction of surface features – a process which is often connected to high ice speeds. Here, the velocity field of the lower part of Kronebreen, Svalbard, is presented for a 40-day period in summer 2001. The obtained glacier activity is compared to other surface velocity measurements from:

- terrestrial photogrammetry in the period 1962–1965 (e.g. Pillewizer and Voigt, 1968),
- terrestrial photogrammetry in the period 1983–1986 (Lefauconnier, 1987),
- repeat SPOT imagery of 1986 (Lefauconnier et al., 1994; Rolstad, 1995),
- terrestrial photogrammetry and stake measurements for 1990 (Melvold, 1992) and
- DInSAR for 1995/1996 (Eldhuset et al., 2003).

Kongsbreen is a tide-water calving glacier formed by two joined ice streams, Kongsvegen and Kronebreen (Fig. 8-9). Kronebreen experienced a major surge in 1868 or 1869. The following front retreat of more than 4 km was interrupted by a surge of Kongsvegen that advanced about 1.5 km into the sea. Since then, the Kongsbreen front has been continuously retreating for more than 4 km. The glacier bed is partially below sea level along a stretch of about 7 km upstream of the front. (After Lefauconnier, 1987; Lefauconnier et al., 1994). (See also Kääb et al., 2005b).

8.4.2 Glacier flow

Image matching using ASTER data from 26 June and 6 August 2001 was applied to derive the flow field of the lowermost 12 km of Kronebreen (for the method see Section 4.4 and Kääb et al. (2005b)). In Figure 8-9 the 100 m spaced measurements are resampled to 200 m spacing for better visibility. Maximum speeds of more than 800 m a^{-1} (2.2 m d^{-1}) are reached just behind the calving front. A marked increase in speed over the entire glacier width can be observed at around 5 km upstream of the front. There, at a transverse step in surface topography, speed increases from up to 1.3 m d^{-1} to up to 1.9 m d^{-1} within a horizontal distance of less than a kilometre. The resultant longitudinal straining is accompanied by enhanced crevassing.

At the confluence with Kongsvegen, but also above this point, the speed maximum of Kronebreen is shifted to its southern margin. On Kongsvegen with speeds known to lie in the range of a few metres per year (Melvold, 1992) no significant displacements can be detected from the 15 m resolution ASTER data. Today, the direction of the middle moraines between Kongsvegen and Kronebreen coincides with the ice flow direction of Kronebreen. Following the 1948 surge of Kongsvegen, the position of the middle moraines continuously shifted reflecting the adjustment of a new mass-flux equilibrium between Kronebreen and Kongsvegen ice streams (Fig. 8-10).

At two cross-sections, the velocity field of July 2001 presented here can be compared to data from the studies listed above (Fig. 8-11). For the lower profile P1 (see Fig. 8-9), the July 2001 data accord well with the August 1986 data. Speeds for June and July 1986 compare well to those from August 1990, both significantly higher than July 2001. The shapes of the 2001, 1990 and 1986 speed cross-profiles resemble one another, however, broad variations occur toward the northern glacier margin. In 1964, the shape of the speed cross-profiles is clearly influenced by the higher ice flux from the post-surge Kongsvegen. For Kronebreen, the July 2001 and the July 1964 speeds coincide well.

At the upper profile P2, all speed cross-profiles included show a very similar shape, but have distinct differences in amplitude. In this comparison, no preferential time period for maximum spring and summer speeds becomes obvious. In contrast to the high speed-variability suggested by Figure 8-11, Eldhuset et al. (2003) (cf. König et al., 2001) found no strong variations in the fringe pattern from a number of ERS 1/2 tandem-mission interferograms over July 1995 to May 1996. They interpret this result as an almost stable ice-velocity field over the investigation period, but also note

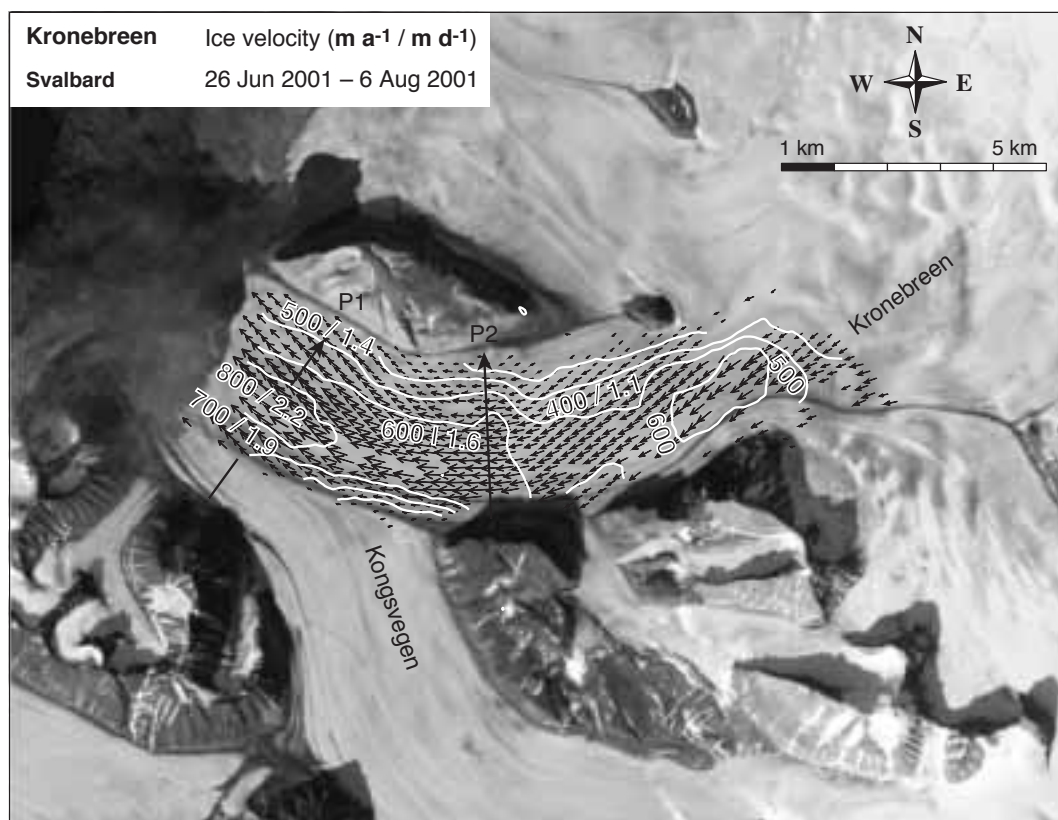


Fig. 8-9 Surface velocity field for a section of Kronebreen, Svalbard, derived from repeat ASTER imagery of summer 2001. Isolines indicate ice speed in metres per year / metres per day. The surface velocities of Kongsvegen are too small to be measured from repeat satellite imagery. For profiles P1 and P2 see Figure 8-11.

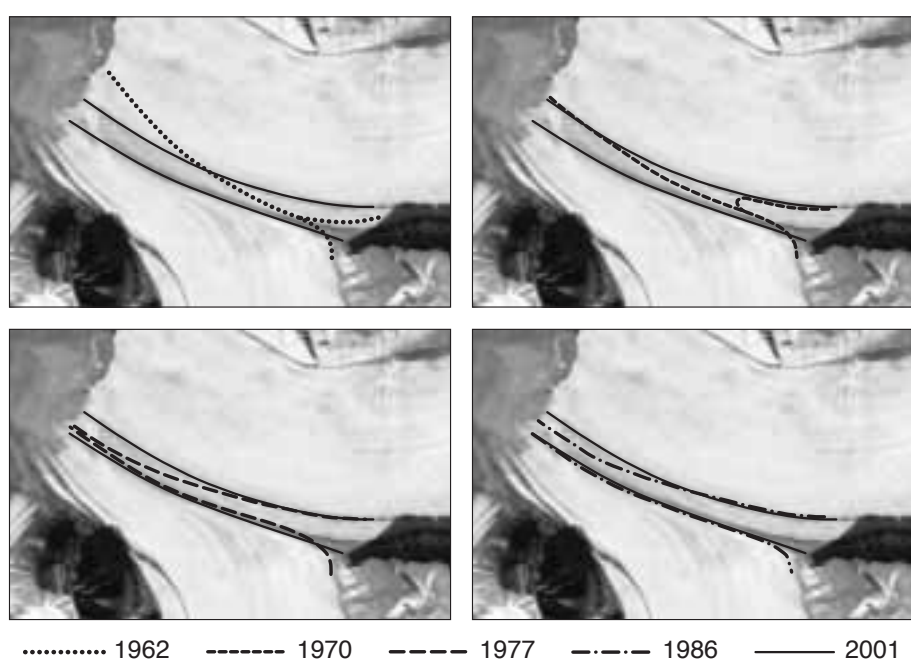


Fig. 8-10 Position of middle moraines between Kongsvegen and Kronebreen at selected times between 1962 and 2001. Data from Lefauconnier (1987), Melvold (1992) and this study. The shift of the moraines reflects the adjustment of ice dynamics following the 1948 surge of Kongsvegen.

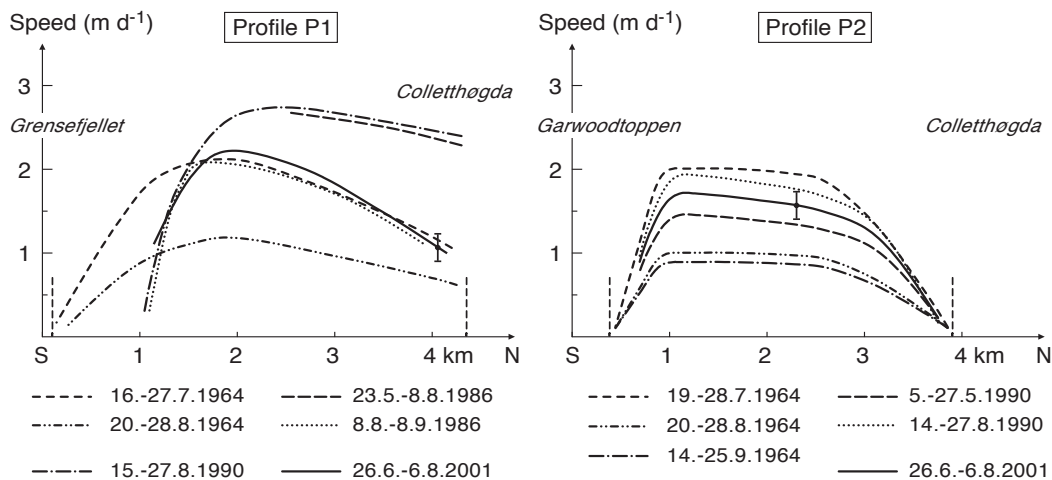


Fig. 8-11 Cross-profiles of ice speed at positions P1 and P2 (see Fig. 8-9). 1964 data from Pillevizer and Voigt (1968), 1986 data from Lefauconnier et al. (1994) and Rolstad (1995), 1990 data from Melvold (1992), and 2001 data from this study. The error bar gives the estimated accuracy for the ice speeds from the 2001 ASTER data.

the problems with coherence and phase unwrapping in the lower, fast-flowing part of Kronebreen. Inter-comparing the data of profiles P1 and P2, the July 2001 velocity field, and additional data from the above mentioned studies shows that the speed variations on Kronebreen happen not synchronously at both profiles.

Kääb et al. (2005b) extended the study presented here using ASTER data of 17 August 2000, 26 June 2001, 6 August 2001 and 12 July 2002, and Landsat ETM+ pan satellite data from 10 July 1999. A thorough description of the method applied and detailed glaciological interpretations can be found in their study.

8.4.3 Conclusions

The July 2001 Kronebreen velocity-field from repeat ASTER imagery shows, in general, a good agreement with other measurements. As also suggested by previous studies, a large spatio-temporal variability of the spring/summer ice speeds becomes evident. At the confluence zone with Kongsvegen, the 1948 surge and – presumably – the changing position of the calving front (exceeding the 2001 position by approximately 3 km in the 1960s) had influence on the flow field. The flow mode of Kronebreen some kilometres upstream of the front did, however, not change substantially since the 1960s. Conclusions about the present seasonal speed-variability of Kronebreen require analyses of more data, for instance, from ASTER and Landsat ETM+ pan (see Kääb et al., 2005b).

For fast flowing glaciers with movement rates of significantly more than several image pixels during the observational period, seasonal velocities may be measured from repeat satellite imagery. The fact that complete surface velocity fields can be thus obtained facilitates comparison with other velocity data, even if they cover only individual points or profiles. Apart from monitoring seasonal velocities for generally fast glaciers, these possibilities are especially useful for observing glacier surges (e.g. Fig. 4-11). For such work the supplementary character of optical methods and DInSAR becomes of great value (see Tab. 4-1)(Kääb et al., 2005b).

8.5 Velocity field during the surge-type movement of Ghiacciaio del Belvedere, Italian Alps

Collaboration

The studies presented here were conducted, to some extent, under mandate or contract to the Italian civil defence authorities and supported by the Comune di Macugnaga. The overall Ghiacciaio del Belvedere project represents a close collaboration between the University of Zurich (Andreas Kääb, Christian Huggel, Wilfried Haeberli), the CNR-IRPI, Torino (Gianni Mortara, Marta Chiarle), Fulvio Epifani (Studio Epifani, Arona), Andrea Tamburini (Enel.Hydro, Seriate), ARPA Piemonte (Marco Cordola, Secondo Barbero), Paolo Semino (Regione Piemonte, Domodossola), and Giorgio Viazzo (Ing. Viazzo, Vercelli) (Kääb et al., 2004).

8.5.1 Background

Since spring 2001 (possibly already starting in autumn 1999, cf. Mazza, 2003), Ghiacciaio del Belvedere (Fig. 8-12) has experienced drastic changes in flow regime and related features. (For details on Ghiacciaio del Belvedere see Mazza, 1998). Starting at the foot of the Monte Rosa east face and continuing down the glacier, exceptional crevassing indicated high stresses and strain rates in the ice. As a consequence, the surface characteristics of the glacier changed from almost complete debris-cover with smooth topography towards a heavily crevassed topography with debris-cover remaining on parts only (Haeberli et al., 2002a; Kääb et al., 2003d; Mazza, 2003; Kääb et al., 2004). Detailed observations of Ghiacciaio del Belvedere

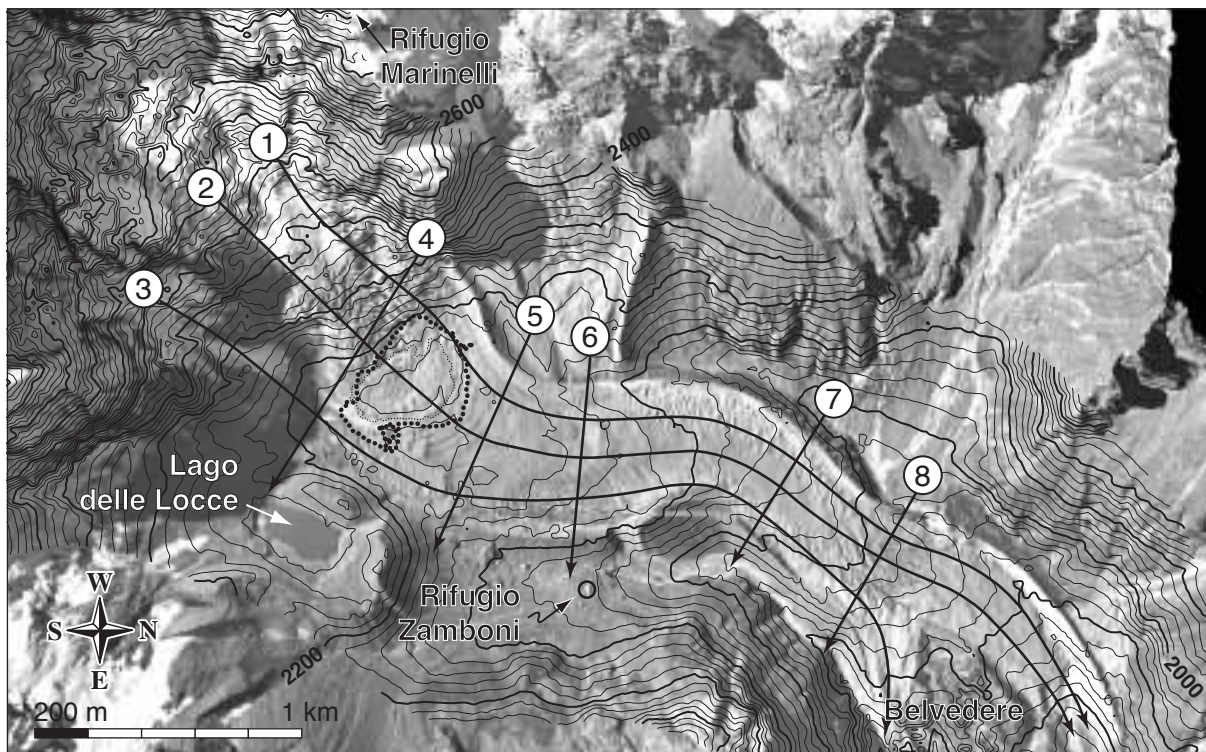


Fig. 8-12 Orthoimage of Ghiacciaio del Belvedere, Italian Alps, from 12 October 1995 (original aerial photo by swisstopo, permission BA057212). Numbers and corresponding lines indicate the elevation profiles of Figures 8-13 and 8-14; arrows give the respective profile direction. The dotted line marks the shoreline of the supraglacial lake at the beginning of July 2002.

had already started in the mid-1980s after a catastrophic outburst of the moraine lake Lago delle Locce in 1979 (Haeberli and Epifani, 1986). In autumn 2001, a small lake developed at an altitude of approximately 2150 m ASL on the flat tongue of Ghiacciaio del Belvedere, at the foot of the Monte Rosa east face. The formation of that lake was attributed to enhanced englacial water pressure linked with the surge-type movement (Haeberli et al., 2002a). Development of a large topographic depression at the glacier surface and rapid evolution of a supraglacial lake is rare on temperate glaciers and had not been observed previously in the European Alps.

Surprisingly, therefore, a huge lake of 150,000 m² area and 3 million m³ volume was encountered during initial control visits in mid-June 2002 (Fig. 8-12) (Kääb et al., 2003d; Tamburini et al., 2003; Kääb et al., 2004). With only a few metres of freeboard left, the lake level was rising at up to 1 m per day. The hydraulic gradient within the ice dam to the east of the lake must have been far over 10 % provoking a high risk of rapid intra-glacial channel development or ice-dam burst. Emergency actions were undertaken by the Italian Civil Protection and the scientists involved, which included continuous lake level monitoring, evacuation of parts of the village Macugnaga, automatic alarm procedures, installation of pumps, and detailed scientific investigations. A cold spell in early July 2002 that significantly reduced meltwater input, together with pumping operations and spontaneous developing sub-glacial drainage, all helped to stabilize and increasingly lower the lake level. By the end of October 2002 the lake area had been reduced to a size of roughly 2,000 – 3,000 m². For details and the recent development see Kääb et al. (2004).

The photogrammetric investigations presented here accompany the scientific activities of the project in order to promote better understanding of the surge-type movement and to aid the prediction of the near-future behaviour of Ghiacciaio del Belvedere. The photogrammetric analyses are based on photographs taken on 12 October 1995, 2 September 1999, 6 September 2001 (all Swiss Federal Office of Topography / swisstopo) and 11 October 2001 (CNR-IRPI, EU-Project Glaciorisk).

8.5.2 Elevation changes

For investigating the thickness changes, longitudinal and transverse profiles were interpolated from 25 m gridded DTMs, which were automatically derived from the aerial photography for the entire glacier. (For the method see Section 3.3.1).

Between 1995 and 1999, the ice thickness of the tongue of Ghiacciaio del Belvedere below the summer 2002 supraglacial lake (i.e. below about 2160 m ASL, or downstream from point $x \approx 1100$ m) was approximately stable (Figs. 8-13 and 8-14). At the zone of the 2002 supraglacial lake, surface lowering of up to -20 to -30 m in total can be observed. In the same time period, the ice thickness in the adjacent parts of the Monte Rosa east face, above the 2002 lake, showed a partial increase in ice thickness of the same order of magnitude.

From September 1999 to September 2001, the glacier thickness grew by about +10 to +15 m a⁻¹ between Lago delle Locce and Rifugio Zamboni, and by about +5 to +10 m a⁻¹ between Rifugio Zamboni and Belvedere. Below this point, no major vertical change was observed. Above the 2002 supraglacial lake (i.e. about 2200–2600 m ASL) the glacier lost up to -15 m a⁻¹ in ice thickness, most pronounced at the orographic left part towards Rifugio Marinelli.

The decrease in ice thickness for parts of the east face drastically accelerated between September and October 2001 with -25 m and more in elevation change over 35 days. Between Lago delle Locce and Belvedere the ice thickness grew by up to +10 m and more in the same time period. Around Belvedere the surface elevation rose by up to

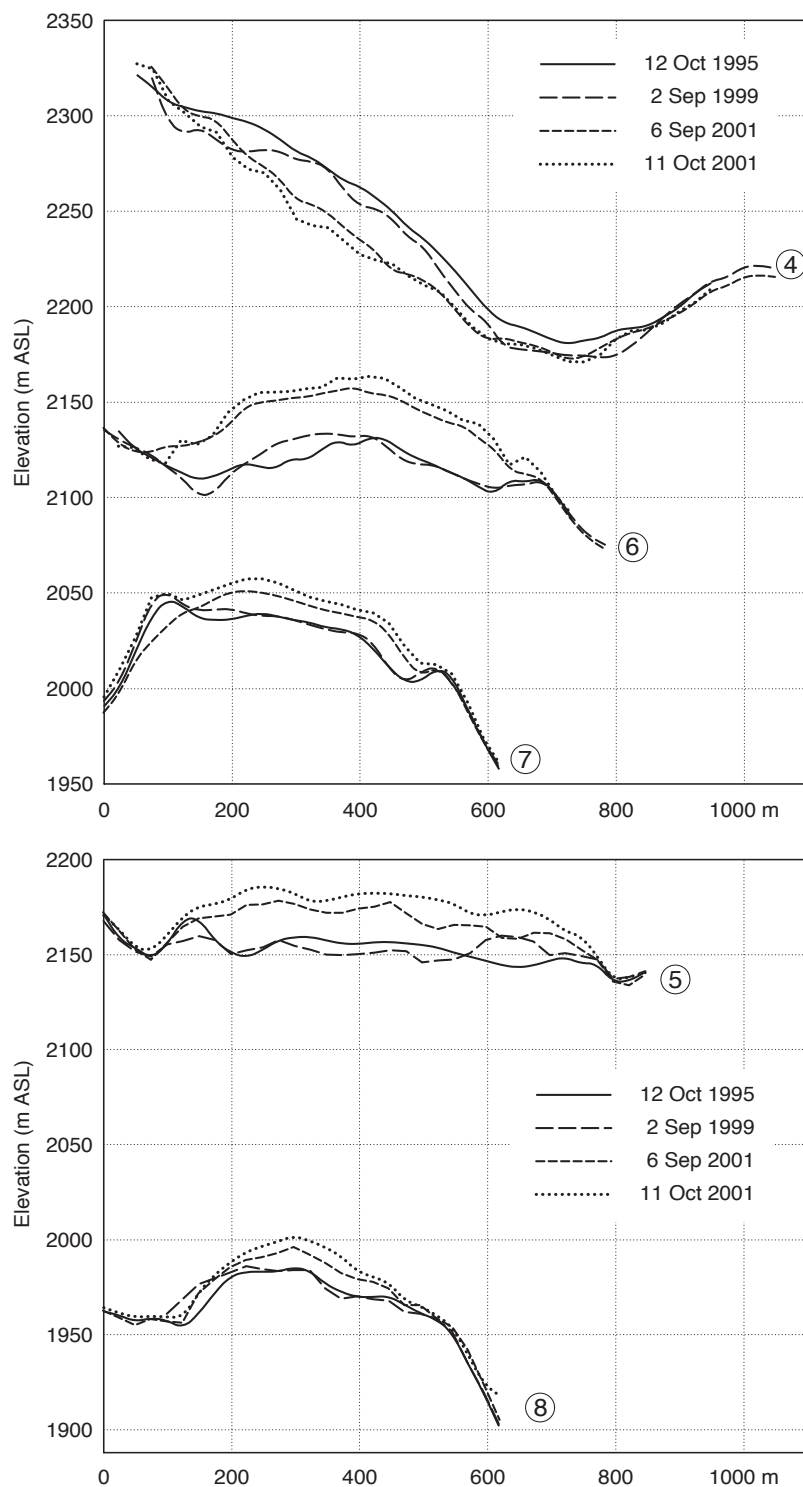


Fig. 8-13 Repeat transverse surface profiles over Ghiacciaio del Belvedere. For profile numbers see Figure 8-12.

5–10 m, indicating that the mass that was mobilized by the surge-type movement had reached the glacier tongues.

Due to local thermokarst processes and problems with the automatic DTM measurement, the elevation changes for the left glacier tongue at the very terminus cannot be interpreted (profiles 1 and 2). A partial advance of up to approximately 70 m can be observed between 1995 and 1999 from the aerial imagery. From 1999 to 2001 no clear advance is visible.

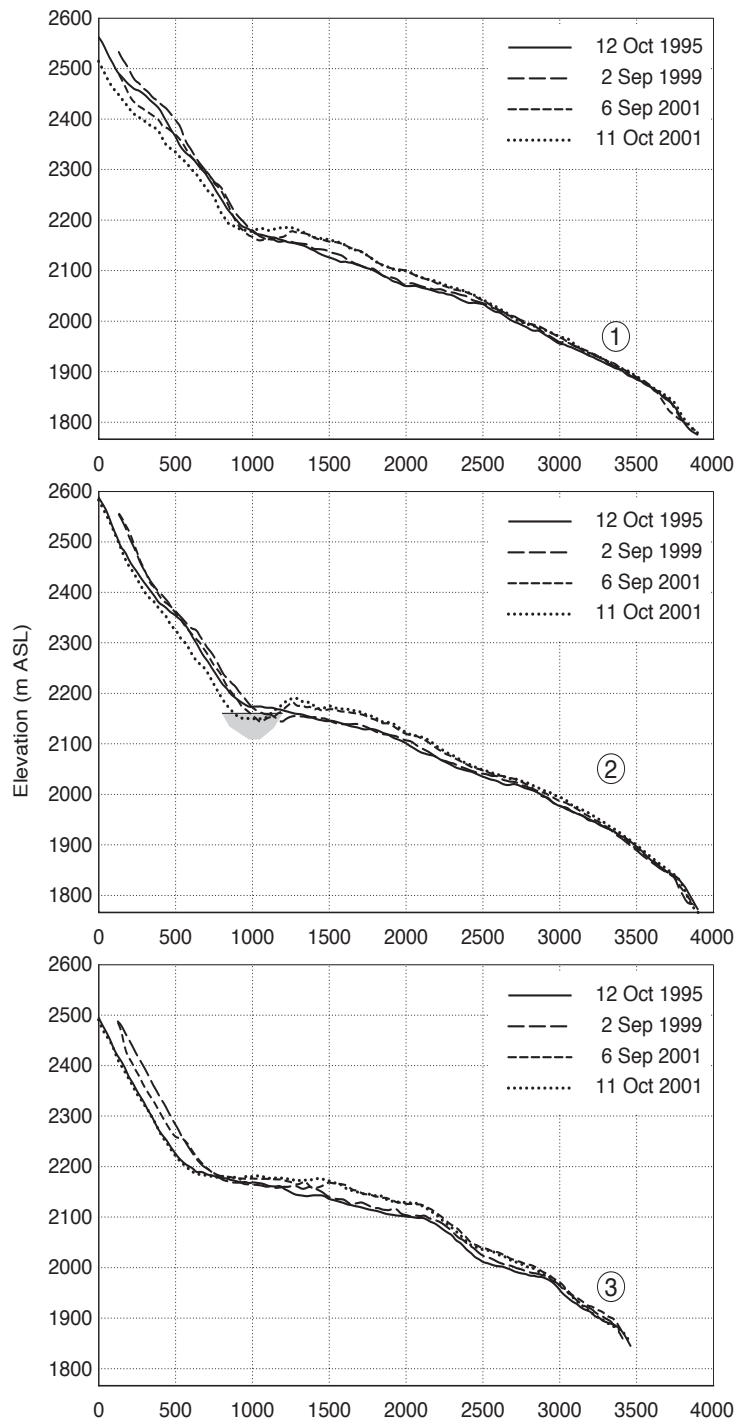


Fig. 8-14 Repeat longitudinal surface profiles over Ghiacciaio del Belvedere. For profile numbers see Figure 8-12. In profile no. 2 the position of the summer 2002 supraglacial lake is indicated schematically.

8.5.3 Ice velocities

Surface velocities on Ghiacciaio del Belvedere were derived from automatic orthoimage matching (see Section 4.4). Due to the long time difference between the 1995, 1999 and September 2001 image acquisition dates, measurements were possible only for selected points (Fig. 8-15). Between 6 September and 11 October 2001 a complete velocity field could be measured.

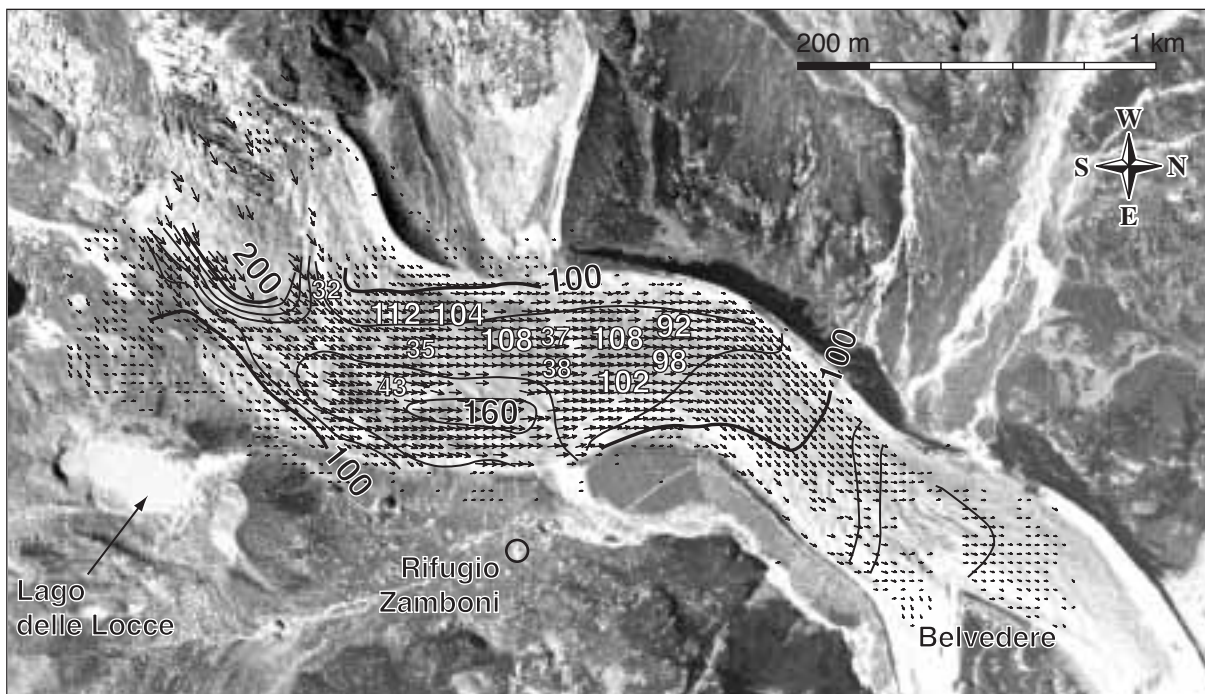


Fig. 8-15 Surface velocity field on Ghiacciaio del Belvedere between 6 September and 11 October 2001. Underlying orthoimage of 11 October 2001 (original air-photo © CNR-IRPI / Glaciorkisk). The black numbers and isolines indicate the glacier speeds of the autumn 2001 period. The large white numbers (92–112) give speeds at selected points between 2 September 1999 and 6 September 2001; the smaller white numbers (32–43) indicate speeds from 12 October 1995 to 2 September 1999. Speeds are given in metres per year.

Between 1995 and 1999, the average horizontal ice speeds on the glacier between Lago delle Locce and Rifugio Zamboni were roughly 35 m a^{-1} , in parts over 40 m a^{-1} . In the mid-1980s speeds of approximately $40\text{--}45 \text{ m a}^{-1}$ were measured terrestrially for the same zone (VAW, 1985; cf. Mazza, 2003). For the period of September 1999 to September 2001, horizontal ice velocities of about 110 m a^{-1} magnitude were measured between Lago delle Locce and Rifugio Zamboni, which represents a drastic increase compared to the time before September 1999.

The velocity field between 6 September and 11 October 2001 on Ghiacciaio del Belvedere (Fig. 8-15) shows a highly coherent ice stream with sharp lateral speed gradients. Glacier speeds close to the moraines are still up to 100 m a^{-1} . Maximum speeds of 200 m a^{-1} and more are found at the foot of the Monte Rosa east face. Flow speed remains above 100 m a^{-1} until halfway between Rifugio Zamboni and Belvedere. Speeds around Belvedere are approximately 40 m a^{-1} . The line of cross-sectional speed maxima along the glacier is strongly S-shaped, swinging from the eastern margin at Rifugio Zamboni to the western margin between Rifugio and Belvedere. The amplitude of the S-shape in speed maximum is similar but more pronounced than the topographic S-shape formed by the lateral moraines of Ghiacciaio del Belvedere.

8.5.4 Conclusions

The photogrammetric analyses suggest that the enhanced movement started somehow simultaneously in the foot zone of the Monte Rosa east face and the flat lower part of Belvedere Glacier, or was, at the beginning of the surge-type behaviour, initially restricted to the flat lower part. The large depression at the foot of the Monte

Rosa east face, which was temporarily filled by the supraglacial lake, might originate in part from strong extending flow and thus mark the upper limit of a decoupled ice mass further downstream. The heavy crevassing and the enormous loss in ice thickness after 1999 observed for the glacier parts above the depression zone could thus be the consequence of a drastically changed stress regime due to sudden lack of support at the slope foot, rather than an active part of the speed-up event. The increase in surface elevation during 1995–1999, as measured for some glacier parts above the depression zone might also indicate the involvement of an unspecified form of ice-damming process occurring at the same time as the formation of the depression.

The autumn 2001 velocity field with its sharp marginal velocity gradients, and an ice-marginal band of strong shearing combined with an undisturbed snow cover on the glacier surface itself, as observed in winter 2002/2003 (Kääb et al., 2004), indicate that the glacier moved as a block by sliding, sediment deformation or internal shearing rather than by enhanced deformation throughout the entire ice column. Such behaviour is typical for glacier surging (Raymond, 1987; Harrison and Post, 2003).

According to the photogrammetric velocity measurements, the surge-type acceleration of Ghiacciaio del Belvedere must have started between 2 September 1999 and 6 September 2001. If one hypothetically assumes (i) a sharp onset of the surge-type movement, (ii) that the glacier speed directly before the surge onset was equal to the average speed between 12 October 1995 and 2 September 1999, and (iii) that the glacier speed directly after the surge onset was equal to the average speed between 6 September 2001 and 11 October 2001, the timing of the surge onset can be estimated in a way that a computed average speed between 2 September 1999 and 6 September 2001 equals the measured one. That way, the beginning of the enhanced speed can be hypothesized for the period around April 2000.

The photogrammetric studies on Ghiacciaio del Belvedere show that reconstruction and interpretation of glacier-dynamical events is very much supported, or even only possible, by (digital) analysis of aerial photographs or other high-resolution stereo imagery. Whereas the construction of repeat DTMs is little dependent on the time intervals between the image acquisition dates, the computation of horizontal surface displacements is strongly influenced by terrain changes over time. For Ghiacciaio del Belvedere, velocity measurements over several years succeeded only for a few selected points, despite the debris cover of the ice. Imaging intervals of a few weeks or months, however, open new perspectives for detailed analysis of glacier dynamics and glacier hazard assessment (see also Fig. 4-12).

9.1 Surface velocity fields of rockglaciers

9.1.1 Introduction

The creep of perennially frozen ground in mountains (here also termed creeping mountain permafrost), best expressed in the form of rockglaciers, is basically defined by its material properties and thermal conditions – and by its deformation. Knowledge about three-dimensional surface velocities contributes towards detecting and understanding the dynamic processes involved in permafrost creep and, generally, in landscape evolution in cold high-mountain environments (Haeberli, 1985; Barsch, 1996; Frauenfelder and Kääb, 2000; Kääb et al., 2003c; Frauenfelder, 2004).

Optimal investigation of permafrost creep requires: (1) area-wide information on kinematics to account for 3-dimensional effects, (2) in view of the low deformation rates, the application of precise high-resolution techniques, and (3) long-term monitoring to document slow temporal changes at a statistically significant level of accuracy. Recent advances especially in image processing enable surface deformation of rockglaciers to be measured with a resolution and accuracy previously not known. Improved process understanding and new insight into rockglacier development result from such measurements. Corresponding findings from surface velocity fields of rockglaciers in the Swiss Alps are the present subject of intercomparison.

9.1.2 Gruben rockglacier

The surface velocity field of Gruben rockglacier, Valais (Fig. 1-3), was derived from aerial photographs taken on 24 September 1970, 2 October 1975 and 10 October 1995 – and also between other periods that are not discussed here. Average displacements 1970–1995 are presented in Figure 9-1 (see also Fig. 6-8). The velocity field of Gruben rockglacier clearly depicts dynamic differences between a periglacial and a glacier-affected part. From 1970 to 1995, the glacier-affected section with its dead ice near the surface has flowed back between lakes no. 3 and 6 towards the Gruben Glacier tongue with surface velocities of up to several metres per year. The different general direction of surface flow within the glacier-affected part as contrasting to the flow direction within the periglacial part corresponds to the different directions of maximum surface slope in each of the two areas. The surface of the periglacial section between lake no. 5 and the front towards the south-west creeps at a velocity of a few decimetres per year. Creep velocities accelerate to about 1 m a^{-1} across and below a transverse bedrock riegel at about 2840 m ASL (Kääb et

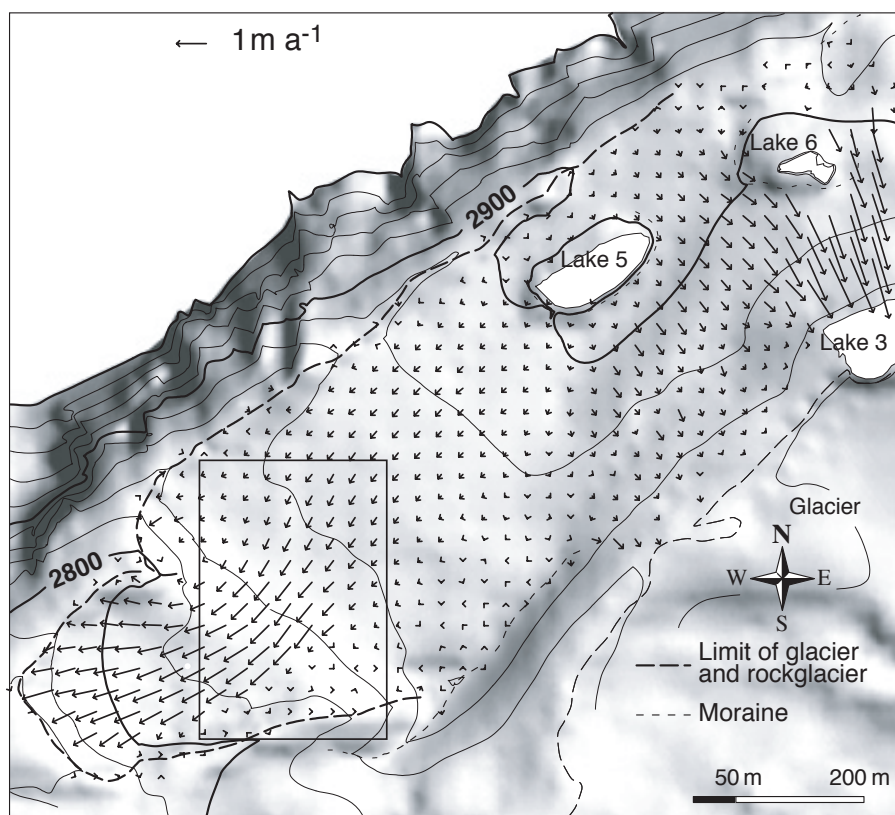


Fig. 9-1 Average horizontal surface velocities on Gruben rockglacier, Valais, measured from aerial photography of 1970 and 1995. The rectangle to the lower left marks the section depicted in Figure 9-28.

al., 1997). Surface speeds continuously increase from lake no. 5 towards the rockglacier front, indicating a prevailing horizontal extension in flow direction.

Detailed analyses and discussions of the Gruben rockglacier kinematics can be found in Kääb et al. (1997). Shallow core drilling, geophysical soundings, lichen-cover studies, modelling of a thermokarst lake, and hazard assessment and mitigation have been conducted in the area (Barsch et al., 1979; Haeberli et al., 1979; Haeberli, 1985; King et al., 1987; Kääb, 1996a; Kääb, 2000; Haeberli et al., 2001; Kääb and Haeberli, 2001). Sections 9.2 and 9.4 of this chapter discuss details of the frontal processes and the flow field of the rockglacier, respectively.

9.1.3 Suvretta rockglacier

Surface displacements of Suvretta rockglacier, Suvretta valley, Upper Engadine (Fig. 1-3), were measured from digital correlation of aerial imagery of 16 September 1992 and 16 September 1997 (Fig. 9-2). A transverse terrain edge at an altitude of about 2600 m ASL divides the rockglacier into a lower steep part, which is depicted in Figure 9-2, and an upper flat part with surface velocities of only a few 0.1 m a^{-1} . On the terrain edge, creep velocities increase to about 1 m a^{-1} , decrease slightly, and increase again to more than 2 m a^{-1} at about 2400 m ASL. Below that zone, surface speed decreases towards a flat, and partially even concave, surface depression. The front has reached the valley bottom, and in that process overridden a stream and a footpath. The maximum speeds and thus the main flux, seems to swing from the east in the upper steep part towards the west further down, before the flow diverges at the valley bottom. This S-shaped flow axis, as observed also in the outline of the creeping mass, might be caused by the high and steep north-eastern flank of the

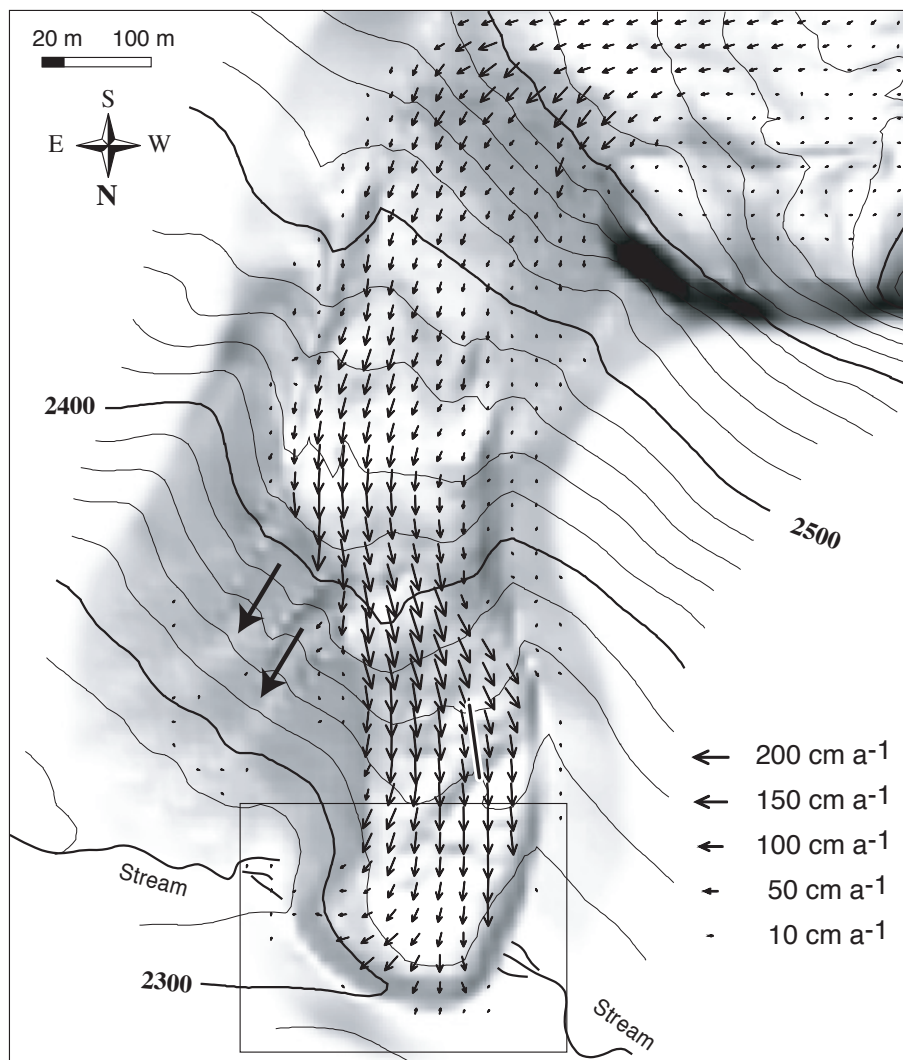


Fig. 9-2 Average horizontal surface velocities on the lower part of Suvretta rockglacier, Grisons, measured from aerial photography of 1992 and 1997. The inset at the terminus indicates the location of Figure 9-16. The line on the rockglacier between 2360 and 2340 m ASL approximates the position of the profile Figure 9-27. The two arrows east of the rockglacier indicate debris flow channels.

rockglacier, which is more exposed to direct incoming solar radiation than other parts, and less insulated due to the lack of coarse rocks on the surface. Both conditions could result in a low ice content (or even absence of ground ice) and a subsequent damming or decelerating effect due to higher viscosity or friction. Low ice content and low material coherence at the north-eastern flank is also indicated by two debris flows marked by arrows in Figure 9-2 (Kääb, 2000).

The mass flux over the terrain edge at 2600 m ASL towards the lower part seems rather low compared to the high velocities and thus anticipated high flux in the lower part. Thinning of the frozen debris by -0.5 m a^{-1} and more at an elevation zone of around 2400 m ASL is compensated to a large extent by corresponding thickening in the lowest part (Kääb, 2000). The average thickness change of the entire part of Suvretta rockglacier below 2600 m ASL amounts to only -0.04 m a^{-1} . This general pattern of change in surface elevation is strongly overlain by the influence of local surface topography (see Section 9.4), and erosion in and above the steep debris-flow breaches in the north-eastern flank. The observed coherent flow on and below the terrain edge at 2600 m ASL indicates supply of frozen debris. However, rockfall over

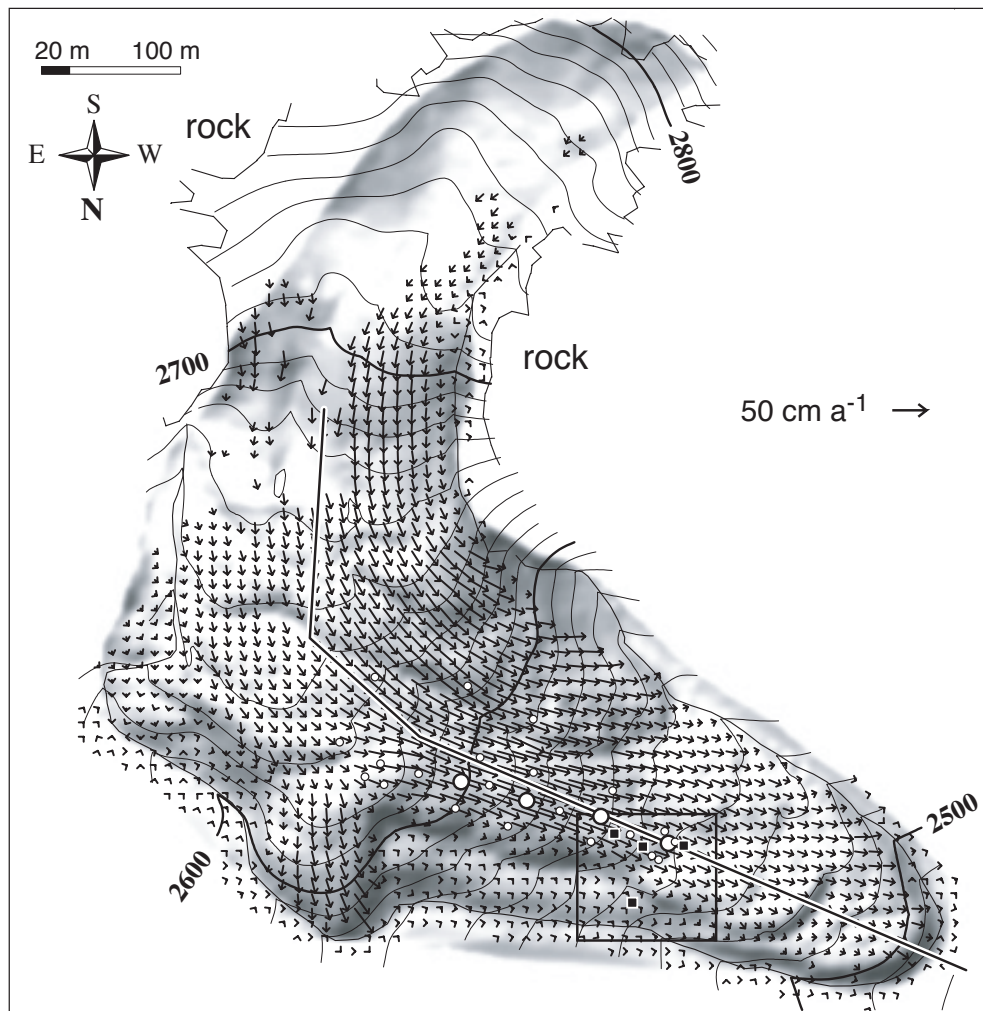


Fig. 9-3 Average horizontal surface velocities on Muragl rockglacier, Grisons, measured from aerial photography of 1981 and 1994. The rectangle to the lower right marks the section depicted in Figure 9-25, the small black rectangles boreholes. The four white large circles indicate selected surface markers for velocity measurements (order from left to right: 208, 206, 204, 202; see Fig. 9-20). The other markers investigated are indicated as smaller circles. For the longitudinal profile see Figure 9-24.

the edge and subsequent refreezing in the lower part might also be a significant process of mass supply.

Geophysical soundings on Suvretta rockglacier are presented by Vonder Mühll (1993). For more details on the behaviour of transverse ridges and the front of Suvretta rockglacier see Sections 9.2 and 9.4, respectively.

9.1.4 Muragl rockglacier

The horizontal surface velocity field (Fig. 9-3) and the thickness changes on Muragl rockglacier between 7 September 1981 and 23 August 1994 show a less uniform picture than Suvretta rockglacier (Kääb and Vollmer, 2000). Except for the zones of perennial ice patches in the upper part of the rockglacier, where surface lowering of up to -0.5 m a^{-1} indicates massive loss of ice, the measurements show elevation changes within the range of $\pm 0.1 \text{ m a}^{-1}$. The increase in thickness at the front of individual flow lobes suggests that elevation changes are influenced by mass advection (see Section 9.4). Over the investigated period, the frozen debris of Muragl rockglacier was creeping with average surface speeds of up to 0.5 m a^{-1} (Fig. 9-3). Maximum creep rates occur in the steeper middle part of the rockglacier. The flow

field reveals a complex system of several flow lobes, separated both laterally and vertically (see Frauenfelder and Kääb, 2000).

Surface strain rates on Muragl rockglacier range between 0.005 a^{-1} and -0.0075 a^{-1} . Largest horizontal extension can be found in places of horizontal flow divergence or longitudinally increasing flow speed. Horizontal compression can be found in places of decreasing flow speed. The partial correlation between the pattern of elevation changes and the distribution of vertical surface strain rates suggests that three-dimensional straining has a significant influence on the temporal development of the surface geometry in the case of Muragl rockglacier (Kääb et al., 2003c). However, in view of the low ice content found in Muragl rockglacier (Arenson et al., 2002), the incompressibility assumption involved in this consideration is certainly critical, and might only be valid qualitatively and over long time periods (see Eq. 2-4) (cf. Arenson et al., 2003).

The measured surface displacements (Fig. 9-3) depict a sharp lateral shearing between the highly active part of the rockglacier and the low or even inactive part to the north-eastern margin (see Frauenfelder and Kääb, 2000). In fact, during borehole drilling in this zone (borehole no. 1; Fig. 9-25), no ice was found, whereas at boreholes no. 2–4 a low ice-content of the matrix was detected (Arenson et al., 2002; Vonder Mühll et al., 2003). In combination with the general topography, the distinct speed gradients clearly indicate an active lobe overriding one or several inactive layers.

More detailed analyses of the Muragl rockglacier kinematics can be found in Kääb (1998a), Frauenfelder and Kääb (2000), Kääb and Vollmer (2000), Kääb (2002a) and Kääb et al. (2003c). A number of geophysical soundings and borehole studies have been conducted (Barsch, 1973; Vonder Mühll and Schmid, 1993; Arenson et al., 2002; Arenson et al., 2003; Vonder Mühll et al., 2003). Details of the flow field and transverse ridges are investigated in Sections 9.2 and 9.4 of this chapter, respectively.

9.1.5 Gufer rockglacier

The surface velocity field of Gufer rockglacier, Valais (Fig. 1-3), has been measured digitally on the basis of aerial photographs from 14 October 1994 and 8 September 2000 (Fig. 9-4). Observed surface speeds continuously increase from a few centimetres and decimetres per year in the upper part to up to 2.5 m a^{-1} in the steep frontal part. Longitudinal extension clearly dominates the surface velocity field. The rockglacier system consists of two or three individual parts with different velocity magnitudes but similar directions. The high surface speeds and strain rates above the north-western front lead to surface destruction for periods longer than several years, and to enhanced rockfall activity endangering a hiking path in front of the rockglacier. Thickness changes (not depicted) were derived from digitally-measured DTMs using the aerial imagery mentioned above. First analyses reveal no significant variations between 1994 and 2000 except for a small zone between 2440 and 2460 m ASL, north-east of the main stream where surface lowering in the order of -5 to -10 cm a^{-1} were found. The zone shows also a local minimum for horizontal speed.

Comparison of the horizontal rockglacier speeds shown here with those derived from aerial imagery of 1976 and 1995 (not presented here) suggest that Gufer rockglacier was about 20–25 % faster in the period 1994–2000 compared to 1976–1995. A preliminary comparison to data for 1950–1962 from Messerli and Zurbuchen (1968) shows speeds that are in part similar, and in part substantially faster for 1994–2000 (Kääb et al., 2005d).

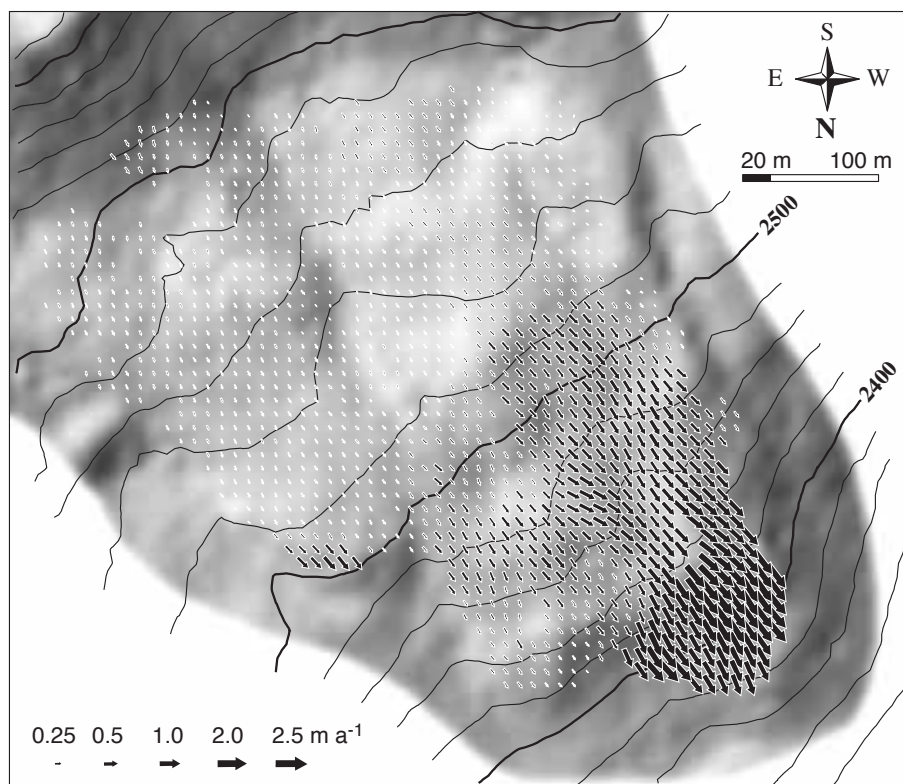


Fig. 9-4 Average horizontal surface velocities on Gufer rockglacier, Valais, measured on the basis of aerial photography from 1994 and 2000.

9.1.6 Murtèl rockglacier

Between 17 September 1987 and 11 September 1996 the surface of Murtèl rockglacier lowered by around -0.04 m a^{-1} on average, considerably more, however, on perennial ice banks in the upper and right part of the rockglacier (Kääb et al., 1998). During the investigated period the horizontal creep rates at the surface amounted to 0.15 m a^{-1} in the steep upper part and decreased to about 0.05 m a^{-1} in the flat lower part (Fig. 9-5). The velocity field points to the existence of two dynamically different parts of the creeping permafrost: high velocities and transverse surface buckling indicate high activity in the inner part; low velocities and lack of significant surface structures point to lower activity in the left and right marginal parts. Horizontal extension prevails in the upper part and horizontal compression in the lower part.

Murtèl rockglacier has been the object of various studies on internal structure, thermal regime, energy balance, rheology, age and evolution (e.g. Haeberli and Vonder Mühll, 1996; Wagner, 1996; Haeberli et al., 1998; Vonder Mühll et al., 1998; Haeberli et al., 1999b; Hoelzle et al., 2001; Arenson et al., 2002; Stocker-Mittaz et al., 2002; Vonder Mühll et al., 2003). The rockglacier kinematics have been discussed by Kääb (1998a), Kääb et al. (1998), Frauenfelder and Kääb (2000), Kääb et al. (2002a) and Kääb et al. (2003c). (See also Figure 7-2 and Section 9.4.2 of this volume).

9.1.7 Becs-de-Bosson rockglacier, Val de Réchy

Collaboration. The photogrammetric measurements on the Becs-de-Bosson rockglacier were performed in close collaboration with Jean-Philippe Dousse and Reynald Delaloye (University of Fribourg, Switzerland).

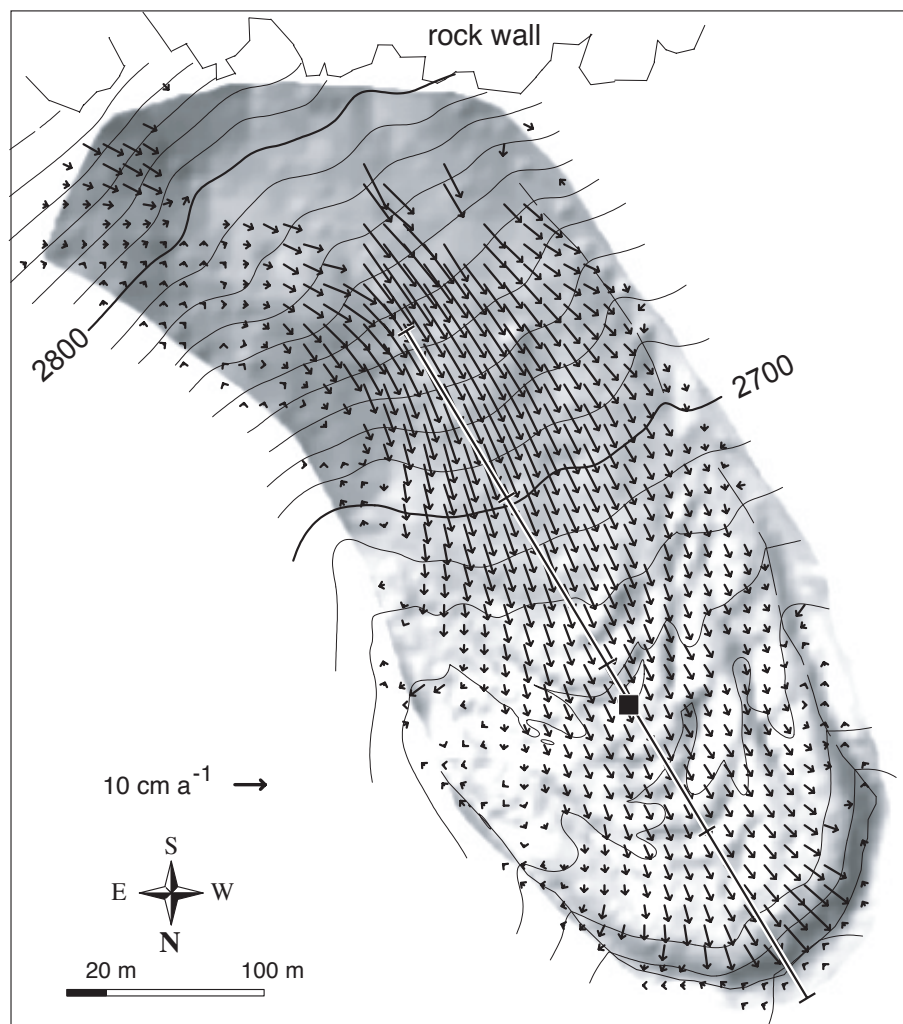


Fig. 9-5 Average horizontal surface velocities on Murtèl rockglacier, Grisons, measured using aerial photography from 1987 and 1996. The small black rectangle indicates the position of the 1987 borehole, the longitudinal line the position of the profile shown in Figure 9-23.

Horizontal surface velocity fields of the Becs-de-Bosson rockglacier in the Val de Réchy (Fig. 1-3) were measured from airphotos of 23 September 1986, 18 September 1991 and 13 September 1999. Figure 9-6 shows the surface velocity field 1986–1999 with maximum speeds of about 1.3 m a^{-1} . Between 1986–1991 and 1991–1999 a significant increase in surface speed could be observed (inset in Fig. 9-6) (Kääb et al., 2005d).

The Becs-de-Bosson rockglacier is subject to extensive investigations related to its dynamics, permafrost distribution, etc. (e.g. Lugon and Delaloye, 2001; Métrailler et al., 2003; Lambiel and Delaloye, 2004; Perruchoud and Delaloye, 2005).

9.1.8 Rockglacier speed and slope

The velocity fields presented above enable various findings on the dynamics of creeping mountain permafrost (Kääb et al., 2003c), including:

- the dependency of creep speed on ground temperature, ice content and surface slope (see this Section and Section 9.3) (Konrad et al., 1999; Kääb et al., 2002a; Frauenfelder et al., 2003a; Ikeda et al., 2003; Kääb et al., 2005d),

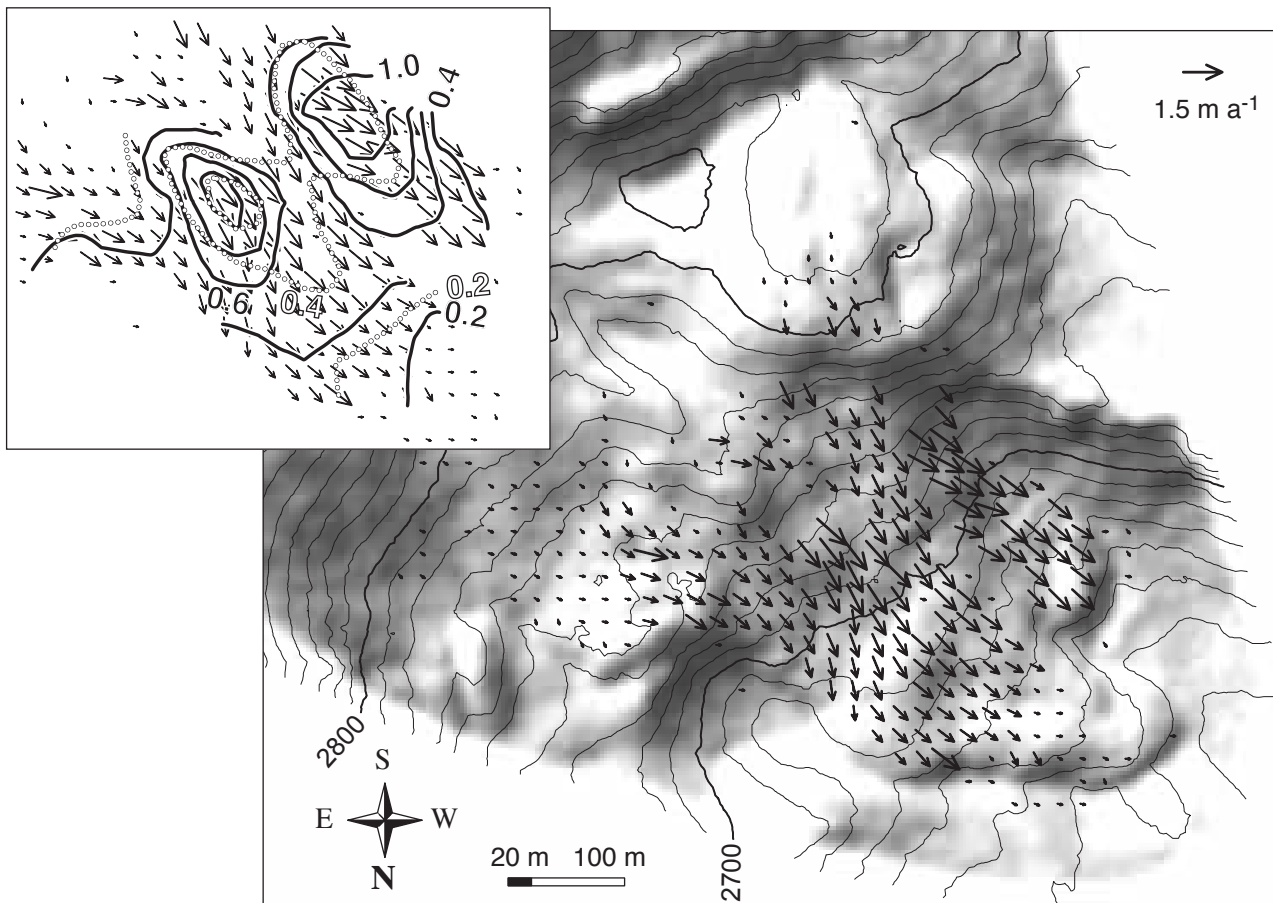


Fig. 9-6 Average horizontal surface velocities on Becs-de-Bosson rockglacier, Valais, measured using aerial photography from 1986, 1991 and 1999. The main panel shows the average velocities 1986–1999. The inset to the upper left shows a comparison between the average speeds over 1986–1991 (white, dotted isolines) and over 1991–1999 (black isolines; speed in m a^{-1} , 0.2 m a^{-1} interval).

- mass advection processes for entire rockglaciers or lobes as well as for individual features of surface topography (see Section 9.4) (Kääb et al., 1998; Kääb and Vollmer, 2000; Kääb et al., 2003c),
- three-dimensional straining and its effects on rockglacier development (Haeberli and Vonder Mühll, 1996; Kääb et al., 1997; Kääb et al., 1998; Kääb et al., 2003c),
- thaw settlement and frost heave (Kääb et al., 1997),
- surface shearing and its effect on surface topography (see Section 9.4) (Kääb et al., 1997),
- rockglacier speed variations with time (see Section 9.3) (Haeberli, 1985; Zick, 1996; Kääb et al., 1997; Frauenfelder and Kääb, 2000; Schneider and Schneider, 2001; Kääb et al., 2003c; Kaufmann and Ladstädter, 2003; Kääb et al., 2005d),
- discontinuities in the velocity field and the surface evolution such as sliding and ruptures (Kaufmann and Ladstädter, 2002; Kaufmann and Ladstädter, 2003; Roer et al., 2005b),
- differential thawing or frost heave processes such as thermokarst (Haeberli, 1985; Kääb et al., 1997; Kääb and Haeberli, 2001), and

- streamlines, age distribution and total age estimates (Kääb et al., 1997; Kääb et al., 1998; Haeberli et al., 1999b; Berthling, 2001; Kääb et al., 2002a; Frauenfelder et al., 2003b).

The potential correlation between surface slope and horizontal deformation is discussed here in more detail for the rockglaciers described above.

Any kind of flow law assumed for rockglacier creep implies that a slope-dependent component of gravity acts as the force which drives deformation. In addition, ice temperature, material density and composition, thickness of the deforming layers, lateral friction, internal structure and other material parameters certainly contribute to the overall surface deformation (Olyphant, 1983; Haeberli, 1985; Whalley and Martin, 1992; Whalley and Azizi, 1994; Azizi and Whalley, 1995; Azizi and Whalley, 1996; Irving, 2000; Arenson, 2002).

Figure 9-7 shows horizontal surface speeds of the above six rockglaciers as a function of the sine of surface slope. In these calculations, the surface slope is derived for an individual data point from the DTMs as the average value of a central grid cell and its eight neighbours. The DTM grid-spacings used are: Suvretta: 10 m; Gruben: 20 m, Gufer: 10 m, Muragl: 10 m, Murtèl: 10 m, Réchy: 20 m. No further longitudinal averaging of surface slope was applied to account for potential stress transfer. Such smoothing would affect the shown scatter plots mainly in a way as to shift individual outliers or less dense clusters horizontally, but not vertically. For all plots such a procedure would strengthen the correlation by reducing the scatter mainly for higher slopes and, therefore, likely increase the slope of a fitting curve.

All scatter plots shown here display a positive correlation between slope and surface speed, except for Suvretta rockglacier when its upper and lower parts are treated as one data set. However, the correlation values differ largely (Tab. 9-1). Linear fits have been performed for all rockglaciers and are based on the complete data sets (solid lines in Fig. 9-7). Power fits are based on the maximum values for each 0.01-slope class only (dashed and dotted lines in Fig. 9-7). Power fits have been calculated for Gufer, Muragl, Murtèl and Réchy rockglaciers.

The best linear correlation is obtained for Murtèl rockglacier, the lowest for Réchy and Muragl rockglacier. For Murtèl and Muragl rockglaciers, this fact is not surprising, considering the internal structure of the two rockglaciers. Murtèl rockglacier has high ice content with comparably low temperature; Muragl rockglacier has low ice content with temperatures close to 0 °C (Arenson et al., 2002). Hence Murtèl rockglacier might have a rheology comparable to pure ice, the deformation of which can be described by Glen's flow law. On the other hand, Muragl rockglacier might have a more complicated rheology involving the interaction of ice and solids and, perhaps crucially, the behaviour of ice close to and at its melting point. For such conditions an exponential-like decrease of ice viscosity and additional interactions between solids and ice are predicted (Paterson, 1994; Davies et al., 2001; Arenson, 2002; Frauenfelder et al., 2003b) (see Section 9.3). In this sense, Muragl rockglacier is certainly less expected to follow a simple flow law compared to Murtèl rockglacier. For Réchy rockglacier the correlation is certainly influenced by the lower spatial resolution applied compared to Muragl, Suvretta, Gufer and Murtèl.

Except for Gruben and Réchy rockglacier, there is a distinct but barely dense cluster of especially high speeds for steeper slopes (Fig. 9-7). This fact might point to a non-linear relationship between slope and deformation for larger slopes. However, a number of other interpretations have to be considered, too. These include sliding or gelifluction-like deformation of the surface layer overlying the deformation of the permafrost body above a certain slope threshold (cf. Ikeda et al., 2003), and the onset

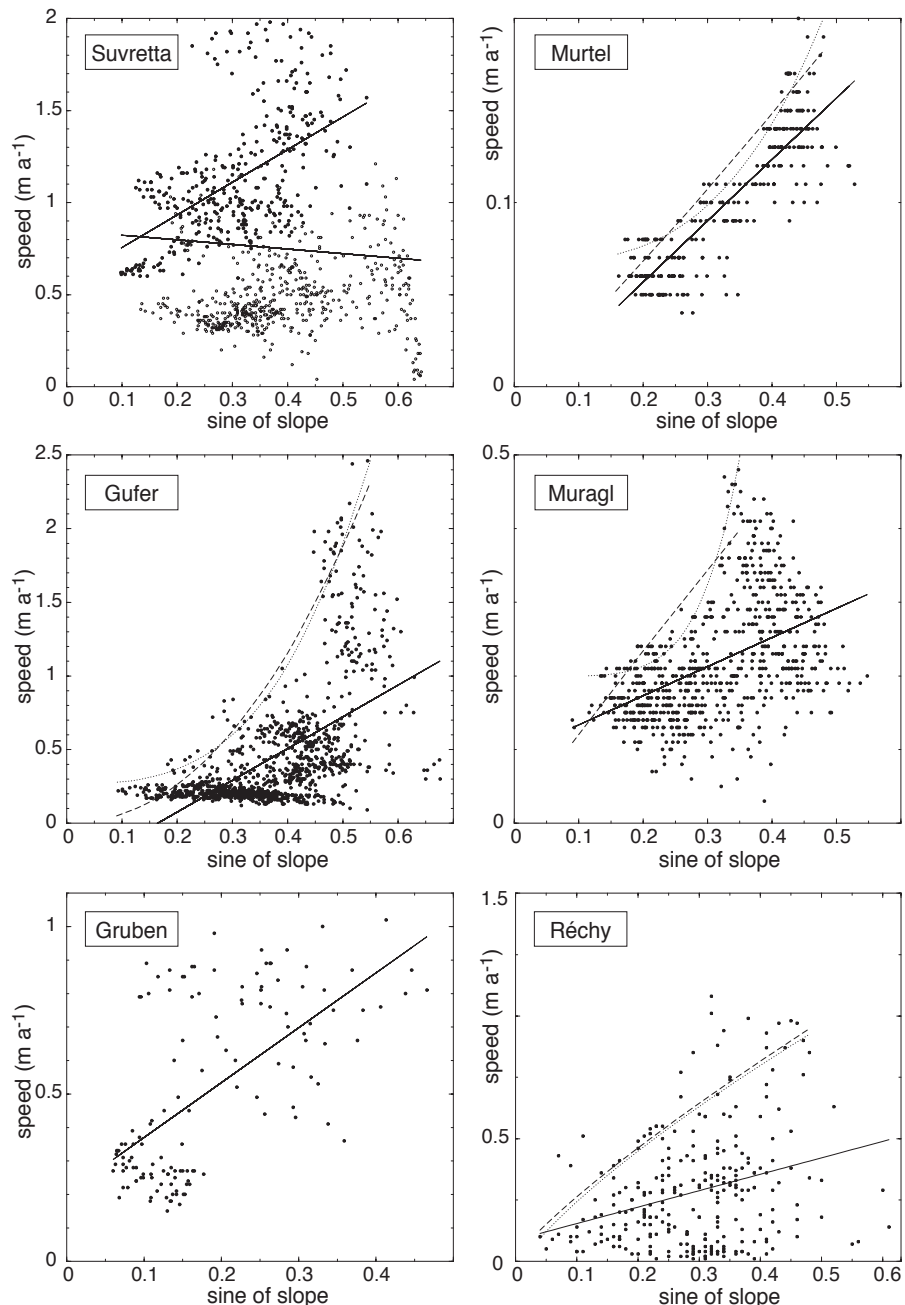


Fig. 9-7 Scatter plots of horizontal surface speed as a function of the sine of surface slope for Gruben, Suvretta, Muragl, Gufer, Murtèl and Becs-de-Bosson (Réchy) rockglaciers. The solid lines are linear fits for the entire data sets of the form $y=a \cdot x + c$. The dashed lines are power fits of the form $y=a \cdot x^b$, the dotted lines are power fits of the form $y=a \cdot x^b + c$. The power fits for Gufer, Muragl, Murtèl and Réchy rockglaciers are based on maximum speed values only. See text for discussion.

or increase of internal shearing processes. As high-resolution measurements confirm, this acceleration for high slopes is in most cases not the result of individually displacing surface boulders but rather of both spatially and temporally coherent processes (Section 9.4).

The vertical scatter in the panels of Figure 9-7 is an expression of different flow conditions for each individual data point due to spatial variations of ice content and ice properties, depth of the deforming layer, lateral and longitudinal effects, etc. Such conditions hinder an individual part of the rockglacier from reaching its hypothetical maximum speed. In a next step, therefore, a data subset consisting of the maximum

Table 9-1 Linear and power fits of horizontal surface velocities as a function of surface slope and computed from the data shown in Figure 9-7.

Rock glacier	coefficient a	exponent b	constant c	correlation R
linear fit (entire set): $v_{hz}^s = a \cdot \sin \alpha + c$				
Suvretta, both parts	-0.2	-	0.8	-0.07
Suvretta, lower part	1.8	-	0.6	0.51
Gufer	2.2	-	-0.3	0.57
Gruben	1.6	-	0.2	0.61
Murtèl	0.3	-	-0.0	0.86
Muragl	0.4	-	0.1	0.47
Réchy	0.7	-	0.1	0.29
power fit (maximum values): $v_{hz}^s = a \cdot (\sin \alpha)^b + c$				
Gufer	15	3.2	0.3	0.95
Murtèl	1.3	3.1	0.07	0.95
Muragl	125	5.8	0.2	0.94
Réchy	1.7	0.8	-0.04	0.82
power fit (maximum values): $v_{hz}^s = a \cdot (\sin \alpha)^b$				
Gufer	8.5	2.2	-	0.93
Murtèl	0.4	1.1	-	0.92
Muragl	1.1	1.0	-	0.86
Réchy	1.7	0.8	-	0.82
power fit (maximum values): $v_{hz}^s = a \cdot (\sin \alpha)^3$				
Gufer	15.6	-	-	-
Murtèl	2.2	-	-	-
Muragl	12.8	-	-	-
Réchy	12.0	-	-	-

speeds for each 0.01 (0.6°) slope class is analyzed. Power fits with and without a constant were applied (Tab. 9-1 and Fig. 9-7). The power fits without a constant approximate a power law like Glen's flow law for ice. Such analyses were not performed for Suvretta and Gruben rockglaciers since they clearly consist of dynamically very different parts. The power fits suggest a flow-law exponent between about 1 and 3. Coefficient a , which summarizes many different material properties such as thickness, ice content or ice properties, shows broad variations between the fits. It should be noted, however, that the coefficient a has a large RMS especially in the power fits including a constant c .

The power fit $v_{hz}^s = a \cdot (\sin \alpha)^b$ can be compared to the horizontal surface speed of a infinite slab deforming in accordance to Glen's flow law for ice:

$$v_{hz}^s = \frac{2A}{n+1} (\rho \cdot g)^n \cdot h^{n+1} \cdot (\sin \alpha)^n , \quad (9-1)$$

with the rate factor A , the flow law exponent n , density ρ , acceleration due to gravity g , and slab thickness h . Thus, for given ρ and h the rate factor A can be estimated from the coefficient a and the exponent b obtained from the power fit. In order to compare this with rate factors usually applied for glaciers, $n=3$ is set (see Tab. 9-1). In the end, approximate rate factors of $2.5 \cdot 10^{-16} \text{ s}^{-1}(\text{kPa})^{-3}$ for Murtèl rockglacier ($h=30 \text{ m}$) and of $2.3 \cdot 10^{-14} \text{ s}^{-1}(\text{kPa})^{-3}$ for Muragl rockglacier ($h=15 \text{ m}$) are obtained. (For depth h see Arenson et al., 2002).

For Gufer rockglacier no depth is known. For $h=15 \text{ m}$ A would be approximately $2.7 \cdot 10^{-14} \text{ s}^{-1}(\text{kPa})^{-3}$; for $h=30 \text{ m}$ A would be approximately $1.7 \cdot 10^{-15} \text{ s}^{-1}(\text{kPa})^{-3}$. Similarly, for Réchy rockglacier no depth is known. For $h=15 \text{ m}$ A would be approximately $2.2 \cdot 10^{-14} \text{ s}^{-1}(\text{kPa})^{-3}$; for $h=30 \text{ m}$ A would be approximately $1.3 \cdot 10^{-15} \text{ s}^{-1}(\text{kPa})^{-3}$. Typical A -values for glacier ice with $n=3$ are $6.8 \cdot 10^{-15} \text{ s}^{-1}(\text{kPa})^{-3}$ for temperate ice, $3.1 \cdot 10^{-15} \text{ s}^{-1}(\text{kPa})^{-3}$ for an ice temperature of -1°C , and $2.4 \cdot 10^{-15} \text{ s}^{-1}(\text{kPa})^{-3}$ for an ice temperature of -2°C (Paterson, 1994).

From inversion of borehole deformation data and iterative adjustment of a corresponding 2D-finite-element model, Wagner (1996) computed different values of A and n for Murtèl rockglacier. While considering the entire deforming column, he found a best fit for $n=2.9$ and $A = 1.5 \cdot 10^{-23} \text{ s}^{-1}(\text{Pa})^{-2.9} = 7.5 \cdot 10^{-15} \text{ s}^{-1}(\text{kPa})^{-2.9}$ for an ice temperature of -1°C . To compare with these results, the above fit for our surface deformation data was performed also for $n=2.9$ (i.e. $v_{hz}^s = a \cdot (\sin \alpha)^{2.9}$), obtaining an $A = 3.9 \cdot 10^{-16} \text{ s}^{-1}(\text{kPa})^{-2.9}$. For a fit of the form $v_{hz}^s = a \cdot (\sin \alpha)^{2.9} + c$ the rate factor A becomes $2.1 \cdot 10^{-16} \text{ s}^{-1}(\text{kPa})^{-2.9}$.

9.1.9 Discussion and conclusions

The speed of the rockglaciers investigated shows a clear dependence on surface slope. The large scatter is, among other factors, the result of the transverse speed profile with highest magnitudes in the centre, even for identical slopes. Since rockglaciers are – in contrast to glaciers – a landform that is usually superimposed on the terrain rather than embedded within valley flanks, the marginal decrease of speed might be due to decreasing ice content, thickness and/or material supply rather than due to marginal friction. Secondly, the large scatter in the plots in Figure 9-7 might be reduced by accounting for longitudinal stress transfer, which smooths the effective surface slope. However, in view of the largely unknown rheology of creeping permafrost the parameterization of such stress-transfer function appears uncertain. The results presented here may serve for such investigations, in particular when inferred into numerical 2D- or 3D-models. Finally, the large scatter in the plots is simply an expression of the large variations of thickness of the deforming layer(s), material properties and/or – perhaps – temperature (Kääb et al., 2005d).

Our estimation of rate factors A from scatter plots of surface speed as a function of slope gives reasonable results when considering the large natural variability of A between different glaciers, and even within one glacier (Paterson, 1994). For Murtèl rockglacier the difference between our rough estimates using an infinite slab and the finite-element model by Wagner (1996) can be explained by the fact that the finite-element model considers the compression effect at the borehole, which is situated in a zone of overall slope decrease, whereas in our calculations such effect falsely alters A (see Figure 9-23).

An increase in vertical scatter (i.e. scatter in speed) above a certain slope can be observed for most of the rockglaciers. Rockglacier surface speed depends, among other factors, on the thickness and on the rate factor of the deforming layer in addition to the surface slope examined here. The scatter observed could thus also

reflect spatial variations of mass thickness. In fact, from Equation 9-1 it can be seen that surface speed is more sensitive to thickness variations when the slopes are large. Furthermore, the increase in speed scatter observed for large slopes seems to be more pronounced for the “warmer” of the investigated rockglaciers, or those situated at lower elevation. In Equation 9-1 surface speed is more sensitive to thickness variations with increasing rate factor A . Larger rate factors are assumed for warm permafrost (see Section 9.3). For colder rockglaciers a simplified glacier-like flow law could apply better than for warmer creeping permafrost as suggested by the correlations presented (Kääb et al., 2005d).

Surface velocity fields of rockglaciers derived from repeat aerial imagery provide a wealth of insights into the dynamics and evolution of creeping mountain permafrost as shown extensively in the corresponding literature. Digital photogrammetric methods in particular permit a density of measurement points as high as a few image pixels. Apart from the statistical abundance provided, such dense data improve the spatial representativity of measurements and reveal a quasi-continuous velocity field.

9.2 Rockglacier advance mechanisms: Suvretta and Gruben rockglaciers, Switzerland

Collaboration

Thekla Reichmuth, student at the Department of Geography, University of Zurich, computed the vector algebra of the measurement rods in the rockglacier front. (See Kääb and Reichmuth, 2005).

9.2.1 Introduction

The advance mechanisms of rockglaciers are some of their most important characteristics. In sharp contrast to glaciers, active rockglaciers have to grow continuously in length due to their thermal condition, which limits ice melt, and due to their solids content, which is usually not being removed from the frontal zone. An exception to the latter can be found only for rockglaciers that terminate above steep terrain leading to a zero-balance between material supply from creep and material loss from erosion.

Theoretical concepts of rockglacier advance have been developed by Wahrhaftig and Cox (1959) and Haeberli (1985), who describe different front characteristics as a function of permafrost creep behaviour. In their descriptions, they consider different vertical profiles of the horizontal velocities, ranging from pure sliding conditions, to a parabolic velocity profile, to restriction of movement to a surface layer only (Fig. 9-8). From considerations about mass conservation and from velocity profiles found during borehole experiments, Haeberli et al. (1998) derive a conceptual model of rockglacier advance: material of the upper layers overrides the lower layers, is subsequently deposited in front of the rockglacier, and is finally overridden again by new material from upper layers (“conveyor belt”, or “caterpillar” effect; Fig. 9-9)

The effective mean advance rate \dot{a} of a rockglacier (see Tab. 9-2) of thickness h is a function of several factors: (1) the vertical variation of horizontal velocity $v_x(z,t)$. (2) The volume is altered by melting and refreezing of ice/water within the advancing material, $b_{ice}(z,t)$, where b_{ice} refers only to the ice volume which exceeds the pore volume (excess ice). (3) The air content $b_{air}(z,t)$ of the rockglacier material at the front might change: a certain fraction of the excess ice volume melting out at the

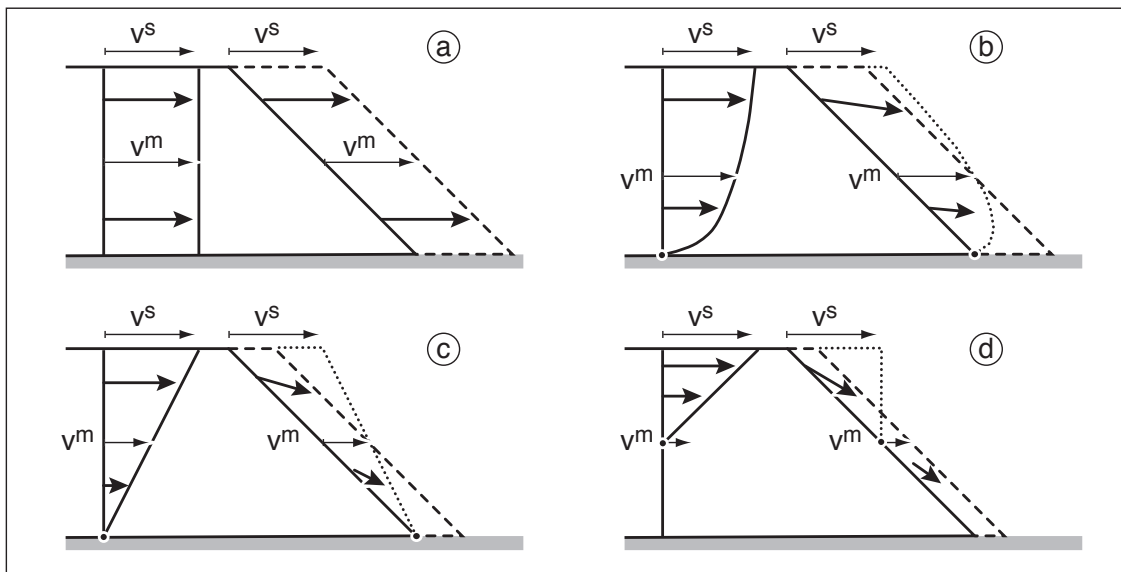


Fig. 9-8 Schemes of rockglacier advance mechanisms as a function of the velocity variation with depth (modified after Wahrhaftig and Cox, 1959). The initial vertical velocity profile within the rockglacier is displayed to the left of each individual panel. The dotted line indicates the hypothetical form of the front after the advected mass is horizontally added to the declined front. The dashed line indicates the form of the front after the advected mass has been distributed evenly over the entire front. The degree of the latter mass redistribution influences the particle vectors (bold arrows) within the front. The thin arrows indicate the surface velocity (v^s) and the mean velocity (v^m) of the deforming column. Icemelt is neglected in the schemes.

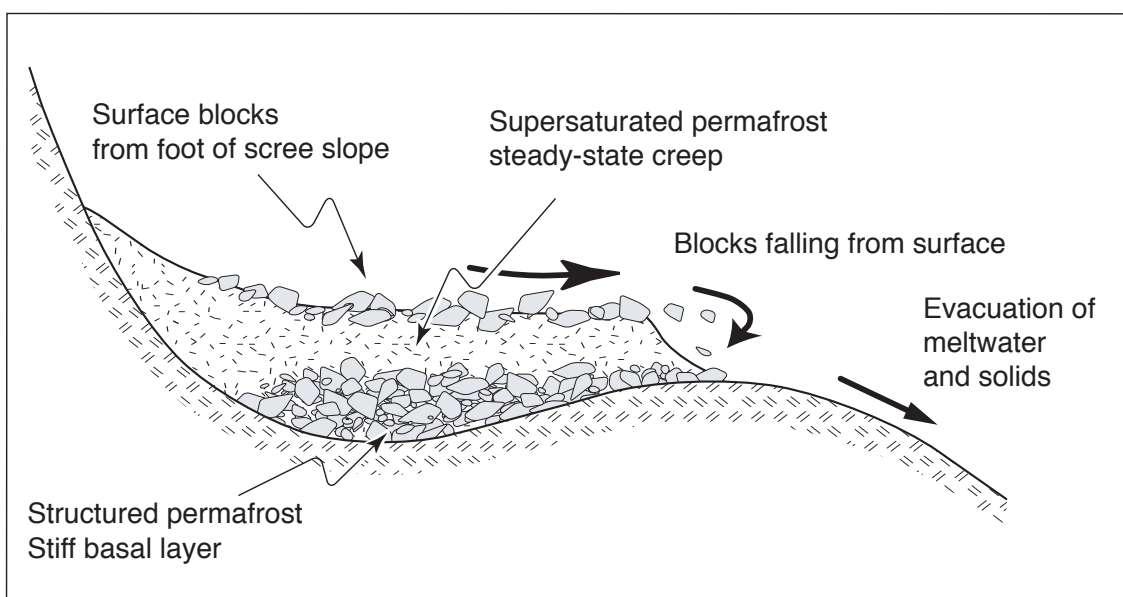


Fig. 9-9 Model of rockglacier advance and structure (after Haeberli et al., 1998).

front, for instance, might be replaced by air, if the material becomes not fully ice-saturated after being incorporated again at the rockglacier base. On the other hand, the air content of unfrozen material (e.g. the active layer) might be filled partially by refreezing water at the base. (4) Erosion and removal of solid material $b_{erosion}(z,t)$ might usually be limited and restricted to fine fractions of the material; accumulation of solids from outside the front system might be only found in rare cases.

$$\dot{a} = \frac{l}{h} \cdot \left(\int_0^h v_x dz + \int_0^h b_{ice} dz + \int_0^h b_{air} dz + \int_0^h b_{erosion} dz \right). \quad (9-2)$$

The few quantitative field investigations on the advance of rockglaciers conducted so far focus mainly on the remote sensing of advance rates (Kääb et al., 1997; Kääb, 1998a; Bauer et al., 2003). In other studies the movement of blocks above the rockglacier front was surveyed (Haeberli, 1985; Koning and Smith, 1999; Lambiel and Delaloye, 2004). These studies revealed a range of ratios between surface speed above the front and mean advance rate. This finding indicates a significant variation of the above processes among different rockglaciers (see Tab. 9-2). Here, it is tried to quantify three-dimensional kinematics in rockglacier fronts using a novel measurement approach.

9.2.2 Method

Even over short time intervals, massive destruction processes such as erosion and rockfall severely complicate the measurement of the dynamics of rockglacier fronts. For this reason, remote sensing has been applied until now to monitor rockglacier fronts. In general, remote sensing is able to detect the effective advance of a front (i.e. the change in its surface geometry), but not the kinematics of the advancing material. Only very-high-resolution data permit the tracking of selected prominent rocks (Bauer et al., 2003). For this, 1–2 m long steel rods were placed at the front of Gruben and Suvretta rockglaciers, Swiss Alps, and their behaviour was monitored over a period of several years until the rods were destroyed. The aim of this approach was to track the position of the rod head B and the head A of a removable extension by polar survey (Fig. 9-10). For that purpose an automatic total station TCA1102 by Leica Geosystems was used (Kääb and Reichmuth, 2005). Terrain surface C and the end of the rod D can then be computed:

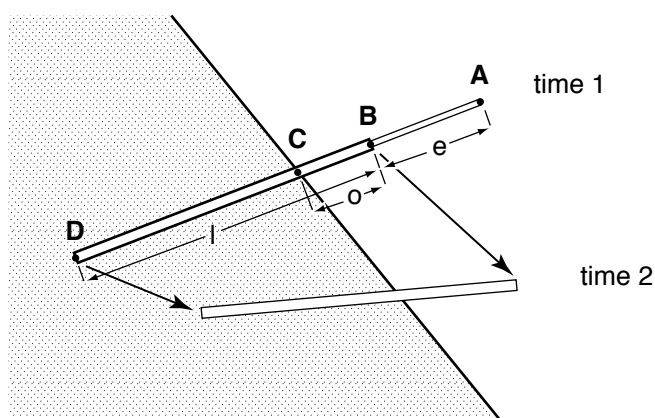


Fig. 9-10 Measurement principle for determining three-dimensional displacements in a rockglacier front from surveying of steel rods. e is an extension fixed only during survey campaigns. The positions of points A and B can be measured, the positions of points C and D can be calculated.

$$\mathbf{C}(t) = \mathbf{B}(t) + \frac{\mathbf{B}(t) - \mathbf{A}(t)}{e} \cdot o(t) \text{ and } \mathbf{D}(t) = \mathbf{B}(t) + \frac{\mathbf{B}(t) - \mathbf{A}(t)}{e} \cdot l \quad (9-3)$$

where the Cartesian coordinates of points A and B are directly measured, the extension e and the rod length l are known, and the offset o from the rod head to the front surface is measured. By this approach, the impact of local erosion and rockfall on the measurement rods was minimized and the three-dimensional behaviour of the front material could be observed to a depth of 1–2 m. The procedure relies on the rods remaining straight, which was not the case for all rods.

9.2.3 Gruben rockglacier front

Figures 9-11 and 9-12 show the measurement setting in the Gruben rockglacier front. At points no. 1–6, rods as described above were installed; at points no. 7–9, small metal bolts were drilled into big rocks and only their velocity but not their rotation was monitored (cf. Lambiel and Delaloye, 2004). Figure 9-13 depicts the position of the rods over time. The main results for the individual rods are:

- No. 6: strong surface-parallel displacement and horizontal emergence; advance of front; downward tilting; rod destroyed after third measurement.
- No. 5: mainly surface-parallel displacement; little front advance; downward tilt; some emergence; rod presumably bent after second measurement.
- No. 4: only slight surface-parallel displacement; horizontal front advance; downward tilting, some submergence.

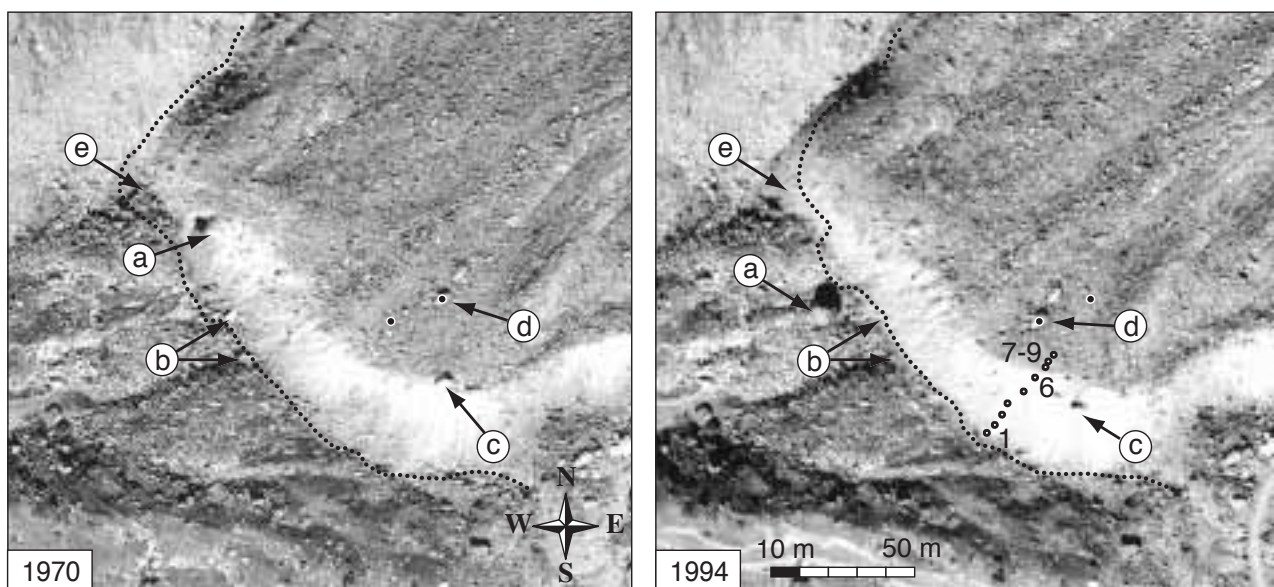


Fig. 9-11 Orthoimages of Gruben rockglacier front in 1970 and 1994. The lines mark the front position at the other of both respective times: (a) a big block, only partially visible in the front in 1970, was emerging from the front and falling down; (b) blocks in front of the rockglacier were overridden; (c) a block was advected over the upper edge of the front and sliding downwards; (d) displacement of a block on the rockglacier surface and (e) clear advance of the front. Numbers indicate the position of measurement rods (see Fig. 9-12). Orthoimage based on photography by swisstopo/flight service (permission BA057212).

- No. 3: surface-parallel displacement; downward tilting; some submergence; rod destroyed after second measurement and possibly already damaged after first period.
- No. 2 and 1: little to no displacement, tilting; significant advance of the front combined with strong submergence of the rods; rod no. 2 was lost after the third measurement.

At the last measurement date, most rods were damaged or covered by debris, or such processes were to be expected soon.

The horizontal velocity components of the rods and bolts (Fig. 9-14) reveal a slow, nearly block-wise movement for the lower 15 m of the front. For the uppermost 5 m a sharp increase in velocity magnitude close to the surface speed can be observed. The horizontal speeds at bolts 7–9 are similar or slightly higher as compared to the speed obtained from multitemporal photogrammetry (see Section 9.1.2). The average advance rate of approximately 0.12 m a^{-1} obtained from the rod measurements is identical to the one obtained from photogrammetry between 1970–1995 (Fig. 9-15) (see also Kääb et al., 1997).

Over a 7-day period in August 1982, Haeberli (1985) measured the movement of three blocks on the rockglacier front with a thin wire. He found horizontal speeds in the order of 1.5 m a^{-1} on top of the front, 0.7 m a^{-1} in the middle, and no significant movement on the base. The order of magnitude of Haeberli's measurements and the results presented here seem to coincide. More detailed comparison is not possible because the observations cover very different segments of a year, and the short-term measurements imply a very different signal-to-noise ratio.

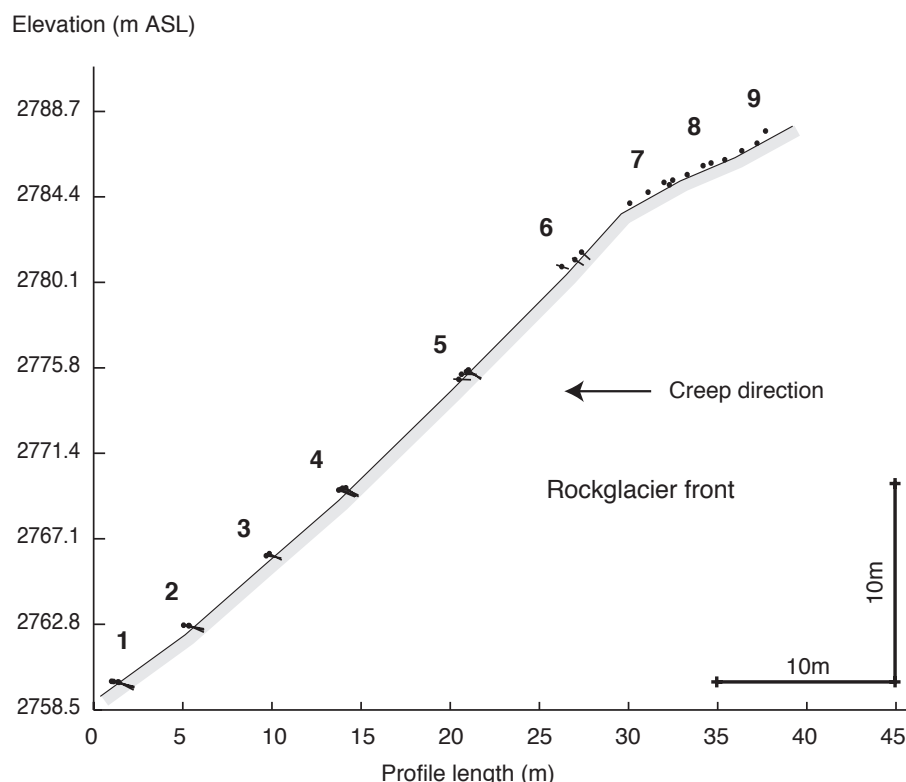


Fig. 9-12 Cross-section of the front of Gruben rockglacier with steel rods for deformation measurement.

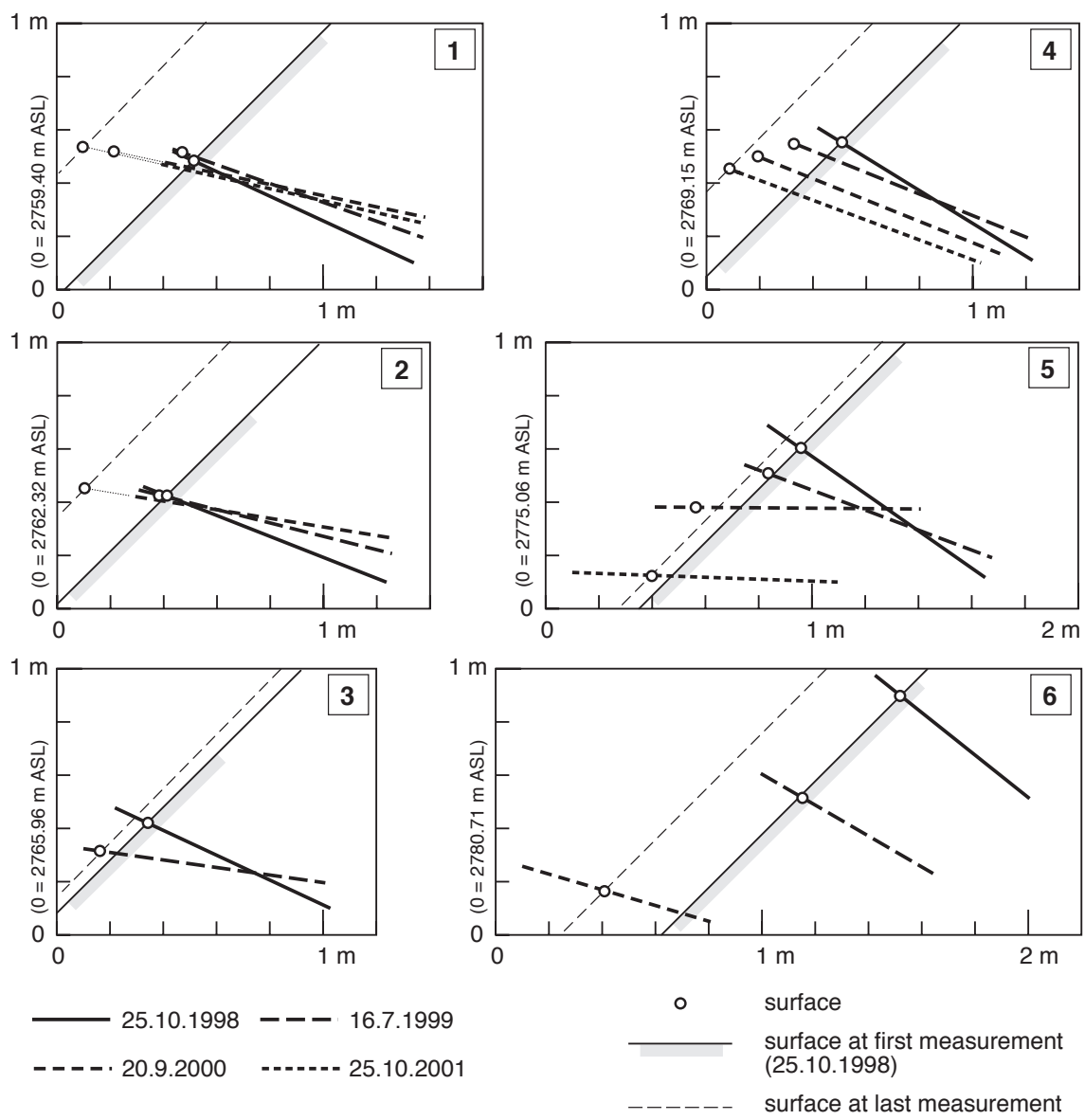


Fig. 9-13 Gruben rockglacier front: detailed displacement of the individual rods in Figure 9-12. Rods nos. 1 and 2 were buried by debris during the observation period.

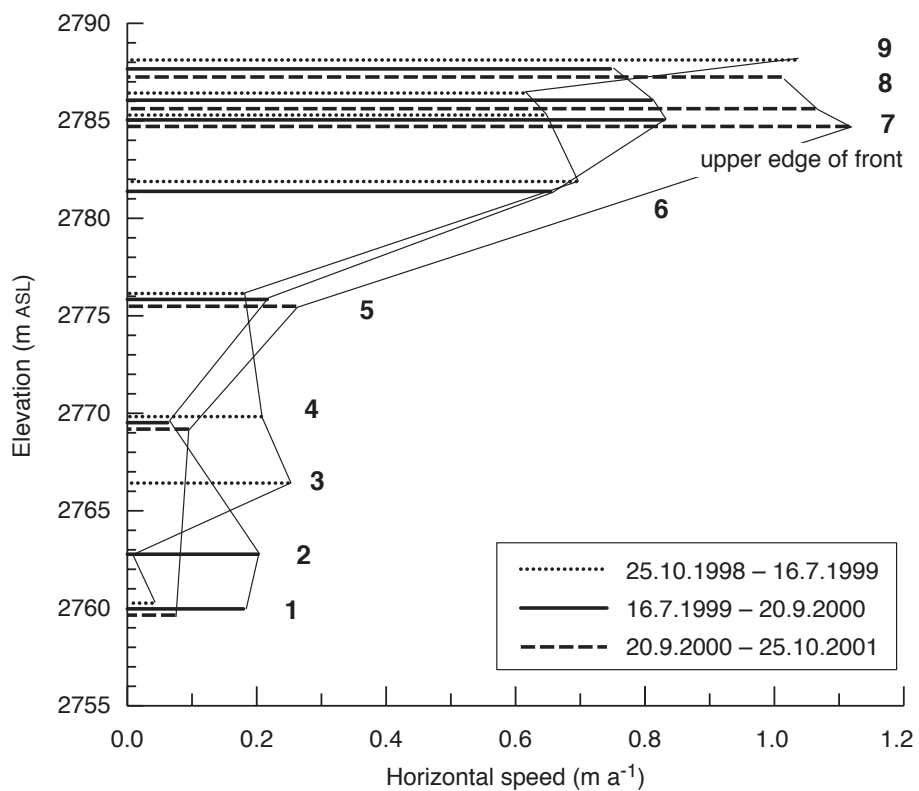


Fig. 9-14 Vertical profile of the horizontal component of rod displacements over the front of Gruben rockglacier (see Figs. 9-13 and 9-12).

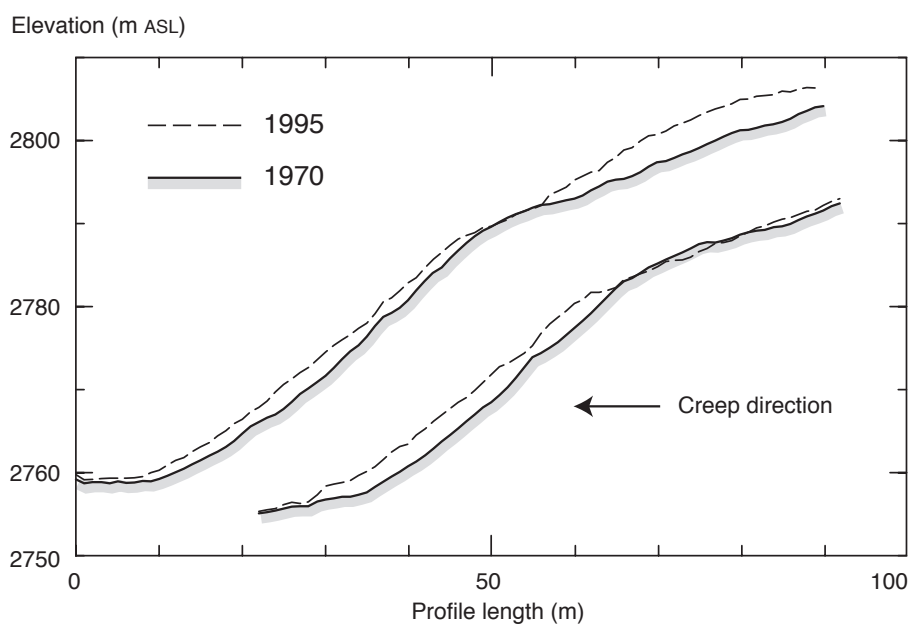


Fig. 9-15 The front of Gruben rockglacier between 1970 and 1995 at two photogrammetric profiles. The position of the two profiles is a few metres to the left or right of the rod profile of Figure 9-11, respectively (see Kääb et al., 1997).

9.2.4 Suvretta rockglacier front

At points no. 1–4 on the Suvretta rockglacier front rods were installed, and at points no. 5–7 bolts were affixed to large rocks (Figs. 9-16 and 9-17). A significantly different behaviour is observed for Suvretta rockglacier, compared to that of the

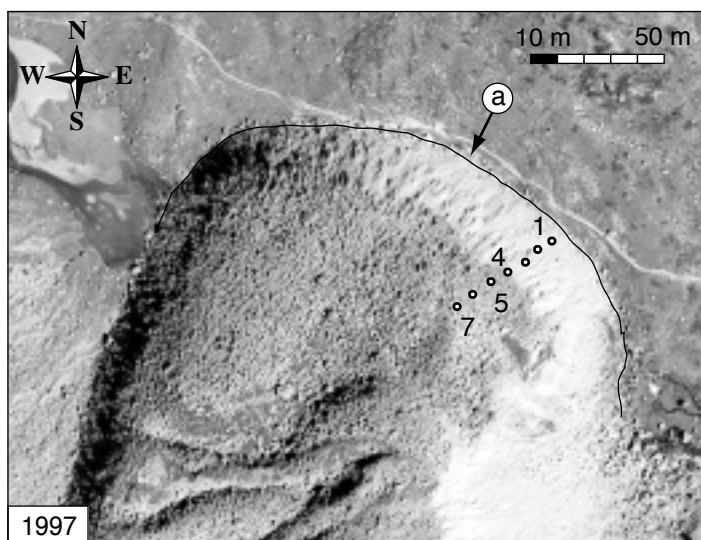


Fig. 9-16 The front of Suvretta rockglacier. The front position of 1992 (line) is overlain on the 1997 orthoimage. At point (a), the advance of the front is large enough to be visible on the image. Numbers and circles indicate the position of measurement rods and bolts (Fig. 9-17). The location of the depicted orthoimage section is shown in Figure 9-2. Orthoimage based on photography by swisstopo/flight service (permission BA057212).

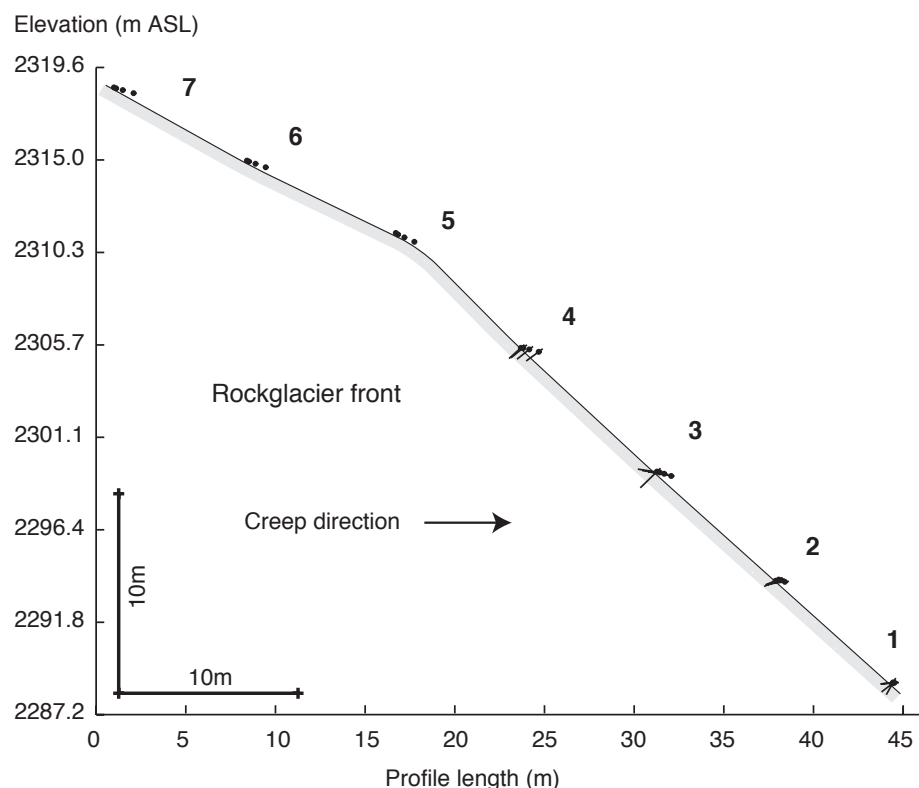


Fig. 9-17 Cross-section of the front of Suvretta rockglacier with steel rods for deformation measurements.

Gruben rockglacier front. The main results for the rod behaviour over time are (Fig. 9-18):

- No. 4: strong horizontal displacement; only slight downward component; little to no tilt; no significant emergence or submergence.
- No. 3: strong horizontal displacement; only slight downward component; no significant tilt; no significant emergence or submergence; after the first measurement the rod was obviously hit by rockfall and bent.
- No. 2: almost exclusively horizontal displacement; minimal submergence; slight tilting and an upward component presumably caused by rockfall impact and displacement of large, individual boulders around the rod.
- No. 1: slight horizontal displacement; strong rotation and bending caused by rockfall impact and individually displacing large boulders around the rod.

At the last measurement date, most rods were damaged or covered by debris, or such processes were to be expected soon.

The horizontal velocity components of the rods and bolts (Fig. 9-19) reveal a linear to slightly parabolic increase towards the upper edge of the front. Surface velocities above the front are slightly higher than for the uppermost rod. The horizontal speeds at bolts 5–7 are almost identical to the speed obtained from multitemporal photogrammetry (0.5 m a^{-1} ; see Section 9.1.3). The average advance rate from the rod measurements of approximately 0.16 m a^{-1} is identical within the significance level to the 1992–1997 advance rate of 0.18 m a^{-1} from photogrammetry.

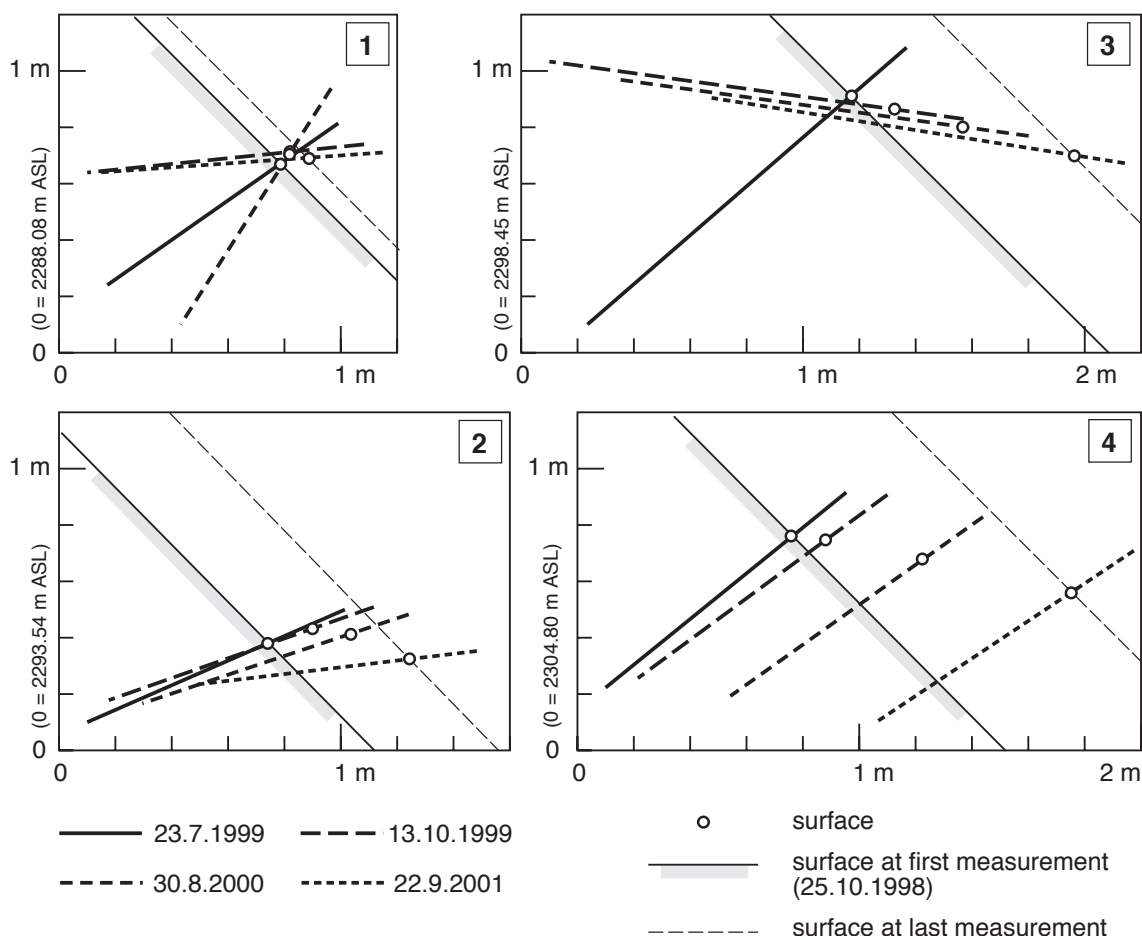


Fig. 9-18 Suvretta rockglacier front: detailed displacement of the individual rods in Figure 9-17.

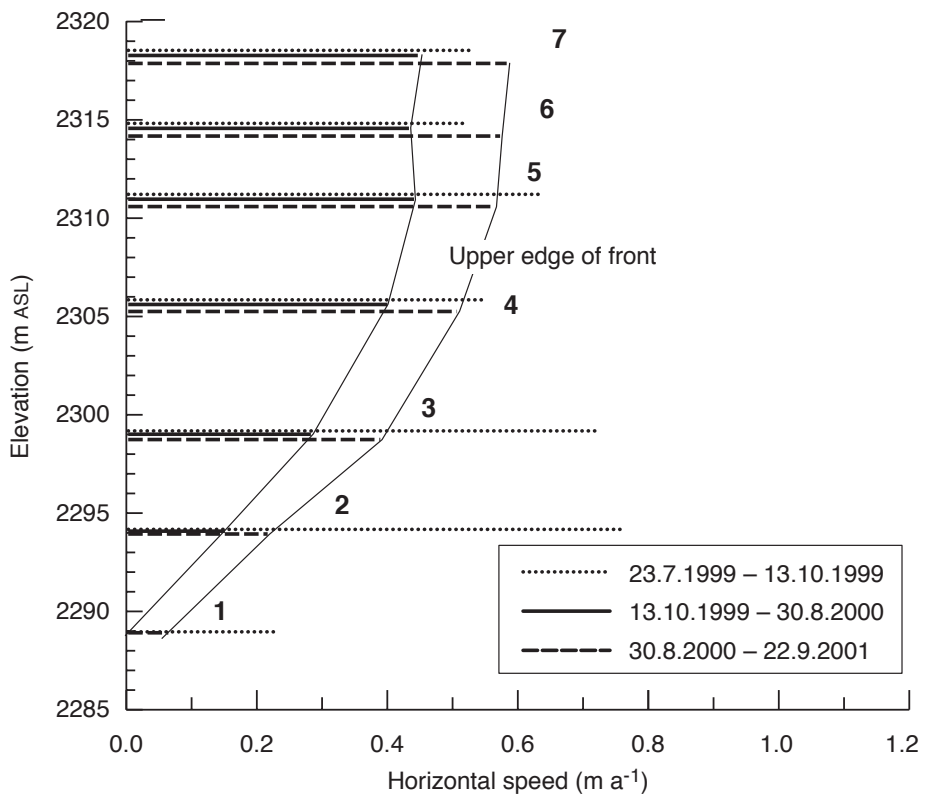


Fig. 9-19 Vertical profile of the horizontal component of rod displacement (see Fig. 9-18) over the front of Suvretta rockglacier (see Fig. 9-17).

9.2.5 Conclusions

The findings of this study rely in parts on the measurement rods remaining straight over the observational period. In some cases, bending was obvious since it took, for instance, place at the airside, or the rod was clearly damaged by rockfall. For the remaining rods possible bending was tested at the observational dates through inserting a smaller rod into the tube-like measurement rods. Finally, a strong discontinuity in the rod deformation over time was treated as sign for rod bending (e.g. Suvretta, rod no. 5).

Gruben and Suvretta rockglacier fronts show significant dynamic differences. The horizontal deformation for Gruben rockglacier front seems to be largely restricted to a 5–10 m thick top layer (layer 1) with at least 0.6 m a^{-1} average horizontal speed. Below this layer a block-wise horizontal speed of about 0.2 m a^{-1} was found (layer 2). These estimates are minimum estimates because thaw settlement originating from greater depths than the rod base reduces the horizontal movement of the rod. With the available measurements alone it is not possible to safely attribute the movement at the base of layer 2 to some kind of sliding of the frozen column. However, the assumption of a sort of shear zone at the base of deforming layers, as found for other rockglaciers (Arenson et al., 2002), might be reasonable for both layers 1 and 2.

From seasonal velocity variations on Gruben rockglacier, Haeberli (1985) estimated that approximately 30 % of the horizontal surface movement could be due to sliding or sediment deformation at the permafrost base. In a 7 m deep borehole on Gruben rockglacier Barsch et al. (1979) found a blocky active layer of about 2 m depth (see Haeberli, 1985), and layers of frozen gravel, frozen sand and ice from 2 to 7 m depth.

These findings neither contradict nor confirm a potential shear horizon of sandy ice within the upper 7 m (cf. Arenson et al., 2002).

The significant downward component of front material and the observed tilt of the rods complete the picture of a surface layer creeping and eroding over the upper front edge. In sum, Gruben rockglacier front seems to act as a combination of cases (a) and (d) in Figure 9-8.

The average horizontal velocity over the 25 m column of Gruben rockglacier front amounts to approximately 0.35 m a^{-1} . In contrast, the average advance rate was determined at 0.12 m a^{-1} (Tab. 9-2). Two-thirds of the frozen mass have, therefore, to be removed by thermal or mechanical erosion (Eq. 9-2). Since the Gruben rockglacier front lies in a vegetated plain or even depression (Fig. 9-15) with no sign of substantial material transport, erosion of solids can be excluded for the most part. Thus, the measurements revealed a thaw settlement, indicating an average excess ice content of two-thirds for the frontal part of Gruben rockglacier.

Both the velocity profile and the rod tilt measured for Suvretta rockglacier front gave a linear to parabolic deformation profile with little downward displacement over the front. Speed tends towards zero towards the rockglacier base. In contrast to Gruben and other rockglaciers (Arenson et al., 2002), deformation in the frontal part of Suvretta rockglacier seems to be distributed over the entire column but not concentrated in thin shear zones. The average horizontal velocity over the 20 m thick front is approximately 0.3 m a^{-1} , contrasting with the average advance rate of 0.16 m a^{-1} . In sum, Suvretta rockglacier front seems to advance like mechanisms (b) or (c) in Figure 9-8. The overall excess ice content in the frontal part of Suvretta rockglacier can be estimated at about 50 %. Removal of fine solids might play a role for the topographic condition found at Suvretta rockglacier, but is still not assumed to have a significant impact on this estimate. Changes in air content are neglected.

Table 9-2 Advance characteristics of selected rockglacier fronts (*: from borehole studies (Arenson et al., 2002); values only for the deforming part of the vertical column at the borehole site).

Rock glacier (period of monitoring)	average surface speed above front (m a^{-1})	average advance rate (m a^{-1})	ratio: advance rate / sur- face speed	average horizontal speed (m a^{-1})	ratio: average speed / surface speed	average excess ice content by volume
Gruben (1970–1995)	0.80	0.12	15 %	0.35	45 %	65 %
Muragl (1981–1994)	0.10-0.15	0.05	30-50 %	0.37 *	88 % *	40-70 % *
Murtèl (1987–1996)	0.05	0.01	20 %	0.05 *	75 % *	90 % *
Suvretta (1992–1997)	0.50	0.16	35 %	0.30	60 %	50 %
Gufer (1994–2000)	1.20	0.20	16 %	—	—	—
Muragl glacier fore- field (1981–1994)	0.50	0.17	35 %	—	—	—

In conclusion, the excess ice content within the Suvretta rockglacier front may be some 15 % lower than for Gruben rockglacier. The excess ice content for both rockglaciers lies in the range found from boreholes within Murtèl rockglacier, and above the values for Muragl and Schafberg rockglaciers. The measurements confirm that material transported towards and down the rockglacier fronts is incorporated at the bottom of the advancing permafrost body and then overridden by it (see also Figs. 9-11 and 9-16). The solid material creeping over the front seems not only to erode at the front by individual events, but also to coherently creep down the front to a significant extent (see Bauer et al., 2003).

Strictly speaking, the deformation of the measurement rods is only able to reflect the deformation of the upper 1–2 m of the rockglacier fronts. In that way, a significant down-slope surface creep was found for the Gruben rockglacier front. The rod measurements alone do not permit to draw conclusions about the thickness of this surface layer. However, at rods where no strong downward component was observed this surface effect can largely be ruled out, and the rods reflect the deformation of depths exceeding the rod length. In case of pure down-slope surface creep, no advance would be observed theoretically except some compression from mass accumulation at the front foot. The fact, that also the upper front sections advanced significantly further supports the suggestion that the rods reflect more than just a down-slope surface creep of the uppermost layer of the front.

The presented study confirms the findings from previous geophysical and borehole studies that the vertical velocity profile and the ice content between individual rock glaciers can vary significantly. These differences are clearly reflected by different advance mechanisms, and can thus be resolved from according measurements. In turn, the differences in advance rate and mechanism have significant impact on the internal age structure of rockglaciers, and on the relations between, for instance, rockglacier length and age, or rockglacier surface velocity and age.

The novel method described above for measuring the kinematics of rockglacier fronts proved to be highly efficient. The characteristics of the advance mechanism and the ice content could clearly be detected and differences between the flow regime of the two investigated rockglaciers identified. The approach appears to be a simple and cheap alternative to, or a preliminary evaluation before borehole measurements in order to assess the vertical velocity profile and overall ice content within rockglaciers. The author considers the combination of such frontal rod measurements with repeat terrestrial close-range techniques such as terrestrial laserscanning (Bauer et al., 2003) or terrestrial photogrammetry as most promising for increasing the understanding of rockglacier advance. The approaches are not restricted to longitudinal profiles as applied here, but are capable of covering entire rockglacier fronts. Complementary insights on the mode of ice loss might be gained from local-scale energy-balance studies over rockglacier fronts, and from water balance/hydrological studies.

9.3 Observed and modelled seasonal variations of rockglacier speed: Muragl rockglacier, Switzerland

9.3.1 Introduction

The deformation magnitude of frozen debris in mountains can change at temporal scales of millennia, decades to centuries, years to decades, or seasons. Speed

variations at diurnal scales are likely to occur, but might not have a relevant influence on the evolution of rockglaciers and alpine landscape.

- Millennia-scale speed variations represent fundamental stages in the rockglacier transport system, such as the origin of a rockglacier itself, impacts from glaciation, or melt-out of the ice content (i.e. formation of relict rockglaciers).
- Speed variations (including de- or re-activation) with frequencies in the order of centuries or several decades can result from general spatio-temporal changes in boundary conditions such as material supply, thermal regime or terrain topography (Barsch, 1996). Comparison of present-day flow fields of rockglaciers with their current shape – that cumulatively reflects their dynamic history – clearly shows such past temporal variability (Frauenfelder and Kääb, 2000).
- Photogrammetric and geodetic monitoring series of up to several decades duration suggest that velocity changes of mountain permafrost creep in pluriannual time scales may be due to variations in weather and climate conditions (Zick, 1996; Kääb et al., 1997; Schneider and Schneider, 2001; Kaufmann and Ladstädter, 2002; Kaufmann and Ladstädter, 2003; Roer et al., 2005a).
- However, the above sensitivity of permafrost creep to external climate forcing is strongly dependent on the individual internal conditions of a rockglacier, as clearly shown by seasonal velocity variations. Related geodetic observations in the Swiss Alps yield seasonal speed variations from nearly zero percent to several tens of percents (Haeberli, 1985; Barsch, 1996; Arenson et al., 2002; Kääb et al., 2003c).

All the above frequencies of speed variability overlay. While long-term variations are mostly relevant to landscape evolution, short-term changes provide insights into the creep mechanisms of rockglaciers. In this study, a monitoring series of seasonal speed variations on Muragl rockglacier is presented and the potential influence of thermal variations on permafrost creep is modelled numerically.

See also Kääb et al. (2005d).

9.3.2 Seasonal velocity variations on Muragl rockglacier

Figure 9-20 shows the horizontal speed of selected markers on Muragl rockglacier (see Fig. 9-3) as measured during repeat polar surveys. In total, measurements were performed for some 20 markers on two flow lobes. The selection shown here appears to be representative for the entire sample.

Surprisingly, the speed of permafrost changes from magnitudes smaller than 0.2 m a^{-1} to up to 1 m a^{-1} within a few months. These “stop-and-go” events happen in a fairly synchronous way over the study area. The average speed over the observational period of 1998 to 2001 is higher than the 1981 to 1994 average speed obtained from photogrammetry by about $+0.1 \text{ m a}^{-1}$ (Fig. 9-20) (Kääb et al., 2005d).

In borehole no. 3 (Fig. 9-25), close to point no. 204, short-term deformation variations were observed by Arenson et al. (2002) (Fig. 9-20). Copying the borehole-derived variations into the other years observed clearly shows that the magnitude, average speed, wavelength and/or onset of the changes vary significantly from year to year. For different reasons, the repeat surveying presented here could not be performed in equal time intervals.

Ground surface temperatures at five locations throughout the study area were measured from miniature temperature loggers placed under large rocks. The temperature series obtained show no marked differences from each other. The onset of rockglacier speed-up is delayed by about 2 months compared to the surface melt-

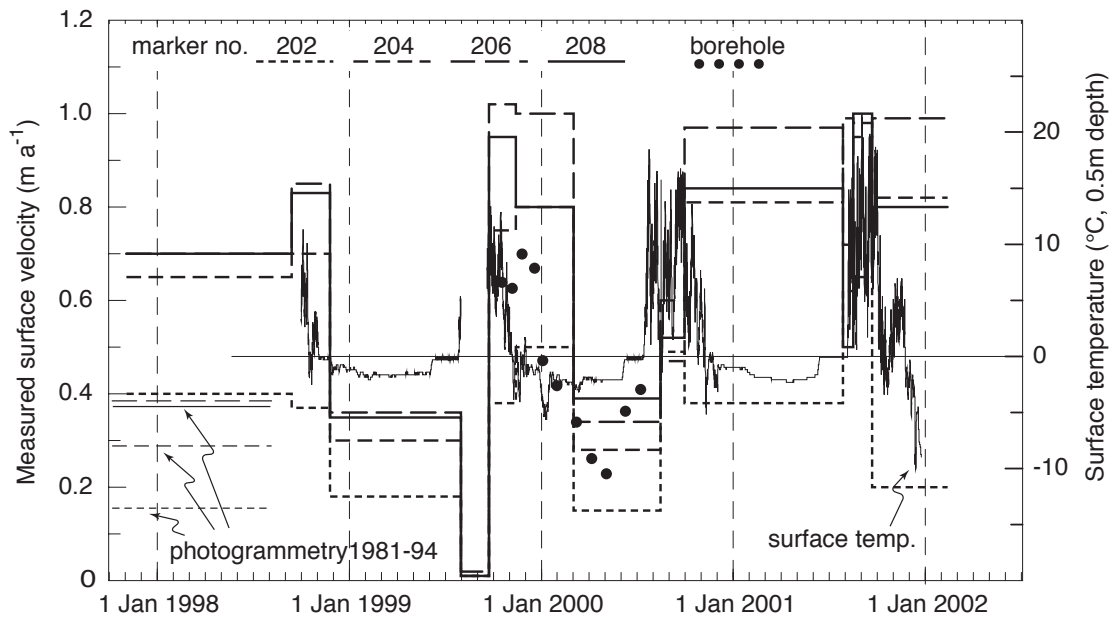


Fig. 9-20 Surface speed variations during 1998–2001 on Muragl rockglacier as measured from repeat terrestrial surveying of markers. To the left, average speeds derived from photogrammetry for 1981 to 1994 are given. The ground surface temperature (thin solid line) was obtained from miniature data loggers at a depth of several decimetres. The dots indicate borehole deformation measurements by Arenson et al. (2002). For location of the markers see Figure 9-3.

out of snow, which is indicated by a ground temperature rise above zero (Fig. 9-20). The time shift of rock glacier speed-up compared to penetration of meltwater into the ground amounts to about 3 to 4 months, as indicated by the rise of the basal temperature of snow (BTS) from permafrost conditions (approximately -3°C) to the so-called “zero-curtain” (0°C). In winter 2002, in-sufficient snow cover and thus lack of insulation led to extraordinary ground cooling.

9.3.3 Numerical model scheme

The possibly sinusoidal form of speed variations on Muragl rockglacier (Arenson et al., 2002) and the clear seasonal cycle suggest a thermal influence on speed. The influence of thermal variations on permafrost creep is numerically modelled here by combining heat conduction with a temperature-dependent rate factor for ice deformation. The model is constructed as follows (Fig. 9-21) (Kääb et al., 2005d):

- A body of pure ice is assumed. This assumption has little effect on the computed heat conduction since the respective heat conductivity coefficients for ice and rock are similar. The assumed constant heat conductivity would, however, not apply for a significant air content of the frozen ground. The ice/debris concentration certainly has an influence on the used creep law. This effect is neglected here as it is considered to not alter in a substantial way the outcomes of the general sensitivity study intended in this investigation. Water penetration and other advective terms are also neglected as a heat transport mechanism. Although these processes could indeed play a significant role in relation to permafrost temperatures close to and at the melting point, not enough is known, for our purposes, about their effects. They might have non-linear (phase transition ice-water!), highly individual consequences for different rockglaciers.
- Since the model in question aims only at simulating short-term variations, the interplay between energy flux through the surface and geothermal heat flux is

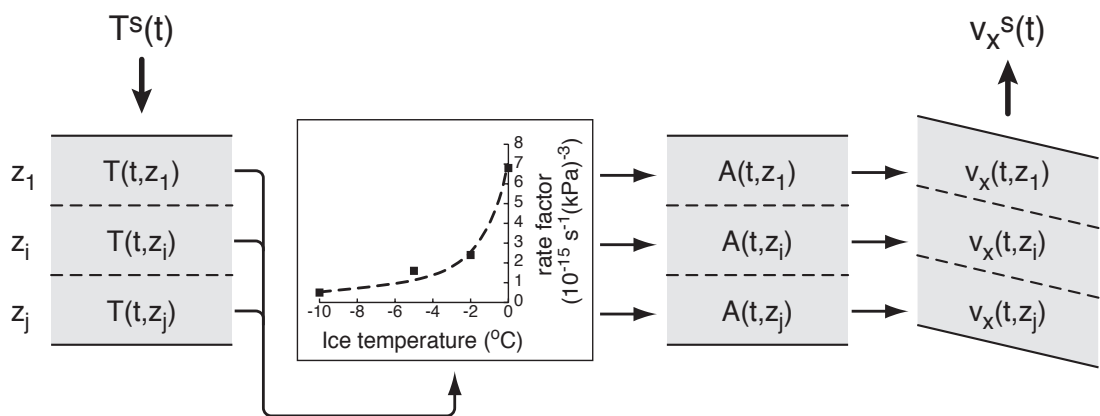


Fig. 9-21 Scheme for simulating changes in surface speed of an ice body due to variations in surface temperature. The temperature of individual layers is computed from heat conduction, and a temperature-dependent rate factor is then estimated empirically for each layer. Integration of the deformation of the individual layers gives the total speed at the surface.

neglected, preferring to keep the temperature constant at the base of the ice body concerned. Such procedure is deduced from measured thermal permafrost behaviour under seasonal temperature variations (Vonder Mühll et al., 1998). The model presented is one-dimensional, i.e. it neglects any lateral influences.

- Model input is a sine-curve of ground surface temperature variations. These range between -3°C and 0°C for the model runs depicted in Figure 9-22. Frequencies for the temperature variations shown in Figure 9-22 are one cycle per one and five years.
- Heat conduction into the ground is computed from

$$\frac{\partial T}{\partial t} = \kappa \frac{\partial^2 T}{\partial z^2} \quad (9-4)$$

(Carslaw and Jaeger, 1959), where T is temperature, t time, κ heat conductivity of ice and z is depth. In the model, heat conduction is calculated for layers with a finite thickness (2–3 m).

- For $T(t)$ obtained for each layer, a temperature-dependent rate factor A is interpolated. For this purpose an exponential curve is fitted into the A factors given by Paterson (1994) for various ice temperatures. Thus one obtains $A(t, z)$ as a function of time and depth. An exponential-like dependency of deformation from temperature seems also to apply to rockglaciers (Arenson et al., 2002; Kääb et al., 2002a; Frauenfelder et al., 2003a). Optionally in the model, the rate factor A is increased for selected layers to simulate shear horizons as found for most rockglaciers (called “soft layer” in Figure 9-22) (see Wagner, 1996; Arenson et al., 2002).
- $A(t, z)$ is then introduced into Glen's flow law integrated for an infinite slab:

$$v_x^s = \frac{2A}{n+1} (\rho g \sin \alpha)^n h^{n+1} \quad (9-5)$$

(Paterson, 1994), where v_x^s is the horizontal surface velocity, ρ the density of ice, g the acceleration due to gravity, α the surface slope and h the column thickness. The flow law exponent n is set at 1 (Wagner, 1996).

- The final model output gives variations of surface speed in dependence on surface temperature variations (Fig. 9-22).

9.3.4 Temperature variations of one-year cycle

Two model runs were computed for a surface temperature variation with a one-year wavelength. Run (1) with an average temperature of -1.5°C throughout the entire column and with a variation magnitude of $\pm 1.5^{\circ}\text{C}$ at the surface (Fig. 9-22), and run (2) with an average ice temperature of close to 0°C (not depicted). Run (1) simulates conditions similar to those for Murtèl rockglacier, for example (Vonder Mühl et al., 1998). Run (2) represents warm rockglaciers, or even temperate glaciers. Both runs aim to cover the range of climate conditions found so far for rockglaciers in the European Alps. For run (2) the temperature of the lowermost layer was kept constant at 0°C . Temperature at the surface was varied as a sine-curve around $T=0^{\circ}\text{C}$ with an amplitude of -1.5°C . Temperatures above 0°C were cut off and set to 0°C . The aim of this procedure is to simulate icemelt at the permafrost table (zero-curtain). Run (2) is not depicted.

The modelled heat conduction with depth is comparable to the one measured in boreholes (Vonder Mühl et al., 1998). For run (1) the temperature maximum reaches a depth of 15 m with a delay of approximately 5–6 months compared to the surface (i.e. a time lag of nearly 50 % of one wavelength of temperature variation). The resulting variations in surface speed are about 8 % (total range) of average speed if no soft layer is assumed. Surface speed varies by approximately 4 % if a layer with a rate factor five times higher than the remaining column is introduced for a depth of 12–15 m, and by about 10 % if the soft layer is in 6–9 m depth. Overall speeds of the soft-layer models are significantly higher than without such layer. Overall speeds are

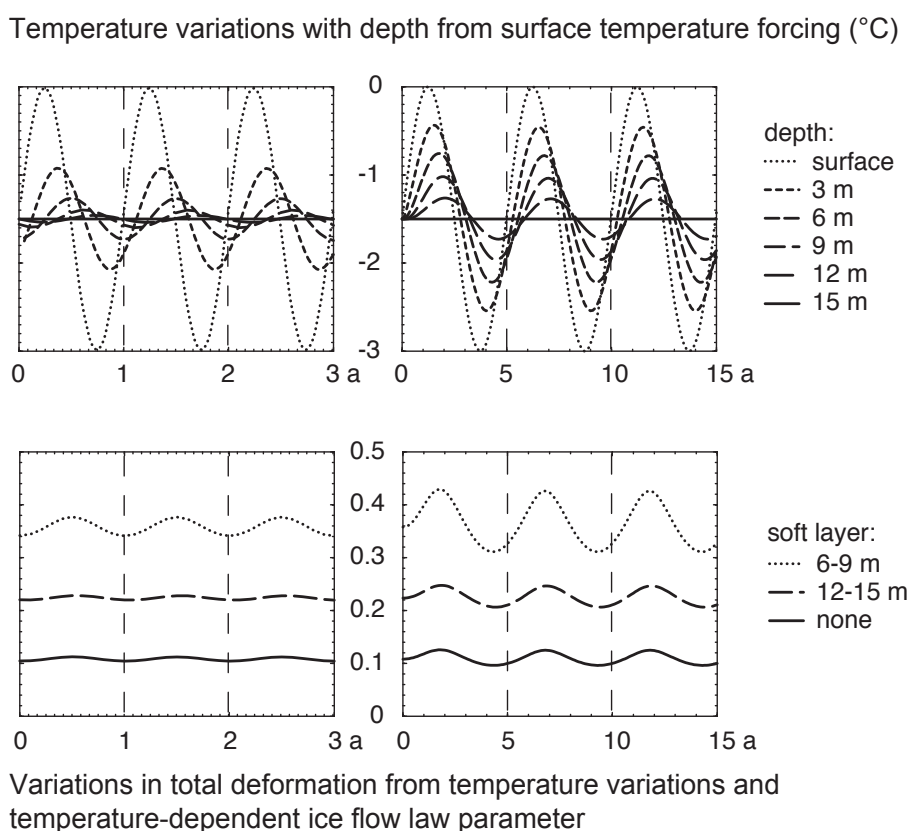


Fig. 9-22 Results from two runs of the model presented in Figure 9-21. Left: surface temperature variations with one-year cycle (i.e. seasonal variations); right: pluriannual temperature variations with five-year cycle. Upper figures: modelled temperature variations at various depths; lower figures: resulting speed variations with and without layers of 5 times increased softness.

also higher with a soft layer in lower depth. For run (2), i.e. temperate ice with penetrating winter coldness, speed variations are in the range of 9 % without soft layer, 6 % for a 12–15 m deep soft layer, and 13 % for a 6–9 m deep soft layer.

9.3.5 Temperature variations of a five-year cycle

A five-year cycle was introduced in the model in order to simulate the effect of one or several especially warm or cold years, or years with different snow depths or timing. Two runs, (3) and (4), were computed in a similar way to the above runs (1) and (2). For a temperature variation with a five-year wavelength, the delay of temperature maximum at 15 m depth amounts to approximately one year (i.e. a time lag of about 25 % of one wavelength of temperature variations). For run (3), surface speeds vary by about 26 % without soft layer, 18 % for a 12–15 m deep soft layer, and 31 % with a 6–9 m deep layer. For run (4), i.e. temperate ice, the respective numbers are 40 %, 37 % and 45 %. For different model runs see Kääb et al. (2005d).

9.3.6 Conclusions

The numerical model for simulating surface speed variations of an ice body driven by surface temperature variations reveals:

- Seasonal surface temperature changes are expected to cause speed variations in the order of 5–15 %, significantly depending on the ice temperature. The latter effect is a consequence of the assumed exponential increase of the rate factor with temperature.
- For pluriannual temperature changes speed variations in the order of 20–40 % or more may be expected. The higher sensitivity compared to seasonal temperature changes is due to the enhanced heat conduction with lower frequency of temperature forcing, or lower thermal attenuation.
- A soft layer within the ice body does not necessarily enhance the speed variability. Depending on its vertical position, it is able both to amplify or compensate the effect of rate-factor change with temperature. Depending on the layer depth, the temperature – and with it the deformation – might reach its maximum at a time when the other layers are comparably warm and fast, or comparably cold and slow.
- The less deep a soft layer is located, the higher the magnitude of temperature variations that reach it. Since the rate factor is assumed to change with temperature it follows that the less deep a soft layer is located the higher are the variations in surface speed of the creeping ice body.
- Since the rate factor, furthermore, is assumed to increase exponentially with temperature, a temperature increase has a much greater influence on deformation than a temperature decrease. As a consequence, the model presented here produces higher overall speeds for settings with a less deep (i.e. warmer) soft layer. The latter conclusion, however, does not consider a variation of average ground temperature with depth. Such an increase of permafrost temperature towards the permafrost base overlays the effect described here, but may be effective, in general, for larger depths of soft layers than applied here.

A number of parameters in the model may be (and were) altered. Such a procedure changes the numbers given above. The basic conclusions given here, however, do not change substantially. It is no doubt true that the inclusion of processes other than one-dimensional heat conduction and viscous temperature-dependent deformation within the model would have significant effect. The interactions between debris and

ice in the matrix, and especially the action of water, can be of major importance. In fact, the model results cannot explain the variability range of 100 % and more of the average speed (i.e. $\pm 50\%$) found for Muragl rockglacier (Section 9.3.2). From borehole studies, this rockglacier is known to have a low ice content with a temperature slightly below or close to $0\text{ }^{\circ}\text{C}$ and a water table was encountered below the permafrost base at a depth of 30–36 m (Arenson et al., 2002; Vonder Mühl et al., 2003). For colder permafrost, observed speed variations are in the range modelled here (Haeberli, 1985; Kääb et al., 1997; Arenson et al., 2002).

For 1971 to 1973, Barsch and Hell (1975) found only slight seasonal velocity variations for Muragl rock glacier (summer speed $\approx 130\%$ of winter speed). For Murtèl rockglacier they found seasonal variations of up to one order of magnitude during the same time period. The borehole studies since 1987 at Murtèl rockglacier and accompanying terrestrial surveys, by way of contrast, revealed little to no speed variations (Wagner, 1996). A clear seasonal cycle in movement was detected by Haeberli (1985) for Gruben rockglacier. All studies revealed greater movements in summer than in winter. Seasonal speed maxima were detected for autumn 1981 and spring 1982 for Gruben rockglacier. From the front measurements at Gruben rockglacier (see Section 9.2), which suggest a shear horizon at 5–10 m depth, it can be expected that seasonal temperature variations will strongly affect the movement of this rockglacier.

The findings suggest that the creep of “warm” permafrost (i.e. slightly below or close to $0\text{ }^{\circ}\text{C}$) is more sensitive to climate forcing than the “cold” one (cf. Ikeda et al., 2003). Furthermore, a rise in rockglacier temperature leads to an exponential increase in average speed (see Frauenfelder et al., 2003a), accompanied by a marked increase in seasonal to pluriannual variability of velocities. At a later stage of increasing rockglacier temperature, a significant loss of ice content by melt-out is able to reduce the deformation rate of the frozen mass again towards its entire deactivation. The model study stresses the importance of learning more about shear zones in rockglaciers. Such layers appear to be an essential part not only of rockglacier thermo-dynamics, but also of their reaction to temperature changes.

For more extensive investigations and possible consequences of rockglacier reaction to temperature changes, see Kääb et al. (2005d).

9.4 Deformation of rockglacier surface topography

Collaboration

The terrestrial measurements on Muragl and Suvretta rockglaciers have been conducted together with or by Monika Weber, and are part of her diploma thesis (Weber, 2003). (See Kääb and Weber, 2004).

9.4.1 Introduction

The high thermal inertia of rockglaciers allows the frozen bodies to continuously deform and preserves their topography over centuries and millennia (Haeberli, 2000; Kääb et al., 2003c). The surface topography of rockglaciers cumulatively reflects their entire dynamic history and thus in a complex way, their present and past internal conditions and environment. Transverse ridges and furrows represent the most prominent expression of rockglacier micro-topography. Understanding the processes involved in the evolution of such structures potentially enables conclusions to be

drawn about the present dynamics of rockglaciers by interpreting their surface topography. Furthermore, such decoding of the surface morphology contributes to the reconstruction of the dynamic and thermal history of rockglaciers (Frauenfelder and Kääb, 2000).

According to main theories on transverse ridges and furrows on rockglaciers (e.g. Wahrhaftig and Cox, 1959; Potter, 1972; Haeberli, 1985; Olyphant, 1987; White, 1987; Loewenherz et al., 1989; Whalley and Martin, 1992; Barsch, 1996; Kääb et al., 1998), these formations might be attributed to:

- external factors, such as variations in debris input or climate conditions, or
- internal factors, such as the dynamic evolution of ridges under compression flow, or disturbance propagation from differential movement of discrete layers (cf. Fletscher, 1974; Fink, 1980).

In addition, it is as yet unknown whether transverse ridges and furrows represent

- dynamic structures, e.g. forming from emergence under compression flow regime (i.e. active formation), or
- thermally shaped forms due to, for instance, differential melt (thermokarst) or frost heave processes (i.e. passive formation).

It is important to note that these four theories do not necessarily contradict each other. One possible process might enhance the other, or a combination might be necessary for the formation of micro-topographic structures. Here, the dynamics of transverse ridges for three rockglaciers in the Swiss Alps are examined.

9.4.2 Transverse ridges on Murtèl rockglacier

The evolution of micro-topography on Murtèl rockglacier is described in detail in Kääb et al. (1998) and a summary given here for the sake of completeness. The results are obtained from photogrammetric longitudinal profiles of surface geometry and velocity with 1 m horizontal spacing, and depicted in Figure 9-23. Also displayed are terms of the kinematic boundary condition at surface (Eq. 2-1): horizontal velocity, change in elevation and the product of slope times speed ($v_x^s \cdot \partial z^s / \partial x$). Over the investigated period 1986–1997, the horizontal creep rates at the surface amount to 0.16 m a^{-1} in the steep upper part and decrease to about 0.05 m a^{-1} in the flat lower part (see Figs. 7-2 and 9-5). The observed velocity increase at the rockglacier front may be related to the increase in slope. However, the measurements might also be affected to some extent by debris sliding along the surface down the front. The elevation changes reveal a more or less constant term of about -0.03 m a^{-1} in decrease of permafrost thickness, overlain by high-frequency variations. These variations clearly coincide with the product of surface slope and horizontal speed, which describes the effect by advection of topography (Eq. 2-1). The transverse buckling becomes first visible in the profile at approximately point $x = 150 \text{ m}$. However, the point of first appearance of the structures needs not necessarily be the zone of their origin. The Murtèl measurements show:

- The longitudinal horizontal surface velocities vary over the ridges in a way that maximum speeds are found on top of the ridges and minimum speeds in the furrows. The variations in speed thus clearly reflect the ridge and furrow topography.
- The distinct ridges of up to 7 m height are advected downstream with a speed that approximates the speed of the entire permafrost body.
- Their formation zone seems to correlate with a distinct decrease in slope, but is also situated in a zone of compression flow.

- The ridges continuously grow under a compression flow regime.
- They seem to decay again towards the front where a short zone of longitudinal extension can be found.
- The age difference between individual ridges is in the order of 300–400 a, as calculated from streamlines (Fig. 7-2) (Kääb et al., 1998; Haeberli et al., 1999b).
- The horizontal compression in the order of 0.001 a^{-1} found for the zone of ridge growth, could theoretically be responsible for a surface uplift over time in the order of the observed ridge heights. (Vertical extension of 0.001 a^{-1} over a 30 m thick incompressible ice slab results in about $+0.03 \text{ m a}^{-1}$ thickness increase)

9.4.3 Transverse ridges on Muragl rockglacier

A profile similar to that for Murtèl rockglacier has also been measured for Muragl rockglacier for the period 1981–1994 (Fig. 9-24). Since Muragl rockglacier is dynamically much more complex than Murtèl rockglacier, the profile includes several individual flow lobes (Fig. 9-3) (see Frauenfelder and Kääb, 2000). Accordingly, the horizontal velocities reflect rockglacier parts of different activity with maximum speeds of 0.45 m a^{-1} . The small-scale topography includes typical transverse ridges and furrows (e.g. at around $x = 350 \text{ m}$; Fig. 9-24, see Fig. 9-25) as well as significantly larger fronts of individual flow lobes or rockglacier generations (e.g. from $x = 400 \text{ m}$ to $x = 550 \text{ m}$). No overall trend of thickness change can be observed. The high-frequency changes of permafrost thickness correspond well with the calculated mass advection ($v_x^s \cdot \partial z^s / \partial x$).

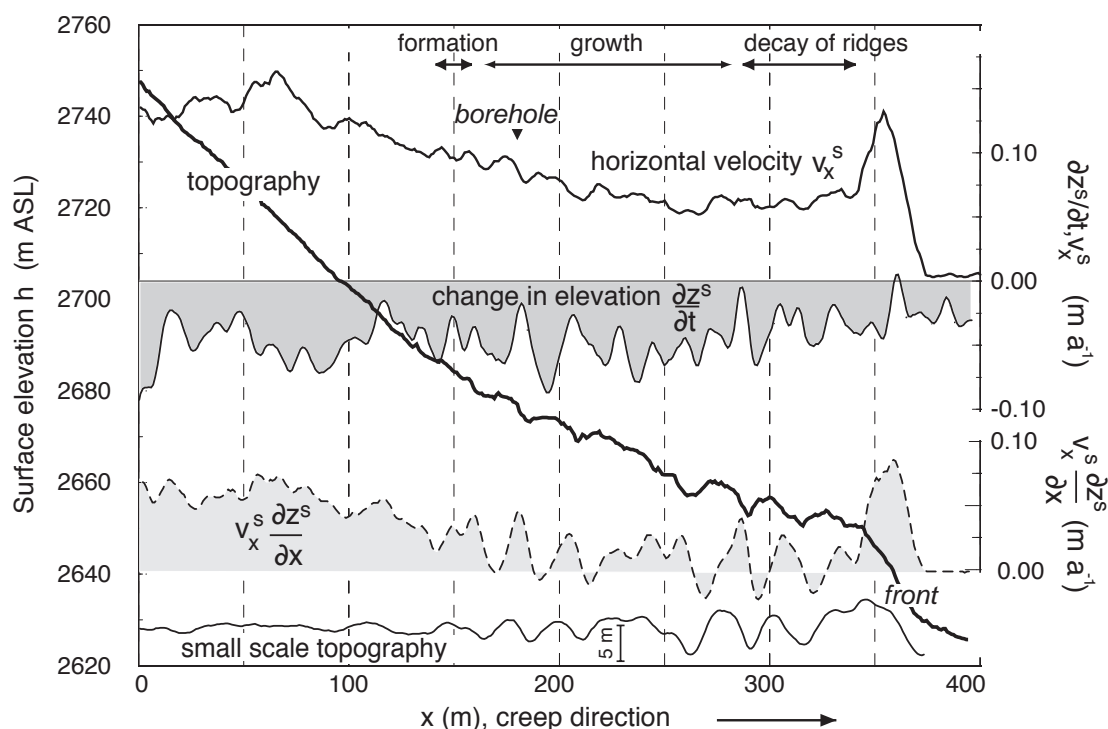


Fig. 9-23 Murtèl rockglacier. Longitudinal profile of rockglacier surface, surface velocities and derived kinematic quantities 1987–1996. The photogrammetric profile measurements have a spatial resolution of 1 m. Surface topography is depicted with two times vertical exaggeration. Small-scale topography is defined as the difference between surface topography at each point and a running average over 200 m (four times vertical exaggeration). For profile location see Figure 9-5.

- As for Murtèl rockglacier, the ridges of up to 2 m height are advected downwards with a speed similar to that of the entire permafrost body.
- Their formation and growth takes place in zones of strong longitudinal compression in the order of -0.003 a^{-1} , and well above a zone of slope decrease. The ridges show a continuous increase in size over a compression zone.
- As for Murtèl rockglacier, local speed maxima are found on top of the ridges, speed minima at furrows.
- The age difference between individual ridges is in the order of 50–70 a, as calculated from streamlines (Frauenfelder and Käab, 2000).
- As for Murtèl rockglacier, the order of horizontal compression of roughly -0.003 a^{-1} found in the zone of ridge growth could theoretically be responsible for a surface uplift in the order of the observed ridge heights. (Vertical extension of 0.003 a^{-1} over a 15 m thick incompressible ice slab results in $+0.04 \text{ m a}^{-1}$ thickness increase).

Figure 9-25 depicts high-resolution measurements of horizontal surface velocities and thickness changes during 1981–1994 for the ridge-and-furrow zone at c. $x = 350 \text{ m}$. South of boreholes 3–4–2, the results illustrate small-scale variations of thickness change from mass advection and an overall thickness increase of roughly $+0.02 \text{ m a}^{-1}$ overlying each other (perhaps from compression or overthrusting?) (Käab and Vollmer, 2000).

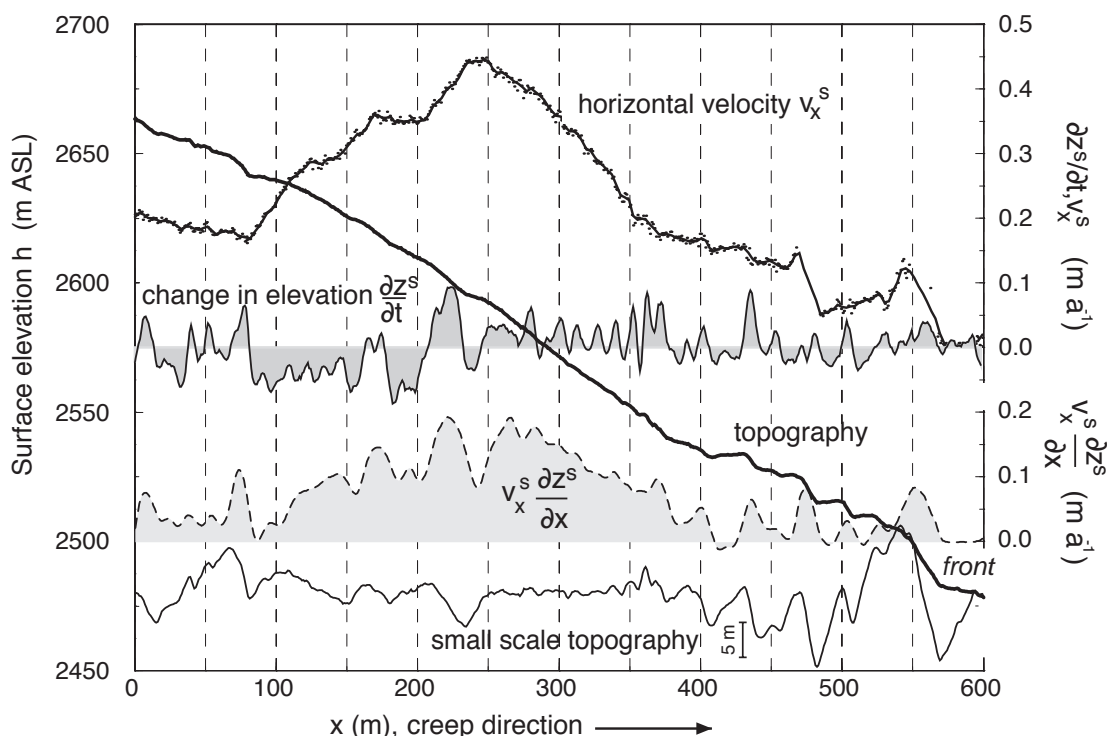


Fig. 9-24 Muragl rockglacier. Longitudinal profile of rockglacier surface, surface velocities and derived kinematic quantities 1981–1994. The photogrammetric profile measurements have a spatial resolution of 1 m. Surface topography is depicted with about two times vertical exaggeration. Small-scale topography is defined as difference between surface topography at each point and a running average over 200 m (four times vertical exaggeration). For profile location see Figure 9-3.

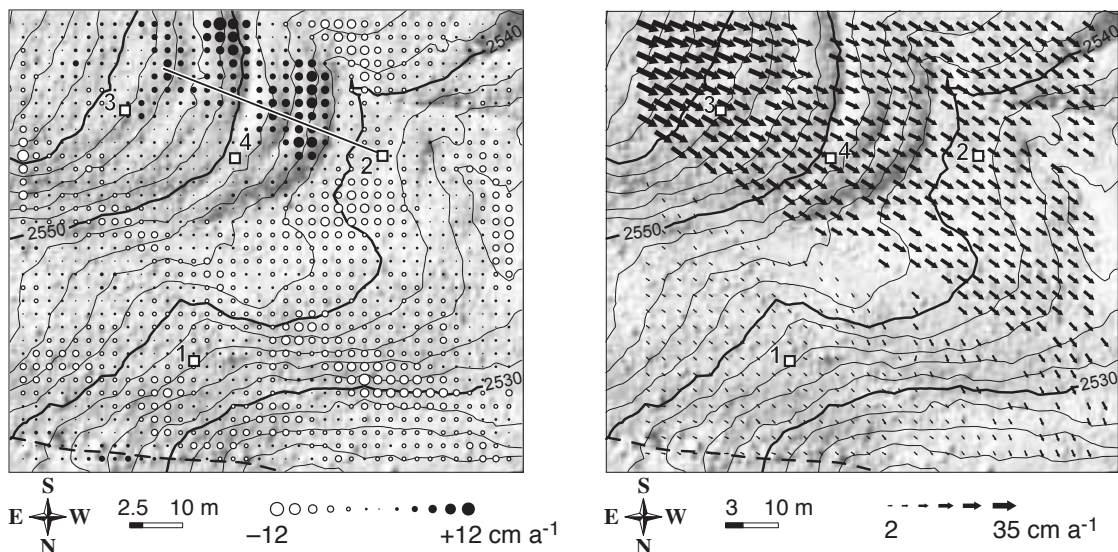


Fig. 9-25 Permafrost thickness changes with 2.5 m spacing (left) and 3 m spaced horizontal displacements (right) measured for a section of the Muragl rockglacier between 1981 and 1994 (see inset in Fig. 9-3). The small rectangles indicate the location of boreholes no. 1–4 (see Arenson et al., 2002). The dashed line to the bottom represents the margin of the rockglacier. The straight line marks the position of the profile in Figure 9-26. Orthoimage based on photography swisstopo/flight service (permission BA057212).

9.4.4 A high-precision profile on Muragl rockglacier

From summer 2001 to summer 2002 high-precision terrestrial measurements of three-dimensional surface velocities were performed for a longitudinal profile south of boreholes 3–4–2. The repeat position of painted marks on boulders was determined by two-way close-range polar survey and levelling. The positional accuracy obtained is estimated to be in the order of a few millimetres (Weber, 2003). Figure 9-26 shows the topography, the horizontal and vertical velocity components obtained, and terms of the kinematic boundary condition (Eq. 2-1). Note that the vertical velocity component is not equivalent to the horizontally fixed thickness change as obtained from photogrammetry ($\partial z^s / \partial t$), but rather linked to the three-dimensional travel of an individual surface particle (v_z^s ; see Eq. 2-2). The measurements and calculations reveal among other findings:

- Horizontal speeds (v_x^s) stay constant or even increase slightly at the top of transverse ridges (see also Fig. 9-23 for Murtèl rockglacier). At the front of the ridges, speed partially decreases more strongly than the overall horizontal speed decrease observed for the profile. In sum, local speed maxima are found on the ridges.
- The vertical velocities (v_z^s) show no distinct small-scale variations. They increase longitudinally in the upper part of the profile but stay nearly constant in the lower part.
- The surface slope ($\partial z^s / \partial x$) is clearly different from the slope of the particle displacement (v_z^s / v_x^s). This fact shows that the surface velocity is not parallel to the surface but rather to a smooth layer at depth. This finding coincides perfectly with observations from borehole inclinometry in the area. Arenson et al. (2002) found a distinct shear horizon in about 15 m depth.
- The slope of particle displacement is, furthermore, not constant but decreasing from -0.28 (-16°) to about -0.12 (-7°), while the overall surface slope is basically

constant at -0.5 (-25°). Thus, the shear horizon seems to emerge significantly towards the surface along the profile. The deformation measurements in boreholes 3 and 4, which are situated near the upper half of the surface profile (see Fig. 9-25), did indeed yield downslope of approximately -0.31 (-18°) for the 2 m thick shear horizon at c. 15 depth (Arenson et al., 2002). The displacement slope for surface particles in the same zone calculated from the profile averages about -0.22 (-13°), i.e. approximately 5° less steep than the slope of the actual shear horizon.

- The overall increase in surface elevation ($\partial z^s / \partial t$) observed from photogrammetry (Fig. 9-25) appears, therefore, to be at least partially an effect of a mass-emergence component. The observed three-dimensional particle displacement is the resultant of (1) basal slope and speed, (2) mass balance, and (3) straining (Eq. 2-1). All three processes could affect the calculated emergence velocity of about 0.13 m a^{-1} . From the above-mentioned borehole measurements, the emergence-velocity component due to basal sliding alone can be expected to be in the order

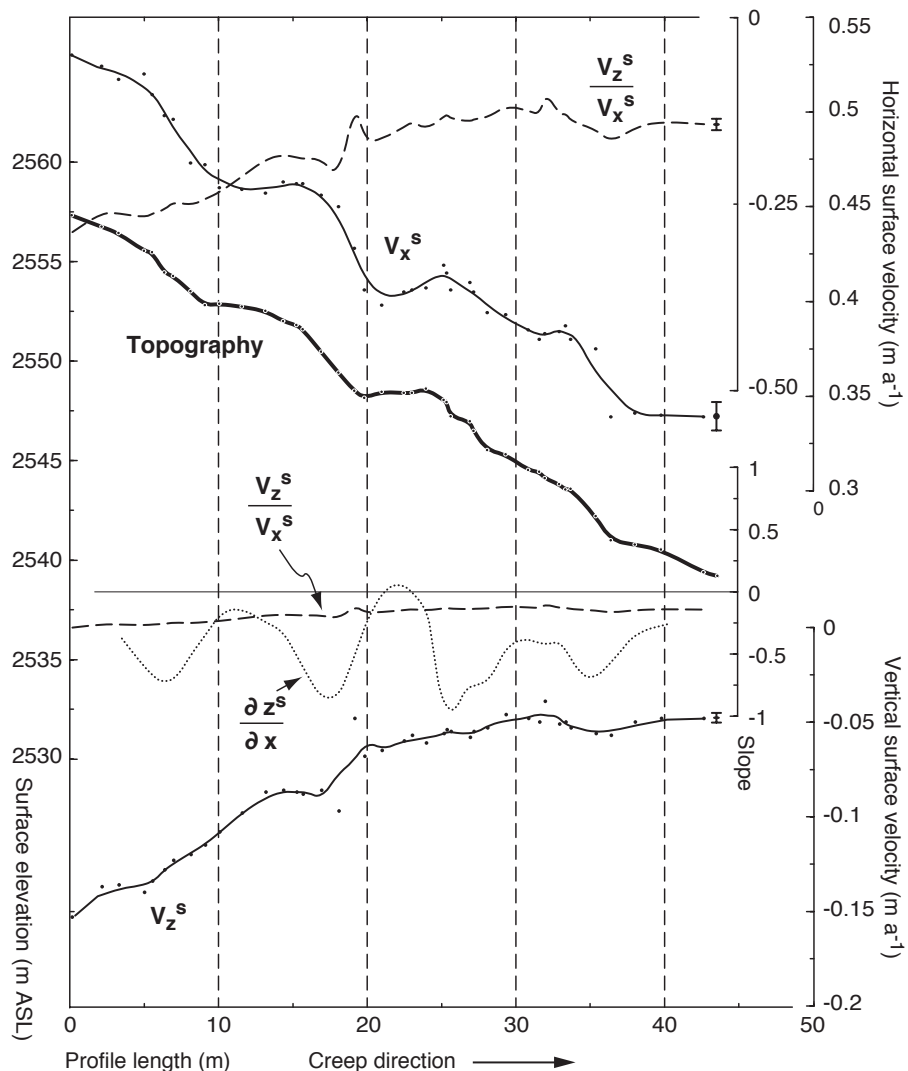


Fig. 9-26 Muragl rockglacier. Longitudinal high-precision profile of rockglacier surface, horizontal and vertical velocities, and derived kinematic quantities for 2001–2002. The data are obtained from polar survey and levelling. v_x^s : horizontal velocity at surface; v_z^s : vertical velocity at surface; $\partial z^s / \partial x$: the slope of surface particle movement v_z^s / v_x^s is depicted twice with different scales. Small dots indicate the raw measurements. Solid lines are interpolated by a running mean. Error bars to the right indicate the measurement accuracy. For profile location see Figure 9-25.

of 0.09 m a^{-1} . The remaining difference compared to the measured emergence velocity could be the result of frost heave (less likely for permafrost, which is close to the melting point) or vertical extension (cf. Arenson et al., 2002).

- The shear horizon still exhibits significant, though not large, small-scale topography. While its slope is roughly constant in the lower part of the profile, it decreases in the upper part. The shear horizon, therefore, seems to have a concave form.

9.4.5 A high-precision profile on Suvretta rockglacier

A high-precision profile similar to that on Muragl rockglacier was measured on Suvretta rockglacier for 2001–2002 (Fig. 9-27) (Weber, 2003):

- The investigated ridges lie in a zone of longitudinal compression in the order of $0.001\text{--}0.002 \text{ a}^{-1}$. Their age difference amounts to only about 20 years.

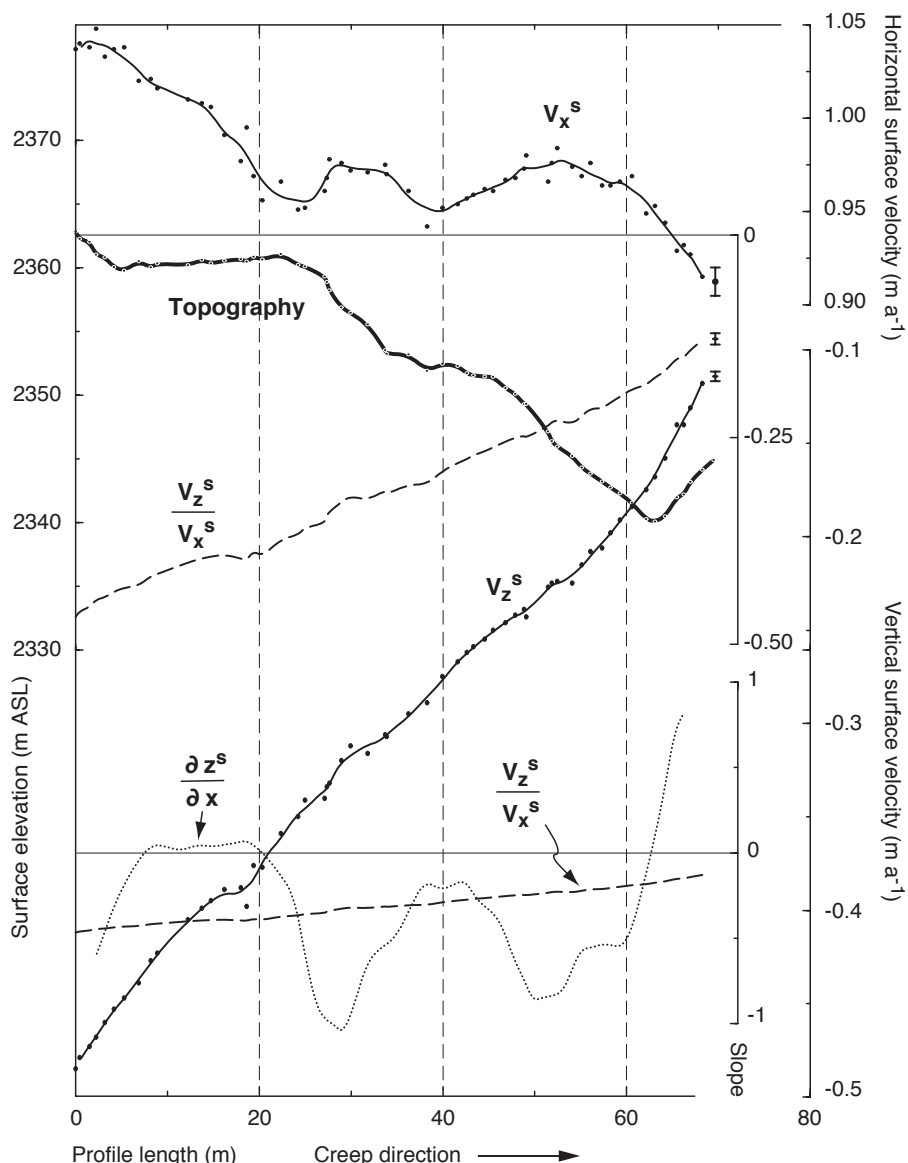


Fig. 9-27 Suvretta rockglacier. Longitudinal high-precision profile of rockglacier surface, horizontal and vertical velocities, and derived kinematic quantities 2001–2002. The data are from polar survey and levelling. v_x^s : horizontal velocity at surface; v_z^s : vertical velocity at surface; $\partial z^s / \partial x$: surface slope; the slope of surface particle movement v_z^s / v_x^s is depicted twice with different scales. Small dots indicate the raw measurements. Solid lines are interpolated by a running mean. Error bars to the right indicate the measurement accuracy. For profile location see Figure 9-2.

- Similar to Muragl and Murtèl rockglaciers, horizontal speed maxima are found on top or in front of the individual ridges.
- Both the vertical velocities and the particle displacement slope show no significant small-scale variations.
- Again, the three-dimensional particle displacement is not parallel to the surface. It is assumed, therefore, that a certain shear horizon exists within the observed section of Suvretta rockglacier.
- Such a potential shear horizon within Suvretta rockglacier shows no significant small-scale topography for the study site, as is to a certain extent apparent for Muragl rockglacier. The shear horizon does, however, also have a concave form with slopes of close to -25° decreasing to about -15° .
- The slope of the shear horizon is not significantly different from the overall surface slope, which is very difficult to determine due to its coarse topography. Thus it is not possible to detect an emerging or submerging flow component to a reliable degree.

9.4.6 Longitudinal ridges on Gruben rockglacier

Gruben rockglacier (Figs. 6-8, 9-1, 9-11 and 9-28) shows no transverse ridges but has distinct longitudinal ones. The fact that a longitudinal extension of up to 0.004 a^{-1} is clearly dominant on its surface (Käab et al., 1997) supports the hypothesis that formation of transverse ridges is favoured by, or even requires, longitudinal compression. We, therefore, further investigated the nature of the longitudinal ridges on Gruben rockglacier by measuring the surface velocity field using high spatial resolution. At an elevation of about 2850 m ASL the surface slope of Gruben rockglacier sharply increases. This surface feature is presumably related to a transverse bedrock riegel at this location, which is also indicated by geoseismic soundings (Käab et al., 1997). Below the riegel zone, surface speeds amount to nearly 1.1 m a^{-1} . A 5 m gridded velocity field for this part was digitally measured on the basis of aerial photography for the period 1970–1975 (Fig. 9-28; for method see Section 4.4). For the surface above the riegel, speeds are in the order of 0.3 m a^{-1} . In order to improve the signal-to-noise ratio for this area, surface velocities were determined using imagery of 1970 and 1995. The latter was not possible for the fast lower area because the high strain rates led to surface destruction in some parts just above the presumed riegel.

Above the riegel zone, the longitudinal ridges are perfectly parallel to the flow direction. Convergent flow, i.e. transverse compression, prevails in this zone (Käab et al., 1997). The ridge size clearly grows along the stream lines of the velocity field until they reach the riegel zone. No significant transverse gradients were found across the ridges. For the area below the riegel zone, the ridges are not parallel to the surface flow. They seem to be advected by the permafrost creep but no longer directly related to the velocity field. The measurements presented here give no direct indication of the ridge formation (pushing from Holocene glacier advances?, cf. Haeberli et al., 1979; Käab et al., 1997), but they suggest that compression might contribute to the growth of ridges also in a transverse mode.

9.4.7 Laboratory experiments

Käab and Weber (2004) (see also Weber, 2003; Weber and Käab, 2003) performed also laboratory experiments on the formation of transverse ridges. Though these experiments should only be interpreted qualitatively, their results show similar

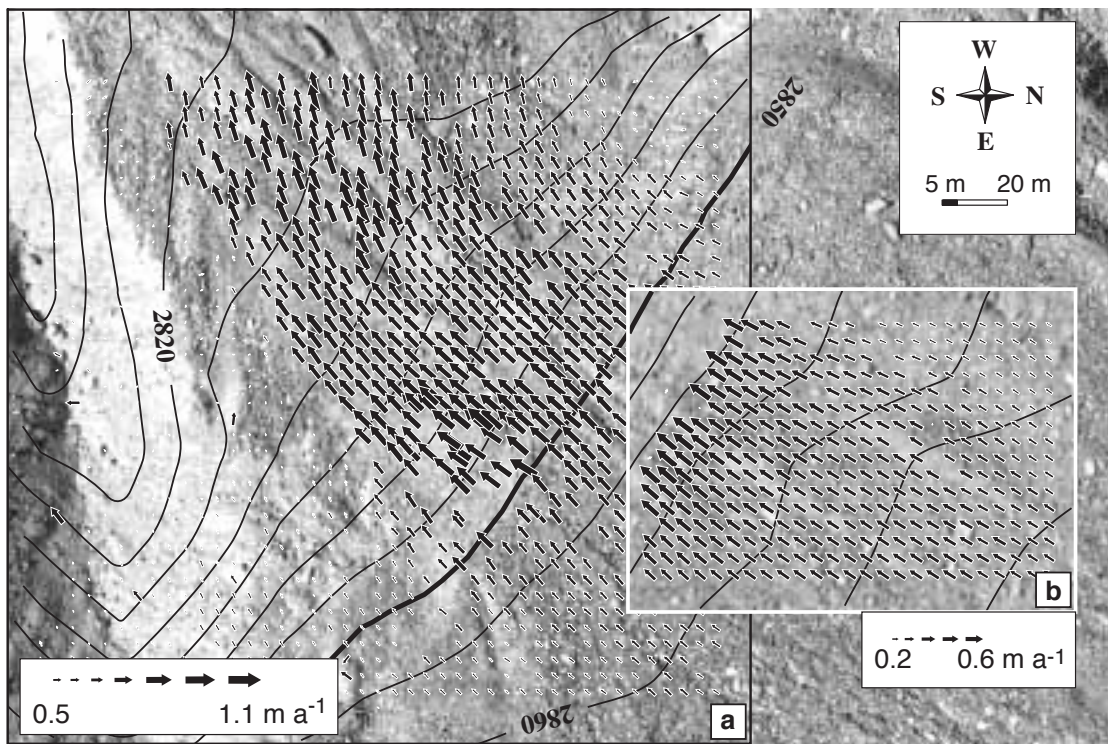


Fig. 9-28 Surface velocities on a section of Gruben rockglacier (see Fig. 9-1) from photogrammetric measurements with 5 m spacing. Inset a: velocities between 1970 and 1975; inset b: between 1970 and 1995. Due to surface destruction measurements in section a were not possible for 1970–1995. Orthoimage based on photography swisstopo/flight service (permission BA057212).

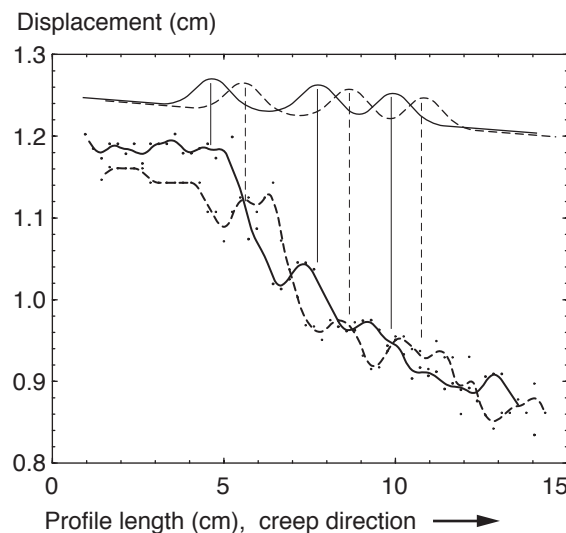


Fig. 9-29 Longitudinal profile of approximately horizontal displacements on the surface of a model mass for the horizontal part of an experimental ramp. The solid line indicates the (interpolated) displacements between times i and $i+1$, the dashed line between times $i+1$ and $i+2$. The small dots mark the original measurements. To the top of the figure, the average position of ridges between times i and $i+1$ (solid) and times $i+1$ and $i+2$ (dashed) is schematically indicated. This topography is only qualitatively reconstructed from the vertical images, which formed also the basis for the displacement measurements. (See Kääb and Weber, 2004).

characteristics as found in the above field experiments. In particular, speed maxima were also found around the ridge tops developing in different mixtures of Xanthan gum, sand, and gravel (Fig. 9-29).

9.4.8 Conclusions and perspectives

Rockglacier micro-topography

The high-precision and high-resolution measurements for Murtèl, Muragl, Suvretta and Gruben rockglaciers clearly indicate that the micro-topography on these rockglaciers is first of all advected downstream, i.e. riding on the creeping bodies. Any process of formation has to be superimposed on the overall permafrost creep. The photogrammetric and terrestrial measurements suggest that compression flow does indeed play a role in the formation of transverse ridges. The overall magnitude of permafrost creep and the degree of straining seem, furthermore, to affect the speed of ridge formation. For Murtèl, Muragl and Suvretta rockglaciers, and for laboratory experiments, horizontal speed shows local maxima on top of the ridges.

From the field measurements and the laboratory experiments using Xanthan-gum/sand/gravel mixtures (Kääb and Weber, 2004) we have developed two theories on possible ridge formation processes (Fig. 9-30):

- *Bulging*: an active process of material uplift under a regime of compressive flow forms the ridges. This process leads to a relative negative speed-component (i.e. a speed-component in upstream direction) on the upstream part of the ridge, and to a relative positive speed-component for the downstream part. The resulting sum (1 in Fig. 9-30) of two speed components, namely a general speed decrease (2 in Fig. 9-30) and the ridge formation (3 in Fig. 9-30), can then be observed at the surface (Figs. 9-23, 9-26 and 9-27).
- *Overthrusting*: faster flow lobes override slower lobes from above. At individual ridges, or lobe fronts, processes similar to the ones taking place at the rockglacier front might occur (see Section 9.2).

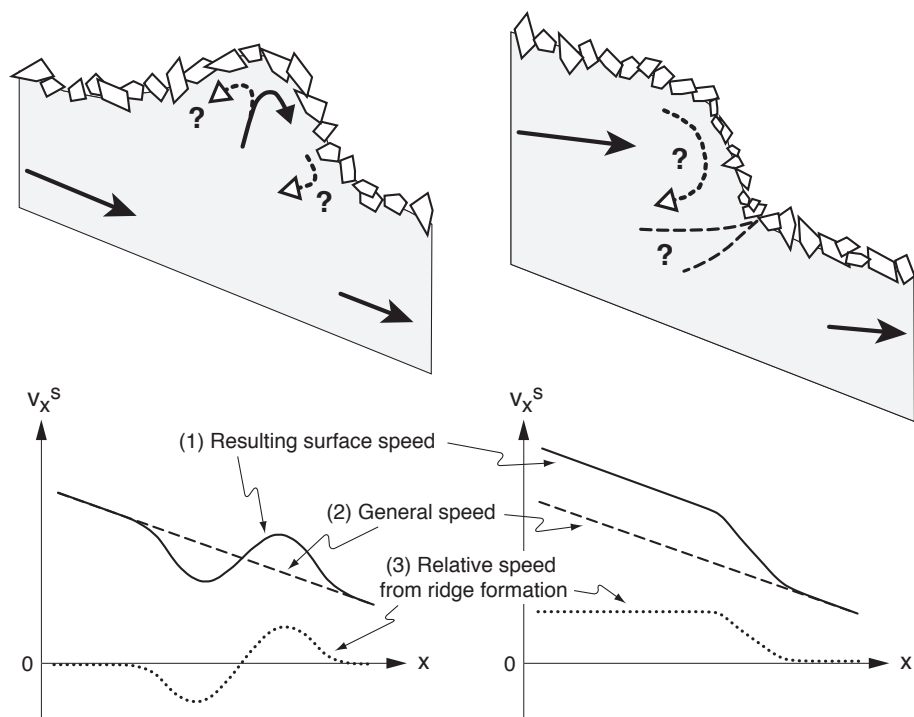


Fig. 9-30 Two hypothetical processes for the formation of transverse ridges on rockglaciers. Left: bulging, right: overthrusting. The lower schemes show how the formation modes lead to different surface velocity profiles. (1) Actual surface velocities are composed by (2) the overall speed gradient (here: decrease) and by (3) the relative speeds connected to the ridge formation itself.

The measurements and additional field interpretation show no clear indication for any of these hypotheses. Moreover, both processes or parts of them seem to be in operation. Overthrusting certainly plays a role for the large-magnitude surface undulations on Muragl (Fig. 9-24) and Suvretta rockglaciers. On the other hand, the velocity profiles obtained for Murtèl (Fig. 9-23) and Muragl (Fig. 9-24) rockglaciers can hardly be explained by overthrusting alone. For the high-precision study site on Muragl rockglacier (Fig. 9-26) some small-scale buckling seems to overlay a general overthrusting of the entire flow lobe onto a slower lower part of the rockglacier.

A thorough investigation of the above theories or development of new ones would be possible from high-precision monitoring over longer time intervals than available here.

For a more detailed discussion of the observations related to ridge formation see Käab and Weber (2004).

Perspectives

The results presented here suggest that high-precision and high-resolution measurements in combination with modelling using the kinematic boundary condition at the surface permit the analysis of the flow characteristics at depth, and the geometry of rockglacier shear horizons or other forms of bedding layers. Such an approach represents an efficient and simple complement to borehole experiments and geophysical soundings. In particular, a combination of the approach shown here and the one presented for investigation of rockglacier front dynamics (Section 9.2) appears promising. A longitudinal profile or entire field of three-dimensional high-precision surface displacements including both, the rockglacier front and surface, will then make it possible to estimate the vertical velocity profile in the frontal part of the rockglacier, and to follow, to a certain extent the depth of a potential shear horizon or other deformation features. Repeat digital photogrammetry of large-scale imagery or terrestrial laserscanning is, next to terrestrial surveying, also able to fulfill these requirements if surface particles are directly tracked in three dimensions (see Section 4.4).

9.5 Permafrost creep within a recently deglaciated glacier forefield: Muragl, Swiss Alps

(See also Käab and Kneisel, 2005).

9.5.1 Introduction

In cold mountains, polythermal glaciers and rockglaciers often exist in close proximity, where climate conditions transit between wet-maritime and dry-continental regimes (Haeberli, 1983b; Barsch, 1996; Humlum, 1998; Ribolini, 1999; Kneisel et al., 2000; Kneisel, 2003; Maisch et al., 2003; Reynard et al., 2003; Lugon et al., 2004). In many situations where these landforms coexist, glaciers have affected adjacent rockglaciers during the Lateglacial and Holocene advance phases, for instance by deformation due to pushing, or by overriding. The present-day massive glacier retreat uncovers forefields, some of which are located within the mountain permafrost belt and contain thick deposits of glacier sediments – both favourable prerequisites for rockglacier formation. Questions arise concerning the extent to which potentially pre-existing permafrost was influenced by overriding during Little Ice Age glacier advances, and the extent to which permafrost and ground ice can

build up, or recover, after ground exposure to the atmosphere due to glacier retreat. So far, ground temperature measurements (BTS) and geophysical soundings have been used to investigate thermal conditions and ground ice occurrences in recently exposed glacier forefields (e.g. Haeberli, 1992b; Kneisel, 1998; Kneisel, 2003).

Here, digital photogrammetric measurements of surface displacement (for the method see Section 4.4) are applied on the Muragl glacier forefield, Swiss Alps, Upper Engadine. In this application, a coherent surface velocity field is viewed as a proxy for frozen debris with an ice content high and long-lasting enough to allow for significant creep of the material (Savigny and Morgenstern, 1986; Bennett and French, 1990; Bennett and French, 1991; Wang and French, 1995; Dallimore et al., 1996; Arenson, 2002).

9.5.2 Study site

The site is close to the well-investigated and currently-active Muragl rockglacier (see Section 9.1.4). The glacier forefield extends in elevation from 2650 m to 2880 m ASL. In the upper part of the cirque from 2880 m to 3080 m ASL, a remnant of the former Muragl glacier exists (as of 2004).

The forefield is located at the lower regional boundary of discontinuous permafrost distribution as inferred by modelling (e.g. Frauenfelder and Kääb, 2000) and measurements of the bottom temperature of the winter snow cover (BTS) (Haeberli, 1992b; Kneisel, 1999). At boreholes in the nearby Muragl rockglacier at an elevation of about 2550 m ASL (i.e. 100 m lower than the forefield investigated) negative ground temperatures close to 0 °C were found (Vonder Mühll et al., 2003). For the Muragl glacier forefield no boreholes are available so far.

The forefield of Muragl glacier is believed to have been more or less completely ice covered at the Little Ice Age glacier maximum at around 1850 (Maisch et al., 2003). The polythermal structure of the historical/Holocene and present-day cirque glacier give rise to a patchy distribution of permafrost occurrences in the highly elevated sediment bed of the forefield (Kneisel, 1998; Kneisel et al., 2000; Maisch et al., 2003).

9.5.3 Surface velocity field

Horizontal surface displacements of 10 m spacing have been measured by matching aerial photographs from 7 September 1981 with those from 23 August 1994 (Fig. 9-31). Measurement accuracy is estimated to be about 0.02–0.03 m a⁻¹ RMS. The results revealed three zones of significant movement. Zone (a) shows surface speeds of up to 0.55 m a⁻¹ (Fig. 9-31). Speeds in the order of 0.50 m a⁻¹ are found above the creep front towards Muragl rockglacier. The front is advancing horizontally by approximately 0.17 m a⁻¹, even more in parts. There seems to be no marked supply by a creep stream from the upper parts of the glacier forefield.

The same applies for zone (b). There, horizontal movement amounts up to 0.16 m a⁻¹. A potential advance of the corresponding front is within the measurement accuracy. Near Lake Muragl in zone (c), the location of a Holocene push moraine, movement in the order of 0.15 m a⁻¹ can be observed. Adjacent to zones (a), (b) and (c), no significant movement during 1981 to 1994 was detected on the Muragl Glacier forefield.

9.5.4 Conclusions

The horizontal surface displacement rates – some of them surprisingly high – in zones (a) and (b) of the Muragl Glacier forefield (Fig. 9-31) seem, for the most part,

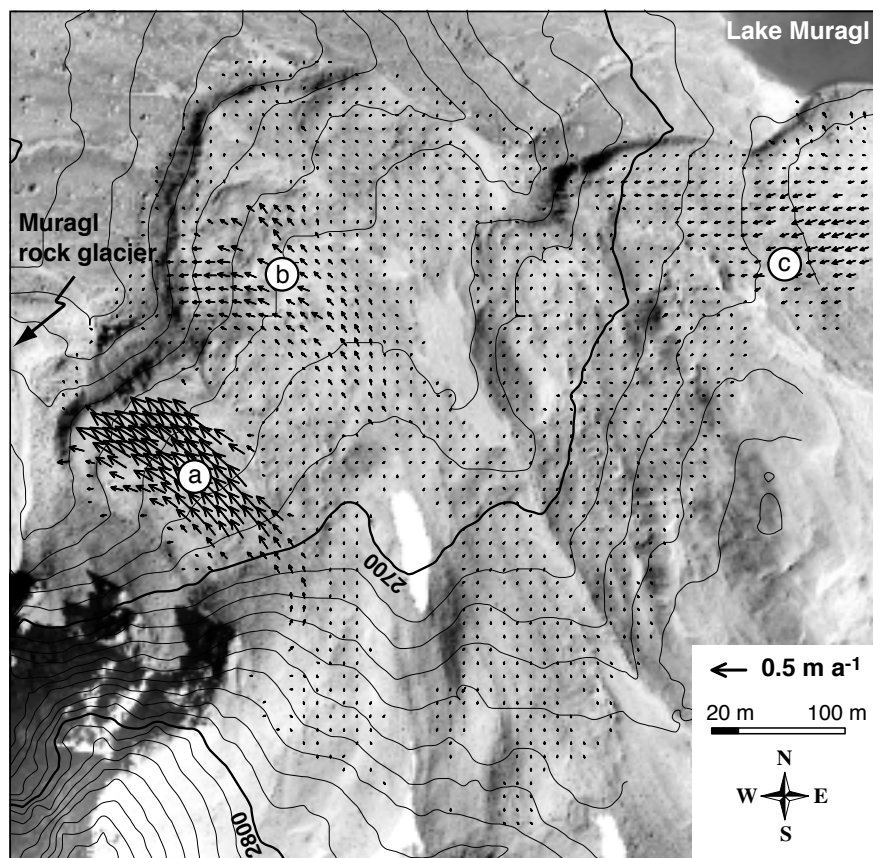


Fig. 9-31 Horizontal surface velocities 1981–1994 on a part of the Muragl Glacier forefield. Orthoimage based on photography swisstopo/flight service (permission BA057212).

to reflect a process of local material mobilization, and not so much the result of material supply over longer distances. These results correspond well with geophysical surveys performed in the area. Geo-electrical soundings for zone (b) gave indications of comparable thin or melting permafrost with an active layer of 2–5 m thickness (Kneisel, 1999). High permafrost temperatures might indeed explain the considerable movement compared to the low slope angle (see Section 9.3). BTS measurements of 1985 (Haeberli, 1992b) and 1996 (Kneisel, 1999) suggest that zones (a) and (b) are the only areas of the forefield sector investigated where permafrost occurrence is likely. (For more details see Kääb and Kneisel, 2005).

The comparably large ratio between surface velocity and advance rate at the front of zone (a) points to a relatively small overall ice content of the body (see Tab. 9-2). Strong oversteepening of the front, as observed in the field, indicates that the movement is restricted, for the most part, to an approximately 10–15 m deep surface layer (see the front of Gruben rockglacier, Section 9.2.3)

Zone (c) is interpreted as part of a push moraine complex (Haeberli, 1979; Haeberli, 1983b). Thus, some downslope creep – back to the area covered by the Little Ice Age glacier – seems reasonable. BTS measurements in the area indicate a likelihood of permafrost; geoelectrical soundings clearly show ice-rich ground (Haeberli, 1992b; Kneisel, 1999; Kääb and Kneisel, 2005).

The good agreement between the photogrammetric measurements presented here and geophysical surveys demonstrates that the investigation of surface kinematics in cold mountain environments can be a suitable tool to detect surface deformation as a proxy for ice-rich permafrost (Kääb and Kneisel, 2005). Combination of

photogrammetry (or other methods of displacement measurement) and geophysics leads to a better understanding of the interplay between ice content and slope deformation (Berthling et al., 1998; Haeberli et al., 1998; Hoelzle et al., 1998; Potter et al., 1998; Konrad et al., 1999; Isaksen et al., 2000; Ikeda et al., 2003; Bucki and Echelmeyer, 2004; Bucki et al., 2004; Lambiel and Delaloye, 2004; Ødegård et al., 2004), and – for the example presented here – to a more sound knowledge of the preservation, or formation, of permafrost in recently deglaciated glacier forefields.

10.1 Kinematics of rock mass creeps at Aletsch and Findelen Glacier, Switzerland

Collaboration

The work on the rock mass creep at Aletsch Glacier was continued and extended as part of the diploma thesis of Mirjam Friedli (Friedli, 2004).

10.1.1 Introduction

The retreat of valley glaciers changes the stress regime of adjacent slopes. Under certain geological circumstances such debuttressing may lead to destabilization and deformation of rock slopes, and to slow rock mass creep among other things (Bovis, 1990; Blair, 1994; Haeberli et al., 1997; Ballantyne, 2002; Matsuoka and Masahiro, 2002). For an overview and nomenclature see Ballantyne (2002). Based on two slope movements of this type it is demonstrated here that the monitoring and modelling techniques applied above to glaciers and rockglaciers can also be used to investigate any other slow mass movement. While glaciers, and perhaps also rockglaciers to a certain extent, consist of an incompressible medium, changes in mass density over time must be considered for rock or debris movements. That requires, in turn, that the kinematic boundary condition (Equations 2-1 and 2-2) be modified. The two-dimensional case may then be written as

$$\frac{\partial z^s}{\partial t} + v_x^s \frac{\partial z^s}{\partial x} - v_x^b \frac{\partial z^b}{\partial x} - \int_{z^b}^{z^s} \frac{\partial v_z}{\partial z} dz - b + \int_{z^b}^{z^s} \frac{\partial \rho}{\partial t} \frac{1}{\rho} dz = 0, \quad (10-1)$$

$$\text{with } v_z^s = v_x^b \frac{\partial z^b}{\partial x} - \int_{z^b}^{z^s} \frac{\partial v_z}{\partial z} dz. \quad (10-2)$$

Rather than applying the relation to ice or ice-rich ground, the mass balance b of a unfrozen mass movement is represented by the addition or removal of mass from the system, such as from deposition or erosion. The term just to the left of the equal sign in Equation 10-1 describes the density change within the vertical column that results in a corresponding change in volume and surface elevation. Density changes, which lead to no geometry change, such as the formation of cavities, are not captured by the kinematic boundary condition for the surface.

In Equation 10-1, change in elevation, horizontal surface velocity and surface slope can be determined on the basis of repeat photogrammetry, other remote sensing techniques, or terrestrial surveying. The resulting term from the kinematic boundary condition that cannot be further resolved using these techniques (i.e. $b+v_z^s+\Delta\rho$), is

the sum of (1) mass changes, (2) density changes, (3) three-dimensional straining, (4) the effect of the differences between basal speed and surface speed, and (5) the effect of non-parallelism between a kinematic bedding plane and the surface. For the studies below it is assumed that processes (4) and (5) dominate over processes (1), (2), and (3), and the latter are neglected for this reason. Under this assumption the resultant term $b+v_z^s+\Delta\rho$ might mainly reflect the topography of a basal horizon under the creeping rock mass.

10.1.2 A rock mass creep at Aletsch Glacier

At its present-day terminus, Great Aletsch Glacier (Fig. 1-3) has lost 300 m and more of ice thickness since the Little Ice Age (Fig. 10-1). That drastic loss in support for the valley flanks in combination with over-steepening due to long-term glacial erosion (Ballantyne, 2002) has led to a number of large-scale mass movements in the area (Matsuoka and Masahiro, 2002). To the south-west of the area investigated here, a rock slope failure occurred during the late 1960s to early 1970s (Fig. 10-1) (SANW, 1982).

Figure 10-2 depicts the horizontal velocity field between 6 September 1976 and 2 October 1995 as determined from orthoimage matching (for method see Section 4.4). Surface displacement over the observational period amounts to 2 m in total (see also Kääb, 2000). Below the 1850 moraine and towards the glacier, measurements were complicated to perform due to surface destruction from moraine erosion. To the south of the area under study, a comparably stable zone can be recognized from random vectors below the significance level. The same applies for the area above the head scarp of the slide. Vertical DTM differences for 1976–1995 indicate a patchy distribution of elevation changes in the zone between the head scarp and the 1850 moraine, including zones of thickness loss of up to -2 m (Fig. 10-3). Uplift in the same order of magnitude clearly dominates below the 1850 moraine. In the freshly exposed moraines adjacent to the current glacier, strong erosion results in thickness loss of up to several metres over the 19 years investigated. Supplementary photogrammetric work including imagery from 1986 and recent terrestrial surveying

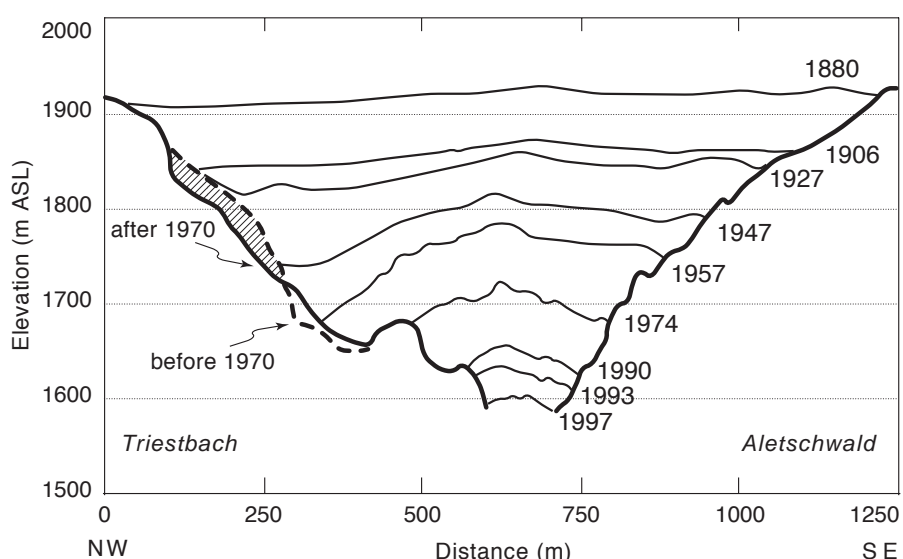


Fig. 10-1 Repeat cross-sections over the tongue of Great Aletsch Glacier, Swiss Alps. Profile location is just outside the lower left corner of Figure 10-2. A rock slope failure to the north-west which occurred during the late 1960s to early 1970s changed the topography. Data provided by M. Aellen and M. Hoelze.

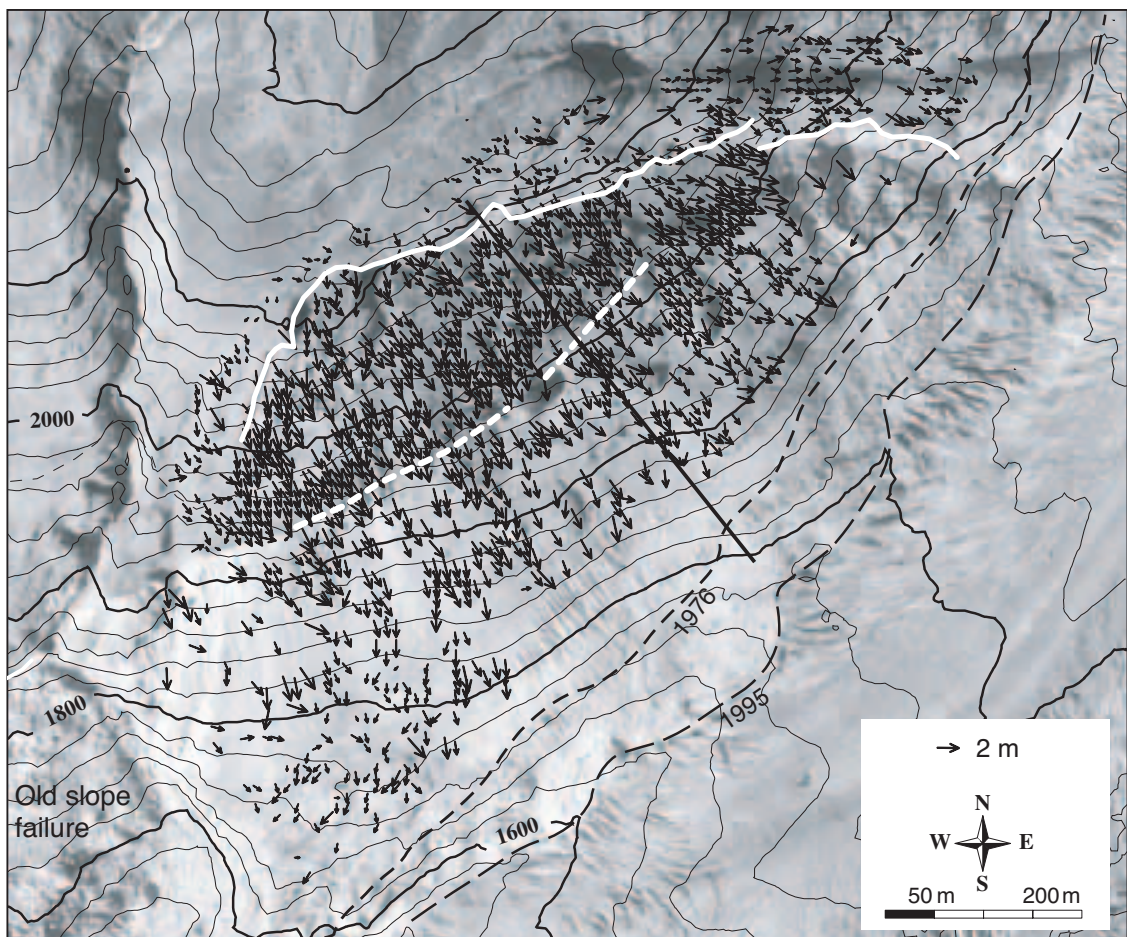


Fig. 10-2

Displacements on a rock mass creep near the tongue of Aletsch Glacier, derived on the basis of orthoimages from 1976 and 1995. In the lower left corner the deposits from a rock slope failure from the late 1960s to early 1970s are located. The solid white line to the north marks the head scarp of the slide; the dashed white line in the centre marks the Little Ice Age (LIA) glacier moraine (about 1850). To the south-east, the glacier boundaries of 1976 and 1995 are marked by black dashed lines. The bold straight line indicates the location of the profile in Figure 10-4. The underlying orthoimage from 1995 is based on aerial photography swisstopo/flight service (permission BA057212). Maximum terrain deformation amounts to 2 m. The retreat of Great Aletsch Glacier from its LIA extent and the accompanying loss of ice thickness (up to 300 m) caused a stress redistribution in the valley flank and related destabilization. See also Fig. 12-5.

of surface markers suggests a step-wise activity of the rock mass creep rather than continuous movement.

For the longitudinal profiles depicted in Figure 10-4, surface topography, thickness changes and horizontal velocities were interpolated, and terms of the kinematic boundary condition calculated. Due to the significance level of at least 0.03 m a^{-1} for the vertical and horizontal displacements, the results should not be interpreted in great detail.

The changes in elevation and the horizontal speeds for the profiles of Figure 10-4 reflect the overall characteristic discussed above. Horizontal speed is largely constant along the profile. Thickness loss prevails in the upper part, surface uplift in the lower part. The high frequencies of the mass-advection term $v_x^s \cdot \partial z^s / \partial x$ show some correlation with the observed elevation changes, suggesting a deep-seated sliding process with the surface topography passively riding on it (see also Figure 4-17).

In the upper part of the profile, between the head scarp and the LIA moraine, the basal slope might be up to 35° or more (from $(b + v_z^s + \Delta\rho)/v_x^s = 0.6$), i.e. steeper than

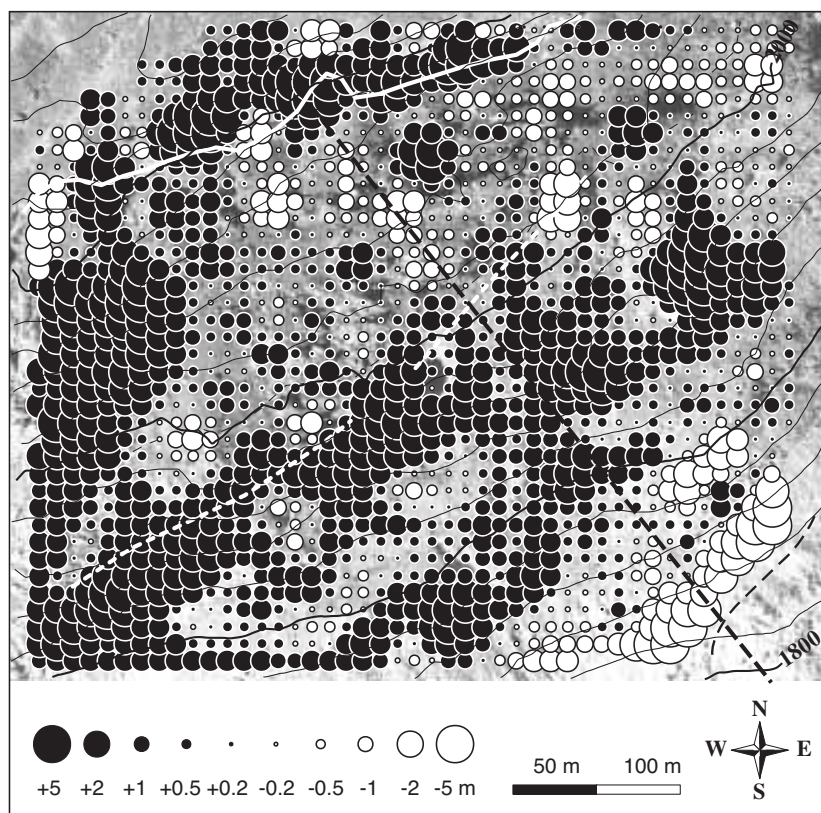


Fig. 10-3 Vertical elevation changes between 1976 and 1995 on the Aletsch rock mass creep (see Figure 10-2).

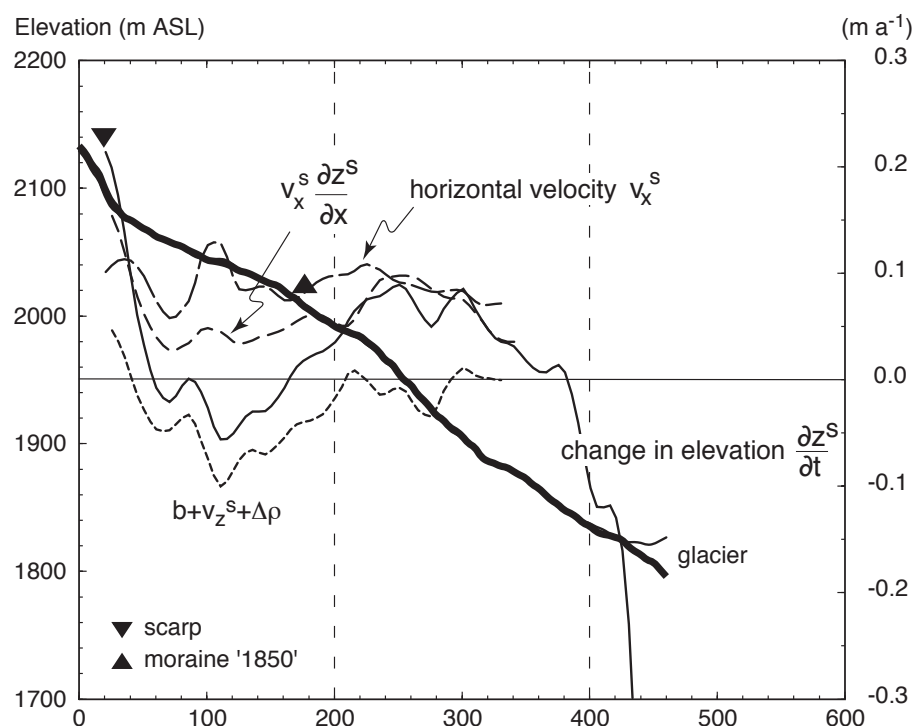


Fig. 10-4 Aletsch rock mass creep. Longitudinal profile of surface, horizontal and vertical velocities, and derived kinematic quantities, 1976–1995. The data are interpolated from the photogrammetric data presented in Figures 10-2 and 10-3. For a description see text. Profile location is given in Figure 10-2.

the surface slope of roughly $20\text{--}25^\circ$. In the lower part, the basal slope is approximately 0° , the surface slope $30\text{--}40^\circ$. Thus, a concave shape of an unspecified basal slide horizon can be deduced at a significant degree.

10.1.3 A rock mass creep at Findelen glacier

As in the case of the rock mass creep at Great Aletsch Glacier, ice thickness loss in the order of 100 m since the LIA has led to destabilization of a rock mass of several million m^3 at Findelen Glacier (local name of the site is Rimpfischwäg). The surface velocity field (Fig. 10-5) and surface elevation changes (Fig. 10-6) have been derived automatically based on aerial photography from 2 September 1985 and 2 September 1999. Horizontal speeds amount to 0.35 m a^{-1} with a highly coherent velocity field with small spatial gradients over large sectors. At the western and eastern margins of

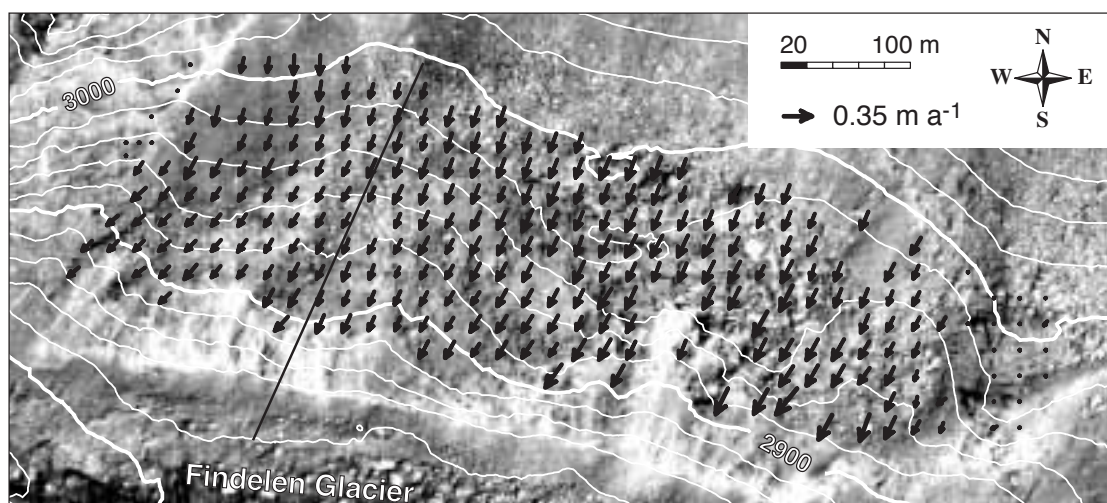


Fig. 10-5 Displacements on a rock mass creep near Findelen Glacier, Swiss Alps, derived on the basis of orthoimages from 1985 and 1999. The black straight line indicates the location of the profile shown in Figure 10-7. Underlying orthoimage of 1999, based on aerial photography © swisstopo/flight service. Maximum terrain deformation amounts to 0.35 m a^{-1} . The retreat of Findelen Glacier since the Little Ice Age (ca. 1850) and the corresponding loss of ice thickness by up to 100 m caused a stress redistribution in the valley flank and related destabilization.

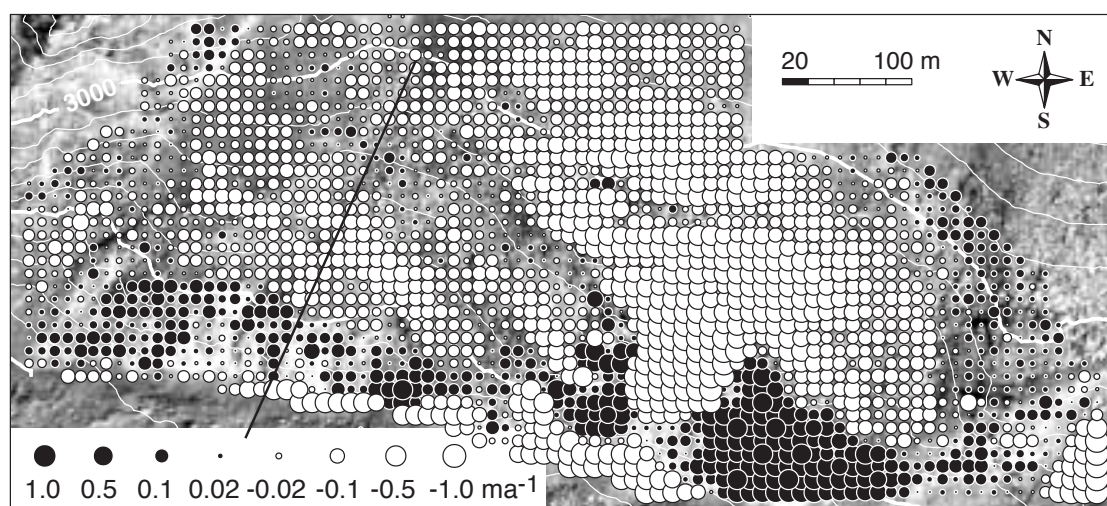


Fig. 10-6 Vertical elevation changes between 1985 and 1999 on the Findelen rock mass creep (see Fig. 10-5).

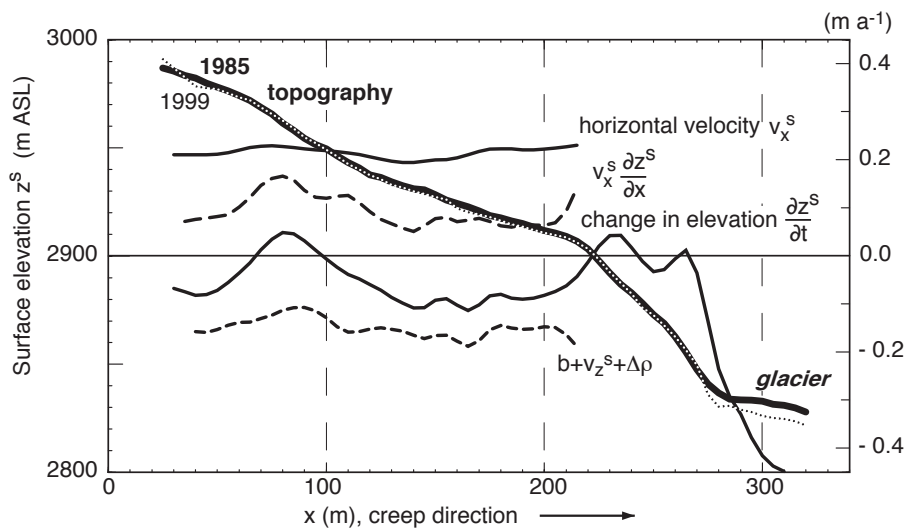


Fig. 10-7 Findelen rock mass creep. Longitudinal profile of surface, horizontal and vertical velocities, and derived kinematic quantities, 1985–1999. The data are interpolated from the photogrammetric data presented in Figures 10-5 and 10-6. For a description see text. Profile location is given in Figure 10-5.

the rock mass creep, velocities sharply decrease to zero values, indicating a distinct marginal shear zone. Surface lowering of up to -1 m a^{-1} prevails on top of the moving mass, while surface uplift in the same order dominates at the steep moraine front towards the glacier. A transverse pattern of alternating zones of elevation losses or constant elevations can be detected for the western part of the slide, which indicates individual lamellas of the moving mass.

A longitudinal profile of interpolated surface geometry, horizontal speed and elevation changes was analyzed in the same way as for Aletsch Glacier (Fig. 10-7). Due to the large change rates on the Findelen rock mass creep, the signal-to-noise ratio of the results is much improved, compared with the Great Aletsch rock mass creep. The accuracy of individual surface displacements or elevation changes is estimated to be about $0.02\text{--}0.03 \text{ m a}^{-1}$ RMS. The mass-advection term $v_x^s \cdot \frac{\partial z^s}{\partial x}$ is almost perfectly parallel to the observed elevation changes, clearly indicating a deep-seated movement on a certain basal horizon. The resultant term of the kinematic boundary condition $(b + v_z^s + \Delta\rho)$, which summarizes mass balance, density change, straining and non-parallelism between surface and basal slope, is primarily attributed to the latter effect from basal slope. The slide surface shows no visual signs of erosion (i.e. $b \approx 0$) and the longitudinal change in horizontal speed is almost zero (i.e. $\partial v_x / \partial x \approx 0$). No statements can be made about density changes, but it appears very unlikely that they could result in up to -0.2 m a^{-1} of vertical change at the surface within a few years. In the model, basal velocity is kept equal to the surface velocity (see Conclusions 10.1.4, below). Under these assumptions the basal slope of the mass movement can be estimated to be about 35° . The surface slope is slightly higher in the upper part, resulting in a relative uplift. In the lower part, above the moraine front, the surface slope is about 15° . The constant overall basal slope points to a predominantly uncurved basal horizon. The superimposed small undulations in the term $b + v_z^s + \Delta\rho$ appear to be above the significance level and might reflect underground topography, or some variations in basal speed, local straining or density changes.

10.1.4 Conclusions and perspectives

The photogrammetric investigations and numerical analyses of this study reveal significant differences between the two rock mass creeps near Aletsch and Findelen Glaciers. The Aletsch rock mass creep seems to represent the movement of partially disintegrated material packages. Both the surface velocity field and the elevation changes show a patchy distribution. The analyses clearly indicate a certain deep-seated movement with a concave basal horizon (Fig. 10-8, left panel). Such an estimation corresponds well with the geological structure in the area. Steep falling schists are found above the head scarp, and amphibolites with a rather flat surface are visible to the south-west of the slide (see small and erratic vectors in Figure 10-2).

Findelen rock mass creep, on the other hand, appears to move largely as one block on a rather even basal horizon (Fig. 10-8, right panel). Some minor internal gradients can, however, also be recognized. Particularly striking is the very sharp velocity gradient at the lateral margins of the slide towards stable terrain. Here, the speed changes from the decimetre-order to zero within a few metres. The sliding speeds on Findelen rock mass creep are significantly higher than at the Aletsch site. Despite the comparably high speed, the surface on the Findelen slide was perfectly preserved in the period 1985–1999.

The assessment of the basal topography performed here using the kinematic boundary condition at the surface depends on assumptions about (i) mass change, (ii) density change, (iii) straining and (iv) basal speed. In the calculations, the three first were set at zero, and the basal velocity was set at the surface velocity. For mass and density changes as well as straining, the zero-assumption might be reasonable over the short time periods considered here, or might to a certain extent be estimated on the basis of photo- and field-interpretation. More care is presumably necessary for estimating the basal velocity. Even if the latter is large, i.e. the moving mass is assumed to predominantly slide, it will in reality not completely equal the surface speed. Introducing a basal speed lower than the surface speed linearly reduces the basal slope obtained (see Eq. 10-2).

The test studies support the application of the combined monitoring and modelling approach of surface kinematics to further mass movements (see e.g. Casson et al., 2003; Delacourt et al., 2004). For demonstration purposes the calculations were performed for selected profiles only (one-dimensional). Actually, the method is an area-wide one if fed with photogrammetric data and the two-dimensional form of the kinematic boundary condition (Kääb and Funk, 1999; Kääb, 2001). As already

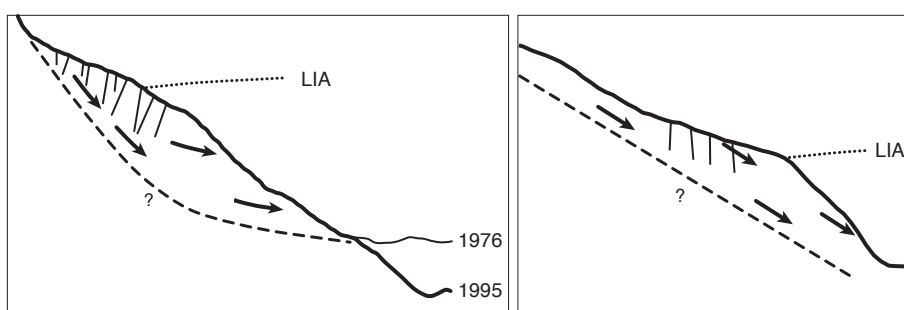


Fig. 10-8 Schemes of the kinematics of Aletsch rock mass creep (left) and Findelen rock mass creep (right) deduced from the profiles shown in Figures 10-4 and 10-7, respectively. LIA: Little Ice Age maximum extent of the respective glaciers. The broken line depicts the suggested form of the basal horizons.

concluded for rockglaciers (see Section 9.4.8), the combination of photogrammetric monitoring and terrestrial high-precision surveying seems to be especially promising. The latter permits the accurate determination of the slide dynamics at selected points or profiles (e.g. Howind and Schmitt, 2001), while photogrammetry provides an overview and ensures spatial representativity. Corresponding efforts are discussed for the Aletsch slide in Friedli (2004). Last but not least, the monitoring and modelling methods presented might gain substantial value if they are combined with geological surveys and geophysical soundings.

The combination of the techniques discussed in Parts II and III of this work enables complex tasks to be solved which arise from the investigation of mountain glaciers and permafrost creep. In this Chapter 11, concepts are presented for satellite-derived glacier inventorying, in the following Chapter 12 space- and airborne assessment of glacier and permafrost hazards. The schemes described are well-tested procedures and should be seen as suggestions. Modifications of the workflow are particularly dependent on the data availability and will need to be in line with the specific results required.

Collaboration

The workflow for glacier inventorying includes work by Frank Paul (Paul, 2004).

11.1 Scheme

Due to difficulties in site access and in order to efficiently cover large areas, regional- or global-scale glacier inventorying has to rely heavily on satellite data (Haeberli, 1998; Haeberli et al., 2000) and requires the extensive application of automatic procedures (e.g. Paul, 2002b; Paul, 2002a; Paul et al., 2002). A typical workflow for (repeat) regional-scale glacier inventorying from (mainly) optical satellite data is shown in Figure 11-1.

Input and output data, or processing steps, comprise:

- *Image pre-processing*, such as destriping, filtering, and other radiometric and geometric corrections.
- *Orientation / georeferencing*: application of the geometric sensor model and set-up of the transformation image-to-ground, and viceversa (Chapter 2).
- *DTM generation*: if the satellite data include along-track or cross-track stereo data, a DTM can be constructed directly (Section 3.4.1). Alternatively, the DTM – necessary for orthoprojection of the image data – can also originate from the SRTM, maps, InSAR, photogrammetry or others (Sections 3.3 and 3.4).
- *Orthorectification* of the applied imagery is necessary for multitemporal applications and for overlay with other data.
- *Multispectral classification* provides surface cover classes such as bare ice, firn and snow (e.g. Fig. 11-2; Section 5.4) (e.g. Hall et al., 1988; Williams et al., 1991, Paul, 2004). Multidimensional classification is necessary for more complex surface cover such as debris-covered ice (Chapter 6) (Paul et al., 2004). The classification may be accompanied by further image correction, for instance due to atmosphere or illumination. Inclusion of SAR data might support, for instance, discrimination of snow facies (Section 5.2).

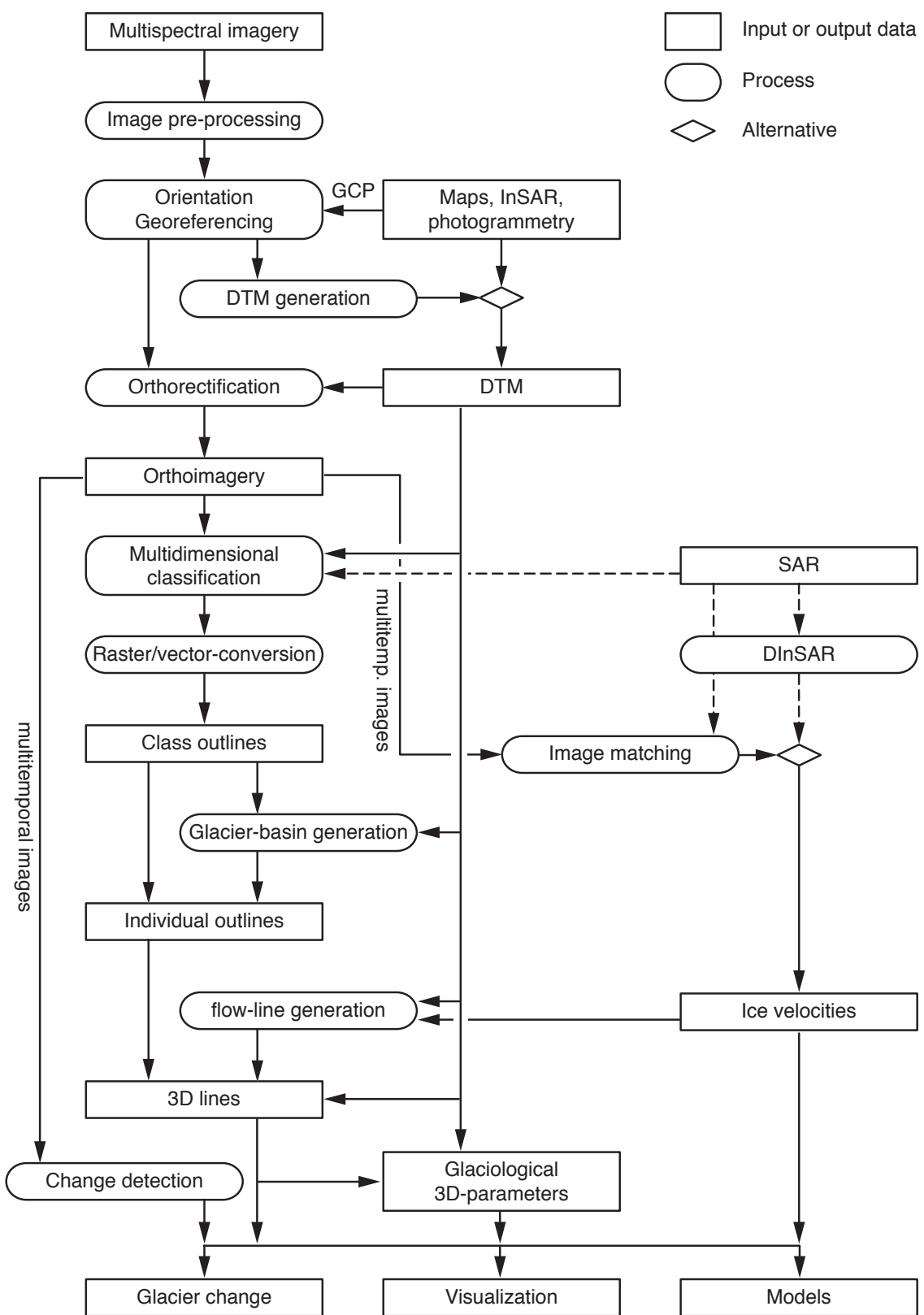


Fig. 11-1 Schematic workflow for (repeat) glacier inventorying from spaceborne optical imagery.

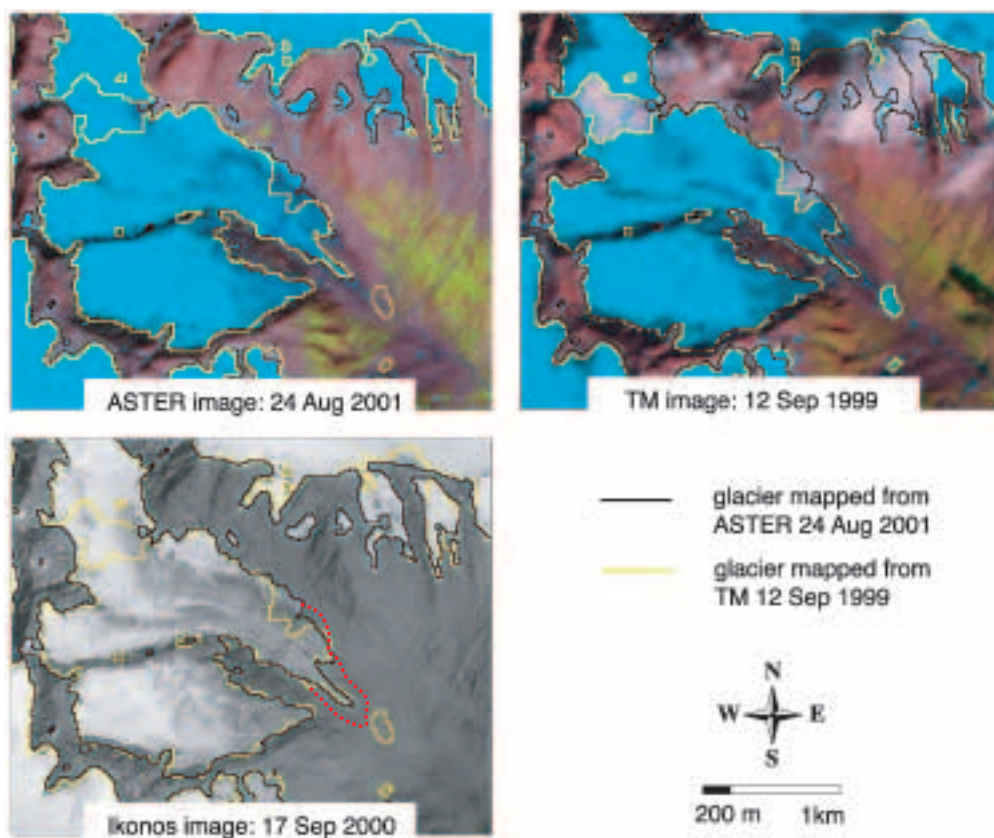


Fig. 11-2 Glacier outlines in the Chelenalp valley, Swiss Alps, as mapped automatically from an ASTER image of 24 August 2001 and a Landsat TM image of 12 September 1999. The debris-covered tongue of Chelenalp gletscher is manually delineated from an Ikonos image of 17 September 2000 (red dashed line). Upper left image: RGB-FCC of ASTER bands 4 3 2, 15 m resolution. Upper right image: RGB-FCC of TM bands 5 4 3, 30 m resolution. Lower left image: Ikonos panchromatic, 1 m resolution. Yellow line: glacier outline automatically computed from a TM 4/5 ratio. Black line: glacier outline automatically computed from an ASTER 3/4 ratio. Largest differences between the TM and the ASTER glacier mapping are due to snow remains in 2001 and clouds in 1999. Largest differences of the TM and ASTER glacier mapping compared to the Ikonos image occur for debris-covered ice which is not detected from the multispectral ratios, but can to some extent delineated manually from the high-resolution Ikonos image.

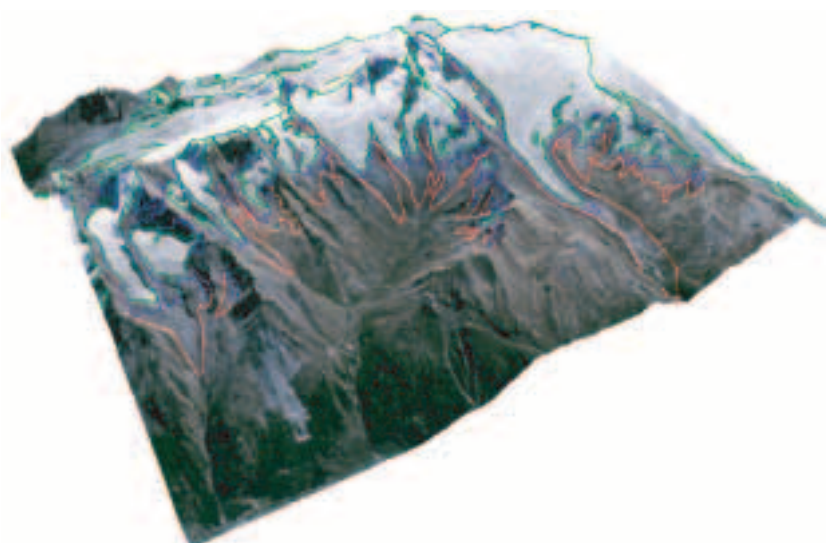


Fig. 11-3 Oblique view of the Täsch valley and Mischabel range, Swiss Alps. Red lines indicate the reconstructed glacier outlines of approx. 1850 (Maisch et al., 1999b); blue lines indicate the glacier outlines of 1973 (Maisch et al., 1999b). The 1998 glacier outlines (green) are automatically derived from Landsat TM multispectral imagery. The underlying surface is an IRS/TM IHS-fusion draped on the DHM25 by swisstopo. (After Kääb et al., 2002b; Paul, 2004).

- *Glacier-basin generation* or generation of any other spatial subdivision of the classified area, and subsequent intersection of such masks with the raw class outlines provides meaningful outlines, e.g. outlines of one individual glacier (Paul, 2002b; Paul et al., 2002; Paul, 2004). In most cases glacier-basins will have to be digitized manually. A DTM might assist such work, or even contribute to partial automation of the process.
- *Flow-line generation*: many glaciological parameters, such as glacier length, refer to central flow lines. Generation of such flow lines can be supported by a DTM or velocity vectors.
- *3D lines*: intersection of the 2-dimensional classification outputs with a DTM provides 3-dimensional lines (e.g. Fig. 11-3).
- *Image matching or DInSAR*: if repeat optical or SAR imagery is available, image matching or DInSAR can reveal ice speeds or velocities (Sections 4.4 and 4.5).
- *Glaciological parameters*: a number of 2- and 3-dimensional glaciological parameters can be derived from the results above, such as glacier length, glacier area, elevation range, aspect, or hypsography (Kääb et al., 2002b; Paul, 2004).
- *Glacier changes* may be derived from repeat application of the above procedure, but also directly from change detection techniques (Fig. 11-4; Section 6.3).

Figures 11-3 and 11-4) show examples of two typical outcomes of the new satellite-derived Swiss glacier inventory, set up for the most part according to the workflow presented here.

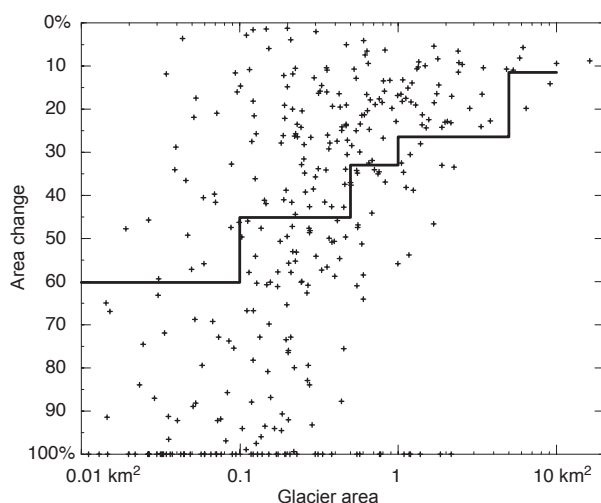


Fig. 11-4 Glacier area changes 1973–98 for a subsample of debris-free glaciers in the Valais and Bernese Alps, Switzerland. The 1973 data are from map, field and aerial photo interpretation (Maisch et al., 1999b), the 1998 data from Landsat TM imagery. The changes are also averaged for different area classes (bold line). The smaller the glaciers, the greater the variance in their behaviour and the higher their average percentage area loss. (See Paul (2004) for a more complete data set).

Collaboration

This chapter represents a shortened version of Kääb et al. (2005a). The results were prepared in collaboration with Christian Huggel, Luzia Fischer, Samuel Guex, Frank Paul, Nadine Salzmann, Stefan Schlaefli, Kostia Schmutz, Demian Schneider (all Department of Geography, University of Zurich), Isabelle Roer (Department of Geography, University of Bonn), Tazio Strozzi (Gamma Remote Sensing, Berne) and Yvo Weidmann (University of Applied Sciences, Muttenz, Basel).

12.1 Introduction

The glacial, paraglacial and periglacial environment is defined, respectively, as the zone of glaciers or their action, the non-glacial zone directly conditioned by glaciation or deglaciation, and the non-glacial zone in cold regions with frost action being the predominant geomorphic process. Disasters originating in that environment can cause thousands of casualties in one event. Related damages or mitigation costs are on the order of several 100 million Euro as a long-term annual average global sum (Kääb et al., 2005c). Glacier and permafrost hazards (here used as a synonym for glacial, peri-, and paraglacial hazards) in high mountains include glacier- and permafrost related floods, stable and unstable glacier length changes as well as glacier fluctuations, glacier- and permafrost-related mass movements, permafrost thaw settlement and frost heave, and hazards from glacier-clad volcanoes (Tab. 12-1). Often, combinations of these (and other) processes lead to the most severe glacier and permafrost catastrophes. Whilst above direct glacier and permafrost hazards are very palpable, so too are indirect hazards, such as changes in dry-season river flows, adverse effects on mountain tourism, and related socio-economic consequences.

Assessment and management of glacial, peri- and paraglacial hazards require the application of modern integrative earth-observation techniques for a number of reasons:

- Typically, related hazard source areas are situated in remote high-mountain regions, often difficult to access physically for topographic, political and/or security reasons (e.g. Caucasus, Colombia, Central Asia, Cashmere, etc.).
- The remote location of most glacial hazard sources, the potential process interactions and chain reactions, and the far reach of some of the high-mountain hazards require remote sensing sensors capable to cover large areas at once.
- Climate change induces disturbance in glacier and permafrost equilibrium and can shift hazard zones beyond historical knowledge. In addition, human settlements and activities increasingly extend towards endangered zones in many regions. As a

result, historical data alone are not sufficient any more for hazard assessments and have to be combined with new observation and modelling approaches (Grove, 1987; Evans and Clague, 1994; Haeberli and Beniston, 1998; Richardson and Reynolds, 2000b; Huggel et al., 2004a; Kääb et al., 2005c).

- Due to the rapid change of high-mountain environments, hazard assessments shall be undertaken routinely and regularly, combined with continuous monitoring. Remote sensing is particularly suited for both regular and rapid observation.

Recent developments in air- and spaceborne remote sensing open up new possibilities for the assessment of natural hazards in general (Mantovani et al., 1996; Sabins, 1997; Ostir et al., 2003) and glacier and permafrost related hazards in particular (this volume and Huggel, 2004; Quincey et al., 2005). Remote sensing will therefore substantially gain importance for such works in the near future. Obstacles to the full exploitation of the remote sensing potential for high-mountain hazard assessments are of technical nature, on the one hand, but also due to the lack of expertise dissemination, on the other hand. This chapter provides an overview of remote sensing methods available for glacier and permafrost hazard assessments in mountains.

12.2 Method overview

12.2.1 Important factors

The applicability of remote sensing for high-mountain hazard assessments is predominantly governed by the following factors:

- The *spatial resolution* of the sensor decides about the degree of detail that can be detected from the data. Often, fine resolution is required to assess important parameters of glacier- and permafrost hazards (e.g. discrimination of debris versus rock surface). In order to characterise spatial resolution, we use here the terms high resolution (< 5 m) and medium resolution (5–100 m). Low (100–1000 m) and very-low resolution systems (> 1000 m) are not covered in this overview (see also Section 2.3).
- The *spatial coverage*, i.e. the ground area or width of the ground track sensed is roughly related to the spatial resolution of the sensor through technical constraints e.g. concerning detectable level of incoming signal strength (sensor noise-level), or onboard-recording and down-link capacities. While, for instance, medium-resolution Landsat, IRS, or ASTER data are very useful for first-order regional-scale hazard assessments, high-resolution IKONOS, QuickBird, or Orbview data are preferable for detailed local-scale investigations. SPOT-5 data (up to 2.5 m resolution, 60 km swath width) combine both advantages to some extent.
- The *temporal resolution*, i.e. revisit time of the remote sensing system has to be in accordance with the rate of hazard development, or the changes observed (see also Section 2.3). The temporal resolution of a system is among others connected to its spatial coverage, and to the pointability of the sensor, e.g. how far the sensor can be rotated in cross-track direction in order to cover areas far off the ground-projected track. As an example, the ASTER visible and near infrared (VNIR) instrument can be pointed up to $\pm 24^\circ$ allowing for repeat imaging as frequently as every two days (and better in high latitudes) for urgent priorities. For instance,

annual resolution might be sufficient to monitor the development of proglacial lakes, whereas repeat times of a few days are required for disaster management in connection with ice-avalanche or landslide induced temporary lakes.

- The *timing* of data acquisition has to be under control of the user, or to coincide with the user needs by chance. The probability for the latter increases with temporal resolution. Timing is of particular importance when remote sensing data are required at a given repeat cycle (e.g. early warning, seasonal restrictions) or when rapid response is needed (e.g. search and rescue operations, disaster management).
- The *section of the electromagnetic spectrum* available determines among others the surface parameters that are recorded at the sensor and the dependence of the sensor to weather and illumination conditions (e.g. all-weather and night-time capability of microwave sensors, night-time capability of thermal infrared sensors) (see also Chapter 5).
- *Stereo, interferometric or ranging capability* of the remote sensing system enables the computation of terrain elevations, often a crucial prerequisite for the analysis of high-mountain hazards in the absence of appropriate topographic maps (see also Chapter 3).
- *Usability of data* for the user, with respect to e.g. existence and access to data archives, speed of on-demand acquisition, speed of delivery, simplicity of data formats and size, financial resources as well as hard- and software resources, and processing and analysis knowledge of the user.

12.2.2 Airborne remote sensing

Airborne remote sensing technologies that are applicable for high-mountain hazard assessments include the following techniques (cf. Tab. 1-1):

- Hard-copy or digital aero-photogrammetry based on frame imagery or linear array CCD sensors (see Sections 3.3.1, 3.3.2 and 3.3.5).
- Airborne hyperspectral remote sensing allows for detailed spectral analysis of the ground surface (e.g. lithology, vegetation, lake water) (e.g. Keller et al., 1998), but is so far little applied directly for mountain hazard assessments due to the high data acquisition costs and the large expertise required for data analysis.
- Airborne laserscanning (see Section 3.3.3).
- Airborne synthetic aperture radar (SAR) (see Section 3.3.4).

Beside many advantages of airborne remote sensing such as level of detail and direct customer control, this class of platforms is often not applicable for areas where major topographic, political, security or financial restrictions are involved. Satellite sensors overcome these restrictions in parts.

12.2.3 Spaceborne remote sensing

Spaceborne remote sensing technologies suitable for high-mountain hazard assessments include the following techniques (cf. Tab. 1-1):

- Optical multispectral spaceborne imaging is often used for detecting hazard source areas and terrain changes, and for mapping of endangered zones (e.g. Buchroithner et al., 1982; Kääb et al., 2000a; Huggel et al., 2002; Kääb et al., 2003d; Huggel et al., 2004c; Liu et al., 2005; Silverio and Jaquet, 2005) (see Chapters 5 and 6).

- Satellite optical stereo (see Section 3.4.1)
- Interferometric SAR (InSAR) (see Sections 3.4.2 and 4.5).

Here, we do not cover terrestrial remote sensing methods since the focus of this chapter is on remote areas. However, it should be stressed that, for instance, terrestrial photogrammetry (Brecher and Thompson, 1993; Kaufmann and Ladstädter, 2004; Pitkänen and Kajutti, 2004), touch-less laser rangers, terrestrial laser scanning (Bauer et al., 2003; Janeras et al., 2004) and terrestrial SAR (Tarchi et al., 2003) can be highly valuable techniques for detailed monitoring tasks (see also Sections 3.4.3 and 4.6).

12.2.4 Image classification

The most common application of remotely sensed image data for high-mountain hazard assessment consists in the interpretation and classification of the image content. Thereby, both the spectral image information and the spatial context of such information are exploited. The technologically simplest form of image analysis (though by no means the least important and easiest analysis!) is the manual mapping of features of interest from the imagery available (Fig. 12-1). In particular under conditions of difficult topography and weak optical contrast, or for highly complex assessment tasks, manual image segmentation might be superior to semiautomatic and automatic techniques. A number of image enhancement and fusion techniques are available to facilitate manual interpretation (e.g. Sections 5.4 and 6.1).

However, for rapid, repeated, and/or large-area quantitative applications, automatic image classification is able to offer valuable support (see Section 5.4). Archived data sets are an invaluable source for comparison between past and present situations (Figs. 12-2 and 12-3) (e.g. Kääb and Haeberli, 2001; Kääb et al., 2003d; Silverio and Jaquet, 2005).

Mountain permafrost, a purely thermal phenomenon, can hardly be remotely sensed in a direct way, but related indicators such as rockglaciers, thaw lakes, polygons, etc. can be detectable in remote sensing data (e.g. Lewkowicz and Duguay, 1999; Frauenfelder et al., 2005; Frohn et al., 2005).

Many glacier- and permafrost-related hazards are connected to terrain changes. Thus, multitemporal applications are of particular interest for assessing high-mountain hazards (e.g. Fig. 12-3). Beside the measurement of outline changes, elevation changes and terrain displacements as discussed in the following sections, a group of change detection techniques are applied (see Section 6.3).

In the microwave spectrum, analysis of the backscatter, the coherence of the SAR interferometric phase, and the signal polarisation is able to support delineation and characterisation of the terrain surface and its dynamic (see Section 5.2). Analysis of the microwave backscatter is, however, seldom used in the context of high-mountain hazards due to the complex electromagnetic nature of the ground reflection and topographically- and sensor-induced geometric problems such as layover and radar shadow. Beside the backscatter amplitude, also interferometric coherence or its spatio-temporal changes (Weydahl, 2001) can be exploited. For instance, interferometric coherence points to stable terrain, whereas its loss over time may hint to changes in surface conditions such as from terrain destruction (cf. Fig. 4-16). Furthermore, the signal (de-)polarisation can be analysed. (See Section 5.2).

Particularly promising for hazard assessment and disaster management is the (multitemporal) fusion of optical and SAR data because it is able to combine the advantages of different sections of the electromagnetic spectrum (Ostir et al., 2003).

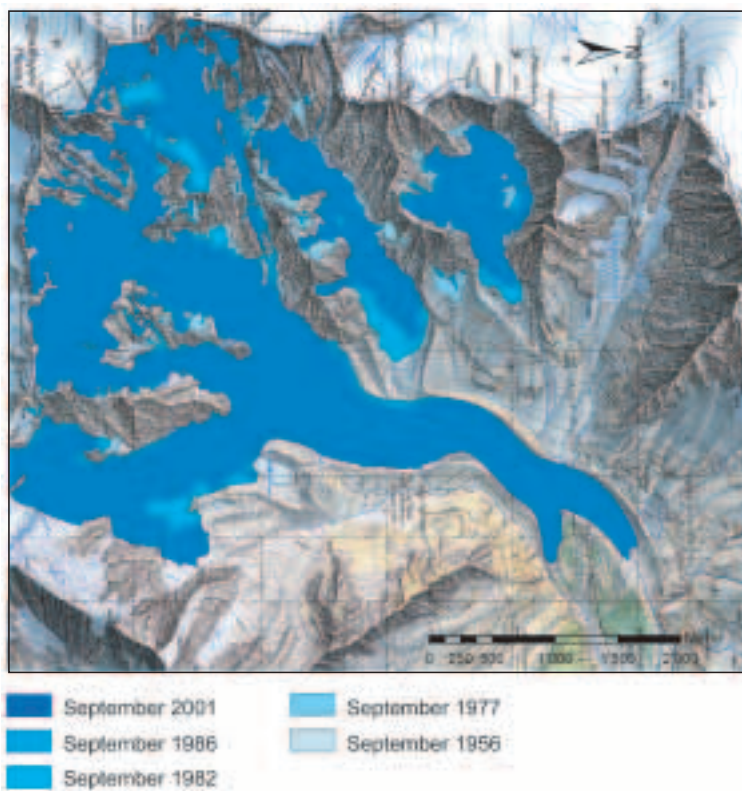


Fig. 12-1 Changes in glacier extent in the Monte Rosa east face as derived from orthophotos between 1956 (light blue) and 2001 (dark blue). In the recently de-glaciated zones drastic mechanical, thermal, hydraulic and hydrological changes affect the frozen and unfrozen rock and debris deposits, and cause increased rock fall activity. (From Fischer, 2004). Background map by swisstopo (permission BA057212).

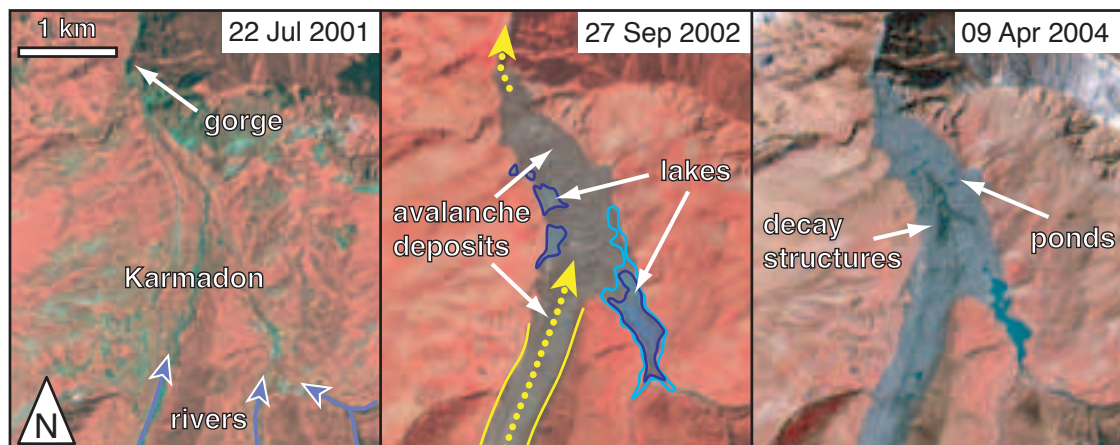


Fig. 12-2 ASTER FCCs of the Karmadon area from before (left) and after (middle and right) the 20 September 2002 Kolka/Karmadon rock-ice avalanche disaster, North Ossetia, Caucasus. During this event, a rock-ice avalanche of several million m³ from the north face of the Kazbek massif sheared off the entire Kolka glacier tongue. This combined avalanche rushed 18 km down the Genaldon valley. Approximately 100 million m³ of ice and debris were deposited near the village of Karmadon where the avalanche was stopped by a narrow gorge (Kääb et al., 2003d; Kotlyakov et al., 2004; Haeberli et al., 2005; Huggel et al., 2005). The rivers in the area (blue arrows) were dammed by the avalanche deposits and formed lakes (dark blue line: lake extent as of 27 September 2002; light blue line: lake extent as of 22 October 2002). On the 09 April 2004 image, the rock-ice dam showed already distinct melt and decay structures. (See also Fig. 6-9).

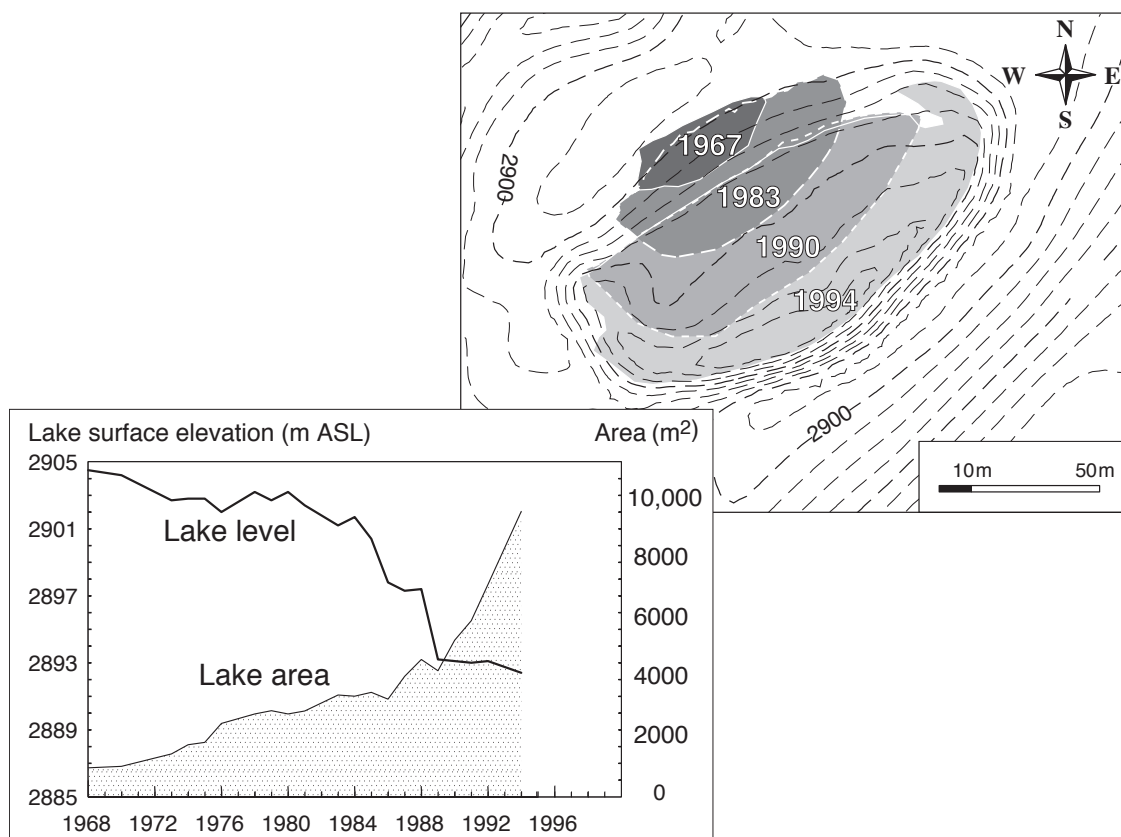


Fig. 12-3 Development of a thermokarst lake on the Gruben rockglacier (see Fig. 6-8) derived from repeat air-photos (from Kääb and Haeberli, 2001).

In that way, for instance, SAR data can bridge gaps in optical time series, which are due to cloud cover. (See Chapter 6).

Accurate co-registration of the repeat data, i.e. identical image and/or ground coordinates for identical (stable) terrain points, is a mandatory prerequisite of any change detection procedure.

12.2.5 Digital terrain models

Satellite stereo

DTMs represent the core of any investigation of high-mountain hazards, because many high-mountain geomorphologic processes are driven by the topographic energy. Furthermore, DTMs are needed for orthorectification of image data, and thus for accurate georeferencing and co-registration with other or repeat data. An efficient spaceborne way to generate such DTMs for nearly any place on the Earth is satellite along-track stereo from sensors such as JERS, ASTER, SPOT-5, IKONOS, QuickBird, or Orbview3. (See Section 3.4.1).

However, large errors in DTMs derived from optical satellite stereo can occur due to the following reasons:

- steep flanks facing away from the oblique stereo sensor (e.g. northern slopes are strongly distorted or even hidden in the back-looking stereo channel for the descending ASTER),
- particularly rough topography with sharp peaks, that are too small to be clearly matched in both stereo partners, and/or

- insufficient optical contrast (e.g. snow cover).

For methods for dealing with such problems see Section 3.4.1, for applications to high mountain hazards Table 12-1.

Photoclinometry, i.e. the inversion of terrain shading to derive terrain geometry is hardly useful for mountain hazard studies because a constant reflectivity over the terrain is necessary in order to attribute changes in reflection to terrain slope and aspect alone.

Radar interferometry; Shuttle Radar Topography Mission

Sensors in the microwave spectrum are able to overcome limitations connected to optical sensors, namely the weather and sunlight dependency. Interferometric synthetic aperture radar (InSAR) is used to generate DTMs (Sections 3.3.4 and 3.4.2). A particularly interesting campaign for regional-scale hazard assessments is the single-pass Shuttle Radar Topography Mission (SRTM) of February 2000. However, due to radar shadow, foreshortening, layover and insufficient interferometric coherence, the SRTM DTM has significant voids in high mountains. In such cases, we regard the fusion between spaceborne photogrammetric DTMs and the SRTM DTM as a promising approach (Sections 3.4.1, 3.4.2 and 3.5) (Kääb, 2005; Kääb et al., 2005a).

Aerial photogrammetry

Aerial photogrammetry is a particularly important tool for hazard assessments in view of the existing archives of analogue airphotos, which represent an invaluable source to quantitatively compare temporal evolutions (Sections 3.3.1, 3.3.2, 4.2 and 4.4). Due to the large technical knowledge and special equipment needed to handle airborne digital imaging, it is difficult to use this technique worldwide, so far. However, the possibility from digital imaging to generate DTMs and orthophotos nearly in real-time (literally "on the flight") has, in theory, an important advantage in disaster management and response.

Laserscanning (airborne LIDAR)

DTM accuracy similar to the one of airborne photogrammetry can be obtained from airborne laserscanning (or light detection and ranging, LIDAR) – a promising technique for glacier and permafrost monitoring (Section 3.3.3). In terms of flight conditions required, laserscanning is comparable to aero-photogrammetry. The resulting high degree of terrain details represented enables new methods of geomorphometric terrain analysis as well as terrain dynamics analysis. If available – what will be rarely the case in remote areas, though – laserscanning is a method, which should be considered whenever accurate DTMs and elevation changes are required for hazard assessments and disaster management.

12.2.6 Terrain elevation changes (DTM differences)

Terrain elevation changes over time, i.e. vertical differences between repeat DTMs, are indicators for glacial and geomorphodynamic processes such as glacier fluctuations and mass movements. Thus, their detection can be an important step of high-mountain hazard assessment and disaster mapping (Section 4.2 and Tab. 12-1). In general, changes in terrain elevation are derived by subtracting repeat DTMs. If the DTMs compared represent independent measurements, the root mean square error (RMS) of an individual elevation change $RMS \Delta h$ can be estimated from the RMS of the repeat (here: two) DTMs (Etzelmüller, 2000):

$$(RMS \Delta h)^2 = (RMS h_1)^2 + (RMS h_2)^2 \quad (12-1)$$

Special pre- and post-processing procedures help to reach or improve the latter accuracy:

Pre-processing, i.e. procedures beforehand the DTM subtraction: As for all multitemporal analyses, accurate co-registration of the multiple DTMs is a necessary prerequisite to obtain elevation changes free of global systematic errors. The co-registration of the DTMs (and other products) can be assured by orienting the original data as one common, multitemporal data set (Toutin, 1995a; Toutin, 1995b; Aniello, 2003), in particular if the repeat DTMs are produced using the same method (e.g. optical stereo). For instance, repeat satellite or aerial imagery should be oriented as one (multitemporal) image block with common ground control points (GCPs) and all the images connected by (multitemporal) tie points (TPs). If the original sensor model and orientation is inaccessible, or the DTMs have different sources, matching between the individual DTMs to be compared is recommended (Section 4.2).

Post-processing of the elevation differences: Once the raw differences between repeat DTMs are computed it is often necessary to filter the elevation differences obtained, because the noise in the derived differences is larger than in the original DTMs (see Equation 12-1). The task is to define a noise model adapted to the nature of the process under investigation. For instance, thickness changes of a debris-free glacier are expected to show a smooth spatial variability so that a coarse filter might be applied. Coarse filters are less suited for mass movements such as landslides with a high spatial variability and with many secondary local terrain movements overlain, because the filter tends to remove important "real" signals. In general, low-pass filters exist in the spatial domain (e.g. median, medium, Gauss, etc.) or for the spectral domain (e.g. fourier or wavelet) (Section 4.2).

Compared to airborne techniques, elevation changes from repeat satellite stereo can only be measured for a limited number of geomorphodynamic processes due to the reduced accuracy of the according DTMs. Nevertheless, the accuracy obtained might be sufficient to detect and quantify large changes in terrain geometry, such as from avalanche deposits or glacier mass changes (Figs. 8-2 and 12-4) (Berthier et al., 2004).

Sometimes, also differential SAR interferometry (DInSAR) can be used to detect vertical terrain changes. However, strictly speaking this technique does track three-dimensional terrain surface shifts rather than elevation changes at fixed positions. The technique is therefore covered in the following section.

12.2.7 Surface displacements

Terrain movements can directly pose a hazard (e.g. landslides) or provoke follow-up processes, which then develop into hazards (e.g. river damming by a glacier surge). The measurement of terrain displacements from repeat image data can thus support high-mountain hazard assessments (Powers et al., 1996; Kääb et al., 1997; Knizhnikov et al., 1998; Kääb and Funk, 1999; Weber and Herrmann, 2000; Jiskoot et al., 2001; Kääb, 2002; Casson et al., 2003; Delacourt et al., 2004).

Image matching techniques can be applied equally to repeat terrestrial photos, air photos, optical satellite images, SAR images, airborne InSAR, or high-resolution DTMs (Chapter 4). The rate of terrain movement, which can be detected at a statistically significant level of accuracy, depends among others on the image pixel size, the temporal baseline, and the terrain preservation between the repeated data acquisitions. From air and high-resolution satellite images slope instabilities such as rock mass movements, or permafrost creep can be detected (Fig. 12-6). Comparably

fast movements, in particular glacier flow (i.e. rates of tens to hundreds of metres per year), can be sometimes quantified from airphotos, but also from medium-resolution satellite imagery (e.g. Landsat ETM+, ASTER) (Section 4.4).

Differential InSAR (DInSAR) enables measuring slow terrain movement with an accuracy of a few millimetres. Applicability of the method depends on terrain topography and SAR imaging geometry, leading to areas of missing information in layover and shadow, and on preservation of interferometric coherence (Section 4.5). In high mountains the presence of snow and its temporal changes have significant influence on the electromagnetic response in the microwave spectrum. Related interferometric de-correlation effects can be avoided by short temporal baselines,

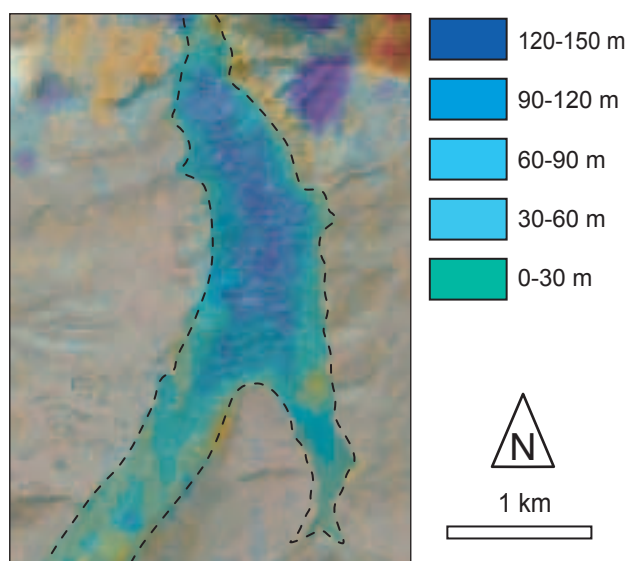


Fig. 12-4 Thickness of the 20 September 2002 avalanche deposits at Karmadon computed from ASTER DTMs of 22 July 2001 and 06 October 2002. The strong elevation changes to the upper right corner are due to errors in the ASTER DTMs in steep slopes. (See also Figs. 6-9 and 12-2).

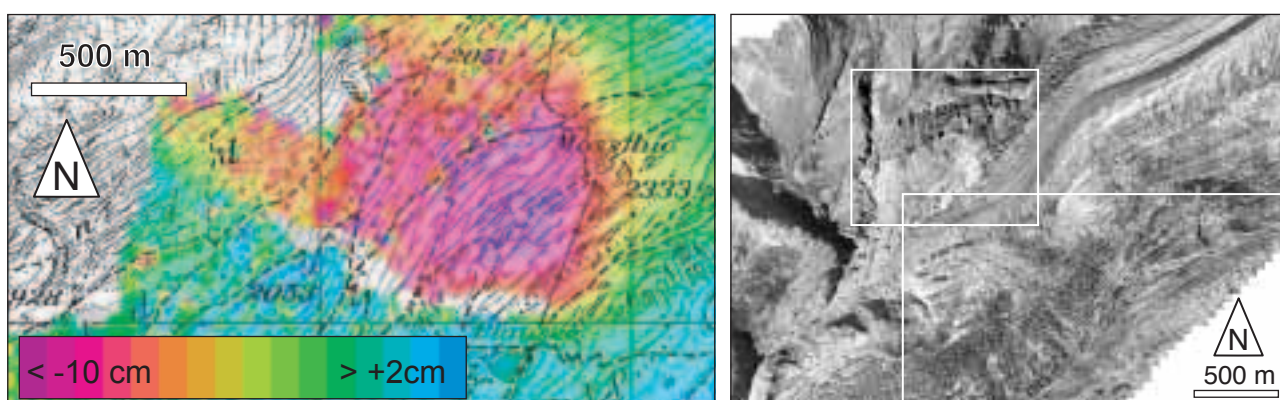


Fig. 12-5 Aletschwald, Swiss Alps. Left panel: displacement magnitude map for a time interval of 1144 days (17 June 1993 - 04 August 1996) derived from repeat JERS SAR data. Displacement direction is assumed to be down-slope to the north-west. As yet the site has not been investigated in detail. However, a number of comparable movements situated nearby and studied already (see lower panel) hint to rock-slope creeping to be the cause for the displacements observed. Right panel: Tongue of Aletsch Glacier with white rectangles indicating the location of this DInSAR study (lower rectangle) and the photogrammetric study Fig. 10-2 (upper rectangle). JERS SAR interferograms processed by Tazio Strozzi, GAMMA Remote Sensing, JERS SAR data courtesy J-2RI-001, © NASDA. Background map by swisstopo (permission BA057212).

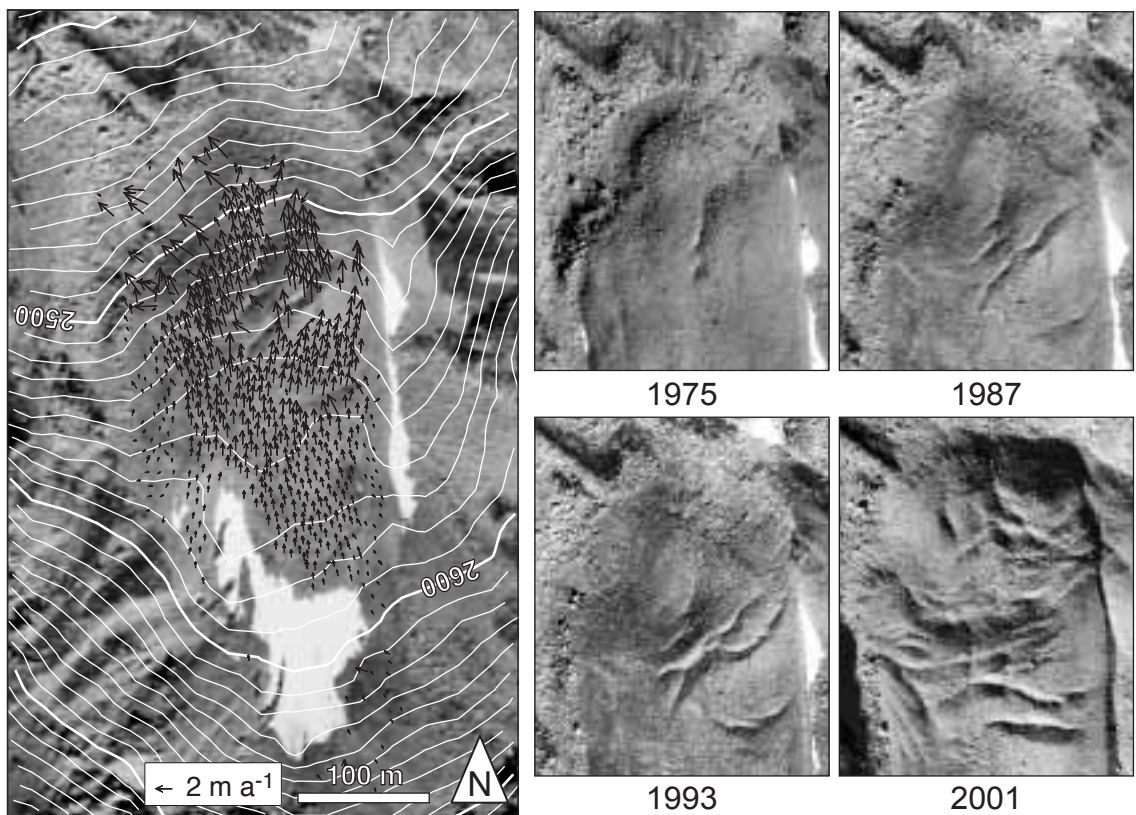


Fig. 12-6 Instability of a rockglacier terminus, Turtmannal, Swiss Alps. Left panel: velocity vectors measured from airphotos of 1987 and 1993; right panels: orthophotos of the terminus section of the rockglacier. Images of 1975, 1987, and 1993 are courtesy of swisstopo (permission BA057212); the 2001 image is a linear array CCD (pushbroom) image taken by the HRSC-A camera, courtesy of Department of Geography, University of Bonn. The rockglacier instability led to enhanced rockfall and required construction of a protection dam (not depicted). (See also Roer et al., 2005b).

when the observed terrain movements are fast enough to be detectable over such short periods. DInSAR directly provides the line-of-sight displacement, i.e. the projection of the actual terrain displacement vector, on the line between terrain point and sensor. Except for high latitudes, where ascending and descending satellite-track azimuths are significantly different, the line-of-sight displacement cannot be well decomposed into horizontal components. The horizontal and vertical displacement components can be separated by combining the line-of-sight displacements measured from ascending and descending orbits, at least in theory. In mountain areas such procedure is often hindered by the fact that slopes which are well visible from the ascending orbit lie in shadow or layover in the descending orbit, and vice versa. The vertical and horizontal components have rather to be estimated or modelled from the type of terrain movement under investigation. Typical DInSAR applications for high-mountain hazard assessments are the detection of rock mass movements, glacier flow and permafrost creep (Figs. 4-16 and 12-5; Section 4.5).

For glacier hazard assessments, DInSAR and optical image matching methods for deriving terrain movement are highly complementary in terms of accuracy and applicability (Section 4.7).

12.3 Detection of hazard sources

A natural hazard can be defined by (a) the kind of physical process involved, (b) the magnitude of the event, and (c) its probability or frequency of occurrence. The detection of potential hazard sources and their characterisation is, therefore, an important first step in assessing glacial, peri- and paraglacial hazards. According to the complex nature of high-mountain processes, multidomain (or multidimensional) classification approaches that integrate spatial, spectral and temporal information are most promising for that task (Section 6.4). No detailed rules for such multidomain classifications can be given due to the variety of specific requirements. In general, however, the combination of a single or repeat DTM(s) with (possibly multitemporal) multispectral data is a particularly powerful tool for detecting potential high-mountain hazard sources.

Selected examples:

- Steep glaciers, a frequent source of ice break-offs and ice avalanches, can be detected on a regional scale through the combination of a multispectral glacier classification with the DTM slope. The result is a map of steep glaciers which are prone to avalanching, i.e. glaciers above a certain slope threshold (Fig. 6-3 right) (Salzmann et al., 2004).
- A texture analysis based on high-resolution satellite (or aerial) imagery combined with DTM slope helps to detect steep, and possibly frozen, debris slopes which may be the source of debris flows (Huggel et al., 2004c).
- Glacier slope, extent of debris cover, thickness changes and ice velocities can help to estimate the evolution of ice-marginal lakes or detecting glacier zones prone to the development of supraglacial lakes (Fig. 6-5) (Paul et al., 2004; Kääb, 2005; Quincey et al., 2005) (cf. Reynolds, 2000).
- Glacier length changes, possibly resulting in a change of ice-avalanche hazard or in the formation of proglacial lakes, can be tracked from multitemporal and -spectral classification (Paul, 2002a; Paul et al., 2004).
- Similarly, the (change in) ice cover on glacier-clad volcanoes can be detected from (repeat) multispectral imagery or aero-photogrammetry. Ice volumes situated on volcanoes can be an important factor for devastating lahars, in particular in connection with volcanic activity (Benson and Follet, 1986; Major and Newhall, 1989; Julio Miranda et al., 2005).
- Freshly deglaciated terrain sections (detectable by multi-temporal and -spectral ice classification) of rock walls (detectable through steep DTM slope, missing vegetation, and possibly texture analysis) indicate zones of potentially enhanced rockfall activity due to the thermal, mechanical, hydraulic and hydrological consequences accompanying glacier retreat (Haeberli et al., 1997).

A second class of multidomain classifications utilises not only the remotely sensed data itself, but also the outputs from process models, which might in turn be fed by remote sensing data. For instance, mountain permafrost distribution is highly dependent on elevation (as a surrogate for air temperature) and direct incoming solar radiation. The latter can be modelled based on a DTM (Hoelzle, 1996). A permafrost distribution map is then a valuable requisite for detecting possible slope instabilities connected to permafrost or permafrost thaw in debris or rock slopes (Zimmermann et al., 1997; Noetzli et al., 2003). As a second example, potentially debris-producing rock walls can be approximated as steep DTM sections without vegetation. Rockfall

modelled from such terrain sections can then support remote sensing-based detection of debris slopes (Zemp et al., 2005).

12.4 Modelling of hazard potentials

Once potential hazard sources have been detected, mass movement models help estimating potentially affected zones. The most important prerequisite of such models is a DTM, best obtained through remote sensing. This relates to the importance of topography for controlling mass-movement downslope propagation. Further, remote sensing supports mass movement modelling by providing model inputs through image classification such as surface cover, surface roughness, material to be potentially mobilised, etc. Types of mass movement models applied to glacial, peri- and paraglacial hazards are (Huggel, 2004):

- *empirical rules and relationships*, where important parameters such as maximum discharge of lake outbursts, starting slope and volume of ice avalanches, or maximum travel distances for glacier floods, debris flows, or ice and rock avalanches are statistically estimated from according events (e.g. Huggel et al., 2004a). Some of these parameters can be derived through remote sensing data from before and/or after an event.
- *numerical models*, where the governing physics of a mass movement type are typically represented by differential equations, which are then solved through numerical methods such as numerical integration, finite differences or finite elements (e.g. Iverson, 1997; Patra et al., 2005). Other applications of the numerical type simulate, for instance, the forces and related movement of point masses (e.g. Bottino et al., 2002). Remotely sensed data are often used to define the boundary conditions of numerical models (e.g. terrain geometry, velocities).
- *probabilistic models*, which result in the probability of a certain action, for instance related to geomorphometric parameters such as slope, slope length, etc. (Mostyn and Li, 1993; Harbitz et al., 2001). Alternatively, a mass movement is modelled by many repeat runs with changing starting, transition and deposition conditions (so-called Monte Carlo models) (Gamma, 2000; Barbolini and Savi, 2001). The resulting pattern of how often a terrain cell is hit by the mass movement then reflects some kind of probability. A similar class of models aims to estimate the possibility of an event, for instance through fuzzy logic. Typically, DTMs (e.g. remote sensing-derived) form the base for 2D probabilistic models.
- *hydrological flow-routing models*, where the mass movement is for the most part purely gravity-driven. Different approaches exist how the (maximum) slope is determined, which decides about the flow direction from one terrain cell to the next (Figs. 12-7, 12-8 and 12-9) (Meissl, 1998; Liang and MacKay, 2000; Dorren, 2003; Dorren and Seijmonsbergen, 2003; Stevens et al., 2003; Huggel et al., 2004c; Salzmann et al., 2004; Sheridan et al., 2004; Noetzli et al., 2005). Hydrological flow-routing models can be modified in order to give some probability measures (Huggel et al., 2003c) or to allow estimates of the mass volumes involved (Iverson et al., 1998). This class of models requires suitable DTMs, which are remote sensing-derived in most cases.
- *physical or laboratory models*, where the terrain and a mass movement process are scaled down to small size and simulated physically in the laboratory. For instance debris flows, or creep of frozen or viscous masses (e.g. Iverson, 1997; Kääb and

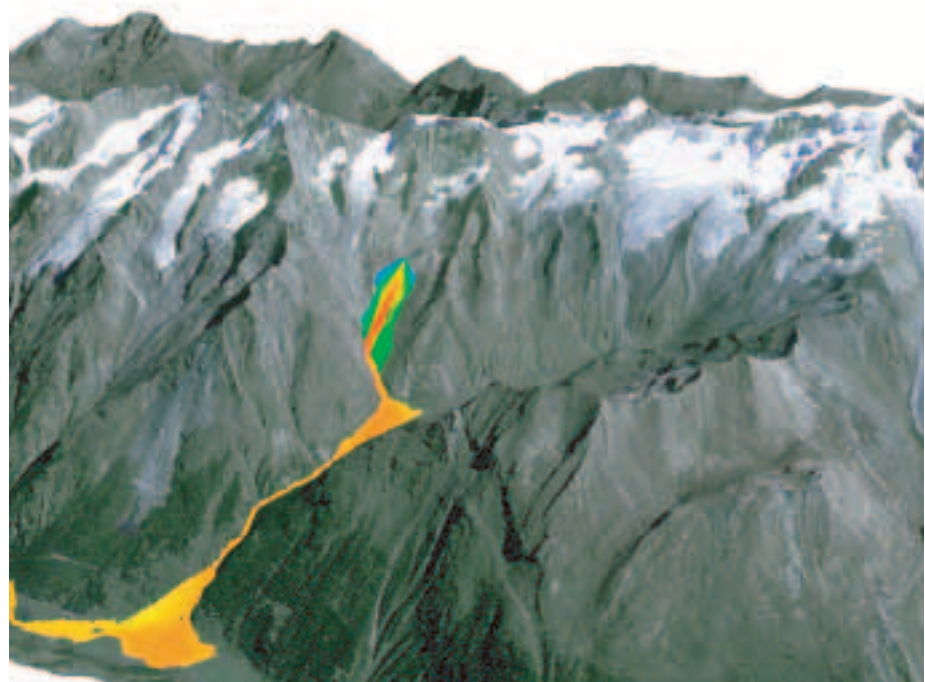


Fig. 12-7 Model of a potential outburst flood / debris flow from the Lake Weingarten, Mischabel range, towards Täsch, Swiss Alps (from Huggel et al., 2003c). The colour transitions from red to blue indicate high to low probabilities of a DTM point to be affected by the modelled debris flow. The elevation difference between Täsch to the lower right of the image section and Lake Weingarten is approximately 1600 m. The underlying image is an oblique perspective of an IRS-pan/Landsat TM fusion draped over the DHM25 by swisstopo (permission BA057212).

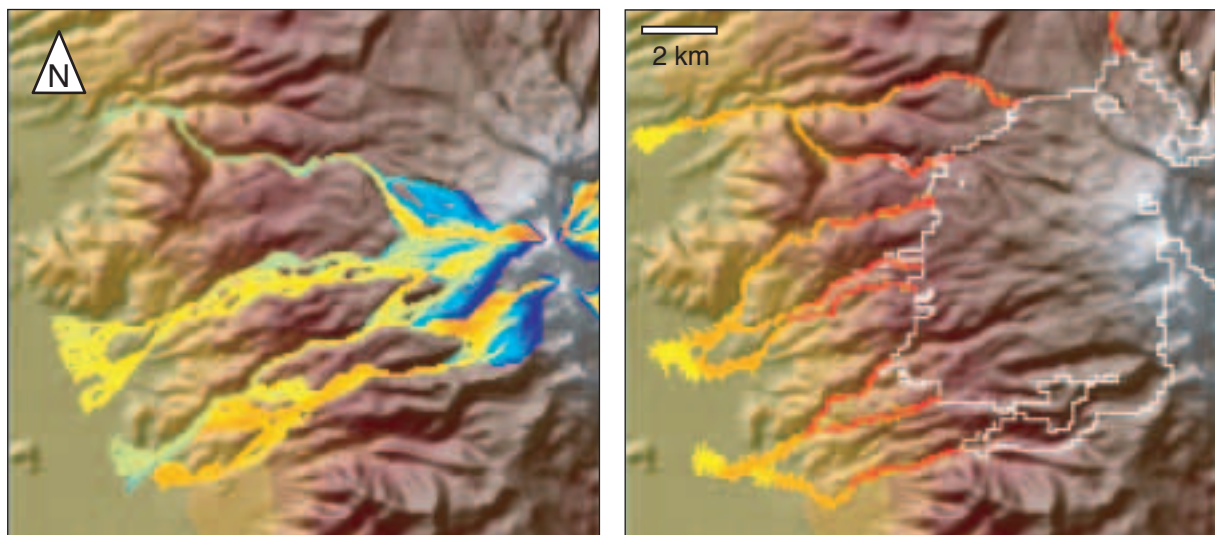


Fig. 12-8 Simulated lahars from the west flank of the ice-clad Iztaccihuatl volcano, Mexico. Background hillshade with colour-coded elevations and topographic base of both model runs is from the SRTM3 DTM. Left: the modified single flow model MSF (Huggel et al., 2003c) initiated at the volcano top and stopped at 19% overall slope. Right: the LAHARZ model (Iverson et al., 1998) with volumes of 100'000 m³ (red), 500'000 m³ (orange), and 1'000'000 m³ (yellow) starting at the so-called high-energy cone of the volcano (white outline). (From Schneider, 2005).

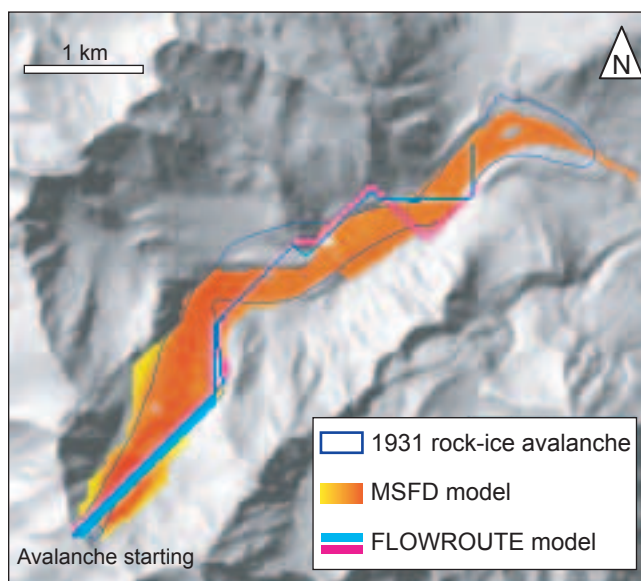


Fig. 12-9 Models of the 1931 rock-ice avalanche from Fletschhorn, Simplon, Swiss Alps. Blue outline: actual avalanche path; yellow to red zone: modified single flow direction model (Huggel et al., 2003c; Noetzli, 2003; Noetzli et al., 2005); blue zones: mass movement model based on energy conservation and impulse; pink zones: as blue zones, but resampled DTM. (From Schlaefli, 2005). Hillshade based on DHM25 by swisstopo (permission BA057212).

Weber, 2004). To such models close-range remote sensing techniques such as particle tracking, or laser and microwave sounders can be applied.

Most outputs of these models are highly sensitive to DTM characteristics such as resolution, level of detail, or vertical and horizontal errors. A sound understanding and evaluation of the remotely sensed DTM used for a simulation is therefore important. Related sensitivity studies can result in multiple model outputs based on different input DTMs and/or different models (Figs. 12-8 and 12-9) (Huggel et al., 2003c; Salzmann et al., 2004).

Geographic information systems (GIS) have become a standard tool for the integration of base data (e.g. digital maps and orthoimages), model input data (e.g. DTMs and terrain classification), model outputs (e.g. affected areas), and – for a number of models – also the model itself.

Depending on the input parameters and/or empirical relations used, models can provide different hazard scenarios (e.g. different distances of reach, relative or absolute probabilities) and hazard maps can be derived. Once a model indicates potentially endangered areas, remote sensing supports the mapping and investigation of settlements and infrastructure at risk, or the assessment of possible chain reactions and secondary effects (e.g. Huggel et al., 2004c).

Spaceborne, airborne and terrestrial methods for glacier and permafrost hazard assessment can be integrated within a down-scaling strategy ranging from first-order assessments with regional coverage towards detailed local investigations (Fig. 12-10). Even when dealing with local problems such as known hazard sources or disaster management, regional-scale first-order assessments should be part of hazard assessments in high mountains in order to account for hazard combinations, chain reactions, and secondary hazards. In particular satellite remote sensing is the method of choice for such work.

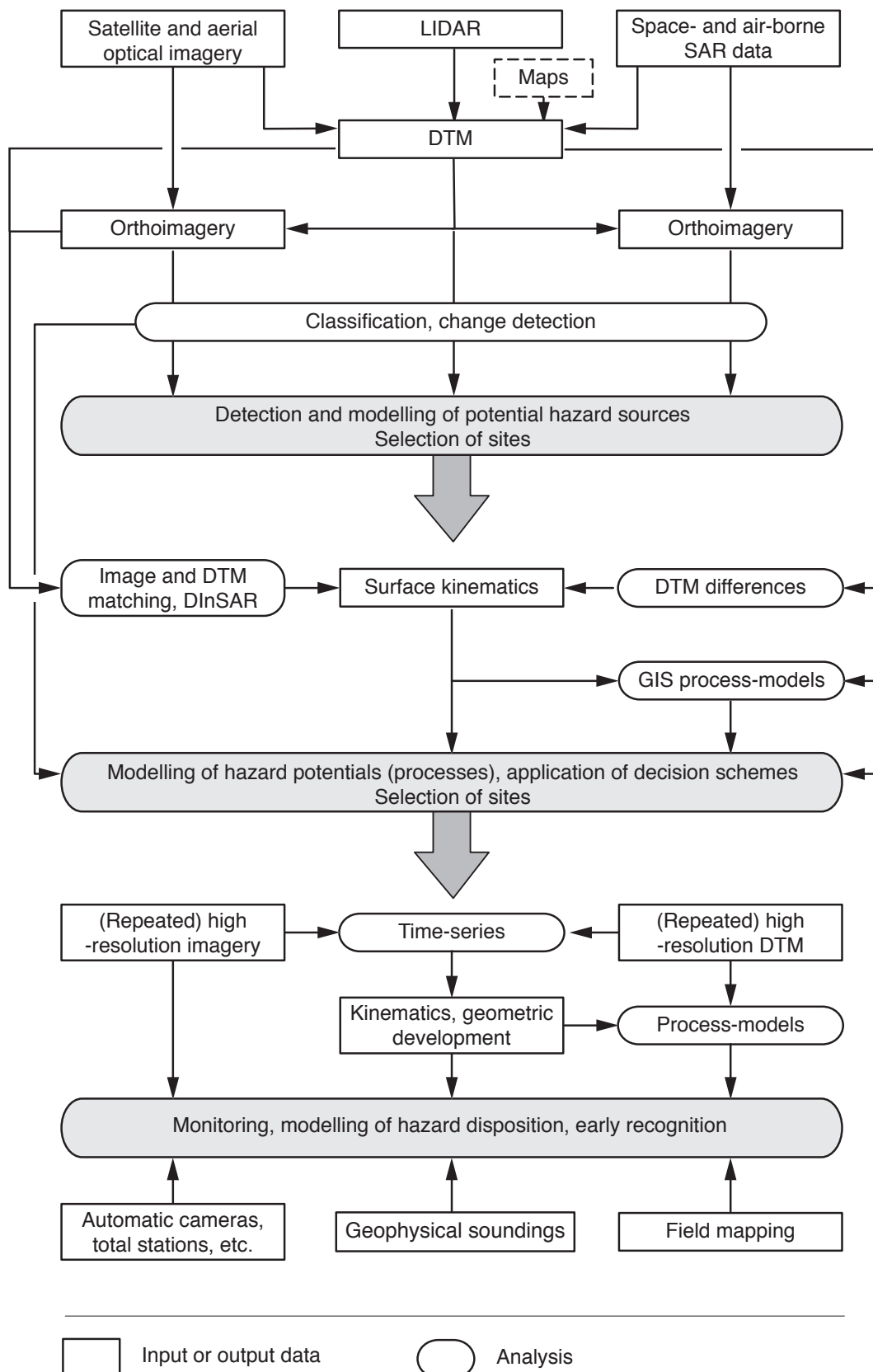


Fig. 12-10 Schematic workflow for assessing glacier- and permafrost-related hazard potentials from space- and airborne data. The scheme describes a downscaling approach from regional-scale assessments using comparably coarse data towards detailed local-scale analyses using data with high temporal and spatial resolution. This sequence includes a decision chain from integrative area-wide first-order evaluations to the selection, and to detailed investigation and monitoring of potentially hazardous sites.

12.5 Disaster management

The above section relates to hazards, i.e. potential processes, the following section to actions after a catastrophic event. Integrating remote sensing in the management of glacier- and permafrost-related disasters can serve three major applied and scientific needs: (i) overview of disaster and damage extent, (ii) frequent monitoring, and (iii) documentation. (i) and (ii) are directed towards search and rescue operations and civil protection, and primarily require a rapid and repeat data acquisition and processing (e.g. Kääb et al., 2003d; Ostir et al., 2003). Due to the limitations of optical remote sensing during cloud cover and night time, the application of (repeat) weather- and sun-independent SAR data can be especially important (Kerle and Oppenheimer, 2002). The major problems related to (i) and (ii) are the enduser-capacity to handle and analyse the data, and the speed of data acquisition and delivery. Remotely sensed documentation of a disaster (iii), even if the data are not analysed immediately, can be an unique source for thoroughly investigating the processes involved, and drawing scientific and applied conclusions of broader interest (Huggel et al., 2005).

The International Charter „Space and Major Disasters“ offers potentially important remote-sensing support for managing large glacier and permafrost disasters. Within this contract, a number of space agencies and commercial satellite companies provide under certain circumstances rapid and free emergency imaging. Currently involved sensors include ENVISAT, ERS, IRS, RADARSAT, or SPOT. Only selected national and international civil protection, rescue and security authorities can activate the Charter (www.disasterscharter.org). Also, the ASTER sensor onboard the Terra spacecraft can be activated for supporting disaster management (Kääb et al., 2003d).

12.6 Conclusions and perspectives

Remote sensing will increasingly become an important and integrative component of managing glacier and permafrost hazards. The best-established and most robust remote-sensing method for detailed investigations considered in this work is aero-photogrammetry, which enables image interpretation, DTM generation, and displacement measurement with centimetre- to metre-accuracy. For regional scale investigations and/or areas that are inaccessible on ground and by airborne platforms, spaceborne optical remote sensing is the tool, which works most robust and is most easily applied. This method enables (semi-)automatic classifications, measurement of strong and large-scale displacements, and for certain instruments also DTM generation – all with an accuracy on the order of metres to tens of metres. Air- and spaceborne photogrammetry are presently converging through the advent of high-resolution space sensors.

SAR data have a large potential to overcome some limitations of optical data, or to complement results from optical data (e.g. DTM generation, displacement measurement with millimetre-accuracy). Thus, the SRTM DTM indeed significantly facilitates hazard assessments in remote high-mountain areas. However, the dissemination of expertise about SAR technology has to be improved, and the analysis methods have to become more robust and cheaper in order to facilitate the widespread application of the technique to glacier and permafrost hazard in mountains. Further research is in particular needed to better understand the complex microwave backscatter mechanisms and to retrieve information about the surface and its changes from it.

Air- and spaceborne remote sensing offers support for assessing the hazard disposition (i.e. the hazard potential), rather than enabling the observation of trigger conditions and the direct short-term forecast of events. In rare occasions, an exception of this general rule might be high-frequency imaging (e.g. monitoring of meteorological events, Kniveton et al., 2000; Buchroithner, 2002b). However, the early warning from impending disasters is an ultimate, long-term goal of earth observation from space and air, and of the related technological development. For the estimation of event magnitude and frequency remote sensing data have typically to be combined with models and/or empirical data.

A major factor currently limiting the accuracy and applicability of spaceborne sensors for glacier and permafrost hazards is their spatial resolution. Data from high-resolution sensors such as IKONOS, QuickBird or Orbview3 open new possibilities in this respect, but are still very expensive and only able to cover small areas. An increasing number of satellites with SAR instruments onboard such as ERS-2, RADARSAT-1, ENVISAT or the planned TerraSAR-X, ALOS and RADARSAT-2, will make SAR a progressively interesting tool for glacier and permafrost hazard assessments.

Spaceborne methods are clearly preferable, or even the only possibility, to obtain base data for regional-scale glacier and permafrost hazard assessments in mountains. Their limitations with respect to spatial resolution and accuracy make these methods rather applicable for the detection of hazard potentials, or for the level of hazard indication maps (scales 1:25'000–1:50'000). For more detailed hazard assessments, above-presented airborne methods, high-resolution spaceborne methods, or terrestrial surveys are necessary.

Modern space technologies enable initial estimation of hazard potentials to be performed by virtually everyone and everywhere, independent of political and geographical restrictions. This fundamental "democratisation" process related to high-mountain (and other) hazards involves a number of new opportunities, dangers and responsibilities for the public, the authorities in charge, and the experts involved. Hazard assessment based on spaceborne remote sensing has, therefore, to follow certain rules considering these responsibilities and the consequences of their disregard.

Table 12-1 Overview of glacier- and permafrost-related hazards in high mountains, hazard descriptions and important remote sensing aspects, and selected remote sensing applications (see also GAPHAZ, 2004; Huggel, 2004; Kääb et al., 2005c; Quincey et al., 2005).

Hazard type	Processes	Remote sensing	Cases and mechanisms Remote sensing applica-tions
(1) Glacier-and permafrost-related floods	(1.1) Breaching of moraine dams Outburst of moraine-dammed lakes. Particularly far reaching glacier disaster (up to hundreds of km). Causes: enhanced runoff; impact waves (1.5); temporary damming/jamming at outlet.	Moraine-dammed lakes usually detectable by remote sensing, in particular optical techniques. Time series particularly useful for assessing lake dynamics and estimating future development. Assessment of moraine dam characteristics requires high-resolution and -precision techniques (dam geometry, deformation, settlement, surface material, etc.). Monitoring of associated glacier characteristics (geometry, surface type), changes and kinematics (thickness changes, velocity) may help assessing the evolution of proglacial lakes.	(Lliboutry et al., 1977; Haeberli, 1983a; Vuichard and Zimmermann, 1987; Costa and Schuster, 1988; Jackson et al., 1989; Reynolds, 1992; Yongjian and Jingshi, 1992; Clague and Evans, 1994; Watanabe and Rothacher, 1996; Popov, 1997; Ames, 1998; Clague and Evans, 2000; Dwivedi et al., 2000; O'Connor et al., 2001; Huggel et al., 2004a)
	(1.2) Failure or overtopping of ice-dams Outburst of ice-dammed lakes. Particularly far reaching glacier disasters. Often repeating for permanent ice dams. Sources: ice-marginal or supraglacial lakes; temporary ice dams from ice avalanches (3.1) or glacier surges (2.1).	Detection of ice-dammed lakes depending on temporal resolution and timing of remote sensing system; detection of ice dams depending on spatial resolution and spectral characteristics. Time series particularly useful. Monitoring of thickness changes and kinematics of long-lasting ice dams supports assessment, e.g. of floatation level.	(Buchroithner et al., 1982; Kääb, 1996b; Ageta et al., 2000; Haeberli et al., 2001; Mool et al., 2001a; Mool et al., 2001b; Huggel et al., 2002; Huggel et al., 2004b) Fig. 12-7
	(1.3) Glacier outbursts Catastrophic water discharge from the en- or subglacial drainage system. Causes: geo-thermal or volcanic activity; temporary en- or subglacial water storage; catastrophic water release connected to surge termination (2.1).	Particularly difficult or impossible to assess due to sub-surface character.	(Clague and Mathews, 1973; Clarke, 1982; Jones et al., 1985; Bruce et al., 1987; Zhang, 1992; Walder and Costa, 1996; Tweed and Russell, 1999; Deline et al., 2004; Kääb et al., 2004)

(1.4) Breaching of thermokarst and supraglacial lakes In ice-rich permafrost or stagnant glacier ice. Progressive lake growth through thermal convection. Causes: similar to (1.1), and progressive melt of ice/permafrost dam.	Detection of related lakes usually requires high image resolution due to the small lake size. Time series particularly useful. Disposition of lake development partially detectable through remote sensing of surface characteristics and kinematics.	(Benn et al., 2000; Reynolds, 2000; Kääb and Haeberli, 2001) (Reynolds, 2000; Kääb and Haeberli, 2001; Wessels et al., 2002) Fig. 6-5, 12-3
(1.5) Displacement waves Displacement-wave impacts on people, natural and artificial lake dams, and other installations. Trigger for a number of lake outburst events of types (1.1) and (1.2). Causes: lake impact from snow-, ice-, rock-avalanches, landslides, debris flows, etc.; floatation of icebergs.	Assessment requires integrative remote sensing and modelling approaches of source processes.	(Haeberli and Röthlisberger, 1975; Vischer, 1979; Vischer et al., 1991; Müller, 1995; Tinti et al., 1999; Walder et al., 2003; Zweifel, 2004) No direct air- and spaceborne remote sensing applications.
(1.6) Enhanced runoff from permafrost Permafrost is for the most part impermeable for surface water, a fact that leads to runoff concentration at the permafrost table, in particular with enhanced surface runoff from snow-melt and intense rainfall; ice melt at permafrost table. Temporary water storage in or underneath permafrost is particularly difficult to investigate but suggested for rare cases (causes: taliks; ice-melt in permafrost; (temporary) water blockage in or under the permafrost?). Both phenomena, runoff concentration and water storage, may lead to unusually enhanced runoff. Potential trigger mechanisms of debris flows (4.3).	Can hardly be investigated by remote sensing.	(Haeberli et al., 1990; Zimmermann and Haeberli, 1992) No published remote sensing applications.

Hazard type	Processes	Remote sensing	Cases and mechanisms Remote sensing applications
(2) Glacier length and volume changes	(2.1) Glacier surge (unstable length change) Temporary instability of large glacier parts with ice velocity increased by an order of magnitude (or more). Usually accompanied by drastic glacier advance. Besides the direct impact from glacier advance (overriding of structures, blockage of rivers, etc.), glacier surges often trigger further hazards such as ice-dammed lakes (1.2). Enhanced englacial water storage, possibly released at surge end (1.3).	Surges can be tracked by high-frequency remote sensing. Former glacier surges, and thus surge-type glaciers, can often be recognised from deformed, so-called "looped" moraines. Geometry changes, if involved in the surge disposition and build-up, can be detected as glacier thickness changes.	(Bruce et al., 1987; Raymond, 1987; Haeberli et al., 2002a; Harrison and Post, 2003; Kääb et al., 2004) (Espizua and Bengochea, 1990; Zhang, 1992; Rolstad et al., 1997; Jiskoot et al., 2001; Luckman et al., 2002; Strozzi et al., 2002; Copland et al., 2003; Dowdeswell and Bennham, 2003) Figs. 4-11, 5-8, 8-13, 8-14, 8-15
	(2.2) Stable glacier advance Advancing glaciers may inundate land, override installations, dam rivers and form lakes (1.2), cause ice break-offs (3.1), etc. Causes: positive mass balance, ice dynamics.	Can usually be monitored by remote sensing. Glacier area changes from repeat imagery, glacier mass changes from repeat DTMs. Forecast best done by a combination of remote sensing, glaciological field work and modelling.	(Tufnell, 1984; Grove, 1987; Mayo, 1988; Yamada and Sharma, 1993) (Kääb, 1996b; Paul, 2002a) and many others (see Sections 5.4 and 6.3)
	(2.3) Glacier retreat Glacier retreat forms usually no direct hazard but is able to trigger a number of secondary hazards such as various slope instabilities (3). Causes (2.2).	Remote sensing see (2.2).	(Grove, 1987) (Silverio and Jaquet, 2005), see (2.2) and (3). Figs. 8-2, 8-3, 8-7, 11-2, 11-3, 12-1
	(2.4) Changes in glacier runoff and seasonality Glacier mass loss leads to reduction of water resources as stored in glaciers and to changes in dry-season river flows. Short-term perspective: increasing discharge due to enhanced melt; long-term perspective: decreasing discharge when glaciers become substantially smaller or disappear. Consequences for drinking water supply, irrigation, hydro-power production, industrial water use, fishery, water quality, etc. Causes see (2.2).	Best investigated through a combination of remote sensing, meteorology, and combined glaciological and hydrological modelling. Remote sensing see (2.2).	(e.g. Wagnon et al., 1999) (Huggel et al., 2003a), see (2.2)

Hazard type	Processes	Remote sensing	Cases and mechanisms Remote sensing applications
(3) Glacial and paraglacial mass movements	(3.1) Ice fall and ice avalanches Ice break-offs and subsequent ice avalanches from steep glaciers. In rare cases detachment of complete glaciers. Particularly dangerous in winter with reduced basal friction, extended runout, and mass gain from snow. Glacier parts can fail due to a failure of the underlaying rock (3.2). Ice avalanches can be triggered by earthquakes. Ice avalanches can trigger lake outbursts (1.5), dam rivers (1.2), transform into mud/debris flows (3.5) (3.6).	Detection of steep glaciers through combination of spectral data with DTM. High-resolution, -precision, and -frequency remote sensing (e.g. terrestrial close range techniques) enables sometimes monitoring of mass changes and kinematics related to entire steep glaciers or unstable sections.	(Röthlisberger, 1981; Alean, 1984; Alean, 1985; Lüthi, 1994; Haeberli et al., 1999a; Margreth and Funk, 1999; Huggel et al., 2004a; Kotlyakov et al., 2004; Van der Woerd et al., 2004; Haeberli et al., 2005; Huggel et al., 2005) (Kääb, 1996b; Clague and Evans, 2000; Kääb, 2000; Kääb et al., 2003d; Salzmann et al., 2004) Figs. 6-4, 12-1, 12-9
	(3.2) Rock fall, rock avalanche Glacier retreat uncovers and debuttresses rock flanks. The related change in thermal, hydrologic, hydraulic and mechanic conditions can lead to rock fall and rock avalanches (fast mass movement). Rock avalanches can carry parts of overlaying glaciers. Rock avalanches can be of increased magnitude in glacial environments (extended runout on glaciers or when combined with ice, mass gain from ice, entrainment of glacier parts through impact, detachment of glaciers overlaying the rock mass breaking off). Rock avalanches can be triggered by earthquakes.	Mapping of rock faces and some boundary conditions (e.g. glacier retreat) possible through remote sensing.	(Plafker and Erikson, 1978; Evans and Clague, 1988; Haeberli et al., 1997; Wegmann and Keusen, 1998; Barla et al., 2000; Deline, 2001; Giani et al., 2001; Haeberli et al., 2005) (Kääb et al., 2003d; Huggel et al., 2005) Fig. 12-1
	(3.3) Landslide / rock slide Among other causes, glacier retreat (2.3) or slope undercutting by floods uncovers and debuttresses rock and debris flanks. The related change in hydrologic, hydraulic and mechanic conditions can lead to mass movements (slow mass movement). These can create secondary hazards such as river dams.	Landslide surface characteristics, geometry and kinematics can be monitored by repeat high-resolution and -precision remote sensing.	(Ballantyne, 2002; Holm et al., 2004; Kääb, 2004) (Mantovani et al., 1996; Kääb, 2002; Singhroy and Molch, 2004) Figs. 10-2, 10-3, 10-5, 10-6, 12-5

(3.4) Destabilization of unconsolidated glacial deposits Glacier retreat (2.3) leaves unprotected and unconsolidated moraine material that is prone to enhanced erosion and debris flows.	Related zones can be detected through remote sensing combined with DTMs. (Huggel et al., 2004b)	(Zimmermann and Haeberli, 1992; Rickenmann and Zimmermann, 1993; Lugon et al., 1999)
(3.5) Debris flows from glacier floods Glacier and permafrost floods (1) are often accompanied by debris flows when erodible material is available in steep parts of the flood path. Such debris flows can show a sequence of erosion and deposition. Debris flow deposits may dam tributaries or main rivers.	Remote sensing with sufficient spatial resolution supports estimating the availability of debris in a potential flood path and its slope (i.e. disposition to erosion or deposition).	see (1)
(3.6) Interaction between volcanic activity and glaciers Potentially among the most devastating glacier disasters. Enhanced geothermal activity, geometric and mechanic changes, deposition of hot eruptive materials, or albedo change by volcanic ash can lead to drastic melt of ice or ice break-off on ice-clad volcanoes and to volcanic landslides or lahars. Ash layers thicker than some mm-cm insulate the underlying ice.	Ice cover on volcanoes and its changes (and partially also volcanic activity) can be monitored by remote sensing.	(Brugmann and Post, 1981; Pierson et al., 1990; Thouret, 1990; Aguilera et al., 2004) (Björnsson et al., 2001; Dean et al., 2004; Julio Miranda et al., 2005) Fig. 12-8

Hazard type	Processes	Remote sensing	Cases and mechanisms Remote sensing applications
(4) Permafrost- and ground ice-related mass movements	(4.1) Adverse effects of permafrost creep Permafrost creep (often forming rockglaciers) can inundate land and destabilize or destroy constructions situated on or in it. Cause: gravity-driven deformation of ice-rich debris.	Monitoring of permafrost deformation by repeat high-resolution optical remote sensing and DInSAR.	(Haeberli, 1992a) (Kääb, 2000; Kääb, 2002; Kenyi and Kaufmann, 2003; Strozzi et al., 2004) (Section 9)

(4.2) Thaw settlement and frost heave Changes in permafrost surface geometry due to changes in ground ice content from ice-lens accumulation or thermokarst processes. Affecting constructions; possibly triggering thermokarst lakes (1.4). Thaw and frost heave processes may be caused by constructions (e.g. changes in snow cover regime, basement heating).	Monitoring of geometry changes from repeat high-precision DTMs. (Kääb et al., 1997) Fig. 6-8	(Haeberli, 1992a; Phillips, 2000; Richardson and Reynolds, 2000a)
(4.3) Debris flows from permafrost Permafrost thaw changes mechanic and hydrological conditions in permafrost. As a consequence the disposition of periglacial debris flows may increase. Temporary runoff concentration (1.6) and ground saturation is, thereby, often involved as trigger.	Only detectable using remote sensing when accompanied by changes in surface geometry (4.2). (Kääb, 1996b; Hoelzle et al., 1998) Fig. 9-2	(Haeberli et al., 1990; Haeberli, 1992a; Zimmermann and Haeberli, 1992)
(4.4) Rockfall from rockglacier front Advance of rockglaciers involves continuous transport of surface debris over the rockglacier front. This may lead to local rockfall endangering people and mountain infrastructure.	Remote sensing see (4.1) (Bauer et al., 2003; Kääb and Reichmuth, 2005) Fig. 9-11	(Haeberli, 1992a; Kääb and Reichmuth, 2005)
(4.5) Destabilization of frozen debris slopes In rare cases entire sections of rockglaciers or frozen debris slopes might destabilize. Reasons largely unknown (dynamic, ground warming, ?). Can lead to (4.1), (4.3), and (4.4).	For slow movements detectable using high-resolution remote sensing ((4.1) and crevasse formation). (Kaufmann and Ladstädter, 2002; Roer et al., 2005b) Fig. 12-6	(Haeberli and Burn, 2002) (Haeberli and Burn, 2002; Noetzli et al., 2003; Haeberli et al., 2005; Noetzli et al., 2005)
(4.6) Rockfall and rock avalanches from frozen rock faces The thermal regime and ground ice in frozen rock faces have complex thermal, mechanical, hydraulic and hydrological effects on rock stability. Related changes can cause mass movements. Processes often also related to surface ice (3.2).	Remote sensing see (3.2). (Fischer, 2004)	(Haeberli et al., 1997; Davies et al., 2001; Bottino et al., 2002; Haeberli and Burn, 2002; Noetzli et al., 2003; Haeberli et al., 2005; Noetzli et al., 2005)

IV. CONCLUSIONS

In this work, each chapter deals with particular issues and conclusions relating to glaciers, rockglaciers, remote sensing, and the methodology of investigation. This concluding chapter offers a summary of methodical perspectives for investigating mountain glaciers and permafrost creep by earth observation technologies and geoinformatics, as follows:

- *DTMs* with a few decimetres of spatial resolution and similar or even better accuracy have become available globally. Glaciological regional-scale analyses can now utilize the vertical dimension in addition to the horizontal ones on a regular basis (Kääb et al., 2002b; Paul, 2004). A major step within this development is most certainly the SRTM. However, DTMs other than SRTM are still necessary for latitudes greater than 60°N or 54°S (i.e. the polar zones), and for filling voids in SRTM DTMs, which occur particularly in high-mountains environments.
- The area-wide availability of medium-resolution and -accuracy *SRTM DTMs* opens perspectives, which have been barely exploited or even imagined to date. For instance, global-scale monitoring of glacier thickness changes from space at time intervals of decades is now feasible (see Section 8.1) (Rignot et al., 2003).
- The rising number of sensors and data, together with the increasing length of corresponding time periods covered, makes *change and time series analyses* even more important and promising. Such possibilities are able to satisfy the growing demand for rapid detection and perception of environmental changes on regional to global scales.
- *Optical remote sensing techniques* are highly developed and robust. They are the “workhorse” of remote investigation of mountain glaciers and permafrost creep. However, the corresponding potential has not been fully exploited by far for global glacier monitoring. On the one hand, it is essential to close the methodical gaps in making these techniques fully operational for standardized, highly automated large-area deployment (see the Global Land Ice Measurements from Space project, GLIMS). While on the other hand, new strategies must be developed and existing ones adapted to the rising technical possibilities (e.g. Williams and Hall, 1998), for instance, for including glacier flow in global-scale observation systems.
- Further progress for the monitoring of mountain glaciers by *spaceborne passive optical sensors* can be expected from increasing spatial and temporal resolution. The latter might be in particular achieved by pointable sensors. The glaciological value of these data is enhanced significantly by the combination with medium resolution DTMs, e.g. from satellite stereo or SAR campaigns, SRTM in particular. Rising radiometric resolution in connection with variable sensor gain settings is able to improve snow classification and image matching (Bindschadler and Vornberger, 2000; Bindschadler, 2003). However, application of remote

sensing techniques for worldwide glacier monitoring is depending strongly on low prices of the satellite data and processing software necessary. (See Bindschadler et al., 2001).

- *Airborne LIDAR*, or *laserscanning*, opens new perspectives for the measurement of high-resolution DTMs in mountain environments (see Section 3.7). Among other applications such as local-scale terrain modelling, repeat laserscanning will in particular be useful for monitoring thickness changes of glaciers or rock glaciers, or for measuring snow depth over large areas. For cryospheric applications, a major advantage of LIDAR as compared to passive optical sensors is the fact that the technique works equally for snow-covered, and snow-free terrain.
- With regard to sensors, further major future perspectives will most likely come from *hyperspectral and microwave sensors*. The potential of SAR systems for investigating ground conditions in particular must be investigated further. In addition, it is of vital importance to further investigate thermal remote sensing data more thoroughly, since energy exchange between ground and atmosphere represents a fundamental factor in the evolution and persistence of surface and sub-surface ice.
- *Multidimensional analysis* will continue to gain importance in glaciology. Perspectives range from sensor fusion (e.g. combining passive systems such as photography or digital cameras with laserscanning, Kraus, 2002), to data merging (e.g. integration of microwave and optical data; e.g. DTM fusion Fig. 3-22), to reinforced development and application of multidimensional classification schemes combining spectral, geometric and multitemporal data (e.g. Paul et al., 2004).
- Understanding and monitoring of high-mountain physical processes relies not only on remotely sensed data, but as well on mathematical process models. As a consequence, the integration of remote sensing data and techniques into *GIS-based numerical process models* should be moved forward.
- *Enhanced utilization of animation and stereo viewing techniques* in glaciological data visualization and exploration will improve the understanding of the usually complex three-dimensional and time-dependent glacial and periglacial processes (Kääb et al., 2003b; Paul et al., 2003).

-
- Both the development of techniques for data acquisition and analysis, and their area-wide application are necessary for *climate-related monitoring* of glaciers and permafrost. Long-term monitoring networks have to adapt continuously to the rising methodical possibilities without losing continuity (Haeberli, 1998; Williams and Hall, 1998). Projecting the overall goals of international climate-related observation systems (see tiers 1-5 in Chapter 1) on mountain glaciers shows that remote sensing methods are already available for most tasks:
 - A number of high-precision techniques for measuring surface velocities and thickness changes, and surface properties such as albedo support detailed process studies on ice flow, creep of frozen ground, and mass balance on a local level (i.e. one single glacier; cf. tier 2).
 - Aero-photogrammetry and laserscanning enable detecting glacier mass changes on a regional scale, at least for areas accessible for aircrafts (cf. tier 3).
 - Glacier length changes can be measured for a large sample of glaciers from medium- and high-resolution satellite optical imagery, in theory on a global level (cf. tier 4).
 - Repeat global glacier inventories (cf. tier 5) can similarly be obtained from spaceborne optical sensors, possibly combined with SAR sensors.

Comparing this list and the techniques discussed in this volume it can be concluded that the largest technological gap exists in the missing possibility to measure glacier volume changes from space (i.e. on a global scale) with an accuracy that is glaciologically necessary (i.e. decimetres to few metres). The largest potential to overcome this problem have – in our view – SAR altimeters, SAR interferometers, a combination of both (e.g. the failed CRYOSAT), DTM_s from high resolution optical sensors (e.g. SPOT5, IKONOS, etc.), and possibly spaceborne LIDAR (e.g. ICESAT).

The rapid development of remote sensing sensors and data availability (e.g. increasing number of sensors and spectral bands, or spatial, spectral, radiometric and temporal resolution) has become a driving force in glacier and permafrost research. A considerable number of “breakthroughs” for investigating mountain glaciers and permafrost creep are based on earth observation technologies and geoinformatics. Along with these great attainments and highly attractive technical perspectives, it is necessary to keep in mind and focus on the fundamental tasks of glaciology: understanding environmental resources and hazards in cold regions, and their change over time.

V. REFERENCES

References

- Abdalati, W. and Krabill, W.B. (1999): Calculation of ice velocities in the Jacobshavn Isbræ using airborne laser altimetry. *Remote Sensing of Environment*, 67(2), 194-204.
- Adalgeirsdotir, G., Echelmayr, K.A. and Harrison, W.D. (1998): Elevation and volume changes on the Harding Icefield, Alaska. *Journal of Glaciology*, 44(148), 570-582.
- Ageta, Y., Iwata, S., Yabuki, H., Naito, N., Sakai, A., Narama, C. and Karma (2000): Expansion of glacier lakes in recent decades in the Bhutan Himalayas. In: Nakawo, M., Raymond, C.F. and Fountain, A., eds., *Debris-Covered Glaciers*, IAHS Publication, 264, 165-175.
- Aguilera, E., Pareschi, M.T., Rosi, M. and Zanchetta, G. (2004): Risk from Lahars in the Northern Valleys of Cotopaxi Volcano (Ecuador). *Natural Hazards*, 33(2), 161-189.
- Al-Rousan, N. and Petrie, G. (1998): System calibration, geometric accuracy testing and validation of DEM & orthoimage data extracted from SPOT stereopairs using commercially available image processing systems. *International Archives of Photogrammetry & Remote Sensing*, 34(4), 8-15.
- Albert, T. (2002): Evaluation of remote sensing techniques for ice-area classification applied to the tropical Quelccaya ice cap, Peru. *Polar Geography*, 26(3), 210-226.
- Alean, J.C. (1984): Untersuchungen über Entstehungsbedingungen und Reichweiten von Eislawinen, Versuchsanstalt für Wasserbau, Hydrologie und Glaziologie ETH Zürich. 74.
- Alean, J. (1985): Ice avalanche activity and mass balance of high-altitude hanging glaciers in the Swiss Alps. *Annals of Glaciology*, 6, 248-249.
- Ames, A. (1998): A documentation of glacier tongue variations and lake development in the Cordillera Blanca, Peru. *Zeitschrift für Gletscherkunde*, 34, 1-36.
- Aniello, P. (2003): Using ASTER DEMs to Produce IKONOS Orthophotos. *Earth Observation Magazine*, 12(5), 22-26.
- Aniya, M. (1999): Recent glacier variations of the Hielos Patagonicos, South America, and their contribution to sea-level change. *Arctic, Antarctic and Alpine Research*, 31(2), 165-173.
- Aniya, M., Sato, H., Naruse, R., Skvarca, P. and Casassa, G. (1996): The use of satellite and airborne imagery to inventory outlet glaciers of the Southern Patagonia Icefield, South America. *Photogrammetric Engineering and Remote Sensing*, 62, 1361-1369.
- Aniya, M., Sato, R., Naruse, P., Skvarca, P. and Casassa, G. (1997): Recent variations in the Southern Patagonia Icefield, South America. *Arctic, Antarctic and Alpine Research*, 29(1), 1-12.
- Arendt, A.A., Echelmeyer, K.A., Harrison, W.D., Lingle, C.S. and Valentine, V.B. (2002): Rapid wastage of Alaska glaciers and their contribution to rising sea level. *Science*, 297(5580), 382-386.
- Arenson, L.U. (2002): *Unstable Alpine permafrost: a potential important natural hazard – Variations of geotechnical behaviour with time and temperature*. PhD thesis, Institute for Geotechnical Engineering, ETH Zurich, 14801.
- Arenson, L., Hoelzle, M. and Springman, S. (2002): Borehole deformation measurements and internal structure of some rock glaciers in Switzerland. *Permafrost and Periglacial Processes*, 13(2), 117-135.
- Arenson, L.U., Springman, S.M. and Hawkins, P.G. (2003): Pressuremeter tests within an active rock glacier in the Swiss Alps. *Proceedings, Eighth International Conference on Permafrost*, Zurich, Balkema, 1, 33-38.
- Armenakis, C. (1984): Deformation measurements from aerial photographs. *International Archives of Photogrammetrie and Remote Sensing*, 25(A5), 39-48.
- Azizi, F. and Whalley, W.B. (1995): Finite element analysis of the creep of debris containing thin ice bodies. *Proceedings, Fifth International Offshore and Polar Engineering Conference*, The Hague, The Netherlands, 336-341.

- Azizi, F. and Whalley, W.B. (1996): Numerical modelling of the creep behaviour of ice-debris mixtures under variable thermal regimes. *Proceedings, Sixth International Offshore and Polar Engineering Conference*, Los Angeles, USA, 362-366.
- Bacher, U., Bludovsky, S., Dorre, E. and Münzer, U. (1999): Precision aerial survey of Vatnajökull, Iceland, by digital photogrammetry. *Proceedings, Third Turkish-German Joint Geodetic Days*, Istanbul, Turkey, 1, 126-136.
- Ballantyne, C.K. (2002): Paraglacial geomorphology. *Quaternary Science Reviews*, 21, 1935-2017.
- Baltsavias, E.P. (1996): Digital ortho-images – a powerful tool for the extraction of spatial- and geo-information. *ISPRS Journal of Photogrammetry and Remote Sensing*, 51(2), 63-77.
- Baltsavias, E.P. (1999): A comparison between photogrammetry and laser scanning. *ISPRS Journal of Photogrammetry and Remote Sensing*, 54(2-3), 83-94.
- Baltsavias, E.P., Li, H., Mason, S., Stefanidis, A. and Sinning, M. (1996a): Comparison of two digital photogrammetric systems with emphasis on DTM generation: case study glacier measurement. *International Archives of Photogrammetry and Remote Sensing*, 31(4), 104-109.
- Baltsavias, E.P., Li, H., Stefanidis, A. and Sinning, M. (1996b): Automatic DSMs by digital photogrammetry. *Surveying World*, 4(2), 18-21.
- Baltsavias, E.P., Favey, E., Bauder, A., Boesch, H. and Pateraki, M. (2001): Digital surface modelling by airborne laser scanning and digital photogrammetry for glacier monitoring. *Photogrammetric Record*, 17(98), 243-273.
- Bamber, J.L., Ekholm, S. and Krabill, W. (1998): The accuracy of satellite radar altimetry data over the Greenland ice sheet determined from airborne laser data. *Geophysical Research Letters*, 25(16), 3177-3180.
- Bamler, R. and Hartl, P. (1998): Synthetic aperture radar interferometry. *Inverse Problems*, 14, R1-R54.
- Barbolini, M. and Savi, F. (2001): Estimate of uncertainties in avalanche hazard mapping. *Annals of Glaciology*, 32, 299-305.
- Barla, G., Dutto, F. and Mortara, G. (2000): Brenva Glacier rock avalanche of 18 January 1997 on the Mont Blanc range, NW Italy. *Landslide News*, 13, 2-5.
- Barmettler, A., Stebler, O., Small, D., Meier, E. and Nüesch, D. (2004): Swiss Alpine Airborne SAR Experiment (SASARE) part II: radar imaging of high alpine glaciers at the VHF-band. *Proceedings, IEEE International Geoscience and Remote Sensing Symposium (IGARSS)*, Anchorage, Alaska, 2, 1121-1123.
- Barsch, D. (1973): Refraktionsseismische Bestimmung der Obergrenze des gefrorenen Schuttkörpers in verschiedenen Blockgletschern Graubündens, Schweizer Alpen. *Zeitschrift für Gletscherkunde und Glazialgeologie*, 9(1,2), 143-167.
- Barsch, D. (1996): *Rockglaciers. Indicators for the present and former geocology in high mountain environments*. Springer, Berlin. 331 pp.
- Barsch, D. and Hell, G. (1975): Photogrammetrische Bewegungsmessungen am Blockgletscher Murtèl I, Oberengadin, Schweizer Alpen. *Zeitschrift für Gletscherkunde und Glazialgeologie*, 11(2), 111-142.
- Barsch, D., Fierz, H. and Haeberli, W. (1979): Shallow core drilling and borehole measurements in permafrost of an active rock glacier near the Grubengletscher, Wallis, Swiss Alps. *Arctic and Alpine Research*, 11(2), 215-228.
- Bauer, A., Paar, G. and Kaufmann, V. (2003): Terrestrial laser scanning for rock glacier monitoring. *Proceedings, Eighth International Conference on Permafrost*, Zurich, Balkema, 1, 55-60.
- Baum, R.L., Messerich, J. and Fleming, R.W. (1998): Surface deformation as a guide to kinematics and three-dimensional shape of slow-moving, clay-rich landslides, Honolulu, Hawaii. *Environmental and Engineering Geoscience*, 4(3), 283-306.
- Bayr, K.J., Hall, D.K. and Kovalick, W.M. (1994): Observations on glaciers in the eastern Austrian Alps using satellite data. *International Journal of Remote Sensing*, 15, 1733-1742.
- Benn, D.I., Wiseman, S. and Warren, C.R. (2000): Rapid growth of a supraglacial lake, Ngozumpa Glacier, Khumbu Himal, Nepal. In: Nakawo, M., Raymond, C.F. and Fountain, A., eds., *Debris-Covered Glaciers*. IAHS publications, 264, 177-185.
- Bennett, L.P. and French, H.M. (1990): In situ permafrost creep, Melville Island, and implications for global change. *Proceedings, 5th Canadian Permafrost Conference*, Québec City, Nordicana, 54, 119-123.
- Bennett, L.P. and French, H.M. (1991): Solifluction and the role of permafrost creep, Eastern Melville Island, N.W.T., Canada. *Permafrost and Periglacial Processes*, 2, 95-102.
- Benson, C.S. and Follet, A.B. (1986): Application of photogrammetry to the study of volcano-glacier interactions on Mount Wrangell, Alaska. *Photogrammetric Engineering and Remote Sensing*, 52(6), 813-827.

- Benveniste, J., Roca, M., Levrini, G., Vincent, P., Baker, S., Zanife, O., Zelli, C. and Bombaci, O. (2001): The radar altimetry mission: RA-2, MWR, DORIS and LRR. *ESA Bulletin*, 106, 67-76.
- Berthier, E., Arnaud, Y., Baratoux, D., Vincent, C. and Remy, F. (2004): Recent rapid thinning of the 'Mer de Glace' glacier derived from satellite optical images. *Geophysical Research Letters*, 31, L17401, doi:10.1029/2004GL020706.
- Berthier, E., Vadon, H., Baratoux, D., Arnaud, Y., Vincent, C., Feigl, K.L., Remy, F. and Legresy, B. (2005): Surface motion of mountain glaciers derived from satellite optical imagery. *Remote Sensing of Environment*, 95(14-28).
- Berthling, I. (2001): *Slow periglacial mass wasting – processes and geomorphological impact. Case studies from Finse, southern Norway and Prins Karls Forland, Svalbard*. Dissertation thesis, Faculty of Mathematics and Natural Sciences, University of Oslo, 113.
- Berthling, I., Etzelmüller, B., Eiken, T. and Sollid, J.L. (1998): Rock glaciers on Prins Karls Forland, Svalbard, I: internal structure, flow velocity and morphology. *Permafrost and Periglacial Processes*, 9(2), 135-145.
- Binaghi, E., Madella, A., Madella, P. and Rampini, A. (1993): Integration of remote sensing images in a G. I. S. for the study of alpine glaciers. In: Winkler, ed., *Remote Sensing for Monitoring the Changing Environment of Europe*, Balkema, Rotterdam, 173-178.
- Binaghi, E., Madella, P., Montesano, M.P. and Rampini, A. (1997): Fuzzy contextual classification of multisource remote sensing images. *IEEE Transactions on Geoscience and Remote Sensing*, 35(2), 326-339.
- Bindschadler, R. (1998): Monitoring ice sheet behaviour from space. *Reviews of Geophysics*, 36(1), 79-104.
- Bindschadler, R. (2003): Tracking subpixel-scale sastrugi with Advanced Land Imager. *IEEE Transactions on Geoscience and Remote Sensing*, 41(6), 1373-1377.
- Bindschadler, R.A., Fahnestock, M.A., Skvarca, P. and Scambos, T.A. (1994): Surface-velocity field of the northern Larsen Ice Shelf, Antarctica. *Annals of Glaciology*, 20, 319-326.
- Bindschadler, R., Vornberger, P., Blankenship, D., Scambos, T. and Jacobel, R. (1996): Surface velocity and mass balance of Ice Streams D and E, West Antarctica. *Journal of Glaciology*, 42(142), 461-475.
- Bindschadler, R., Fahnestock, M. and Sigmund, A. (1999): Comparison of Greenland ice sheet topography measured by TOPSAR and airborne laser altimetry. *IEEE Transactions on Geoscience and Remote Sensing*, 37(5), 2530-2535.
- Bindschadler, R. and Vornberger, P. (2000): Detecting ice-sheet topography with AVHRR, RESURS-01, and Landsat TM imagery. *Photogrammetric Engineering and Remote Sensing*, 66(4), 417-422.
- Bindschadler, R., Dowdeswell, J., Hall, D. and Winther, J.G. (2001): Glaciological applications with Landsat-7 imagery: early assessments. *Remote Sensing of Environment*, 78(1-2), 163-179.
- Bishop, M.P., Shroder, J.F. and Ward, L.J. (1995): SPOT multispectral analysis for producing supraglacial debris-load estimates for Batura Glacier, Pakistan. *Geocarto International*, 10(4), 81-90.
- Bishop, M.P., Shroder, J.F., Hickman, B.L. and Copeland, L. (1998): Scale-dependent analysis of satellite imagery for characterization of glacier surfaces in the Karakoram Himalaya. *Geomorphology*, 21, 217-232.
- Bishop, M.P., Shroder, J.F. and Hickman, B.L. (1999): High resolution satellite imagery and neuronal networks for information extraction in a complex mountain environment. *Geocarto International*, 14, 17-26.
- Bishop, M.P., Kargel, J.S., Kieffer, H.H., MacKinnon, D.J., Raup, B.H. and Shroder, J.F. (2000): Remote-sensing science and technology for studying glacier processes in high Asia. *Annals of Glaciology*, 31, 164-170.
- Bishop, M., Bonk, R., Kamp Jr., U. and Shroder Jr., J.F. (2001): Terrain analysis and data modeling for alpine glacier mapping. *Polar Geography*, 25(3), 182-201.
- Bishop, M.P., Colby, J.D., Luval, J.C., Quattrochi, D. and Rickman, D.L. (2004): Remote-sensing science and technology for studying mountain environments. In: Bishop, M.P. and Shroder Jr., J.F., eds., *Geographic Information Science and Mountain Geomorphology*, Springer, Praxis, Chichester, UK, 147-187.
- Bishop, M.P. and Shroder Jr., J.F. (2004): GIScience and mountain geomorphology: overview, feedbacks, and research directions. In: Bishop, M.P. and Shroder Jr., J.F., eds., *Geographic Information Science and Mountain Geomorphology*, Springer, Praxis, Chichester, UK, 1-31.
- Björnsson, H., Rott, H., Gudmundsson, S., Fischer, A., Siegel, A. and Gudmundsson, M.T. (2001): Glacier-volcano interactions deduced by SAR interferometry. *Journal of Glaciology*, 47(156), 58-70.
- Blair, R.W. (1994): Moraine and valley wall collapse due to rapid deglaciation in Mount Cook National Park, New Zealand. *Mountain Research and Development*, 14(4), 347-358.

- Blatter, H. (1995): Velocity and stress fields in grounded glaciers: a simple algorithm for including deviatoric stress gradients. *Journal of Glaciology*, 41(138), 333-344.
- Bolch, T. and Kamp, U. (2003): Qualitätsanalyse digitaler ASTER-Geländemodelle von Hochgebirgsregionen (Cerro Sillajhuay, Chile/Bolivien). *Kartographische Nachrichten*, 53(5), 217-224.
- Bottino, G., Chiarle, M., Joly, A. and Mortara, G. (2002): Modelling rock avalanches and their relation to permafrost degradation in glacial environments. *Permafrost and Periglacial Processes*, 13(4), 283-288.
- Bourdelles, B. and Fily, M. (1993): Snow grain size determination from Landsat imagery. *Annals of Glaciology*, 17, 87-92.
- Bovis, M.J. (1990): Rock-slope deformation at Affliction Creek, southern Coast Mountains, British Columbia. *Canadian Journal of Earth Sciences*, 27, 243-254.
- Brändli, M. (1996): Hierarchical models for the definition and extraction of terrain features. In: Burrough, P.A. and Frank, A.U., eds., *Geographic Objects with Indeterminate Boundaries*, Taylor and Francis, London, 257-270.
- Brazier, V., Kirkbride, M.P. and Owens, I.F. (1998): The relationship between climate and rock glacier distribution in the Ben Ohau Range, New Zealand. *Geografiska Annaler, Series A*, 80A(3-4), 193-205.
- Brecher, H. and Thompson, L.G. (1993): Measurement of the retreat of Qori Kalis in the tropical Andes of Peru by terrestrial photogrammetry. *Photogrammetric Engineering and Remote Sensing*, 59, 1017-1022.
- Brecher, H.H. (1986): Surface velocity determination on large polar glaciers by aerial photogrammetry. *Annals of Glaciology*, 8, 22-26.
- Briese, C. and Kraus, K. (2003): Datenreduktion dichter Laser-Geländemodelle. *ZfV - Zeitschrift für Geodäsie, Geoinformation und Landmanagement*, 128(5), 312-317.
- Bronge, L.B. and Bronge, C. (1999): Ice and snow-type classification in the Vestfold Hills, East Antarctica, using Landsat-TM data and ground radiometer measurements. *International Journal of Remote Sensing*, 20, 225-240.
- Brown, D.G., Lusch, D.P. and Duda, K.A. (1998): Supervised classification of types of glaciated landscapes using digital elevation data. *Geomorphology*, 21, 233-250.
- Brown, J., Ferrians Jr., O.J., Heginbottom, J.A. and Melnikov, E.S. (2001): Circum-arctic map of permafrost and ground ice conditions. National Snow and Ice Data Center/World Data Center for Glaciology. Digital media. Boulder, CO.
- Bruce, R., Cabera, G.A., Leiva, J.C. and Lenzano, L.E. (1987): The 1985 surge and ice dam of Glaciar Grande del Nevado del Plomo, Argentina. *Journal of Glaciology*, 33(113), 131-132.
- Brugmann, M.M. and Post, A. (1981): Effects of volcanism on the glaciers of Mount St. Helens. *US Geological Survey Circular*, 850-D, 11.
- Buchroithner, M. (2002a): Creating the virtual Eiger North Face. *ISPRS Journal of Photogrammetry and Remote Sensing*, 57(1-2), 114-125.
- Buchroithner, M.F., Jentsch, G. and Waniverhaus, B. (1982): Monitoring of recent glaciological events in the Khumbu Area (Himalaya, Nepal) by digital processing of Landsat MSS data. *Rock Mechanics*, 15(4), 181-197.
- Buchroithner, M. and Kirschenbauer, S. (1998): Derivation of relief information from various cartographic representations. *Wiener Schriften zur Geographie und Kartographie*, 11, 65-75.
- Buchroithner, M.F. (2002b): Meteorological and earth observation remote sensing data for mass movement preparedness. *Advances in Space Research*, 29(1), 5-16.
- Bucki, A.K. and Echelmeyer, K.A. (2004): The flow of Fireweed rock glacier, Alaska, USA. *Journal of Glaciology*, 50(168), 76-86.
- Bucki, A.K., Echelmeyer, K.A. and MacInnes, S. (2004): The thickness and internal structure of Fireweed rock glacier, Alaska, USA, as determined by geophysical methods. *Journal of Glaciology*, 50(168), 67-75.
- Buckley, A., Hurni, L., Kriz, K., Patterson, T. and Olsenholter, J. (2004): Cartography and visualization in mountain geomorphology. In: Bishop, M.P. and Shroder Jr., J.F., eds., *Geographic Information Science and Mountain Geomorphology*, Springer, Praxis, Chichester, UK, 253-287.
- Bull, W.B., King, J., Kong, F., Moutoux, T. and Phillips, W.M. (1994): Lichen dating of coseismic landslide hazards in alpine mountains. *Geomorphology*, 10, 253-264.
- Burga, C., Frauenfelder, R., Ruffet, J., Hoelzle, M. and Kääb, A. (2004): Vegetation on Alpine rock glacier surfaces: a contribution to abundance and dynamics on extreme plant habitats. *Flora*, 199, 505-515.

- Buziek, G., Dransch, D. and Rase, W.-D. (Editors), 2000. *Dynamische Visualisierungen - Grundlagen und Anwendungsbeispiele für kartographische Animationen*. Springer Verlag, Berlin Heidelberg New York.
- Campbell, J.B. (2002): *Introduction to remote sensing. Third edition*. Taylor and Francis, London. 621 pp.
- Carslaw, H.S. and Jaeger, J.C. (1959): *Conduction of heat in solids*. Oxford Science Publications. Clarendon Press, Oxford. 510 pp.
- Casassa, G., Brecher, H., Rivera, A. and Aniya, M. (1997): A century-long record of glacier O' Higgins, Patagonia. *Annals of Glaciology*, 24, 106-110.
- Casassa, G., Rivera, A., Aniya, M. and Naruse, R. (2002): Current knowledge of the Southern Patagonia Icefield. In: Casassa, G., Sepulveda, F. and Sinclair, R., eds., *The Patagonian Icefields. A unique natural laboratory for environmental and climate change studies*, Kluwer Academic / Plenum Publishers, 67-83.
- Casson, B., Delacourt, C., Baratoux, D. and Allemand, P. (2003): Seventeen years of the "La Clapière" landslide evolution analysed from ortho-rectified aerial photographs. *Engineering Geology*, 68(1-2), 123-139.
- Chandler, J. (1999): Effective application of automated digital photogrammetry for geomorphological research. *Earth Surface Processes and Landforms*, 24(1), 51-63.
- Chikita, K., Jha, J. and Yamada, T. (1999): Hydrodynamics of a supraglacial lake and its effect on the basin expansion: Tsho Rolpa, Rolwaling valley, Nepal Himalaya. *Arctic, Antarctic and Alpine Research*, 31, 58-70.
- Chorowicz, J., Parrot, J.-F., Taud, H., Hakdaoui, M., Rudant, J.P. and Rouis, T. (1995): Automated pattern-recognition of geomorphic features from DEMs and satellite images. *Zeitschrift für Geomorphologie. Supplementband*, 101, 69-84.
- Clague, J.J. and Mathews, W.H. (1973): The magnitude of jökulhlaups. *Journal of Glaciology*, 33(113), 501-504.
- Clague, J.J. and Evans, S.G. (1994): *Formation and failure of natural dams in the Canadian Cordillera*. Geological Survey of Canada, Bulletin, 464, Ottawa.
- Clague, J.J. and Evans, S.C. (2000): A review of catastrophic drainage of moraine-dammed lakes in British Columbia. *Quaternary Science Reviews*, 19(17-18), 1763-1783.
- Clark, R.N. (1999): Spectroscopy of rocks and minerals, and principles of spectroscopy. In: Rencz, A.N., ed., *Remote Sensing for the Earth Sciences. Manual of Remote Sensing*, 3rd Edition, John Wiley and Sons, New York, 3, 3-58.
- Clarke, G.K.C. (1982): Glacier outburst floods from 'Hazard Lake', Yukon Territory, and the problem of flood magnitude prediction. *Journal of Glaciology*, 28(98), 3-21.
- Cloude, S.R. and Papathanassiou, K.P. (1998): Polarimetric SAR interferometry. *IEEE Transactions on Geosciences and Remote Sensing*, 36(5), 1551-1565.
- Colesanti, C., Ferretti, A., Prati, C. and Rocca, F. (2003): Monitoring landslides and tectonic motions with the Permanent Scatterers Technique. *Engineering Geology*, 68(1-2), 3-14.
- Coltellini, M., Fornaro, G., Franceschetti, G., Lanari, R., Migliaccio, M., Moreira, J.R., Papathanassiou, K.P., Puglisi, G., Riccio, D. and Schwäbisch, M. (1996): SIR-C/X-SAR multifrequency multipass interferometry: A new tool for geological interpretation. *Journal Of Geophysical Research*, 101, 23127-23148.
- Conway, H., Rasmussen, L.A. and Marshall, H.P. (1999): Annual mass balance of Blue Glacier, USA. *Geografiska Annaler, Series A*, 81A(4), 509-520.
- Copland, L., Sharp, M.J. and Dowdeswell, J.A. (2003): The distribution and flow characteristics of surge-type glaciers in the Canadian High Arctic. *Annals of Glaciology*, 36, 73-81.
- Cosandier, D. (1999): *Generating a digital elevation model and orthomosaic from pushbroom imagery*. PhD thesis, Department of Geomatics Engineering, University of Calgary, Calgary, 277 pp.
- Costa, J.E. and Schuster, R.L. (1988): The formation and failure of natural dams. *Geological Society of America Bulletin*, 100, 1054-1068.
- Crippen, R.E. (1988): The dangers of underestimating the importance of data adjustments in band rationing. *International Journal of Remote Sensing*, 9(4), 767-776.
- Crippen, R.E. (1992): Measuring of subresolution terrain displacements using SPOT panchromatic imagery. *Episodes*, 15, 56-61.
- Crosetto, M. (2002): Calibration and validation of SAR interferometry for DEM generation. *ISPRS Journal of Photogrammetry and Remote Sensing*, 57(3), 213-227.
- Cuartero, A., Felicísimo, A.M. and Ariza, F.J. (2005): Accuracy, reliability, and depuration of SPOT HRV and Terra ASTER digital elevation models. *IEEE Transactions on Geoscience and Remote Sensing*, 43(2), 404-407.

- Curlander, J.C. and McDonough, R.N. (1991): *Synthetic Aperture Radar, Systems & Signal Processing, Introduction to SAR. Second edition.* J. Wiley & Sons Inc, New York. 672 pp.
- Dallimore, S.R., Nixon, F.M., Egginton, P.A. and Bisson, J.G. (1996): Deep-seated creep of massive ground ice, Tuktoyaktuk, NWT, Canada. *Permafrost and Periglacial Processes*, 7, 337–347.
- Davies, M.C.R., Hamza, O. and Harris, C. (2001): The effect of rise in mean annual temperature on the stability of rock slopes containing ice-filled discontinuities. *Permafrost and Periglacial Processes*, 12(1), 137-144.
- Davis, C.H., Klueve, C.A., Haines, B.J., Perez, C. and Yoon, Y.T. (2000): Improved elevation-change measurement of the southern Greenland ice sheet from satellite radar altimetry. *IEEE Transactions on Geoscience and Remote Sensing*, 38(3), 1367-1378.
- Deakin, R.E. and Kildea, D.G. (1999): Note on standard deviation and RMS. *The Australian Surveyor*, 44(1), 74-79.
- Dean, K.G., Dehn, J., Papp, K.R., Smith, S., Izbekov, P., Peterson, R., Kearney, C. and Steffke, A. (2004): Integrated satellite observations of the 2001 eruption of Mt. Cleveland, Alaska. *Journal of Volcanology and Geothermal Research*, 135(1-2), 51-73.
- Delacourt, C., Allemand, P., Casson, B. and Vadon, H. (2004): Velocity field of "La Clapière" landslide measured by the correlation of aerial and QuickBird satellite images. *Geophysical Research Letters*, 31(15), L15619, doi:10.1029/2004GL020193.
- Deline, P. (2001): Recent Brenva rock avalanches (Valley of Aosta): new chapter in an old story? *Supplementi di Geografia Fisica e Dinamica Quaternaria*, 5, 5-63.
- Deline, P., Diolaiuti, G., Kirkbride, M.P., Mortara, G., Pavan, M., Smiraglia, C. and Tamburini, A. (2004): Drainage of ice-contact Miage lake (Mont Blanc Massif, Italy) in September 2004. *Geografia Fisica e Dinamica Quaternaria*, 27, 113-119.
- Della Ventura, A., Rampini, A., Rabagliati, R. and Serandrei Barbero, R. (1983): Glacier monitoring by satellite. *Il Nuovo Cimento*, C-1(6), 211-221.
- Della Ventura, A., Rampini, A. and Serandrei Barbero, R. (1987): Development of a satellite remote sensing technique for the study of alpine glaciers. *International Journal of Remote Sensing*, 8, 203-215.
- Dikau, R., Brabb, E.E., Mark, R.K. and Pike, R.J. (1995): Morphometric landform analysis of New Mexico. *Zeitschrift für Geomorphologie. Supplementband*, 101, 109-126.
- Dikau, R., Cavallin, A. and Jäger, S. (1996a): Databases and GIS for landslide research in Europe. *Geomorphology*, 15(3-4), 227-239.
- Dikau, R., Gärtner, H., Holl, B., Kienholz, H., Mani, H.P. and Zimmermann, M. (1996b): Untersuchung zur Murgangaktivität im Mattertal, Wallis, Schweiz. *Proceedings, Interpraerent*, Garmisch-Partenkirchen, 1, 397-408.
- Dorren, L.K.A. (2003): A review of rockfall mechanics and modelling approaches. *Progress in Physical Geography*, 27(1), 69-87.
- Dorren, L.K.A. and Seijmonsbergen, A.C. (2003): GIS-based rockfall modelling at regional scale. *Geomorphology*, 56(1-2), 49-64.
- Dowdeswell, J.A., Unwin, B., Nuttall, A.M. and Wingham, D.J. (1999): Velocity structure, flow instability and mass flux on a large Arctic ice cap from satellite radar interferometry. *Earth and Planetary Science Letters*, 167(3-4), 131-140.
- Dowdeswell, J.A. and Benham, T.J. (2003): A surge of Perseibreen, Svalbard, examined using aerial photography and ASTER high-resolution satellite imagery. *Polar Research*, 22(2), 373-383.
- Dozier, J. (1989): Spectral signature of alpine snow cover from Landsat 5 TM. *Remote Sensing of Environment*, 28, 9-22.
- Dransch, D. (1997): *Computer-Animation in der Kartographie. Theorie und Praxis.* Springer Verlag, Berlin Heidelberg New York.
- Duan, J. and Grant, G.E. (2000): Shallow landslide delineation for steep forest watersheds based on topographic attributes and probability analysis. In: Wilson, J.P. and Gallant, J.C., eds., *Terrain analysis*, Wiley, New York etc., 311-329.
- Dwivedi, S.K., Acharya, M.D. and Simard, R. (2000): The Tam Pokhari glacier lake outburst flood of 3 September 1998. *Journal of Nepal Geological Society*, 22, 539-546.
- Ebner, H. (1987): Digital terrain models for high mountains. *Mountain Research and Developement*, 7(4), 353-356.
- Echelmeyer, K.A., Harrison, W.D., Larsen, C.F., Sapiano, J., Mitchell, J.E., DeMallie, J., Rabus, B., Adalgeirs Þóttir, G. and Sombardier, L. (1996): Airborne surface profiling of glaciers: a case-study in Alaska. *Journal of Glaciology*, 42(142), 3-9.

- Eckert, S. and Kellenberger, T. (2002): Qualitätsanalyse automatisch generierter digitaler Geländemodelle aus ASTER Daten. *Proceedings, 22. Wissenschaftlich-Technische Jahrestagung*, Neubrandenburg.
- Eckert, S., Kellenberger, T. and Itten, K. (2005): Accuracy assessment of automatically derived digital elevation models from ASTER data in mountainous terrain. *International Journal of Remote Sensing*, 26(9), 1943-1957.
- Eiken, T., Hagen, J.O. and Melyold, K. (1997): Kinematic GPS survey of geometry changes on Svalbard glaciers. *Annals of Glaciology*, 24, 157-163.
- Eisenbeiss, H., Baltsavias, E., Pateraki, M. and Zhang, L. (2004): Potential of Ikonos and Quickbird imagery for accurate 3D-point positioning, orthoimage and DSM generation. *International Archives of Photogrammetry and Remote Sensing*, 35(B3), 522-528.
- Eldhuset, K., Andersen, P.H., Hauge, S., Isaksson, E. and Weydahl, D.J. (2003): ERS tandem INSAR processing for DEM generation, glacier motion estimation and coherence analysis on Svalbard. *International Journal of Remote Sensing*, 24(7), 1415-1437.
- Engeset, R.V. (1999): Comparison of annual changes in winter ERS-1 SAR images and glacier mass balance of Slakbreen, Svalbard. *International Journal of Remote Sensing*, 20(2), 259-271.
- ERSDAC (1999a): ASTER User's Guide. Part I(2), Earth Remote Sensing Data Analysis Center, Tokyo, Japan.
- ERSDAC (1999b): ASTER User's Guide. Part II(2), Earth Remote Sensing Data Analysis Center, Tokyo, Japan.
- Espizua, L.E. and Bengoechea, J.D. (1990): Surge of Grande del Nevado Glacier (Mendoza, Argentina) in 1984: its evolution through satellite images. *Geografiska Annaler*, 72A(3-4), 255-259.
- Etzelmüller, B. (2000): On the quantification of surface changes using grid-based digital elevation models (DEMs). *Transactions in GIS*, 4(2), 129-143.
- Etzelmüller, B., Vatne, G., Ødegård, R. and Sollid, J.L. (1993): Mass balance and changes of surface slope, crevasse and flow pattern of Erikbreen, northern Spitsbergen: an application of a geographical information system (GIS). *Polar Research*, 12(2), 131-146.
- Etzelmüller, B. and Björnsson, H. (2000): Map analysis techniques for glaciological applications. *International Journal of Geographical Information Science*, 14(6), 567-581.
- Etzelmüller, B., Hoelzle, M., Heggem, E.S.F., Isaksen, K., Mittaz, C., Vonder Mühl, D., Ødegård, R.S., Haeberli, W. and Sollid, J.L. (2001a): Mapping and modelling the occurrence and distribution of mountain permafrost. *Norwegian Journal of Geography*, 55(4), 186 -194.
- Etzelmüller, B., Ødegård, R.S., Berthling, I. and Sollid, J.L. (2001b): Terrain parameters and remote sensing data in the analysis of permafrost distribution and periglacial processes: principles and examples from Southern Norway. *Permafrost and Periglacial Processes*, 12(1), 79-92.
- Evans, A.N. (2000): Glacier surface motion computation from digital image sequences. *IEEE Transactions on Geoscience and Remote Sensing*, 38(2), 1064-1072.
- Evans, I.S. and McClean, C.J. (1995): The land surface is not unifractal: variograms, cirque scale and allometry. *Zeitschrift für Geomorphologie. Supplementband*, 101, 127-147.
- Evans, S.G. and Clague, J.J. (1988): Catastrophic rock avalanches in glacial environment. *Proceedings, 5th International Symposium on Landslides*, Lausanne, 2, 1153-1158.
- Evans, S.G. and Clague, J.J. (1994): Recent climatic change and catastrophic geomorphic processes in mountain environments. *Geomorphology*, 10, 107-128.
- Falk, D., Brill, D. and Stork, D. (Editors), 1986. *Seeing the light. Optics in nature, photography, color, vision and holography*. Wiley, New York, 446 pp.
- Faller, N.P. and Meier, E.H. (1995): First results with the airborne single-pass DO-SAR interferometer. *IEEE Transactions on Geoscience and Remote Sensing*, 33(5), 1230-1237.
- Favay, E., Geiger, A., Gudmundsson, G.H. and Wehr, A. (1999): Evaluating the potential of an airborne laser scanning system for measuring volume changes of glaciers. *Geografiska Annaler*, 81A(4), 555-561.
- Ferretti, A., Prati, C. and Rocca, F. (2001): Permanent Scatterers in SAR interferometry. *IEEE Transactions of Geosciences and Remote Sensing*, 39(1), 8-20.
- Fink, J. (1980): Surface folding and viscosity of rhyolite flows. *Geology*, 8, 250-254.
- Finsterwalder, R. (1931): Geschwindigkeitsmessungen an Gletschern mittels Photogrammetrie. *Zeitschrift für Gletscherkunde und Glazialgeologie*, 19, 251-262.
- Finsterwalder, R. and Rentsch, H. (1980): Zur Höhenänderung von Ostalpengletschern im Zeitraum 1969-1979. *Zeitschrift für Gletscherkunde und Glazialgeologie*, 16, 111-115.

- Fischer, L. (2004): *Monte Rosa Ostwand - Geologie, Vergletscherung, Permafrost und Sturzereignisse in einer hochalpinen Steilwand*. Diploma thesis, Department of Geography, University of Zurich, and Department of Earth Sciences, ETH Zurich.
- Fletscher, R.C. (1974): Wavelength selection in the folding of a single layer with power-law rheology. *American Journal of Science*, 274, 1029-1043.
- Floricioiu, D. and Rott, H. (2001): Seasonal and short-term variability of multifrequency, polarimetric radar backscatter of alpine terrain from SIR-C/X-SAR and AIRSAR data. *IEEE Transactions on Geoscience and Remote Sensing*, 39(12), 2634 –2648.
- Flotron, A. (1979): Verschiebungsmessungen aus Luftbildern. *Mitteilungen der Versuchsanstalt für Wasserbau, Hydrologie und Glaziologie der ETH Zürich*, 41, 39-44.
- Forster, R.R., Rignot, E., Isacks, B.L. and Jezek, K.C. (1999): Interferometric radar observations of Glaciares Europa and Penguin, Hielo Patagonico Sur, Chile. *Journal of Glaciology*, 45(150), 325-337.
- Forster, R.R., Jezek, K.C., Koenig, L. and Deeb, E. (2003): Measurement of glacier geophysical properties from InSAR wrapped phase. *IEEE Transactions on Geosciences and Remote Sensing*, 41(11), 2595-2604.
- Förstner, W. (2000): Image preprocessing for feature extraction in digital intensity, color and range images. In: Dermanis, A., Grün, A. and Sansò, F., eds., *Geomatic Methods for the Analysis of Data in the Earth Sciences*. Lecture Notes in Earth Sciences, Springer, 95, 165-189.
- Fox, A.J. and Nuttall, A.M. (1997): Photogrammetry as a research tool for glaciology. *Photogrammetric Record*, 15(89), 725-738.
- Fox, A.J. and Gooch, M.J. (2001): Automatic DEM generation for antarctic terrain. *Photogrammetric Record*, 17(98), 275-290.
- Frank, T.D. (1988): Mapping dominant vegetation communities in the Colorado Rocky Mountain Front Range with Landsat TM. *Photogrammetric Engineering and Remote Sensing*, 54(12), 1727-1734.
- Fraser, C.S., Baltsavias, E.P. and Grün, A. (2002): Processing of Ikonos imagery for submetre 3D positioning and building extraction. *ISPRS Journal of Photogrammetry and Remote Sensing*, 56(3), 177-194.
- Frauenfelder, R. (2004): *Regional-scale modelling of rockglacier distribution and dynamics, and its implications for paleo-permafrost reconstruction*. PhD thesis, Department of Geography, University of Zurich.
- Frauenfelder, R., Allgöwer, B., Haeberli, W. and Hoelzle, M. (1998): Permafrost investigations with GIS - a case study in the Fletschhorn area, Wallis, Swiss Alps. *Proceedings, Seventh International Conference on Permafrost*, Yellowknife, Canada, Collection Nordicana, 57, 291-295.
- Frauenfelder, R. and Kääb, A. (2000): Towards a palaeoclimatic model of rock glacier formation in the Swiss Alps. *Annals of Glaciology*, 31, 281-286.
- Frauenfelder, R., Haeberli, W. and Hoelzle, M. (2003a): Rockglacier occurrence and related terrain parameters in a study area of the Eastern Swiss Alps. *Proceedings, Eighth International Conference on Permafrost*, Zurich, Balkema, 1, 253-258.
- Frauenfelder, R., Laustela, M. and Kääb, A. (2003b): Velocities and relative surface ages on selected Alpine rockglaciers. *Proceedings, Turbulenzen in der Geomorphologie. Jahrestagung der Schweizerischen Geomorphologischen Gesellschaft*, Erstfeld, Mitteilungen der Versuchsanstalt für Wasserbau, Hydrologie und Glaziologie, ETH Zürich, 184, 103-118.
- Frauenfelder, R., Zgraggen-Oswald, S., Huggel, C., Kääb, A., Haeberli, W., Galushkin, I. and Polkvoj, A. (2005): Permafrost distribution assessments in the North-Ossetian Caucasus: first results. *Geophysical Research Abstract, European Geosciences Union*, 7, 01619.
- Frezzotti, M., Capra, A. and Vittuari, L. (1998): Comparison between glacier ice velocities inferred from GPS and sequential satellite images. *Annals of Glaciology*, 27, 54-60.
- Friedli, M. (2004): *Kinematik von Fellsackungen*. Diploma thesis, Department of Geography, University of Zurich, in prep. pp.
- Friedman, K.S., Clemente, C.P., Pichel, W.G. and Li, X. (1999): Routine monitoring of changes in the Columbia Glacier, Alaska, with synthetic aperture radar. *Remote Sensing of Environment*, 70, 257-264.
- Frohn, R.C., Hinkel, K.M. and Eisner, W.R. (2005): Satellite remote sensing classification of thaw lakes and drained thaw lake basins on the North Slope of Alaska. *Remote Sensing of Environment*, in press.
- Fruneau, B., Achache, J. and Delacourt, C. (1996): Observation and modelling of the Saint-Etienne-de-Tinée landslide using SAR interferometry. *Tectonophysics*, 265(3-4), 181-190.
- Fujimura, S. and Kiyasu, S. (1999): Classification of terrain objects using hyperdimensional (multi-temporal multispectral) images through purpose-oriented feature extraction. *Proceedings, IEEE Geoscience and Remote Sensing Symposium, IGARSS'99*, Hamburg, 1192-1194.

- Funk, M. and Hoelzle, M. (1992): Application of a potential direct solar radiation model for investigating occurrences of mountain permafrost. *Permafrost and Periglacial Processes*, 3(2), 139-142.
- Gamache, M. (2004): Free and Low Cost Datasets for International Mountain Cartography. *Proceedings, 4th ICA Mountain Cartography Workshop*, Vall de Nuria, Catalonia, Spain.
- Gamma, P. (2000): *dfivalk - Ein Murgang-Simulationsprogramm zur Gefahrenzonierung*. PhD thesis, Department of Geography, University of Berne, Geographica Bernensia G66.
- Gansser, A. (1970): Lunana, the peaks, glaciers and lakes of northern Bhutan. *The Mountain World, Schweizerische Stiftung für Alpine Forschungen*, 1970, 117-131.
- Gao, J. and Liu, Y.S. (2001): Applications of remote sensing, GIS and GPS in glaciology: a review. *Progress in Physical Geography*, 25(4), 520-540.
- GAPHAZ (2004): Joint international working group on glacier and permafrost hazards in mountains. Commission on Cryospheric Sciences and International Permafrost Association. <http://www.geo.unizh.ch/gaphaz>.
- Garvin, J.B. and Williams, R.S. (1993): Geodetic airborne laser altimetry of Breidamerkurjökull and Skeidararjökull, Iceland, and Jakobshavn Isbræ, West Greenland. *Annals of Glaciology*, 17, 379-385.
- Geist, T., Lutz, E. and Stötter, J. (2003): Airborne laser scanning technology and its potential for applications in glaciology. *Proceedings, ISPRS Workshop on 3-D reconstruction from airborne laserscanner and INSAR data*, Dresden, Germany.
- Geist, T. and Stötter, H. (2003): First results of airborne laser scanning technolgy as a tool for the quantification of glacier mass balance. *EARSel eProceedings*, 2(1), 8-14.
- Gens, R. and van Genderen, J.L. (1996): SAR interferometry - Issues, techniques, applications. *International Journal of Remote Sensing*, 17, 1803–1835.
- Georgopoulos, A. and Skarlatos, D. (2003): A novel method for automating the checking and correction of digital elevation models using orthophotographs. *Photogrammetric Record*, 18(102), 156-163.
- Giani, G.P., Silvano, S. and Zanon, G. (2001): Avalanche of 18 January 1997 on Brenva glacier, Mont Blanc Group, Western Italian Alps: an unusual process of formation. *Annals of Glaciology*, 32, 333-338.
- Gillespie, A.R., Kahle, A.B. and Walker, R.E. (1986): Color enhancement of highly correlated images: I. Decorrelation and HSI contrast stretches. *Remote Sensing of Environment*, 20, 209-235.
- Goldstein, R.M., Engelhardt, H., Kamb, B. and Frolich, R.M. (1993): Satellite radar interferometry for monitoring ice sheet motion: application to an Antarctic ice stream. *Science*, 262(5139), 1525-1530.
- Gorbunov, A.P. and Titkov, S.N. (1992): Dynamics of rock glaciers of the northern Tien Shan and the Djungär Ala Tau, Kazakhstan. *Permafrost and Periglacial Processes*, 3, 29-39.
- Gratton, D.J., Howarth, P.J. and Marceau, D.J. (1990): Combining DEM parameters with Landsat MSS and TM imagery in a GIS for mountain glacier characterization. *IEEE Transactions on Geoscience and Remote Sensing*, 28(4), 766-769.
- Gratton, D.J., Howarth, P.J. and Marceau, D.J. (1993): Using Landsat-5 Thematic Mapper and digital elevation data to determine the net radiation field of a mountain glacier. *Remote Sensing of Environment*, 43, 315-331.
- Greuell, W. and de Ruyter de Wildt, M. (1999): Anisotropic reflection by melting glacier ice: measurements and parametrizations in Landsat TM bands 2 and 4. *Remote Sensing of the Environment*, 70, 265-277.
- Griffiths, G.A. and McSaveney, M.J. (1983): Distribution of mean annual precipitation across some steepland regions of New Zealand. *New Zealand Journal of Science*, 26(2), 197-209.
- Gross, H.N. and Schott, J.R. (1998): Application of spectral mixture analysis and image fusion techniques for image sharpening. *Remote Sensing of Environment*, 63(85-94).
- Grove, J.M. (1987): Glacier fluctuations and hazards. *Geographical Journal*, 153, 351-369.
- Gruber, S. (2000): *Slope instability and permafrost. A spatial analysis in the Matter Valley, Switzerland*. Master thesis, Department of Geography, Justus-Liebig-University of Giessen, Giessen, 66 pp.
- Gruber, S. and Hoelzle, M. (2001): Statistical modelling of mountain permafrost distribution: local calibration and incorporation of remotely sensed data. *Permafrost and Periglacial Processes*, 12(1), 69-77.
- Gruber, U. (2001): Using GIS for Avalanche Hazard Mapping in Switzerland. *Proceedings, ESRI International User Conference*, San Diego.
- Grün, A. and Sauermann, H. (1977): Photogrammetric determination of time-dependent variations of details of a glacier surface using a non-metric camera. *Proceedings, Symposium on dynamics of temperated glaciers and related problems.*, München.

- Grün, A. and Baltsavias, E.P. (1987): High-precision image matching for digital terrain modelling. *Photogrammetria*, 42, 97-112.
- Grün, A. and Baltsavias, E.P. (1988): Geometrically constrained multiphoto matching. *Photogrammetric Engineering and Remote Sensing*, 54(5), 633-641.
- Grün, A. and Zhang, L. (2002): Automatic DTM generation from three-line-scanners (TLS) images. *Proceedings, International Symposium Photogrammetry meets Geoinformatics - Kartdagrar 2002*, Jönköping, Sweden.
- Gudmundsson, G.H. (1997): Ice deformation at the confluence of two glaciers investigated with conceptual map-plane and flowline models. *Journal of Glaciology*, 43(145), 537-547.
- Gudmundsson, G.H. and Bauder, A. (1999): Towards an indirect determination of the mass-balance distribution of glaciers using the kinematic boundary condition. *Geografiska Annaler*, 81A(4), 575-583.
- Gudmundsson, G.H., Bassi, A., Vonmoos, M., Bauder, A., Fischer, U.H. and Funk, M. (2000): High-resolution measurements of spatial and temporal variations in surface velocities of Unteraargletscher, Bernese Alps, Switzerland. *Annals of Glaciology*, 31, 63-68.
- Guglielmin, M., Cannone, N. and Dramis, F. (2001): Permafrost-glacial evolution during the Holocene in the Italian Central Alps. *Permafrost and Periglacial Processes*, 12(1), 111-124.
- Guth, P.L. (1995): Slope and aspect calculations on gridded digital elevation models: Examples from a geomorphometric toolbox for personal computers. *Zeitschrift für Geomorphologie. Supplementband*, 101, 31-52.
- Gyasi-Agyei, Y., Willgoose, G. and De Troch, F. (1995): Effects of vertical resolution and map scale of digital elevation models on geomorphological parameters used in hydrology. *Hydrological Processes*, 9, 363-382.
- Häberling, C. (1999): Symbolisation in topographic 3D-maps - conceptual aspects for user-oriented design. *Proceedings, 19th ICA Conference*, Ottawa, Canada, 2, 1037-1044.
- Häberling, C. and Hurni, L. (2002): Mountain cartography: revival of a classic domain. *ISPRS Journal of Photogrammetry and Remote Sensing*, 57(1-2), 134-158.
- Haeberli, W. (1979): Holocene push-moraines in alpine permafrost. *Geografiska Annaler, Series A*, 61A, 43-48.
- Haeberli, W. (1983a): Frequency and characteristics of glacier floods in the Swiss Alps. *Annals of Glaciology*, 4, 85-90.
- Haeberli, W. (1983b): Permafrost-glacier relationships in the Swiss Alps – today and in the past. *Proceedings, Fourth International Conference on Permafrost*, Fairbanks, Alaska, National Academy Press, Washington, 415-420.
- Haeberli, W. (1985): *Creep of mountain permafrost*. Mitteilungen der Versuchsanstalt für Wasserbau, Hydrologie und Glaziologie der ETH Zürich, 77. 142 pp.
- Haeberli, W. (1992a): Construction, Environmental Problems and Natural Hazards in Periglacial Mountain Belts. *Permafrost and Periglacial Processes*, 3(2), 111-124.
- Haeberli, W. (1992b): Possible effects of climatic change on the evolution of Alpine permafrost. In: Boer, M. and Koster, E., eds., *Greenhouse-impact on cold-climate ecosystems and landscapes*, Catena Supplement, 22, 23-35.
- Haeberli, W. (1996): On the morphodynamics of ice/debris-transport systems in cold mountain areas. *Norwegian Journal of Geography*, 50, 3-9.
- Haeberli, W. (1998): Historical evolution and operational aspects of worldwide glacier monitoring. In: Haeberli, W., Hoelzle, M. and Suter, S., eds., *Into the second century of world glacier monitoring: prospects and strategies*. Studies and reports in hydrology, UNESCO, Paris, 56, 35-51.
- Haeberli, W. (2000): Modern research perspectives relating to permafrost creep and rock glaciers. *Permafrost and Periglacial Processes*, 11, 290-293.
- Haeberli, W. and Röhlisberger, H. (1975): Beobachtungen zum Mechanismus und zu den Auswirkungen von Kalbungen am Grubengletscher (Saastal, Schweiz). *Zeitschrift für Gletscherkunde und Glazialgeologie*, 11(2), 221-228.
- Haeberli, W., King, L. and Flotron, A. (1979): Surface movement and lichen-cover studies at the active rock glacier near the Grubengletscher, Wallis, Swiss Alps. *Arctic and Alpine Research*, 11(4), 421-441.
- Haeberli, W. and Fisch, W. (1984): Electrical resistivity soundings of glacier beds: a test study on Grubengletscher, Wallis, Swiss Alps. *Journal of Glaciology*, 30(106), 373-376.
- Haeberli, W. and Epifani, F. (1986): Mapping the distribution of buried glacier ice - an example from Lago Delle Locce, Monte Rosa, Italian Alps. *Annals of Glaciology*, 8, 78-81.

- Haeberli, W. and Schmid, W. (1988): Aerophotogrammetrical monitoring of rock glaciers. *Proceedings of the 5th International Conference on Permafrost*, 1, 764-769.
- Haeberli, W., Rickenmann, D., Zimmermann, M. and Rösli, U. (1990): Investigation of 1987 debris flows in the Swiss Alps: general concept and geophysical soundings, *Hydrology in Mountainous Regions II, Artificial Reservoirs, Water and Slopes*, IAHS, 194, 303-310.
- Haeberli, W. and Hoelzle, M. (1995): Application of inventory data for estimating characteristics of and regional climate-change effects on mountain glaciers: a pilot study with the European Alps. *Annals of Glaciology*, 21, 206-212.
- Haeberli, W. and Vonder Mühl, D. (1996): On the characteristics and possible origins of ice in rock glacier permafrost. *Zeitschrift für Geomorphologie*, 104, 43-57.
- Haeberli, W., Wegmann, M. and Vonder Mühl, D. (1997): Slope stability problems related to glacier shrinkage and permafrost degradation in the Alps. *Elogiae Geologicae Helvetiae*, 90, 407-414.
- Haeberli, W. and Beniston, M. (1998): Climate change and its impacts on glaciers and permafrost in the Alps. *AMBIO*, 27(4), 258-265.
- Haeberli, W., Hoelzle, M., Kääb, A., Keller, F., Vonder Mühl, D. and Wagner, S. (1998): Ten years after drilling through the permafrost of the active rock glacier Murtèl, Eastern Swiss Alps: answered questions and new perspectives. *Proceedings, 7th International Conference on Permafrost*, Yellowknife, Canada, 403-410.
- Haeberli, W., Kääb, A., Hoelzle, M., Bösch, H., Funk, M., Vonder Mühl, D. and Keller, F. (1999a): *Eisschwund und Naturkatastrophen im Hochgebirge*. Schlussbericht NFP31. vdf Hochschulverlag an der ETH Zürich, Zürich. 190 pp.
- Haeberli, W., Kääb, A., Wagner, S., Geissler, P., Haas, J.N., Glatzel-Mattheier, H., Wagenbach, D. and Vonder Mühl, D. (1999b): Pollen analysis and 14C-age of moss remains recovered from a permafrost core of the active rock glacier Murtèl/Corvatsch (Swiss Alps): geomorphological and glaciological implications. *Journal of Glaciology*, 45(149), 1-8.
- Haeberli, W., Cihlar, J. and Barry, R. (2000): Glacier monitoring within the Global Climate Observing System - a contribution to the Fritz Müller memorial. *Annals of Glaciology*, 31, 241-246.
- Haeberli, W., Kääb, A., Vonder Mühl, D. and Teyssiere, P. (2001): Prevention of debris flows from outbursts of periglacial lakes at Gruben, Valais, Swiss Alps. *Journal of Glaciology*, 47(156), 111-122.
- Haeberli, W. and Burn, C.R. (2002): Natural hazards in forests: glacier and permafrost effects as related to climate change. In: Sidle, R.C., ed., *Environmental change and geomorphic hazards in forests*. IUFRO Research Series, CABI Publishing, Wallingford/New York, 9, 167-202.
- Haeberli, W., Kääb, A., Paul, F., Chiarello, M., Mortara, G., Mazza, A. and Richardson, S. (2002a): A surge-type movement at Ghiacciaio del Belvedere and a developing slope instability in the east face of Monte Rosa, Macugnaga, Italian Alps. *Norwegian Journal of Geography*, 56(2), 104-111.
- Haeberli, W., Maisch, M. and Paul, F. (2002b): Mountain glaciers in global climate-related observation networks. *World Meteorological Organization Bulletin*, 51(1), 18-25.
- Haeberli, W., Brandova, D., Burga, C., Egli, M., Frauenfelder, R., Kääb, A., Maisch, M., Mauz, B. and Dikau, R. (2003): Methods for absolute and relative age dating of rock-glacier surfaces in alpine permafrost. *Proceedings, Eighth International Conference on Permafrost*, Zurich, Switzerland, Balkema, 1, 343-348.
- Haeberli, W. and Burn, C.R. (2003): Natural hazards in forests: glacier and permafrost effects as related to climate change. In: Sidle, R.C., ed., *Environmental Change and Geomorphic Hazards in Forests*. IUFRO Research Series, CABI Publishing, Oxon, United Kingdom.
- Haeberli, W., Huggel, C., Kääb, A., Oswald, S., Polvoj, A., Zotikov, I. and Osokin, N. (2005): The Kolka-Karmadon rock/ice slide of 20 September 2002 - an extraordinary event of historical dimensions in North Ossetia (Russian Caucasus). *Journal of Glaciology*, in press.
- Hagen, J.O., Melvold, K., Eiken, T., Isaksson, E. and Lefauconnier, B. (1999): Mass balance methods on Kongsvegen, Svalbard. *Geografiska Annaler*, 81A(4), 593-601.
- Hall, D.K., Chang, A.T.C. and Siddalingaiah, H. (1988): Reflectances of glaciers as calculated using Landsat 5 Thematic Mapper data. *Remote Sensing of Environment*, 25(3), 311-321.
- Hall, D., Chang, A.T.C., Foster, J.L., Benson, C.S. and Kovalick, W.M. (1989): Comparison of in situ and Landsat derived reflectances of Alaskan glaciers. *Remote Sensing of Environment*, 28, 493-504.
- Hall, D.K., Bindschadler, R.A., Foster, J.L., Chang, A.T.C. and Siddalingaiah, H. (1990): Comparison of in situ and satellite derived reflectances of Forbindels Glacier, Greenland. *International Journal of Remote Sensing*, 11, 493 - 504.
- Hall, D.K., Williams, R.S. and Bayr, K.J. (1992): Glacier recession in Iceland and Austria. *EOS Transactions, American Geophysical Union*, 73(12), 129,135,141.

- Hall, D.K., Riggs, G.A. and Salomonson, V.V. (1995a): Development of methods for mapping global snow cover using Moderate Resolution Imaging Spectroradiometer (MODIS) data. *Remote Sensing of Environment*, 53, 127-140.
- Hall, D.K., Williams, R.S. and Sigurdsson, O. (1995b): Glaciological observations on Bruarjökull, Iceland, using synthetic aperture radar and Thematic Mapper satellite data. *Annals of Glaciology*, 21, 271-276.
- Harbitz, C., Harbitz, A. and Nadim, F. (2001): On probability analysis in snow avalanche hazard zonation. *Annals of Glaciology*, 32, 290-298.
- Hardy, C.C. and Burgan, R.E. (1999): Evaluation of NDVI for monitoring moisture in three vegetation types of the western U.S. *Photogrammetric Engineering and Remote Sensing*, 65(5), 603-610.
- Harris, C. and Haeberli, W. (2003): Warming permafrost in the mountains of Europe. *World Meteorological Organization Bulletin*, 52(3), 252-257.
- Harrison, W.D. and Post, A.S. (2003): How much do we really know about glacier surging? *Annals of Glaciology*, 36, 1-6.
- Hauber, E., Slupetzky, H., Jaumann, R., Wevel, F., Gwinner, K. and Neukum, G. (2000): Digital and automated high resolution stereo mapping of the Sonnblick glacier (Austria) with HRSC-A. *Proceedings, EARSeL-SIG-Workshop Land Ice and Snow*, Dresden, Germany, 246-254.
- Hauck, C. (2001): *Geophysical methods for detecting permafrost in high mountains*. PhD thesis, Versuchsanstalt für Wasserbau, Hydrologie und Glaziologie der ETH Zürich, Zürich, 204 pp.
- Hellwich, O. (1999): An alternative paradigm for data evaluation in remote sensing using multisensor data fusion. *Proceedings, IEEE Geoscience and Remote Sensing Symposium, IGARSS'99*, Hamburg, 299-301.
- Hirano, A., Welch, R. and Lang, H. (2003): Mapping from ASTER stereo image data: DEM validation and accuracy assessment. *ISPRS Journal of Photogrammetry and Remote Sensing*, 57(5-6), 356-370.
- Hoelzle, M. (1992): Permafrost occurrence from BTS measurements and climatic parameters in the eastern Swiss Alps. *Permafrost and Periglacial Processes*, 3(2), 143-147.
- Hoelzle, M. (1996): Mapping and modelling of mountain permafrost distribution in the Alps. *Norwegian Journal of Geography*, 50, 11-15.
- Hoelzle, M. and Haeberli, W. (1995): Simulating the effects of mean annual air temperature changes on permafrost distribution and glacier size. An example from the Upper Engadin, Swiss Alps. *Annals of Glaciology*, 21, 400-405.
- Hoelzle, M., Wagner, S., Käab, A. and Vonder Mühll, D. (1998): Surface movement and internal deformation of ice-rock mixtures within rock glaciers in the Upper Engadin, Switzerland. *Proceedings, 7th International Conference on Permafrost*, Yellowknife, Canada, 465-472.
- Hoelzle, M., Mittaz, C., Etzelmüller, B. and Haeberli, W. (2001): Surface energy fluxes and distribution models of permafrost in European mountain areas: an overview of current developments. *Permafrost and Periglacial Processes*, 12(1), 53-68.
- Hofmann, C., Schwäbisch, M., Och, S., Wimmer, C. and Moreira, J.R. (1999): Multipath P-Band interferometry - first results. *Proceedings, Fourth International Airborne Remote Sensing*, Ottawa, 2, 732-737.
- Hofmann, W. (1958): Bestimmung von Gletschergeschwindigkeiten aus Luftbildern. *Bildmessung und Luftbildwesen*, 3, 71-88.
- Holben, B.N. and Justice, C.O. (1981): An examination of spectral band rationing to reduce the topographic effect on remotely sensed data. *International Journal of Remote Sensing*, 2(2), 115-133.
- Holm, K., Bovis, M. and Jakob, M. (2004): The landslide response of alpine basins to post-Little Ice Age glacial thinning and retreat in southwestern British Columbia. *Geomorphology*, 57(3-4), 201-216.
- Honikel, M. (1999): Strategies and methods for the fusion of digital elevation models from optical and SAR data. *Proceedings, Joint ISPRS/EARSeL Workshop "Fusion of Sensor Data, Knowledge Sources and Algorithms for Extraction and Classification of Topographic Objects"*, Valladolid, Spain, 83-89.
- Honikel, M. (2002): *Fusion of spaceborne stereo-optical and interferometric SAR data for digital terrain model generation*. Mitteilungen des Institutes für Geodäsie und Photogrammetrie, 76.
- Hook, S.J., Gabell, A.R., Green, A.A. and Kealy, P.S. (1992): A comparison of techniques for extracting emissivity information from thermal infrared data for geologic studies. *Remote Sensing of the Environment*, 42, 123-135.
- Hook, S.J., Abbott, E.A., Grove, C., Kahle, A.B. and Palluconi, F. (1999): Use of multispectral thermal infrared data in geological studies. In: Rencz, A.N., ed., *Remote Sensing for the Earth Sciences. Manual of Remote Sensing*, 3rd Edition, John Wiley and Sons, New York, 3, 59-110.
- Howind, J. and Schmitt, G. (2001): Geodätische Überwachung einer Grosshangbewegung in Ebnit/Vorarlberg. *Zeitschrift für Vermessungswesen*, 126(1), 1-5.

- Hubbart, A., Willis, I., Sharp, M., Mair, D., Nienow, P., Hubbard, B. and Blatter, H. (2000): Glacier mass-balance determination by remote sensing and high resolution modelling. *Journal of Glaciology*, 46(154), 491-498.
- Huber, S. and Sieber, R. (2001): From flatland to spaceland. Concepts for interactive 3D navigation in high standard atlases. *Proceedings, 20th International Cartographic Conference ICC*, Beijing, China, 2, 841-848.
- Huber, S., Sieber, R. and Wipf, A. (2003): Multimedia in der Gebirgskartographie – 3D-Anwendungen aus dem "Atlas der Schweiz - interaktiv 2". *Kartographische Nachrichten*, 53(5), 217-224.
- Huggel, C. (1998): *Periglaziale Seen im Luft- und Satellitenbild*. Diploma thesis, Department of Geography, University of Zurich.
- Huggel, C. (2004): *Assessment of glacial hazards based on remote sensing and GIS modeling*. Department of Geography, University of Zurich, Physical Geography Series, 44.
- Huggel, C., Kääb, A., Haeberli, W., Teyssiere, P. and Paul, F. (2002): Satellite and aerial imagery for analysing high mountain lake hazards. *Canadian Geotechnical Journal*, 39(2), 316-330.
- Huggel, C., Haeberli, W., Kääb, A., Ayros, E. and Portocarrero, C. (2003a): Assessment of glacier hazards and glacier runoff for different climate scenarios based on remote sensing data: a case study for a hydropower plant in the Peruvian Andes. *EARSeL eProceedings*, 2, 22-33.
- Huggel, C., Kääb, A. and Haeberli, W. (2003b): Regional-scale models of debris flows triggered by lake outbursts: the June 25, 2001 debris flow at Täsch (Switzerland) as a test study. In: Rickenmann and Chen, eds., *Debris Flows Hazards Mitigation: Mechanics, Prediction and Assessment*, Millpress, Rotterdam.
- Huggel, C., Kääb, A., Haeberli, W. and Krummenacher, B. (2003c): Regional-scale GIS-models for assessment of hazards from glacier lake outbursts: evaluation and application in the Swiss Alps. *Natural Hazards and Earth System Science*, 3(6), 647-662.
- Huggel, C., Haeberli, W., Kääb, A., Bieri, D. and Richardson, S. (2004a): Assessment procedures for glacial hazards in the Swiss Alps. *Canadian Geotechnical Journal*, 41(6), 1068-1083.
- Huggel, C., Kääb, A., Reynolds, J.M. and Heald, A. (2004b): Impact-oriented models for potential lake outbursts and ASTER-based application in the Peruvian Andes. *Proceedings, Fachtagung Schweizerische Geomorphologische Gesellschaft*, Erstfeld, 129-143.
- Huggel, C., Kääb, A. and Salzmann, N. (2004c): GIS-based modeling of glacial hazards and their interactions using Landsat TM and Ikonos imagery. *Norwegian Journal of Geography*, 58, 61-73.
- Huggel, C., Zgraggen-Oswald, S., Haeberli, W., Kääb, A., Polkvoj, A., Galushkin, I. and Evans, S.G. (2005): The 2002 rock/ice avalanche at Kolka/Karmadon, Russian Caucasus: assessment of extraordinary avalanche formation and mobility, and application of QuickBird satellite imagery. *Natural Hazards and Earth System Sciences*, 5, 173-187.
- Humlum, O. (1998): The climatic significance of rock glaciers. *Permafrost and Periglacial Processes*, 9(4), 375-395.
- Hurni, L., Kääb, A. and Häberling, C. (2000): Kartographische Darstellungen glazialer Phänomene. Zeitliche Entwicklung und heutiger Stand. *Salzburger Geographische Arbeiten*, 36, 23-38.
- Ikeda, A., Matsuoka, N. and Kääb, A. (2003): A rapidly moving small rock glacier at the lower limit of the mountain permafrost belt in the Swiss Alps. *Proceedings, Eighth International Conference on Permafrost*, Zurich, Balkema, 1, 455-460.
- IPCC (2001a): Climate Change 2001 - Impacts, Adaption and Vulnerability. Intergovernmental Panel on Climate Change. Third Assessment Report of the Working Group II.
- IPCC (2001b): Climate Change 2001 - The Scientific Basis. Intergovernmental Panel on Climate Change. Third Assessment Report of the Working Group I.
- Irving, D.H.B. (2000): *The application of geotechnical centrifuge modelling to the deformation of permafrost*. PhD thesis, University of Cardiff.
- Isakowski, Y. (2003): *Animation mit SVG als Visualisierungsmethode von räumlich-zeitlichen Prozessen in der Glaziologie*. Diploma thesis, FB Vermessungswesen/ Kartographie, HTW Dresden (FH); Institut für Kartographie, ETH Zürich.
- Isaksen, K., Ødegård, R.S., Eiken, T. and Sollid, J.L. (2000): Composition, flow and development of two tongue-shaped rock glaciers in the permafrost of Svalbard. *Permafrost and Periglacial Processes*, 11, 241-257.
- Iverson, R.M. (1997): The physics of debris flows. *Reviews of Geophysics*, 35(3), 245-296.
- Iverson, R.M., Schilling, S.P. and Vallance, J.W. (1998): Objective delineation of lahar-inundation hazard zones. *Geological Society of America Bulletin*, 110(8), 972-984.
- Jackson, L.E., Hungr, J.S., Gardner, J.S. and Mackay, C. (1989): Cathedral Mountain debris flows. *Bulletin International Association of Engineering Geology*, 40, 35-54.

- Jacobs, J.D., Simms, E.L. and Simms, A. (1997): Recession of the southern part of Barnes Ice Cap, Baffin Island, Canada, between 1961 and 1993, determined from digital mapping of Landsat TM. *Journal of Glaciology*, 43(143), 98-102.
- Janeras, M., Navarro, M., Arnó, G., Ruiz, A., Kornus, W., Talaya, J., Barberà, M. and López, F. (2004): LIDAR applications to rock fall hazard assessment in Vall de Núria. *Proceedings, 4th ICA Mountain Cartography Workshop*, Vall de Núria, Catalonia, Spain.
- Jiskoot, H., Pederson, A.K. and Murray, T. (2001): Multi-model photogrammetric analysis of the 1990s surge of Sortebræ, East Greenland. *Journal of Glaciology*, 47, 677-687.
- Jones, D.P., Richer, K.E., Desloges, J.R. and Maxwell, M. (1985): Glacier outburst flood on the Noeick river, Geological Survey of Canada. Open file report, Vancouver, Canada.
- Joseph, G. (2000): How well do we understand Earth observation electro-optical sensor parameters. *ISPRS Journal of Photogrammetry and Remote Sensing*, 55, 9-12.
- Joughin, I., Winebrenner, D., Fahnestock, M. and Kwok, R.K., W. (1996): Measurement of ice-sheet topography using satellite radar interferometry. *Journal of Glaciology*, 42(140), 10-22.
- Joughin, I.R., Kwok, R. and Fahnestok, M.A. (1999a): Interferometric estimation of three-dimensional ice-flow using ascending and descending passes. *IEEE Transactions on Geoscience and Remote Sensing*, 36(1), 25-37.
- Joughin, I., Gray, L., Bindschadler, R., Price, S., Morse, D., Hulbe, C., Mattar, K. and Werner, C. (1999b): Tributaries of West Antarctic ice streams revealed by RADARSAT interferometry. *Science*, 286(5438), 283-286.
- Julio Miranda, P., Gonzales-Huesca, A.E., Delgado Granados, H. and Kääb, A. (2005): Ice-fire interactions on Popocatépetl volcano (Mexico): case study of the January 22, 2001 eruption. *Zeitschrift für Geomorphologie*, in press.
- Kääb, A. (1996a): Photogrammetrische Analyse von Gletschern und Permafrost. *Vermessung Photogrammetrie Kulturtechnik*, 1996(12), 639-644.
- Kääb, A. (1996b): *Photogrammetrische Analyse zur Früherkennung gletscher- und permafrostbedingter Naturgefahren im Hochgebirge*. Mitteilungen der Versuchsanstalt für Wasserbau, Hydrologie und Glaziologie der ETH Zürich, 145, Zürich. 182 pp.
- Kääb, A. (1998a): Oberflächenkinematik ausgewählter Blockgletscher des Oberengadins, *Beiträge aus der Gebirgs-Geomorphologie. Jahrestagung 1997 der Schweizerischen Geomorphologischen Gesellschaft*. Mitteilungen der Versuchsanstalt für Wasserbau, Hydrologie und Glaziologie der ETH Zürich, Zürich, 158, 121-140.
- Kääb, A. (1998b): Visualisierung glazialer und periglazialer Prozesse: Probleme und Ansätze. *Wiener Schriften zur Geographie und Kartographie*, 11, 94-101.
- Kääb, A. (2000): Photogrammetry for early recognition of high mountain hazards: new techniques and applications. *Physics and Chemistry of the Earth, Part B*, 25(9), 765-770.
- Kääb, A. (2001): Photogrammetric reconstruction of glacier mass balance using a kinematic ice-flow model: a 20-year time-series on Grubengletscher, Swiss Alps. *Annals of Glaciology*, 31, 45-52.
- Kääb, A. (2002): Monitoring high-mountain terrain deformation from air- and spaceborne optical data: examples using digital aerial imagery and ASTER data. *ISPRS Journal of Photogrammetry and Remote Sensing*, 57(1-2), 39-52.
- Kääb, A. (2004): *Mountain glaciers and permafrost creep. Methodical research perspectives from earth observation and geoinformatics technologies*. Habilitation thesis, Department of Geography, University of Zurich, 205 pp.
- Kääb, A. (2005): Combination of SRTM3 and repeat ASTER data for deriving alpine glacier flow velocities in the Bhutan Himalaya. *Remote Sensing of Environment*, 94(4), 463-474.
- Kääb, A., Gudmundsson, G.H. and Hoelzle, M. (1998): Surface deformation of creeping mountain permafrost. Photogrammetric investigations on rock glacier Murtèl, Swiss Alps. *Proceedings, 7th International Permafrost Conference*, Yellowknife, Canada, 531-537.
- Kääb, A., Haeberli, W. and Gudmundsson, G.H. (1997): Analysing the creep of mountain permafrost using high precision aerial photogrammetry: 25 years of monitoring Gruben rock glacier, Swiss Alps. *Permafrost and Periglacial Processes*, 8(4), 409-426.
- Kääb, A. and Funk, M. (1999): Modelling mass balance using photogrammetric and geophysical data. A pilot study at Gries glacier, Swiss Alps. *Journal of Glaciology*, 45(151), 575-583.
- Kääb, A. and Vollmer, M. (2000): Surface geometry, thickness changes and flow fields on creeping mountain permafrost: automatic extraction by digital image analysis. *Permafrost and Periglacial Processes*, 11(4), 315-326.
- Kääb, A., Haeberli, W., Huggel, C. and Paul, F. (2000a): Glacier- and permafrost-related hazards in high mountains: integrative assessment in the Swiss Alps based on remote sensing and geo-information systems. *Proceedings, X Congresso Peruano de Geología*, Lima, CD-ROM.

- Kääb, A., Huggel, C. and Paul, F. (2000b): Früherkennung hochalpiner Naturgefahren mittels Fernerkundung. *Proceedings, Interpraevent 2000*, Villach, 1, 49-60.
- Kääb, A. and Haeberli, W. (2001): Evolution of a high-mountain thermokarst lake in the Swiss Alps. *Arctic, Antarctic, and Alpine Research*, 33(4), 385-390.
- Kääb, A. and Vollmer, M. (2001): Digitale Photogrammetrie zur Deformationsanalyse von Massenbewegungen im Hochgebirge. *Vermessung Photogrammetrie Kulturtechnik*, 99(8), 538-543.
- Kääb, A., Isaksen, K., Eiken, T. and Farbrot, H. (2002a): Geometry and dynamics of two lobe-shaped rock glaciers in the permafrost of Svalbard. *Norwegian Journal of Geography*, 56, 152-160.
- Kääb, A., Paul, F., Maisch, M., Hoelzle, M. and Haeberli, W. (2002b): The new remote sensing derived Swiss glacier inventory: II. First results. *Annals of Glaciology*, 34, 362-366.
- Kääb, A., Huggel, C., Paul, F., Wessels, R., Raup, B., Kieffer, H. and Kargel, J. (2003a): Glacier monitoring from ASTER imagery: accuracy and applications. *EARSel eProceedings*, 2, 43-53.
- Kääb, A., Isakowski, Y., Paul, F., Neumann, A. and Winter, R. (2003b): Glaziale und periglaziale Prozesse: Von der statischen zur dynamischen Visualisierung. *Kartographische Nachrichten*, 53(5), 206-212.
- Kääb, A., Kaufmann, V., Ladstädter, R. and Eiken, T. (2003c): Rock glacier dynamics: implications from high-resolution measurements of surface velocity fields. *Proceedings, Eighth International Conference on Permafrost*, Zurich, Balkema, 1, 501-506.
- Kääb, A., Wessels, R., Haeberli, W., Huggel, C., Kargel, J. and Khalsa, S.J.S. (2003d): Rapid ASTER imaging facilitates timely assessment of glacier hazards and disasters. *EOS Transactions, American Geophysical Union*, 84(13), 117,121.
- Kääb, A. and Weber, M. (2004): Development of transverse ridges on rockglaciers. Field measurements and laboratory experiments. *Permafrost and Periglacial Processes*, 15(4), 379-391.
- Kääb, A., Huggel, C., Barbero, S. et al. (2004): Glacier hazards at Belvedere Glacier and the Monte Rosa east face, Italian Alps: processes and mitigation. *Proceedings, Interpraevent*, 1, 67-78.
- Kääb, A. and Kneisel, C. (2005): Permafrost creep within a recently deglaciated glacier forefield: Muragl, Swiss Alps. *Permafrost and Periglacial Processes*, in press.
- Kääb, A. and Reichmuth, T. (2005): Advance mechanisms of rockglaciers. *Permafrost and Periglacial Processes*, 16(2), 187-193.
- Kääb, A., Huggel, C., Fischer, L. et al. (2005a): Remote sensing of glacier- and permafrost-related hazards in high mountains: an overview. *Natural Hazards and Earth System Sciences*, 5, 527-554.
- Kääb, A., Lefauconnier, B. and Melvold, K. (2005b): Flow field of Kronebreen, Svalbard, using repeated Landsat7 and ASTER data. *Annals of Glaciology*, 42, in press.
- Kääb, A., Reynolds, J.M. and Haeberli, W. (2005c): Glacier and permafrost hazards in high mountains. In: Huber, U.M., Bugmann, H.K.M. and Reasoner, M.A., eds., *Global Change and Mountain Regions (A State of Knowledge Overview)*. Advances in Global Change Research, Springer, Dordrecht, 225-234.
- Kääb, A., Frauenfelder, R. and Roer, I. (2005d): On the reaction of rockglacier creep to surface temperature variations. *Global and Planetary Change*, submitted.
- Karma, Ageta, Y., Naito, N., Iwata, S. and Yabuki, H. (2003): Glacier distribution in the Himalayas and glacier shrinkage from 1963 to 1993 in the Bhutan Himalayas. *Bulletin of Glaciological Research*, 20, 29-40.
- Kaser, G., Juen, I., Georges, C., Gómez, J. and Tamayo, W. (2003): The impact of glaciers on the runoff and the reconstruction of mass balance history from hydrological data in the tropical Cordillera Blanca, Perú. *Journal of Hydrology*, 282(1-4), 103-144.
- Kaufmann, V. (1998a): Deformation analysis of the Doesen rock glacier (Austria). *Proceedings, Seventh International Conference on Permafrost*, Yellowknife, Canada, Collection Nordicana, 57, 551-556.
- Kaufmann, V. (1998b): Geomorphometric monitoring of active rock glaciers in the Austrian Alps. *Proceedings, 4th International Symposium on High-Mountain Remote Sensing Cartography*, Karlstadt, Sweden, 97-113.
- Kaufmann, V. and Plösch, R. (2000): Reconstruction and visualisation of the retreat of two small cirque glaciers in the Austrian Alps since 1850. In: Buchroithner, M., ed., *High Mountain Cartography 2000*. Kartographische Bausteine, Dresden University of Technology, 18, 239-253.
- Kaufmann, V. and Ladstädter, R. (2002): Spatio-temporal analysis of the dynamic behaviour of the Hochebenkar rock glaciers (Oetztal Alps, Austria) by means of digital photogrammetric methods. *Grazer Schriften der Geographie und Raumforschung*, 37, 119-140.
- Kaufmann, V. and Ladstädter, R. (2003): Quantitative analysis of rock glacier creep by means of digital photogrammetry using multi-temporal aerial photographs: two case studies in the Austrian Alps. *Proceedings, Eighth International Conference on Permafrost*, Zurich, Balkema, 1, 525-530.

- Kaufmann, V. and Ladstädter, R. (2004): Documentation of the retreat of a small debris-covered cirque glacier (Goessnitzkees, Austrian Alps) by means of terrestrial photogrammetry. *Proceedings, 4th ICA Mountain Cartography Workshop*, Vall de Núria, Catalonia, Spain.
- Keller, P., Keller, I. and Itten, K.I. (1998): Combined hyperspectral data analysis of two Alpine lakes using CASI and DAIS 7915 imagery. *Proceedings, EARSeL workshop*, Zurich, CD-ROM.
- Kelley, R., Engeset, R., Kennett, M., Barrett, E.C. and Theakstone, W. (1997): Characteristic snow and ice properties of a Norwegian ice cap determined from complex ERS SAR. *Proceedings, 3rd ERS Symposium (ESA)*, Florence, Italy, CD-ROM.
- Kennett, M. and Eiken, T. (1997): Airborne measurement of glacier surface elevation by scanning laser altimeter. *Annals of Glaciology*, 24, 293-296.
- Kenyi, L.W. and Kaufmann, V. (2000): Detection and quantification of rock glacier deformation using ERS D-InSAR data. *Proceedings, ERS-Envisat Symposium "Looking down to Earth in the New Millennium"*. 16-20 October 2000, Gothenburg, Sweden, ESA Publications Division, SP-461.
- Kenyi, L.W. and Kaufmann, V. (2001): Estimation of alpine permafrost surface deformation using InSAR data. *Proceedings, IEEE International Geoscience and Remote Sensing Symposium*, Sydney, Australia, CD-ROM.
- Kenyi, L.W. and Kaufmann, V. (2003): Measuring rock glacier surface deformation using SAR interferometry. *Proceedings, Eighth International Conference on Permafrost*, Zurich, Balkema, 1, 537-541.
- Kerle, N. and Oppenheimer, C. (2002): Satellite remote sensing as a tool in lahar disaster management. *Disasters*, 26(2), 140-160.
- Kersten, T. and Meister, M. (1993): Grosser Aletschgletscher. Photogrammetrische Auswertungen als Grundlage für glaziologische Untersuchungen. *Vermessung Photogrammetrie Kulturtechnik*, 91(2), 75-80.
- King, L., Fisch, W., Haeberli, W. and Waechter, H.P. (1987): Comparison of resistivity and radio-echo soundings on rock-glacier permafrost. *Zeitschrift für Gletscherkunde und Glazialgeologie*, 23(1), 77-97.
- Kirkbride, M.P. (1993): The temporal significance of transitions from melting to calving termini at glaciers in the central Southern Alps of New Zealand. *The Holocene*, 3, 232-240.
- Kirkbride, M. (1995): Ice flow vectors on the debris-mantled Tasman glacier, 1957-1986. *Geografiska Annaler, Series A*, 77A(3), 147-157.
- Kirkbride, M.P. and Warren, C.R. (1999): Tasman glacier, New Zealand: 20th-century thinning and predicted calving retreat. *Global and Planetary Change*, 22, 11-28.
- Klein, A.G. and Isacks, B.L. (1999): Spectral mixture analysis of Landsat Thematic Mapper images applied to the detection of the transient snowline on tropical Andean glaciers. *Global and Planetary Change*, 22, 139-154.
- Knap, W.H., Brock, B.W., Oerlemans, J. and Willis, I.C. (1999): Comparison of Landsat-TM derived and ground-based albedos of Haut Glacier d'Arolla, Switzerland. *International Journal of Remote Sensing*, 20(17), 3293-3310.
- Kneisel, C. (1998): Occurrence of surface ice and ground ice/permafrost in recently deglaciated glacier forefields, St. Moritz area, Eastern Swiss Alps. *Proceedings, Seventh International Conference on Permafrost*, Yellowknife, Canada, Collection Nordicana, 57, 575-581.
- Kneisel, C. (1999): *Permafrost in Gletschervorfeldern*. Trierer Geographische Studien, 22. 156 pp.
- Kneisel, C. (2003): Sporadic and discontinuous mountain permafrost occurrences in the Upper Engadine, eastern Swiss Alps. *Proceedings, Eighth International Conference on Permafrost*, Zurich, Balkema, 1, 561-566.
- Kneisel, C., Haeberli, W. and Baumhauer, R. (2000): Comparison of spatial modelling and field evidence of glacier/permafrost-relations in an Alpine permafrost environment. *Annals of Glaciology*, 31, 269-274.
- Kniveton, D.R., De Graff, P.J., Granica, K. and Hardy, R.J. (2000): The development of a remote sensing based technique to predict debris flow triggering conditions in the French Alps. *International Journal of Remote Sensing*, 21(3), 419-434.
- Knizhnikov, Y.F. and Nikitin, A.V. (1997): Cartographic representation of the velocity field for a mountain glacier. *Proceedings, International Cartographic Conference*, Stockholm, 1, 294-298.
- Knizhnikov, Y.F., Gelman, R.N., Osipova, G.B. and Tsvetkov, D.G. (1998): Aerophotogrammetric study of ice movement in surging glaciers. *Zeitschrift für Gletscherkunde und Glazialgeologie*, 34(1), 69-84.
- Koelemeijer, R., Oerlemans, J. and Tjemkes, S. (1993): Surface reflectance of Hintereisferner, Austria, from Landsat 5 TM imagery. *Annals of Glaciology*, 17, 17-22.
- König, M., Winther, J.-G. and Isaksson, E. (2001): Measuring snow and ice properties from satellite. *Reviews of Geophysics*, 39(1), 1-27.

- König, M., Winther, J.-G., Kohler, J. and König, F. (2004): Two methods for firn-area and mass-balance monitoring of Svalbard glaciers with SAR satellite images. *Journal of Glaciology*, 50(168), 116-128.
- Koning, D.M. and Smith, D.J. (1999): Movement of King's Throne rock glacier, Mount Rae area, Canadian Rocky Mountains. *Permafrost and Periglacial Processes*, 10(2), 151-162.
- Konrad, S.K., Humphrey, N.F., Steig, E.J., Clark, D.H., Potter Jr., N. and Pfeffer, W.T. (1999): Rock glacier dynamics and paleoclimatic implications. *Geology*, 27(12), 1131-1134.
- Kotlyakov, V.M., Rototaeva, O.V. and Nosenko, G.A. (2004): The September 2002 Kolka glacier catastrophe in North Ossetia, Russian Federation. evidence and analysis. *Mountain Research and Development*, 24(1), 78-83.
- Krabill, W.B., Thomas, R.H., Martin, C.F., Swift, R.N. and Frederick, E.B. (1995): Accuracy of air-borne laser altimetry over the Greenland ice sheet. *International Journal of Remote Sensing*, 16(7), 1211-1222.
- Krainer, K. and Mostler, W. (2000): Reichenkar rock glacier: a glacier derived debris-ice system in the western Stubai Alps, Austria. *Permafrost and Periglacial Processes*, 11(3), 267-275.
- Kraus, K. (2002): Laser-Scanning – ein Paradigma-Wechsel in der Photogrammetrie. *Vermessung Photogrammetrie Kulturtechnik*, 100(10), 620-624.
- Krummenacher, B. and Keusen, H.R. (1997): Steinschlag-Sturzbahnen – Modell und Realität. *Mitteilungen der Schweizerischen Gesellschaft für Boden- und Felsmechanik*, 135.
- Krummenacher, B., Budmiger, K., Mihailovic, D. and Blank, B. (1998): *Periglaziale Prozesse und Formen im Furggental*, Gemmipass, 56. Eidgenössisches Institut für Schnee und Lawinenforschung, Davos.
- Kurnatowska, A.M. (1998): Large-scale vegetation mapping in mountain environments using remote sensing and plant physiology methods. In: Nieuwenhuis, G.J.A., Vaughan, R.A. and Molenaar, M., eds., *Operational Remote Sensing for Sustainable Development*, Balkema, Lisse, 61-65.
- Ladstädter, R. (1999): *Automatisierte Messung von Geländemodellen und Fließrektoren aus digitalen, multitemporalen Orthophotos - ein neuer Ansatz für das Blockgletscher-Monitoring*. Diploma thesis, Technical University of Graz, Austria.
- Ladstädter, R. (2001): Blockgletscher-Monitoring mittels Digitalphotogrammetrie. *Proceedings, 21. Wissenschaftlich-technische Jahrestagung*, Konstanz, 10, 459-466.
- Lambiel, C. and Delaloye, R. (2004): Contribution of real-time kinematic GPS in the study of creeping mountain permafrost: examples from the Western Swiss Alps. *Permafrost and Periglacial Processes*, 15(3), 229 - 241.
- Laustella, M., Egli, M., Frauenfelder, R., Käab, A., Maisch, M. and Haeberli, W. (2003): Weathering rind measurements and relative age dating of rockglacier surfaces in crystalline regions of the Eastern Swiss Alps. *Proceedings, Eighth International Conference on Permafrost*, Zurich, Switzerland, Balkema, 2, 627-632.
- Lefaouconnier, B. (1987): *Fluctuation glaciaires dans le Kongsfjord, 79°N, Spitsbergen, Svalbard; analyse et conséquences*. PhD thesis, Université de Grenoble.
- Lefaouconnier, B., Hagen, J.O. and Rudant, J.P. (1994): Flow speed and calving rate of Kronebreen glacier, Svalbard, using SPOT images. *Polar Research*, 13(1), 59-65.
- Lefsky, M.A., Cohen, W.B., Acker, S.A., Parker, G.G., Spies, T.A. and Harding, D. (1999): Lidar remote sensing of the canopy structure and biophysical properties of Douglas-fir/western hemlock forests. *Remote Sensing of the Environment*, 70, 339-361.
- Lenk, U. (2003): Triangulation und adaptive Triangulation - ein Verfahren zur Ausdünnung unregelmässig verteilter Massenpunkte in der Geländemodellierung. *Zeitschrift für Vermessungswesen*, 128(1), 47-56.
- Lerjen, M., Käab, A., Hoelzle, M. and Haeberli, W. (2003): Local distribution pattern of discontinuous mountain permafrost. A process study at Flüela Pass, Swiss Alps. *Proceedings, Eighth International Conference on Permafrost*, Zurich, Switzerland, Balkema, 2, 667-672.
- Lewkowicz, A.G. and Duguay, C.R. (1999): Detection of permafrost features using SPOT panchromatic imagery, Fosheim Peninsula, Ellesmere Island, N.W.T. *Canadian Journal of Remote Sensing*, 25(1), 34-44.
- Li, Z., Xu, Z., Cen, M. and Ding, X. (2001): Robust surface matching for automated detection of local deformations using least-median-of-squares estimator. *Photogrammetric Engineering and Remote Sensing*, 67(11), 1283-1292.
- Liang, L. and MacKay, D.S. (2000): A general model of watershed extraction and representation using globally optimal flow paths and up-slope contributing areas. *International Journal of Geographic Information Science*, 14(4), 337-358.
- Lillesand, T.M. and Kieffer, R.W. (2000): *Remote Sensing and image interpretation - fourth edition*. Wiley, New York etc.

- Lipton, A.E. and Ward, J.M. (1997): Satellite-view biases in retrieved surface temperatures in mountain areas. *Remote Sensing of the Environment*, 60, 92-100.
- Liu, J.G., Mason, P.J., Clerici, N., Chen, S., Davis, A., Miao, F., Deng, H. and Liang, L. (2005): Landslide hazard assessment in the Three Gorges area of the Yangtze river using ASTER imagery: Zigui-Badong. *Geomorphology*, 61(1-2), 171-187.
- Lliboutry, L., Morales, A.B., Pautre, A. and Schneider, B. (1977): Glaciological problems set by the control of dangerous lakes in Cordillera Blanca, Peru I, historic failure of moranic dams, their causes and prevention. *Journal of Glaciology*, 18(79), 239-254.
- Lobben, A. (2003): Classification and application of cartographic animation. *The Professional Geographer*, 55(3), 318-328.
- Loewenherz, D.S., Lawrence, C.J. and Weaver, R.L. (1989): On the development of transverse ridges on rock glaciers. *Journal of Glaciology*, 35(121), 383-391.
- Lougeay, R. (1974): Detection of buried glacial and ground ice with thermal infrared remote sensing. In: Santeford, H.S. and Smith, J.L., eds., *Advanced concepts and techniques in the study of snow and ice resources*, National Academy of Sciences, Washington D.C., 487-494.
- Lougeay, R. (1982): Landsat thermal imaging of alpine regions. *Photogrammetric engineering and remote sensing*, 269-273.
- Lucchitta, B.K. and Ferguson, H.M. (1986): Antarctica – measuring glacier velocity from satellite images. *Science*, 234(4780), 1105-1108.
- Luckman, A., Murray, T. and Strozzi, T. (2002): Three-dimensional surface flow evolution throughout a glacier surge measured by satellite radar interferometry. *Geophysical Research Letters*, 29(23), 10.1029/2001GL014570.
- Luckman, A., Murray, T., Jiskoot, H., Pritchard, H. and Strozzi, T. (2003): ERS SAR feature-tracking measurement of outlet glacier velocities on a regional scale in East Greenland. *Annals of Glaciology*, 36, 129-134.
- Lugon, R., Vonder Mühll, D. and Gardaz, J.M. (1999): La lave torrentielle de la moraine du Glacier du Dolent (Val Ferret, Massif du Mont Blanc). *Proceedings, Fachtagung der Schweizerischen Geomorphologischen Gesellschaft*, 29-36.
- Lugon, R. and Delaloye, R. (2001): Modelling alpine permafrost distribution, Val de Réchy, Valais Alps (Switzerland). *Norwegian Journal of Geography*, 55, 224-229.
- Lugon, R., Delaloye, R., Serrano, E., Reynard, E., Lambiel, C. and Gonzalez-Trueba, J.J. (2004): Permafrost and Little Ice Age glacier relationships, Posets Massif, Central Pyrenees, Spain. *Permafrost and Periglacial Processes*, 15(3), 207-220.
- Lüthi, M. (1994): *Stabilität steiler Gletscher: Eine Studie über den Einfluss möglicher Klimaänderungen; Untersuchungen am Beispiel eines Hängegletschers in der Westflanke des Eigers*. Diploma thesis, VAW, ETH Zurich.
- Lutz, E., Geist, T. and Stötter, J. (2003): Investigations of airborne laser scanning signal intensity on glacial surfaces - Utilizing comprehensive laser geometry modelling and orthophoto surface modelling (A case study: Svartisheibreen, Norway). *Proceedings, ISPRS Workshop on 3-D reconstruction from airborne laserscanner and INSAR data*, Dresden, Germany.
- Maas, G. (1997): *Mehr bildtechniken in der digitalen Photogrammetrie*. Mitteilungen des Institutes für Geodäsie und Photogrammetrie. ETH Zurich, 62, Zurich. 118 pp.
- Madson, S.N., Martin, J.M. and Zebker, H.A. (1995): Analysis and evaluation of the NASA/JPL TOPSAR across-track interferometric SAR system. *IEEE Transactions on Geoscience and Remote Sensing*, 33, 383-391.
- Maisch, M., Haeberli, W., Frauenfelder, R. and Kääb, A. (2003): Lateglacial and Holocene evolution of glaciers and permafrost in the Val Muragl, Upper Engadine, Swiss Alps. *Proceedings, Eighth International Conference on Permafrost*, Zurich, Balkema, 2, 717-722.
- Maisch, M., Haeberli, W., Hoelzle, M. and Wenzel, J. (1999a): Occurrence of rocky and sedimentary glacier beds in the Swiss Alps as estimated from glacier-inventory data. *Annals of Glaciology*, 28, 231-235.
- Maisch, M., Wipf, A., Denneler, B., Battaglia, J. and Benz, C. (1999b): *Die Gletscher der Schweizer Alpen: Gletscherhochstand 1850 - Aktuelle Vergletscherung - Gletscherschwund-Szenarien 21. Jahrhundert*. Schlussbericht NFP31. vdf Hochschulverlag, ETH Zurich.
- Major, J.J. and Newhall, C.G. (1989): Snow and ice perturbation during historical volcanic eruptions and the formation of lahars and floods. *Bulletin of Volcanology*, 52, 1-27.
- Mantovani, F., Soeters, R. and Van Westen, C.J. (1996): Remote sensing techniques for landslide studies and hazard zonation in Europe. *Geomorphology*, 15(3-4), 213-225.
- Margreth, S. and Funk, M. (1999): Hazard mapping for ice and combined snow/ice avalanches - two case studies from the Swiss and Italian Alps. *Cold Regions Science and Technology*, 30(1-3), 159-173.

- Markham, B.L. and Barker, J.L. (1985): Spectral characterization of the Landsat Thematic Mapper sensors. *International Journal of Remote Sensing*, 6(5), 697-716.
- Marshall, G.J., Rees, W.G. and Dowdeswell, J.A. (1995): The discrimination of glacier facies using multitemporal ERS - 1 SAR data. In: Askne, J., ed., *Sensors and environmental applications of remote sensing*, Balkema, Rotterdam, 263-269.
- Martin, H.E., Whalley, W.B., Orr, J. and Caseldine, C. (1994): Dating and interpretation of rock glaciers using lichenometry, South Tröllaskagi, North Iceland. In: Stötter, J. and Wilhelm, F., eds., *Environmental Change in Iceland*. Münchener Geographische Abhandlungen, Reihe B, München, 12, 205-224.
- Matsuoka, N. and Masahiro, A. (2002): Rock slope failures associated with deglaciation: some examples from glaciated valleys in the Swiss Alps. *Annual Report of the Institute of Geoscience. University of Tsukuba*, 28, 11-16.
- Mattar, K.E., Vachon, P.W., Geudtner, D., Gray, A.L., Cumming, I.G. and Brugman, M. (1998): Validation of alpine glacier velocity measurements using ERS tandem-mission SAR data. *IEEE Transactions on Geosciences and Remote Sensing*, 36(3), 974-984.
- Mätzler, C. (1987): Applications of the interaction of microwaves with the natural snow cover. *Remote Sensing Reviews*, 2, 259-392.
- Mayo, L.R. (1988): Advance of Hubbard Glacier and closure of Russel Fjord, Alaska - environmental effects and hazards in the Yakutat area. In: Galloway, J.P. and Hamilton, T.P., eds., *Geological studies in Alaska*. US Geological Survey Circular, 1016, 4-16.
- Mazza, A. (1998): Evolution and dynamics of Ghiacciaio Nord delle Locce (Valle Anzasca, Western Alps) from 1854 to the present. *Geografia Fisica e Dinamica Quaternaria*, 21, 233-243.
- Mazza, A. (2003): The kinematics wave theory: a possible application to "Ghiacciaio del Belvedere" (Valle Anzasca, Italian Alps). Preliminary hypothesis. *Terra Glacialis*, 6, 23-36.
- McDermid, G.J. and Franklin, S.E. (1994): Spectral, spatial and geomorphometric variables for the remote-sensing of slope processes. *Remote Sensing of Environment*, 49(1), 57-71.
- McDermid, G.J. and Franklin, S.E. (1995): Remote sensing and geomorphometric discrimination of slope processes. *Zeitschrift für Geomorphologie. Supplementband*, 101, 165-185.
- McSaveney, M.J., Chinn, T.J. and Hancox, G.T. (1992): Mount Cook rock avalanche of 14 December 1991, New Zealand. *Landslide News*, 6, 32-34.
- Meissl, G. (1998): *Modellierung der Reichweite von Felsstürzen – Fallbeispiele zur GIS-gestützten Gefahrenbeurteilung aus dem Bayrischen und Tiroler Alpenraum*. Innsbrucker Geographische Studien, Innsbruck.
- Melvold, K. (1992): Study of glacier motion on Kongsvegen and Kronebreen, Svalbard, Department of Geography, University of Oslo. 1.
- Mennis, J.L. and Fountain, A.G. (2001): A spatio-temporal GIS database for monitoring alpine glacier change. *Photogrammetric Engineering and Remote Sensing*, 67(8), 967-975.
- Messerli, B. and Zurbuchen, M. (1968): Blockgletscher im Weissmies und Aletsch und ihre photogrammetrische Kartierung. *Schweizer Alpen Club - Die Alpen*, 3, 139-152.
- Métrailler, S., Delaloye, R. and Lugon, R. (2003): Recent evolution of permafrost in both Becs-de-Bosson and Lona glacier/rock glacier complexes (western Swiss Alps). *Proceedings, Eighth International Permafrost Conference, Extended Abstracts*, Zurich, 107-108.
- Meyer, M., Haslinger, E., Häusler, H., Leber, D. and Wangda, D. (2003): The glacial chronology of eastern Lunana (NW Bhutan-Himalaya). *Proceedings, 16th INQUA Congress*, Reno, The Desert Research Institute, Reno, Abstract no. 54-10, 170.
- Michel, R. and Rignot, E. (1999): Flow of Moreno Glaciär, Argentina, from repeat-pass Shuttle Imaging Radar images: comparison of the phase correlation method with radar interferometry. *Journal of Glaciology*, 45(149), 93-100.
- Mitchell, H.L., Fryer, J.G. and Pâquet, R. (2002): Integration and filtering of 3D spatial data using a surface comparison approach. *Proceedings, Symposium on Geospatial Theory, Processing and Applications*, Ottawa, Canada.
- Mittaz, C., Hoelzle, M. and Haeberli, W. (2000): First results and interpretation of energy-flux measurements of Alpine permafrost. *Annals of Glaciology*, 31, 275-280.
- Mohr, J.J., Reeh, N. and Madsen, S.N. (1998): Three-dimensional glacial flow and surface elevation measured with radar interferometry. *Nature*, 391(6664), 273-276.
- Mool, P.K., Bajracharya, S.R. and Joshi, S.P. (2001a): *Inventory of glaciers, glacial lakes and glacial lake outburst floods. Nepal*. International Centre for Integrated Mountain Development, Kathmandu, Nepal. 365 pp.

- Mool, P.K., Wangda, D., Bajrachary, S.R., Kunzang, K., Gurung, D.R. and Joshi, S.P. (2001b): *Inventory of glaciers, glacial lakes and glacial lake outburst floods. Bhutan*. International Centre for Integrated Mountain Development, Kathmandu, Nepal. 227 pp.
- Moore, I.D. (1992): SRAD: direct, diffuse, reflected short wave radiation, and the effects of topographic shading. Terrain analysis programs for the environmental sciences (TAPES) radiation program documentation, Centre for Resource and Environmental Studies, Australian National University, Canberra.
- Moorman, B.J. and Vachon, P.W. (1998): Detecting ground ice melt with interferometric synthetic aperture radar. *Proceedings, 20th Canadian Symposium on Remote Sensing*, Calgary, Canada.
- Mora, P., Baldi, P., Casula, C., Fabris, M., Ghirotti, M., Mazzini, M. and Pesci, A. (2003): Global Positioning Systems and digital photogrammetry for the monitoring of mass movements: application to the Ca' di Malta landslide (northern Apennines, Italy). *Engineering Geology*, 68(1-2), 103-121.
- Mostyn, G.R. and Li, V. (1993): Probabilistic slope analysis - state of play. *Proceedings, Conference on Probabilistic Methods in Geotechnical Engineering*, Canberra, Australia, A.A. Balkema, Rotterdam, 89-110.
- Mouat, D.A., Mahin, G.G. and Lancaster, J. (1993): Remote sensing techniques in the analysis of change detection. *Geocarta International*, 2(39-50).
- Mulders, M.A. (2001): Advances in the application of remote sensing and GIS for surveying mountainous land. *International Journal of Applied Earth Observation and Geoinformation*, 3(1), 3-10.
- Müller, D. (1995): *Auflaufen und Überschwappen von Impulswellen an Talsperren*. Mitteilungen VAW / ETH Zürich, 137.
- Munechika, C.K., Warnick, J.S., Salvaggio, C. and Schott, J.R. (1993): Resolution enhancement of multispectral image data to improve classification accuracy. *Photogrammetric Engineering and Remote Sensing*, 59(1), 176-172.
- Murray, T., Strozzi, T., Luckman, A., Pritchard, H. and Jiskoot, H. (2002): Ice dynamics during a surge of Sortebræ, East Greenland. *Annals of Glaciology*, 34, 323-329.
- Nagler, T., Mayer, C. and Rott, H. (2002): Feasibility of DInSAR for mapping complex motion fields of Alpine ice- and rock-glaciers. *Proceedings, 3rd International Symposium on Retrieval of Bio- and Geophysical Parameters from SAR Data for Land Application*, Sheffield, UK, SP, 475, 377-382.
- Nakawo, M., Yabuki, H. and Sakai, A. (1999): Characteristics of Khumbu Glacier, Nepal Himalaya: recent change in the debris-covered area. *Annals of Glaciology*, 28, 118-122.
- Netanyahu, N.S., Le Moigne, J. and Masek, J.G. (2004): Georegistration of Landsat data via robust matching of multiresolution features. *IEEE Transactions on Geoscience and Remote Sensing*, 42(7), 1586-1600.
- Noetzli, J. (2003): *Felsstürze aus Permafrost über Gletschern*. Diploma thesis, Department of Geography, University of Zurich.
- Noetzli, J., Hoelzle, M. and Haeberli, W. (2003): Mountain permafrost and recent Alpine rock-fall events: a GIS-based approach to determine critical factors. *Proceedings, 8th International Conference on Permafrost*, Zurich, Balkema, 827-832.
- Noetzli, J., Huggel, C., Hoelzle, M. and Haeberli, W. (2005): GIS-based modelling of rock/ice avalanches from Alpine permafrost areas. *Computational Geosciences*, in press.
- Nogami, M. (1995): Geomorphometric measures for digital elevation models. *Zeitschrift für Geomorphologie. Supplementband*, 101, 53-67.
- Norvelle, R. (1996): Using iterative orthophoto refinements to generate and correct digital elevation models (DEM's), *Digital Photogrammetry: an Addendum to the Manual of Photogrammetry*, American Society for Photogrammetry and Remote Sensing, Falls Church, 151-155.
- Nunez, J., Otazu, X., Fors, O., Prades, A., Pala, V. and Arbiol, R. (1999): Multiresolution-based image fusion with additive wavelet decomposition. *IEEE Transactions on Geoscience and Remote Sensing*, 37(3), 1204-1211.
- O'Connor, J.E., Hardinson, J.H. and Costa, J.E. (2001): Debris flows from failures of Neoglacial-age moraine dams in the Three Sisters and Mount Jefferson wilderness areas, Oregon. *US Geological Survey Professional Paper*, 1606.
- Ødegård, R., Isaksen, K., Eiken, T. and Sollid, J.L. (2004): Terrain analyses and surface velocity measurements of Hiorthfjellet rock glacier, Svalbard. *Permafrost and Periglacial Processes*, 14(4), 359-365.
- Oerlemans, J., Anderson, B., Hubbard, A. et al. (1998): Modelling the response of glaciers to climate warming. *Climate Dynamics*, 14, 267-274.
- Olyphant, G.A. (1983): Computer simulation of rock-glacier development under viscous and pseudoplastic flow. *Geological Society of America Bulletin*, 94, 499-505.

- Olyphant, G.A. (1987): Rock glacier response to abrupt changes in talus production. In: Giardino, J.R., Shroder, J.F. and Vitek, J.D., eds., *rock glaciers*, 55-64.
- Ostir, K., Veljanovski, T., Podobnikar, T. and Stancic, Z. (2003): Application of satellite remote sensing in natural hazard management: the Mount Mangart landslide case study. *International Journal of Remote Sensing*, 24(20), 3983-4002.
- Oswald, S. (2001): *Kartierung und Modellierung von periglazialen Murgängen*. Diploma thesis, Department of Earth Sciences, ETH Zurich, and Department of Geography, University of Zurich.
- Paar, G., Bauer, A. and Kaufmann, V. (2001): Rock glacier monitoring using terrestrial laser scanning. Abstract. *Proceedings, 1st European Permafrost Conference*, Rome, 58-59.
- Painter, T.H., Dozier, J., Roberts, D.A., Davis, R.E. and Green, R.O. (2003): Retrieval of subpixel snow-covered area and grain size from imaging spectrometer data. *Remote Sensing of Environment*, 85(1), 64-77.
- Paterson, W.S.B. (1994): *The Physics of Glaciers. Third edition*. Elsevier, Oxford, etc. 380 pp.
- Patra, A.K., Bauer, A.C., Nichita, C.C. et al. (2005): Parallel adaptive numerical simulation of dry avalanches over natural terrain. *Journal of Volcanology and Geothermal Research*, 139(1-2), 1-21.
- Paul, F. (2001): Evaluation of different methods for glacier mapping using Landsat TM. *EARSeL eProceedings*, 1, 239-245.
- Paul, F. (2002a): Changes in glacier area in Tyrol, Austria, between 1969 and 1992 derived from Landsat 5 Thematic Mapper and Austrian Glacier Inventory data. *International Journal of Remote Sensing*, 23(4), 787-799.
- Paul, F. (2002b): Combined technologies allow for rapid analysis of glacier changes. *EOS, Transaction, American Geophysical Union*, 83(23), 253,260,261.
- Paul, F. (2004): *The new Swiss glacier inventory 2000 – Application of remote sensing and GIS*. PhD thesis, Department of Geography, University of Zurich.
- Paul, F., Kääb, A., Maisch, M., Kellenberger, T. and Haeberli, W. (2002): The new remote-sensing-derived Swiss glacier inventory: I. Methods. *Annals of Glaciology*, 34, 355-361.
- Paul, F., Kääb, A., Maisch, M., Kellenberger, T. and Haeberli, W. (2003): Das neue Schweizer Gletscherinventar 2000: Anwendungen in der Gebirgskartographie. *Kartographische Nachrichten*, 53(5), 212-217.
- Paul, F., Huggel, C. and Kääb, A. (2004): Mapping of debris-covered glaciers using multispectral and DEM classification techniques. *Remote Sensing of Environment*, 89(4), 510-518.
- Paul, F. and Kääb, A. (2005): Challenges for glacier inventorying from multispectral satellite data in the Canadian Arctic: Cumberland Peninsula, Baffin Island. *Annals of Glaciology*, 42, in press.
- Paul, F., Machguth, H. and Kääb, A. (2005): On the impact of glacier albedo under conditions of extreme glacier melt: the summer of 2003 in the Alps. *EARSeL eProceedings*.
- Pellemans, A.H.J.M., Jordans, R.W.L. and Allewijn, R. (1993): Merging multispectral and panchromatic SPOT images with respect to the radiometric properties of the sensor. *Photogrammetric Engineering and Remote Sensing*, 59(1), 81-87.
- Perruchoud, E. and Delaloye, R. (2005): Surveying the (seasonal) variations in rock glacier activity using GPS technique (western Swiss Alps). *Proceedings, 2nd European Conference on Permafrost*, Potsdam, Germany, Terra Nostra, GeoUnion Alfred-Wegener-Stiftung, Berlin, 2005/2, 99-100.
- Phillips, J.D. (1995): Nonlinear dynamics and the evolution of relief. *Geomorphology*, 14, 57-64.
- Phillips, M. (2000): *Influences of snow supporting structures on the thermal regime of the ground in alpine permafrost*. Swiss Federal Institute for Snow and Avalanche Research. Eidgenössische Forschungsanstalt WSL, Davos. 146 pp.
- Pierson, T.C., Janda, R.J., Thouret, J.C. and Borrero, C.A. (1990): Perturbation and melting of snow and ice by the 13 November 1985 eruption of Nevado del Ruiz, Colombia, and consequent mobilization, flow and deposition of lahars. *Journal of Volcanology and Geothermal Research*, 41, 17-66.
- Piesbergen, J. (2002): *ERS-1-SAR-Verarbeitungs- und Datenfusionsmethoden zur Schneekartierung im Hochgebirge*. Remote Sensing Series, 33. Remote Sensing Laboratories, Zurich. 170 pp.
- Pietroniro, A. and Leconte, R. (2000): A review of Canadian remote sensing applications in hydrology, 1995-1999. *Hydrological Processes*, 14, 1641-1666.
- Pike, R. (2000): Geomorphometry - diversity in quantitative surface analysis. *Progress in Physical Geography*, 24(1), 1-20.
- Pilgrim, L. (1996a): Robust estimation applied to surface matching. *ISPRS Journal of Photogrammetry and Remote Sensing*, 51, 243-257.
- Pilgrim, L.J. (1996b): Surface matching and difference detection without the aid of control points. *Survey Review*, 33(259), 291-303.

- Pillewizer, W. and Voigt, U. (1968): Block movement of glaciers, *Geodätische und geophysikalische Veröffentlichungen*, Berlin, R III.
- Pitkänen, T. and Kajutti, K. (2004): Close-range photogrammetry as a tool in glacier change detection. *ISPRS International Archives of Photogrammetry, Remote Sensing and Spatial Information Sciences*, XXXV(B7), 769-773.
- Plafker, G. and Erikson, F.E. (1978): Nevados Huascaran avalanches, Peru. In: Voight, B., ed., *Rock-slides and Avalanches. Natural Phenomena*, Elsevier, Amsterdam, 1, 277-314.
- Pohl, C. and Van Genderen, J.L. (1998): Multisensor image fusion in remote sensing: concepts, methods and applications. *International Journal of Remote Sensing*, 19(5), 823-854.
- Poli, D. (2002): General model for airborne and spaceborne linear array sensors. *International Archives of Photogrammetry and Remote Sensing*, 34(B1), 177-182.
- Popov, N. (1997): Glacial debris-flows mitigation in Kazakstan: assessment, prediction and control. *Proceedings, Debris-flow hazard mitigation: mechanics, prediction, and assessment*, San Franciso, American Society of Civil Engineers, 113-122.
- Potter, N. (1972): Ice-cored rock glacier, Galena Creek, Northern Absaroka Mountains, Wyoming. *Geological Society of America Bulletin*, 83, 3025-3058.
- Potter, N., Steig, E.J., Clark, D.H., Speece, M.A., Clark, G.M. and Updike, A.B. (1998): Galena Creek rock glacier revisited - New observations on an old controversy. *Geografiska Annaler*, 80A(3-4), 251-265.
- Powers, P.S., Chiarle, M. and Savage, W.Z. (1996): A digital photogrammetric method for measuring horizontal surficial movements on the Slumgullion earthflow, Hinsdale county, Colorado. *Computers and Geosciences*, 22(6), 651-663.
- Pulliainen, J., Engdahl, M. and Hallikainen, M. (2003): Feasibility of multi-temporal interferometric SAR data for stand-level estimation of boreal forest stem volume. *Remote Sensing of Environment*, 85(4), 397-409.
- Purdie, J. and Fitzharris, B. (1999): Processes and rates of ice loss at the terminus of Tasman glacier, New Zealand. *Global and Planetary Change*, 22, 79-91.
- Quincey, D., Lucas, R.M., Richardson, S.D., Glasser, N.F., Hambrey, M.J. and Reynolds, J.M. (2005): Optical remote sensing techniques in high-mountain environments: application to glacial hazards. *Progress in Physical Geography*, in press.
- Quinn, P., Beven, K., Chevallier, P. and Planchon, O. (1991): The prediction of hillslope flow paths for distributed hydrological modelling using digital terrain models. *Hydrological Processes*, 5, 59-79.
- Quinn, P.F., Beven, K.J. and Lamb, R. (1997): The $\ln(a/\tan b)$ index: how to calculate it and how to use it within the TOPMODEL framework. In: Beven, K.J., ed., *Distributed hydrological modelling, applications of the TOPMODEL concept*, Wiley, Chichester, 31-52.
- Rabus, B., Eineder, M., Roth, A. and Bamler, R. (2003): The shuttle radar topography mission - a new class of digital elevation models acquired by spaceborne radar. *ISPRS Journal of Photogrammetry and Remote Sensing*, 57(4), 241-262.
- Ranchin, T. and Wald, L. (1998): Sensor fusion to improve the spatial resolution of images: the ARSIS method. *Proceedings, 17th EARSeL Symposium*, Lyngby, Denmark, Balkema, Rotterdam, 445-451.
- Ranzi, R., Grossi, G., Iacovelli, L. and Taschner, S. (2004): Use of multispectral ASTER images for mapping debris-covered glaciers within the GLIMS project. *Proceedings, IEEE International Geoscience and Remote Sensing Symposium*, Anchorage, 2, 1144-1147.
- Rasemann, S., Schmidt, J., Schrott, L. and Dikau, R. (2004): Geomorphometry in mountain terrain. In: Bishop, M.P. and Shroder Jr., J.F., eds., *Geographic Information Science and Mountain Geomorphology*, Springer, Praxis, Chichester, UK, 101-145.
- Rasmussen, L.A. (1988): Bed topography and mass-balance distribution of Columbia Glacier, Alaska, U.S.A., determined from sequential aerial photography. *Journal of Glaciology*, 34(117), 208-216.
- Raup, B., Scharfen, G., Khalsa, S. and Kääb, A. (2001): The design of the GLIMS (Global Land Ice Measurements from Space) glacier database. *Eos Transactions supplement, American Geophysical Society*, 82(47).
- Raymond, C.F. (1987): How do glaciers surge. A review. *Journal of Geophysical Research*, 92(B9), 9121-9134.
- Reeh, N., Madsen, S.N. and Mohr, J.J. (1999): Combining SAR interferometry and the equation of continuity to estimate the three-dimensional glacier surface vector. *Journal of Glaciology*, 45(151), 533-538.

- Rencz, A., Harris, J., Sangster, D. and Budkewitsch, P. (2003): Spectral characteristics of bedrock map units using Landsat TM, radar and topographic data in an arctic environment: Borden Peninsula, Nunavut Territory, Canada. *Canadian Journal of Remote Sensing*, in press.
- Renouard, L., Perlant, F. and Nonin, P. (1995): Comparison of DEM generation from SPOT stereo and ERS interferometric SAR data. *EARSeL Advances in Remote Sensing — Topography from Space*, 4(2), 103-109.
- Rentsch, H., Welsch, W., Heipke, C. and Miller, M. (1990): Digital terrain models as a tool for glacier studies. *Journal of Glaciology*, 36(124), 273-278.
- Reynard, E., Lambiel, C., Delaloye, R., Devaud, G., Baron, L., Chapellier, D., Marescot, L. and Monnet, R. (2003): Glacier/permafrost relationships in forefields of small glaciers (Swiss Alps). *Proceedings, Eighth International Conference on Permafrost*, Zurich, Switzerland, Balkema, 2, 947-952.
- Reynolds, J.M. (1992): The identification and mitigation of glacier-related hazards: examples from the Cordillera Blanca, Peru. In: McCall, G.J.H., Loming, D.J.C. and Scott, S.C., eds., *Natural and man-made geohazards*, London, 143-157.
- Reynolds, J.M. (2000): On the formation of supraglacial lakes on debris-covered glaciers. In: Nakawo, M., Raymond, C.F. and Fountain, A., eds., *Debris-Covered Glaciers*. IAHS publications, 264, 153-161.
- Ribolini, A. (1999): Areal distribution of rock glaciers in the Argentera Massif (Maritime Alps) as a tool for recent glacial evolution reconstruction. *Geografia Fisica e Dinamica Quaternaria*, 22, 83-86.
- Richards, J.A. (1993): *Remote sensing digital image analysis - an introduction. Second edition*. Springer, Berlin. 334 pp.
- Richards, K., Arnold, N., Lane, S., Chandra, S., El-Hames, A., Mattikalli, N. and Chandler, J. (1995): Numerical landscapes: static, kinematic and dynamic process-form relations. *Zeitschrift für Geomorphologie. Supplementband*, 101, 201-220.
- Richardson, S.D. and Reynolds, J.M. (2000a): Degradation of ice-cored moraine dams: implications for hazard development, *Debris Covered Glaciers*, IAHS Publication 264, 187-197.
- Richardson, S.D. and Reynolds, J.M. (2000b): An overview of glacial hazards in the Himalayas. *Quaternary International*, 65/66, 31-47.
- Rickenmann, D. and Zimmermann, M. (1993): The 1987 debris flows in Switzerland: documentation and analysis. *Geomorphology*, 8, 175-189.
- Rignot, E., Forster, R. and Isacks, B. (1996): Interferometric radar observations of Glaciar San Rafael, Chile. *Journal of Glaciology*, 42(141), 279-291.
- Rignot, E., Hallet, B. and Fountain, A. (2002): Rock glacier surface motion in Beacon Valley, Antarctica, from synthetic-aperture radar interferometry. *Geophysical Research Letters*, 29(12), 1607.
- Rignot, E., Rivera, A. and Casassa, G. (2003): Contribution of the Patagonia Icefields of South America to sea level rise. *Science*, 302, 434-437.
- Rivera, A., Acuna, C., Casassa, G. and Bown, F. (2002): Use of remote sensing and field data to estimate the contribution of Chilean glaciers to the sea level rise. *Annals of Glaciology*, 34, 367-372.
- Rivera, A., Casassa, G., Bamber, J. and Kääb, A. (2005): Ice elevation changes in the Southern Patagonia Icefield, using ASTER DEMs, aerial photographs and GPS data. *Journal of Glaciology*, 51(172), in press.
- Roer, I., Kääb, A. and Dikau, R. (2005a): Rockglacier acceleration in the Turtmann valley (Swiss Alps) - probable controls. *Norwegian Journal of Geography*, 59(2), 157-163.
- Roer, I., Kääb, A. and Dikau, R. (2005b): Rockglacier kinematics derived from small-scale aerial photography and digital airborne pushbroom imagery. *Zeitschrift für Geomorphologie*, 49(1), 73-87.
- Rolstad, C. (1995): *Satellite -and aircraft images for determination of glacier dynamics*. Master thesis, Department of Geography, University of Oslo.
- Rolstad, C., Amlen, J., Hagen, J.O. and Lundén, B. (1997): Visible and near-infrared digital images for determination of ice velocities and surface elevation during a surge on Osbornebreen, a tide-water glacier in Svalbard. *Annals of Glaciology*, 24, 255-261.
- Rosenblüth, B., Fuenzalida, H. and Aceituno, P. (1997): Recent temperature variations in southern South America. *International Journal of Climatology*, 17, 67-85.
- Röthlisberger, H. (1981): Eislawinen und Ausbrüche von Gletscherseen, *Jahrbuch der Schweizerischen Naturforschenden Gesellschaft, wissenschaftlicher Teil*, 1978, 170-212.
- Röthlisberger, H. and Aellen, M. (1970): Bewegungsregistrierung an der Zunge des Giétroletschers. *Schweizerische Bauzeitung*, 43(88), reprint.
- Rott, H. (1976): Analyse der Schneeflächen auf Gletschern der Tiroler Zentralalpen aus Landsat-Bildern. *Zeitschrift für Gletscherkunde und Glazialgeologie*, 12(1), 1-18.
- Rott, H. (1994): Thematic studies in alpine areas by means of polarimetric SAR and optical imagery. *Advances in Space Research*, 14(3), 217-226.

- Rott, H. and Markl, G. (1989): Improved snow and glacier monitoring by the Landsat Thematic Mapper. *Proceedings, Workshop on Landsat Thematic Mapper applications*, ESA, SP-1102, 3 - 12.
- Rott, H. and Strobl, D. (1992): Synergism of SAR and Landsat TM imagery for thematic mapping in complex terrain. *Advances in Space Research*, 12(7), 425-431.
- Rott, H. and Siegel, A. (1997): Glaciological studies in the Alps and in Antarctica using ERS interferometric SAR. *Proceedings, ERS SAR Interferometry, ESA Fringe'96 Workshop*, Zurich, ESA SP 406, II, 149-159.
- Rott, H. and Siegel, A. (1999): Analysis of mass movement in alpine terrain by means of SAR interferometry. *Proceedings, IEEE Geoscience and Remote Sensing Symposium, IGARSS'99*, Hamburg, 1933-1936.
- Rowan, L.C. and Mars, J.C. (2003): Lithologic mapping in the Mountain Pass, California area using Advanced Spaceborne Thermal Emission and Reflection Radiometer (ASTER) data. *Remote Sensing of Environment*, 84(3), 350-366.
- Sabins, F.F. (1997): *Remote sensing: principles and interpretation*. Freeman, New York.
- Sabins, F.F. (1999): Remote sensing for mineral exploration. *Ore Geology Reviews*, 14(3-4), 157-183.
- Salisbury, J.W., D'Aria, D.M. and Wald, A. (1994): Measurements of thermal infrared spectral reflectance of frost, snow, and ice. *Journal of Geophysical Research*, 99(B12), 24235-24240.
- Salzmann, N. (2002): *Modellierung von Gefahrenpotentialen durch Eislawinen mittels Fernerkundung und GIS*. Diploma thesis, Department of Geography, University of Zurich.
- Salzmann, N., Kääb, A., Huggel, C., Allgöwer, B. and Haeberli, W. (2004): Assessment of the hazard potential of ice avalanches using remote sensing and GIS-modelling. *Norwegian Journal of Geography*, 58, 74-84.
- Sandmeier, S. and Itten, K. (1997): A physically-based model to correct atmospheric and illumination effects in optical satellite data of rugged terrain. *IEEE Transactions on Geoscience and Remote Sensing*, 35(3), 708-717.
- SANW (1982): Die Gletscher der Schweizer Alpen 1973/74 und 1974/75, Glaziologische Kommission der Schweizerischen Akademie der Naturwissenschaften.
- Savigny, K.W. and Morgenstern, N.R. (1986): In situ creep properties in ice-rich permafrost soil. *Canadian Geotechnical Journal*, 23, 504-514.
- Scambos, T.A., Dutkiewicz, M.J., Wilson, J.C. and Bindschadler, R.A. (1992): Application of image cross-correlation to the measurement of glacier velocity using satellite image data. *Remote Sensing of Environment*, 42(3), 177-186.
- Schenk, T., Krupnik, A. and Postolov, Y. (2002): Comparative study of surface matching algorithms. *International Archives of Photogrammetry and Remote Sensing*, 32(B4), 518-524.
- Schlaefli, S. (2005): *Interaktive, GIS-basierte Modellierung von Murgängen, Fels- und Eislawinen*. Diploma thesis, Department of Geography, University of Zurich.
- Schläpfer, D., Bojinski, S., Schaeppman, M. and Richter, R. (2000): Combination of geometric and atmospheric correction for AVIRIS data in rugged terrain. *Proceedings, AVIRIS workshop*, JPL, Pasadena.
- Schmidt, J. and Dikau, R. (1999): Extracting geomorphometric attributes and objects from digital elevation models - semantics, methods, future needs. In: Dikau, R. and Saurer, H., eds., *GIS for earth surface systems*, Borntraeger, Berlin, 153-173.
- Schmugge, T.J., Kustas, W.P. and Humes, K.S. (1998): Monitoring land surface fluxes using ASTER observations. *IEEE Transactions on Geoscience and Remote Sensing*, 36(5), 1421-1430.
- Schneider, B. and Schneider, H. (2001): Zur 60jährigen Messreihe der kurzfristigen Geschwindigkeitsschwankungen am Blockgletscher im Äusseren Hochebenkar, Ötztaler Alpen, Tirol. *Zeitschrift für Gletscherkunde und Glazialgeologie*, 37(1), 1-33.
- Schneider, D. (2005): *Modeling of lahar hazard potentials on glacier covered volcanoes: Iztaccíhuatl, Mexico*. Diploma thesis, Department of Geography, University of Zurich.
- Schowengerdt, R.A. (1997): *Remote sensing. Models and methods for image processing - second edition*. Academic Press, San Diego and Chestnut Hill.
- Schuler, D.L., Ainsworth, T.L., Lee, J.S. and De Grandi, G.F. (1998): Topography mapping using polarimetric SAR data. *International Journal of Remote Sensing*, 19(1), 141-160.
- Schwäbisch, M. and Moreira, J.R. (1999): The high resolution airborne interferometric SAR AeS-1. *Proceedings, Fourth International Airborne Remote Sensing*, Ottawa, 1, 540-547.
- Seko, K., Yakubi, H., Nakawo, M., Sakai, A., Kadota, T. and Yamada, Y. (1998): Changing surface features of Khumbu glacier, Nepal Himalayas revealed by SPOT images. *Bulletin of Glacier Research*, 16, 33-41.

- Sheridan, M.F., Hubbard, B., Carrasco-Nunez, G. and Siebe, C. (2004): Pyroclastic flow hazard at Volcan Citlaltepetl. *Natural Hazards*, 33(2), 209-221.
- Shroder Jr., J.F. and Bishop, M.P. (2004): Mountain geomorphic systems. In: Bishop, M.P. and Shroder Jr., J.F., eds., *Geographic Information Science and Mountain Geomorphology*, Springer, Praxis, Chichester, UK, 33-73.
- Sidjak, R.W. and Wheate, R.D. (1999): Glacier mapping of the Illecillewaet icefield, British Columbia, Canada, using Landsat TM and digital elevation data. *International Journal of Remote Sensing*, 20, 273-284.
- Silverio, W. and Jaquet, J.-M. (2005): Glacial cover mapping (1987-1996) of the Cordillera Blanca (Peru) using satellite imagery. *Remote Sensing of Environment*, 95, 342-350.
- Simard, R. (1987): Digital stereo processing of satellite image data. *Advances in Space Research*, 7(11), 227-235.
- Simone, G., Farina, A., Morabito, F.C., Serpico, S.B. and Bruzzone, L. (2002): Image fusion techniques for remote sensing applications. *Information Fusion*, 3(1), 3-15.
- Singh, A. (1989): Digital change detection techniques using remotely sensed-data. *International Journal of Remote Sensing*, 10(6), 989-1003.
- Singhroy, V. and Molch, K. (2004): Characterizing and monitoring rockslides from SAR techniques. *Advances in Space Research*, 33(3), 290-295.
- Skvarca, P., Raup, B. and De Angelis, H. (2003): Recent behaviour of Glaciar Upsala, a fast-flowing calving glacier in Lago Argentino, southern Patagonia. *Annals of Glaciology*, 36, 184-188.
- Sloan, V.F. and Dyke, L.D. (1998): Decadal and millennial velocities of rock glaciers, Selwyn Mountains, Canada. *Geografiska Annaler, Series A*, 80A(3-4), 237-249.
- Squarezoni, C., Delacourt, C. and Allemand, P. (2003): Nine years of spatial and temporal evolution of the La Valette landslide observed by SAR interferometry. *Engineering Geology*, 68(1-2), 53-66.
- Stebler, O., Meier, E. and Nüesch, D. (2002): Multi-baseline polarimetric SAR interferometry – first experimental spaceborne and airborne results. *ISPRS Journal of Photogrammetry and Remote Sensing*, 56(3), 149-166.
- Stebler, O., Barmettler, A., Divis, L., Small, D., Schwerzmann, A., Meier, E. and Nüesch, D. (2004): Swiss Alpine Airborne SAR Experiment (SASARE) part I: Multi-baseline polarimetric SAR interferometry studies at L- and P-band. *Proceedings, IEEE International Geoscience and Remote Sensing Symposium (IGARSS)*, Anchorage, Alaska, 2, 1116-1120.
- Stenoien, M.D. and Bently, C.R. (2000): Pine Island Glacier, Antarctica: a study of the catchment using interferometric synthetic aperture radar and radar altimetry. *Journal of Geophysical Research -Solid Earth*, 105(B9), 21761-21779.
- Stevens, N.F., Manville, V. and Heron, D.W. (2003): The sensitivity of a volcanic flow model to digital elevation model accuracy: experiments with digitised map contours and interferometric SAR at Ruapehu and Taranaki volcanoes, New Zealand. *Journal of Volcanology and Geothermal Research*, 119(1-4), 89-105.
- Stevens, N.F., Garbeil, H. and Mouginis-Mark, P.J. (2004): NASA EOS Terra ASTER: Volcanic topographic mapping and capability. *Remote Sensing of Environment*, 90, 405-414.
- Sties, M., Krüger, S., Mercer, J.B. and Schnick, S. (2000): Comparison of digital elevation data from airborne laser and interferometric SAR systems. *International Archives of Photogrammetry and Remote Sensing*, 33, 866-873.
- Stocker-Mittaz, C., Hoelzle, M. and Haeberli, W. (2002): Modelling alpine permafrost distribution based on energy-balance data: a first step. *Permafrost and Periglacial Processes*, 13(4), 271-282.
- Strozzi, T., Wegmüller, U., Tosi, L., Bitelli, G. and Spreckels, V. (2001): Land subsidence monitoring with differential SAR interferometry. *Photogrammetric Engineering and Remote Sensing*, 67(11), 1261-1270.
- Strozzi, T., Luckman, A., Murray, T., Wegmüller, U. and Werner, C.L. (2002): Glacier motion estimation using SAR offset-tracking procedures. *IEEE Transactions on Geosciences and Remote Sensing*, 40(11), 2384-2391.
- Strozzi, T., Gudmundsson, H. and Wegmüller, U. (2003a): Estimation of the surface displacement of Swiss alpine glaciers using satellite radar interferometry. *EARSel eProceedings*, 2(1), 3-7.
- Strozzi, T., Kääb, A., Frauenfelder, R. and Wegmüller, U. (2003b): Detection and monitoring of unstable high-mountain slopes with L-band SAR interferometry. *Proceedings, IGARSS'03*, Toulouse, France.
- Strozzi, T., Wegmüller, U., Kääb, A. and Frauenfelder, R. (2003c): Satellite radar interferometry for detecting and quantifying mountain permafrost creep. *Proceedings, Eighth International Permafrost Conference, Extended Abstracts*, Zurich, 155-156.

- Strozzi, T., Wegmüller, U., Wiesmann, A. and Werner, C. (2003d): Validation of the X-SAR SRTM DEM for ERS and JERS SAR geocoding and 2-pass differential interferometry in alpine regions. *Proceedings, IGARSS'03*, Toulouse, France.
- Strozzi, T., Kääb, A. and Frauenfelder, R. (2004): Detecting and quantifying mountain permafrost creep from in-situ, airborne and spaceborne remote sensing methods. *International Journal of Remote Sensing*, 25(15), 2919-2931.
- Stumm, D. (2001): *Erkennung geomorphologischer Formen mit Hilfe von GIS und Fernerkundung*. Diploma thesis, Department of Geography, University of Zurich.
- Sun, G., Ranson, K.J., Kharuk, V.I. and Kovacs, K. (2003): Validation of surface height from Shuttle Radar Topography Mission using Shuttle laser altimeter. *Remote Sensing of Environment*, 88(4), 401-411.
- Tamburini, A., Mortara, G., Belotti, M. and Federici, P. (2003): The emergency caused by the "Short-lived Lake" of the Belevdere Glacier in the summer 2002 (Macugnaga, Monte Rosa, Italy). Studies, survey techniques and main results. *Terra Glacialis*, 6, 37-54.
- Tarchi, D., Casagli, N., Fanti, R., Leva, D.D., Luzi, G., Pasuto, A., Pieraccini, M. and Silvano, S. (2003): Landslide monitoring by using ground-based SAR interferometry: an example of application to the Tessina landslide in Italy. *Engineering Geology*, 68(1-2), 15-30.
- Taschner, S. and Ranzi, R. (2002): Comparing the opportunities of Landsat-TM and ASTER data for monitoring a debris covered glacier in the Italian Alps within the GLIMS project. *Proceedings, IEEE International Geoscience and Remote Sensing Symposium, IGARSS 2002*, Toronto, Canada, 4, 1044-1046.
- Thouret, J.C. (1990): Effects of the November 13, 1985 eruption on the snow pack and ice cap of Nevado del Ruiz volcano, Colombia. *Journal of Volcanology and Geothermal Research*, 41, 177-201.
- Tinti, S., Maramai, A. and Cerutti, A.V. (1999): The Miage Glacier in the Valley of Aosta (western Alps, Italy) and the extraordinary detachment which occurred on August 9, 1996. *Physics and Chemistry of the Earth, Part A-Solid Earth and Geodesy*, 24(2), 157-161.
- Toutin, T. (1995a): Multi-source data fusion with an integrated and unified geometric modelling. *EARSeL Journal - Advances in Remote Sensing*, 4(2), 118-129.
- Toutin, T. (1995b): Multi-source data integration: comparison of geometric and radiometric methods. *International Journal of Remote Sensing*, 16(15), 2795-2811.
- Toutin, T. (2001): DEM generation from new VIR Sensors: Ikonos, ASTER and Landsat 7. *Proceedings, IGARSS '01*, Sydney, Australia.
- Toutin, T. (2002a): DEM from stereo Landsat 7 ETM data over high relief areas. *International Journal of Remote Sensing*, 23(10), 2133-2139.
- Toutin, T. (2002b): Three-dimensional topographic mapping with ASTER stereo data in rugged topography. *IEEE Transactions on Geoscience and Remote Sensing*, 40(10), 2241-2247.
- Toutin, T. (2004): Geometric processing of remote sensing images: models, algorithms and methods. *International Journal of Remote Sensing*, 25(10), 1893-1924.
- Toutin, T. and Gray, L. (2000): State-of-the-art of elevation extraction from satellite SAR data. *ISPRS Journal of Photogrammetry and Remote Sensing*, 55(1), 13-33.
- Toutin, T. and Cheng, P. (2001): DEM generation with ASTER stereo data. *Earth Observation Magazine*, 10(6), 10-13.
- Toutin, T. and Cheng, P. (2002): Comparison of automated digital elevation model extraction results using along-track ASTER and across-track SPOT stereo images. *Optical Engineering*, 41(9), 2102-2106.
- Tucker, E.G., Lancaster, S.T., Gasparini, N.M., Bras, R.L. and Rybarczyk, S.M. (2001): An object-oriented framework for distributed hydrologic and geomorphic modeling using triangulated irregular networks. *Computers & Geosciences*, 27(8), 959-973.
- Tufnell, L. (1984): *Glacier hazards*. Longman, London.
- Tweed, F.S. and Russel, A.J. (1999): Control on the formation and sudden drainage of glacier-impounded lakes: implications for jökulhlaup characteristics. *Progress in Physical Geography*, 23(1), 79-110.
- UNESCO (2003): *Water for People, water for life. The United nations world water development report*. UNESCO Publishing / Berghahn Books, Oxford, New York. 576 pp.
- Ustin, S.L., Smith, M.O., Jacquemoud, S., Verstraete, M.M. and Govaerts, Y. (1999): Geobotany: Vegetation mapping for Earth Sciences. In: Rencz, A.N., ed., *Remote Sensing for the Earth Sciences. Manual of Remote Sensing*, 3rd Edition, John Wiley and Sons, New York, 3, 189-248.

- Vachon, P.W., Geudtner, D., Gray, A.L., Mattar, K., Brugman, M. and Cumming, I.G. (1996): Air-borne and Spaceborne SAR Interferometry: Application to the Athabasca Glacier Area. *Proceedings, IGARSS '96*, Lincoln, Nebraska, 2255-2257.
- Vadon, H. and Massonet, D. (2000): Earthquake displacement fields mapped by very precise correlation; complementarity with radar interferometry. *Proceedings, IEEE International Geoscience and Remote Sensing Symposium*, New York, IEEE Institute of Electrical and Electronics Engineers, 6, 2700-2702.
- Vadon, H. and Berthier, E. (2004): Measurement of glacier velocity fields using very precise multi-temporal correlation on high resolution Spot5 images. *International Archives of Photogrammetry and Remote Sensing*, 35(B7), 830-835.
- Van der Veen, C.J., Krabill, W.B., Csatho, B.M. and Bolzan, J.F. (1998): Surface roughness on the Greenland ice sheet from airborne laser altimetry. *Geophysical Research Letters*, 25(20), 3887-3890.
- Van der Woerd, J., Owen, L.A., Tapponnier, P., Xu, X.W., Kervyn, F., Finkel, R.C. and Barnard, P.L. (2004): Giant, similar to M8 earthquake-triggered ice avalanches in the eastern Kunlun Shan, northern Tibet: Characteristics, nature and dynamics. *Geological Society of America Bulletin*, 116(3-4), 394-406.
- Van Puymbroeck, N., Michel, R., Binet, R., Avouac, J. and Taboury, J. (2000): Measuring earthquakes from optical satellite images. *Applied Optics*, 39(20), 3486-3494.
- Van Westen, C.J. (1994): GIS and landslide hazard zonation: a review, with examples from the Andes of Colombia. In: Price, M.F. and Heywood, D.I., eds., *Mountain Environments and Geographic Information Systems*, Taylor & Francis Ltd., London, 135-165.
- Van Zyl, J.J. (2001): The Shuttle Radar Topography Mission (SRTM): a breakthrough in remote sensing of topography. *Acta Astronautica*, 48(5-12), 559-565.
- Vaseghi, S.V. (1996): *Advanced Signal Processing and Digital Noise Reduction*. Wiley, Chichester.
- VAW (1985): Studi sul comportamento del Ghicacciaio del Belvedere, Macugnaga, Italia. Relazione, Versuchsanstalt für Wasserbau, Hydrologie und Glaziologie.
- Vermote, E., Tanré, D., Deuze, J.L., Herman, M. and Morcette, J.J. (1997): Second simulation of the satellite signal in the solar spectrum: an overview. *IEEE Transactions on Geoscience and Remote Sensing*, 35(3), 675-686.
- Vischer, D., Funk, M. and Müller, D. (1991): *Interaction between a reservoir and a partially flooded glacier: problems during the design stage*.
- Vischer, D.L. (1979): Kalbungswelle beim Aufbrechen einer überstaute Gletscherzunge, *Mitteilungen der VAW / ETH Zürich*, 41, 315-329.
- Viviroli, D. and Weingartner, R. (2003): The significance of mountains as sources of the world's fresh water. *GALIA*, 11(3), 182-187.
- Volesky, J.C., Stern, R.J. and Johnson, P.R. (2003): Geological control of massive sulfide mineralization in the Neoproterozoic Wadi Bidah shear zone, southwestern Saudi Arabia, inferences from orbital remote sensing and field studies. *Precambrian Research*, 123(2), 235-247.
- Vollmer, M. (1999): *Kriechender alpiner Permafrost: Digitale photogrammetrische Bewegungsmessung*. Diploma thesis, Department of Geography, University of Zurich.
- Vonder Mühl, D. (1993): *Geophysikalische Untersuchungen im Permafrost des Oberengadins*. PhD thesis, Versuchsanstalt für Wasserbau, Hydrologie und Glaziologie der ETH Zürich, ETH Zürich, 222 pp.
- Vonder Mühl, D.S. and Schmid, W. (1993): Geophysical and photogrammetrical investigation of rock glacier Muragl I, Upper Engadin, Swiss Alps. *Proceedings of the 6th International Conference on Permafrost, Beijing*, 1, 214-219.
- Vonder Mühl, D., Stucki, T. and Haeberli, W. (1998): Borehole-temperatures in alpine permafrost: a ten year series. *Proceedings, Seventh International Conference on Permafrost*, Yellowknife, Canada, Collection Nordicana, 57, 1089-1095.
- Vonder Mühl, D.S., Arenson, L.U. and Springman, S.M. (2003): Temperature conditions in two Alpine rock glaciers. *Proceedings, Eighth International Conference on Permafrost*, Zurich, Balkema, 2, 1195-1200.
- Vuichard, D. and Zimmermann, M. (1987): The 1985 catastrophic drainage of a moraine-dammed lake, Khumbu Himal, Nepal: causes and consequences. *Mountain Research and Development*, 7(2), 91-110.
- Wagner, S. (1996): *Dreidimensionale Modellierung zweier Gletscher und Deformationsanalyse von eisreichem Permafrost*. Mitteilungen der Versuchsanstalt für Wasserbau, Hydrologie und Glaziologie der ETH Zürich, 146, Zürich. 133 pp.
- Wagnon, P., Ribstein, P., Kaser, G. and Berton, P. (1999): Energy balance and runoff seasonality of a Bolivian glacier. *Global and Planetary Change*, 22, 49-58.

- Wahrhaftig, C. and Cox, A. (1959): Rock glaciers in the Alaska Range. *Bulletin of the Geological Society of America*, 70, 383-436.
- Wake, C.P. and Searle, M.P. (1993): Rapid advance of Pumarikish Glacier, Hispar Glacier Basin, Karakoram Himalaya. *Journal of Glaciology*, 39(131), 204-206.
- Walder, J.S. and Driedger, C.L. (1994): Rapid geomorphic change caused by glacial outburst floods and debris flows along Tahoma Creek, Mount Rainier, Washington, U.S.A. *Arctic and Alpine Research*, 26, 319-327.
- Walder, J.S. and Driedger, C.L. (1995): Frequent outburst floods from South Tahoma Glacier, Mount Rainier, U.S.A.: relation to debris flows, meteorological origin and implications for subglacial hydrology. *Journal of Glaciology*, 41(1-10).
- Walder, J.S. and Costa, J.E. (1996): Outburst floods from glacier-dammed lakes: the effect of mode of lake drainage on flood magnitude. *Earth Surface Processes and Landforms*, 21, 701-723.
- Walder, J.S., Watts, P., Sorensen, O.E. and Janssen, K. (2003): Water waves generated by subaerial mass flows. *Journal of Geophysical Research*, 108 (B5), 2236-2255.
- Walsh, S.J., Butler, D.R. and Malanson, G.P. (1998): An overview of scale, pattern, process relationships in geomorphology: a remote sensing and GIS perspective. *Geomorphology*, 21, 183-205.
- Wan, Z. and Dozier, J. (1989): Land-surface temperature measurements from space: physical principles and inverse modeling. *IEEE Transactions on Geoscience and Remote Sensing*, 36(4), 1282-1289.
- Wang, B. and French, H.M. (1995): In situ creep of frozen soil, Fenghuo Shan, Tibet Plateau, China. *Canadian Geotechnical Journal*, 32, 545-552.
- Wang, Z. and Li, S. (1998): A study of the upheaval and subsidence of permafrost through INSAR techniques. In: Akasofu, S.I., ed., *International cooperation in Arctic research; detecting global change and its impacts in the western Arctic*. Program and Abstracts - Arctic Science Conference Collection Nordicana, American Association for the Advancement of Science, Arctic Division, Fairbanks, AK, United States Quebec, PQ, Canada, 49, 72-73.
- Wang, Z. and Li, S. (1999): Detection of winter frost heaving of the active layer of arctic permafrost using SAR differential interferometry. *Proceedings, IEEE Geoscience and Remote Sensing Symposium IGARSS'99*, Hamburg, 1946-1948.
- Warren, S.G. (1982): Optical properties of snow. *Reviews of Geophysics and Space Physics*, 20, 67-89.
- Watanabe, T. and Rothacher, D. (1996): The 1994 Lugge Tsho glacial lake outburst flood, Bhutan Himalaya. *Mountain Research and Development*, 16, 77-81.
- Weber, D. and Herrmann, A. (2000): Contribution of digital photogrammetry in spatio-temporal knowledge of unstable slopes: the example of the Super-Saute landslide (Alpes-de-Haute-Provence, France). *Bulletin de la Societe Geologique de France*, 171(6), 637-648.
- Weber, M. (2003): *Oberflächenstrukturen auf Blockgletschern*. Diploma thesis, Department of Geography, University of Zurich.
- Weber, M. and Kääb, A. (2003): Laboratory experiments towards better understanding of surface buckling of rock glaciers. *Proceedings, Eighth International Permafrost Conference, Extended Abstracts*, Zurich, 183-184.
- Wechsler, S.P. (2000): *Effect of DEM uncertainty on topographic parameters, DEM scale and terrain evaluation*. PhD thesis, College of Environmental Science and Forestry, State University of New York, Syracuse, 380 pp.
- Wegmann, M. and Keusen, H.R. (1998): Recent geophysical investigations at a high alpine permafrost construction site in Switzerland. *Proceedings, Seventh International Conference on Permafrost*, Yellowknife, Canada, Collection Nordicana, 57, 1119-1123.
- Wegmüller, U., Strozzi, T. and Werner, C. (1998): Characterisation of differential interferometry approaches. *Proceedings, EUSAR'98*, Friedrichshafen, Germany.
- Wehr, A. and Lohr, U. (1999): Airborne laser scanning - An introduction and overview. *ISPRS Journal of Photogrammetry and Remote Sensing*, 54(2-3), 68-82.
- Weibel, R. and Brändli, M. (1995): Adaptive methods for the refinement of digital terrain models for geomorphometric applications. *Zeitschrift für Geomorphologie, Supplementband*, 101, 13-30.
- Weidmann, Y. (2004): *Kombination von ASTER- und SRTM-Höhenmodellen für die Abschätzung von Naturgefahren im Pamir Gebirge, Tadschikistan*. Diploma thesis, University of Applied Sciences, Muttenz, Basel.
- Wessels, R., Kargel, J.S. and Kieffer, H.H. (2002): ASTER measurement of supraglacial lakes in the Mount Everest region of the Himalaya. *Annals of Glaciology*, 34, 399-408.
- Weydahl, D.J. (2001): Analysis of ERS tandem SAR coherence from glaciers, valleys, and fjord ice on Svalbard. *IEEE Transactions on Geoscience and Remote Sensing*, 39(9), 2029-2039.

- Whalley, W.B. and Martin, H.E. (1992): Rock glaciers. Part II: Models and mechanisms. *Progress in Physical Geography*, 16(2), 127-186.
- Whalley, W.B. and Azizi, F. (1994): Rheological models of active rock glaciers: evaluation, critique and a possible test. *Permafrost and Periglacial Processes*, 5(1), 37-51.
- Wheatley, J.M., Wilson, J.P., Redmond, R.L., Ma, Z. and DiBenedetto, J. (2000): Automated land cover mapping using Landsat Thematic Mapper images and topographic attributes. In: Wilson, J.P. and Gallant, J.C., eds., *Terrain analysis*, Wiley, New York etc., 355-389.
- Whillans, I.M., Jackson, M. and Tseng, Y.H. (1993): Velocity pattern in a transect across Ice Stream B, Antarctica. *Journal of Glaciology*, 39(133), 562-572.
- Whillans, I.M. and Tseng, Y.-H. (1995): Automatic tracking of crevasses on satellite images. *Cold Regions Science and Technology*, 23(2), 201-214.
- White, S.E. (1987): Differential movement across ridges on Arapaho rock glaciers, Colorado Front Range, US. In: Giardino, J.R., Shrader, F. and Vitek, J.D., eds., *Rock glaciers*, Allen & Unwin, London, 145-149.
- Williams, R.S., Hall, D.K. and Benson, C.S. (1991): Analysis of glacier facies using satellite techniques. *Journal of Glaciology*, 37, 120-127.
- Williams, R.S., Hall, D.K., Sigurdsson, O. and Chien, J.Y.L. (1997): Comparison of satellite-derived with ground-based measurements of the fluctuations of the margins of Vatnajökull, Iceland, 1973-1992. *Annals of Glaciology*, 24, 72-80.
- Williams, R.S. and Hall, D.K. (1998): Use of remote sensing techniques. In: Haeberli, W., Hoelzle, M. and Suter, S., eds., *Into the 2nd century of world glacier monitoring: Prospects and strategies: A contribution to the International Hydrological Programme (IHP), and the Global Environmental Monitoring System (GEMS)*, World Glacier Monitoring Service, UNESCO Publishing, Studies and Reports in Hydrology, Paris, 56, 97-111.
- Wilson, J.P. and Gallant, J.C. (Editors), 2000. *Terrain analysis. Principles and applications*. Wiley, New York, etc., 479 pp.
- Wimmer, C., Siegmund, R., Schwäbisch, M. and Moreira, J.R. (2000): Generation of high-precision DEMs of the Wadden Sea with airborne interferometric SAR. *IEEE Transactions on Geoscience and Remote Sensing*, 38, 2234-2245.
- Winter, R. (2001): *Entwicklung geeigneter Ansätze und Methoden zur kartographischen Visualisierung mehrdimensionaler glaziologischer Prozesse*. Diploma thesis, Institut für Kartographie, Technische Universität Dresden, 99 pp.
- Winther, J.-G., Gerland, S., Ørbæk, J.B., Ivanov, B., Blanco, A. and Boike, J. (1999): Spectral reflectance of melting snow in a high Arctic watershed on Svalbard: some implications for optical satellite remote sensing studies. *Hydrological Processes*, 13(12-13), 2033-2049.
- Winther, J.G. (1993): Landsat TM derived and in situ summer reflectance of glaciers in Svalbard. *Polar Research*, 12, 37-55.
- WMO (1997): World Meteorological Organisation (WMO). Global Hierarchical Observing Strategy (GHOST). *WMO*, 862.
- Wrobel, B. and Schlüter, M. (1997): Digital terrain model generation in the Antarctic – A challenging task for digital photogrammetry. *Proceedings, 2nd Turkish-German Joint Geodetic Days*, Berlin, Germany, 407-416.
- Xin, L., Guodong, C., Qingbai, W. and Yongjian, D. (1999): Chinese Cryospheric Information System. *Proceedings, The 20th Asian Conference on Remote Sensing*, Hong Kong.
- Yamada, T. and Sharma, C.K. (1993): Glacier lakes and outburst floods in the Nepal Himalaya, *IAHS Publ. 218, Snow and Glacier Hydrology*, Oxford, 319-330.
- Yocky, D.A. (1996): Multiresolution wavelet decomposition image merger of Landsat Thematic Mapper and SPOT panchromatic data. *Photogrammetric Engineering and Remote Sensing*, 62(9), 1067-1074.
- Yongjian, D. and Jingshi, L. (1992): Glacier lake outburst flood disaster in China. *Annals of Glaciology*, 16, 180-184.
- Zahnen, N., Jung-Rothenhäusler, F., Oerter, H., Wilhelms, F. and Miller, H. (2003): Correlation between Antarctic dry snow properties and backscattering characteristics in RADARSAT SAR imagery. *EARSeL eProceedings*, 2, 140-148.
- Zavorin, I. and Le Moigne, J. (2005): Use of multiresolution wavelet feature pyramids for automatic registration of multisensor imagery. *IEEE Transactions on Image Processing*, 14(6), 770-782.
- Zemp, M., Kääb, A., Hoelzle, M. and Haeberli, W. (2002): GIS-based modelling of glacial sediment balance. *Proceedings, ESRI User Conference*, San Diego.

- Zemp, M., Kääb, A., Hoelzle, M. and Haeberli, W. (2005): GIS-based modelling of glacial sediment balance. *Zeitschrift für Geomorphologie, Supplements*, 138, 113-129.
- Zeng, Q., Cao, M., Feng, X., Liang, F., Chen, X. and Sheng, W. (1983): A study of spectral reflection characteristics for snow, ice and water in the north of China. In: Goodison, B., ed., *Hydrological applications of remote sensing and remote data transmission*, IAHS, 145, 451-462.
- Zhang, L. and Grün, A. (2004): Automatic DSM generation from linear array imagery data. *International Archives of Photogrammetry and Remote Sensing*, 15(B3), 128-133.
- Zhang, W. (1992): Identification of glaciers with surge characteristics on the Tibetan Plateau. *Annals of Glaciology*, 16, 168-172.
- Zhou, J., Civco, D.L. and Silander, J.A. (1998): A wavelet transform method to merge Landsat TM and SPOT panchromatic data. *International Journal of Remote Sensing*, 19(4), 743-757.
- Zhukov, B., Oertel, D., Lanzl, F. and Reinhäeckel, G. (1999): Unmixing-based multisensor multiresolution image fusion. *IEEE Transactions on Geoscience and Remote Sensing*, 37(3), 1212-1226.
- Zick, W. (1996): Bewegungsmessungen 1965-1994 am Blockgletscher Macun I (Unterengadin/Schweiz) - neue Ergebnisse. *Zeitschrift für Geomorphologie N.F., Supplement-Band*, 104, 59-71.
- Zimmermann, M. and Haeberli, W. (1992): Climatic change and debris flow activity in high-mountain areas - a case study in the Swiss Alps. In: Boer, M. and Koster, E., eds., *Catena Supplement 22*, 59-72.
- Zimmermann, M., Mani, P., Gamma, P., Gsteiger, P., Hunziker, G. and Heiniger, O. (1997): *Beurteilung der Murganggefährdung mit Hilfe eines Geographischen Informationssystems. Analyse der räumlichen Entwicklung infolge von Klimaänderungen*. Schlussbericht NFP31. Verlag der Fachvereine ETH Zurich, Zurich.
- Zollinger, S. (2003): *Ableitung von Parametern für die Identifikation und Beobachtung gefährlicher Gletscherseen in Nepal aus ASTER Satellitendaten*. Diploma thesis, Department of Geography, University of Zurich.
- Zomer, R., Ustin, S. and Ives, J. (2002): Using satellite remote sensing for DEM extraction in complex mountainous terrain: landscape analysis of the Makalu Barun National Park of eastern Nepal. *International Journal of Remote Sensing*, 23(1), 125-143.
- Zong, J., Davies, R., Muller, J.P. and al., e. (2002): Photogrammetric retrieval of cloud advection and top height from the multi-angle imaging spectroradiometer (MISR). *Photogrammetric Engineering and Remote Sensing*, 68(8), 821-829.
- Zwally, H.J. and others, a. (2002): ICESat's laser measurements of polar ice, atmosphere, ocean, and land. *Journal of Geodynamics*, 34, 405-445.
- Zweifel, A. (2004): *Impulswellen: Effekte der Rutschdichte und der Wassertiefe*. Mitteilungen VAW / ETH Zürich, 186.

SCHRIFTENREIHE PHYSISCHE GEOGRAPHIE

- Vol. 5 J. Suter (ed.): **Kurzfassungen der Vorträge Hauptversammlung der Deutschen Quartärvereinigung in Zürich.**
(84 pp, 1982, CHF. 20.–, ISBN 3 85543 201 5)
- Vol. 10 R. Vuagneux: **Gletschergeschichtliche Untersuchungen im Gebiet Flüelapass (Kt. Graubünden, Schweiz).**
(249 pp, 1983, CHF. 30.–, ISBN 3 85543 206 6)
- Vol. 11 W. A. Keller (ed.): **Beiträge zur angewandten physischen Geographie.**
(89 pp, 1983, CHF. 18.–, ISBN 3 85543 207 4)
- Vol. 12 O. Gisler: **Die meteorologischen Beobachtungen von Schaffhausen (1794–1845) und Zürich (1767–1802) nebst einigen Betrachtungen über historische Niederschlagsreihen.**
(190 pp, 1983, CHF. 30.–, ISBN 3 85543 208 2)
- Vol. 15 R. Bless: **Beiträge zur spät- und postglazialen Geschichte der Gletscher im nordöstlichen Mont Blanc Gebiet.**
(116 pp, 1984, CHF. 25.–, ISBN 3 85543 211 2)
- Vol. 21 R. A. Hipp: **Zur Landschaftsgeschichte der Region Bischofszell. Eine glazialmorphologische Arbeit.**
(125 pp, 1986, CHF. 30.–, ISBN 3 85543 217 1)
- Vol. 22 W. Wetter: **Spät- und postglaziale Gletscherschwankungen im Mont Blanc-Gebiet: Untere Vallée de Chamonix – Val Montjoie.**
(275 pp, 1987, CHF. 35.–, ISBN 3 85543 218 X)
- Vol. 23 **Beiträge zur Geomorphologie der Alpen und des Alpenvorlandes: Kurzfassung der Vorträge. Jahresversammlung der Schweizerischen Geomorphologischen Gesellschaft und des Deutschen Arbeitskreises für Geomorphologie anlässlich der 167. Jahresversammlung der Schweizerischen Naturforschenden Gesellschaft in Luzern.**
(52 pp, 1987, CHF. 10.–, ISBN 3 85543 219 8)
- Vol. 24 **Exkursionsführer Teil A: Rhonegletscher. Hauptsymposium «Eiszeitforschung» im Rahmen der 167. Jahresversammlung der Schweizerischen Naturforschenden Gesellschaft in Luzern.**
(73 pp, 1987, CHF. 25.–, ISBN 3 85543 220 1)
- Vol. 25 **Exkursionsführer Teil B: Mittelland. Hauptsymposium «Eiszeitforschung» im Rahmen der 167. Jahresversammlung der Schweizerischen Naturforschenden Gesellschaft in Luzern.**
(69 pp, 1987, CHF. 20.–, ISBN 3 85543 221 X)
- Vol. 26 W. A. Keller: **Liste der ^{14}C -Daten 1975–1987.**
(60 pp, 1988, CHF. 20.–, ISBN 3 85543 222 8)
- Vol. 29 P. Fitze, U. Capaul, R. Meuli, M. Achermann: **Landschaftsökologisches Forschungsprojekt «Gubrist». Ergebnisse der Beobachtungsperiode 1983–1988.**
(85 pp, 1989, CHF. 20.–, ISBN 3 85543 225 2)
- Vol. 30 U. Capaul: **Erfassung der atmosphärischen Metalleinträge auf Waldlichtungen des Gubrist.**
(150 pp, 1989, CHF. 25.–, ISBN 3 85543 226 0)
- Vol. 31 St. Bader: **Die Modellierung von Nettobilanzgradienten spätglazialer Gletscher zur Herleitung der damaligen Niederschlags- und Temperaturverhältnisse dargestellt an ausgewählten Beispielen aus den Schweizer Alpen.**
(110 pp, 1990, CHF. 30.–, ISBN 3 85543 227 2)
- Vol. 32 T. Häberle: **Spät- und postglaziale Gletschergeschichte des Hörgárdalur-Gebietes, Tröllaskagi, Nord Island.**
(210 pp, 1991, CHF. 40.–, ISBN 3 85543 228 4)
- Vol. 33 M. Maisch: **Die Gletscher Graubündens. Rekonstruktion und Auswertung der Gletscher und deren Veränderungen seit dem Hochstand von 1850 im Gebiet der östlichen Schweizer Alpen (Bündnerland und angrenzende Regionen).**
(Teil A: Grundlagen-Analysen-Ergebnisse 320 pp, CHF. 50.–, Teil B: Verzeichnisse-Datenkataloge-Gletscherkarten 130 pp, 1992, CHF. 30.–, ISBN 3 85543 229 5)
- Vol. 34 K. Graf: **Pollendiagramme aus den Anden. Eine Synthese zur Klimageschichte und Vegetationsentwicklung seit der letzten Eiszeit.**
(120 pp, 1992, CHF. 40.–, ISBN 3 85543 230 1)
- Vol. 35 A. Walker: **Grossräumige Austauschprozesse der Atmosphäre als Ursache von Starkgewittern. Herkunft und Entwicklung von starken Unwettern in gemäßigten Breiten analysiert anhand des Wasserdampfabsorptionsbandes der geostationären Satelliten METEOSAT und GOES.**
(166 pp, 1992, CHF. 35.–, ISBN 3 85543 231 7)
- Vol. 36 K. F. Kaiser: **Klimageschichte vom späten Hochglazial bis ins frühe Holozän, rekonstruiert mit Jahrringen und Molluskenschalen aus verschiedenen Vereisungsgebieten.**
(203 pp, 1993, CHF. 40.–, ISBN 3 85543 232 5)

SCHRIFTENREIHE PHYSISCHE GEOGRAPHIE

- Vol. 37 M. Egli: **The Influence of Increased NH₄⁺ Deposition Rates on Aluminium Chemistry and Alkalinity in the Percolate of Acid Soils.** (156 pp, 1995, CHF. 25.–, ISBN 3 85543 233 3)
- Vol. 38 A. Burri: **Retrospektive Erfassung von Veränderungen bodenchemischer Parameter unter spezieller Berücksichtigung der Azidität. Eine Darstellung für den Zeitraum zwischen 1969 und 1993 am Beispiel der Waldböden bei Möhlin/AG.** (164 pp, 1996, CHF. 30.–, ISBN 3 85543 234 1)
- Vol. 39 O. Keller und E. Krayss: **Quartärgeologie zwischen Bodensee und Säntis.** (Ostschweiz). Führer zu den Exkursionen der AGAQ-Arbeitstagung 1999 in Kirchberg bei Wil SG. (60 pp, 1999, CHF. 15.–, ISBN 3 85543 295 X)
- Vol. 40 A. Wipf: **Die Gletscher der Berner, Waadtländer und nördlichen Walliser Alpen.** Eine regionale Studie über die Vergletscherung im Zeitraum «Vergangenheit» (Hochstand von 1850), «Gegenwart» (Ausdehnung im Jahr 1973) und «Zukunft» (Gletscherschwund-Szenarien, 21. Jahrhundert). (280 pp, 1999, CHF. 40.–, ISBN 3 85543 296 8)
- Vol. 41 M. Maisch, D. Vonder Mühl und M. Monbaron (Hrsg.): **Entwicklungstendenzen und Zukunftsperspektiven in der Geomorphologie.** Publikation zur Jahrestagung der Schweizerischen Geomorphologischen Gesellschaft (SGmG) anlässlich des 180. Jahrestreffens der Schweizerischen Akademie der Naturwissenschaften (SANW) in Winterthur (11.–13. Oktober 2002) (130 pp, 2002, CHF. 35.–, ISBN 3 85543 237 6)
- Vol. 42 C. Hitz: **Inventur und Dynamik der organischen Substanz in Böden der alpinen Stufe. Untersuchungen im Vereina-Tal, GR, Schweiz.** (223 pp, 2002, CHF. 35.–, ISBN 3 85543 238 4)
- Vol. 43 C. Benz: **Der würmeiszeitliche Rheingletscher-Maximalstand. Digitale Rekonstruktion, Modellierung und Analyse mit einem Geographischen Informationssystem.** (181 pp, 2003, CHF. 30.–, ISBN 3 85543 239 2)
- Vol. 44 Ch. Huggel: **Assessment of Glacial Hazards based on Remote Sensing and GIS Modeling.** (72 pp, 5 papers im Anhang, 2004, CHF. 35.–, ISBN 3 85543 240 6)
- Vol. 45 R. Frauenfelder: **Regional-scale modeling of the occurrence and dynamics of rockglaciers and the distribution of paleopermafrost.** (67 pp, 5 papers im Anhang, 2004, CHF. 35.–, ISBN 3 85543 241 4)
- Vol. 46 H. Machguth, St. Margreth (Hrsg.): **Baikal Exkursion 2004:** Ein wissenschaftlicher Überblick zum Baikal-Raum und Reisebericht. (144 pp, 2005, CHF. 25.–, ISBN 3 85543 242 2)
- Vol. 48 A. Kääb: **Remote Sensing of Mountain Glaciers and Permafrost Creep.** (266 pp, 2005, CHF. 40.–, ISBN 3 85543 244 9)

Ausserhalb der Schriftenreihe:

- M. Maisch, C.A. Burga, P. Fitze:
Lebendes Gletschervorfeld. Von schwindenden Eisströmen, schuttreichen Moränenwällen und wagemutigen Pionierpflanzen im Vorfeld des Morteratschgletschers. Führer und Begleitbuch zum Gletscherrlehrpfad. Gemeinde Pontresina, Geographisches Institut der Universität Zürich. (138 pp, 1999, 2. ergänzte Auflage, CHF. 20.–)
- K. Graf:
Bolivien – Probleme und Chancen der Dritten Welt, bearbeitet für den Geographieunterricht an Gymnasien. (150 pp, 1998, CHF. 35.–) Spanische Ausgabe (280 pp, 2003, CHF. 30.–)
- M. Maisch und P. Wick:
CD-Rom zum Themenheft «Gletscher» (Unterrichtsmaterialien, Bilder, Grafiken, Aufgabenblätter, Kopiervorlagen). Ergänzung zur Sondernummer «Die neue Schulpraxis» (dns-Heft 6/7, Juni/Juli 04, 150 pp, 2004, CHF. 25.–; inkl. Heft CHF. 30.–)

Bezugsadresse:

Geographisches Institut der Universität Zürich
Schriftenreihe Physische Geographie
Winterthurerstrasse 190
CH-8057 Zürich
E-mail: maisch@geo.unizh.ch
ax: +41 (0)44 635 68 48